

GEOFORSCHUNGSZENTRUM POTSDAM
STIFTUNG DES ÖFFENTLICHEN RECHTS

Scientific Technical Report

ISSN 1610-0956

Identification of Parameters Controlling the Accretive and
Tectonically Erosive Mass-Transfer Mode at the South-Central
and North Chilean Forearc Using Scaled 2D Sandbox
Experiments

Jo Lohrmann

Dissertation zur Erlangung des Doktorgrades
im Fachbereich Geowissenschaften an der Freien Universität Berlin

begutachtet durch
Prof. Dr. Onno Oncken
Prof. Dr. Hans-Jürgen Götze

2002

Der Versuchung widerstehen durch Vermehrung ihrer Varianten.

Resist temptation by multiplying its varieties.

Dill Bitterfit, 1992

Abstract	5
1 Introduction and Theoretical Background	7
1.1 Objectives	7
1.2 Mass-transfer modes at convergent margins	10
1.3 Mechanical Concepts	12
1.4 Analogue simulations	15
1.5 Scaled 2D sandbox experiments	15
2 Method and Basic Studies of Material Properties	21
2.1 Introduction	21
2.2 Theoretical background	22
2.3 Material properties	23
2.3.1 Material characterisation	23
2.3.2 Results	26
2.4 Sandbox experiments: Basic parameter studies	30
2.4.1 The sandbox apparatus	30
2.4.2 Experimental setup of the basic parameter studies	32
2.4.3 1 st Series: Variation of internal wedge properties	33
2.4.4 2 nd Series: Variation of basal material properties	49
2.5 Application to nature	53
2.6 Conclusions	55
3 The Accretive Forearc of Southern Chile	57
3.1 The South Chilean Forearc	57
3.1.1 Database obtained from nature	57
3.1.2 Mass-transfer concept derived from field data	61
3.2 Experimental setup of the two-level experiments	61
3.3 Experimental results of the two-level experiments	63
3.4 Interpretation of the results of the two-level experiments	73
3.4.1 Changes in structural and geometrical wedge evolution	73
3.4.2 State of stress of the wedge segments	75
3.5 Comparison with the South Chilean Forearc	79
3.5.1 Mass balance of basally- accreted sediments at the South Chilean Forearc	79
3.5.2 Kinematics of experiments and the South Chilean Forearc	81
3.5.3 Discussion	82
3.5.4 Summary	86
4 The Tectonically-Erosive Forearc of Northern Chile	87
4.1 The North Chilean Forearc	87
4.1.1 Database obtained from nature	87
4.1.2 Previously-published concepts of tectonic erosion	91
4.2 Experimental setup	94
4.2.1 Experimental concept to simulate steady-state tectonic erosion	94
4.2.2 Setup of the 1 st series (mass-transfer processes)	95
4.2.3 Setup of the 2 nd series (mechanics)	96
4.3 Results of experiments simulating steady-state tectonic erosion	97
4.3.1 Experimental results of the 1 st series (mass transfer)	97
4.3.2 Experimental results of the 2 st series (mechanics)	110
4.3.3 Summary of experimental results of 1 st and 2 nd series	112
4.4 Interpretation of experimental results	112
4.4.1 Mass transfer	113
4.4.2 Mechanics	114
4.4.3 Summary of the basally erosive process	118

4.5	Comparison with the North Chilean Forearc	119
4.6	Discussion of published concepts	120
4.7	Discussion of inconsistencies	121
4.7.1	Geometric and kinematic inconsistencies?	121
4.7.2	Inconsistencies of the erosion ratios (basal erosion versus frontal erosion)	123
4.7.3	Mechanical inconsistencies	124
4.8	Conclusions	126
5	Final Discussion	127
5.1	Hierarchical order of parameters controlling the mass transfer at convergent forearcs	127
5.2	Restrictions of quantitative critical-taper analysis of convergent wedges in nature	134
	Appendices	143
A	Experiments directly used in this study	143
B	Experiments indirectly used in this study	189
C	Zusammenfassung	229
D	Lebenslauf	233

Abstract

This study attempts to identify and quantify the parameters that control mass-transfer modes in brittle tectonically erosive and accretive forearc settings. Scaled analogue simulations, which are specifically designed for this task, are compared with the convergent Chilean Margin that demonstrates both of these mass-transfer modes. Analogue simulation of geodynamic processes requires granular materials (e.g. sand) that deforms similarly to typical crustal rocks. Accordingly, a parameter study is performed, which yields general insight in the basic mechanics of highly-idealised convergent sand wedges.

Static and dynamic shear tests are employed to obtain the frictional strength of different sand types. The analysed sand types are characterised by an elastic frictional-plastic behaviour with a transient strain-hardening and strain-softening phase prior to the transition to stable sliding. This complex material behaviour is comparable to that of natural rocks. However, it is in conflict with the assumption of an ideal cohesionless Coulomb Material with constant frictional properties, which is commonly used in mechanical interpretations of convergent forearcs, fold-and-thrust belts, and orogens. The influence of these transient material properties on the kinematics, growth mechanisms, and internal deformation of convergent sand wedges results in wedge segments with different characteristics, i.e. frontal-deformation zone at the wedge tip, frontal-imbrication in the centre and internal-accumulation zone at the rear of the wedge. This wedge segmentation varies — depending on material compaction — from well defined segments with straight slopes to wedges with continuous convex topographic profiles. A new strategy of critical-taper analysis is developed, which is restricted to individual wedge segments and considers this complex material behaviour. The analysis shows that for most materials, only one wedge segment (frontal-imbrication zone) is critically-tapered during material addition to the front of the wedge. Taper and bulk strength of the wedge segments are controlled by the frictional strength of active faults. Wedge segmentation is caused by a bulk wedge-strength increase toward the rear of the wedge. This is due to rotation of faults into mechanically less-favourable orientations and plastic material hardening.

On this basis, the two mass-transfer modes of the North and South Chilean Forearc are investigated, steady-state tectonic erosion and coeval frontal and basal accretion, respectively. Several scenarios of these mass-transfer modes are simulated by systematic variation of parameters. In these experimental series, the parameters varied are: amount of material supplied, presence of mechanically weak layers as potential detachments, frictional strength and surface roughness of the subduction interface, as well as transport capacity of the ‘subduction channel’. The latter is determined by the inlet capacity (i.e. amount of material underthrust beneath the wedge) and global capacity (i.e. amount of material subducted to greater depth). The experiments are analysed with respect to fault kinematics, wedge geometry, particle-displacement field, subsidence pattern and mass-transfer rates. These features of the convergent sand wedges are compared with the respective features of the North and South Chilean Forearc and probable scenarios of the mass-transfer mode at these forearc settings are identified. This links the natural observation with experimental mass-transfer mode and thus identifies the parameters, which control the mass-transfer mode in nature.

The sediments entering the trench at the South Chilean Forearc are partly frontally accreted and partly underthrust with the potential to be basally accreted beneath the Coastal Cordillera, as inferred by interpretations of reflection seismic lines and surface geology. In the related experiments, this mass-transfer mode is produced in a setup that shows weak-layer decoupling within the incoming sand-layer above a high-friction basal detachment. Similar to the purely frontally-accretionary wedges of the basic parameter study, this complex mode of sediment accretion also results in kinematically-segmented sand wedges. Here, basal accretion causes uplift, bending, and horizontal extension of the overlying wedge segment. Syn-uplift tilting and syn-uplift extension at the surface are indicators of this basal mass-transfer process. These kinematic features are identified at the South Chilean Forearc, which supports the primary suggestion from field data that basal accretion takes place beneath the Coastal Cordillera. However, comparison of the mass balance of the experiments and nature shows that only a minor amount of the underthrust material is accreted onto the base of the forearc wedge, whereas the major part is subducted to greater depth. Critical-taper analysis of the complex accretionary sand wedges shows

that no wedge segment is in a critical state of stress: Wedge segments formed by frontal accretion are maintained in a stable state of stress because wedge properties change due to fault-rotation, stepping of the basal detachment in to various materials at different levels, or tilting of the whole segment by basal accretion. The segment formed by basal accretion is in a subcritical state of stress during the whole experimental run, as its adjustment to the critical state is inhibited by a continuous increase in normal load due to material addition to the overlying frontally-accretionary segment.

Steady-state tectonic erosion, as observed at the North Chilean Forearc, only occurs in sand wedges above a high-friction basal detachment, without material supply (no incoming sand-layer). Here, four mass-transfer processes are identified: i) frontal erosion, ii) basal erosion, iii) underthrusting, and iv) basal accretion of formerly-eroded material. These mass-transfer processes require a thick basal shear zone with particular kinematics. In the lower part of this shear zone, frontally- and basally-eroded material is continuously underthrust by penetrative shearing, whereas in the upper part material is removed from the base of the wedge (basal erosion) along reactivated localised shear zones. Frontal erosion causes subsidence by wedge-internal extension due to gravitational collapse, which is identified at the North Chilean Forearc. This subsidence overprints the subsidence and uplift resulting from basal erosion and basal accretion, respectively. Therefore, a well-defined wedge segmentation, as observed in accretionary settings, is not present in tectonically-erosive wedges, and thus particular basal mass-transfer processes cannot be identified from near-surface data. Consequently, the exact position of basal erosion occurring along the North Chilean Forearc cannot be reconstructed, although basal erosion is evident from geophysical and geological data. Analysis of the experiments shows that the rates of basal erosion are strongly dependent on the physical properties of the wedge material. Specific strength ratios between the basal detachment, the material transported within the basal shear zone ($\chi_L > 1$), and the overlying wedge material ($\chi_U \approx 0.94$) are required to enable basal mass removal. As minor changes of the strength of only one of these materials would prevent basal erosion, it is suggested that basal erosion is a very sensitive process in nature. Therefore, the required conditions in nature are considered rather to occur frequently than be continuously present. A plausible process, which might be able to bring about these conditions is the variation of pore pressure during the postseismic phase of subduction earthquakes.

Among the broad range of forearc settings present at convergent margins, the specific mass-transfer modes investigated at the North and South Chilean Forearc considered as representative for other forearc settings of similar style. Hence, the experimental results of this study allow a general systematic evaluation of the parameters, which control mass-transfer modes of convergent forearc settings and their specific influence on shaping forearc architecture. In the hierarchy of these parameters, the ratio between the inlet capacity and global capacity (IC/GC ratio) plays the most superior role. Assignment of the North and South Chilean Forearc to this systematics shows that the difference of their mass-transfer modes is caused by different IC/GC ratios and a different amount of sediment supply. This shows that such a systematics can be used to determine the IC/GC ratio of forearc settings by the identification and comparison of several features of mass-transfer processes, mass-transfer rates, kinematics and wedge geometry in nature and experiment.

Chapter 1

Introduction and Theoretical Background

1.1 Objectives

Convergent plate boundaries severely influence the economic and hazard potential of the earth, as these are the most dynamic regions on the crust. At these locations large deposits of mineral resources are available and the most frequent and strongest earthquakes take place. Therefore, to understand the geodynamic processes, which cause large-scale mass transfer and deformation at convergent margins is of fundamental importance. Within such a frame, this study focuses on the identification and evaluation of parameters, which control the tectonic growth mechanisms of the brittle crust (i.e. mass-transfer modes) present at convergent margins.

The classification of convergent forearc settings (Fig. 1.1) using specific patterns and styles of deformation, characteristic particle paths, and wedge geometry show that various mass-transfer modes are active at convergent plate boundaries (accretive, stagnant to erosive, cf. Section 1.2; Cloos and Shreve, 1988b; von Huene and Scholl, 1991; Lallemand et al., 1994b). This infers that each of these mass-transfer modes is governed by mechanical processes, which are in turn controlled by a specific combination of parameters. Several researchers have attempted to identify these parameters from geophysical and geological field data to understand the control and mechanics of the various mass-transfer modes. However, comparison of parameters between individual forearcs shows that too many parameters change in nature to unequivocally show that specific parameter combinations characterise particular mass-transfer modes (e.g. Jarrard, 1986; von Huene and Scholl, 1991; Lallemand et al., 1994b). Nevertheless, these investigations revealed parameters that have the potential to influence the

mechanics of mass-transfer modes (e.g. velocity of plate convergence, obliquity of plate convergence, sediment supply to the trench basin, asperities on top of the oceanic crust, dip of the subducting slab, geometry of the forearc wedge; cf. Section 1.2). Scaled analogue or numerical simulations of geodynamic processes have the capability to solve the above mentioned problems, as these methods enable the investigation of individual parameters by systematic variation in series of experiments (cf. Section 1.3.).

In this study, 2D sandbox simulations were chosen for this task, as their high resolution of deformation structures and particle paths enable comparison of the experimental results with geological and geophysical data obtained in nature. A strategy is required to link the understanding of the mechanics, which resulted from the analysis of the analogue simulations, with the style of deformation in nature. Critical-taper theory is a concept with a high potential to understand orogeny, owing mainly to its simplistic and straightforward way to link the force balance of an orogen in self-similar growth mode to its bulk geometry, mechanical properties and kinematics (cf. Section 1.3; Chapple, 1978; Davis et al., 1983). This approach has been successfully used to explain the mechanics of fold-and-thrust belts, forearc wedges as well as entire orogenic belts (Davis et al., 1983; Platt, 1986; Willett, 1992). Scaled analogue experiments with granular materials (e.g. sand), in particular, were able to link the internal structural evolution and related particle-displacement field to the material properties, thereby yielding a first-order approach to understand the mechanics of different deformation styles that may be applied to nature (e.g. Malavieille, 1984; Huiqi et al., 1992; Lallemand et

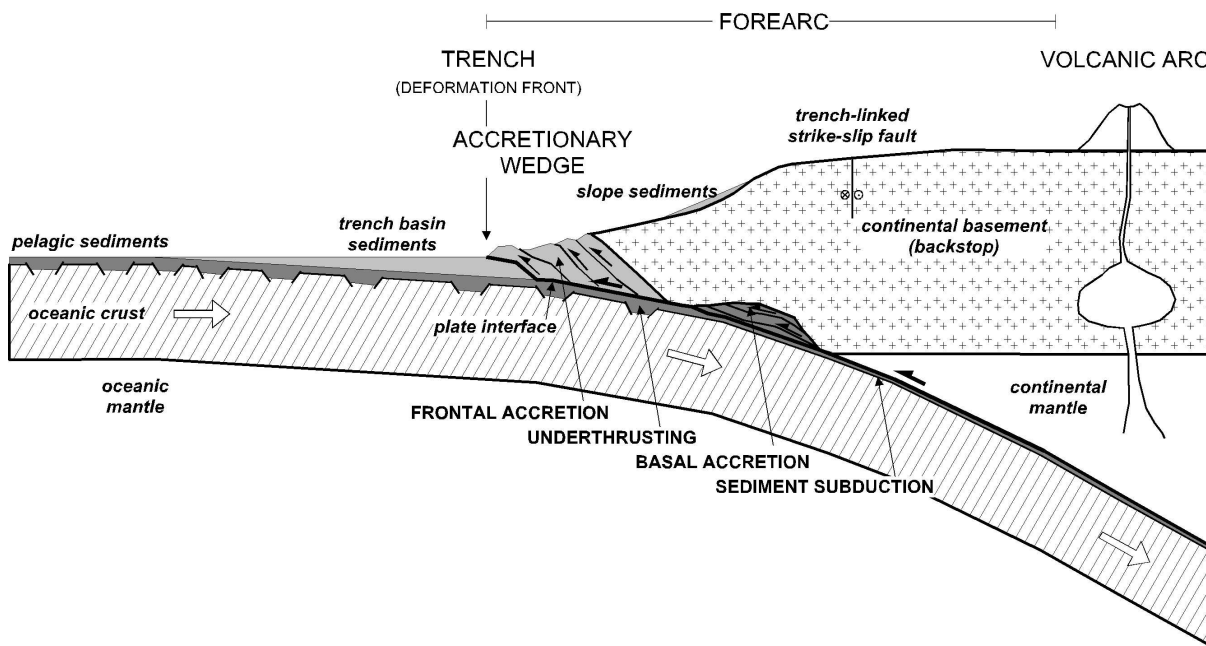


Figure 1.1: General sketch of a convergent margin indicating the principle morphological elements, sedimentary deposits and deformation processes. Trenchward from the backstop an accretionary prism is formed by frontal accretion of the upper portion of the incoming sediments. The lower portion of the sediments are either basally accreted or subducted to greater depth.

al., 1994b; Gutscher et al., 1996; Wang and Davis, 1996). Accordingly, the concept of this study is twofold:

- i) A basic parameter study was performed to quantify material properties with emphasis on finding sand types which are suitable to simulate the material behaviour of the brittle crust. Based on series of sandbox experiments performed with these sand types, I analysed the ability of the critical-taper analysis to evaluate the influence of specific properties on the mechanics of convergent wedges (Chapter 2).
- ii) These findings are applied to experiments, which were based on the specific features of accretive and non-accretive forearcs in nature (Chapter 3 and 4, respectively) to study their controlling parameters.

The second part of this study focuses on the convergent Chilean Forearc, as it shows a fundamental change from a purely tectonically erosive margin in the north to an accretive margin in the south, with associated kinematic domains (Fig. 1.2; Rutland, 1971; Ziegler et al., 1981; Behrmann et al., 1994; Scheuber et al., 1994). To test the experimental

results, two study areas, the North Chilean Forearc between 22 and 24°S, and the South Chilean Forearc between 37 and 40°S, were chosen, which have identical plate kinematic boundary conditions (present convergence rate about 6–7 cm a⁻¹ with 10–20° obliquity), but represent two end-members of mass transfer modes (Fig. 1.2). These are thought to be representative for other continental margins of similar style. In the case of the Chilean margin, parameters which significantly differ along strike are considered to be of major importance. In the north, the hyperarid climate (< 50 mm a⁻¹ precipitation) has led to a sediment-starved trench, lacking an accretionary wedge (Fig. 1.2; Bangs and Cande, 1997). This is in contrast with the south, which is characterised by high precipitation rates of 2000 mm a⁻¹, a trench fill, which exceeds 2 km in thickness, and an accretionary wedge. According to these differences, this study focuses on the investigation of the following parameters: sediment supply to the oceanic plate, the mechanical behaviour of sediments entering the trench, as well as surface properties (roughness and friction) of the oceanic basement. Different experimental setups were designed to determine the influence of these particular parameters. With these series of experiments the hypothesis can be tested, if only the sediment

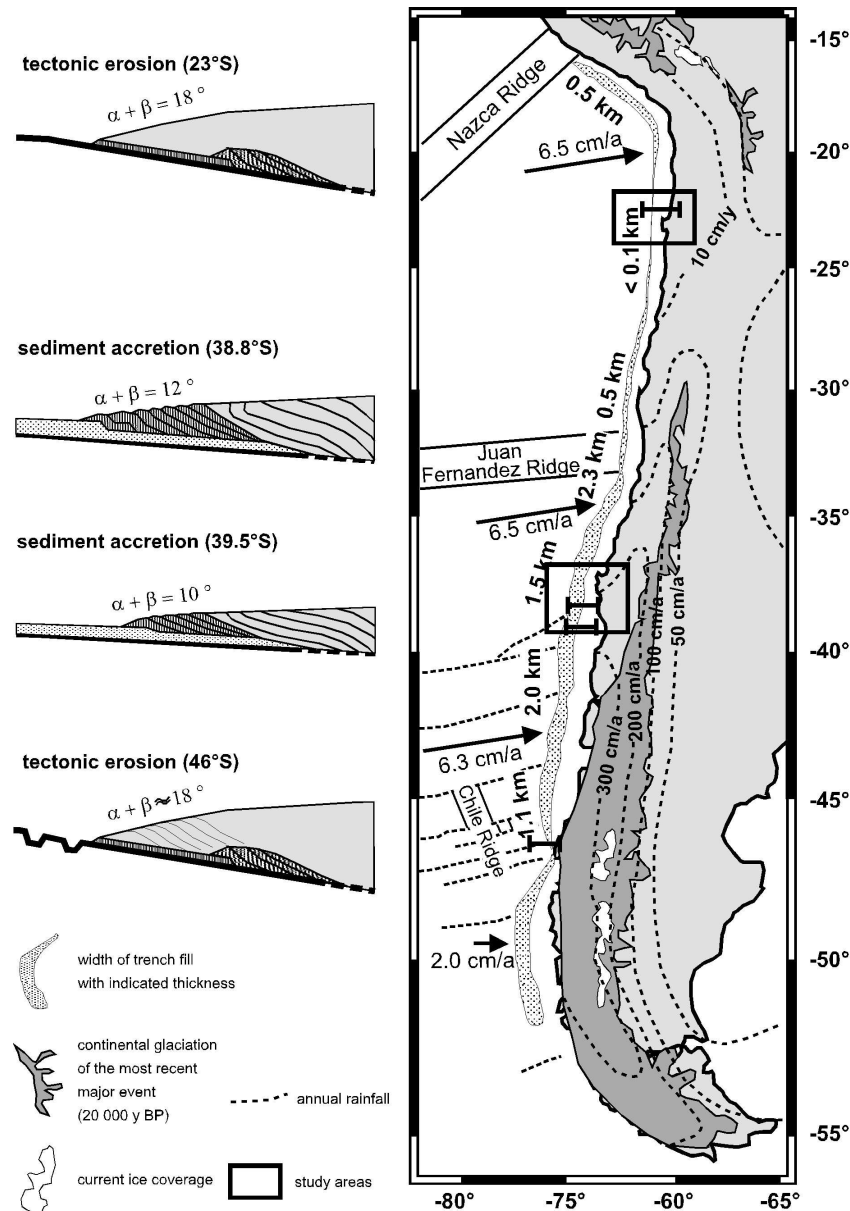


Figure 1.2: Mass-transfer modes at the convergent margin of Chile: The north/south variation of climate and sediment supply to the trench basin are proposed to be the important parameters controlling the mass-transfer mode ($\alpha + \beta$ – taper of the forearc wedge; modified after Bangs and Cande, 1997).

supply, as suggested by Bangs and Cande (1997), or a combination of several parameters, causes the change in mass-transfer mode along the Chilean Margin (Chapter 5).

An additional aim of this study is to test and establish links between mass-transfer modes and deformation onshore and offshore by comparison of the experimental results with the concepts based on surface studies and geophysical data. Because the study areas differ in the amount of data, which have

been acquired and interpreted, this study covers different topics at the North and South Chilean Forearc. A large geological and geophysical database of the tectonically-erosive North Chilean Forearc exists and detailed knowledge of the kinematics present in the onshore and offshore area is available. A large portion of this is due to 9 years work done by the SFB 267. Nevertheless, several concepts of the processes (frontal and basal erosion, cf. Section 1.2), which cause the tectonically-erosive mass-

transfer mode are still under consideration (cf. Section 4.1.2), as the mutual relationships of these processes and their mechanics are not well understood. Therefore, this study attempts to understand the mass-transfer processes of tectonically-erosive sand wedges and thus provide a concept of its mechanics (Section 4.4.2). Comparison of experiment and nature should show, if this concept is also appropriate to explain the processes in nature (Section 4.7.3). In contrast, a detailed database of the accretive South Chilean Forearc has been acquired and analysed by SPOC (Subduction Processes off Chile) and the SFB 267 during that time that this study was in progress and the concepts about its kinematics and mass-transfer processes were still incomplete. However, the general mechanical concepts of accretive forearc settings are well understood and investigated in nature and experiment. Based on published analogue simulations supplemented by experiments performed in this study, a possible scenario for the specific mass-transfer mode active at the South Chilean is discussed (Section 3.5). The resulting conceptual model may help to interpret the newly-acquired database.

1.2 Mass-transfer modes at convergent margins

Von Huene and Scholl (1991) classified convergent margins with respect to the main mass-transfer modes into accretive and non-accretive. An accretive margin is characterised by the presence of a growing frontal-accretionary wedge, whereas non-accretive margins are characterised by its absence.

The subducted oceanic plate contributes sediments to the forearc (Fig. 1.1). The incoming pile of sediment on top of the oceanic crust is composed of pelagic and hemipelagic material (thickness: 200–600 m; von Huene and Scholl, 1991), which are present at both accretive and non-accretive forearc systems. Terrigenous material reaches a maximum thickness in trench basins of accretive margins (thickness up to 1–6 km; von Huene and Scholl, 1991). Forearcs, as revealed from reflection seismic data, consists of a continental basement wedge, sometimes together with obducted basaltic oceanic fragments, and, if present, a frontal-accretionary wedge (Fig. 1.1). The accretionary wedge is mechanically weak and therefore accumulates most of deformation. The basement wedge has considerably greater strength and may be even considered

as rigid and serves as a backstop for frontal deformation.

The deformation processes, which take place at accretive margins, are well known, since the related tectonic structures are preserved in recent and fossil accretionary complexes. During the subduction of the oceanic crust, the sedimentary cover is either (partly) offscraped (e.g. along a basal detachment at the top of the oceanic basement or the pelagic sediments) and added to the upper plate, or is transported on top of the oceanic crust to greater depth (Fig. 1.1). It may potentially reach mantle depth as suggested by isotopic signatures in arc melts (Morris et al., 1990; Stern, 1991; Leeman et al., 1994). The corridor through which sedimentary material is transferred to greater depths is named the *subduction channel* (Fig. 1.3 a; Cloos and Shreve, 1988b; Cloos and Shreve, 1988a). Material addition at the frontal and basal part of an accretionary wedge occurs in two different modes (Fig. 1.1): Frontal accretion results in the formation of an imbricate fan (e.g. Seely et al., 1974; Karig and Sharman, 1975), whereas underplating, i.e. basal accretion beneath the wedge takes place by duplex formation and antiformal stacking (e.g. Moore et al., 1982; Westbrook et al., 1982; Platt et al., 1985). Before the sediments are basally accreted, they pass internally undeformed through the subduction channel, i.e. are underthrust.

Frontal and basal accretion leads to characteristic growth patterns of the forearc area. Uplift is slow in the case of frontal accretion, whereas it may be rapid in the case of basal accretion. High rates of frontal accretion lead to dominant horizontal growth of the wedge and therefore trench advance and trenchward migration of the volcanic arc may occur (Stern, 1989). Basal accretion affects mainly the vertical growth of the wedge and is not able to change the lateral position of the trench-arc system. However, basal accretion provides a mechanism to exhume high P/low-T metamorphic rocks to upper crustal levels in the rear part of the wedge, as commonly observed in nature (Platt, 1986).

With their subduction-channel model, Cloos and Shreve (1988b; 1988a) presented a detailed classification of convergent margins with regard to the mass-transfer processes observed in nature (frontal and basal accretion, underthrusting, basal erosion) and related deformation patterns. This conceptual model (Fig. 1.3 a) concentrates on the accretive mass-transfer modes and explains the two general accretive modes with the mass balance between the incoming sediments, the frontal inlet capacity of

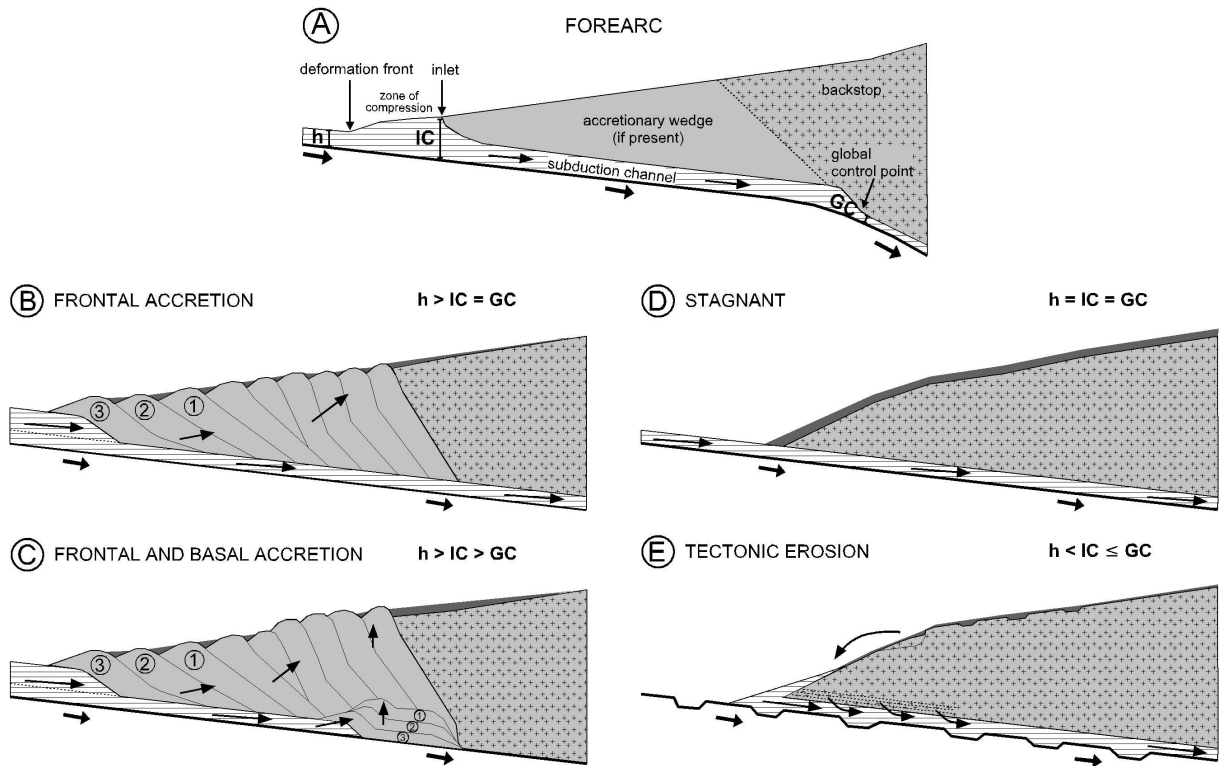


Figure 1.3: a) Major features of the subduction-channel concept (Cloos and Shreve, 1988a) for an accretive forearc. The balance of sediment thickness (h), inlet capacity (IC) and global capacity (GC) of the subduction channel determine the mass-transfer mode. The height of the inlet capacity determines the thickness of the underthrust sediments beneath the frontal part of the accretionary wedge. At the global control point, the global capacity of the subduction channel is measured. The global control point is located where the channel capacity decreases because of a sharp increase in the density of the overlying rocks, in the surface slope or in the dip of the subducted plate. For the case of a b) purely frontally-accretive forearc, c) coeval frontally- and basally-accretive forearc, d) stagnant forearc, e) tectonically-erosive forearc with frontal and basal erosion (numbers indicate the sequence of thrust initiation).

the subduction channel and its global capacity at greater depths:

- purely frontal accretion: Nearly the total volume of incoming sediments is frontally accreted, as the inlet capacity of the subduction channel is zero or very small compared to the volume of incoming sediments (Fig. 1.3 b).
- coeval frontal accretion and underthrusting: The lower part of the incoming sediments is underthrust beneath the forearc wedge, as the inlet capacity allows the partial bypassing of the incoming sediments. If the global capacity of the subduction channel is smaller than the volume of underthrust sediments, basal accretion takes place (Fig. 1.3 c).

Most of the accretive margins show partial underthrusting of the incoming sediments. Typical

frontally-accretive margins with more than 60% frontal accretion of the incoming sediments comprise only about 20% of the total length of convergent margins [e.g. Barbados (Moore et al., 1982), Cascadia (Hyndman et al., 1993), Sunda, (Kopp et al., 2002)], whereas accretive margins with less than 20% frontal accretion and more than 80% underthrusting of the incoming sediments are identified along 30% of the total length of convergent margins [e.g. Makran (Platt et al., 1985); Alaska, (Gutscher et al., 1998a); Mediterranean Ridge (Kukowski et al., 2002)].

Nearly half of the total length of convergent margins belong to the non-accretive type without an accretionary prism. With respect to the concept of Cloos and Shreve (1988b; 1988a) two types of non-accretive mass-transfer modes are expected to occur in nature:

- stagnation: All of the incoming sediments are subducted, as the subduction channel is able to transport the total volume of incoming sediments (Fig. 1.3 d).
- tectonic erosion: Instead of adding material to the upper plate, material is removed (Fig. 1.3 e).

The identification and investigation of tectonic erosion is more difficult than that of accretive processes, as the structures (e.g. fault planes related to tectonic erosion) of the former are continuously destroyed by the erosive process itself. The worldwide percentage of stagnant and erosive margins is still unknown, since many forearc settings, formerly believed to be stagnant, have been now identified as erosive margins (Scholl and von Huene, 2001).

The concept of tectonic erosion was developed to explain significant subsidence and truncation of continental crust observed at several convergent margins (North Chile, Japan, Peru, Costa Rica; Miller, 1970; Rutland, 1971; Scholl et al., 1980; Hussong and Uyeda, 1982; Cloos and Shreve, 1988b; von Huene and Lallemand, 1990). The most important features needed to identify tectonic erosion are material consumption and thinning of the forearc, trench retreat (Miller, 1970; von Huene and Cullotta, 1989; von Huene and Lallemand, 1990; von Huene and Scholl, 1991) and inland migration of the volcanic front (Stern, 1989; Scheuber and Reutter, 1992; Scheuber, 1994).

Two processes cause the consumption and thinning of the upper plate (von Huene and Lallemand, 1990), i.e. frontal and basal erosion: Frontal erosion loosens and removes material from the frontal slope of the forearc. In morphological lows on the oceanic plate, frontal-slope material is transported into the subduction channel. This can explain the truncation of continental crust, but not, the subsidence and thinning of the forearc. These are caused by basal erosion, i.e. the removal of mass at the base of the wedge. The frontally and basally-eroded material is transported in the subduction channel to greater depth or is basally accreted, as it is also has been shown for accretive margins. In contrast to the accretive margins, the material in the subduction channel consists of internally-deformed slope sediments and continental basement.

Systematic investigation of several convergent margins suggest that only under specific conditions erosive or accretive mass-transfer modes can occur (Hilde, 1983; Karig and Kagami, 1983; Jarrard,

1986; von Huene and Lallemand, 1990; Lallemand et al., 1994b; Bangs and Cande, 1997). The most non-accretive margins are characterised by a high convergence rate, no or a minor amount of incoming sediments, a steep dip and pronounced morphology of the oceanic plate due to unfilled depressions (cf. Section 4.1). In contrast, accretive margins mostly show a low convergence rate, a thick pile of sediments on top of the oceanic crust and a shallower dip of the subducting plate.

1.3 Mechanical Concepts

Several concepts for the mechanics of fold-and-thrust-belts, accretionary wedges, and even entire orogens have been developed since the thin-skinned nature of these wedge-shaped bodies were identified. These concepts explain deformation and displacement occurring on top of a weak basal detachment, i.e. an interface of lower friction than the wedge material. However, these concepts apply different rheologies. Elliot (1976) found a simple analytical expression that employs realistically geological parameters to estimate the shear stress necessary to initiate displacement along an inclined basal interface. This concept is partially independent of a specific rheology. However, it is successful in explaining the basic processes of deformation related to thrust sheets. In contrast, the concept of Chapple (1978) uses a simple mathematical description and a perfectly plastic rheology, which is best applicable to displacements on top of a very weak interface such as shales or evaporites.

With the critical-taper approach (Davis et al., 1983; Dahlen, 1984; Dahlen et al., 1984), which is based on the Coulomb Failure Criterion (equation 1.9 in Section 1.5), a much wider range of physical properties of wedge-shaped bodies can be included in an elasto-plastic concept. The critical-taper theory also allows for the inclusion of wedges that deform on top of relatively strong interfaces (Davis et al., 1983). The latter approach has recently become the most widely-used mechanical concept for accretionary or orogenic wedges. It allows the description of the geometry and state of stress within a wedge as a simple function of only few parameters, i.e. effective basal and internal friction, basal and internal pore pressure parameters, as well as cohesion (Fig 1.4 a and b). In these concepts the mechanics of horizontally-compressed wedges are considered to be analogous to wedges, which form in front of a moving bulldozer. The soil in front of the bulldozer deforms internally until the wedge attains a steady

state. This initial deformation phase is named the adjustment stage in this study. The steady-state phase is geometrically characterised by a constant wedge taper, i.e. critical taper. The critical-taper theory (Davis et al., 1983; Dahlen, 1984; Dahlen et al., 1984) assumes that the actively-accreting wedge attains its critical taper, where the whole wedge is on the verge of Coulomb Failure (Fig. 1.4 a). This theory shows that any wedge will evolve towards a dynamically steady state with a balance between material input, wedge taper, the mechanical properties of the wedge itself, and the mechanical properties of the basal shear zone. The critical taper is defined as (Davis et al., 1983):

$$\alpha + \beta = \Psi_b + \Psi_0 \quad (1.1)$$

where α is the surface slope, β is the basal dip and Ψ_b and Ψ_0 are the angles between the maximum principle stress orientation and the basal detachment and the surface, respectively. The critical-taper equation is only valid for a homogeneous wedge with uniform properties, i.e. one for which the densities of rocks, frictional properties and the pore pressure ratios are constant. In the following the exact solution of the critical-taper equation for non-cohesive wedges of Dahlen (1984) is presented. This equation can be also used as a good approximation for cohesive wedges, if the differential stresses are much larger than the cohesion, so that the influence of the cohesion is negligible low. This is the case, if the cohesion is very low, or if the study area is at a great depth in the internal part of the wedge, where the differential stress ($\Delta\sigma = \sigma_1 - \sigma_3$) is very large. The stress orientation Ψ_0 can also be written in the explicit form:

$$\Psi_0 = \frac{1}{2} \arcsin \left(\frac{\sin \alpha'}{\sin \Phi_I} \right) - \frac{1}{2} \alpha \quad (1.2)$$

with Φ_I as the angle of internal friction and the effective surface slope (α'):

$$\alpha' = \arctan \left(\frac{1 - \frac{\rho_w}{\rho}}{1 - \lambda} \right) \tan \alpha \quad (1.3)$$

which is influenced by the density of the wedge material (ρ), the density of the overlying water column (ρ_w) and the pore-pressure parameter λ . If a wedge is dry and subaerial, then $\lambda = 0$ and $\rho_w = 0$, so that $\alpha' = \alpha$. Also, the stress orientations in terms of β can be written in the explicit form:

$$\Psi_b = \frac{1}{2} \arcsin \left(\frac{\sin \Phi'_B}{\sin \Phi_I} \right) - \frac{1}{2} \Phi'_B \quad (1.4)$$

The effective basal friction (Φ'_B) influenced by the pore pressure is given as:

$$\Phi'_B = \arctan \mu'_B \quad (1.5)$$

The effective coefficient of basal friction (μ'_B) is defined as:

$$\mu'_B = \mu_B \left(\frac{1 - \lambda_b}{1 - \lambda} \right), \quad (1.6)$$

where λ_b is the pore-pressure parameter of the basal detachment and μ_B is the basal friction. Under dry conditions, $\lambda_b = 0$ and $\lambda = 0$, so that $\Phi'_B = \Phi_B$.

Insertion of (1.2) and (1.4) into the critical taper equation (1.1) leads to a simple expression for dry, subaerial wedges:

$$\begin{aligned} \alpha + \beta &= \frac{1}{2} \arcsin \left(\frac{\sin \Phi'_B}{\sin \Phi_I} \right) - \frac{1}{2} \Phi'_B \\ &- \frac{1}{2} \arcsin \left(\frac{\sin \alpha'}{\sin \Phi_I} \right) + \frac{1}{2} \alpha \end{aligned} \quad (1.7)$$

As an alternative to the mathematical solution of Dahlen (1984), Mohr Diagrams as presented by Lehner (1986), graphically illustrate the internal state of stress in a wedge and its internal slip lines, i.e. fault planes potentially (re-)activated in the wedge (Fig. 1.4 b). From this, the limiting states of stress

$$\sigma_z = \frac{\tau_{crit}}{\sigma_N} \quad (1.8)$$

with τ_{crit} as critical shear stress and σ_N as normal stress can be obtained for any point at the depth z . Using the pole construction method (Terzaghi, 1943), the Mohr Circles provide the actual orientation and the sense of possible motion for the set of slip lines of the wedge. Stresses determined by the second intersection with the Mohr Circle of any line passing through the pole, act on a plane with the same orientation as a line in physical space. Slip lines, which plot at the intersection of the Mohr Circle and the failure curve (i.e. critical point; A in Fig. 1.4 b) indicate the related faults can become active. Slip lines, which meet the Mohr Circle above the critical point (B in Fig. 1.4 b) show the related faults will be further active, whereas slip lines below the critical point (C in Fig. 1.4 b) denote inactive faults.

Dynamic equilibrium of a wedge, as expressed by stable sliding of a wedge over its base without internal deformation, will only be affected by changes of

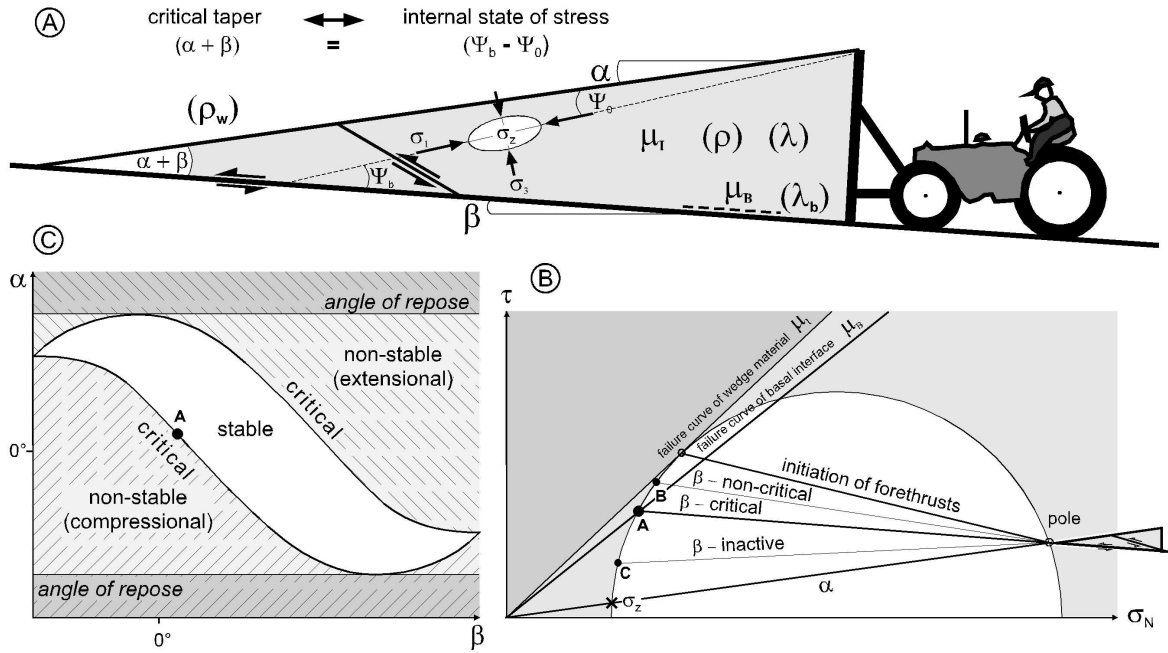


Figure 1.4: a) Convergent wedge and its controlling parameters: α – surface slope; β – basal dip; μ_I – coefficient of internal friction; μ_B – coefficient of basal friction; λ – internal pore-pressure parameter; λ_b – basal pore-pressure parameter; ρ – density of rocks; ρ_w – density of seawater (σ_1 – maximum principle stress; σ_3 – minimum principle stress; Ψ_0 – angle between σ_1 and surface slope; Ψ_b – angle between σ_3 and wedge base; after Davis et al.1983). b) Mohr Diagram of a critically-tapered wedge, with potential states of stress at the depth z (σ_z) indicated, as determined from the basal dip for a given surface slope after Lehner (1986; for further explanation see Section 1.3). The point A marks an activated basal detachment, point B an active basal detachment and point C an inactive basal detachment. c) α/β -diagram with indicated states of stress and stability field (white area) of a convergent wedge with a specific friction ratio (μ_B/μ_I ; modified after Dahlen, 1984). The point A marks the wedge shown in (a).

its boundary conditions (e.g. its mechanical properties, material supply, amount of material eroded, etc.). Accordingly, a convergent wedge can exhibit three dynamic states (i.e. state of stress; Fig. 1.4 b and c; Dahlen, 1984):

- i) In the stable state, the wedge does not need to accommodate minor changes in its boundary conditions as long as these do not lead to a state of near-failure throughout.
- ii) At the limits of the stable state, i.e. the critical state, equilibrium is achieved between the basal traction, and the stresses acting at the rear of the wedge, i.e. the wedge is at failure throughout during slip over its base. Such a critically-tapered wedge is indicated by continuously-active faults.
- iii) In the non-stable state, the wedge is in a sub-critical or supra-critical state and has to adjust its shape to a critical state by internal

deformation, i.e. by shortening in case of the sub-critical state or by extension in case of the supra-critical state.

A wedge, which is in a critical state of stress, will grow self-similarly by adjusting its critical shape during material addition (or removal) by internal deformation. Strain rates are largest where modification of the wedge shape is caused by changed parameters, as the new parameters determine another critical taper, to which the wedge has to adjust. In fossil orogenic belts, this is obvious e.g. from repeated reactivation of faults, formation of out-of-sequence faults, domains of diffuse wedge-internal deformation with second-generation fabrics, or from synconvergent extensional collapse of parts of the wedge. How to identify a critically-tapered wedge, is still a point of discussion. However, distributed and frequent seismicity indicates that a wedge is at failure throughout and this is interpreted as a critically-tapered wedge. The to-

pography of a critically-tapered wedge should reveal key information about its mechanical properties. On the other hand, the discontinuous topography of a non-stable wedge and its localised seismicity should allow identification of domains of active mass transfer and localised deformation.

Lallemand et al. (1994b) showed that the different mass-transfer modes of forearc wedges are characterised by typical wedge tapers: The truly accretive wedges show small wedge tapers, whereas non-accretive wedges have large wedge tapers. This observation may suggest that each mass-transfer mode corresponds to a different dynamical state or that the stability field (Fig. 1.4 c) changes from one mass-transfer mode to another. The latter suggestion implies that the mass-transfer modes are controlled by material properties, as the shape and the position of a stability field is controlled by the internal and basal mechanical properties of the wedge.

1.4 Analogue simulations

Analogue simulation is a forward modelling method used to investigate the geometrical, kinematic, and dynamical evolution of deformation in the crust. In analogue experiments, materials are chosen to simulate specific rheologies, which are deformed by forces operating in a similar way to nature. Silicone putty, honey, wax, and synthetic resins are commonly used analogue materials for simulating viscous rheologies in the lower crust or mantle (e.g. Gosh and Ramberg, 1968; Cobbold et al., 1971; McClay, 1976; Weijmar and Schmelting, 1986; Shemenda and Grocholsky, 1992; Wosnitza, 2002). Granular materials such as sand, micro glass beads, dry mortar or flour are used for the brittle behaviour of the upper crust (e.g. Hubbert, 1951; Malavieille, 1984; McClay and Ellis, 1987; Mulugeta and Koyi, 1987; Cobbold et al., 1989). Different apparatuses have been developed to simulate compressional, strike slip or extensional stress regimes [pure-shear box (Cadell, 1888), simple-shear box (Harris and Cobbold, 1984), extension boxes (McClay and Ellis, 1987), and centrifuges (Koyi, 1988)].

Analogue simulations help understand deformation processes by causing structures similar to those in nature. In contrast to geodynamic settings in nature, analogue experiments are performed within a fixed reference frame, so that a detailed detection of deformation is possible. One of the major advantages of analogue simulations compared to observation in nature is the well-directed simplifica-

tion of analogue experiments. In nature, multiple processes interact complexly, so that the observed structures are a product of all of them. The setup of analogue experiments can exclude most of the processes, so that the deformation is mainly produced by the processes for which the experiment was designed. This simplification enables a systematic investigation of parameters and their influence on the system.

Despite simplification, comparison between the experimental results and nature is allowed, when the analogue experiments are ‘properly’ scaled. Hubbert (1937) showed that the physical properties of a body change, when its size is changed. He concluded that the results of analogue experiments are only realistic, if they fulfil three scaling rules:

- Two bodies are geometrically similar when all corresponding lengths are proportional, and all corresponding angles of the two bodies are equal.
- Kinematic similarity is achieved, if two geometrically similar bodies undergo similar changes of shape or position (or both). Additionally, time-dependent deformation only achieves this similarity, if the time required for any given change in the two bodies is proportional.
- Two bodies, which are geometrically and kinematically similar, are only dynamically similar if the ratio between the forces acting on corresponding particles in the two bodies is constant.

In the next section, I will show how these scaling rules have been applied to analogue experiments performed with granular material (i.e. sandbox experiments).

1.5 Scaled 2D sandbox experiments

Before the scaling rules of Hubbert (1951) were established, the pioneering model studies of Hall (1815) and Cadell (1888) had revealed that the fault geometries in the models are in good accordance with those in nature, except for the difference in size. Therefore, they claimed that the geometrical similarity between their models and nature allowed their comparison. Hubbert (1951) used sand for his analogue experiments and inferred that the deformation behaviour of sand is applicable to the

behaviour of brittle rocks, as it obeys the pressure-dependent and time-independent Coulomb Failure Criterion:

$$\tau_{crit} = C + \mu\sigma_N, \quad (1.9)$$

where τ_{crit} is the shear stress at failure (i.e. critical shear stress), C is the cohesion, μ is the coefficient of friction and σ_N is the normal stress (for further discussion see Section 2.2 and 2.5). According to the scaling rules (cf. Section 1.4), the geometrical dimensions as well as the body (gravitational, inertial, and buoyancy), frictional and cohesion forces must all be scaled by a common constant (K , i.e. overall effective scaling factor) derived from (Ramberg, 1981):

$$\frac{C}{\rho \cdot a} = K \frac{C_M}{\rho_M \cdot a_M}, \quad (1.10)$$

where subscript M denotes the analogue model and C is the cohesion, ρ is the density, and a the acceleration due to body forces. Thus, sandbox experiments carried out in a normal gravity field (g – acceleration due to gravity) are dynamically scaled down by:

$$\frac{C \cdot \rho_M \cdot g_M}{\rho \cdot a \cdot C_M} = K \quad (1.11)$$

A sandbox experiment is ‘properly’ scaled, if it meets this condition. Several researchers had applied this scaling condition to their sandbox simulations and successfully drawn conclusions on a multitude of questions (see below, e.g. Hubbert, 1937; Malavieille, 1984; Mulugeta, 1988; Davy and Cobbold, 1991; Byrne et al., 1993; Kukowski et al., 1994; Lallemand et al., 1994a; Storti and McClay, 1995). Also, all experiments of this study follow this rule (cf. Section 2.4.1).

On this basis, convergent sandbox simulation becomes an effective tool to demonstrate the consequences of the critical-taper theory and to investigate the mass-transfer processes, kinematical and dynamical evolution of crustal wedges.

Davis et al. (1983) applied sandbox experiments to confirm their critical-taper theory. They used a 2D shear box with a variable basal dip, in which a conveyor belt was drawn toward a rigid backwall to transfer basal-shear forces to a frontally-accretionary sand wedge. The geometries of the experiments with different basal inclinations are in good agreement with the prediction of the theory: the surface slope of the wedge decreased with an increase in the basal dip.

Mulugeta (1988) and Huiqi et al. (1992) studied the influence of internal and basal friction on the geometries of convergent sand wedges. Loose sand with a low friction produced larger wedge tapers than compacted sand, where the latter is characterised by a high friction (Mulugeta, 1988). In contrast, using sandpaper as a conveyor belt with high friction caused larger wedge tapers than a plastic sheet with lower friction (Fig. 1.5; Huiqi et al., 1992). The results of both studies are in accordance with the critical-taper theory. However, the convex topographies of the convergent sand wedges were not self-similar, as predicted by the theory. Mulugeta (1992) suggested that this inconsistency was caused by deformation partitioning into brittle and ductile components. Diffuse compaction of the sand (i.e. ductile deformation) observed in internal parts of the wedge should increase the cohesion of the sand, and thus cause the convex wedge shape. However, this was not quantitatively validated.

The internal kinematics of convergent sand wedges built by frontal accretion show strong similarities with experiments performed in various laboratories. Low basal friction causes dominant frontal accretion, whereas highly frictional interfaces (sandpaper; i.e. high-friction interface) induce underthrusting of the incoming sand-layer (Fig. 1.5; e.g. Huiqi et al., 1992; Gutscher et al., 1998b). The incoming sand-layer is incorporated by forethrusts into a piggyback sequence of imbricates. Mulugeta (1992) showed that propagation of the frontal thrust is not a continuous process. Despite the fact that the rigid backwall is continuously under stress, the evolving thrust show stick-slip behaviour. However, Mulugeta and Koyi (1992) did not suggest a mechanical explanation of this behaviour.

Thrusts in the internal part of a wedge are steeply inclined and movement along these thrusts has ceased (Fig 1.5). Occasional reactivation of some of these thrusts leads to wedge-internal out-of-sequence deformation. The back rotation of the internal thrusts is caused by the subsequent stacking of imbricates and their passive transport on top of active imbricates (Fig. 1.5). Nieuwland (2000) developed a method of in-situ stress measurements in sandbox experiments to directly investigate the relation between internal kinematics and the stress regime. Although the experiments did not reach the steady-state phase (cf. Section 1.3), the stress measurements suggested that changes in the dynamic equilibrium between stress and strain are balanced by changes in the wedge taper. These changes of

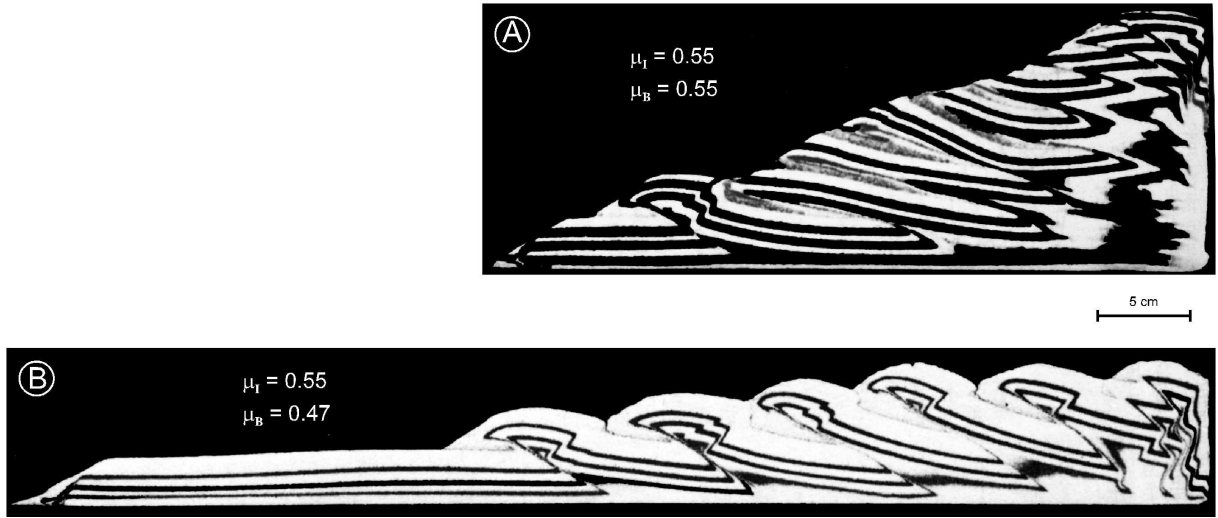


Figure 1.5: Frontally-accretionary sand wedges and their dependence on a change of basal friction: a) The large wedge taper results from high basal friction (sandpaper). b) The small wedge taper results from low basal friction (drafting film); (μ_B – coefficient of basal friction, μ_I – coefficient of internal friction; modified after (Huiqi et al., 1992)).

wedge geometry are achieved by the reactivation of localised out-of-sequence thrusts.

Platt (1988) developed a mechanical concept for the regular spacing of thrusts in imbricate fans, and therefore the spacing of thrusts in experimental sand wedges can be used as evidence of their mechanical properties. Colletta et al. (1991) and Huiqi et al. (1992) performed systematic studies on this topic. They confirmed the theoretical prediction of Platt (1988): the spacing of thrusts is proportional to the thickness of the incoming layer and the basal friction. Gutscher (1998b), however, showed that the proportional relationship between fault spacing, layer thickness and mechanical properties is not realised in experiments with significantly high basal friction. This mass transfer shows a cyclic behaviour, which alternates from failure of the incoming sand-layer at the deformation front to underthrusting of long thrust slices (Gutscher et al., 1996; Gutscher et al., 1998a). This cyclic behaviour has been explained by analysis of the forces present in the model (cf. Section 2.4.4.2 and 3.4.1).

To simulate the deformation processes of nature, boundary effects in the sandbox experiment have to be reduced. The rigid backwall is suggested to be one of the most influencing restrictions in sandbox devices. To solve this problem, Byrne et al. (1993) introduced a backstop with significantly greater yield strength than the incoming granular material. They showed that the general structures

	high μ_b	low μ_b
IC > GC IC = 2 cm GC = 1 cm	1 $\alpha = 10^\circ$ $\alpha = 16^\circ/5^\circ$ 	4 $\alpha = 6^\circ$ $\alpha = 7^\circ$
IC = GC IC = 1.6 cm GC = 1.6 cm	3 $\alpha = 10^\circ$ $\alpha = 31^\circ/5^\circ$ 	7 $\alpha = 5^\circ$ $\alpha = 11^\circ$
IC < GC IC = 1.3 cm GC = 2 cm	6 $\alpha = 10^\circ$ $\alpha = 32^\circ/25^\circ$ 	5 $\alpha = 6^\circ$ $\alpha = 18^\circ$

Figure 1.6: Results of a series of accretive experiments simulating different mass balances between the inlet capacity (IC) and global capacity (GC) with the initial surface slope (dashed lines and upper α -values) and the final surface slope (solid lines and lower α -values). Backthrusts and normal faults are indicated schematically ('+' represents material addition; '-' represents material loss; modified after Gutscher et al. (1998b)).

in the accretionary complex only weakly depend on the strength and geometry of the backstop. Nevertheless, such a backstop undergoes deformation itself, so that it is able to reduce the artificial deformation due to the rigid backwall.

Recently, such deformable backstops were commonly introduced in experiments, so the experimen-

tal mass-transfer mode can be favourably compared with nature (Kukowski et al., 1994; Gutscher et al., 1998a; Gutscher et al., 1998b). These studies investigated the influence of the different ratios between the incoming material and rearward material loss, as well as the basal friction, on the mass-transfer mode, kinematics and dynamics of accretive forearcs. To simulate a rearward material loss, i.e. transport of underthrust sediments to greater depth, the rigid backwall of the sandbox is lifted, so that material leaves the system through a ‘subduction window’. The height of the subduction window determines the amount of rearward material loss. Thus the height of the ‘subduction window’ determines the global capacity (GC) and the thickness of the incoming sand-layer represents the inlet capacity (IC) of the simulated forearc setting, in terms of the subduction-channel concept of Cloos and Shreve (1988b; 1988a; cf. Section 1.2). Kukowski et al. (1994) and Gutscher et al. (1998b) showed that dominant trench retreat always occurs, if the rearward material loss is greater than the volume of incoming material (i.e. $IC > GC$; Fig 1.6).

In the same way that convergent forearc settings are investigated with analogue simulation techniques, several studies have been concerned with fold-and-thrust belts (e.g. Corrado et al., 1998; Leturmy et al., 2000), as the investigations of Coulomb Wedges are meaningful for both accretionary wedges and fold-and-thrust belts. The main topics of these investigations were the influence of palaeomorphology and syntectonic sedimentation on thrust systems as well as the evolution of multi-layered systems.

Lallemand et al. (1992a) and Dominguez et al. (1998) supplemented the studies of accretive settings with their simulation of a non-accretive forearc settings. They showed that asperities along the basal interface cause short-term tectonic erosion (Fig. 1.7). This experimental setup was used to simulate the subduction of seamounts and aseismic ridges. The subduction of asperities results in a drastic modification of the wedge taper, and thickening of the wedge due to the inactivation of the trailing forethrust. Tectonic erosion, accompanied by a pronounced trench retreat, dominates the wedge above the trailing edge of the asperity. After subduction of the seamount the formerly accretive mass-transfer mode is re-established.

Interpretation of sandbox experiments can only be considered with respect to natural settings, when the limitations of the simulation are known. One

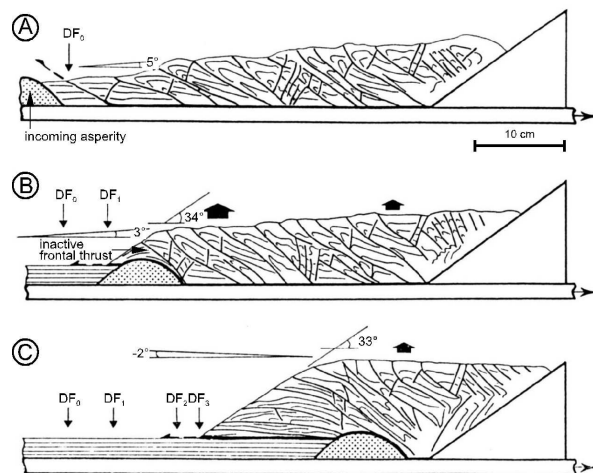


Figure 1.7: Line drawings of three stages of an experiment simulating seamount subduction. a) Before the asperity crosses the deformation front (DF; represents the trench), a typical frontal-accretionary wedge has developed. b) The asperity is underthrust beneath the wedge and ‘trench retreat’ begins. c) Advanced ‘trench-retreat’ and a steep surface slope is caused by further underthrusting of the asperity; modified after Lallemand et al. (1992).

of the most obvious limitations of sandbox experiments is the missing influence of pore pressure, since the experiments are done under dry conditions. Therefore, the wedge tapers of the experimental sand wedges are higher than those of submarine wedges, as the differential stresses are higher and the overlying water column is absent in the experimental systems. To prevent this limitation the laboratory at the Université Rennes presented a method to simulate deformation coupled with fluid flow (Cobbold and Castro, 1999; Cobbold et al., 2001). They showed that compressed air could be used as pore fluid in a dry sand package verifying Darcy’s law. They produced a realistic range of pore pressure parameters from 0.0 (air pressure) to 1.0 (lithostatic pressure). This method was applied to homogenous compressive sand wedges and resulted in typical lower wedge tapers. It was also used for a multi-layered sand wedge in which detachment activation due to increased pore pressure was reached (Cobbold et al., 2001). This method is advantageous to specific investigations of the direct influence of pore pressure. However, this technique requires a complex experimental setup and is therefore not suitable for investigations in which relative changes in wedge geometry are investigated. In addition, it is possible to simulate the consequences of

overpressured layers (i.e. weakening of specific layers) in dry sandbox experiments with the help of different materials, so that it is not necessary to use such a complicate experimental setup.

Another limitation of sandbox experiments is the narrow range through which material properties change during the experiments. In general, granular materials are characterised by load- and deformation-dependent properties to a small degree. Therefore it is difficult to simulate well-directed transient material properties during the experiment, as it is suggested in natural forearc settings, for example, due to dewatering or metamorphism. In analogue experiments, the packing, distribution and size of the grains cannot be accurately scaled and the faults do not occur as discrete failure planes but as dilatant shear zones. Therefore the faulting processes cannot be interpreted in small scales.

Chapter 2

Method and Basic Studies of Material Properties

2.1 Introduction

The critical-taper theory predicts a certain wedge taper for a convergent wedge (i.e. theoretical critical Coulomb Wedge) in a critical state of stress (cf. Section 1.3). Despite successful application of the critical-taper theory (Malavieille, 1984; Huiqi et al., 1992; Lallemand et al., 1994b; Gutscher et al., 1996; Wang and Davis, 1996), more-detailed descriptions of experiments performed with scaled analogue materials and their mechanical analysis reveal that the wedge taper does not match this predicted geometry (cf. Section 1.4). Hence, the theoretical critical Coulomb Wedge (Davis et al., 1983; Dahlen, 1984) may not adequately describe the deformation patterns of convergent non-cohesive sand wedges and their characteristic convex topography (Mulugeta, 1988; Mulugeta and Koyi, 1992).

From critical-taper theory it follows that only three fundamental material properties control the critical wedge geometry, the internal kinematics, and the internal stress regime (assuming a wedge remains at hydrostatic fluid pressure): internal and basal friction, and cohesion (cf. Chapter 1.3.). Hence, an explicit understanding of the deformation processes and the discrepancies described above requires that specific attention needs to be given to the properties of analogue materials, so that they properly represent natural materials.

Several authors have investigated the physical properties of dry granular materials, such as quartz sand (Hubbert, 1937; Mulugeta, 1988; Krantz, 1991; Huiqi et al., 1992; Lallemand et al., 1994a; Gutscher et al., 1996; Cobbold, 1999) From their results, average material parameters were used to determine an overall effective scaling factor (cf. Section 1.5) and to describe the analogue material.

Recent, more detailed analyses on granular-material behaviour have proposed a refined treatment of analogue experiments (Krantz, 1991; Schellart, 2000). Accordingly, deformation behaviour for small normal stresses (0–400 Pa), as is the case in common laboratory setups, is more complex than previously assumed and, in addition, internal friction also depends on rounding, sphericity, and grain size. Krantz (1991) revealed that the preparation technique (sifted, poured or sprinkled) of the sand is decisive in determining the internal friction and that friction differ significantly for fault initiation and for reactivated faults. This latter feature is well known from experiments performed on natural rocks (Brace and Byerlee, 1966; Byerlee, 1978; Paterson, 1978) and forms the basis for assessing the strength of the continental crust (Davis and von Huene, 1987). This may be of major importance since only one set of basal and internal friction is implicitly used in the critical-taper theory.

Additionally, in the context of the critical-taper approach, the influence of the basal detachment on dry, subaerial Coulomb Wedges is described by the basal friction (Φ_b), which has been investigated by several researchers (Huiqi et al., 1992; Kukowski et al., 1994; Lallemand et al., 1994a; Gutscher, 1996). Several parameters (roughness, adhesion, ploughing) control the basal friction in the brittle field (Straffelini, 2001). In natural forearc wedges, a variation in the roughness of the plate interface is apparent from bathymetric data (e.g. Hilde, 1983; Lallemand et al., 1994b; von Huene et al., 1999): The topography of oceanic basement with asperities of different scales (aseismic ridges, seamounts, inherited highs and lows, horst and graben structures) enter the trench. Therefore, Jarrard (1986), Lallemand et al. (1994b), and Kukowski et al. (2001a)

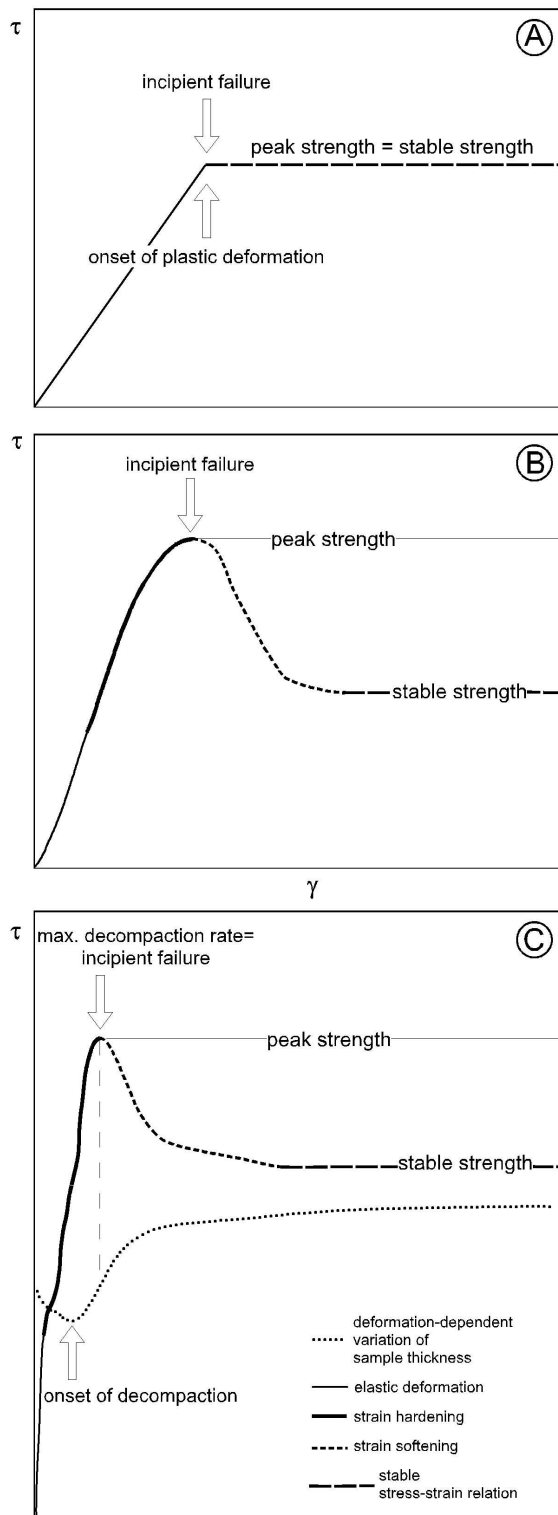


Figure 2.1: Plots of shear stress (τ) as a function of angular shear (γ) show that the material behaviour of a) an ideal Coulomb Material is distinctly different from that of b) natural rocks (modified after Jaeger and Cook, 1969) and c) granular analogue material.

suggested that the variation of basal friction induced by the roughness might play a major role in the kinematics and dynamics of natural forearc wedges.

However, this has not been experimentally investigated. If the roughness has such an impact on the basal friction that the mechanical wedge behaviour is influenced, it should be observable in analogue experiments designed to answer to this question (cf. Section 2.4.4).

The above-mentioned restrictions may be an oversimplification of the critical-taper approach and the consequences for experimental wedges has not been established. Accordingly, proper representation of natural systems in experiments must

- identify the factors that control material properties and use these to choose materials according to the behaviour of natural rocks in the brittle field (cf. Section 2.3.2 and 2.5), and
- based on these results, define a strategy that is appropriate to extend the analysis of accretionary wedges, fold-and-thrust belts, and orogenic belts (cf. Section 2.4.3.2 and 2.5).

These two issues are studied with a mechanical-property analysis and the first series of convergent sandbox experiments (cf. Section 2.4.3). These experiments focus on previously determined material properties and the associated kinematic evolution of convergent sand wedges. First, the dependence of the mechanical properties of granular analogue materials (quartz sand) on standard handling techniques was analysed by shear tests (cf. Section 2.3). Then the role of material properties which showed variations during ongoing deformation are demonstrated and the potential of quartz sand to be used for scaled analogue experiments is established (cf. Section 2.4.3). On the base of the first series of experiments, a new strategy of critical-taper analysis is developed and tested. Then, a second series of experiments was performed to investigate only the influence of basal roughness on the evolution of convergent sand wedges (cf. Section 2.4.4). There, I show how the new strategy of critical-taper analysis can be applied to the understanding of the mechanics of scaled analogue experiments.

2.2 Theoretical background

The Coulomb Failure Criterion (equation 1.9 in Section 1.5), as used in the critical-taper theory, defines the behaviour of the theoretical Coulomb Wedge.

In the critical-taper theory, the Coulomb-type Material is defined to be non-cohesive ($C = 0$) and characterised by a linear elastic stress-strain relationship, until pressure-dependent failure occurs (Fig. 2.1 a). Thus, the critical shear stress (t'_{crit}) in this simplified modification is written as:

$$t'_{crit} = \mu \cdot \sigma_n, \quad (2.1)$$

where μ is the coefficient of friction and σ_n is the normal stress. In Section 2.3.2, I will show that this simplification typically only causes a negligible error in the sandbox simulations. Then t'_{crit} is implemented in the mechanical analysis of convergent sand wedges. As the stresses, which act on the wedge material, have to exceed this critical shear stress at pervasive failure, t'_{crit} corresponds to the *frictional strength* of the wedge material in the terms of Ranalli (1987). Only in the cases where the critical shear stress is strongly influenced by the cohesion (cf. Section 2.3.2), will t_{crit} (equation 1.9 in Section 1.5) be considered and the term *strength* is correspondingly used.

When the frictional strength is exceeded, subsequent plastic deformation follows under constant shear stress. The frictional strength of a Coulomb-type Material at failure (i.e. the *peak strength*) is equal to that, which is present during persistent deformation (i.e. *stable strength*; Fig. 2.1 a). However, mechanical experiments on natural rocks have established that a distinction must be made between the properties of an undeformed and deformed material (Brace and Byerlee, 1966; Byerlee, 1978; Paterson, 1978): Undeformed materials have higher frictional strengths than fractured materials (Fig. 2.1 b). The frictional strength of the latter is only controlled by that of existent faults.

In agreement with this observation, wedge materials, such as natural rocks or granular analogue materials, show a more complex behaviour during the phase of plastic deformation than that described by the Coulomb Failure Criterion (Fig. 2.1 b and c). Investigations of bulk solids have shown that granular materials display a complex strain-dependent behaviour during initial failure (Vaid and Sasitharan, 1992; Chu, 1995; Schanz and Vermeer, 1996). They proposed that these materials exhibit elastic-frictional properties, with strain hardening prior to failure and subsequent strain softening, until a dynamically constant shear load is reached (Fig. 2.1 c). This evolution is related to a compaction-decompaction cycle. Values of friction derived from laboratory experiments show that a peak friction

may be assigned to the initial yield strength of the samples, while a lower stable friction is linked to stable sliding. It should be noted that the stress-strain curves of rocks are comparable to that of granular materials. However, in case of rocks, strain-hardening and strain-softening effects also depend on strain rate, temperature, effective stresses, gauge compaction, and roughness of the sliding surface.

Despite the more complex material behaviour of rocks, a ‘Coulomb Rheology’ may be used to describe the mechanical behaviour of the upper brittle crust on a regional scale (Davis et al., 1983). This is justified from the observation that rocks are penetrated by fractures, micro-cracks and mechanical heterogeneities of any orientation (Sibson, 1974; Brudy et al., 1997). Failure by reactivation, therefore, will occur prior to attaining the peak strength related to undeformed rocks. Accordingly, stable sliding can be assumed to control the critical taper of a compressive wedge in nature. The elastic-frictional behaviour of rocks with strain hardening and strain softening then can be substituted by that of an ideal cohesionless ‘Coulomb Material’ for investigations on a regional scale.

In contrast, the simplistic assumption of a ‘Coulomb Rheology’ may not apply to the behaviour of granular analogue material. It might therefore not be justified to use granular materials to simulate the behaviour of the brittle upper crust. In addition, the critical-taper approach may not be adequate enough to describe sandbox experiments. Instead, the identification of the currently active state of basal and internal friction (peak or stable friction) of sand wedges may be more appropriate.

2.3 Material properties

2.3.1 Material characterisation

To evaluate the influence of internal and basal frictional strength (i.e. frictional strength of wedge material and frictional strength along the detachment at the wedge base; cf. Section 1.3) on the evolution of convergent sand wedges, the possible influence of all other material properties has to be excluded. Therefore, in all experiments, which were performed in this study, I employed the same sand (S30T, Quaternary, glacial, almost pure quartz sand from Königslutter, Germany). This sand was washed and dried at high temperature by the distributing company, so that the finest fraction ($< 20 \mu\text{m}$) was removed. Consequently, the size of the well-rounded,

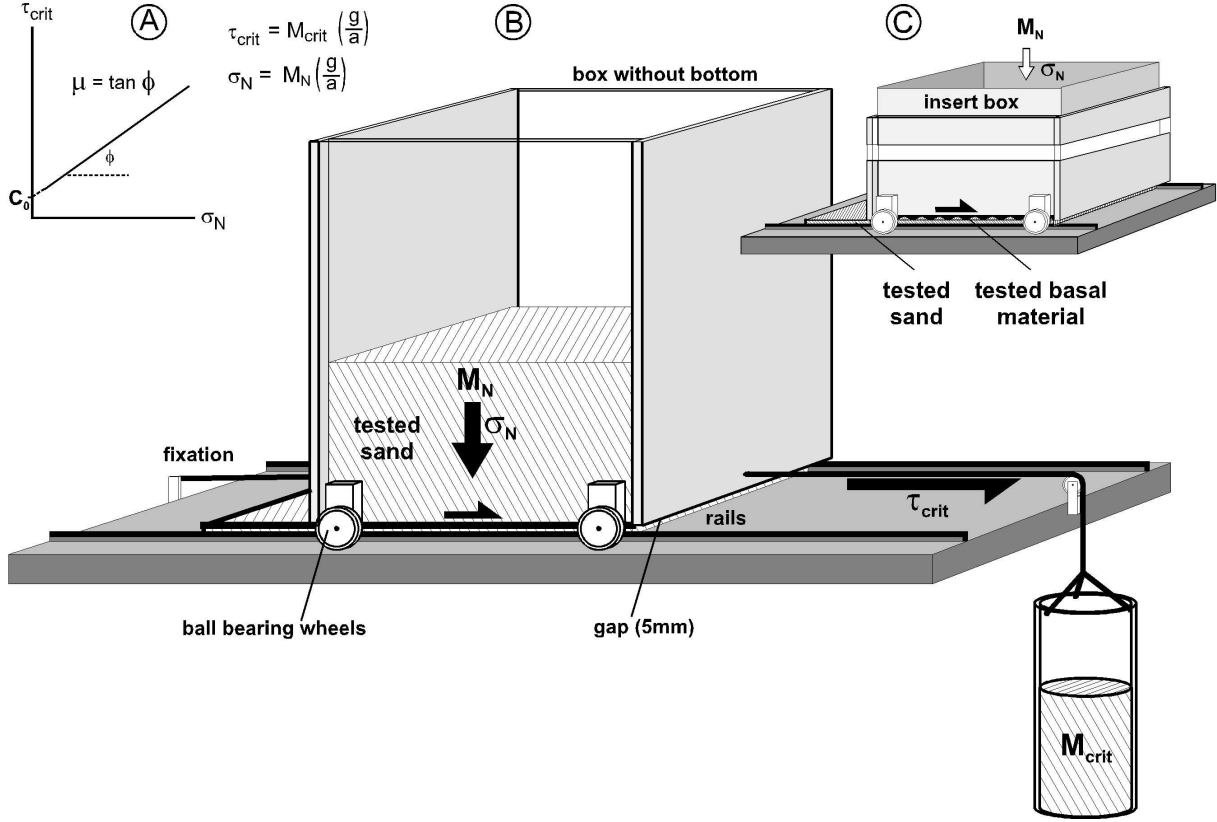


Figure 2.2: Hubbert-type shear box used to measure physical properties of granular materials. a) Critical shear stress (τ_{crit}) as function of normal stress (σ_N) for an analogue material. The slope gradient of the line represents the angle of friction (Φ). The intersection of the line with the ordinate represents the cohesion (C_0). b) Setup used to determine internal friction and cohesion; c) Setup used to determine the basal friction between granular materials and the materials of the basal interface (μ – coefficient of friction; M_N – normal load; M_{crit} – critical mass of shear load; g – acceleration due to gravity, a – area of fault plane).

sand type	grain size spectra [μm]	filling method	grain-size distribution	grain-size	ρ [g/cm]	μ_P	C_P [Pa]	μ_S	C_S [Pa]
SIF	< 400	sifted	inhomo	fg	1.67	0.72 ± 0.01	28 ± 10.3	0.54 ± 0.02	83 ± 11
SHF	220–400	sifted	homo	fg	1.65	0.68 ± 0.02	49 ± 15	0.55 ± 0.02	75 ± 12
SIC1	> 400	sifted	inhomo	cg	1.67	0.62 ± 0.02	80 ± 25	0.52 ± 0.02	75 ± 16
SHC	400–630	sifted	homo	cg	1.67	0.65 ± 0.02	45 ± 17	0.55 ± 0.01	72 ± 8
PIF	< 400	poured	inhomo	fg	1.54	0.44 ± 0.02	123 ± 13	0.53 ± 0.02	95 ± 24
PHF	220–400	poured	homo	fg	1.5	0.47 ± 0.02	99 ± 18	0.52 ± 0.02	78 ± 21
PIC1	> 400	poured	inhomo	cg	1.54	0.49 ± 0.02	62 ± 22	0.52 ± 0.02	71 ± 22
PHC	400–630	poured	homo	cg	1.51	0.55 ± 0.02	26 ± 14	0.54 ± 0.02	53 ± 15

Table 2.1: Physical properties of sands measured with the Hubbert-type shear box. Grey rows indicate the sands used for the sandbox experiments of Section 2.4.3 (ρ – density, μ_P – peak friction, C_P – peak cohesion, μ_S – stable friction, C_S – stable cohesion, inhomo – inhomogeneous, homo – homogeneous, fg – fine-grained, cg – coarse-grained).

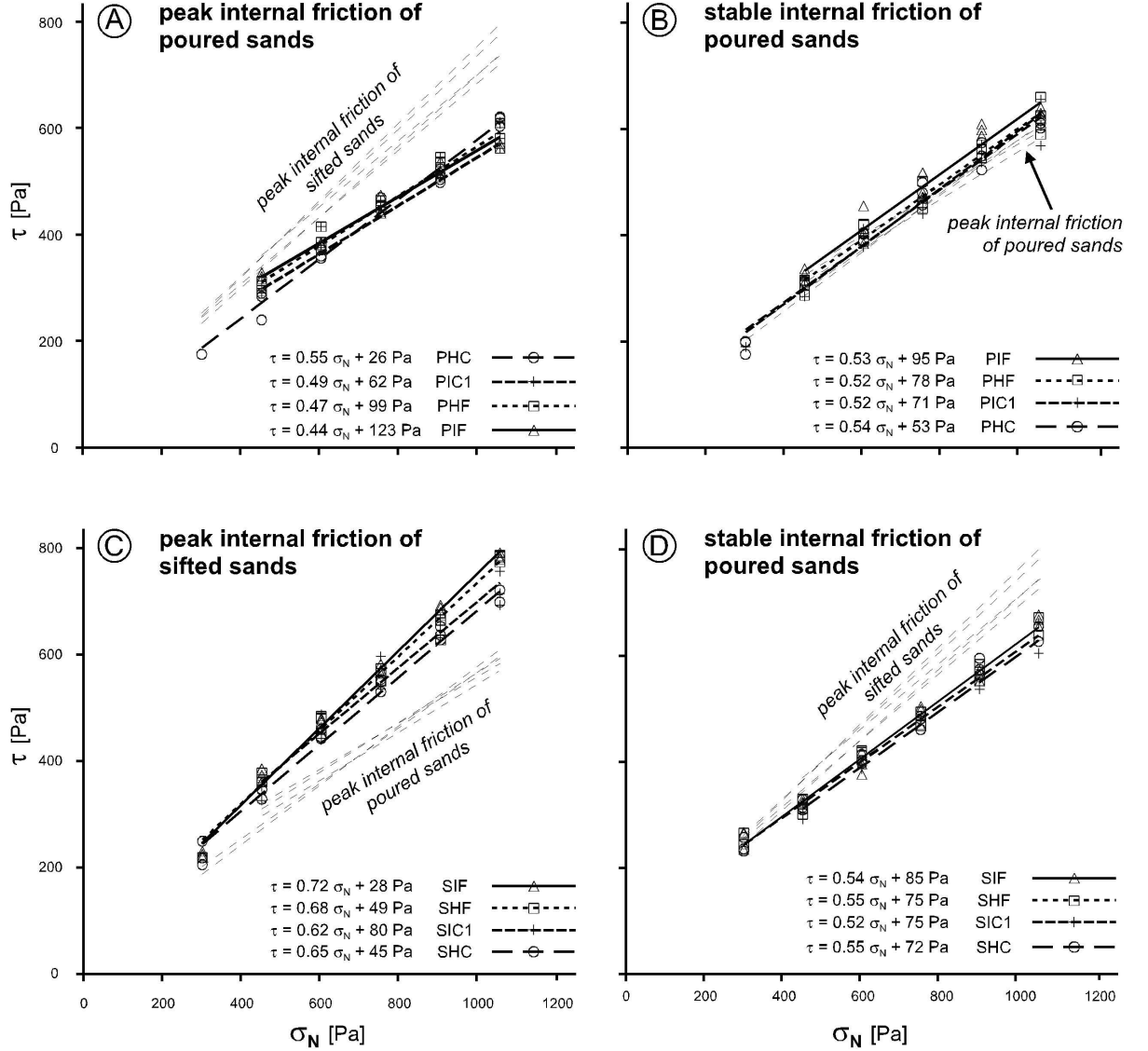


Figure 2.3: Shear stress (τ) plotted as a function of normal stress (σ_N) for poured (a, b) and sifted sands (c, d) in the Hubbert-type shear box. Peak internal friction (a, c), stable internal friction (b, d), and related cohesion are derived from linear regression analysis applied to these data (for error and nomenclature of sands see Tab. 2.1 and Section 2.3.1.).

moderately-spherical grains varies between 20 and 800 μm . Grain-size distribution is nearly symmetrical with a maximum at 350 to 400 μm . To obtain materials with different properties, the sand was separated into different grain-size fractions. To measure the material properties a shear apparatus was filled using two different methods; sifting and pouring (Tab. 2.1). From now on the different sand fractions (poured or sifted) are named as different *sands*. Conveyor belts, which simulated the detachment at the wedge base (cf. Section 2.4),

were covered with paper, latex gum, or sandpaper (< 400 μm). Paper and latex gum are characterised by a smooth surface, whereas the sandpaper has a significantly rough surface.

The mechanical properties of the different sands were measured with a modified Hubbert-type shear box (Hubbert, 1951), which allows the determination of the ratio of normal stress to shear stress at failure (Fig. 2.2 a). Strength at failure was measured by increasing the shear load until initial failure occurred. The mass (M_{crit} in Fig. 2.2) of the

shear load was determined to calculate the internal peak strength (Fig. 2.2 b). In a second step, the shear load was again increased until renewed slip in the sheared sand occurred. This provided the stable internal strength of deformed material. For the measurement of the basal properties between the different sands and the paper material, I employed a box, the bottom of which was attached to the material of the conveyor belt, which was set on top of a thin layer of sand (Fig. 2.2 c). The technique to measure peak basal strength and stable basal strength was the same as described for the internal properties.

To minimise error, these measurements were repeated up to six times using different normal loads for each sand (1.5 kg to 4 kg, in steps of 0.5 kg) and an experiment was repeated for each normal load three times. The coefficient of friction and the cohesion were then determined by linear regression analysis (Fig. 2.2 a and 2.3). For the coefficient of friction, standard error of all measurements was smaller than ± 0.02 (Tab. 2.1). Cohesion, however, could only be determined with a precision of ca. 30% with this method.

In addition, a disadvantage of this method is that it introduces another error: The measurement is performed under static conditions, i.e. the fault plane is reactivated and not continuously active as e.g. often observed in sandbox experiments. Therefore, the results of these static measurements were confirmed by selected dynamic measurements performed in a ring-shear tester (Schulze, 1994), which measures the material strength during ongoing deformation (Fig. 2.4 a). Two shear-load cycles were performed with the same normal load (Fig. 2.4 b). The peak strength of the first cycle was used to calculate the peak friction, whereas the peak strength of the second cycle led to the *stable static friction* (i.e. the friction, which was overcome at the moment of fault reactivation). The *stable dynamic friction* for continuously-active faults is given by the constant strength during further deformation. These measurements record deformation-dependent compaction and decompaction. The comparison of the two methods (shear box, ring-shear tester) showed that the measurements with the ring-shear tester are faster, more precise with a standard error smaller than 0.007 and provide more detailed results. Therefore, the basal properties between one specific sand and latex gum or sandpaper were measured only with the ring-shear tester. These measurements were repeated six times to minimise error.

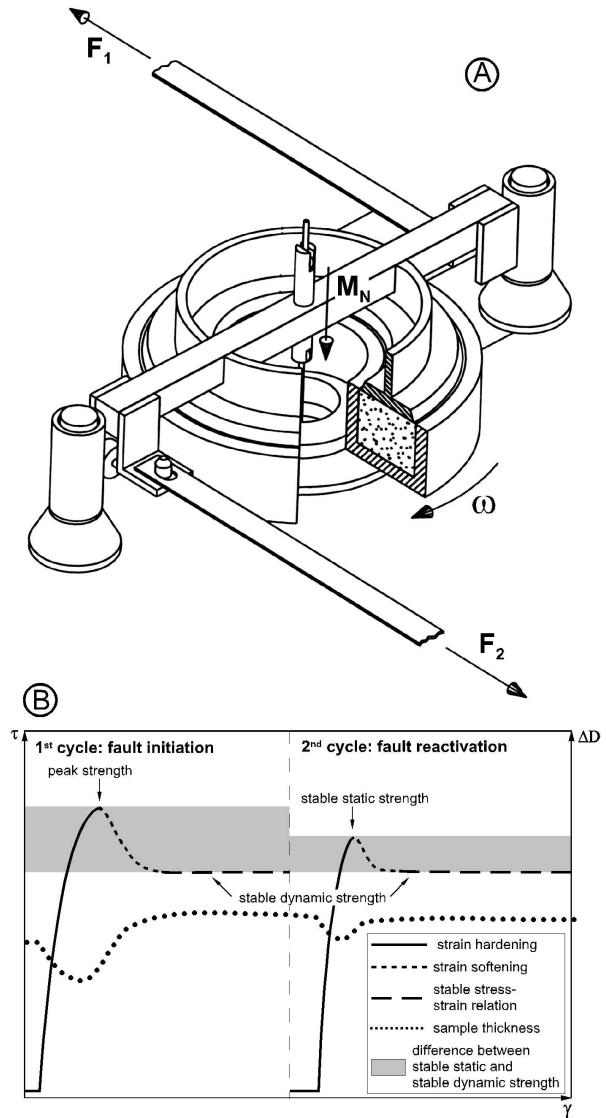


Figure 2.4: a) Ring-shear tester used to determine physical properties of granular materials in a dynamic mode (M_N – normal load; ω – angular velocity, F_1 and F_2 – measured shear force; modified after Schulze, 1994). b) Stress-strain curve and variations of sample thickness (ΔD) as a function of angular shear (γ) derived from two load cycles with undeformed and deformed material (τ – shear stress).

2.3.2 Results

Sand density was mainly controlled by the technique used to fill the shear box. The densities of poured sands had a smaller range and were also significantly lower ($1.5\text{--}1.54\text{ g cm}^{-3}$) than those of the sifted sands ($1.65\text{--}1.67\text{ g cm}^{-3}$, Tab. 2.1). Whereas sifting generated more densely packed

well-compacted sands, pouring always produced undercompacted materials. For both filling techniques, sifting and pouring, a homogeneous sand always had a lower density and higher porosity than an inhomogeneous sand.

Since the cohesion of the sands was very low (< 130 Pa; Tab. 2.1) when compared to the normal stress acting in the ring-shear tester, Hubbert-type shear box and the sandbox experiments (experiments in this chapter > 1000 Pa; experiments in Chapter 3 and 4 > 6000 Pa) the critical shear stress was mainly governed by the friction. Therefore, the simplified critical shear stress τ'_{crit} (equation 2.1 in Section 2.2) and the corresponding frictional strength was used for these materials. Moreover, the cohesion did not correlate with either sand density or degree of compaction. Therefore, this study mainly focuses on friction. From this point onwards friction is always given in terms of the dimensionless coefficient of friction and named *friction* throughout.

Results of static measurements

Static measurements showed that peak internal friction was clearly a function of the filling technique of the shear box. Pouring the sand resulted in significantly lower peak friction (0.44–0.55) than sifting (0.62–0.72; Fig. 2.3 a and c; Tab. 2.1). These ranges do not overlap, revealing that friction was mainly controlled by compaction and density. In addition, peak internal friction was affected by grain size and degree of homogeneity, resulting in minor variation of this parameter. In sifted sands, peak friction increased with grain-size heterogeneity and decreasing grain size. In contrast, poured sands showed increasing peak friction with increasing grain size and homogeneity.

There was a remarkable difference between peak and stable friction (Fig. 2.3 b and d; Tab 2.1). Stable friction of the different sands did not show the well-defined separation between the two techniques of shear box filling. All sands investigated in this study had nearly the same stable internal friction (0.52–0.56), with no systematic influence from the grain size and grain-size distribution.

With the Hubbert-type shear box, basal friction were only measured between the paper used as conveyor belt and those sands, which were used in the sandbox experiments of the basic parameter study (Tab. 2.2; Fig. 2.5 a and b). These measurements revealed that the peak basal friction and stable basal friction were lower than the respective internal frictions, while the trends of both basal and internal

frictions are comparable. The inhomogeneous sifted sand with small grain size (< 400 μm) had the highest peak basal friction (SIF: 0.53 ± 0.02). Whereas the equivalent poured sand had the smallest peak basal friction (PIF: 0.38 ± 0.02). The stable basal friction of the investigated sands ranged from 0.45 to 0.55.

Results of dynamic measurements

The results of the dynamic measurements performed in the ring-shear tester confirm the results of the static measurements for the internal material properties with respect to the peak strength of undeformed materials (Tab. 2.3). However, comparison of the static and dynamic measurements indicates that the stable strength measured in the Hubbert-type shear box is always lower than the stable dynamic strength of deformed materials: For the basal shear zone, test runs showed that the friction for stable sliding in identical materials, with an identical filling technique, is 0.07 lower for dynamic measurements than for static measurements (Tab. 2.2). Therefore, the results of the stable basal friction, measured in the shear box, were corrected by this amount for use in further interpretations. This difference can probably be ascribed to repeated stops and reactivation of slip imposed by the mechanical setup of the shear box, whereas the stable dynamic strength of the dynamic measurements is related to ongoing shear zone development.

Comparison of peak and stable dynamic strength of various sands showed that poured sands have a small ratio of peak strength to stable dynamic strength, whereas this ratio was high for sifted sands (with equivalent ratios of peak versus stable dynamic friction, Fig. 2.6). In addition, dynamic measurements performed in the ring-shear tester showed a transient strength development of all samples during increasing shear deformation along with a systematic compaction-decompaction cycle. Early diffuse deformation was associated with sample compaction, followed by a stage of dilatancy of the granular material during the pre-failure deformation. Increasing plastic deformation, during increasing shear load, was associated with plastic hardening of the samples in this stage (Fig. 2.6). Failure, i.e. formation of a localised shear zone, is inferred to occur near peak strength and peak decompaction rate, as also observed in the analysis of granular materials (Han and Drescher, 1993; Anand and Gu, 2000). Subsequent strength drop of the material and the transition to stable sliding was associated with a decreasing decompaction rate.

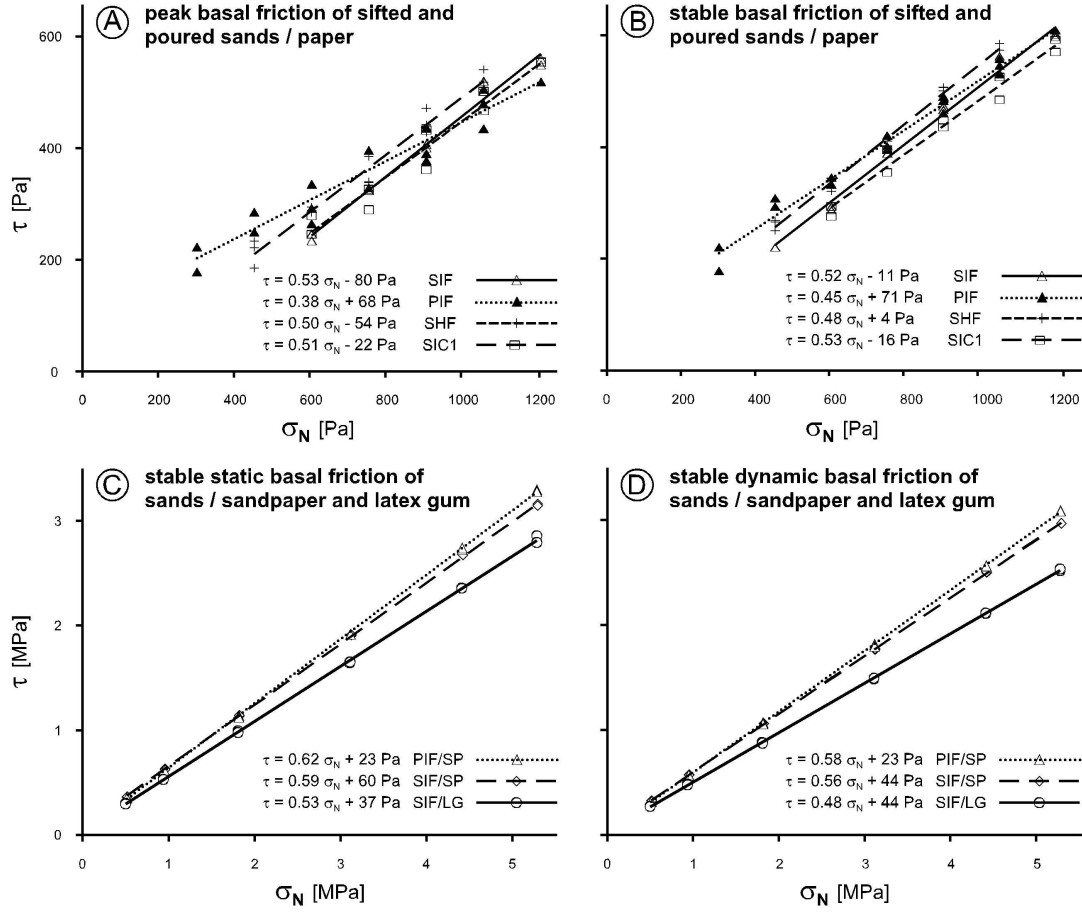


Figure 2.5: Shear stress (τ) plotted as a function of normal stress (σ_N) for basal materials and different sands in the Hubbert-type shear box (a, b) and in the ring-shear tester (c, d). Peak, stable static, and stable dynamic basal friction are derived from linear regression analysis applied to these data (for errors see Tab. 2.2 and Section 2.3.1; for nomenclature of sands see Tab. 2.1; SP – sandpaper, LG – latex gum).

sand type	grain size spectra [μm]	basal interface material	μ_P	μ_{SS}	μ_D
SIF	< 400	paper	0.53 ± 0.02	0.52 ± 0.02	...
SIF	< 400	paper	0.54 ± 0.01	0.51 ± 0.02	0.45 ± 0.01
SHF	220–400	paper	0.50 ± 0.02	0.48 ± 0.02	<i>0.41</i>
SIC1	> 400	paper	0.51 ± 0.02	0.53 ± 0.01	<i>0.46</i>
PIF	< 400	paper	0.38 ± 0.02	0.45 ± 0.01	<i>0.37</i>
SIC2	< 630	sandpaper	...	0.590 ± 0.003	0.558 ± 0.003
PIC2	< 630	sandpaper	...	0.616 ± 0.002	0.579 ± 0.002
SIC2	< 630	latex gum	...	0.534 ± 0.006	0.479 ± 0.007

Table 2.2: Basal friction between different basal interfaces and sands used in the sandbox experiments of this chapter. Grey rows indicate materials used in the experiments of Section 2.4.3 and 2.4.4. The results from the ring-shear tester are in bold types. All other values were measured with the Hubbert-type shear box. Stable dynamic friction, which was calculated from the stable friction measured with the Hubbert-type shear box using the experimentally-derived correction value (0.07), are marked in italics (for nomenclature see Tab. 2.1; μ_P – peak friction, μ_{SS} – stable static friction, μ_D – stable dynamic friction)

material	grain size spectra [μm]	ρ [g/cm ³]	μ_P	C_P [Pa]	μ_{SS}	C_{SS} [Pa]	μ_D	C_D [Pa]
SIF	< 400	1.73	0.72 ± 0.01	67 ± 8.3	0.58 ± 0.02	82 ± 13	0.53 ± 0.01	75 ± 10.5
SIC2	< 630	1.732 ± 0.008	0.731 ± 0.006	63.5 ± 19.8	0.601 ± 0.002	89.6 ± 7.4	0.568 ± 0.002	66.5 ± 5.0
PIC2	< 630	1.526 ± 0.005	0.658 ± 0.004	24.2 ± 12.3	0.658 ± 0.004	43.6 ± 12.1	0.612 ± 0.002	50.8 ± 5.4
glass beads	200 – 300	1.6 ± 0.002	0.522 ± 0.004	...	0.449 ± 0.003	...	0.432 ± 0.002	...
dry mortar	...	1.734 ± 0.009	0.706 ± 0.004	53.7 ± 12.5	0.700 ± 0.007	54.3 ± 21.3	0.664 ± 0.004	24.1 ± 13.1

Table 2.3: Physical properties of different granular materials used in this study, obtained with the ring-shear tester. The results of SIF (grey row) verify the precision of the static measurements (same nomenclature as Tab. 2.1; ρ – density, μ_P – peak friction, C_P – peak cohesion, μ_{SS} – stable static friction, C_{SS} – stable static cohesion, μ_D – stable dynamic friction, C_D – stable dynamic cohesion).

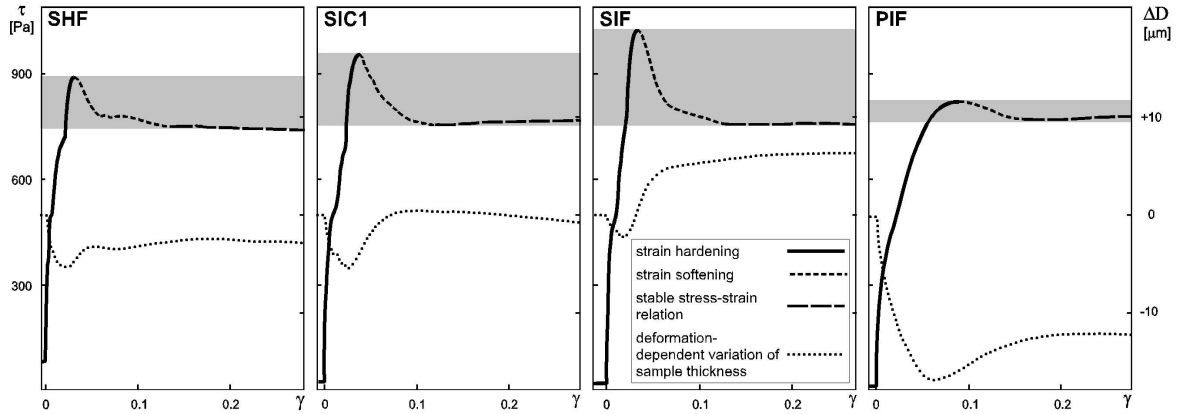


Figure 2.6: Plots of shear-stress (τ) and variation of sample thickness (ΔD) as a function of angular shear (γ) for different sands derived from ring-shear tests. The difference between peak and stable strength (grey area) is related to the initial degree of compaction of the tested sands.

The degree of compaction and strain hardening prior to pervasive deformation mainly depended on the filling technique. Well-compacted sifted sands only exhibited minor compaction during this stage (e.g. SIF in Fig. 2.6). In contrast, undercompacted poured sands showed a high degree of compaction (e.g. PIF in Fig. 2.6). In all sands, the onset of plastic deformation occurred before peak strength was reached. The well-compacted sifted sands showed substantial dilatancy during deformation, whereas the undercompacted poured sands only showed minor decompaction in the localised shear zone. Thus, sifted and poured sands have quite different decompaction characteristics. This resulted in nearly the same stable dynamic friction for all sands once the stage of stable sliding was reached. Moreover, three of the tested sands showed a slight strain hardening (SIC1, PIF) or slight strain softening (SHF) during more advanced stages of shearing.

In the ring-shear tester, basal shear tests of latex gum and sandpaper were only performed with the sands SIC2 and PIC2, which were also used in corresponding sandbox experiments (Tab. 2.2).

In contrast to the stress-strain curves of internal shear zones and basal shear zones in contact with paper, the stress-strain curves of basal shear zones in contact with latex gum and sandpaper did not show a significant decrease in shear stress after the initial failure. The shear stress increased continuously until the stable dynamic strength was achieved (Fig. 2.7). Consequently, peak basal friction did not exist between these basal materials and the sands. In contrast, the stress-strain curves of pre-sheared basal-shear zones were characterised by a remarkable increase followed by a decrease of the shear stress during initial reactivation. Therefore, the stable static friction was determined from these measurements. The stable static friction between the sandpaper and poured sand (0.62 ± 0.002) was slightly higher than that of the sandpaper relative to sifted sand (0.59 ± 0.002 ; Fig. 2.5 c and d, Tab. 2.2). In contrast, the stable dynamic frictions between sandpaper and the sifted and poured sands were nearly similar (0.56 and 0.58, respectively). This stable dynamic friction nearly matched the stable dynamic friction of internal shear zones. Al-

though the basal-shear zone between latex gum and sifted sand showed smaller values for both stable static friction (0.53 ± 0.02) and stable dynamic friction (0.47 ± 0.02) compared to the sandpaper, latex gum reached the highest basal friction of all basal materials with a smooth surface ever tested in the laboratory.

The stable dynamic strength between sandpaper and SIC2 was characterised by a load-dependence at minor normal stresses (< 1500 Pa), which was not observed for the stable dynamic friction of shear zones within sand. The former decreased exponentially with increasing normal load towards the stable dynamic friction (Fig. 2.8). This load-dependence is ascribed to the increased dilatation and the strong influence of cohesion at small normal stresses.

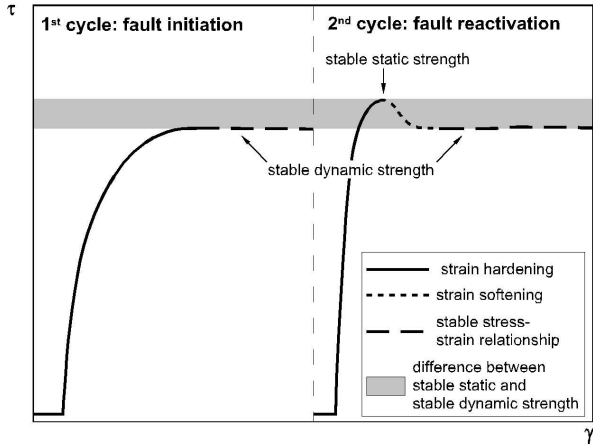


Figure 2.7: Schematic diagram of shear-stress (τ) as a function of angular shear (γ) of high-frictional basal materials (sandpaper and latex gum) in two load cycles. The postfailure strain-softening effect only occurs during reactivation of faults and not fault initiation.

The measurements reported here suggest that the filling technique has a major influence on peak internal friction, confirming the results of an earlier parameter study (Krantz, 1991). Furthermore, measurements in this study reveal that stable internal friction of the different sands is nearly uniform. Hence, I conclude that stable internal friction is not influenced by the method of filling the shear box. Changes in grain size and homogeneity cause only minor changes in the stable friction. Moreover, the sands showed no compaction-dependent variation of cohesion, as was the case for the sand used by Mulugeta et al. (1988; 1992). In addition, the results of

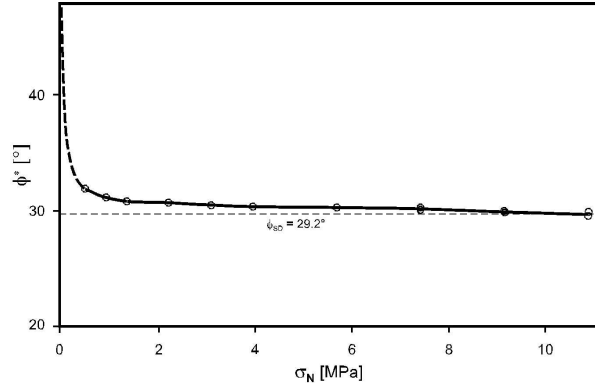


Figure 2.8: Effective basal friction angle ($\Phi^* = \arctan(\tau/\sigma_N)$; in the terms of Jaeger and Cook, 1969) as a function of normal stress (σ_N) shows the load-dependence of friction in a shear zone between sandpaper and SIC2 at small normal loads (Φ_{SD} – angle of stable dynamic friction).

the ring-shear tests reveal that sands typically used as analogue material show transient, deformation-dependent friction with elastic-plastic behaviour, as well as initial strain hardening and strain softening. The choice of the basal material has major influence on the stable dynamic basal friction, and is not so strongly influenced by the filling technique. Moreover, significantly high basal friction is only achieved with a rough basal material (sandpaper). Here, the dynamic stable strength is strongly load-dependent at small normal loads (< 1500 Pa).

2.4 Sandbox experiments: Basic parameter studies

2.4.1 The sandbox apparatus

All experiments presented in this study were performed with the modular 2D-sandbox apparatus of the analogue laboratory at the GFZ (Fig. 2.9). In the glass-sided box (width 20 cm), a conveyor belt is moved by an electric motor to converge an overlying sand layer or a wedge-shaped body towards the rigid backwall. Plane-strain deformation in the 2D-setup is guaranteed by perfectly-parallel glass panes and transport direction. These requirements minimise boundary effects and allow a careful monitoring of the experiments. The reproducibility of the experiments was tested in several test runs. These experiments also showed results comparable to those obtained in a similar experimental setup in the analogue laboratory at the Université Montpellier.

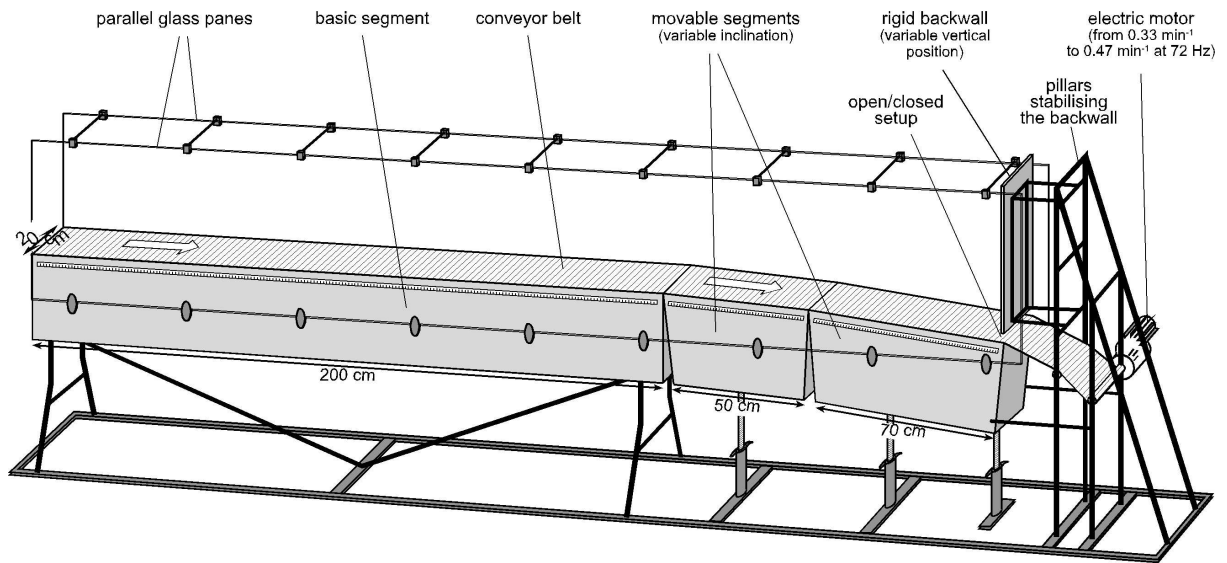


Figure 2.9: The 2D sandbox apparatus used for all experiments presented in this study.

According to the scaling rules (Hubbert, 1937 cf. Section 1.4.), the scaling of the sandbox experiments of this study to nature is calculated with the cohesion and material density by using equation 1.11 in Section 1.5, as the experiments of this study are performed under normal gravity. For the mean values of cohesion (marine sediments: 5–20 MPa; Jaeger and Cook, 1969; Hoshino et al., 1972; analogue materials used: 30–130 Pa) and density (marine sediments: $2300\text{--}2500\text{ kg m}^{-3}$; analogue materials used: $1500\text{--}1700\text{ kg m}^{-3}$), a scaling factor of $K = 10^5$ was calculated. This scaling factor has to be applied to the geometric dimensions as well as body, frictional and cohesive forces to obtain the proper scaling.

In each series of systematic experiments only one parameter per experiment was changed, to see the impact of this parameter. The parameters that were possible to vary in this experimental setup were:

1. geometric parameters:

- *basal dip*: moveable apparatus segments of 50 and 70 cm length allowed variations in the basal dip from 0 to 10° . In this study, systematic variations of the basal dip were not investigated. Therefore the basal dip was held constant within one series of experiments. The basal dip in one series was in accordance with the basal dip observed in the natural system (i.e. in-

clination of the subducting plate), which was simulated (Chapter 3, 4).

- *initial wedge geometry*: The preparation of different initial wedge geometries was only limited by the angle of repose of the analogue material used. Except for the basic parameter studies, the initial geometry of the experiments were chosen to be close to the geometry of a wedge in steady state to minimise the adjustment stage (cf. 1.3).
- *thickness of incoming sand-layer*: The thickness of the incoming sand-layer was varied to investigate its influence on mass-transfer modes.
- *length of incoming sand-layer*: The length of the incoming sand-layer was limited by the length of the conveyor belt. This parameter controlled the total throughput of material in one experiment. Low material-transfer rates required a larger throughput to produce significant changes in the experiment. In this study, the experiments used conveyor belts of 2–10 m length.
- *output of material*: The rigid backwall could be lifted to open a ‘subduction window’ (cf. Section 1.5). In this study, a setup with an open ‘subduction window’ will be named an open setup. Other experiments show that an open setup could

cause significant changes of the internal kinematics and mass-transfer modes, with respect to those performed in a closed setup (cf. Section 1.5; Kukowski et al., 1994; Gutscher et al., 1998b). In the experiments of this study, an open setup was used only to allow a net negative mass balance, but without changing the internal kinematics of the wedge (for further information see Section 4.2).

2. mechanical properties:

- *properties of the granular material:* The internal material properties such as angle of friction, cohesion and density can be changed by using different granular materials. In this study, the internal friction was varied systematically during the series of the basic parameter investigations (Section 2.4.3). In the other series which were concerned with the mass-transfer modes at the Chilean Margin (Chapter 3 and 4), only one sand (SIC2) was used to simulate the brittle crust. Other materials were only used, when changes of the mechanical properties in the forearc setting in nature were also evident.
- *basal material properties:* Both the basal friction and the basal roughness were systematically varied in the experiments of this study, to simulate the different mechanical properties of the plate interface in nature.
- *velocity:* As the deformation behaviour of the material used is not time-dependent, the velocity of the conveyor belt of about $1\text{-}4\text{ cm min}^{-1}$ does not influence the experimental results. Nevertheless, large experiments were done at smaller velocities to avoid overstress of the apparatus.

The experiments were monitored to obtain data for analysis of wedge and fault geometry, kinematics, displacement field, and mass balance. Therefore, thin marker layers and triangular-shaped markers of coloured sand were incorporated within the incoming sand-layer, sand wedge, and backstop to enable observation of deformation structures and particle paths. The coloured sand had a slightly higher cohesion (120 Pa), and nearly the same peak internal friction ($\mu_{PI} = 0.7$) as the sifted sands. Tests established that a small volume of sand, with

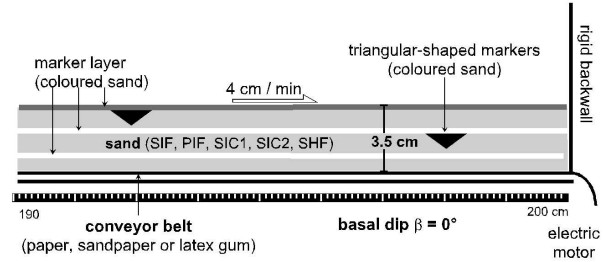


Figure 2.10: Setup of the sand box experiments of the basic parameter study. Only the tested sands were varied between experiments in the first series. In the second series only the basal material was changed.

properties differing from the bulk sand properties, has no influence on the fault geometry and kinematics of the sand wedge.

A digital video camera and a reflex-lens camera with fixed lateral views documented the experimental runs. Photographs were taken on every 10 cm conv. The video camera recorded continuously. The video helped to determine the velocity of deformation processes and the activity of faults. The photographs were digitised with a CAD-system with respect to the wedge geometry, marker layers, fault geometries, and position of the triangular-shaped markers. These line drawings were used as database for further analysis (Appendix).

Interpretations, based on the comparison of results of different experiments, only lead to reliable results, when the initial adjustment phase of the experiments was ignored. The initial adjustment phase is characterised by strong changes of wedge taper and kinematics compared to those observed in the later steady-state phase (cf. Section 2.4.3).

2.4.2 Experimental setup of the basic parameter studies

Two series of scaled sandbox experiments with a highly-idealised setup were performed to study the influence of material properties on the kinematics, growth mechanisms, and internal deformation patterns of sand wedges. The sandbox employed for all basic parameter studies had a length of 2 m and a basal dip of 0° (Fig. 2.10). The incoming sand-layer had a thickness of 35 mm.

In the first series of experiments, only the sand was varied between four experiments (Tab. 2.1). The criteria to select the sands for the sandbox experiments were: filling technique, grain size, distribution of grain size, as well as peak internal friction. Because different sands overly the conveyor

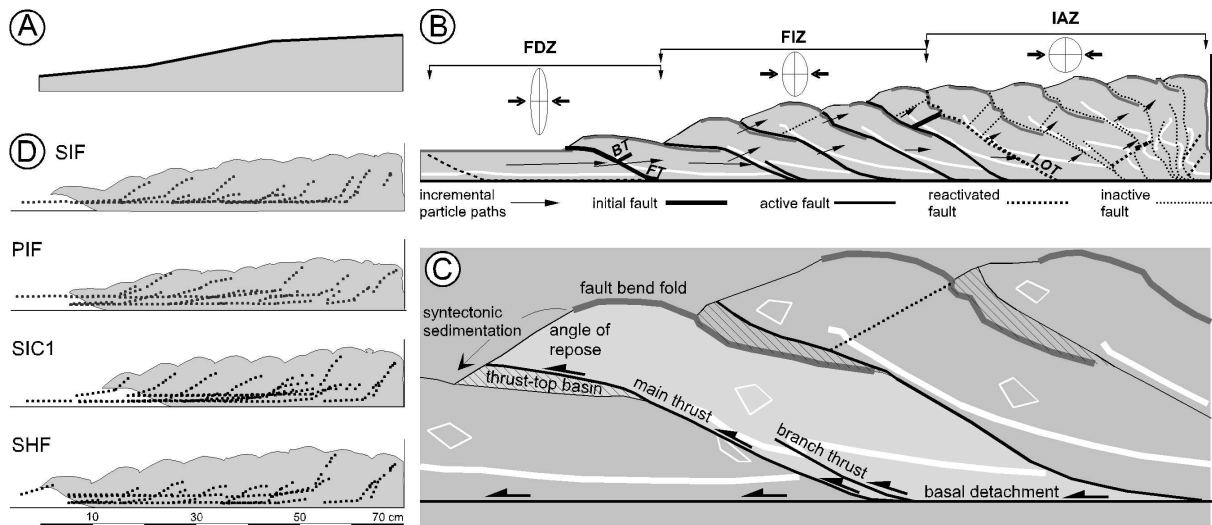


Figure 2.11: Common features of the convergent sand wedges consisting of different sands. a) The overall wedge geometry is characterised by three domains with different surface slopes. b) The kinematic segments (FDZ – frontal-deformation zone; FIZ – frontal-imbrication zone, IAZ – internal-accumulation zone) show unique internal kinematics, horizontal shortening rates and incremental particle paths (FT – forethrust; BT – backthrust, LOT – leading out-of-sequence thrust). c) Internal kinematics of an individual thrust slice with formation of a subsequently overthrust ‘thrust-top basin’. d) Total displacement fields in the sand wedges do not show any substantial difference.

belt (paper), which was held identical in all experiments, this also resulted in a relative change of the basal properties.

In the experiments of the second series the roughness of the basal material was varied, whereas the same sand (SIC2) was always used. Sandpaper was used as material with a high roughness. The corresponding material with low roughness was latex gum, as this material, among the materials with a smooth surface, showed the smallest difference in the basal friction compared to sandpaper.

2.4.3 1st Series: Variation of internal wedge properties

2.4.3.1 Experimental results

In the following, the common and contrasting features of the sand wedges of the first series are emphasized to evaluate the influence of the varied properties of the sand. The common features indicate the general evolution of a convergent sand wedge in a frontally-accretive mode, whereas the contrasting features refer to the influence internal friction has on the kinematics and dynamics of convergent sand wedges.

Common features

The shortening of the incoming sand-layer resulted in a sand wedge with fore- and backthrusts in a frontally-accretive mode. A steady-state wedge geometry was achieved after all the segments of the wedge, which are defined in this section, were assembled. In all experiments, the steady-state wedge shape was characterised by up to three domains, each with a different surface slope (from the wedge tip to the rear; Fig. 2.11 a):

- i) the frontal surface slope changed its inclination (i.e. transient surface slope), but never reached the steepness of the surface slope of the adjacent segment,
- ii) a steeply-inclined surface slope with constant inclination over time, and
- iii) a shallow and constant surface slope. The boundary between the latter two segments was in some cases indistinct, or even formed a gradual transition zone.

These three domains coincided with domains within unique structural styles and, in particular, with different kinematics (Fig. 2.11 b):

- i) In the *frontal-deformation zone* (FDZ), the incoming material formed new thrust slices.

	experiment		amount of FIZ segments	taper of FIZ	taper of IAZ	slice length/ thickness	thrust displacement/ slice length
	wedge material	basal material		[°]	[°]		
PIF	paper		2	7.8 ± 0.4 5.2 ± 0.3	...	2.8	0.22
SHF	paper		1	7.8 ± 0.7	-3.9 ± 0.3	4.5	0.41
SIC1	paper		1			4.1	0.43
SIF	paper		1	11.3 ± 0.7	2.7 ± 0.6	4.6	0.41
SIC2	latex gum		0	...	10.5 - 12.5	5.7	0.5
SIC2	sandpaper		0	...	13.5 - 20.5	5.7	0.73

Table 2.4: Quantitative results of the sandbox experiments concerning the internal and basal material properties (the systematically-varied materials are in bold type; for nomenclature see Tab. 2.1)

Such a thrust slice belonged to the FDZ until it was incorporated into the adjacent (more steeply tapered) wedge segment. In the first step of initial faulting, a pair of conjugate fore- and back thrusts broke through the incoming sand-layer. After 1–3 cm conv., the back-thrust ceased, when it reached the tip of the previously-formed thrust slice. Subsequently, the hinterland-dipping thrusts were the dominant faults. This segment included up to 3 imbricates.

- ii) The *frontal-imbrication zone* (FIZ) is located next to the FDZ. The FIZ contained several thrusts, all of which were continuously active, maintaining a constant surface slope as the wedge volume increased. The more internal forethrusts in the FIZ were back-rotated during piggy-back translation.
- iii) In the *internal-accumulation zone* (IAZ), the adjustment of the wedge geometry to the continuously-increasing wedge volume was produced by occasional reactivation of some or all of the earlier-formed thrusts. This deformation rather caused vertical uplift than horizontal shortening. Fault planes were further back-rotated and eventually became inactive. The IAZ was separated by the leading out-of-sequence thrust (LOT) toward the FIZ.

In individual thrust slices, most deformation took place along the base (Fig. 2.11 c). However, a small component of internal strain occurred in two strain patterns:

- localised shear displacement along distinct branch thrusts, and
- diffuse intergranular deformation.

In all experiments, bulk particle paths were nearly identical (Fig. 2.11 d). Incremental analysis of the displacement field exposed three well-defined domains of mass transfer, from the wedge tip to the rear, which correlated to the domains of similar surface slope and internal kinematics described above (Fig. 2.11 b). These incremental displacement fields also demonstrate that the wedges were kinematically segmented. Material which moved through the FDZ showed the largest horizontal displacement and most variable uplift (i.e. most variable inclination of particle paths). As material moved into the FIZ, horizontal displacement diminished, with only moderate uplift, where both became continuously smaller toward the rear of this domain. In the IAZ, material velocities slowed down further. This zone comprised the smallest horizontal displacements and the steepest inclination, when compared to the other domains.

Contrasting features

Wedge tapers were determined by measuring the slope of the line linking the tips of the thrust sheets (wedge taper = α , since $\beta = 0^\circ$) of the three kinematic segments every 10 cm conv. The resulting average wedge taper of the surface slopes were subsequently analysed.

Systematic variation in wedge geometry of the different sand wedges was only observed in the surface slope of the FIZ (Fig. 2.12, Tab. 2.4). Here, the surface slopes varied between 7.8 and 11.3° . In addition, the PIF surface slope showed a decrease from 7.8° at the front to 5.2° at the rear. The SIC1 surface slope had a large error in its mean value. This error was caused by measuring the taper in this experiment at different stages of new imbricates incorporation. In the other experiments (SIF, PIF, SHF), taper measurements were always performed

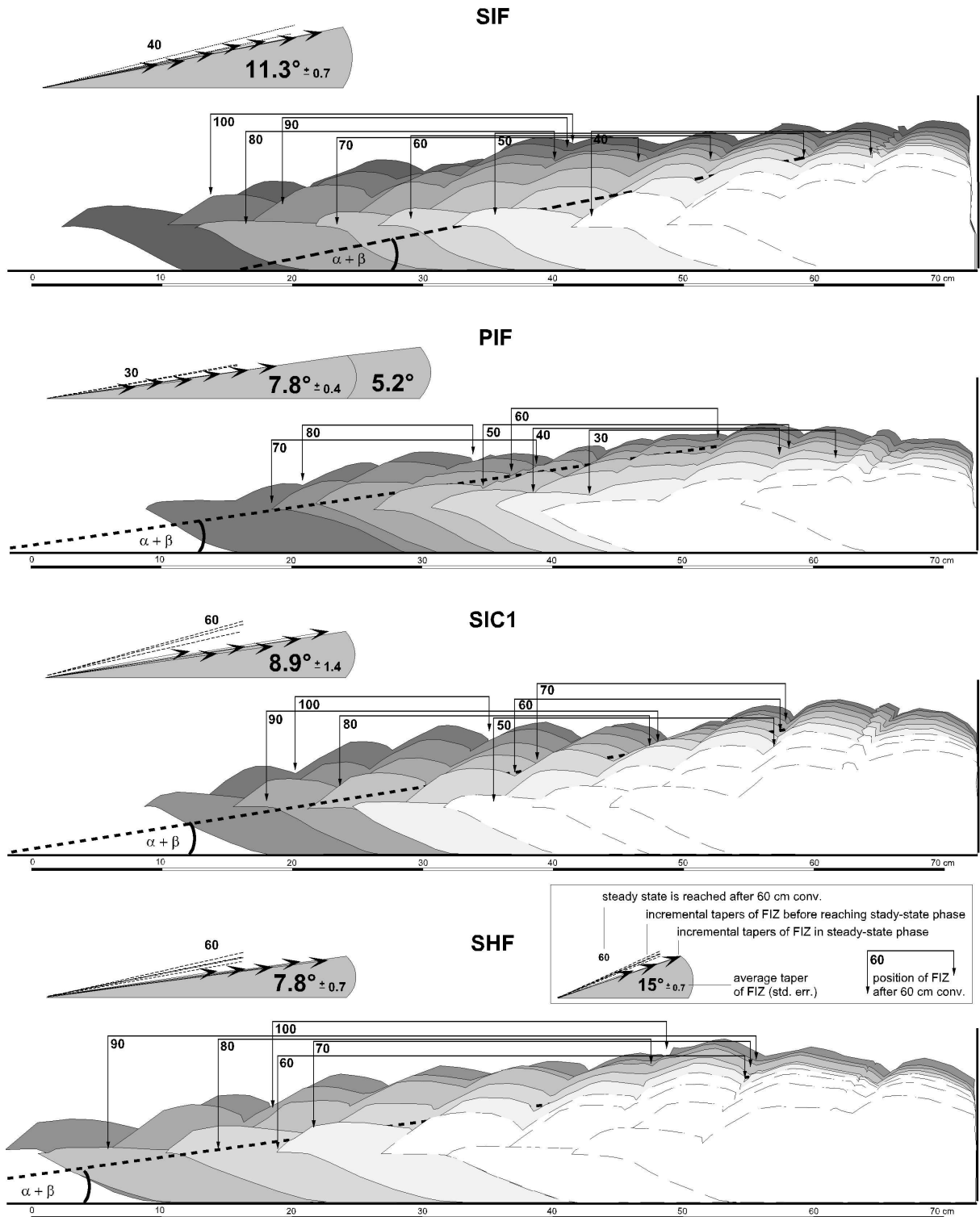


Figure 2.12: Wedge geometry plotted after every 10 cm conv. Thin dashed lines indicate the geometries before the wedge has reached steady-state stage; solid lines indicate the steady-state geometries. The wedge taper of the frontal-imbrication zone during its evolution was determined from these diagrams. The sand wedge that consists of PIF, shows two continuously deforming domains with differently inclined surface slopes during the last two stages of convergence.

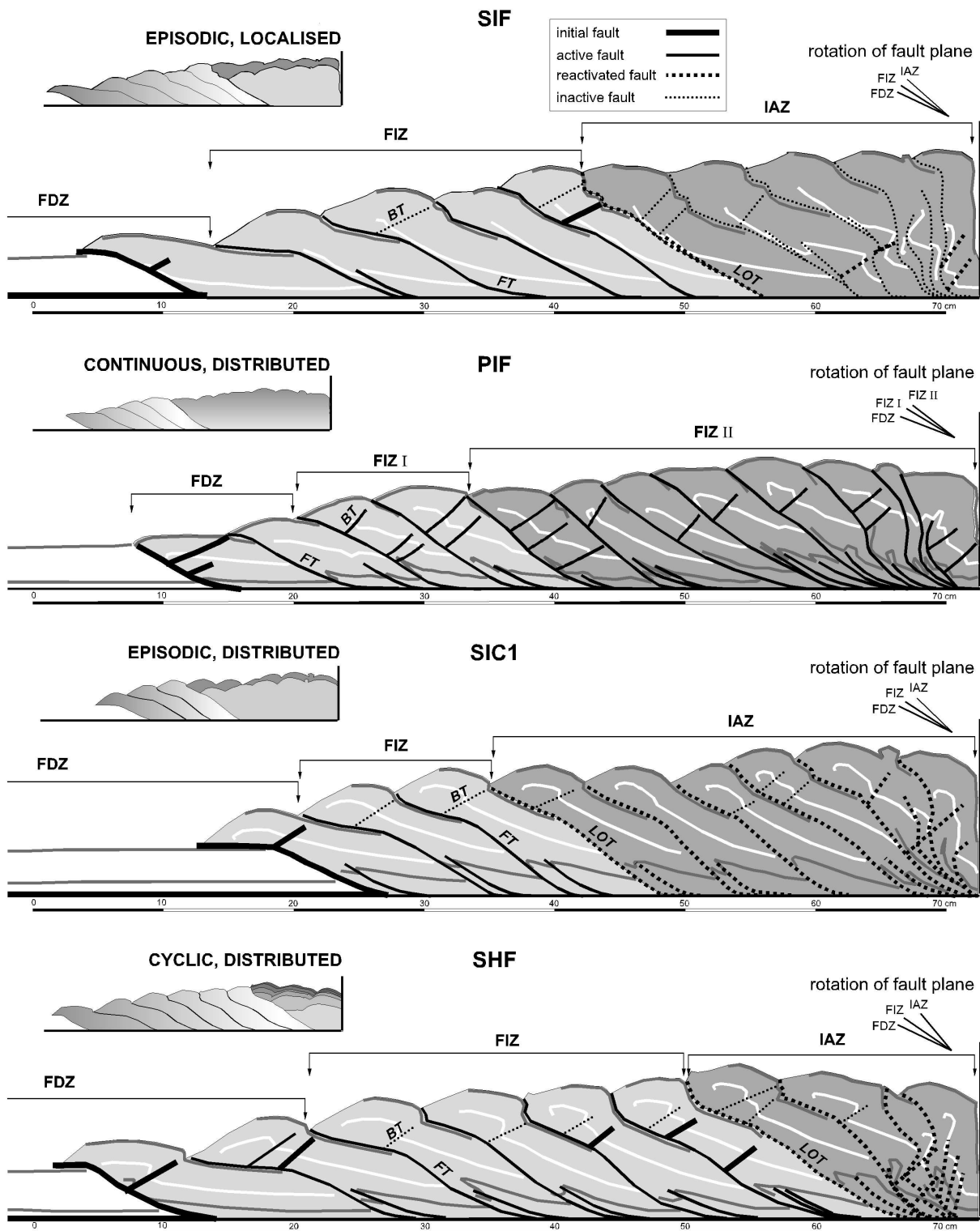


Figure 2.13: Kinematic features of the convergent sand wedges. The kinematics and modes of wedge adjustment (see sketches on the left) of the internal-accumulation zone (IAZ) are different in each experiment, whereas the kinematics of the other wedge segments are similar (FDZ – frontal-imbrication zone, FIZ – frontal-imbrication zone, FT – forethrust, BT – backthrust).

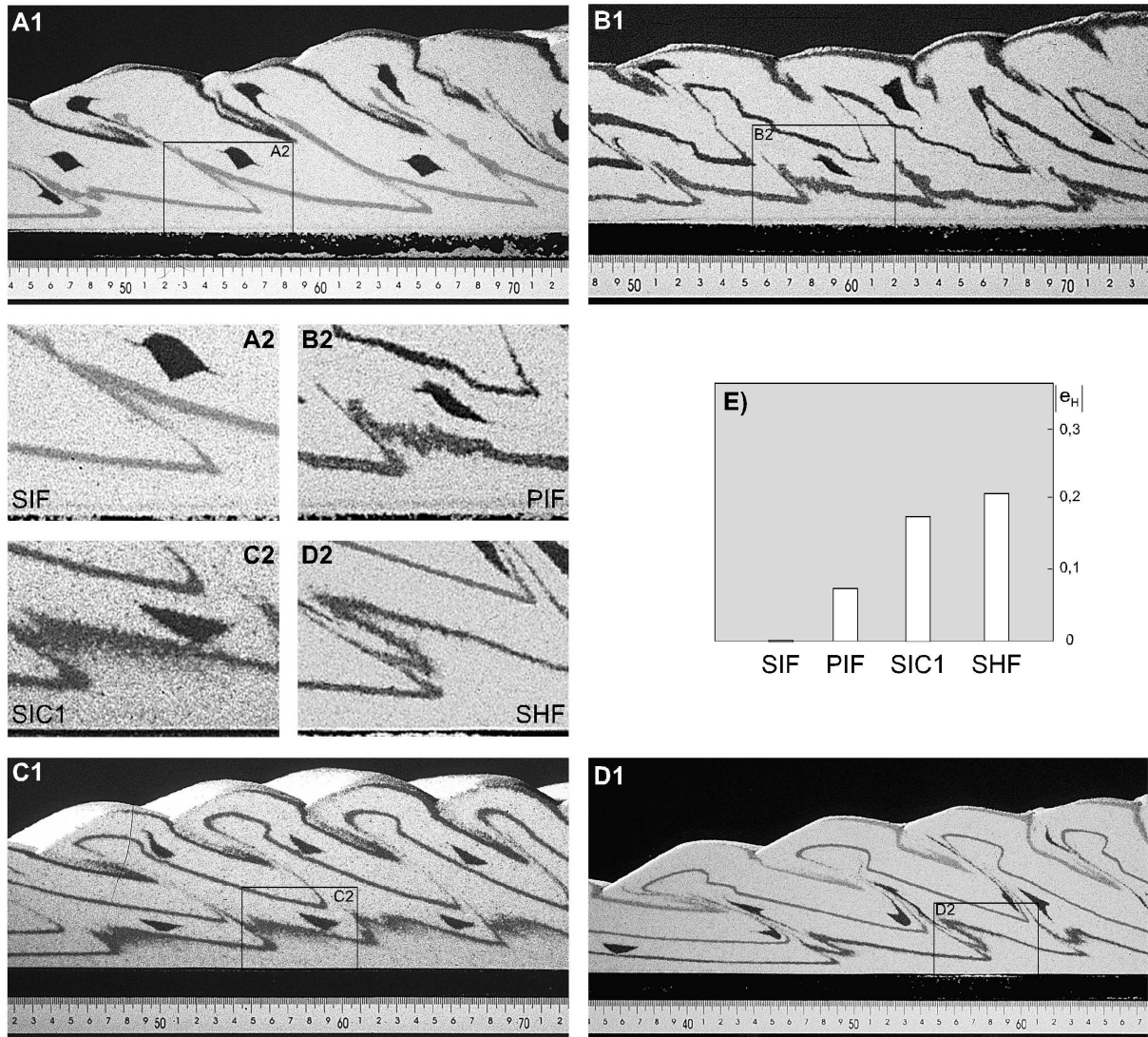


Figure 2.14: Detail (a1-d1 not to scale; a2-d2 at the same scale) shows different degrees of diffuse deformation within the imbricates. The photographs of the different experiments show (a-d) the total diffuse deformation accumulated in the frontal-deformation zone (FDZ) and the frontal-imbrication zone (FIZ). e) Horizontal shortening (e_H) due to diffuse intergranular deformation of an imbricate during its evolution in the frontal-imbrication zone.

at the same stage of imbricate incorporation, which prevented this ambiguity.

In addition, the shortening required to reach steady state varied from one experiment to another. In the experiment with PIF, the steady-state phase was attained most rapidly (after 30 cm conv.), whereas the experiments with SIC1 and SHF reached this stage only after 60 cm conv.

The main difference in the kinematics of the different sand wedges was observed in the IAZ (Fig. 2.13). The faults were either reactivated occasionally (SIC1, SHF), or were persistently in-

active except for reactivation of the LOT (SIF; Fig. 2.13). This different kinematic behaviour of the IAZ caused different modes of wedge adjustment. Occasional reactivation of all the out-of-sequence thrusts (SIC1, SHF) led to an episodic or cyclic wedge adjustment, which was also related to distributed deformation in the IAZ. Reactivation of only the LOT, without segment-internal deformation (SIF), led to localised and episodic wedge adjustment. The PIF sand wedge lacked an IAZ and a well-defined slope segmentation. Here, all thrusts were continuously active, and, accordingly, showed

no rearward limit of the FIZ. The FDZ and FIZ differed in only one kinematic aspect, observed in all sand wedges: Only the sand wedge, which consisted of poured sand (PIF) was capable of forming several initial backthrusts within one thrust slice in the FDZ. The other sand wedges, which consisted of sifted sand, showed only one initial backthrust per imbricate. More than one backthrust per imbricate in sifted-sand experiments only occurred in the FIZ during the formation of fault-bend folds above foot-wall ramps.

The different sand wedges also showed variable imbricate geometry. The average ratio of the length of the thrust slices to their thickness increased proportionally with the peak internal friction and ranges between 2.8 in the sand wedge with the smallest peak internal friction (PIF), and 4.6 in the sand wedge with the highest peak internal friction (SIF; Tab. 2.4). The average ratio of thrust displacement to thrust-slice length suggests a similar positive dependency on peak internal friction, although the thrust-displacement ratio was not as sensitive as the slice-length ratio (Tab. 2.4). The sifted sands with high peak internal friction were capable of producing a large thrust-displacement ratio (0.41–0.43), whereas this ratio was small (0.22) in case of the poured sand (PIF), which was characterised by low peak friction.

The sand wedges also differed with respect to the internal strain of the thrust slices. Comparison of strain between the experiments requires a segment, which is in steady state and shows the same kinematics in all experiments. Therefore, the only segment, which is suitable for this strain comparison, is the FIZ. The internal strain varied with respect to localisation and amount (Fig. 2.14): In well-compacted sands with high internal friction (SIF), strain was exclusively accumulated by localised deformation at distinct branch thrusts (Fig. 2.14 a). In all other sands, deformation occurred by a combination of localised strain and diffuse, intergranular deformation (Fig. 2.14 b-d). In addition, the amount of this diffuse deformation differed (Fig. 2.14 e). It is important to notice that the initially undercompacted PIF material showed only minor diffuse deformation in the FIZ, whereas the well-compacted sifted sands SHF and SIC 1 exhibited substantial diffuse deformation in this segment. In contrast to this observation, the total amount of diffuse deformation (i.e. the diffuse deformation accumulated in the FDZ and FIZ) increased with a decrease of the peak internal friction.

Conclusions of the experimental results

The results show that convergent sand wedges are kinematically segmented. On the base of geometrical and kinematical analysis, I define three segments in which convergent sand wedge are typically divided (from the front to the rear):

1. The FDZ is characterised by continuous slip of its thrusts during the underthrusting of the incoming sand-layer or the initiation of a new frontal thrust. This results in a constant and high material flux through this segment. The FDZ taper is transient, although it never attains the steepness of the FIZ.
2. Also, the FIZ shows continuously-active thrusts. However, new thrusts are not initiated here. The FIZ attains the largest taper of all segments, which keeps constant during material addition.
3. Material is discontinuously added to the IAZ by intermittent slip of the steeply back-rotated thrusts. In this small-tapered segment, initiation of thrusts does also not take place.

This kinematic segmentation suggest that each part of convergent sand wedges is in a certain state of stress. I investigate this in the next section.

2.4.3.2 Mechanical analysis

Quantitative analysis of Coulomb Wedges based on the critical-taper theory has been performed using two strategies:

- To determine the general state of stress (critical, sub-critical or stable; cf. Section 1.3), the friction of the wedge material and the basal interface needed to be known or assumed (Dahlen, 1984; Mulugeta, 1988; Adam, 1996; Adam and Reuther, 2000).
- Unknown material properties (either the friction of wedge material or that of the basal interface) are determined by assuming a critical state of stress (Davis and von Huene, 1987; Lallemand et al., 1994b; Kukowski et al., 2002).

However, the material and kinematic analyses presented in this chapter (cf. Section 2.3.2 and Section 2.4.3.1) show that such a critical-taper analysis can not apply to the sand wedges documented here: The actual frictional strength, which controls

the wedge geometry and the state of stress are unknown, as the friction of the sand and the basal interface change during shear zone formation (from peak friction to stable dynamic friction). Also, the kinematic segmentation indicates that a general homogeneous state of stress can not be assumed for the whole wedge. Therefore, I used another strategy than described above, to identify the state of stress in the individual wedge segments: I used the geometrical and kinematic features of the identified segments, to predict the most reasonable state of stress for each of them. Then, I applied a critical-taper analysis to identify the actual frictional strengths (internal and basal), which control the taper of a segment assumed to be in the critical state of stress. Finally, the previous assumption was tested by plotting the observed kinematical and geometrical features of these segments in Mohr Diagrams. The following states of stresses were assumed for the individual segments in this analysis:

1. The FIZ is assumed to be in a critical state of stress, since its constant and steep taper during continuous activity of the thrusts indicates the adjustment of the predicted threshold of a critically-tapered wedge. The friction of the fault material was possibly near the stable dynamic internal friction, as it was continuously deformed. Also, the basal interface below the FIZ was continuously active, suggesting that stable dynamic friction was also attained here.
2. The transient FDZ taper and continuous failure of the thrusts suggested a non-critical state of stress in this segment, as these indicated that an equilibrium of forces is not achieved, which would represent a critical state. As the FDZ taper is less than that of the FIZ, I assume that the FDZ is in a sub-critical state of stress. Moreover, the occurrence of thrust initiation and continuous deformation indicates that both peak and stable dynamic friction control the evolution of this segment.
3. Repeated reactivation of thrusts and the constant IAZ taper suggest that the IAZ exceeds the threshold of a critically-tapered wedge and is in a stable state of stress. However, this suggestion does not explain the small IAZ taper (for further discussion see below). The absence of thrust initiation indicates that the differential stress does not exceed the peak frictional strength.

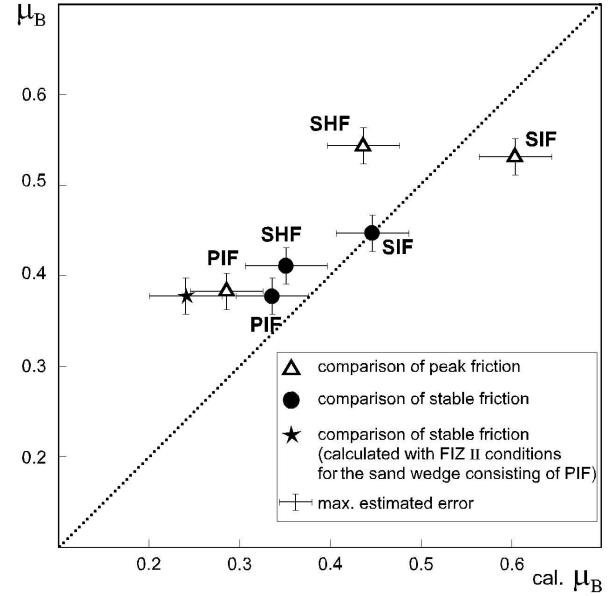


Figure 2.15: Comparison of calculated values of basal friction ($\text{cal.}\mu_B$), which employ equation 1.7 with measured values of basal friction (μ_B). Dotted line represents the line of best fit of measured and calculated values.

These assumptions suggest that only one segment of the wedge (FIZ) is critically-tapered and suitable for quantitative critical-taper analysis. Thus, I attempt to evaluate the hypothesis, which is supported by the observed fault kinematics of the FIZ: Here, the internal and basal friction in the stable dynamic state should control the taper. Hence, a critical-taper analysis was performed on the FIZs of the sand wedges made of SIF, PIF, and SHF. The wedge which consisted of SIC1 could not be used for the critical-taper analysis, as the error of the measured wedge taper was too large to expect a reasonable result (cf. Section 2.4.3.1).

Critical-taper analysis of the FIZ

The critical-taper analysis made use of the results from the previous analysis and from measurements in the Hubbert-type shear box (Tab. 2.1 and 2.3). The stable friction measured with the static approach was corrected by the empirically-derived value from dynamic measurements with the ring-shear tester (cf. Section 2.3.2) and used as stable dynamic friction.

The critical-taper equation (1.7, Section 1.3) allows the iterative calculation of the friction value of the basal detachment below the FIZ, as all other variables are given. Basal friction values were calcu-

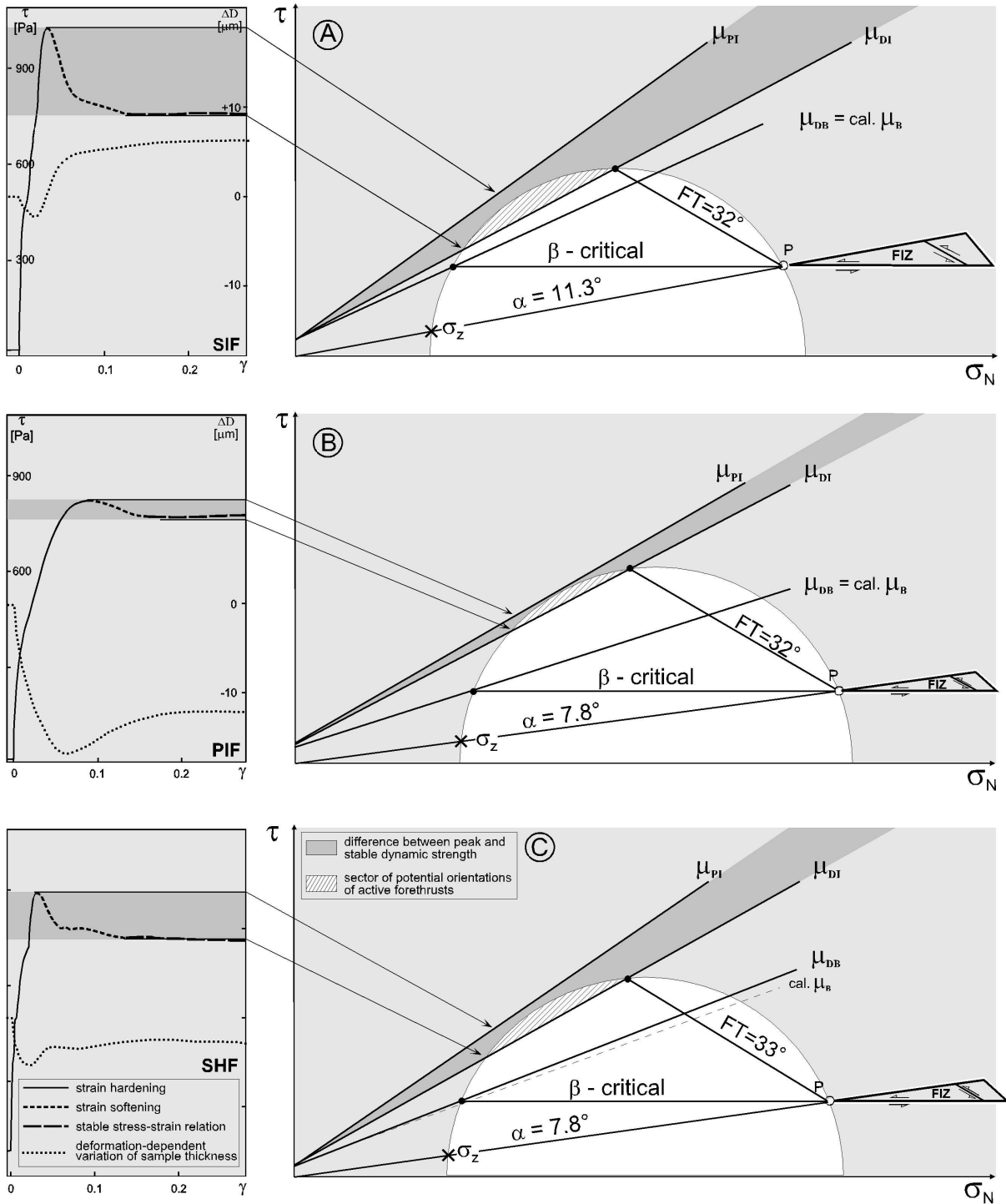


Figure 2.16: Mohr Diagrams show the state of stress required for the critically-tapered frontal-imbrication zone (FIZ) at the depth z (σ_z) in the sand wedges consisting of a) SIF, b) PIF, c) SHF. The constraints used for construction are the failure curves as measured for peak internal friction (μ_{PI}), stable dynamic internal friction (μ_{DI}) and for stable dynamic basal friction (μ_{DB}), the wedge taper ($\alpha + \beta$) measured in the sandbox experiments, and the dip of the trailing internal forethrust (FT) of the FIZ. The Mohr Diagrams are accompanied by the stress-strain curves of the respective materials to illustrate the frictional strength development in the shear zones during deformation under the load conditions of the FIZ. (cal. μ_B – basal friction calculated with stable dynamic internal friction, P – pole; τ – shear stress; σ_N – normal stress; γ – angular shear).

lated assuming first stable dynamic internal friction and then peak internal friction and were then compared with the basal friction values obtained from the shear-box tests.

Analysis shows that only the stable dynamic friction (basal and internal) lead to results reasonably consistent with the experimental observations (Fig. 2.15). Here, the wedge that consisted of SIF showed a perfect match between the measured and calculated basal friction. In contrast, the measured absolute values of basal friction slightly exceeded the calculated absolute values of the PIF and SHF wedge. Under consideration of the estimated maximum error (from measurements of surface slope and friction), a minor difference between measured basal friction and calculated basal friction (< 0.01) was still observed for the wedge, which was built of SHF.

Depiction of the above described relationship in Mohr Diagrams (Fig. 2.16) shows the stresses required for contemporaneous active slip at the wedge base and on the internal thrusts of the FIZ, i.e. the critical state. The constraints, which were used for construction, were the failure curves as measured (for peak and stable dynamic internal friction of wedge material, and its base), the wedge tapers measured in the sandbox experiments, and the dip of the trailing internal thrust of the FIZ (FT in Fig. 2.16). This part of the FIZ is a key for understanding the mechanical conditions for deformation, since its analysis illustrates the extreme conditions under which critical behaviour occurs.

As inferred from the results shown in Fig. 2.15, the SIF wedge (Fig. 2.16 a) shows a very close match between the measured and calculated basal friction. This result is derived with the assumption that bulk wedge strength in this part of the FIZ is determined by the stable friction of the trailing active thrust. To maintain slip on this thrust, after its back-rotation, the differential stress must increase. In this case, thrusts of various orientations can be reactivated, if the material has reached stable sliding conditions. However, the peak strength of unfailed SIF material was not reached, and therefore, no new structures were formed. This example can, accordingly, be seen to support the aforementioned hypothesis of stable friction being the key property controlling critical taper.

Since the PIF experiment showed a continuously-decreasing taper across its FIZ, I separately analysed the frontal and rear part (see next section). The frontal part showed similar behaviour to the SIF wedge with respect to friction dependence, and

with respect to fault reactivation without formation of a new fault generation (Fig. 2.16 b). Closer inspection, however, revealed minor internal deformation of the imbricates of the PIF material during active fault slip in the FIZ. Therefore, wedge adjustment in the FIZ was achieved by internal localised fault slip and minor diffuse grain-scale deformation (cf. Fig. 2.14). As shown by the critical-taper analysis, however, the wedge taper seemed to be also controlled by the frictional strength at stable-sliding conditions.

Whilst the stress-strain curve of the SHF material was similar to that of the SIF material, the sand wedge consisting of SHF showed substantial diffuse deformation in the FIZ (cf. Fig. 2.14). Similar to the result shown in Fig. 2.15, the Mohr Diagram demonstrates a minor difference between the calculated and the measured basal friction for stable sliding (Fig. 2.16 c).

The mismatch between the measured and calculated basal friction (PIF, SHF) was proportional to the increase in diffuse deformation. The differential stress in both of these wedges was close to the peak internal friction (Fig. 2.16 b and c). Therefore I suggest, that in these cases the differential stress reached the frictional strength at which the sand diffusely deforms prior pervasive failure. Accordingly, sands with a large difference between peak and stable dynamic frictional strength (e.g. SHF) should show a larger mismatch than sands in which peak and stable dynamic frictional strength are nearly similar (e.g. PIF): in the former the phase of diffuse deformation is only reached, if a significantly high differential stress acts on the material. The stress-strain curves of PIF, SHF, and SIF support this suggestion (Fig. 2.16 b and c). The latter showed the largest difference between peak and stable dynamic frictional strength. Consequently, diffuse deformation of this sand would indicate the highest differential stress. However, such a high differential stress was not attained in the wedge consisting of SIF, as here diffuse deformation did not take place. This interpretation is supported by the Mohr Diagram (Fig. 2.16 a), in which the Mohr Circle is well below the failure of undeformed SIF.

The critical-taper analysis of the FIZs consisting of PIF and SHF shows that the basal shear stress is slightly higher than the shear stress required for the critical state of stress (Fig. 2.15). This suggests that the FIZ of these sand wedges are in a 'nearly critical state of stress', as continuous material addition permanently perturbs their attainment of the 'exactly critical state'. However, this increase of basal

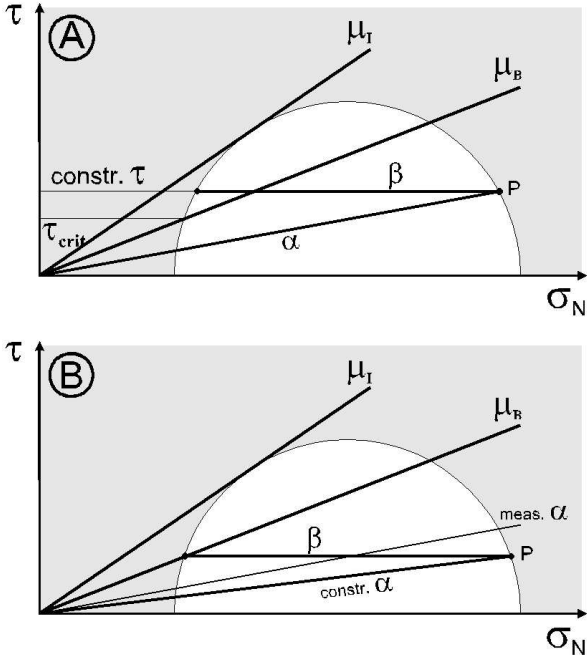


Figure 2.17: Generalised Mohr Diagrams of a subcritically-tapered wedge plotted under the assumption of a) critical geometry; b) critical basal shear stress. (μ_I – internal friction, μ_B – basal friction, α – surface slope, β – basal dip, constr. – constructed, meas. – measured, τ – shear stress, σ_N – normal stress, P – pole).

shear stress can not be validated, as it is within the error.

I conclude from the analysis of the FIZ of all wedges that its taper and internal kinematics are predominantly controlled by the friction of faults that have reached the state of stable sliding. However, with increasing diffuse deformation in the critically-tapered segment, mechanical critical-taper analysis leads to results which are inconsistent with frictions measured with the standard measuring-techniques applied here. Peak frictional strength does not directly influence the state of stress of the FIZ, as the differential stress does not exceed it. As the observed kinematics are fully explained by the assumption of a (nearly) critical state of stress, it is used for further interpretations.

Interpretation of the FDZ

In the critical-taper theory, the subcritical state of stress as assumed for the FDZ, is described by a basal shear stress, which overcomes that required for a critically-tapered wedge. Thus, a wedge in a subcritical state of stress has to enlarge its taper

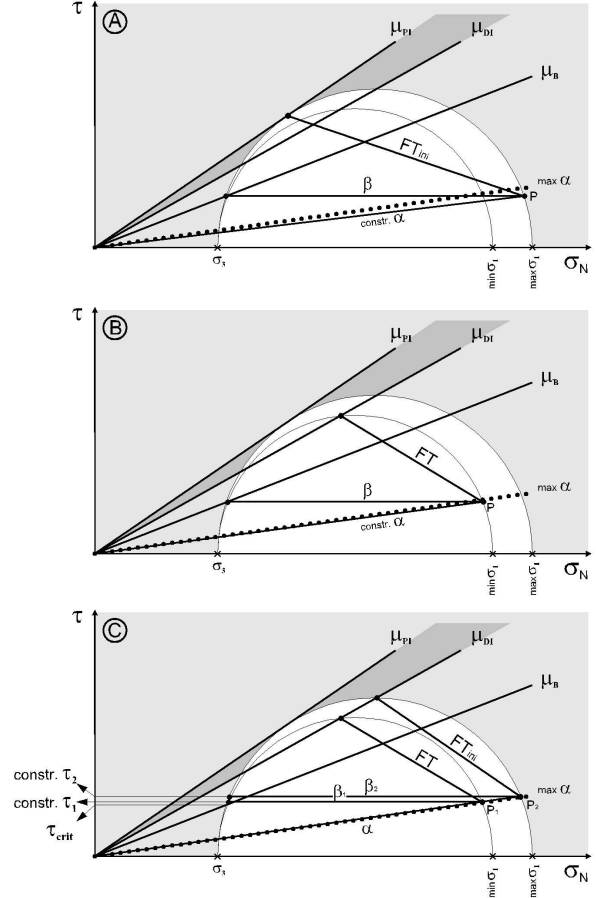


Figure 2.18: Qualitative Mohr Diagrams showing the extreme states of stress of the FDZ: a) the maximum differential stress is reached during fault initiation, b) the minimum differential stress is reached during the underthrusting phase, c) the FDZ attains its largest taper (μ_{PI} – peak internal friction, μ_{DI} – stable dynamic internal friction, μ_B – basal friction, α – surface slope, β – basal dip, FT_{ini} – initiated forethrust, FT – trailing forethrust, constr. – constructed, τ – shear stress, σ_N – normal stress, σ_1 – maximum principle stress; σ_3 – minimum principle stress).

by thrusting (cf. Section 1.3). In general, two types of Mohr Diagrams describe the subcritical state of stress, depending on the assumed input parameters (Fig. 2.17):

1. The measured taper is assumed to be critical and is used to determine the pole: The orientation of the basal interface intersects the Mohr Circle above the critical point (i.e. the intersection of Mohr Circle and failure curve of the basal interface). This shows directly that the shear stress acting on the basal interface ex-

ceeds that, which is required for the critical state of stress, such as required for the subcritical state (Fig. 2.17 a).

2. The basal shear stress is assumed to be critical and is plotted at the critical point: The taper constructed in the Mohr Diagram is lower than that measured. This shows that the assumed basal shear stress is too low for this wedge, as the wedge taper increases with higher basal shear stresses. Therefore, this plot shows indirectly that the wedge is in a subcritical state (Fig. 2.17 b).

The FDZ with its non-constant deformation behaviour (i.e. episodic thrust initiation, strong back-rotation of thrusts, transient taper) showed all features of a segment in a subcritical state of stress and does not provide the data to perform a quantitative analysis. Nevertheless, I tested the reliability of this hypothesis in qualitative Mohr Diagram, which only considers the relative relationship between the observed kinematic and mechanical conditions, and results in relative differential stresses. It was not possible to directly determine the maximum FDZ taper, and therefore the constructed tapers of the FDZ, in its extreme states of stress, were compared with the taper of the FIZ. This is allowed, since the maximum measured FDZ taper is close to FIZ taper and the relative differential stress for the critical state of stress in the FIZ is the minimum relative differential stress for the whole wedge. A reduction of the relative differential stress beyond that required for the critical state conflicts with the observation of continuous deformation in the FIZ and FDZ. For the clarity of the following argumentation, I use only one state of basal friction and do not distinguish between different states of basal friction (peak or stable dynamic). This is possible, as test plots have shown that in this qualitative analysis the difference of 30% between these states does not change the general statement of this interpretation. However, in quantitative critical-taper analysis, this simplification would lead to wrong results, therefore this distinction is made again in Section 2.4.4.

The geometrical and kinematical features observed in the FDZs of all the sandbox experiments, indicate that the state of stress in the FDZ ranges between three extreme cases:

- In the moment a new thrust is initiated, the slip lines of the basal interface and the new thrust (FT_{ini} in Fig. 2.18 a) reach the critical point controlled by the basal friction and

the peak internal friction. The constructed taper is smaller than the maximum FDZ taper (Fig. 2.18 a). This matches the general Mohr Diagram 2 of subcritically-tapered wedges (Fig. 2.17 b).

- During the underthrusting phase of the incoming sand-layer when no new thrust is initiated, the minimum differential stress is present in the FDZ, as all thrusts are active. Assuming the basal shear stress to be critical, the Mohr Diagram reveals a lower taper, than the maximum FDZ taper (Fig. 2.18 b). Again, this is in agreement with the general Mohr Diagram 2 (Fig. 2.17 b).
- Under the conditions of the maximum FDZ taper, the basal stress exceeds the critical point for the whole range of possible differential stresses (Fig. 2.18 c). This matches the general Mohr Diagram 1 of subcritically-tapered wedges (Fig. 2.17 a).

Thus, the FDZ is a subcritically-tapered segment, as all extreme states of stress are shown to be in the subcritical state.

Interpretation of the IAZ and FIZ II: Are wedge mechanics transient?

Segmentation of the wedges, as identified from kinematic analysis, is not directly explained by the mechanical analysis presented above, and even appears to be in conflict with measured friction values in the case of the PIF wedge: The shallower surface slope (5.2°) in the rear part of the PIF experiment results in an underestimation of the basal friction (0.24) at constant internal friction or an overestimate of the internal stable friction (0.73) at constant basal friction (Fig. 2.15). The latter value is well below the peak frictional strength of undeformed material. These results indicate that the friction values as measured are not valid for the more internal parts of this sand wedge.

A more detailed analysis of the states of stress of the rear parts of the sand wedges, provides a more straightforward explanation. The experiments show that slip on some of the faults in the FIZ proceeds at differential stresses higher than necessary to overcome the frictional strength of optimally-oriented faults which have reached the state of stable sliding (FT in Fig. 2.16). This is a consequence of antithetic rotation of the faults into a mechanically less-favourable position once they have left the FDZ and entered the FIZ (Fig. 2.13).

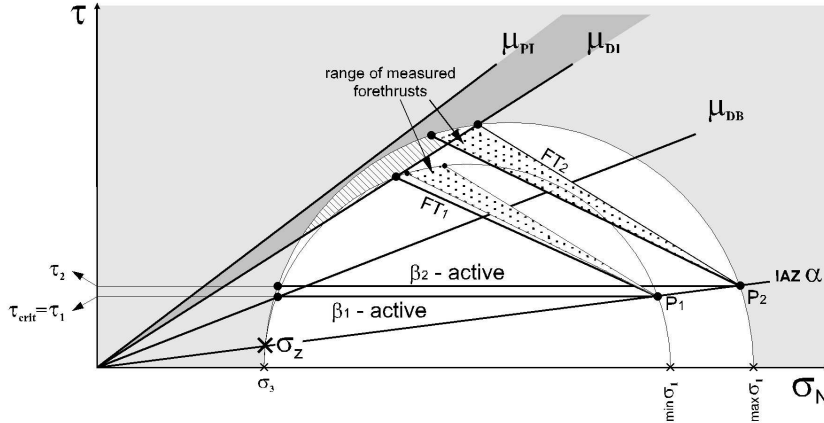


Figure 2.19: Schematic Mohr-Diagram illustrates the kinematics of the minimum and maximum differential stress in the IAZ (subscripts 1 and 2 indicate the minimum and maximum states of stress, respectively; hatched sectors indicate potential orientations of active forethrusts; μ_{PI} – peak internal friction, μ_{DI} – stable dynamic internal friction; μ_{DB} – stable dynamic basal friction, α – surface slope, β – basal dip, FT – steepest potential inclination of a reactivated forethrust, τ – shear stress; σ_N – normal stress; σ_1 – maximum principle stress; σ_3 – minimum principle stress).

As a consequence, differential stresses required for slip increase towards the boundary between the FIZ and IAZ, i.e. the bulk strength of the wedge is not reached.

An important implication is that the boundaries of the FIZ, i.e. the segment limits within the wedge, are controlled by key mechanical boundary conditions: The boundary between the FDZ and the FIZ is a zone of minimum wedge strength since it shows an optimally-oriented leading fault, once it has reached the stage of stable sliding. Wedge strength increase due to fault rotation and strain hardening by diffuse deformation toward the boundary of the FIZ to the IAZ evolves to a point where two possible effects can occur:

- Slip on a rotated fault may eventually require differential stresses beyond the upper bound of plastic hardening of the thrust sheets near peak frictional strength of the material. Subsequent failure will then produce second generation faults crosscutting the earlier structures with a stress drop and a renewed transition to stable sliding. This should result in weakening of the bulk wedge strength and an equivalent increase in taper.
- Peak strength is not reached and rotated faults are inactivated, because convergence is entirely taken up by the basal shear zone which fails throughout. Accordingly, deformation in the wedge will cease, leading to a transition into

a stable state of stress below the current bulk wedge strength.

Thus, the horizontal length of the FIZ and the FDZ, is controlled by a deformation-dependent strength threshold (i.e. bulk wedge strength), reached after active faults have rotated through a critical angle.

In agreement with this argument and critical-wedge theory, the decrease in wedge taper of the IAZ must be due to an increase of the frictional strength ratio between the wedge itself and the wedge basis. I consider that the influence of the rigid backwall (which was similar in all experiments) for the variable wedge taper in the IAZ is not important at distances larger than experiment thickness, because there is a lack of a systematic relationship between the width and number of thrust slices at this distance. This increase in frictional strength ratio could be due to three aspects:

- Since the friction of wedge-internal faults controls wedge taper, transient increase in stable dynamic friction can potentially cause a decrease in wedge taper. However, the material analysis in the ring-shear tests does not support the assumption that stable dynamic friction changes relevantly.
- Similarly, weakening of the basal shear zone by a deformation-dependent process was not observed, nor could a load-dependent change

in friction be established. Ring-shear tests and the variable (by a factor of as much as 1.5; from 1200 to 1800 Pa) normal load at the downdip end of the FIZ-IAZ boundary in the experiments described here, show no significant change of friction at pressures above 200 Pa, similar to the results of Schellart, (2000).

- The only remaining explanation for the low taper of the IAZ and its kinematic properties is an increase in bulk wedge strength which, as argued above, could be due to progressive fault-rotation and associated plastic-hardening in the thrust sheets as proposed by Mulugeta (1988). The reactivation of the faults in the stable state of stress requires fluctuation of the differential stresses beyond the frictional strength threshold, as e.g. expected from discontinuous material addition to the IAZ. To illustrate this in a schematic Mohr Diagram, I use a specific IAZ taper and the inclination of the active basal detachment (Fig. 2.19). The slip line of the basal detachment at the critical point (i.e. intersection of the Mohr Circle with the failure curve of the continuously-active basal interface) determines the minimum differential stress under these conditions. In this state of stress, no back-rotated thrust in the IAZ is activated. The Mohr Circle position of the maximum differential stress is somewhat beneath the peak frictional strength of the wedge material. Here, all back-rotated thrust of the IAZ are reactivated and slip at the base proceeds under higher than minimum conditions.

The observed inconsistencies between measured and calculated basal friction for the rear segment of PIF wedge, require that material properties vary during such experimental runs. Transient, i.e. deformation-dependent changes of properties, apparently occurred in several instances: Material analysis has established an elastic-plastic material behaviour with a strain-hardening and strain-softening cycle during initial diffuse deformation and fault formation (cf. Section 2.3) — a behaviour which is well known in soil mechanics (e.g. Schanz and Vermeer, 1996) but has not as yet been considered in geodynamic analogue simulations (cf. Section 2.2). This short-term transient effect, however, only affected fault material in the FDZ. After slip of a few millimetres, all the materials reached

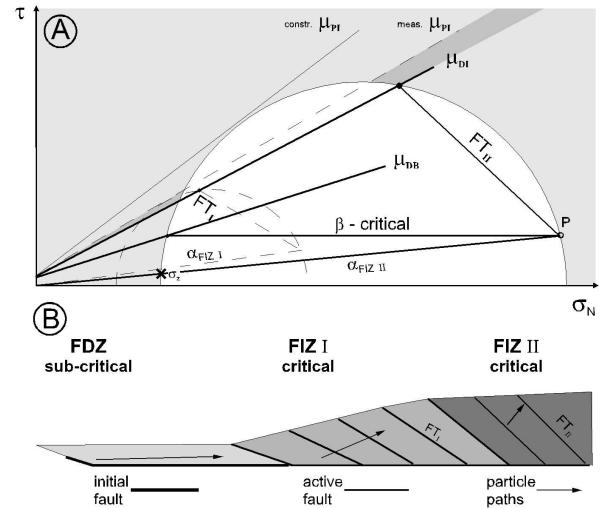


Figure 2.20: a) Schematic Mohr Diagram for the sand wedge consisting of PIF to illustrate the different state of stress in the rearward part of the FIZ (FIZ_{II} – solid lines) compared to its frontal part (FIZ_I – dashed lines). The constructed value for peak internal friction (μ_{PI}) is only semi-quantitative, as the influence of the rigid backwall is not considered here (meas. μ_{PI} – peak internal friction as measured, μ_{DI} – stable dynamic internal friction, μ_{DB} – stable dynamic basal friction, α – surface slope, β – basal dip, FT – trailing forethrust, τ – shear stress, σ_N – normal stress). b) For orientation, the general geometry of the sand wedge.

the phase of stable sliding found to be the relevant property controlling the critically-tapered segments. This phase may exhibit a long-term transient change of friction. As hinted by the stress-strain curves in Fig. 2.16, minor changes may occur, both in terms of weakening or of strengthening, by a few percent. This effect again only affects the faults and is considered negligible.

More importantly, changes of mechanical properties that are related to initially undercompacted materials, e.g. PIF material, may be relevant (see compaction curves in Fig. 2.16). To maintain slip on the progressively-steepening faults in the entire actively-deforming zone of the PIF experiment, differential stresses must steadily increase to exceed the equally-increasing wedge strength. Because of the small initial difference between peak and stable frictional strength of PIF material and the absence of newly formed out-of-sequence faults, this necessitates an increase of the peak frictional strength of the material within the thrust sheets (Fig. 2.20). This is probably achieved by progressive compaction and deformation of the initially-

undercompacted material during initial shear zone evolution in the FDZ. This transient deformation-dependent increase in peak friction is, at present, not quantitatively accessible, and can only be estimated by inference.

In undercompacted sands (e.g. PIF), it is probable that bulk compaction and peak friction increase equally with increasing deformation (cf. Section 2.3.2). At the same time, friction within faults converges toward a similar average value, independent of the material type (cf. Section 2.3.2). Accordingly, with increasing deformation all materials should converge on the behaviour typical of sifted sands, with high differences between peak and stable frictional strength, and an equivalent deformation localisation. Based on the semi-quantitative analysis of wedge-internal frictional strength from Fig. 2.20, I infer that the peak friction of undercompacted sand increased and reached the peak friction of the well-compacted SIF material during the initial compaction phase.

A key consequence of this argument is that the bulk strength of a particular, critically-tapered wedge segment is neither identical to the frictional strength measured from deformed materials for stable frictional sliding, nor to the peak strength of undeformed materials. Moreover, the occurrence of two or more different critically-tapered segments in a single wedge implies that a critical-taper analysis of such wedges cannot be performed with average values of material properties extrapolated from experimental data. Consequently, a critical-taper analysis requires that the different kinematic wedge segments as well as the stages of the development of bulk wedge strength are identified.

2.4.3.3 Summary: The influence of friction on wedge mechanics

The influence of the varied parameters on the investigated features of the sand wedges are presented in Fig. 2.21. These schematic diagrams are based on the correlation of the quantitative and qualitative results of the sandbox experiments, and measurements of material properties. Grain size, grain-size distribution and filling technique influence the peak internal and peak basal friction, whereas the stable dynamic internal and stable dynamic basal friction is influenced only by grain size and grain-size distribution (Fig. 2.21 a and b).

The features of the convergent sand wedges which are mainly formed during the initial failure of the material (slice length; slice-internal deformation)

are linked to peak friction. As put forward by Platt (1988), thrust-slice length is mainly a function of the thickness of the incoming layer and the frictional strength of the footwall. In experiments, in which the thickness of the incoming sand-layer was held constant, the direct dependency of the slice length on the peak internal friction and peak basal friction was observed (Fig. 2.21 c and d). Also, the total amount of slice-internal diffuse deformation is mainly influenced by the peak internal friction, as the highest amount of the diffuse deformation takes place before and during the initial failure of the sand in the FDZ (Fig. 2.21 c). In contrast, the small amount of diffuse deformation, which takes place during later stages of deformation within the FIZ, is not related to the peak internal friction (Fig. 2.21 c). The peak internal friction is a transient material property (see below and Section 2.4.3.2). The newly-established peak internal friction during the experimental run and the diffuse deformation within the FIZ are a function of grain size, grain-size distribution and filling technique (Fig. 2.21 a and b). The diffuse deformation within the FIZ is the only feature which is not directly influenced by the material properties used in the critical-taper theory, i.e. internal and basal friction (Fig. 2.21 c-f).

Based on the discussion in Section 2.4.3.2, the initial peak friction controls the range, in which the bulk wedge strength can vary during the experimental run: As the initial peak friction indicates the degree of compaction of the sand, a small initial peak friction (e.g. PIF) denotes undercompaction (cf. Section 2.3.3). In Section 2.4.3.2, I suggested that peak friction of such sands increases during the deformation in compressive sand wedges by compaction. Therefore this newly-established peak friction corresponds to the initial peak friction of well-compacted sands (e.g. SIF). It thus follows that a sand with a small initial peak friction is able to vary its peak internal friction and bulk wedge strength over a large range (Fig. 2.21 a). Consequently, the bulk wedge strength strongly increases in such a sand wedge and thrusts are continuously activated, although they are steeply inclined by back-rotation. The higher the peak internal friction is, the smaller the range of transient bulk wedge strength (Fig. 2.21 a). In these cases, a wedge adjusts its geometry by reactivation of favourably-orientated thrusts, because this mode is kinematically more suitable than the initiation of new thrusts. Consequently, initial peak friction

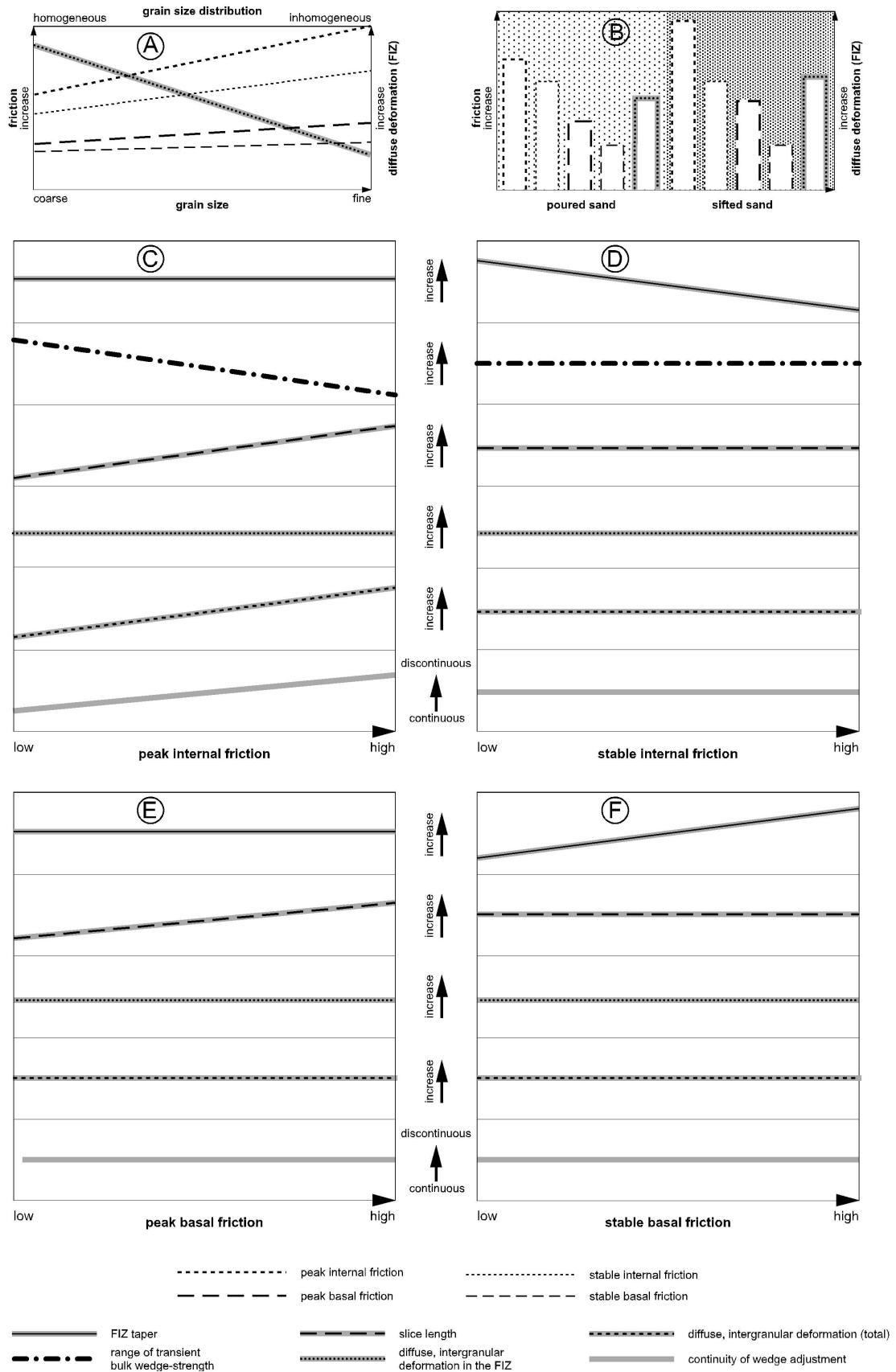


Figure 2.21: Schematic diagrams show the dependence of the frictional properties on a) grain size and grain-size distribution, and b) filling method, as well as the dependence of the investigated wedge features on c) peak internal friction, d) stable internal friction, e) peak basal friction, and f) stable basal friction.

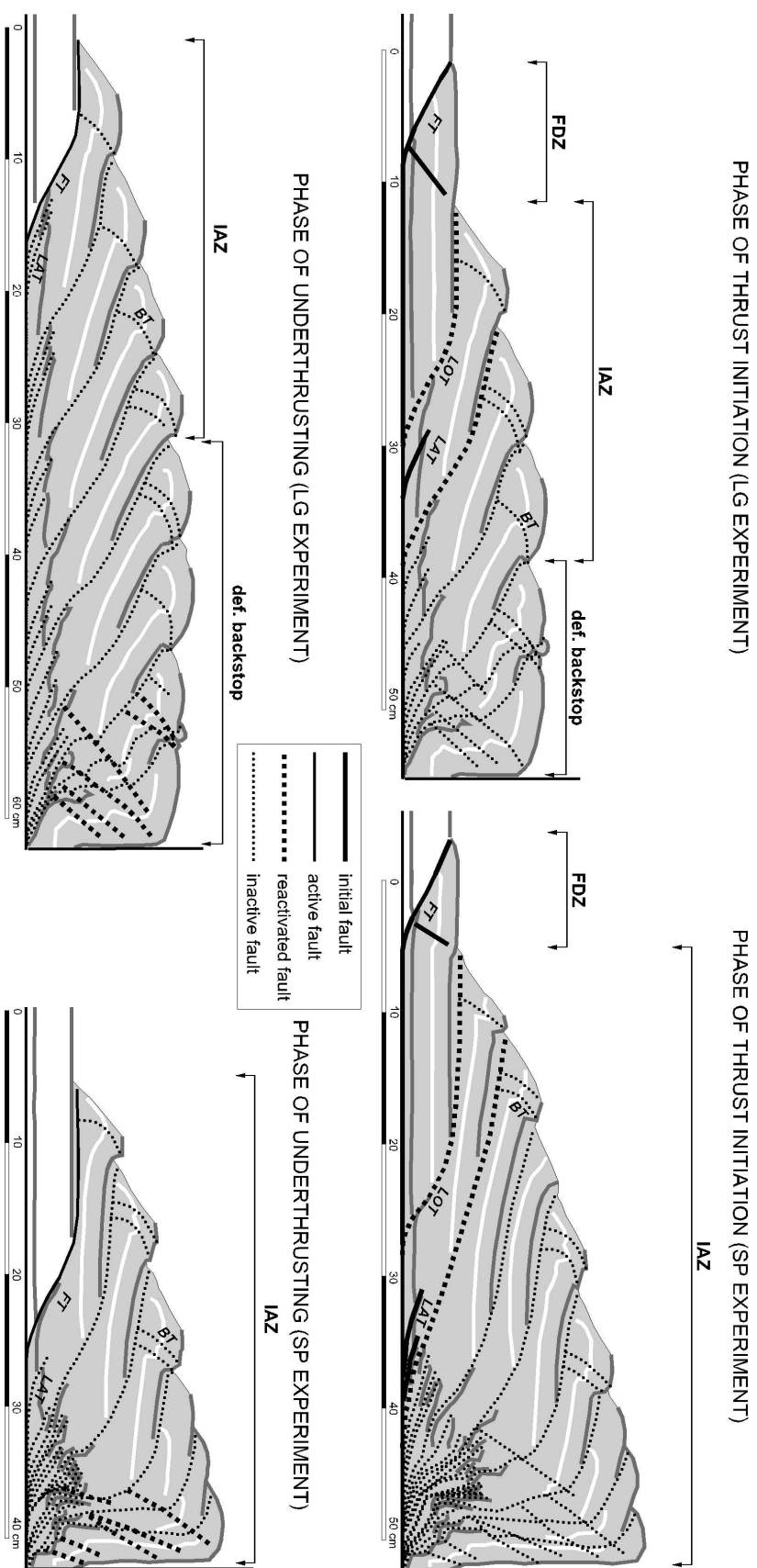


Figure 2.22: Kinematic features of the high-friction experiments in both deformation phases, fault initiation and underthrusting (LOT – leading out-of-sequence thrust, LAT – low angle thrust).

causes the rear parts of a wedge to adjust its geometry by episodic or cyclic reactivation of back-rotated thrusts or the continuous motion of the thrusts.

The wedge taper of the FIZ is the only feature, which is influenced by a combination of the stable internal and stable basal friction of all active faults (Fig. 2.21 e and f). The critical-taper analysis shows that the critical taper only depends on these two material properties (cf. Section 2.4.3.2), and is not influenced by other internal or basal material properties not considered in the critical-taper equation (Fig. 2.21 c and d).

2.4.4 2nd Series: Variation of basal material properties

2.4.4.1 Experimental Results

Based on the mechanical and dynamical interpretation of the frontally-accretionary wedges previously described in this chapter, the influence of varied basal properties on the wedge segmentation, kinematics and mass transfer is shown below. In the following, the contrasting features between the sand wedges of the first series (low basal friction – *low-friction experiments*) and the second series (high basal friction – *high-friction experiments*) are emphasised to evaluate the influence of low and high friction of the basal detachment. The identification of the contrasting features between the sand wedges formed on top of latex gum (i.e. *LG experiment*) and sandpaper (i.e. *SP experiment*) show whether high basal friction induced by high roughness influences wedge evolution.

Contrasting features between the 1st and 2nd series

The sand wedges of the two series differed mainly in their internal kinematics. In the high-friction experiments, longer thrust slices and larger thrust displacements than in the low-friction experiments were produced (Tab. 2.4). The sand wedges with the high-friction basal detachment showed deformation cycles alternating between initiation of a new thrust slice and underthrusting of the incoming sand-layer (Fig. 2.22). During the underthrusting phase, only the frontal thrust was active, while all other internal thrusts were inactive. At the moment of thrust initiation in the front of the wedge, underthrusting of the frontal thrust slice ceased. During the initiation of a pair of conjugated fore- and backthrust in front of the wedge, two types of wedge-internal deformation contemporaneously

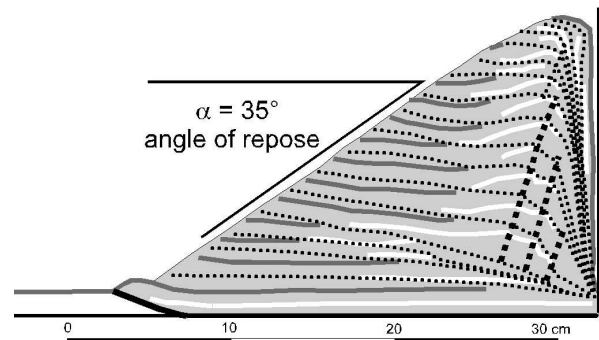


Figure 2.23: Experiment #2.13, another SP experiment with very large thrust displacements. The large thrust displacements cause a steep surface slope with the angle of repose (activity of faults is marked as in Fig. 2.22).

occurred: reactivation of the LOT and the adjacent forethrust, as well as initiation of low-angle thrusts (LAT in Fig. 2.22) at the base of the frontal thrust slice. All other internal thrusts were inactive during both deformation phases. The LOT of the high-friction experiments was always the second thrust from the front. This well-defined deformation cycle was not observed in the low-friction experiments, which were characterised by continuous wedge-internal deformation in the FIZ (cf. Section 2.4.3.1).

In both types of experiments, low-friction and high-friction experiments, the frontal thrust slice was continuously truncated at the front by slumping and attained the angle of repose (Fig. 2.11 c and Fig. 2.22). The truncation lasted as long as the tip of wedge was thrust over the incoming layer. Since the thrust displacements were larger in the high-friction experiments, the frontal part of these wedges were more truncated than the low-friction wedges. In experiments with very large thrust displacements, not only the front of a single thrust slice but the whole wedge suffered truncation and its surface slope steepened up to the angle of repose (Fig. 2.23). In this case, the surface slope was independent of the basal dip and basal friction, since the angle of repose is only controlled by the internal friction itself.

In the high-friction experiments only continuous activity of the frontal thrust was identified. Therefore, these wedges lacked a FIZ, as the area, which was at failure throughout, was reduced to a single thrust. In consequence, the high-friction wedges formed mainly an IAZ, whereas the low-friction wedges show a succession in FIZ and IAZ (Figs. 2.13 and 2.24). The comparison of the geome-

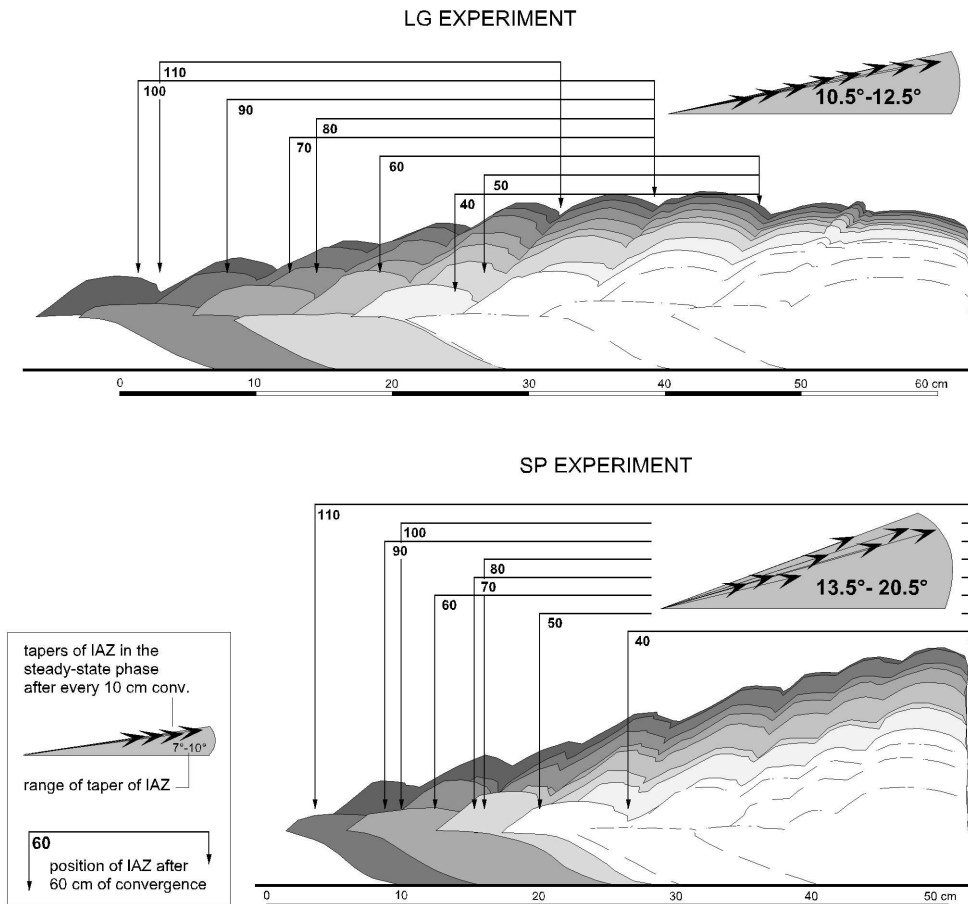


Figure 2.24: Wedge geometry of the high-friction experiments, plotted after every 10 cm conv. Dashed lines indicate the geometries of the adjustment stage; solid lines indicate the steady-state geometries.

try of the IAZs revealed another substantial difference between low-friction and high-friction experiments: The IAZ of high-friction wedges achieved large wedge tapers, which varied strongly during the experimental runs, whereas the IAZ of low-friction wedges was characterised by a small and constant wedge taper (Tab. 2.4). These large changes in the wedge tapers of the high-friction wedges support the interpretation that the wedge mainly consisted of an IAZ, since the IAZ is a stable segment in terms of critical-taper theory and it is therefore able to achieve a range of various wedge tapers.

Contrasting features between LG and SP experiment

Although both high-friction wedges exhibited nearly the same average slice length (20 cm), the thrust displacements differed (Tab. 2.4). The thrusts in the LG wedge reached only an average displacement of 10 cm, whereas the average thrust

displacement of the SP wedge was 14.7 cm. Therefore the ratio between thrust displacement and slice length was significantly larger in the SP wedge (0.73), compared to the LP wedge (0.5). This difference crucially influenced the displacement field: In the SP wedge, the internal part of the wedge was nearly vertically uplifted due to underthrusting of long slices (Fig. 2.25). In contrast, the shallowly-inclined particle paths of the LG experiment displayed a passive rearward transport on top of the frontal imbricates, which were formerly accreted in a more frontal position on the sand wedge.

The geometry of the LG wedge showed a convex surface slope. In contrast, the SP wedge was characterised by a straight surface slope (Fig. 2.24). The underthrusting in the SP wedge caused an uplift of the whole wedge, so that the SP wedge consisted only of an IAZ. In the LG wedge, the IAZ was smaller, as the underthrusting induced only an uplift of the adjacent three slices. The rear-

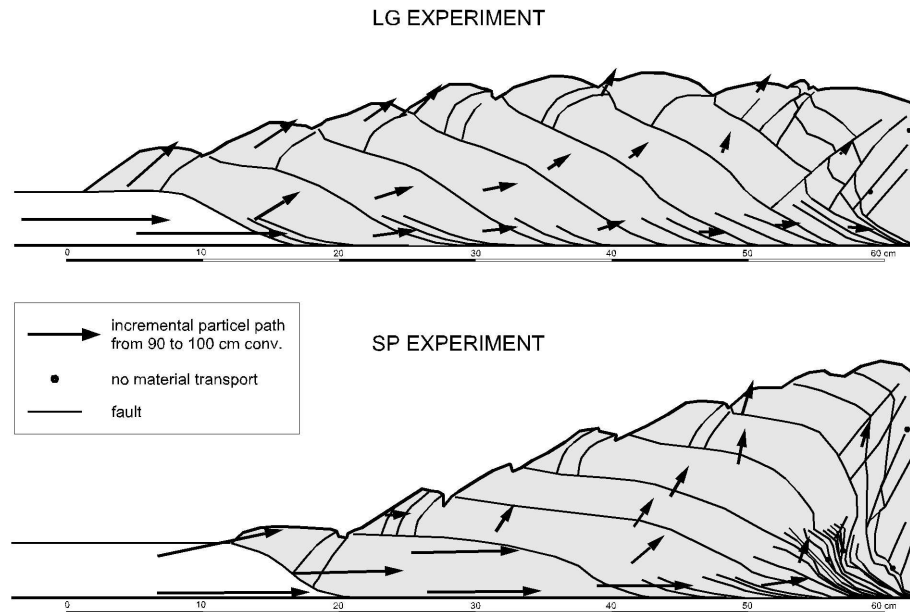


Figure 2.25: Incremental particle paths of the high-friction experiments detected using the triangular-shaped markers.

ward part of this wedge showed only minor displacements, which were accumulated by newly-formed backthrusts close to the rigid backwall. The influence of the rigid backwall cannot be excluded for this part of the wedge. Consequently, the rearward part of the LG-wedge is defined as deformable backstop and is not further interpreted in this chapter (see also Section 3.4.2.).

In the SP wedge, the wedge taper of the IAZ measured after every 10 cm conv. varied from 13.5 up to 20.5°. In contrast, the IAZ of the LP wedge only achieved wedge tapers from 10.5 to 12.5° (Fig. 2.24, Tab. 2.4).

In conclusion, the sand wedges with high basal friction were characterised by large thrust displacements, long thrust slices, the absence of a FIZ, and large wedge tapers of the IAZ.

2.4.4.2 Interpretation

This section focuses on the role of high basal friction in wedge mechanics to explain the absence of a FIZ, the steep wedge taper of the IAZ, as well as the mechanism of underthrusting in high-friction experiments. This mechanics analysis is restricted to semi-quantitative inspections, since the stable IAZ achieved a range of different wedge tapers, so that the analysis cannot be based on one specific value.

Gutscher et al. (1998a) explained the cycles of underthrusting and thrust initiation by an analysis

of forces at work. In their study, the different forces which are required for underthrusting and fault initiation were calculated. The force which is required to underthrust the incoming layer is equal to the frictional strength along the surface of the incoming layer plus the frictional strength along the ramp and the force required to uplift the overlying portion of the wedge along the ramp (Fig. 2.26 b). The force, which is required to initiate a new thrust is equal to the frictional strength along the conveyor belt and along the new initiated ramp thrust, plus the forces required to uplift the toe along the frontal ramp (Fig. 2.26 a). Comparison of the two forces showed that after a certain thrust displacement the forces of underthrusting overcome the forces of fault initiation, so that further underthrusting is not possible and this force balance can be used to predict slice lengths (Fig. 2.26 c and d). Gutscher et al. (1998a) showed that the predicted slice length fits very well with the slice length observed in their experiments, which were performed with large initial wedges. Their study shows that the thrust displacement increases with increasing basal friction, and that wedge taper and basal friction are the crucial parameters which mainly influences maximum thrust displacement.

The thrust displacements observed in the SP and LG experiments showed also that thrust displacements are larger in the case of higher basal friction.

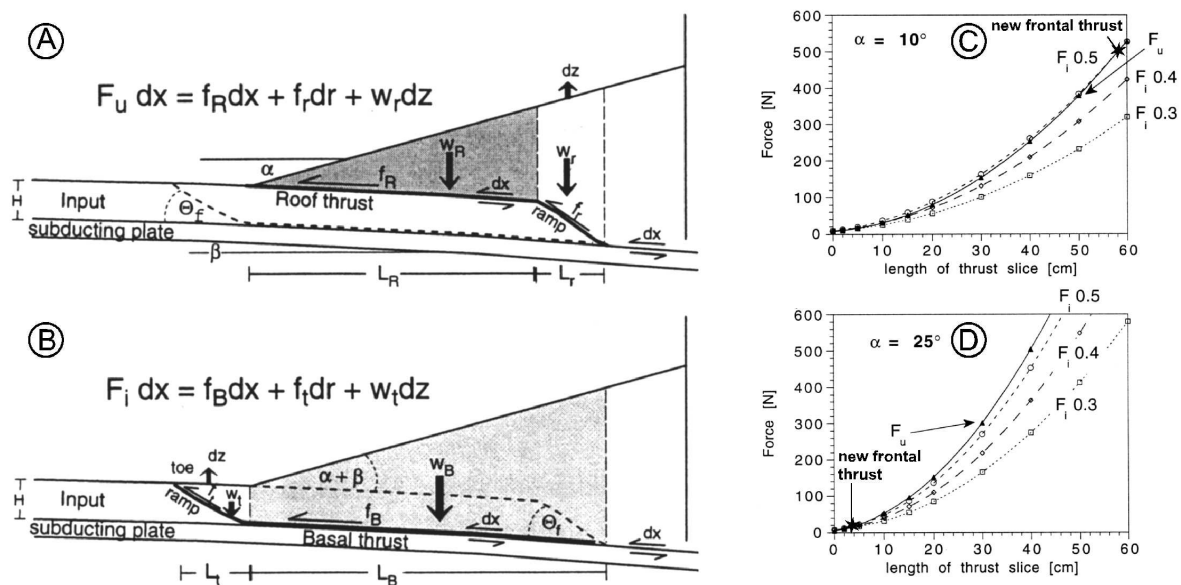


Figure 2.26: Diagram showing a generalised thrust wedge with the work calculated for motion along fault surfaces. a) F_u is the force required to advance an underthrusting unit an incremental distance dx ; b) F_i is the force required to initiate a new basal and frontal thrust with incremental displacement dx . F_u and F_i versus length of thrust slice for three basal frictions (0.3; 0.4; 0.5) and for c) a surface slope of 10° and d) a surface slope of 25° , calculated with the conditions Gutscher et al. (1998a) used; modified after Gutscher (1996).

Therefore, Gutscher's et al. (1998) interpretation of the cyclic deformation and large thrust displacements is favoured for the SP and LG experiment.

Large thrust displacements have one more impact on wedge mechanics: The frontal part of the wedge is controlled by different basal frictional strengths during the two phases of the deformation cycle: During the phase of underthrusting the basal detachment steps up to the surface of the incoming sand-layer, so that the stable dynamic frictional strength of SIC2 is the currently effective basal frictional strength (Tab. 2.3). In the case of thrust initiation the frontal part of the wedge is controlled by the peak frictional strength of the conveyor belt.

Following the strategy of analysing the low-friction experiments (cf. Section 2.4.3.2), the two deformation phases with different basal frictional strength had to be treated separately. In terms of critical-taper theory, wedges reach the existence limit, if their basal friction is equal to their internal friction (Dahlen, 1984). This is the case during the underthrusting phase, which is characterised by steepening of the frontal wedge taper up to the angle of repose, due to consumption of frontal wedge material. On the basis of the results of the second SP experiment (Fig. 2.23), it is suggested that a

wedge at its existent limit always tends to achieve the angle of repose (for further discussion of this process cf. Section 4.4.2). In both of the high-friction experiments, the SP and LG experiment, the angle of repose was only attained in single imbricates, as the incoming sand-layer failed to build up a new thrust slice before underthrusting proceeded so far as to enable the truncation of the whole overlying wedge. Since the latex gum had a lower friction than the sandpaper, a new thrust was initiated after a shorter underthrust displacement in the LG experiment. In consequence, the adjustment to the angle of repose during the underthrusting phase was interrupted earlier in the LG experiment than in the SP experiment, resulting in smaller wedge tapers in the LG experiment.

To show that the high-friction experiments are forced to produce stable sand wedges due to this process, Mohr Diagrams of the phase of thrust initiation were plotted (Fig. 2.27). The observation of the contemporaneous initiation of frontal and wedge-internal thrusts indicates that during this deformation phase, the maximum state of stress up to the peak internal frictional strength is reached within the wedge. The constructed critical-wedge tapers for the LG experiment (9.3°) and the SP ex-

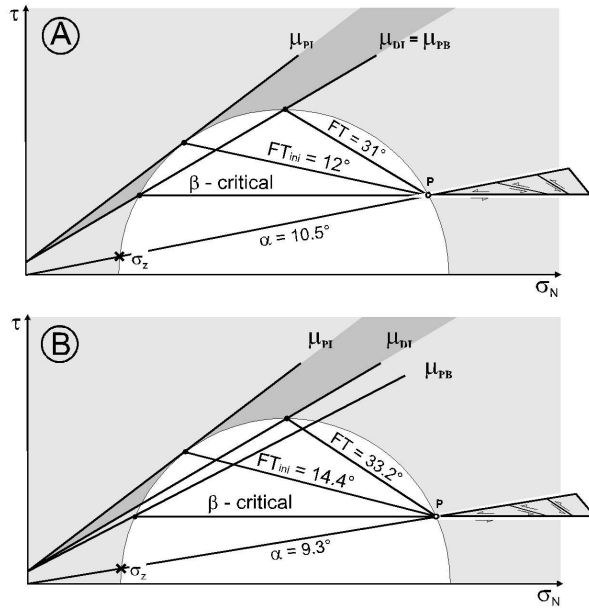


Figure 2.27: Mohr Diagrams show the state of stress required for the initiation of new thrusts (FT_{ini}), assuming a critically-tapered a) SP wedge and B) LG wedge. The constraints used for construction are the measured peak internal friction (μ_{PI}), stable dynamic internal friction (μ_{DI}) and peak basal friction (μ_{PB}), and the dip of the trailing out-of-sequence thrust (FT). For both experiments the constructed surface slope (α) is smaller than the measured surface slopes in the experiments (β – basal dip; τ – shear stress; σ_N – normal stress; σ_z – state of stress at the depth z ; P – pole).

periment (10.5°) are much smaller than observed in the experiments. This means that the wedge taper, which was attained under the conditions of the underthrusting phase, was in the stable state during thrust initiation. These stable wedges only have to adjust their geometry to continuous material addition and not to critical taper, which is already exceeded. Therefore, such wedges are not able to keep a critically-tapered geometry and to build a FIZ. As shown by the Mohr Diagrams, the wedges should adjust their geometry during the phase of thrust initiation by initiation of low-angle thrusts and the reactivation of back-rotated thrusts. Although a wedge in a stable state should show smaller dips of these thrusts than revealed from the Mohr Diagrams of a critical state, these characteristic features were also observed in the LG and SP experiments.

I suggest that the wedge taper of the high-friction experiments was not controlled by a stress balance under constant wedge properties, which is explained

by the critical-taper theory. In contrast, these wedges are controlled by a balance of two states of stress under temporally changing wedge properties.

The steeper wedge taper of the IAZ in the high-friction wedges compared to the IAZ of the low-friction wedges can be explained on the basis of the above mentioned interpretation. Both IAZs of the high-friction and low-friction wedges were shifted to a stable wedge geometry due to a change in the wedge properties. However, the position of the change of wedge property as well as the changed wedge properties themselves were different in the two types of experiments. The bulk wedge strength increased in the rear part of the wedge in the low-friction experiments, whereas the basal friction increased in the frontal part of the wedge of the high-friction experiments. Consequently, the different positions and geometries of the IAZs are caused by the basic difference in their boundary conditions.

2.5 Application to nature

In Chapter 3 and 4, sandbox simulations are used to investigate natural forearc settings. This is only possible, if the mechanics of the sandbox experiments represents those of nature. Applicability of the arguments derived from the here presented analysis to natural convergent wedges also strongly requires that natural rocks behave similarly to the used analogue material. Although more diverse, stress-strain curves of rocks are very similar to the stress-strain curves of the investigated sands (Jaeger and Cook, 1969; Paterson, 1978). At a larger scale moreover, the shape of the strength curve of faults in the brittle upper crust derived from laboratory tests matches the presented results for large sand samples (Fig. 2.28; Marone, 1998). Both, the brittle crust and the analogue materials, exhibit elastic, frictional plastic material behaviour with an initial strain hardening and strain softening cycle.

The proper choice of analogue material is required to reproduce the overall wedge geometry of the individual kinematic segments in natural wedges, as well as to allow the comparison of their internal deformation patterns and kinematics. The relevant features are the initial difference between peak and stable frictional strength, long-term transient evolution of the fault itself and deformation-dependent evolution of the peak frictional strength of the material. However, even in the brittle field, natural rocks will invariably experience a variety of

other processes that may cause transient mechanical behaviour. It should be noted, that the scaling of these various transient mechanical phenomena and its establishment in natural rocks, as well as in analogue materials, is an as yet unresolved problem (Paterson, 2001). In consequence, the identification of general similarities is the only viable strategy at present.

Brittle upper crustal rocks, from the results presented in this chapter, are best represented by sifted, inhomogeneous, fine-grained sands (similar to SIF or SIC2). Therefore, all sandbox experiments presented in Chapter 3 and 4 were constructed with SIC2. Unlithified, incompletely-compacted sediments with a low ratio of peak frictional strength to stable frictional strength are best represented by poured sand, whereas sediments with a high strength ratio (peak/stable) may react like sifted homogenous sand. Typical low porosity basement rocks show a continuous increase in strength during the stable-sliding phase (Paterson, 1978). These rocks are best simulated by sifted inhomogeneous, coarse grained sands such as SIC1, which also exhibit a slight strain hardening during advanced stages of shearing. However, the stress-strain curves of this analogue material and the basement rocks are significantly different during initial failure. Consequently, a transfer of the experimental results with this sand to natural systems is only possible, if the investigated processes are independent of initial failure (like deformation processes in the FIZ or IAZ). Correlation in all cases, is however, dependent on two aspects:

- The stress-strain curves of the analogue materials only image the mechanical evolution of fault material and not that of the surrounding material.
- Mechanical properties of the analogue material are measured at sample scales similar to those used in the scaled analogue experiment itself. Data from natural rocks, however, represent small samples, the properties of which cannot directly be extrapolated to scales of friction-controlled orogenic wedges.

The kinematic segmentation is not exclusive to experimental wedges and can be used to test the applicability of the arguments described above to natural wedges. I expect, however, that segmentation in natural wedges may be affected by additional aspects, such as variation in dip of the basal

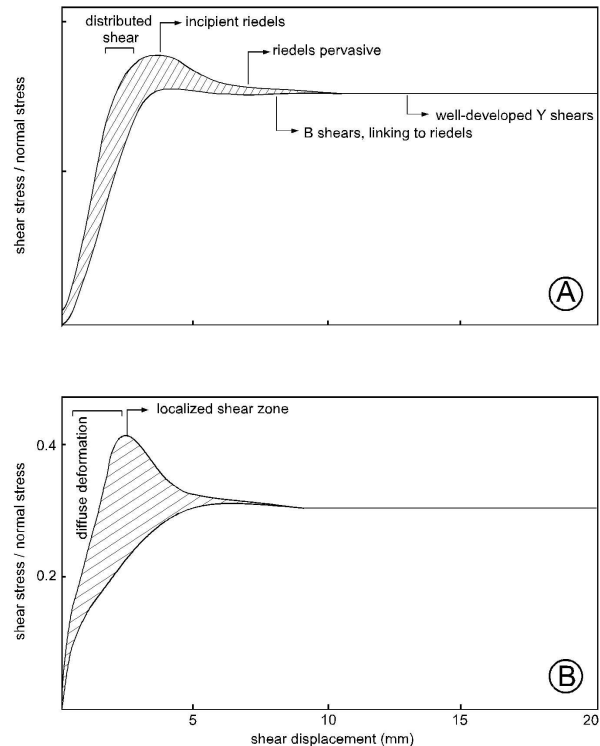


Figure 2.28: a) Sketch of a stress-strain curve during shear zone evolution in the upper brittle crust (modified after Marone (1998)), b) sketch of a stress-strain curve of a granular analogue material (hatched area – range of initial stress-strain behaviour that is controlled by the degree of compaction).

detachment, changes of rock properties by variations in cohesion (Zhao et al., 1986), mineral reactions, changes in pore pressure, and formation of anisotropic fabrics.

Deformation or load-dependent changes in cohesion, in particular, have been invoked to explain the convex shape of natural as well as of analogue wedges (Zhao et al., 1986; Mulugeta and Koyi, 1992). The underlying assumption, is however, that of an ideal Coulomb Material with deformation-independent friction and accordingly, deformation-independent bulk material properties controlling the wedge. This study, in contrast, shows that the taper of individual segments in a critical and stable state of stress is entirely controlled by the friction of faults, because the frictional strength of granular materials during stable sliding is always lower than the peak strength of the undeformed material. Transient, deformation-dependent properties within the thrust sheets only determine to which degree the faults may be rotated without becoming inactive. Accordingly, increasing cohesion can only

play a role in the latter aspect and, indirectly, support an increase in rearward bulk wedge strength. To have an effect on the taper of a wedge, fault material must also be affected by cohesion enhancement. While this may occur in natural systems (by solution-precipitation processes and fault sealing, etc.), no evidence is available to support this inference for faults in analogue materials. The convex shape of convergent analogue wedges cannot be the simple consequence of an increase of the cohesion of the undeformed wedge material. I expect a contribution of the latter aspect in natural wedges (as suggested by Zhao; 1986), but emphasise that here again the friction of fault materials, including their cohesion, are the key elements controlling the taper and strength of wedges.

2.6 Conclusions

This chapter shows that the dynamics of convergent sand wedges can only be correctly described if a more complex material behaviour than previously assumed is considered. Sand exhibits an elastic/frictional plastic behaviour with transient strain hardening prior to failure and subsequent strain softening until the onset of stable sliding at constant friction. Although more diverse, stress-strain curves of natural rocks are very similar to the stress-strain curves of the sands investigated here. This confirms that sand can be considered a suitable analogue material for the simulation of crustal deformation in the brittle field.

The influence of preparation techniques on the friction of sand analogue materials, as well as friction of the basal detachment, are responsible for kinematic and dynamic segmentation of convergent sand wedges. Based on kinematic analysis, only parts of a wedge are critically tapered. Critical-taper analysis for individual wedge segments, whether in a critical or a stable state of stress, leads in the case of localised wedge-internal deformation to an excellent agreement between theoretical prediction and measured friction values. Nevertheless, only a critically-tapered segment allows complete quantitative evaluation. As a result, the strength of critically-tapered wedge segments is mainly controlled by the frictional strength of the faults which have reached the state of stable sliding. However, in the case of diffuse wedge-internal deformation caused by differential stress, only slightly below the peak internal friction, the mismatch between measured and predicted friction values suggest a 'nearly critical state of stress'. This

is due to the perturbation of boundary conditions by continuous material addition. While this allows a mechanical analysis based on the Coulomb Failure Criterion, it requires unambiguous identification of the critical state of stress within a specific segment. Moreover, the occurrence of two or more critically-tapered segments in a single wedge implies that a critical-taper analysis of such wedges cannot be performed with average values of material properties extrapolated from experimental data. In consequence, the critical-taper analysis requires identification of the different kinematic wedge segments, as well as of the specific stages of the development of frictional strength.

The frontally-accretionary sand wedges investigated in this chapter show three different patterns of kinematic segmentation, according to the amount of critically-tapered segments (Tab. 2.4). Two critically-tapered segments occur in sand wedges, which were formed by undercompacted sand upon a low-friction detachment. In undercompacted materials, peak strength of the material must increase as a consequence of pervasive deformation and bulk compaction. This deformation-dependent transient property shifts the position of the strength limits that control the wedge segments toward the rear. In such cases, the taper may continuously decrease resulting in a convex geometry, although it is critical throughout. Also, mechanical properties predicted from taper analysis in these cases increasingly diverge from experimentally-obtained data, supporting the inference of deformation-dependent transience. Standard measuring techniques for these properties establish only the long-term development of shear-zone properties and, so far, do not allow the quantification of the friction of intervening material.

One critically-tapered segment occurs in every sand wedge, which is formed of well-compacted sand above a low-friction detachment. In these sand wedges, bulk wedge strength is not constant, as a consequence of progressive fault rotation into mechanically less-favourable orientations and associated plastic hardening in the thrust sheets by pervasive deformation. Bulk wedge strength increases toward the rear and influences the wedge segmentation. The critical segment is separated from the stable segment (with all other conditions kept constant) by a frictional strength limit. At this limit, the condition for continuous slip on previously established and rotated faults is exceeded, resulting in either inactivation of the fault with discontinuous reactivation or in renewed failure.

If the stable strength of the basal detachment exceeds about 80% of the stable strength of wedge material, the sand wedge does not form any critically-tapered segment. In these sand wedges, the frictional strength of the basal detachment is not constant, as a consequence of a relocation of the basal detachment during two different deformation phases. A sand wedge which is subject to temporary varying conditions is not able to adjust its geometry to one of these conditions. The adjustment to the steepest wedge taper is perturbed by the relocation of the basal detachment. Under the new conditions, the wedge taper attained before, is a taper in a stable state of stress. As consequence of the stable geometry in the frontal wedge the incoming material is directly incorporated in a wedge, which does not have to achieve a critical taper.

Chapter 3

The Accretive Forearc of Southern Chile

3.1 The South Chilean Forearc

3.1.1 Database obtained from nature

Since the Tertiary, the South Chilean Forearc (Fig. 3.1) has been accretive, with possible changes between the accretive and erosive mode (Bangs and Cande, 1997). Bangs and Cande (1997) have suggested that the current accretive stage is linked to the initiation of glacial erosion in the Main Cordillera (Pleistocene) and the related increase in sedimentation into the trench basin (cf. Fig. 1.2). During the Lower Pliocene and then again since the Pleistocene frontal accretion formed a small accretionary prism in front of an older accretionary complex (Palaeozoic; Fig. 3.2 and 3.3; Bangs and Cande, 1997; Díaz-Naveas, 1999). The lack of accreted sediments of Mesozoic to Miocene times and of the Upper Pliocene indicates non-accretive or tectonically-erosive phases of the South Chilean Margin (Bangs and Cande, 1997). In this study, I focus only on the accretive processes underlying the Neogene geodynamic evolution of the South Chilean Forearc (Miocene-Recent) between 37–40° S (Fig. 3.1).

Depth-migrated reflection-seismic lines at 38 and 39° S (RC 2901, lines 730, 732) (Díaz-Naveas, 1999) image the main structures of the South Chilean Offshore Forearc (Fig. 3.2 and 3.3): The dip of the upper oceanic plate is equal in both seismic lines ($\beta = 5^\circ$). Only the upper portion of sediment, which enters the trench on top of oceanic crust, is presently frontally accreted. The 20–40 km wide frontal-accretionary wedge at the lower slope is formed by three to five imbricates. This wedge is compressed against a continental basement wedge that forms the middle slope, which is covered by

Eocene to Neogene slope sediments. The surface slope of the lower and middle slope is different in both seismic lines (38° S: $\alpha = 6^\circ$, 39° S: $\alpha = 4^\circ$) and shows a large variability along trench (Ladage et al., 2002).

Trench-parallel shelf basins are located within the upper slope. The Arauco Basin in the north is bordered by the Mocha High to the Valdivia Basin in the south (Fig. 3.1). Although, both basins are characterised by Neogene syn-sedimentary normal faults, their different sedimentary record demonstrates independent evolution (Mordojovich, 1981).

The lower portion of the incoming sediments is underthrust beneath the frontally-accretionary wedge (Fig. 3.2 and 3.3). They are internally undeformed and can be identified in the seismic lines up to 30 km landwards of the trench. It is unknown whether the underthrust sediments are (partly) basally accreted beneath the Coastal Cordillera or further subducted beneath the magmatic arc. The thickness of sediments entering the trench varies significantly along-strike (38° S – 4000 m; 39° S – 1600 m). Furthermore, the ratio of frontally accreted to underthrust sediments is larger at 38° S (3.33) than at 39° S (1.25).

The South Chilean onshore Forearc (37–40° S) shows a morphological zonation related to kinematic domains (from W to E; Fig. 3.1):

- i) The Arauco Peninsula is the only location which shows onshore trench-parallel shelf basins. The current kinematic state of the Arauco Peninsula is syn-uplift extension perpendicular to the trench axis (Lavenu and Cembrano, 1999). The main tectonic structures in this area are nearly N-S striking horst- and graben-structures with several 100 m displacement of Neogene sediments

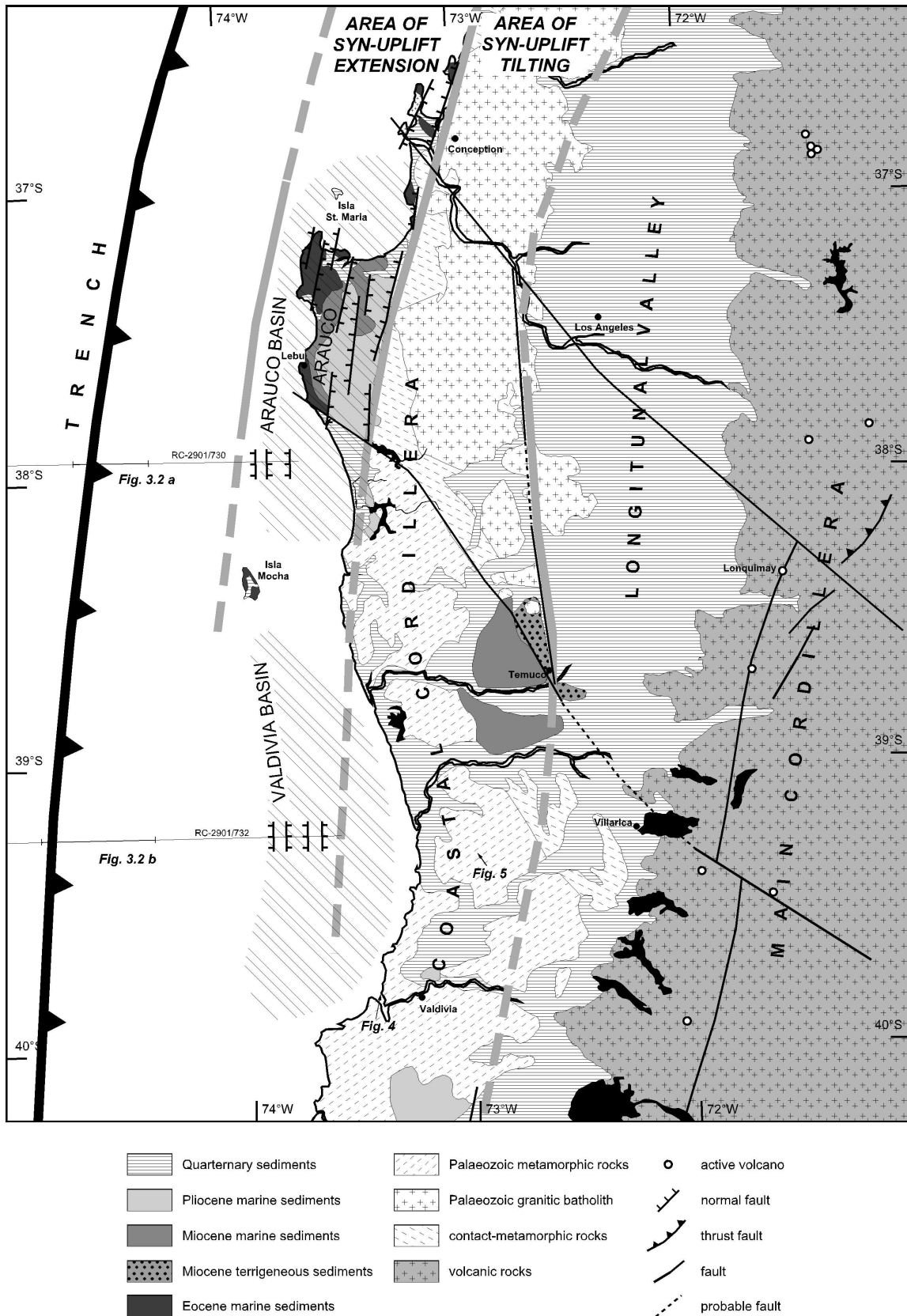


Figure 3.1: Geological map of the South Chilean Forearc with morphotectonic domains indicated; compiled from SERNAGEOMIN (1980), Mordojovich (1981), Boettcher (1999), and pers. comm. H. Ehtler.

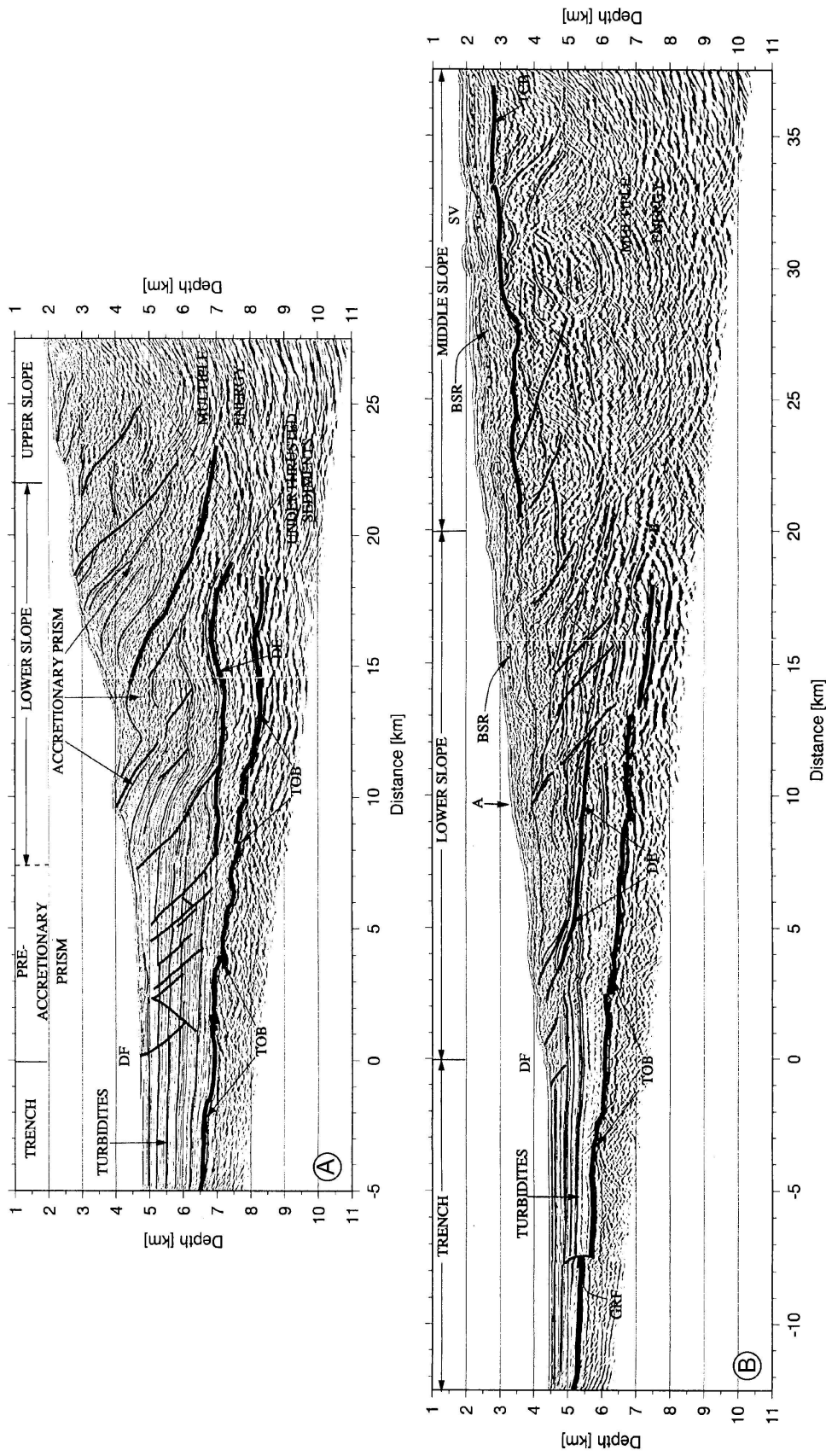


Figure 3.2: Interpretation of depth-migrated line a) 730 and b) line 732 (RC 2901; for location see Fig. 3.1) of Díaz-Naveas (1999) (v. e. = 1.3, DF – deformation front, TOB – top of oceanic basement, DE – basal detachment of the frontal-accretionary wedge, TCB – top of continental basement, GRF – growth fault, SV – submarine valley, BSR – bottom-simulating reflector).

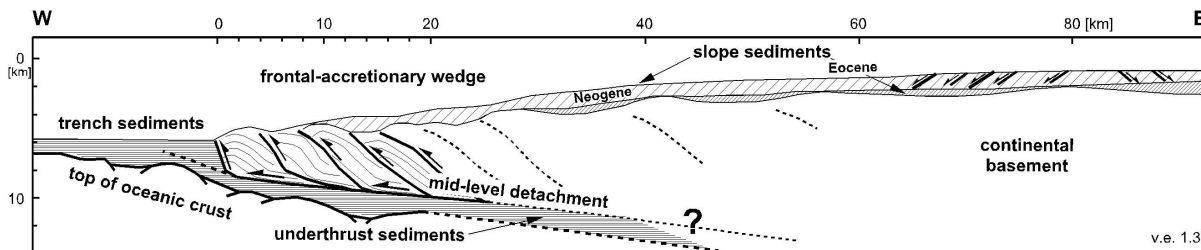


Figure 3.3: Cross-sectional sketch of the South Chilean Forearc based on the interpreted reflection seismic sections (Fig. 3.2), modified after Díaz-Naveas (1999).

(Boettcher, 1999). This region is characterised by distributed crustal seismicity, which implies current tectonic activity of the continental crust (Asch et al., 2001). The sedimentary fill of the shelf basins records frequent changes of marine and continental facies since the Eocene to the Quaternary (Pineda, 1986; Jordan et al., 2001).

- ii) The Coastal Cordillera shows a decreasing surface elevation from north to south (700–300 m a.s.l.). Between 37–38° S, the Coastal Cordillera consists of a Palaeozoic granitic batholith and its adjacent contact-metamorphic rocks (Hervé, 1977). Because of the absence of Neogene rocks in this region, the Neogene kinematics remain uncertain. Nevertheless, minor normal faults in unconsolidated soils indicate the recent extensional state of the Coastal Cordillera (pers. comm. S. Potent, 2001). Further south (38–40° S), the Coastal Cordillera is composed of metaclastic rocks, metacherts, metabasalts, ultramafic rocks, and high P/T metamorphic rocks of blueschist facies (Aguirre et al., 1972; Martin et al., 1999). This metamorphic unit is interpreted as a Palaeozoic accretionary complex (Kato and Godoy, 1995; Martin et al., 1999; Gräfe et al., 2000). This part of the Coastal Cordillera preserves some indication of Neogene kinematics: Near to the coast are three lakes, which are now not connected to the Pacific Ocean (Fig. 3.1). These lakes were formed by tilting and uplifting during Quaternary times so that rivers were dammed in their valleys (Kaizuka et al., 1973). Evidence for this syn-uplift tilting of this region is validated by terraces along the coast line, which show a slight inclination towards the east (Fig. 3.4). Although the exact age of the terraces is not known, the tilting might have taken place during the Neogene, because
- their well-preservation and the presence of unconsolidated dune sand suggests that their formation is younger than Miocene. In contrast to the kinematics of the northern region (37–38° S), this southern region (38–40° S) is not marked by large-scaled horst and graben structures. Only small-scale normal faults with only several metres displacement in unconsolidated Quaternary sands and soils indicate extension (Fig. 3.5; pers. comm. H. Ehtler 2001). Crustal seismicity in the Coastal Cordillera is located along prominent NW–SE trending fault zones and does not reflect a distributed tectonic activity (Asch et al., 2001).
- iii) In the Longitudinal Valley (average elevation 100 m a.s.l.), continental Quaternary sediments of a few 100 m to several 1000 m thickness indicate a relative subsidence of local basins with respect to the Coastal and Main Cordilleras (Kelm et al., 1994). The Longitudinal Valley was originally described as graben or half-graben structure (Cisternas and Frutos, 1994). However, this interpretation is still controversially discussed. The eastern border of the Longitudinal Valley with the Main Cordillera is an inactive normal fault that was active until the Middle Miocene (Lavenu and Cembrano, 1999; Jordan et al., 2001). Lavenu and Cembrano (1999) interpreted the N–S striking lineament of the western border of the Longitudinal Valley as strike-slip and reverse faults, whereas McDonough et al. (in prep.) suggest an eastward-dipping normal fault at crustal scale as the border of the Longitudinal Valley.
 - iv) The position of the magmatic arc in the Main Cordillera (elevation 2.5 km a.s.l.) has been largely stable throughout the Mesozoic-Cenozoic, with only a small current shift (35 km since Pliocene times) towards the trench (Stern, 1989).



Figure 3.4: To the west of Valdivia, Neogene terraces in different levels (arrows) indicate uplift. They are slightly inclined towards the east (for location see Fig. 3.1).

3.1.2 Mass-transfer concept derived from field data

The syn-uplift extension of the Coastal Cordillera during the Neogene and current seismicity distribution at the South Chilean Forearc (Asch et al., 2001) suggest that basal accretion of all or part of the subducted sediment beneath the Coastal Cordillera is the most probable current mass-transfer mode. This would imply that the centre of basal accretion is probably up to 100 km landward of the trench.

Whereas the recently acquired data suggests the above-mentioned general mass-transfer mode, a specific understanding of this process requires more detailed data. With this in mind, the aim of analogue simulation in this study is to develop differ-

ent scenarios of basally-accretive systems to identify the influence of the variable parameters on the kinematics and mechanics. The parameter which is observed as variable input parameter in nature, is the sediment supply. Based on the basic parameter studies (Section 2.4.4.), the mechanical parameters of the basal interface were expected to crucially influence the mass-transfer mode proposed for the South Chilean Forearc. Therefore both of these parameters, sediment supply and mechanical properties of the basal interface, were varied in the following analogue simulations.

3.2 Experimental setup of the two-level experiments

In analogue experiments reported in literature two experimental setups are known to produce underthrusting of the incoming sand-layer beneath the accretionary wedge:

- This setup requires a basal interface with a high friction with respect to the overlying material (e.g. sandpaper, latex gum) as well as a mechanically-consistent, incoming sand-layer (Huiqi et al., 1992; Gutscher et al., 1996; and Section 2.4.4.). Strong coupling between the basal detachment and the incoming sand-layer results from these boundary conditions, which causes long thrust slices to be transported for a long distance beneath the frontal accretionary wedge before a new thrust slice is initiated in



Figure 3.5: Small-scaled, NNW-SSE striking normal faults in Quaternary sediments in the Coastal Cordillera (for location see Fig. 3.1).

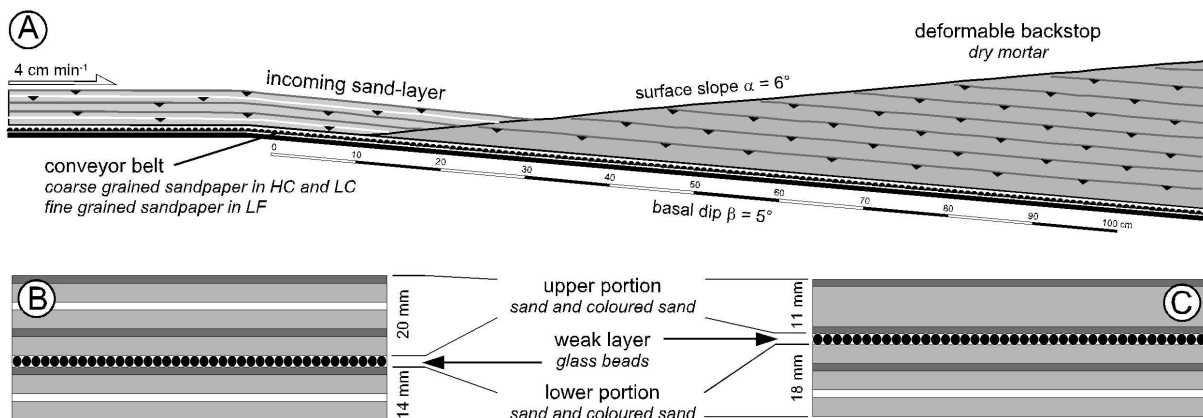


Figure 3.6: a) Setup of the two-level experiments. The incoming sand-layer is differently stratified in b) the LF and LC experiments and in c) the HC experiment (for nomenclature of the experiments see Tab. 3.1). The glass-bead layer serves as a potential mid-level detachment.

front of the wedge tip. In this experimental setup, frontal accretion and sediment underthrusting occur in alternation rather than simultaneously (cf. Section 2.4.4.). This is not observed at the South Chilean Margin, and therefore this setup cannot be used to simulate this mass-transfer mode.

- This setup (Fig. 3.6), which leads to basal accretion, differs from the first one in that the incoming sand-layer consists of two materials of different mechanical properties. A thin layer consisting of micro glass beads ($\mu_D = 0.43$, Tab. 2.3), which are considerably weaker than sand, and allow mechanical decoupling between the upper and lower parts of the incoming sand-layer. Therefore, such an experimental setup provides the possibility to activate detachments at two levels: one within the incoming sand-layer along the glass-bead layer (i.e. *mid-level detachment*) and the other one at the basal interface (i.e. *basal detachment*). In the text below, these experiments are known as *two-level experiments*. In a two-level experiment, the lower part of the incoming sand-layer is underthrust beneath the accretionary wedge, while the upper part of the layer is simultaneously frontally accreted (Turrini and Ravaglia, 1999; Huhn et al., 2000; Huhn, 2002; Kukowski et al., 2002).

At the South Chilean Margin, seismic studies reveal a decoupling between the upper and lower portion of the incoming sediment pile (Fig. 3.3). Therefore the two-level setup was chosen to simulate the

mass-transfer process of the South Chilean Forearc (Fig. 3.6, Tab. 3.1). Tab. 3.1 lists the initial conditions and the nomenclature of certain experiments in this series. Test runs showed, that a glass-bead layer was only activated as mid-level detachment under certain conditions: The minimum thickness of the glass-bead layer needed to be 3 mm thick and the upper portion of the incoming sand-layer had to be 10 mm thick. Therefore, it was not possible to scale the incoming sand-layer to the South Chilean trench-basin fill. Nevertheless, relative variations of the position of the thin, weak layer within the incoming material and its thickness allow the simulation of the variation in sediment stratification as observed at the South Chilean trench basin. This limitation still permits a general evaluation of the influence of the varied parameters (thickness of the incoming sand-layer; properties of the basal interface), but not a direct comparison of mass-transfer rates between experiment and nature. Since the lower portion of the incoming sediments is suggested to be underthrust for a long distance beneath the South Chilean Forearc (ca. 100 km, Section 3.1.2), the experimental conditions have to be capable of large thrust-displacements. As seen in the basic parameter studies (Section 2.4.4.), thrust displacements mainly depend on the basal friction and the largest displacements results from a high-friction and rough conveyor belt. Therefore the experiments to simulate the South Chilean Forearc were performed with conveyor belts which consisted of sandpaper. Variations in the mechanical properties of the basal interface were investigated by using fine and coarse-grained sandpaper.

experiment	position of glass-bead layer	thickness of incoming layer [mm]		conveyor belt	
		upper portion	lower portion	sandpaper	μ_{DB}
HC	high	11	18	coarse grained (> 0.63)	0.61 ± 0.01
LC	low	20	14	coarse grained (> 0.63)	0.61 ± 0.01
LF	low	20	14	fine grained (< 0.4)	0.55 ± 0.002

Table 3.1: Setup and nomenclature of the two-level experiments performed, with respect to the South Chilean Forearc. In all experiments, the sand used (SIC2) has a stable dynamic friction (μ_{DI}) of 0.57; (μ_{DB} – stable dynamic friction).

The basal friction of the coarse-grained sandpaper ($\mu_{DB} = 0.61 \pm 0.01$) exceeds the internal friction of the used sand (SIC2, $\mu_{DB} = 0.57 \pm 0.002$). Contrastingly, the basal friction of the fine-grained sandpaper ($\mu_{DB} = 0.55 \pm 0.005$) nearly matches the internal friction of the sand (for further information about the materials used see Tab. 2.3).

A deformable backstop, which consisted of dry mortar, was used in all experiments. The higher stable dynamic internal friction ($\mu_{DI} = 0.66$) correlated with that of the sand of the incoming layer and simulated the formerly-accreted material of the South Chilean metamorphic Forearc wedge. The initial surface slope (6°) of the backstop was designed to represent the natural surface slope. Although this surface slope could not be expected in the experiments under dry conditions, an initial surface slope at the experiment reduces the adjustment phase in the beginning of the experimental run. Furthermore, the basal dip of the oceanic plate of the natural forearc (5°) was adopted for the experimental setup.

3.3 Experimental results of the two-level experiments

The experimental setup described-above produced highly-complex convergent sand wedges, which showed more contrasting rather than common features. Nevertheless, a general overview of the mass-transfer mode and kinematics is given in the following section ‘common features’. The section ‘contrasting features’ focuses on the individual specific evolution of the three experiments.

Common features

In all of the two-level experiments, the upper part of the incoming sand-layer was frontally accreted and formed an imbricate fan (i.e. *frontal-accretionary wedge*) on top of an active detachment (i.e. *mid-level detachment*), which was located within the glass-bead layer (Fig. 3.7 a). The

lower part of the incoming sand-layer was underthrust and basally accreted (i.e. *basal-accretionary complex*) beneath the frontal part of the backstop by the formation of hinterland-dipping duplexes. At the leading edge of the basal-accretionary complex, the active detachment stepped down to the basal sandpaper interface (Fig. 3.7 a). Active basal accretion caused passive uplift and bending of the overlying material. Near-surface extension was initiated by this bending at the midpoint of uplift, as shown by tension cracks in the backstop. The active tension cracks were located directly above the midpoint of uplift, whereas on both sides the uplifted area was tilted without significant extension. The tension cracks, which were visible in these parts of the experiments, were formed at earlier stages of the experiment. The area of uplift was bordered to the rear by persistently-active backthrusts (i.e. *trailing backthrust*). Due to this type of mass transfer, the ratio of frontally to basally-accreted material corresponded with the ratio of the thickness of the upper to the lower portion of the incoming sand-layer (Tab. 3.2).

The kinematics of the frontal-accretionary wedge of the two-level experiments were comparable with those of the high-friction experiments (Fig. 3.7 and Section 2.4.4). A cyclic deformation was observed, which altered between an underthrusting and an initiation phase of a new frontal thrust in the upper portion of the incoming sand-layer. The LOT was the second thrust from the front and only two of the frontal in-sequence thrusts were reactivated (LOT1 in Fig. 3.7). All the other previously formed and back-rotated thrusts of the frontal-accretionary wedge were inactive until the late stages of an experimental run.

In contrast to the high-friction experiments, the two-level experiments did not show the initiation of new low-angle thrusts in previously-incorporated imbricates during the fault-initiation phase. However, a continuously diffuse thickening of the glass-bead layer was observed at the base of the individual imbricates, which suggests that the basal de-

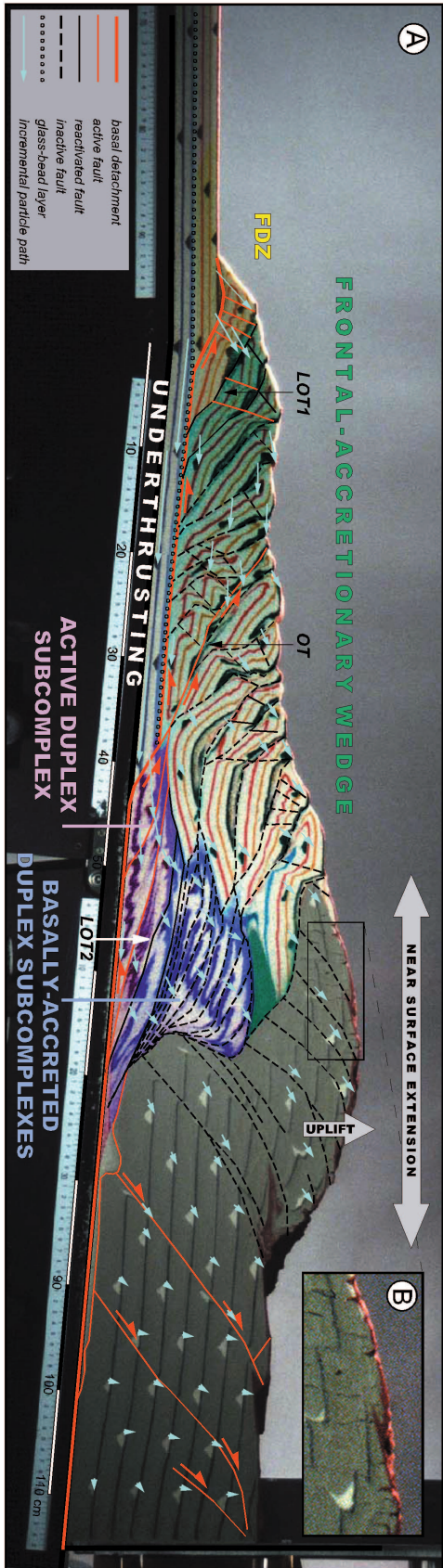


Figure 3.7: a) The LF experiment after 220 cm conv., indicating kinematics and incremental particle paths between 210 and 220 cm conv. The leading out-of-sequence thrust 1 (LOT1) is the boundary between the frontal-deformation zone (FDZ) and the rear part of the frontal accretionary wedge, LOT2 is the boundary between the continuously-active duplex sub-complex and the basally-accreted duplex sub-complexes (OT – out-of-sequence thrust initiated in the late phase of the experiment). b) Tension cracks indicate horizontal extension due to bending.

	HC experiment	LC experiment	LF experiment
ratio of incoming layer (upper portion/lower portion)	0.61	1.43	1.43
volume of frontally-accreted material [cm ³]	210	340	350
volume of basally-accreted material [cm ³]	310	250	260
ratio of frontally/basally-accreted material	0.68	1.36	1.35
total uplift [cm]	9.4	9.7	13.4
ratio of min. thrust (displacement/slice length)	0.56	0.54	0.52

Table 3.2: Quantitative results of the two-level experiments (for nomenclature of the experiments see Tab. 3.1)

formation, as observed in the high-friction experiments, also occurred here.

Another important difference between the high-friction experiments and the frontal-accretionary wedge of the two-level experiments was the irregularity of the length of imbricates in the latter. In the two-level experiments the slice length and therefore the thrust displacement strongly varied (see further description in ‘contrasting features’). As described in Section 2.4.4., a large ratio of thrust displacement and slice length, in excess of 0.5, is a characteristic feature of high-friction sand wedges. Selected measurements of single imbricates show that the ratio of thrust displacement and slice length exceeded 0.5 in both cases of long and short thrust slices.

The basal-accretionary complex consisted of several sub-complexes, which were stacked upon another. Each of these sub-complexes were formed by hinterland-dipping duplexes at the wedge base. The lower portion of the incoming sand-layer was not internally deformed and underthrust beneath the frontal-accretionary wedge, until the formation of a new forethrust indicated the initiation of a new duplex. The initial duplexes had a variable length from a few centimetres up to 10–15 cm in all experiments. A new duplex was internally deformed by several narrowly-spaced forethrusts during the successive accretion into the basal-accretive complex.

The basal-accretionary complex demonstrated a unique kinematic and geometrical segmentation. The most frontal thrusts were continuously active. This frontal part was bordered by a LOT towards the rear part (LOT2 in Fig. 3.7) with strongly back-rotated, reactivated thrusts. The continuously-active frontal part showed a steeper slope than the rear part within one sub-complex.

The following aspects show more contrasting than common features and are discussed in detail in the next section. Nevertheless, some similarities

observed in all experiments (HC, LC, LF) are mentioned below.

The stacking of the sub-complexes of hinterland-dipping duplexes was triggered by the initiation of trailing, persistently-active backthrusts in the backstop (Fig. 3.12). During the initial adjustment phase (for definition see Section 2.4.1.) of one experiment the first underthrust duplex caused several short-active backthrusts in the backstop (Fig. 3.12). New backthrusts were initiated in the footwall of the adjacent one. While a duplex sub-complex was formed, no new backthrust was initiated and the previously-formed backthrust was active during the whole formation of the duplex sub-complex. In the moment when a new backthrust was initiated, the whole frontal part of the sub-complex was underthrust beneath the LOT. This underthrusting took place simultaneously with further frontal material addition to the sub-complex. After the underthrusting of the sub-complex, the formerly-reactivated thrusts in the overlying sub-complex were inactive during the rest of the experimental run, i.e. the sub-complex was basally accreted against the overlying material.

Also, common geometrical features were rare in the two-level experiments (Fig. 3.10). Only the frontal part of the frontal-accretionary wedge and the rear part above the basal-accretionary complex showed some similarities. The central part of the wedge, where the lower portion of the incoming sediments was underthrust, differed in all of the experiments (for further discussion, see next section).

The frontal part of the frontal-accretionary wedge was characterised in all experiments by a significant fluctuation of the surface slope during the experimental runs (Fig. 3.8). This is ascribed to the irregularity of the slice lengths and thrust displacements, since large thrust displacements of long imbricates caused a truncation of the frontal part of the wedge and steepening of the surface slope up to the angle

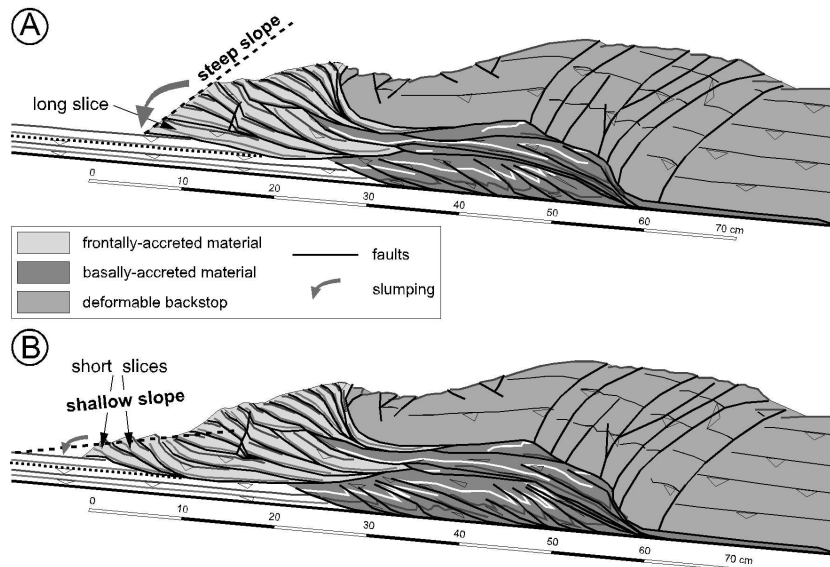


Figure 3.8: a) Underthrusting of a long thrust slice causes the steepening of the frontal wedge taper (long-slice event). b) Frontal accretion of short slices cause a shallow wedge taper. These examples are from the HC experiment after 150 and 170 cm conv., respectively.

of repose (35° , Fig. 3.8 a, cf. also Fig. 2.23). During the shorter underthrusting phase, only one frontal imbricate was truncated and a shallow frontal surface slope (measured over several imbricates) was formed (Fig. 3.8 b, cf. also Fig. 2.22 c and d).

The rear edge of the area of basal accretion was marked by a topographic high that correlates with the position of maximum total uplift (Fig. 3.10).

Contrasting features

The values for all quantitative comparisons, which are presented in the following section, were measured in each of the experiments after 180 cm conv. (Fig. 3.9), as this was the final stage of the smallest experiment (LC experiment, for nomenclature of experiments see Tab. 3.1).

The topography of the LC and HC wedges was comparable at the rear part, beneath which basal accretion took place (Fig. 3.10): In both experiments the topography was divided into two parts. A topographic high formed the rear part, whereas the surface of the frontal part was nearly horizontal in the LC experiment, and irregular in the HC experiment. In contrast, the same area of the LF experiment did not show this division and was marked only by a huge topographic-high with a larger surface elevation than the topographic highs of the other two experiments (LC, HC ; Tab. 3.2).

The variable topography of the frontal-accretionary wedge, beneath which the material

of the lower part of the incoming sand-layer was underthrust (Fig. 3.8, Appendix), was marked by an additional feature in the late stages of the LF experiment: The fluctuation between a steep and shallow frontal slope ceased in this experiment after ca. 100 cm conv. (Appendix). From then on the frontal-accretionary wedge built up a convex topography, which is typical for frontal-accretionary wedges (see also Section 2.4.3.).

As the topographic evolution of these experiments was directly linked to their structural evolution, the geometrical fluctuations of the frontal- and basal-accretionary complexes were investigated by a comparison of thrust slice length. This comparison is based on the video sequences of the experimental runs, since the serial photographs did not have the temporal resolution required to measure all initial slice lengths. In the video sequences, the amount of total convergence was measured when a new fault was initiated. The relative distance of convergence between one thrust initiation and the next was used to gauge the relative slice length: The relative amount of convergence is proportional to thrust-slice length and displacement. The events of the initiation of long imbricates in the upper portion of the incoming sand-layer (i.e. long-slice event), which caused a significant steepening of the frontal wedge-taper (Fig. 3.8), were differently distributed during the experimental runs (Fig. 3.11): In the HC experiment the first of these long-slice

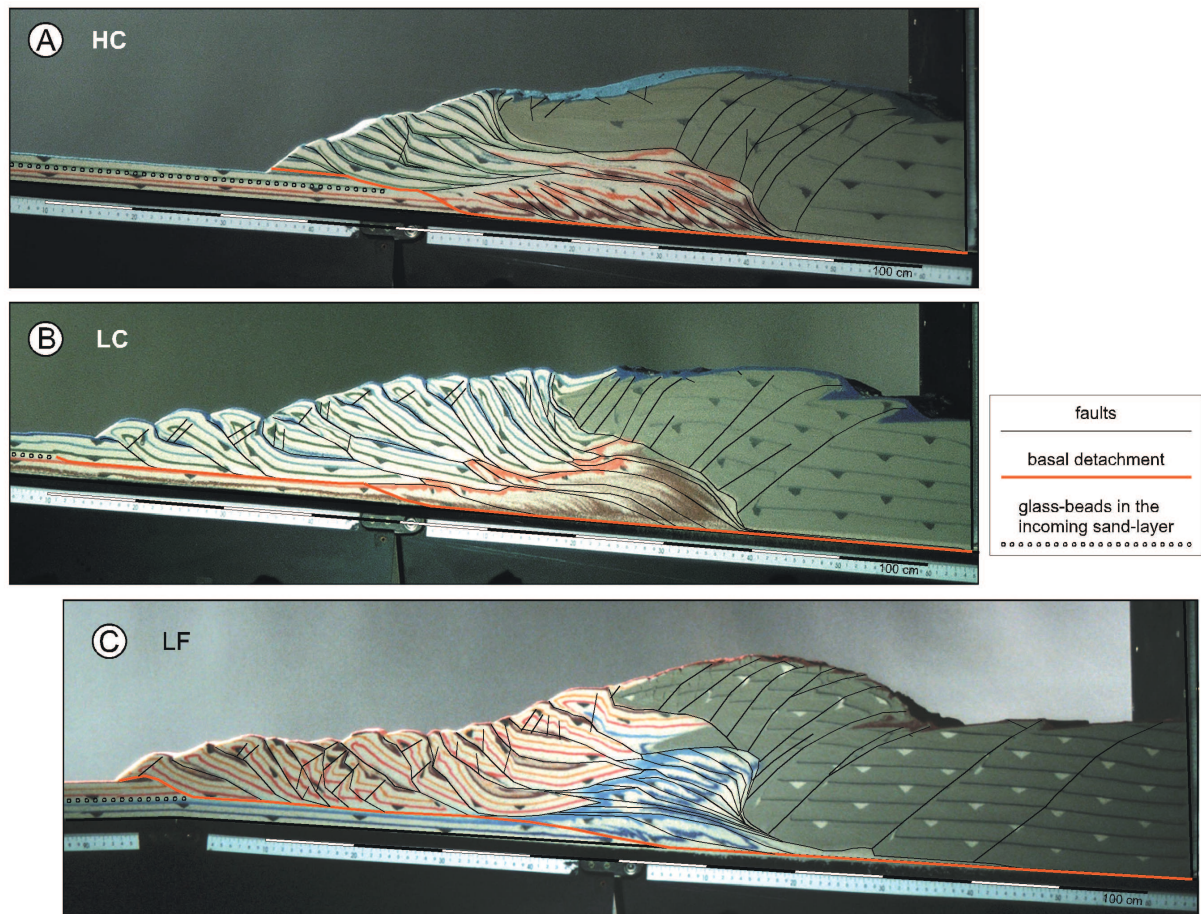


Figure 3.9: Photographs after 180 cm conv. of the two-level experiments, which were used as database for quantitative comparisons (see Tab. 3.2; vertically aligned on the initial tip of the backstop wedge). a) HC experiment, b) LC experiment, c) LF experiment. Detailed kinematics are indicated in Fig. 3.7).

events occurred after 78 cm conv. This was followed by five other events until the experiment finished after 210 cm conv. (Fig. 3.11 a). In contrast, the LF and LC experiments showed only two long-slice events during the whole experimental run (Fig. 3.11 b and c). In the LC experiment the long slices were initiated during the later stages of the experimental run (after 120 cm conv.), whereas the long slices occurred only in the early stages of the LF experiment (up to 90 cm conv.). During the later stages of the LF experiment (after 90 cm conv.) slices of nearly similar length formed the frontal-accretionary wedge with the convex topography (Fig. 3.9 c). The kinematics of the rear segment with the shallow surface slope of this frontal-accretionary wedge were characterised by an active out-of-sequence thrust (after 150 cm conv.) within the segment (OT in Fig. 3.7). In the other experiments (LC, HC), active out-of-sequence thrusts within the internal parts of the frontal-accretionary

wedges were not observed (Fig. 3.9 a and b).

Furthermore, the initial length of the duplexes, which were formed in the lower portion of the incoming sand-layer, differed between the experiments (Fig. 3.11). All duplexes in the LF and HC experiment had an initial minimum length of more than 5 cm, which was immediately reduced after the initiation by duplex-internal diffuse deformation. In addition, two phases of diffuse deformation occurred in the LC experiment, without the previous initiation of a localised ramp at the front (80–10 and 135–180 cm conv.; Fig. 3.11 b). The initial maximum lengths of duplexes were smaller in the LF experiment than in the other two experiments (LC, HC), so that the range of length variation was smaller, and the distribution of slice length was more even in the LF experiment (Fig. 3.11).

Another important difference between the experiments was the length and the displacement of the duplex sub-complexes. Fig. 3.12 shows that the

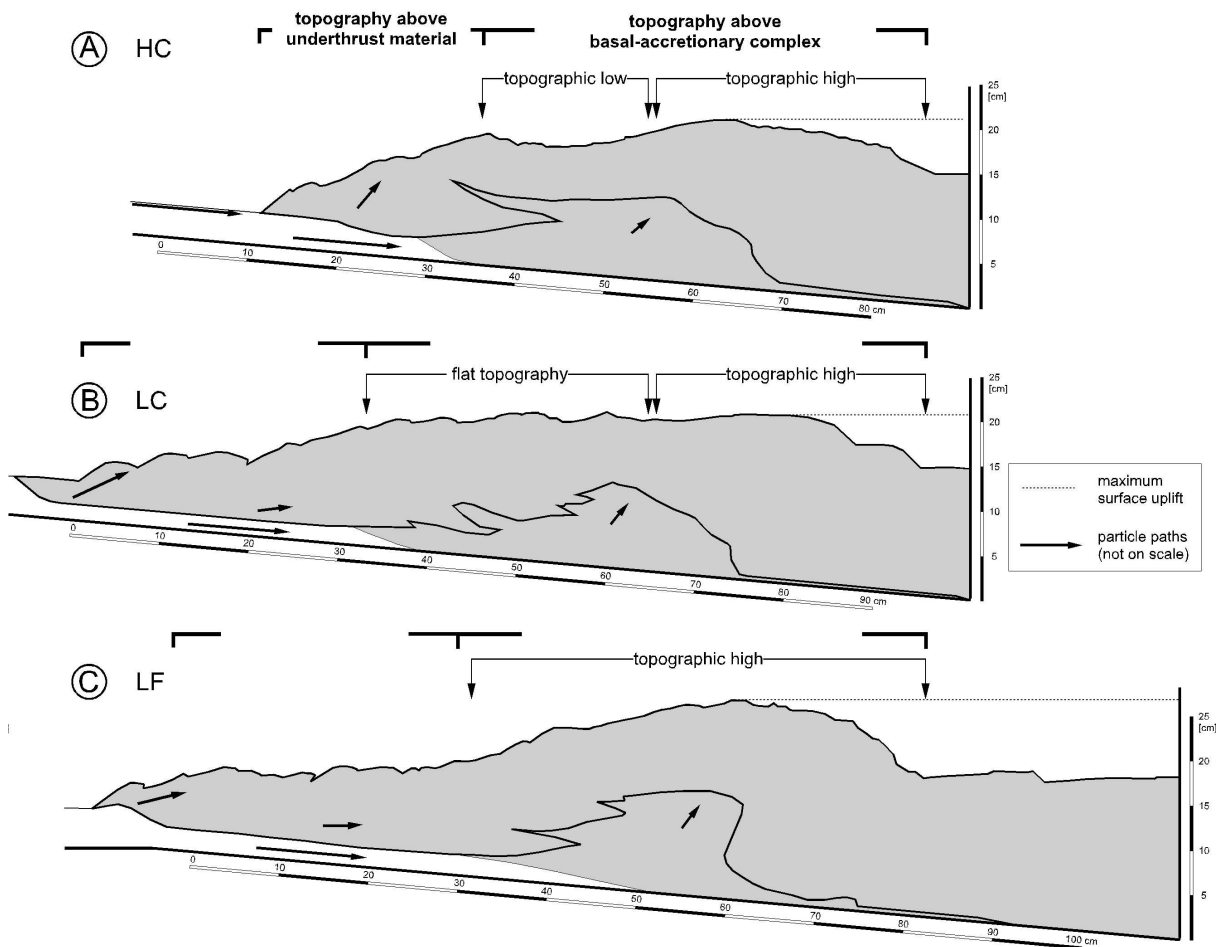


Figure 3.10: Comparison of the topography above the basal-accretionary complexes of the a) HC experiment, b) LC experiment, c) LF experiment, each after 180 cm conv.

smaller sub-complexes of the LF experiment were more highly stacked than the larger sub-complexes of the two other experiments (LC, HC). This observation was quantitatively supported by the comparison of the total length of the whole duplex complex and the maximum surface uplift caused by basal accretion in the experiments with the same volume of basally-accreted material (Tab. 3.2, LC and LF): The length of the duplex complex was shorter in the experiment which was performed with fine-grained sandpaper (LF – 35.5 cm), than that which formed on top of coarse-grained sandpaper (LC – 47.5 cm). As a consequence of the larger horizontal shortening of the lower portion of the incoming sand-layer in the LF experiment, the maximum total surface uplift was larger in this experiment (13.4 cm), than that in the LC experiment (9.7 cm). Although the LC and HC experiments differed in the volume of basally-accreted material, stacking

of the duplex sub-complexes caused approximately the same maximum total uplift in both experiments (9.7 and 9.4 cm, respectively). This observation also supports the interpretation that the surface uplift is not directly linked to the thickness of the lower portion of the incoming sand-layer.

As consequence of more localised and higher uplift in the LF experiment, bending of the overlying material and near-surface extension which were caused by basal accretion of the duplex sub-complexes, were stronger in this experiment with the fine-grained sandpaper (LF; Fig. 3.7 b), than in both experiments with the coarse-grained sandpaper (LC, HC; Fig. 3.9 a and b).

During the experimental runs, the position of the midpoint of maximum surface uplift and therefore the position of the centre of basal accretion did not remain stationary. Mapping of the incremental maximum surface uplift (Fig. 3.13) revealed that

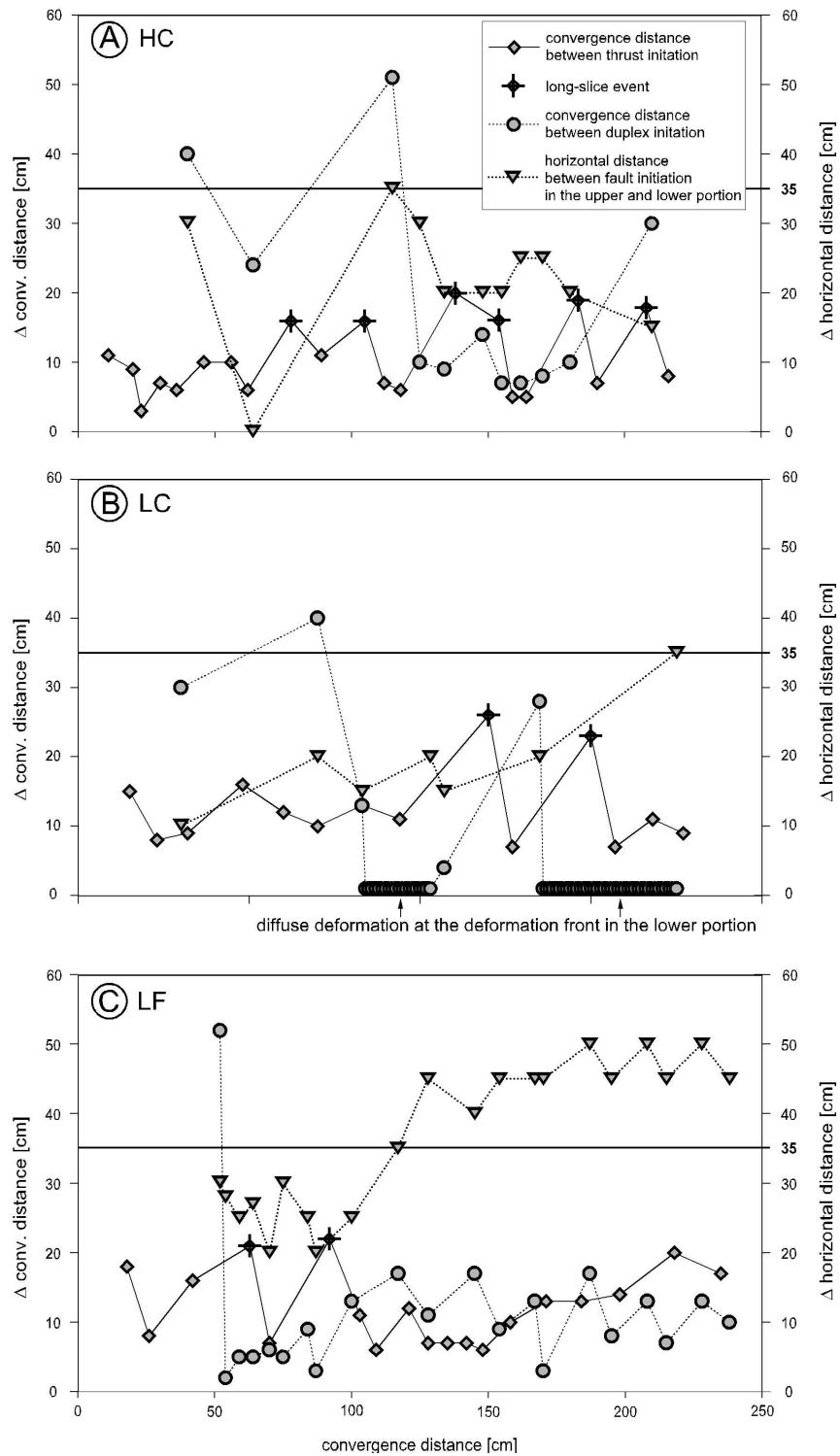


Figure 3.11: Relative convergence distance between the initiation of imbricates and duplexes (Δ conv. distance), and the horizontal distance of the loci of fault initiation in the upper and lower portion of the incoming sand-layer (Δ horizontal distance), as a function of total convergence distance. For the a) HC experiment, b) LC experiment, c) LF experiment.

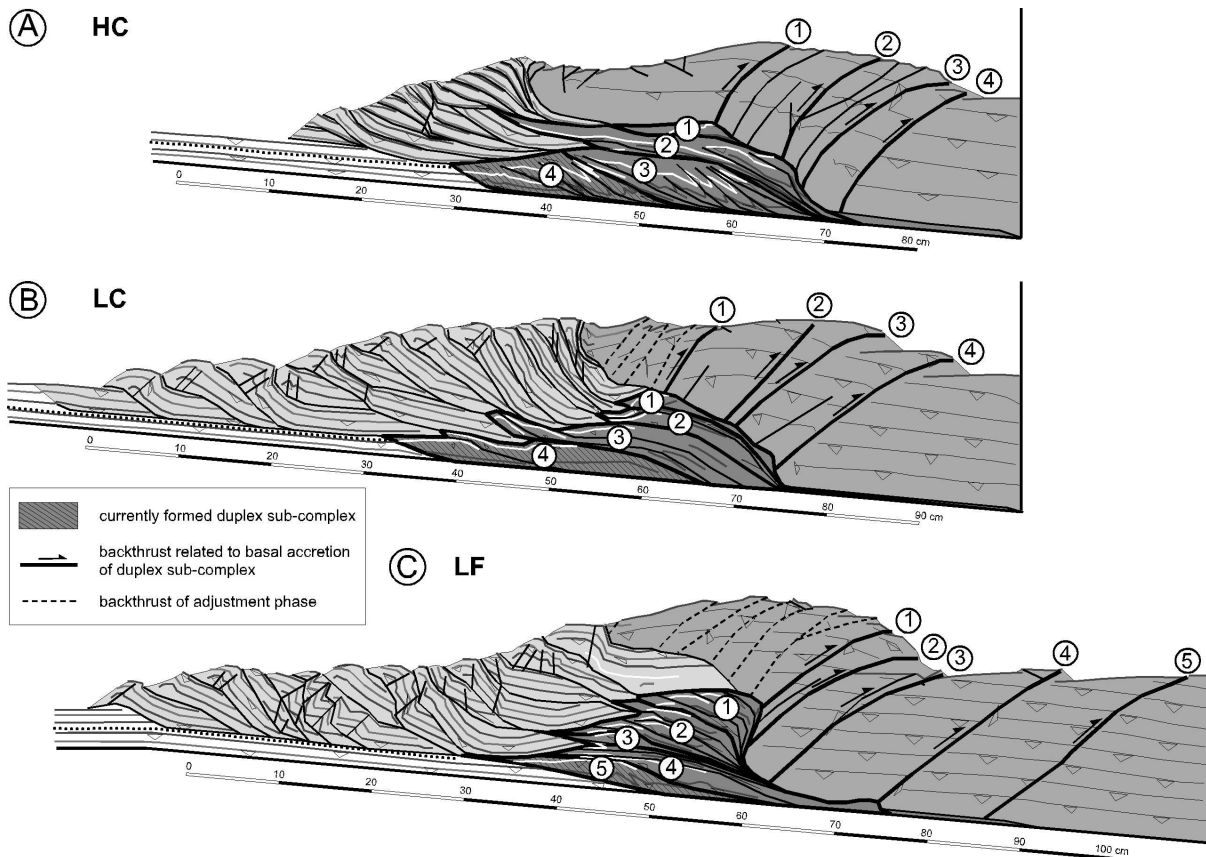


Figure 3.12: Basal accretion of duplex sub-complexes is connected with the initiation of a new backthrust in a) HC experiment, b) LC experiment, c) LF experiment (numbers indicate the age of the formation of duplex sub-complexes and backthrust). The ratio between thrust displacement and the length of the sub-complexes controls the total amount of uplift.

the migration patterns of the different experiments were not similar (Fig. 3.14). In the LF experiment an even topography was formed above the basal-accretionary complex. In contrast, the LC and HC experiments produced topographies with distinct lows above the basally-accreted material. If the wedge above the basally-accreted material had an even topography, the position of maximum uplift continuously migrated towards the rear of the sand wedge, and incremental uplift rates decreased over time (Fig. 3.14 c). If a topographic low developed above the basal-accretionary complex, the position of incremental maximum uplift was shifted towards the topographic low, and the incremental uplift rate increased (Fig. 3.14 a and b). This shift of the midpoint of uplift resulted in compensation of the topographic low until a more even topography was re-established. After compensation, the rearward migration of the midpoint of uplift began again (Fig. 3.14 b).

Three mechanisms to compensate the topographic lows were observed in fast-motion of the video sequences (Fig. 3.15):

- i) The position of the initiation of duplexes took place in a more frontal position beneath the topographic low. Further underthrusting of the incoming sand-layer along a localised thrust or the diffuse deformation within the newly-formed duplex caused an increase of uplift at a more frontal position (Fig. 3.15 a).
- ii) The displacement rates of the duplex sub-complexes were temporarily increased. This mechanism was less effective with respect to shifting the position of surface uplift than (i), however, it still enabled the compensation of a topographic low (Fig. 3.15 b).
- iii) Long slices in the upper portion of the incoming sand-layer were underthrust far beneath

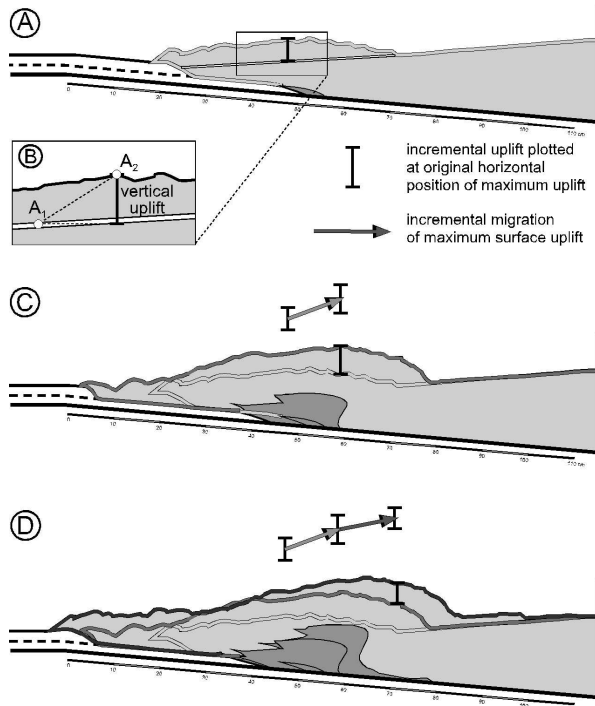


Figure 3.13: Method to measure the incremental vertical uplift and map the incremental migration of maximum surface uplift. Wedge geometries a) after 0 and 50 cm conv., c) after 50 and 100 cm conv., and d) after 100 and 170 cm conv. b) A reference point in two stages of convergence (A_1 , A_2) is used to measure the vertical uplift.

the frontal-accretionary wedge and reached the position of the topographic low. This compensation mechanism of topographic lows was the only one which did not result in a relocation of the centre of basal accretion. However, this mechanism was observed only once in all of the experiments (LC experiment, 120–130 cm conv., Fig. 3.15 c).

Differences in the displacement field of the experiments were most clearly seen in the incremental particle paths of later stages of the experimental run, in which different kinematic domains were developed. The LF experiment possessed three well-defined particle-path domains which correlated with the domains of different inclinations of the surface slope (Fig. 3.16 c). Frontal accretion caused uplift and rearward transport at the wedge tip in the area of the steep frontal surface slope. The adjacent domain with the shallow surface slope was characterised by nearly base-parallel transport with a very small component of uplift. This domain was

located above the underthrust material. In turn, the third domain with a stronger inclined surface slope showed a larger component of uplift, which resulted from basal accretion.

These three domains of particle paths were also present in the LC experiment (Fig. 3.16 b). However, between the two rear domains there was no remarkable change in the inclination of the surface slope.

The HC experiment was characterised by a steep frontal slope without any significant change during the investigated convergence steps. In this experiment, the pattern of particle paths did not allow the division into different domains (Fig. 3.16 a). However, inspection of the kinematics suggested a division into two domains:

- the frontal domain, in which uplift was caused by frontal accretion
- the rear domain, in which basal accretion caused the uplift component

A central domain with nearly base parallel transport was missing in this experiment.

Conclusions of experimental results

In summary, the variation of sediment supply mainly resulted in changing the distribution of material volumes (frontally versus basally accreted). In contrast, the roughness of the basal interface determined the length of the duplex sub-complexes. Fine-grained sandpaper produced shorter duplexes with larger thrust displacements. Both of the varied input parameters, sediment supply and roughness of the basal interface, were not able to change the general mass-transfer mode.

Basal accretion took place by initiation of single duplexes and the stacking of duplex sub-complexes. As the experiments with different thicknesses of the lower portion of the incoming sand-layer (HC and LC) showed the same uplift rates, I conclude that the uplift rate was not a function of the thickness of the incoming sand-layer. Therefore, the uplift caused by basal accretion was mainly produced by the stacking of the sub-complexes. Moreover, the distribution of vertical load significantly controlled the migration of the position of basal accretion.

The kinematics of the frontal-accretionary wedge indicated a high-friction wedge. The relative high basal friction of the frontal-accretionary wedge (glass beads $\mu_D = 0.43$) confirmed this suggestion. However, it does not explain the occurrence of the

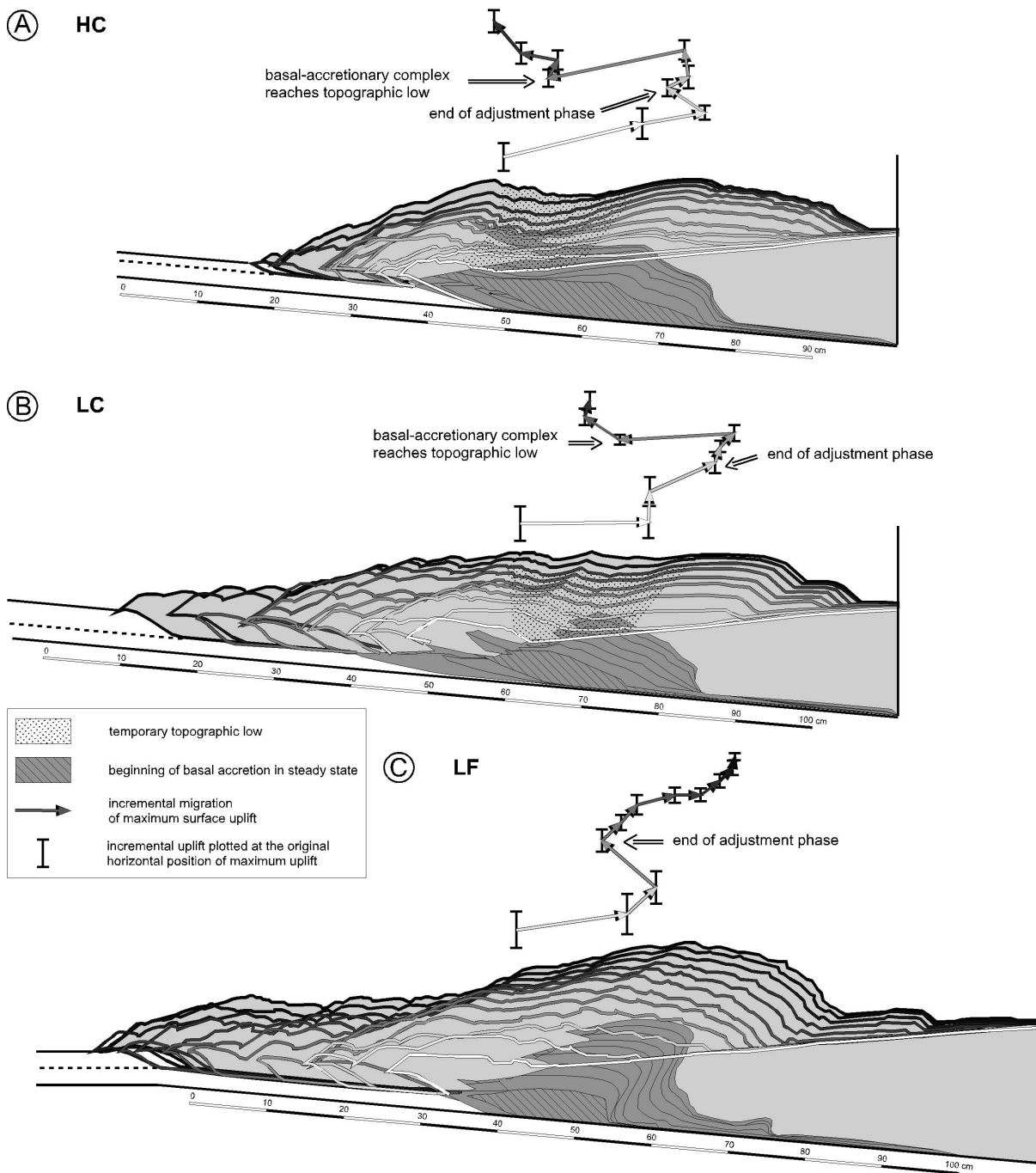


Figure 3.14: Migration of the midpoint of uplift in the a) HC experiment, b) LC experiment, c) LF experiment.

long-slice events in the upper part of the incoming sand-layer (further discussion cf. Section 3.4.1).

The number of kinematic segments in the two-level experiments varied in each experiment. The determination of wedge segments was more difficult in these two-level experiments than in the one-layer experiments, since the kinematic domains did not

always coincide with the geometrical segmentation. Therefore, the topographical signal was not an explicit feature of the actual particle paths. Nevertheless, in every experiment only one segment always contained continuously-active thrusts: the youngest duplex sub-complex. This suggests a critical state of stress of this segment (further discussion cf. Sec-

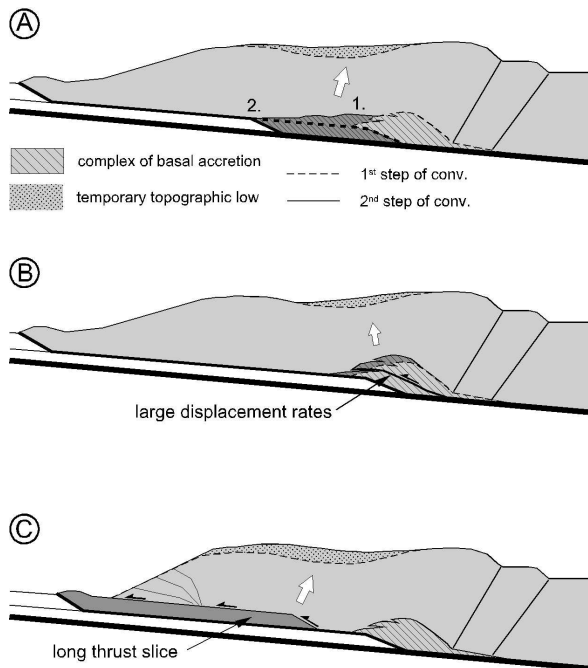


Figure 3.15: Mechanisms to compensate for a topographic low by wedge-internal deformation: a) The onset of failure in the lower portion of the incoming sand-layer migrates towards a more frontal position; b) increase in the displacement rate of a duplex sub-complex; c) underthrusting of longer imbricates at the base of the frontal-accretionary wedge.

tion 3.4.2). All other wedge segments showed reactivated or inactive thrusts, which infers that these segments were in a stable state, such as the IAZs of the one-layer experiments (cf. Section 2.4.3.2).

3.4 Interpretation of the results of the two-level experiments

3.4.1 Changes in structural and geometrical wedge evolution

All two-level experiments were characterised by different phases in the structural and geometrical evolution: Large thrust displacements episodically occurred in the frontal-accretionary wedge, as well as in the basal-accretionary complex. However, the frontal and basal deformation processes were not mutually caused, as the long-slice events in the frontal-accretionary wedge did not correlate either to long-slice events in the basal-accretionary complex, nor to the underthrusting events of duplex sub-complexes (Fig. 3.11). The alternation of long and short slices in the frontal-accretionary wedge

occurred only when the horizontal distance between the deformation front of the wedge and the deformation onset in the lower portion of the incoming sand-layer was less than 35 cm (Fig. 3.11). This was the case during all the HC and LC experiments and during the first 100 cm conv. in the LF experiment. During this stage of the experiments the position of deformation onset in the lower portion of the incoming sand-layer migrated towards the deformation front. The deformation front itself migrated rearwards. Thus the distance between the deformation front and the deformation onset in the lower portion was not able to increase despite continuous material addition. In the later stages of the LF experiment, the distance between the deformation front and the deformation onset in the lower portion increased to 45–50 cm, because the frontal-accretionary wedge formed the central wedge segment. After the formation of this wedge segment the alternation between long and short slices in the frontal part of the wedge ceased.

The comparison of the frontal-accretionary wedge of the two-level experiments with the purely frontal-accretive, high-friction experiments investigated by Gutscher et al. (1998a) and in Section 2.4.4, provide a good opportunity to discuss the phenomenon of alternation of slice length.

Gutscher et al. (1998a) observed an alternation of long and short slices during one-layer experiments they had performed in an open setup (for the definition 'open setup' see, Section 2.4.1). However, my high-friction experiments of the basic parameter study (Section 2.4.4) did not show alternation between long and short slice length. Also, the one-layer experiment of Gutscher et al. (1998a) in a closed setup formed only slices of similar length. Therefore, the alternation of slice length is not typical of high-friction experiments. However, the alternation always occurred when the experimental setup allowed rearward material loss of the material previously accreted to the frontal wedge: In the one-layer experiments this is caused by the open setup, whereas in the two-level experiments, rearward material loss with regard to the frontal-accretionary wedge occurred by out-of-sequence thrusting, underthrusting and basal accretion. However, the two-level experiments indicated that a spatial relationship of frontal accretion and the site of material loss was necessary to produce the alternation of long and short thrust slices.

Gutscher et al. (1998a) showed theoretically that thrust displacements are mainly influenced by the overlying wedge thickness (cf. Section 2.4.4.2 and

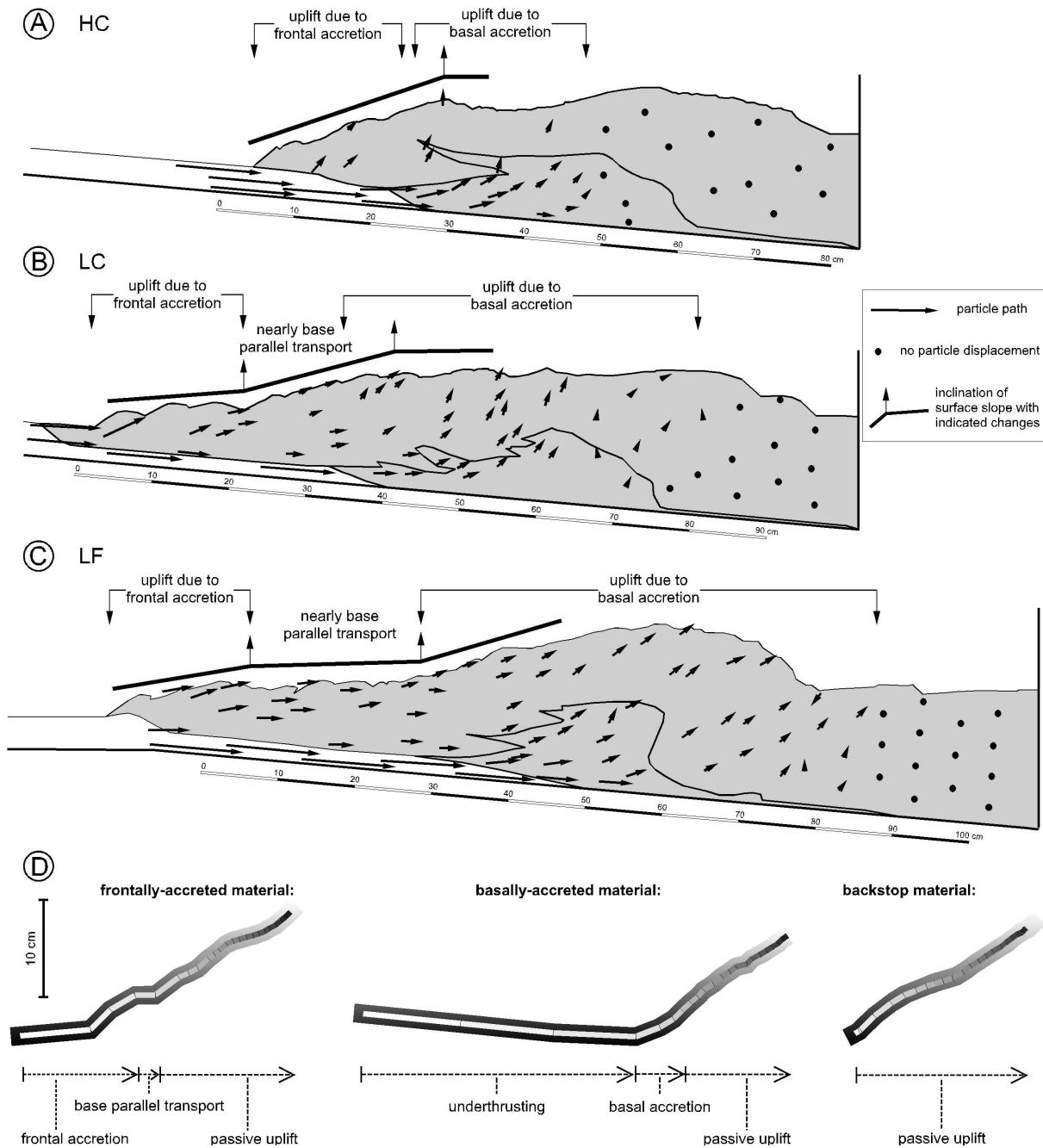


Figure 3.16: Comparison of the incremental displacement fields of the two-level experiments between 170-180 cm conv. of the a) HC experiment; b) LC experiment; c) LF experiment. d) Total particle paths (0-220 cm conv.) from selected triangular-shaped markers of the LF experiment with increments indicated every 10 cm conv.

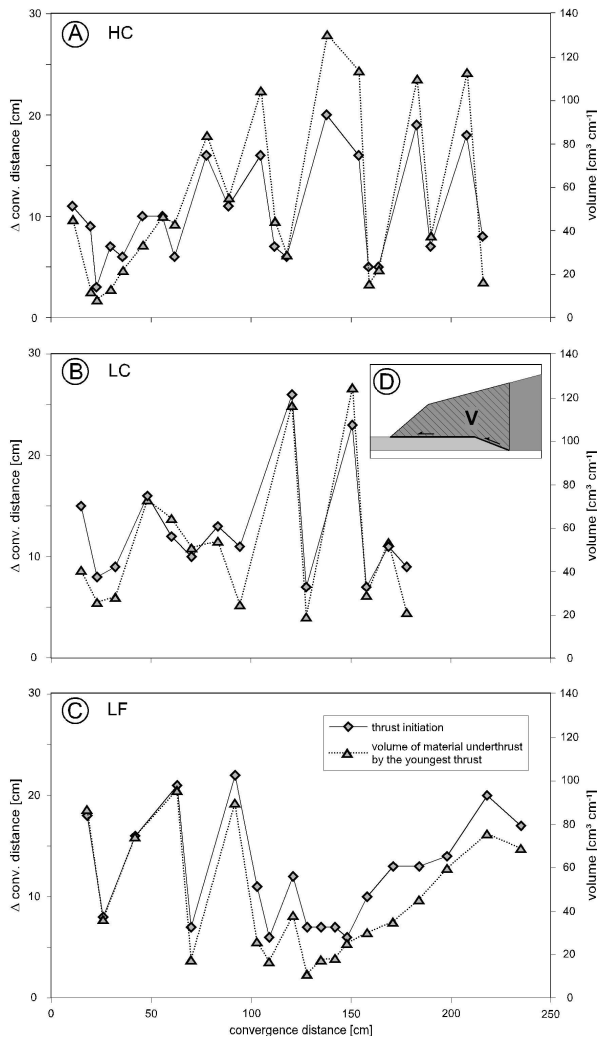


Figure 3.17: Relative convergence distance between the initiation of imbricates (Δ conv. distance) and cross-sectional area of the wedge above the currently underthrust imbricate (A in Fig. d), as a function of total convergence distance. a) HC experiment; b) LC experiment; c) LF experiment

Fig. 2.26 c and d). The wedge thickness, which is controlled by the wedge taper, was inversely proportional to the maximum thrust displacement. Large thrust displacements steepen the surface slope, so that a successively larger wedge thickness had to be uplifted by the underthrust sequence. They argued that the increase in wedge taper caused the observed decrease in slice length. However, their argumentation fails to explain the repeated occurrence of long slices in their experiments and also in the frontal-accretionary wedge of two-level experiments: In both types of experiments, these long slices were underthrust far beneath the wedge,

where the steep surface slope was already present. Therefore this observation does not confirm the direct influence of wedge thickness on slice length (Fig. 3.17).

The results of the one-layer experiments in the open setup suggested that the alternation in slice length is only controlled by continuously changing forces (frictional and gravitational forces). However, the observations of the two-level experiments inferred that a force that discontinuously changes during the experimental run might control the alternation in slice length: The long-slice events only occurred, when the central segment of the frontal-accretionary wedge was absent. In this case,

- discontinuous deformation processes in the basal-accretionary complex,
- the changing inclination of the glass-bead layer above the basal-accretionary complex, and
- the changing volume and shape of the basal-accretionary complex

are able to directly influence the processes at the deformation front. Although measurement of forces was not possible in the experimental setup used, I suggest from these observations that the resistance at the rear of the frontal-accretionary wedge mainly controlled the alternation of slices length.

3.4.2 State of stress of the wedge segments

The critical-taper theory is able to estimate the state of stress in wedges which grow geometrically self-similar, since a homogeneous stress field is assumed here. As described above, the two-level experiments did not meet this condition. In this case, I propose that the estimation of the state of stress is also possible for geometrically self-similar wedge segments, since this was successfully carried out for the basic parameter experiments (Section 2.4.). Therefore, I separately analysed each phase and segment of the different dynamical states using semi-quantitative Mohr Diagrams. These investigations were not able to study the whole wedge evolution with linked processes such as described in Section 3.4.1. However, they lead to a better understanding of why one segment is shifted into a non-critical state of stress. The probable occurrence of different non-critical wedge segments with different wedge tapers in the two-level experiments

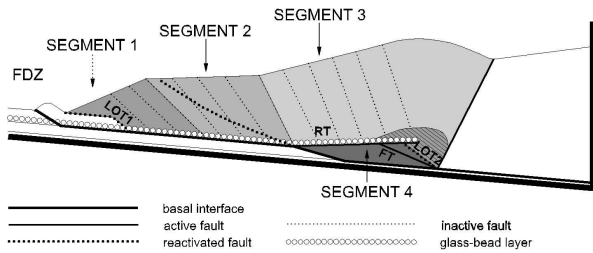


Figure 3.18: The critical-taper analysis is based on this kinematic segmentation of the LF experiment. The leading out-of-sequence thrust 1 (LOT1) is the boundary between the frontal-deformation zone (FDZ) and segment 1, LOT2 is the boundary between segment 4 and the basally-accreted duplex sub-complexes (FT – continuously-active, trailing forethrust of segment 4).

infers that each segment was shifted by a modification of a certain parameter (e.g. internal, basal friction, surface slope) into a non-critical state. In this section, these controlling parameters for each segment will be identified. Moreover, I will estimate, under which specific conditions these segments were in a non-critical state.

On the basis of the geometrical and kinematic segments of the LF experiment (Fig. 3.18) which were defined in Section 3.3, the following critical-taper analysis was performed. The LF experiment was chosen for the critical-taper analysis because this experiment possessed, in addition to the wedge segments also observed in the other experiments (LC, HC), a central stable segment. Moreover, the LF experiment showed the best-defined wedge segments, i.e. each wedge segment was characterised by its own kinematic, geometrical features and mass-transfer process. In contrast, the LC- and HC experiment formed wedge segments, which consisted of inherited geometries or they did not show differences in the mass-transfer process (cf. Section 3.3).

Segment 1 was in a stable state and showed the typical features of a frontal-accretionary wedge, which was formed above a relatively high-friction interface (glass beads). In Section 2.4.4, I explained that the stable state of such a wedge segment is due to the change of the basal properties. During the initiation of a new frontal thrust, the basal interface is located within the glass-bead layer, which has a lower friction than the sand/sand interface during the underthrusting phase. This decrease of the basal friction changed the formerly-shaped wedge into the stable state.

Segment 2 had also obtained a stable state and showed a lower wedge taper compared to segment 1.

Here, the basal properties were constant, as the basal interface of this segment was located within the glass-bead layer during its whole evolution. As was argued in Section 2.4.2, the bulk wedge strength of internal wedge segments increases by the back-rotation of thrusts. This increase of internal wedge strength can stabilise a low wedge taper. Because material is added and thus the differential stress increases, the thrusts in this segment have either to be reactivated or new thrusts with a lower dip have to be initiated. In the LF experiment it was observed that the decrease in wedge taper coincided with the back-rotation of thrusts. Therefore I suggest that increased bulk wedge strength is due to the back-rotation of thrusts in segment 2. Reactivation of thrusts during the growth of the segment was not observed. Nevertheless, in the later stage of the experiment, an out-of-sequence thrust with a lower dip than the back-rotated thrusts was initiated (OT in Fig. 3.7). This late initiation of the out-of-sequence thrust infers that new thrusts in this segment require a larger spacing than the frontally-initiated thrusts. This suggestion is in accordance with the results of Platt (1988), in that the spacing of thrusts depends on the thickness of the incoming layer. In the case of segment 2, the incoming layer is the segment 2, which was considerably thicker than the undeformed incoming sand-layer. Therefore, the initiation of a new thrust in this segment required a large horizontal length of the segment. This observation also supports the suggestion of an increase in bulk wedge strength by thrust-rotation: Without an increase of bulk wedge strength, the initiation of the out-of-sequence thrust and the inactivation of back-rotated thrust are not possible.

I suggested that segment 3 is again a stable segment with inactive thrusts, which exhibited a steeper surface slope than segment 2. Material of segment 2 was continuously transformed into that of segment 3 during the experimental run due to the formation of segment 4 at its base. The parameter which changed between segment 2 and 3 was not mechanical, but geometrical, i.e. the basal dip decreased from 5 to -1° . For the construction in the Mohr Diagram (Fig. 3.19), I used the most shallowly-inclined thrust (FT = 23° in Fig. 3.19) as the boundary condition and assumed that its slip-line orientation belongs to thrusts which are just not activated. Under these conditions, the constructed critical taper is 9° ($\alpha = 10^\circ$; $\beta = -1^\circ$). The passive basal uplift and rotation of the previously stable

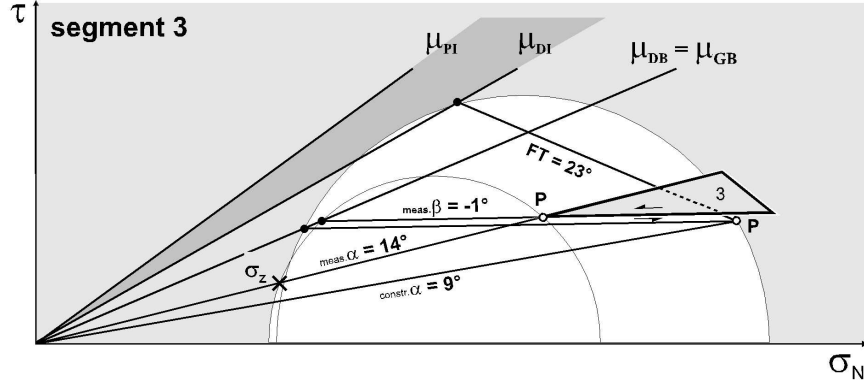


Figure 3.19: Comparison of measured and constructed surface slope (meas. α , constr. α , respectively) of segment 3 in the LF segment (see Fig. 3.18). The constraints used for Mohr Circle construction are the stable dynamic internal friction (μ_{DI}) and stable dynamic basal friction (μ_{DB}) of the glass beads (μ_{GB}), the wedge taper (meas. α +meas. β) measured in the sandbox experiments, and the dip of the shallowest-inclined inactive forethrust (FT) (τ – shear stress, σ_N – normal stress, σ_z – state of stress at the depth z ; μ_{PI} – peak internal friction, P – pole).

wedge segment caused a taper of 12–13° in the experiment, which was higher than the constructed critical taper (Fig. 3.19). Thus, the rotation of the segment enabled it to maintain the stable state: Here, the differential stress was sufficiently large to maintain shearing along the mid-level detachment, but did not allow the activation of thrusts in any orientation, since the differential stress did not overcome the failure curve of pre-sheared sand.

Segment 4 was the only segment in the two-level experiments which showed continuous failure along its thrusts. Therefore, I suggested that this segment was in a critical state. The upper boundary of this segment was formed by an active wedge-internal shear zone within the glass-bead layer, i.e. the roof thrust of the duplex sub-complex, which was active along its whole length. Therefore segment 4 did not have a frictionless surface, in contrast to all other segments described in this study. The segment overlying segment 3 induced an additional normal stress on the latter. The additional normal stress was not produced by the force balance of the active segment, but instead by the inherited wedge geometry of the overlying segment. To regard to all acting stresses, a Mohr Diagram of segment 4 has to consider the surface slope of segment 3 (Fig. 3.20 b). The basal interface was located between the sand and the sandpaper. The characteristic features of this segment were a shallowly-inclined roof thrust (–1 to –2°, RT in Fig. 3.20) and also shallowly-inclined trailing forethrusts (23°, FT in Fig. 3.20). Therefore, the Mohr Diagrams of this segment were constructed with the measured stable dynamic fric-

tion according to SIC2, glass beads, and sandpaper and the inclinations of the trailing active forethrust and roof thrust within the glass-bead layer.

The Mohr Diagram shows that an activation of the basal detachment on top of the sandpaper could only occur under the above-mentioned conditions, i.e. if a certain normal stress acted on the sandpaper interface (σ_{N2} in Fig. 3.20 a), which was larger than the normal stress required to activate a mid-level detachment in the glass-bead layer (σ_{N1} in Fig. 3.20 a). In the experiment, this normal stress was produced by the overlying segment 3.

Fig. 3.20 b shows a Mohr Diagram in which the trailing forethrust is plotted as the steepest active thrust and reveals a state of stress different to the previously-suggested critical one: The constructed basal shear stress overcomes that one required for basal-detachment activation. Thus, I propose a subcritical state of stress in segment 4. The mismatch between the observed and constructed inclination of the roof thrust validates this interpretation, as the subcritical state of stress in terms of critical-taper theory is characterised by a shallower roof thrust than that in a critical state. However, the characteristic transient taper, as observed in the subcritical segments of the basic-parameter experiments (FDZ in Section 2.4.3.2), was not observed in segment 4 (taper = β +RT) of the LF wedge. This inconsistency might be explained by the continuous material addition to the overlying segment during the experimental run. This increase in normal load does not allow the steepening of the roof thrust. Instead, strongly back-rotated thrusts became ac-

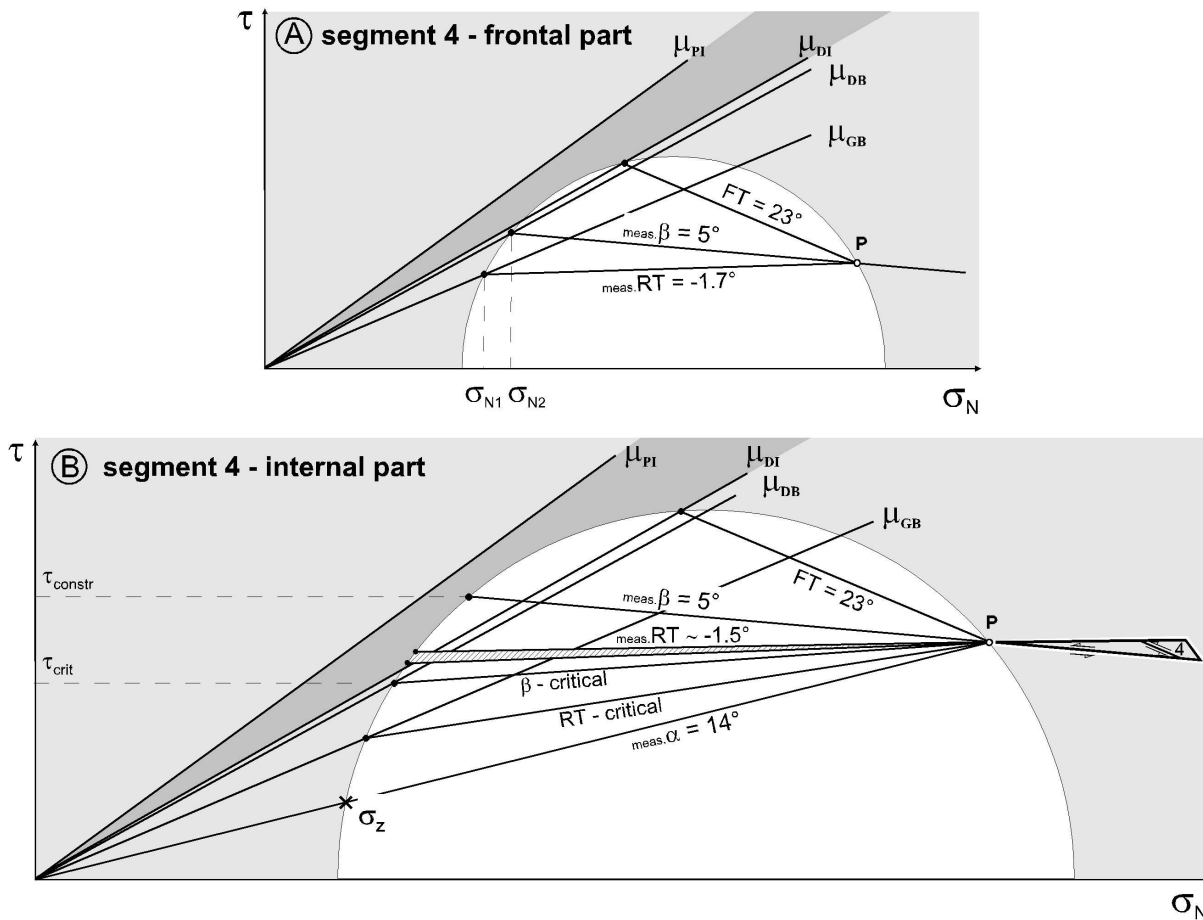


Figure 3.20: Mohr Diagrams of segment 4 in the LF experiment (see Fig. 3.18). The constraints used for construction are the measured peak internal friction (μ_{PI}), stable dynamic internal friction (μ_{DI}) and stable dynamic basal friction (μ_{DB}) of SIC2 with respect to the fine-grained sandpaper, as well as the stable dynamic friction of the glass beads (μ_{GB}), the wedge taper ($\text{meas.}\alpha + \text{meas.}\beta$) measured in the sandbox experiments, and the dip of the trailing internal forethrust (FT) and roof thrust ($\text{meas.}RT$) of the active duplex sub-complex. a) Mohr Diagram shows the assumed critical state of stress of segment 4, with indicated normal stresses required for continuously-active detachments within the glass-bead layer, and along the sandpaper interface (σ_{N1}, σ_{N2} , respectively). b) Comparison of the constructed critical state of stress with the state of stress present in segment 4. (τ – shear stress, σ_N – normal stress, τ_{crit} – critical shear stress of the basal interface, τ_{constr} – shear stress acting on the basal interface, P – pole).

tive. However, basal accretion only took place when a stable duplex segment with inactive thrusts was formed by their back-rotation in the rear part of segment 4. Therefore the duplex sub-complexes with continuously-active thrusts became larger during the experimental run and effective stacking due to the basal accretion of sub-complexes ceased.

I conclude that, based on this critical-taper analysis, the stable states of segment 1 and 3 could occur only under certain conditions. Segment 1 remained only in stable state because the initial setup with the glass-bead layer, which acted as a relatively high

frictional base. A setup with a low-friction mid-level detachment would have caused a critical state of stress in segment 1. This scenario is most conceivable in nature, where high pore pressures are able to produce very low strength of the individual layers.

The stable state of segment 3 was reached by strong passive bulk rotation. This rotation depended on the inclination of the roof thrust of the duplex complex. Other mechanical and geometrical conditions would have led to a lower inclination of the roof thrust, so that passive rotation of the

overlying segment would have shifted the overlying segment in a subcritical or critical state.

The only segment of the frontal-accretionary wedge, which would remain stable under any conditions is the segment 2, as the thrust rotation, which caused the stable state in segment 2, is a self-induced process within the system. As discussed in Section 3.4.1, the formation of this segment was responsible for the change of kinematics from alternation between long and short thrust slices to thrust slices of similar length. Therefore, I suggest that the change of kinematics in the LF experiment is not a function of the special initial conditions of the experiment, but describes the general behaviour of two-level systems which undergoes much convergence.

3.5 Comparison with the South Chilean Forearc

The analogue simulations yield a detailed database for the complex accretionary process of two-level systems. Although nature does not provide the observer with such a detailed database, it is possible to draw some conclusions for the mass-transfer process acting at the South Chilean Margin, by comparison of the main kinematic features and mass-transfer rates of experimental and natural systems.

The experiments have shown that the partial underthrusting of incoming sediments, such as observed at the South Chilean Margin, leads to basal accretion beneath the forearc wedge and uplift of the overlying material. An area of minor Neogene uplift in the South Chilean Forearc is observed between the shore line and the boundary of the Coastal Cordillera and the Longitudinal Valley (Section 3.1.1 and Fig. 3.1). Therefore, I suggest that basal accretion took and is taking place beneath this region during the different Neogene accretionary phases of this forearc system. To validate this suggestion, the kinematic domains observed in nature have to match those of the analogue experiments. Moreover, the uplift rates during particular time intervals, as measured for the South Chilean Forearc provide important information about its basal mass-transfer mode. Below, the rates of basal accretion during the Miocene, Pliocene and Quaternary are estimated as exactly as possible from published data. On this basis, the natural and experimental system are compared.

3.5.1 Mass balance of basally-accreted sediments at the South Chilean Forearc

To estimate the thickness of the sediment pile which was basally-accreted during the individual time intervals, two simplified assumptions are made:

1. The shape of the uplifted area is assumed to be rectangular, since only the length and height of the uplifted area could be estimated from the geological record, but not its exact shape. The true shape of the uplifted area possibly lies between a triangle ABC and a rectangle ABDE in Fig. 3.21 a. I chose the latter, which is always the maximum overestimation, for the calculation.
2. As seen in the experiments, uplift is accomplished by fault-bend folding, so that the basally-accreted area has to be constructed correctly with dip-domain boundary projection.

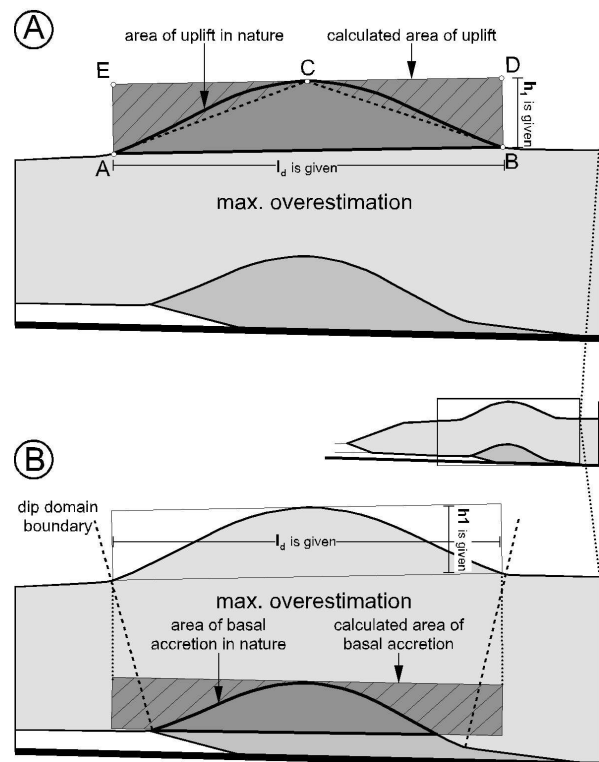


Figure 3.21: Assumptions which were made to calculate the thickness of basally-accreted sediments from field data (shaded area – estimated error; for acronyms see Fig. 3.22 and Section 3.5.1). a) the shape of the area of surface uplift is rectangular, b) the area of surface uplift is equal to the area of basally-accreted sediments.

Here, the depths of basal accretion and inclination of the dip-domain boundary strongly influences the volume of the area of basal accretion. Because both parameters are unknown in the nature, I use the depth-independent assumption that the uplifted area is equal to the basally-accreted area. Calculations of the area of basal accretion, which are based on this assumption, result in maximum values (Fig. 3.21 b).

The area of basal accretion (A'_1) during one time interval is given by

$$A'_1 = t \cdot V \cdot x, \quad (3.1)$$

where t is the duration of the time interval, V is the velocity of plate convergence, and x the thickness of the basally-accreted layer (Fig. 3.22 a).

The area of uplift (A_1) during the same time interval is given by

$$A_1 = l_d \cdot h_1 \quad (3.2)$$

where l_d is the length of the uplifted area as observed from field data, and h_1 the uplift during the time interval (t ; Fig. 3.22 a). h_1 is determined by the deposition depth of the sediments (d_1), their current elevation (d_2), as well as the difference between the current sea level (sl_2) and that during deposition (sl_1) (Fig. 3.22 b):

$$h_1 = d_1 + d_2 + (sl_2 - sl_1) - h_2 \quad (3.3)$$

The uplift (h_2), which took place after the time interval of interest (Fig. 3.22 a), must be considered, since d_2 reflects the total amount of uplift.

The second assumption

$$A'_1 = A_1 \quad (3.4)$$

allows the calculation of the thickness of basally-accreted layer (x), using equations 3.1 and 3.2:

$$x = \frac{l_d \cdot h_1}{t \cdot V}. \quad (3.5)$$

The database used for the calculation of basal accretion in Quaternary, Pliocene and Miocene time is summarised in Tab. 3.3. The average convergence rate of the Nazca Plate during the Quaternary is 8 cm a^{-1} (DeMets et al., 1994). The current convergence rate of 6.5 cm a^{-1} suggests a decrease of convergence velocity since the beginning of the Quaternary (Angermann et al., 1999). For the calculation

of thickness of the basally-accreted material during this time interval, I used a convergence rate of 8 cm a^{-1} which leads to a maximum value. An increase in convergence velocity up to 11.2 cm a^{-1} was determined for Pliocene and Miocene time (Pardo-Casas and Molnar, 1987), which is considered for the calculation of basally-accreted material during these time intervals.

For all calculations, the same length of the area of uplift is used, since the geological record does not provide detailed data to allow this value to be estimated for each time interval separately. However, offshore drilling shows that Miocene and Pliocene shelf sediments are still in a shelf position 35–40 km seaward of the current shore line (Bangs and Cande, 1997). This suggests that this region was not uplifted since the Miocene and marks the maximum western border of the uplifted area. The eastern border is indicated by the most eastern occurrence of the Miocene marine-continental transition, which is observed 40 km landward of the current shore line (Elgueta et al., 2001). Therefore the minimum length of the uplifted area is estimated to be 80 km.

To estimate the uplift during different time intervals, the deposition depths of the sediments from individual time intervals, and the sea level changes needed to be known. The data of sea level changes are taken from Haq (1988). Deposition depths of the sediments in the study area are rare in the literature, and are only known from some selected localities. These data are used here to calculate the general uplift in the region between 38–40° S, which is a crude approximation. The following data of each time interval were available:

- Quaternary: Quaternary beach terraces are located 50 m a.s.l. at the islands Mocha and St. Maria as well as on the Arauco Peninsula (Nelson and Manley, 1992; Boettcher, 1999).
- Pliocene: Pliocene shelf sediments are found today at 100–150 m a.s.l. on the Arauco Peninsula (Pineda, 1986). These sediments were deposited at water depths of ca. 50 m (pers. comm. K. Bandel, 2001).
- Miocene: The Miocene marine-continental transition, which marks the Miocene sealevel, is exposed today at 500 m a.s.l. (Elgueta et al., 2001).

All assumptions and approximations, which were made in the calculation of the thickness of the basally-accreted sediment pile, lead to maximum

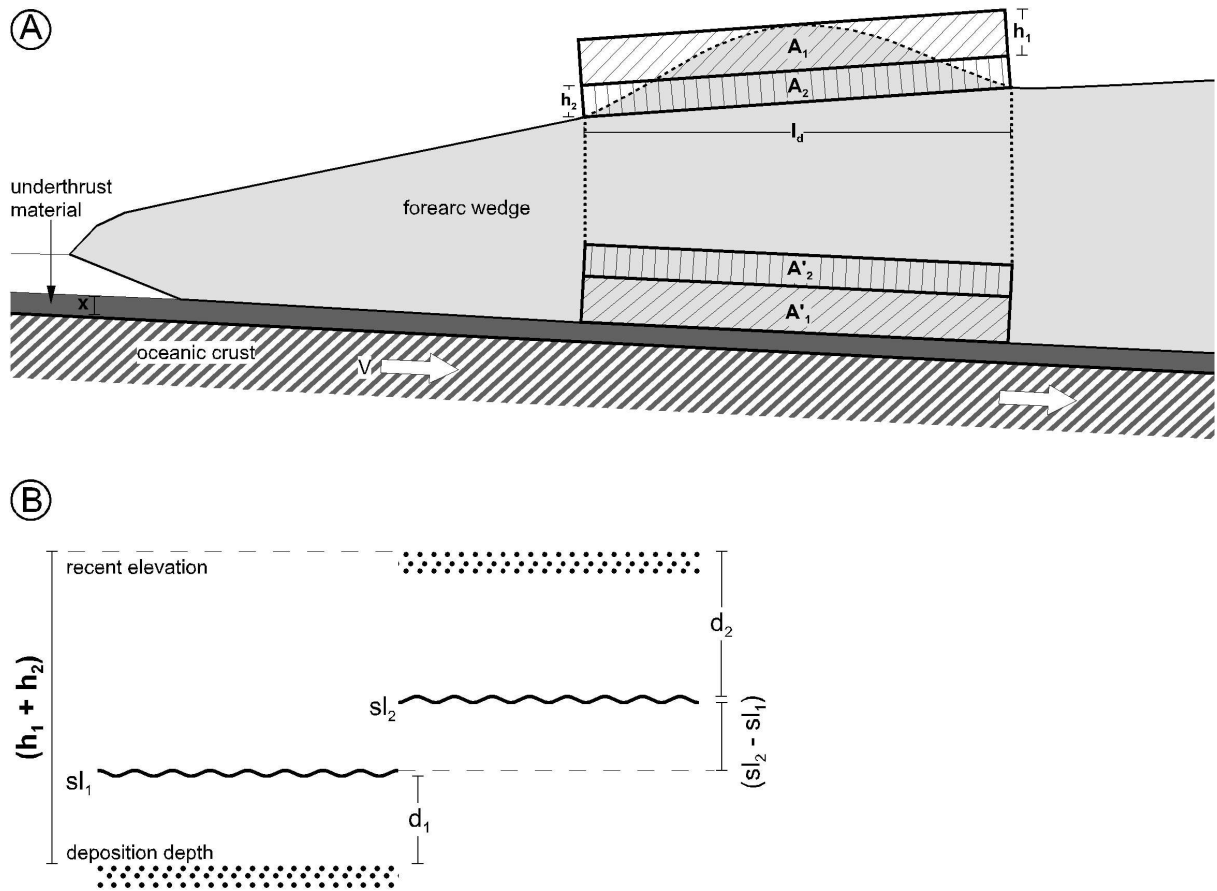


Figure 3.22: a) Definition of the geometrical parameters used for the calculation of the thickness of basally-accreted material (x): A_1 – area of surface uplifted during the calculated time interval (t), A'_1 – area of basally-accreted sediments during t , A_2 – area of surface uplifted after t , A'_2 – area of basally accreted sediments after t , l_d – length of uplifted area, h_1 – vertical uplift during t (see also Fig. b), h_2 – vertical uplift after t . b) Definition of geometrical parameters used for the calculation of h_1 : d_1 – deposition depths of the sediments deposited during t , d_2 – recent elevation of the sediments above sealevel, sl_1 – sealevel during the calculated time interval, sl_2 – recent sealevel.

values. However, this value does not exceed 80 m for the Quarternary, and is even less (0–10 m) for the Pliocene and the Miocene (Tab. 3.3). An underthrust sedimentary layer with such a small thickness is not able to form duplexes over the whole length of the area of basal accretion. Therefore, the result suggest that short duplexes probably form a hinterland-dipping antiformal stack. Nevertheless, the estimated thickness is quite small, when compared to the thickness of sediments, which were underthrust during the current mass-transfer mode (max. 1300 m; Díaz-Naveas, 1999), and will be discussed further in Section 3.5.3.

3.5.2 Kinematics of experiments and the South Chilean Forearc

Two typical kinematic surface-patterns, which were caused by basal accretion, were observed in the experiments (cf. Section 3.3):

- syn-uplift extension occurred directly above the centre of current basal accretion,
- syn-uplift tilting occurred on both sides of the centre of basal accretion.

The evidence from the onshore region of the South Chilean Margin suggests that both kinematic

	t [a]	V [m a ⁻¹]	l_d [m]	d_1 [m]	d_2 [m]	h_1 [m]	h_2 [m]	$sl_2 - sl_1$ [m]	x [m]
Quaternary	1800000	0.080	80000	0	50	150	0	100	83
Pliocene	3500000	0.112	80000	50	100–150	0– 50	150	0	0–10
5 Miocene	18500000	0.112	80000	0	500	200–250	150–200	-100	8–10

Table 3.3: Database and results of the calculation of the thickness of basally-accreted material (x) beneath the South Chilean Forearc (for acronyms see Fig. 3.22 and Section 3.5.1). Sea level data from Haq et al., 1988

patterns are also present in nature: Syn-uplift extension of the Arauco Peninsula marks the position of the centre of basal accretion. The Coastal Cordillera South of 38° S, which is characterised by syn-uplift tilting to the east, is comparable with the rear part of the area of uplift in the experiments (Fig. 3.7). In this southern region (38–40° S), I suggest that the midpoint of uplift is located in the shelf, where the Valdivia Basin shows syn-sedimentary normal faults (Fig. 3.1 and 3.3; Mordojovich, 1981; Díaz-Naveas, 1999). This correlation of the kinematic domains shows a significant difference between experimental and natural systems: At the South Chilean Forearc, the centre of basal accretion seems to be at the same position with respect to the Coastal Cordillera, because the features of syn-uplift extension are present in the Miocene to Quaternary sediments in exactly the same position (at the Arauco Peninsula or in the Valdivia Basins). In contrast, all two-level experiments reveal migration of the midpoint of uplift, frontwards or backwards.

Moreover, all two-level experiments were characterised by a persistently-active, trailing backthrust, which formed the rear border of the area of uplift. There is no clear evidence for such a backthrust at the South Chilean Forearc. Nevertheless, the border between the Coastal Cordillera and the Longitudinal Valley (Fig. 3.1) could be a good candidate for this backthrust, as this lineament separates the area of uplift (Coastal Cordillera) and the area of relative subsidence (Longitudinal Valley).

The alternation between long and short slices is another feature of experimental basal-accretive systems, although this feature does not apparently occur under any conditions, as seen in the experiments. The small frontal-accretionary wedge of the South Chilean Forearc consists of only three to five slices, the length of which do not differ significantly (Fig. 3.2 and 3.3; Díaz-Naveas, 1999).

3.5.3 Discussion

The differences above-described between the experiments and nature will be discussed in this section, to decide whether these differences are indicators of additional processes, which are not considered in the sandbox simulations.

The stationary area of uplift in nature might be explained by the processes observed in the experiments. It is seen that in the experiments, a small deviation in wedge topography from an ‘ideal’ wedge shape is able to cause migration of the midpoint of uplift. In this case, the midpoint of uplift migrates towards the direction of the deviation. In the case of an ‘ideal’ wedge shape, the midpoint of uplift migrates backwards.

The midpoint of uplift of the South Chilean Forearc was located near or at the coast during the Miocene-Quaternary. This means that the area of uplift was (partly) in an onshore position, where the high precipitation rates (present-day rate $> 2000 \text{ mm y}^{-1}$), suggest a strong influence of surface-erosive material transfer on the dynamics and kinematics of the forearc. The strong dependence of wedge dynamics and mass-transfer mode on surface-material transfer was shown by Beaumont et al. (1992) and Willett et al. (1993). The continuous mass removal at the South Chilean onshore Forearc due to erosion might produce a deviation from an ‘ideal’ wedge topography at a fixed position. In this case, the midpoint of uplift is not able to migrate landward, as the uplift has to permanently compensate the continuous mass removal at the same position.

The thickness of the basally-accreted material is another difference between nature and experiments. The significantly reduced thickness of basally-accreted material in nature could be explained in one of three ways:

- i) The thickness of basally-accreted sediments is equal to the thickness of the underthrust sediments. Consequently, the thickness of underthrust sediments must have been significantly

less during Miocene to Quaternary times, when compared to the current thickness, as also considered by Bangs and Cande (1997). This interpretation requires that sediments of reduced thickness (< 100 m) were underthrust 100 km before they were basally accreted, since this is the distance between the trench and the midpoint of uplift. However, it is not mechanically possible to underthrust a very thin sediment pile for such a long distance, because the underthrust distance is also a function of thickness, as the slice length is a function of thickness (this is also to be seen in the initial stages of the HC and LC experiment, Appendix).

- ii) The process of basal accretion is not a continuous process. However, a continuous process was assumed to calculate the thickness of basally accreted sediments. If basal accretion took place periodically, a larger thickness of basally-accreted material is necessary to cause the observed uplift. The two-level experiments show that basal accretion was a continuous process during the Neogene, when consider over a timescale of tens of million years. Features of an alternation of fast uplift and stagnation of uplift, which would be caused by changes in basal accretion, are absent in the sedimentary record in South Chile. Only a change in the general mass-transfer mode could lead to an interruption of basal accretion, e.g. tectonic erosion or stagnation of the mass transfer processes. Although a tectonical-erosive phase

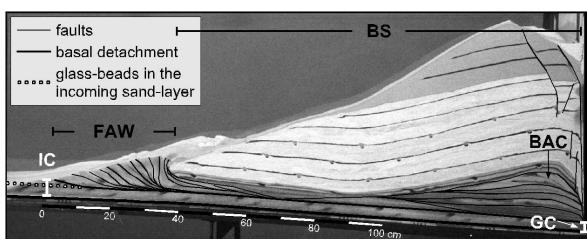


Figure 3.23: Two-level experiment in an open setup after 135 cm conv. The global capacity (GC) is smaller than the inlet capacity (IC) and the thickness of the sand layer beneath the glass-bead layer. The backstop (BS) shows uplift and bending due to partial basal accretion of the lower portion of the incoming sand-layer. The kinematics in the rear part of the backstop are strongly influenced by the backwall and cannot be compared with the experiments of this study (FAW – frontal-accretionary wedge, BAC – basal-accretionary complex; modified after Kukowski et al., 1997).

during Miocene and Pliocene times has been considered by mass-balance calculations of the South Chilean Forearc (Kopf, 1995; Bangs and Cande, 1997; Behrmann and Kopf, 2001), this interpretation cannot be used for the Quaternary accretionary phase of the South Chilean Forearc. There is no evidence of a change of mass-transfer mode during the current accretionary phase (Pleistocene to Recent), during which it has been shown that sediments were underthrust (Bangs and Cande, 1997; Díaz-Naveas, 1999).

- iii) Only one part of the underthrust sediments is basally accreted, so that the thickness of the basally-accreted sediments is less than the thickness of the underthrust sediments. In this scenario the underthrust sediments, which are not basally accreted, are transported to mantle depth and leave the forearc system. Consequently, the subduction interface never steps down to the top of the oceanic basement. According to the subduction-channel model (cf. Section 1.2.) this occurs if the global capacity of the subduction channel, which is controlled by wedge geometry and overlying rock density, is smaller than the volume of underthrust sediments (Cloos and Shreve, 1988a). In sandbox experiments, Kukowski et al. (1997) studied such a system with a mid-level detachment in an open setup to increase the global capacity (Fig. 3.23). These experiments reveal that the near-surface kinematic domains are similar to those observed in two-level experiments presented in this study, although the underthrust pile of sand is only partially basally accreted. Moreover the open setup of these experiments enables a more rearward position of the centre of basal accretion compared to the experiments of this study, even beneath a thick overlying backstop.

I favour the third interpretation to explain the reduced thickness of the basally-accreted sediments at the South Chilean Margin (Fig. 3.24), particularly for the present mass-transfer phase. This would also explain the large distance between the trench and the midpoint of uplift observed at the South Chilean Forearc (ca. 100 km compared with e.g. Makran 50 km; Kukowski et al., 2001b; Huhn, 2002).

However, the second interpretation could be used to explain the difference of the thickness of basally-accreted sediments between Miocene/Pliocene

(max. 10 m) and Quaternary times (80 m). An indication of a change in the mass-transfer mode is given by the absence of frontally-accreted sediments of Miocene and Upper Pliocene age (Behrmann and Kopf, 2001). Either these sediments were never accreted (stagnant mass transfer, Section 1.2.) or these accreted sediments were tectonically eroded during a later phase. These changes in the frontal mass-transfer mode could also lead to a decrease of total basally-accreted material, if the basal mass transfer changes simultaneously.

In addition, the reduced thickness of basally-accreted material and the minor uplift, lead to another difficulty in the interpretation. In the previous section (Section 3.5.2), I suggested that the lineament at the eastern border of the Coastal Cordillera might be the trailing backthrust. If this lineament acts only as this trailing backthrust, the relative displacement between the Coastal Cordillera and the Longitudinal Valley has to be equal to the total uplift due to basal accretion (150–200 m). However, the large thickness of Quaternary sediments in the Longitudinal Valley (up to 3000 m; Kelm et al., 1994) indicates a much larger relative displacement of these two domains. Therefore, I suggest that the Longitudinal Valley has undergone active subsidence. Subsidence at such a rate cannot be produced by the dynamics of a convergent forearc. Therefore, this subsidence is due to other forces (e.g. corner flow in the mantle wedge), which were not considered in these experiments. Jordan et al. (2001) discussed changes of the mantle rheology due to an increase in convergence velocity, as possible a reason for extension in this region. The interpretation, that the Longitudinal Valley is a half-graben with its main normal fault at the western border of the valley (Cisternas and Frutos, 1994; McDonough et al., in prep.), is in good agreement with this suggestion (Fig. 3.24).

However, this hypothesis does not allow the existence of the trailing backthrust observed in the experiments. The shape of the uplifted area in the experiments differs significantly from the uplifted area in nature: The uplifted area in nature is as long as the scaled length of this area in the experiments (ca. 100 km), but it is fiftyfold thinner than the scaled height of the experiments (compare: 200 m uplift in nature with 10 km scaled uplift in the experiments). In consequence, continental crust overlying the duplex complex does not need to be flexed so strongly as in the experiment. Therefore it is possible that the natural uplift due to basal accretion is not com-

pensated by a localised backthrust, but by flexural bending.

The absence of the alternation between short and long slices in nature can be explained by processes observed in the experiments. On one hand it is possible that the few slices preserved at the natural frontal-accretionary wedge are not statistically representative and alternation does occur. On the other hand it is possible that the South Chilean accretionary wedge really is in a constant mode. The LF experiment showed that a constant mode is present, when a long stable segment (segment 2) is formed between the segment 1 and segment 3. At the South Chilean Forearc the distance between the area of uplift (marking the segment 3) and the frontally accretive wedge is ca. 30–40 km. Thus, this central part of the wedge is as long as the accretionary wedge itself. This part of the wedge consists of continental basement, which was accreted during the Palaeozoic. The tectonic structures were reactivated only during the Eocene, and not during the current accretionary phase (Fig. 3.3; Díaz-Naveas, 1999). This indicates that this long segment is in a stable state. Therefore I suggest that the South Chilean Forearc possesses a stable segment 2, as it was observed in the LF experiment.

Validation of the suggestions discussed above about the evolution of the mass-transfer modes at the South Chilean Forearc necessitates additional field investigations. On the basis of the sandbox simulations, I suggest the two following key localities, which are recently investigated by the SFB 267, University Hamburg (Reuther and Potent, 2001) and SPOC:

- The area of syn-uplift extension is best to be investigated in the offshore region south of 38° S, as the offshore has not suffered much surficial-eosive material transfer and the sediments of the whole Neogene are conserved here. On the basis of seismic investigations, the exact position and volume of basally-accreted material could be quantified.
- The whole area of syn-uplift tilting is only located in onshore regions, as it is suggested by the sandbox simulations. More detailed data about the uplift-history of the terraces of these regions can provide better insight in the potential minor migration of the centre of basal accretion.

3.5.4 Summary

In the analogue simulations, syn-uplift extension and syn-uplift tilting of the overlying wedge indicated basal accretion. As these kinematic features were also identified along the South Chilean Forearc, I suggest that basal accretion takes place beneath the Arauco Peninsula and the adjacent region (37–38° S), and beneath the upper shelf in the region from 38 to 40° S. However, mass balance of basally accreted material at the South Chilean Forearc infers that only the minor portion of the underthrust sediments is basally accreted whereas the major portion is subducted to greater depth. The kinematics of this mass-transfer mode is in good agreement with experiments performed in an open setup.

The complex accretive experiments showed that a kinematic segmentation of the South Chilean Forearc wedge has to be expected. Although the recently available data are not detailed enough to identify segment boundaries, I consider that the kinematic and morphological domains of the South Chilean Forearc are caused by such segmentation.

The sandbox experiments were not able to simulate the kinematics landward of the uplifted area (Longitudinal Valley). However comparison of nature and experiment suggest that the Longitudinal Valley is subsiding due to crustal extension that is not due to the mass-transfer processes of the brittle forearc crust.

Chapter 4

The Tectonically-Erosive Forearc of Northern Chile

4.1 The North Chilean Forearc

4.1.1 Database obtained from nature

At the North Chilean Forearc (20–30° S), tectonic erosion has led to landward migration of the trench-arc systems by some 200 km since the Jurassic (Miller, 1970; Rutland, 1971; Kulm et al., 1977; Stern, 1991; von Huene and Scholl, 1991; Scheuber and Reutter, 1992). Based on results of geophysical investigations, Miller (1970) first suggested that the continental crust of the North Chilean Forearc was thinned and consumed over a length of several hundred kilometres. Then, Rutland (1971) identified four magmatic arcs (Jurassic-Lower Cretaceous, Middle Cretaceous, Upper Cretaceous-Palaeogene, Miocene-Recent) which are juxtaposed and become progressively younger from the coast to the Main Cordillera. Both Miller (1970) and Rutland (1971) postulated that a tectonically erosive mechanism was responsible for the consumption of the missing continental crust. Von Huene and Culotta (1989) and von Huene and Lallemand (1990) described the tectonically erosive mode with frontal and basal erosion of the forearc wedge (Section 1.2 and 4.1.2). This tectonically erosive mass-transfer mode has resulted in $35 \text{ km}^3 \text{ Ma}^{-1} \text{ km}^{-1}$ (i.e. km^3 material loss $\text{Ma}^{-1} \text{ km}^{-1}$ trench length) since the Jurassic (Scheuber et al., 1994), with related trench retreat of 0.7 km km^{-1} since the upper Miocene (Pelz, 2000).

The present North Chilean Forearc extends from the trench to the Atacama Faults System, which was formed as trench-linked, strike-slip fault (in terms of Woodcock, 1986; Fig. 4.1). The forearc shows a complex pattern of Neogene deformation partitioning and vertical motion (Pelz, 2000). The

ongoing tectonic erosion mainly controls the evolution and architecture of the forearc. This process is suggested to be in steady state as the absence of oceanic ridges and the rather equal distribution of other asperities on the oceanic crust (topographic highs and lows, seamounts, horst-, and graben-structures) in the area from 22 to 24° S, suggest that the mass-transfer mode was not disturbed over the last 10th of Ma (von Huene et al., 1999; Pelz, 2000). Therefore this work will focus mainly on the Neogene evolution of the forearc in this area.

In the study area nearly no sediment ($\sim 100 \text{ m}$) is deposited on the oceanic basement of the Nazca Plate (Fig. 4.2). Therefore, the horst and graben structures which developed during flexural bending at the outer bulge as well as additional highs and lows of the oceanic crust, form morphological asperities of 1500–3000 m amplitude when entering the trench (Schweller et al., 1981; von Huene et al., 1999; Buske et al., 2002). The trench along the sediment-bare part of the descending Nazca Plate is the deepest region of the Peru-Chile Margin with water depths up to 8000 m. The Nazca plate dips with about 10° beneath the offshore forearc (Wigger et al., 1994; Buske et al., 2002).

The North Chilean Forearc itself is characterised by pronounced morphological and related-kinematic domains (Fig. 4.1 b and 4.2; Adam and Reuther, 2000; Pelz, 2000):

1. The steeply-dipping offshore forearc (α from 2.5 up to 9°) undergoes subsidence and trench-normal extension, which becomes younger toward the coast (Fig. 4.2; Hinz et al., 1998; Pelz, 2000). The offshore forearc can be subdivided into a lower, middle and upper slope on the basis of geometrical, morphological and kinematic features (Fig. 4.1 b; von Huene et al., 1999).

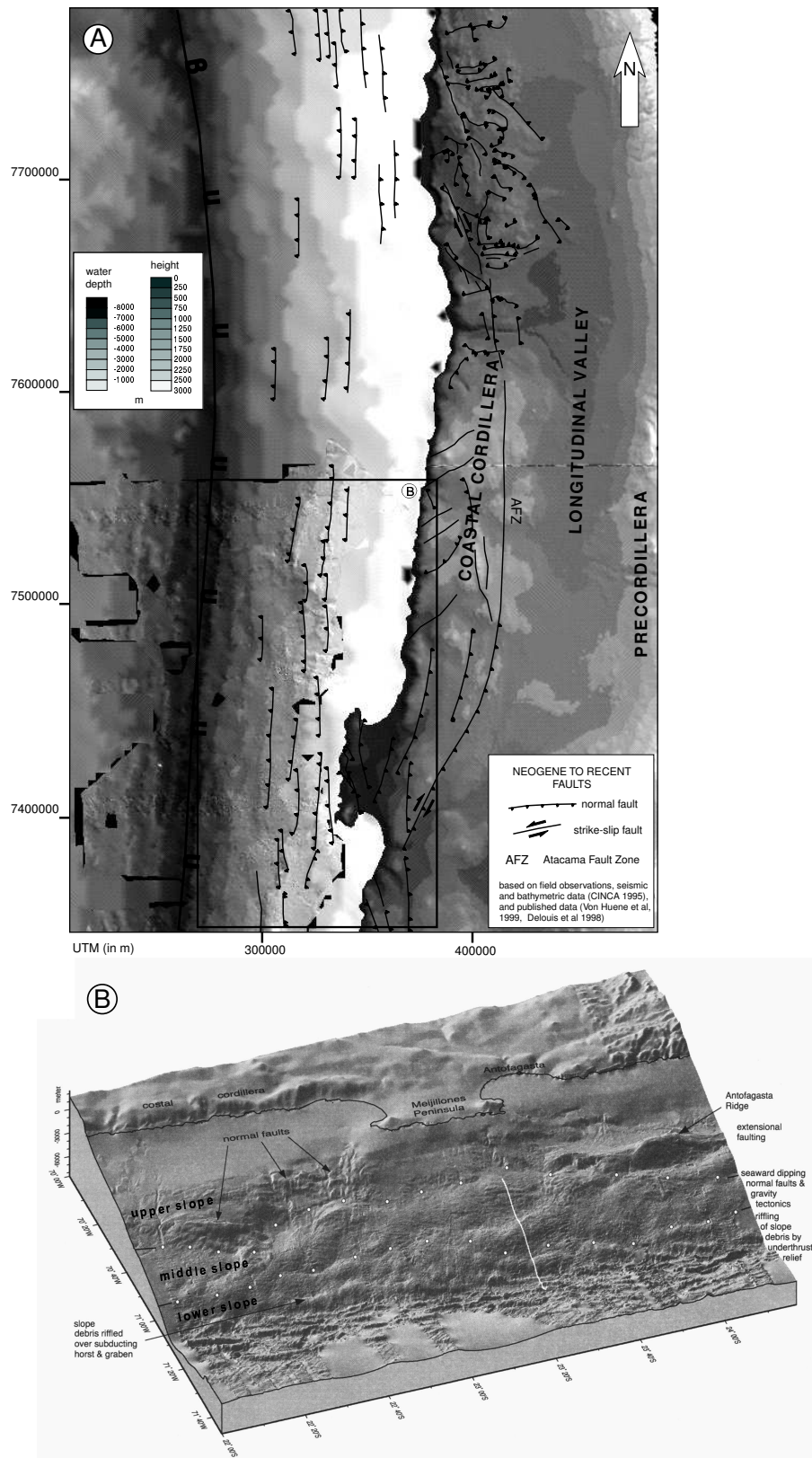


Figure 4.1: a) Structural map of the North Chilean Forearc between 21 and 24°S compiled by Pelz (2000); (AFZ – Atacama Fault Zone). b) Morphotectonic domains of the offshore forearc (von Huene and Ranero, 2002).

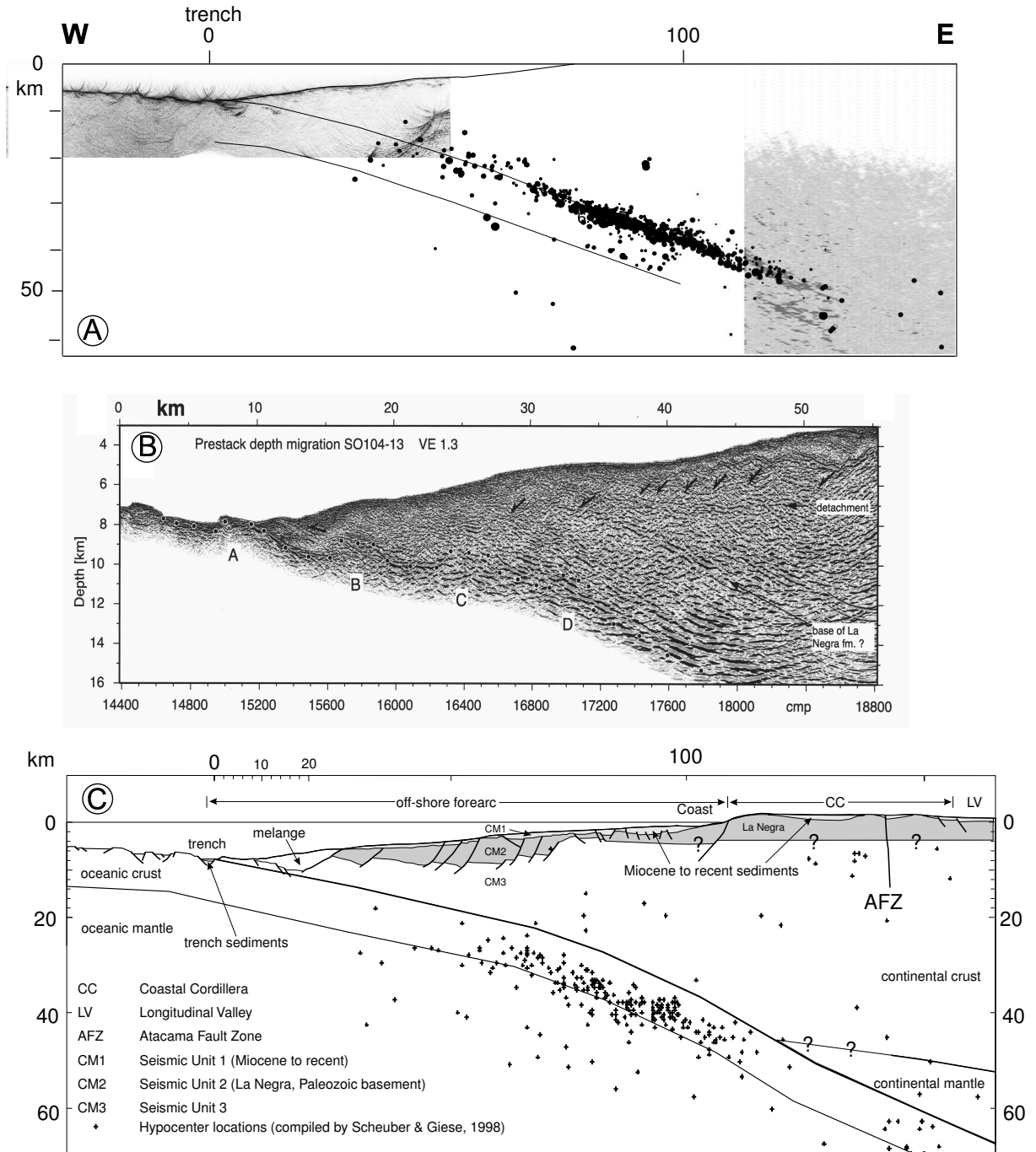


Figure 4.2: Cross-sectional images of the North Chilean Forearc based on the seismic data of CINCA '95 (SO104-13), and ANCORP '96 and field observation. a) Broad depth-range seismic image of the subducted Nazca Slab; black dots indicate hypocenters of the aftershock sequence of the Antofagasta earthquake (1995) (Buske et al., 2002 in press). b) Prestack-depth migration of SO104-13; arrows indicate normal faults (von Huene and Ranero, 2002 in press). c) Crustal cross-section of the North Chilean Forearc at 22° S compiled by Pelz (2000).

- (a) The lower slope shows the steepest surface inclination at 9° (Pelz, 2000). This frontal prism (in terms of von Huene, 2001) is the only part of the forearc which shows trench-normal compression by thrusting (von Huene and Scholl, 2001). The frontal prism consists of a melange, which was interpreted as continental crust fractured by tectonic erosion and the erosional debris derived from the continental slope (Hinz et al., 1998).
- (b) The middle slope is inclined at 6° and is characterised by N–S trending, inactive normal faults (Pelz, 2000). Pelz (2000) dated the end of this extensional deformation at the Lower Miocene based on the sedimentary record in the prestack depth-migrated seismic line of CINCA SO104-13. Additionally, von Huene and Ranero (2002) also showed recently active normal faults in the middle slope, which meet low-angle detachments in depths of ca. 5 km on the base of the newly prestacked and depth-migrated profile of SO104-13.
- (c) The shallow upper slope ($2.5\text{--}4^\circ$) shows also N–S trending normal faults. However, these normal faults were all recently active and have larger displacements than the faults of the middle slope (Pelz, 2000).

The lower and middle slope is covered by erosional debris, which indicates continuous slope failure by gravitational collapse. The erosional debris is transported down slope and deposited in the trench at the tip of the frontal prism (Fig. 4.1 b; von Huene et al., 1999). The middle and upper slope consists of the rocks of the Jurassic magmatic arc, which are overlain by Miocene sediments (Hinz et al., 1998). Sub-aerial Upper Miocene sequences were bored by a piston corer at 1800 m water depth, suggesting a fast rate of subsidence since deposition (Kudrass et al., 1998).

2. The Coastal Escarpment is characterised by the steepest topographical gradient observed at the North Chilean Forearc: Here, the topography rises to 1000–1500 m a.s.l. within a horizontal distance of only 2.5 km (Fig. 4.2 c). The Coastal Escarpment marks the transition between the subsiding off-shore area and the uplifting onshore area. Also at the

Coastal Escarpment, N–S trending, active normal faults indicate trench-normal extension. However, the displacement of these dominantly W-dipping normal faults cannot be determined by field data. Nevertheless, Pelz (2000) suggested that these normal faults do not cause all of the huge difference in the topographical elevation. Based on the reflection seismic lines and sedimentological investigations of the CINCA cruise SO-104, the total vertical displacement of the unconformity between the Jurassic magmatic rocks and the Miocene sediments in the first 60 km from the coast is estimated at 1500–2000 m (Pelz, 2000). However, at the Coastal Escarpment, the normal faulting is accompanied by a regional uplift rate of 0.1 mm Ma^{-1} (Radke, 1989).

3. The Coastal Cordillera reaches an altitude of 1200–1600 m a.s.l. (Fig. 4.2 c). This area shows transtensional deformation with a component of 5% E–W extension up to the eastern border marked by the Atacama Fault System. The trench-normal component of the extension is dominantly accommodated by E-dipping normal faults (Pelz, 2000). The Neogene uplift rate of the Coastal Cordillera ($0.05\text{--}0.07 \text{ mm Ma}^{-1}$; Pelz, 2000) is lower than that of the Coastal Escarpment. The Atacama Fault System shows reactivations with different orientations of displacement (sinistral and dextral) during the Neogene evolution of the North Chilean Forearc (Armijo and Thiele, 1990; Delouis et al., 1998).

The region east of the Atacama Fault system is divided into three morphotectonic domains:

- The Longitudinal Valley (1000 m altitude) is a morphological depression and traps sediments derived from the Main Cordillera since the Miocene (Mortimer et al., 1974; Victor, 2000).
- East of the Longitudinal Valley, the Precordilleran Monocline forms the western flank of the Altiplano Plateau rising to 4000–5000 m. The Precordilleran Monocline is due to Miocene uplift above E-dipping crustal thrusts (Victor, 2000).
- The present magmatic arc is located some 50 km east from the border of the Altiplano Plateau.

Seismic data acquired by the CINCA 95 and ANCORP 96 projects, and analysis of the aftershock sequence of the Antofagasta 1995 earthquake ($M = 8.0$) lead to a seismic image of the seismogenic zone along the subduction interface (Shapiro et al., 2001; Buske et al., 2002). Here, a low velocity zone with a thickness of 800–1600 m was identified, which extends from the trench as far as the Precordilleran Monocline (ANCORP and group, 1999; Husen et al., 1999; Patzwahl et al., 1999; Lüth, 2000). This feature can be interpreted as a subduction channel. The thickness of the aftershock sequence distribution is around 3000 m, which may indicate the width of active deformation along the seismogenic plate interface, including the subduction channel and the damage zone surrounding it (Fig. 4.2 a; Patzwahl et al., 1999; Patzig et al., 2001; Buske et al., 2002).

4.1.2 *Previously-published concepts of tectonic erosion*

A well-known tectonically erosive process observed at other recent convergent margins is the tectonic erosion by seamount or oceanic-ridge subduction (e.g. Lallemand et al., 1992a; Lallemand et al., 1994a; Dominguez et al., 1998; Ranero and von Huene, 2000). This short-term tectonic erosion would not be able to produce the arc retreat of 200 km since the Jurassic, which occurs along ca. 400 km strike (Clift et al., 2002), as observed at the North Chilean Forearc. Therefore the tectonically-erosive process, which affects the North Chilean Forearc, is suggested to be rather a persistent process (von Huene et al., 1999; Pelz, 2000). From here on this mode of tectonic erosion will be named *steady-state tectonic erosion*.

Steady-state tectonic erosion is restricted to convergent margins that are characterised by a low thickness of sediments in the trench (≤ 200 m), a high orthogonal convergence rate (≥ 10 cm Ma^{-1}), and a rough subduction interface (sediment-bare, faulted oceanic crust, fault offset ≥ 700 m, roughness coefficient, which is defined by volumes of topographic highs and lows of the seafloor over a distance integrated over several transects, $RC \approx 15$, Lallemand et al., 1994b). Therefore, a mechanical concept of steady-state tectonic erosion has to present a process, which is controlled by one or more of these characteristic parameters. Such a concept may be valid, if it is able to explain the typical features which are observed at all of the recent tectonically erosive forearcs: strong forearc

subsidence, trench- and arc-retreat, large wedge tapers and the absence of a frontal-accretionary wedge (Section 1.2).

4.1.2.1 Chain-saw model

One of the first mechanical concepts was the chain-saw model of Schweller et al. (1981) and Hilde (1983), in which basal tectonic erosion is used to explain forearc subsidence (Fig. 4.3 a). This model attempts to demonstrate that the morphological asperities of the oceanic crust cause basal tectonic erosion of the forearc by mechanical abrasion. This concept was disproved for the North Chilean Forearc, since the bulk rate of transported upper crustal material in the lows of the oceanic crust since the Jurassic ($56 \text{ km}^3 \text{Ma}^{-1} \text{km}^{-1}$; von Huene et al., 1999) is greater than the tectonic erosion rate derived from the arc retreat ($35 \text{ km}^3 \text{Ma}^{-1} \text{km}^{-1}$; Scheuber et al., 1994). However, this calculation of the erosion rate caused by the filling of the lows is a crude estimation, as it is not possible to reconstruct the potential geometry of the subducted lows from the Jurassic to the Recent. Additionally, Pelz (2000) noticed that the fill of lows with upper crustal material does not explain the process of basal erosion, since the lows will be filled the moment they reach the wedge tip. This means that frontal erosion is caused by this process.

4.1.2.2 Frontal and basal erosion by gravitational collapse and hydro-fracturing

Based on morphotectonic analysis it has been shown that frontal erosion of the steep lower slope is caused by gravitational collapse, as the lower and middle slopes were observed to be covered by erosional debris at all tectonically erosive forearcs [e.g. Chile (von Huene et al., 1999); Costa Rica (Ranero and von Huene, 2000), Peru, Japan (von Huene and Lallemand, 1990)].

Based on the observation of overpressured accretive forearc systems (Platt, 1990), basal erosion at the Japan-, and Peru-Trench has been suggested to be caused by the fragmentation of the whole upper plate by hydro-fracturing (Fig. 4.3 b; Murauchi and Ludwig, 1980; von Huene and Culotta, 1989; von Huene and Lallemand, 1990; Lallemand et al., 1994b). This process might soften the base of the upper plate and produce clasts and slivers to form a melange. Continuous hydro-fracturing along the base of the forearc requires overpressured pore

fluids along the whole length of the area of basal erosion and a convergence velocity which is higher than the dewatering process of the underthrust sediments (von Huene and Scholl, 1991). Until now, these pre-requisites have not been investigated for tectonically erosive forearcs, so that this concept remain hypothetical. Moreover, this concept shows only a possibility of fracturing and weakening of the wedge base and not a possibility to transport the produced melange to greater depth. The transport mechanism is suggested to be the same as in the chain-saw model (von Huene and Culotta, 1989), which did not apply to the North Chilean Forearc (see Section 4.1.2.1).

4.1.2.3 Subduction channel concept

One of the first mechanical concepts capable of explaining contrasting deformation processes and mass-transfer modes at accretive and non-accretive margins was the subduction-channel concept (see Section 1.2 and Fig. 4.3 c; Cloos and Shreve, 1988b; Cloos and Shreve, 1988a). They assumed that the subducting sediment deforms as a viscous material once it is dragged into the subduction channel, which is defined as a relatively narrow basal shear zone along the subduction interface. In this concept steady-state tectonic erosion is achieved when the tensile principle component of the effective stress exceeds the strength of the wedge-material. This explanation is comparable with that derived from the critical-taper theory (see Section 4.1.2.4). However, this concept is restricted to viscous flow within the subduction channel and does not take into account the brittle material behaviour in forearc wedges. To attain the required conditions in a natural system, Cloos and Shreve (1988a) also proposed hydro-fracturing to weaken the wedge material (see Section 4.1.2.2).

4.1.2.4 Steady-state tectonic erosion in terms of critical-taper theory

Based on the critical-taper theory (see Section 1.3, Davis et al., 1983; Dahlen, 1984; Dahlen et al., 1984), Lallemand (1994b) suggested that the large variations in surface inclination observed at tectonically erosive forearcs are an expression of a change in the material properties of the wedge. This suggestion led to the concept that each part of the continental slope of the North Chilean Forearc (see Section 4.1.1) shows a unique structural style and mass-transfer processes (frontal erosion, basal erosion,

underthrusting, and basal accretion; von Huene et al., 1999; Adam and Reuther, 2000).

To explain the mechanics of these basal mass-transfer processes, a critical-taper analysis was applied to each part of the North Chilean Forearc presented in Section 4.1.1 assuming a Mohr Coulomb Rheology for the forearc (Fig. 4.3 d; Adam and Reuther, 2000). Applying this approach, basal erosion can only occur under very specific conditions: the basal friction has to be equal or larger than the internal friction. Under these conditions, the strength ratio $\chi = \mu_B \setminus \mu_I \geq 1$, so that the wedge reaches its limit of existence (Dahlen, 1984). This state of stress leads to internal slip lines oriented parallel to the wedge base and large wedge tapers. A change of these conditions in the down-dip direction along the wedge base (e.g. strain softening, increasing pore pressure) leads to stronger-inclined slip lines, whereas the slip lines parallel to the wedge base have no possibility to be (re-)activated. The following mechanical concept for erosive mass transfer is suggested from the critical-taper analysis for the North Chilean Forearc by Adam and Reuther (2000): active forethrusts parallel to the wedge base are able to form a new subduction interface within the wedge. The material in the footwall of this new subduction interface is transported arcward on top of the subducting oceanic crust, i.e. the wedge undergoes basal erosion and a subduction channel is established. If the subduction interface is blocked and steeper fault planes are activated (caused by changing boundary conditions lower down), a re-entry of eroded material into the wedge results and basal accretion occurs. Adam and Reuther (2000) concluded that basal erosion is restricted to the frontal part of the forearc wedge with the steepest surface slopes, i.e. lower and middle slope (which are the best candidates to be wedge segments at their limit of existence); the upper slope is the area beneath which underthrusting takes place; and the onshore forearc undergoes basal accretion.

Until now, the concept of Adam and Reuther (2000) is the only one in which all the features typical of steady-state tectonic erosion are explained with respect to the observed natural properties, as they explain the required high strength ratio with a very high basal friction indicated by the sediment-bare and rough oceanic plate. However, critical-taper analysis only provides the prediction of the state of stress with slip-line orientation and wedge geometry, and is not able to estimate, whether the required forces of the predicted mass-transfer mode are actually reached in such a system. Moreover,

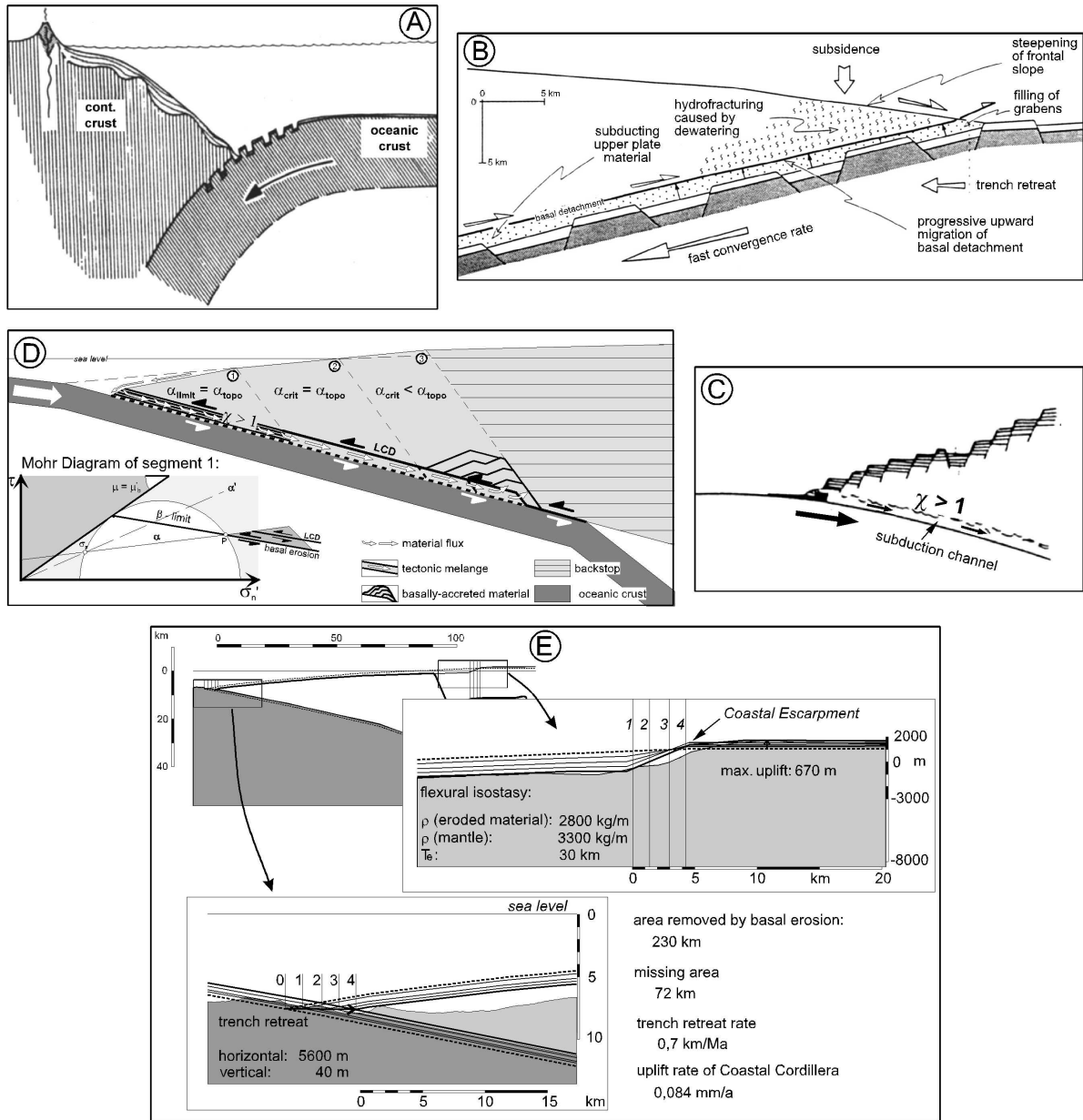


Figure 4.3: Concepts of steady-state, tectonic erosion: a) chain-saw model after Schweller et al. (1981) and Hilde (1983); b) hydro-fracturing of the whole frontal part of the forearc wedge after von Huene and Culotta (1989) and Lallemand et al. (1994); c) subduction channel concept after Cloos and Shreve (1988b) (χ – strength ratio of basal and internal frictional strength) ; d) critical-taper theory applied to the North Chilean Forearc with frontal and basal erosion of segment 1, underthrusting beneath segment 2, and basal accretion beneath segment 3, after Adam and Reuther (2000) (LCD - newly-formed lower crustal detachment; notation of the Mohr Diagram is the same as used elsewhere in this study e.g. Fig. 2.16); and e) results of the incremental forward modelling of mass removal at the North Chilean Forearc after Pelz (2000). For further explanations, see Section 4.1.2.

until now, it has not univocally been shown, how a critically-tapered wedge segment can be identified in nature, so that the critical taper analysis performed for the North Chilean Margin has to assume a critically-tapered segment without any prior evidence.

4.1.2.5 Geometrical forward modelling with implemented effects of isostatic rebound

Only Pelz (2000) estimated the rates of tectonic erosion at the North Chilean Forearc with respect to both tectonic erosion processes, frontal and basal erosion (Fig. 4.3 e). However, for the reconstruction of the eroded mass, he did not assume a specific mechanical concept of basal erosion. This study is based on a forward modelling method described by von Huene and Lallemand (1990) and required the reconstruction of the geometry of the forearc of the Upper Miocene as a starting model. According to the field data (see Section 4.1.1), the offshore forearc was uplifted by 1800 m and the onshore forearc subsided to its initial position, as calculated with the estimated uplift rates, without changing the observed inclination of the surface slope. Pelz (2000) used this starting geometry in computational forward modelling with flexural isostatic compensation. He incrementally reconstructed the volume of basally-eroded material with respect to an assumed trailing edge of basal erosion (i.e. the position, where basal erosion of the wedge base ceases; Trailing Edge of Basal Erosion – *TEBE*). The *TEBE* position was calculated from

- the boundary between uplifting and subsiding parts of the forearc (Coastal Escarpment) and
- through the assumption that shear deformation occurs in the subsiding part down to the basal interface, where the shear angle is based on average inclinations of normal faults in the forearc.

Pelz (2000) concluded that the volume of material removed by basal erosion exceeds that removed by frontal erosion by a factor of at least 3. The total volume of tectonically-eroded material (frontally- and basally-eroded material) amounts to $38 \text{ km}^3 \text{ Ma}^{-1} \text{ km}^{-1}$ since the Upper Miocene. This corresponds to a trench-retreat rate of 0.7 km Ma^{-1} since the Upper Miocene. Pelz (2000) showed that the relatively slow uplift of the Coastal Cordillera is largely driven by flexural isostatic rebound caused

by the tectonic erosion of continental material and corresponding unloading of the subducted oceanic plate. There is no evidence for major underplating of the eroded material as far east as the Longitudinal Valley.

4.1.2.6 Conclusions

The quantification of basally-eroded mass requires the determination of the *TEBE* from field data. As the mechanisms of basal erosion and the related deformation processes within the wedge has not been well understood until now, different positions of *TEBE* were assumed, which differed in more than 50 km horizontal distance in the studies concerning the North Chilean Forearc (compare Sections 4.1.2.4 and 4.1.2.5; Adam and Reuther, 2000; Pelz, 2000). The simulation of steady-state tectonic erosion in scaled sandbox experiments provide the possibility to observe the deformation processes caused by this mass-transfer mode. The aim of this study is to experimentally test the mechanical concepts of steady-state tectonic erosion in the brittle field. It will give insight in the wedge-internal deformation processes caused by different mass-transfer processes, so that the deformation related to the basal erosion process can be evaluated.

4.2 Experimental setup

4.2.1 Experimental concept to simulate steady-state tectonic erosion

Convergent forearc setting, which show significant trench-retreat, were previously investigated using two types of analogue experimental concepts (see Section 1.4.):

- Short-term tectonic erosion is caused by asperities on the oceanic crust (seamounts, oceanic ridges), which induce offscraping of forearc material for a geologically-short period (Fig. 1.7; Lallemand et al., 1994a; Dominguez et al., 1998). After such an asperity has been subducted to greater depth, the forearc will switch back to its previous mass-transfer mode. This concept is inadequate to describe the steady-state tectonic erosion observed at the North Chilean Forearc (see Section 4.1.2).
- A net negative mass balance of an accretive system has been forced by an open setup (Kukowski et al., 1994; Gutscher, 1996). The

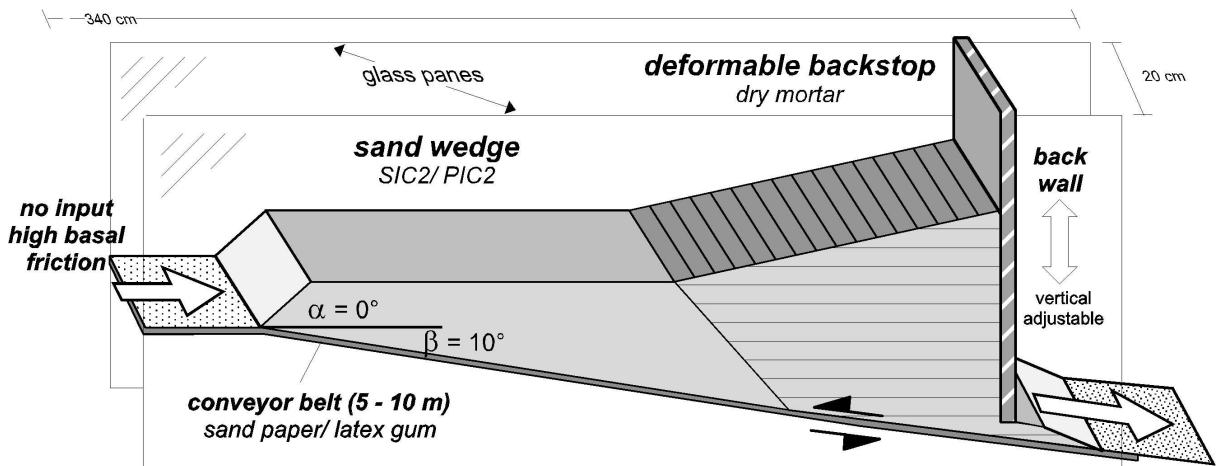


Figure 4.4: Experimental setup of the 1st and 2nd series of the tectonically-erosive experiments (Tab. 4.1).

thickness of the subduction channel was determined by how high the backwall is lifted and is not controlled by the dynamic system itself. In this case, the mass-transfer modes of the frontal sand-wedge (accretive or non-accretive) is insignificant, since the experiments showed a net material loss at the rear. This concept is not appropriate for the mass-transfer mode of the Northern-Chilean Forearc, as the kinematic domains of Northern Chile indicate a material loss in the frontal and basal part, and not in the rear (see Section 4.1.1).

Since none of the experimental concepts presented so far appears adequate to investigate the mass-transfer mode of the North Chilean Forearc, the working group of the GFZ geodynamic laboratory developed a specific setup for these experiments (Fig. 4.4, Kukowski et al., 1999; Adam et al., 2000; Kukowski et al., 2002):

To simulate a subduction interface, a conveyor belt was used, which had nearly the same friction as the wedge material, as required by the mechanical concept discussed by Adam and Reuther (2000, see Section 4.1.2.4). There was no incoming sand-layer on top of the conveyor belt, as this would render the required high frictional strength of the basal interface ineffectual. Furthermore, tectonic erosive margins have been shown to be characterised by the absence or only a very small thickness of sediment entering the trench (see Section 1.2).

On top of the conveyor belt, an initial sand wedge was prepared of ca. 110 cm length and an initial wedge taper of 10° ($\alpha = 0^\circ$, $\beta = 10^\circ$). A deformable backstop consisting of dry mortar separated the

sand wedge from the rigid backwall. Therefore, potential boundary effects due to the rigid backwall were negligible in the area of interest. To simulate steady-state tectonic erosion, which occurs over several million years (> 300 km total convergence in nature), the experiments were performed with large total convergence (300–850 cm conv.). As these experiments were the first experiments to simulate steady-state tectonic erosion, some details in the general geometry (e.g. the surface slope of the backstop, the dip of the boundary between the sand wedge and the backstop) was varied from one experiment to the next. These changes were made only to ensure a proper experimental run with these heavy sand wedges and it was shown that they did not influence the experimental results.

This principle experimental setup were used in two series of experiments. With the first series the mass-transfer processes of steady-state tectonic erosion were studied in detail. The second series were to investigate the mechanics of this mass-transfer mode.

4.2.2 Setup of the 1st series (mass-transfer processes)

In the first series, different scenarios of steady-state tectonic erosion were performed. Although the Northern-Chilean Forearc does not indicate basal accretion (see Section 4.1.1 and 4.2.1.5), several experiments with basal accretion were performed, since it was important to know if the applied concept (see Section 4.2.1) was able to simulate steady-state tectonic erosion caused by the properties used and not by a net negative mass balance.

The nomenclature of the experiments, the used materials, and their properties are listed in Tab. 4.1. In the following the intention and specific features of the experimental setup are mentioned:

SSC experiment (SIC2, sandpaper, closed setup)

With the SSC experiment the experimental concept (see section 4.2.1) was tested. The sand wedge of this first experiment had a very narrow wedge tip, which resulted in thickening by thrusting during the adjustment phase. This initial deformation complicated the deformation analysis of the steady-state phase. Therefore, the thickness of this sand wedge, after the initial adjustment phase, was used as initial thickness for the further experiments, so that initial thrusting was avoided.

PSC experiment (PIC2, sandpaper, closed setup)

In comparison to the SSC experiment, the internal material properties of the PSC experiment were changed by using another filling technique of the sand (PIC2 instead of SIC2; cf. Tab. 2.3). This experiment was designed for the second series which concerned the mechanics. As it showed a particular mode of basal accretion, it was also included in the first series.

SSO experiment (SIC2, sandpaper, open setup)

The mechanical conditions of the SSO experiments were similar to those used in the SSC experiment. However, the SSO experiment was performed in an open setup. The amount the rigid backwall was lifted, was equal to the thickness of the 'subduction channel' (i.e. basal shear zone) established in the experiments which were performed in a closed setup. This avoided material loss from the rear of the sand wedge, observed in the experiments of Gutscher (1996; cf. Section 4.2.1). Instead, this experimental setup allowed rearward material transfer within the basal shear zone beyond the rigid backwall. The amount the backwall was lifted determined the height of the global control point in terms of Cloos and Shreve (1988b; cf. Section 1.2).

ASO (anisotropic sand wedge, sandpaper, open setup)

This experiment differed from the SSO experiment in the choice of material. This wedge was prepared

with two materials: Lens-shaped bodies consisting of sifted sand (SIC2) were surrounded by thin, weak layers (micro glass beads) in the lower part of the wedge (cf. Appendix and Fig. 4.13 d and e). These represented overpressured shear zones or a fractured, weakened base of a forearc wedge, as indicated by the observed structures in subduction channels (e.g. Costa Rica; Ranero and von Huene, 2000). As it was expected that detachments would preferentially occur along the glass-bead layers, this wedge was named anisotropic sand wedge, as opposed to the other tectonically-erosive experiments, which were named here isotropic sand wedges. The ASO experiment was only interpreted with regards to mass-transfer rates and not mechanics.

4.2.3 Setup of the 2nd series (mechanics)

The experiments of the second series were constructed to study the mechanics of steady-state tectonic erosion. In addition to the experiments of the first series performed in a closed setup (SSC, PSC; cf. Section 4.2.2), this series included the SLC experiment (SIC2, Latex gum, Closed setup). The SLC experiment differed from the SSC experiments by its basal material properties: The conveyor belt consisted of latex gum, which was characterised by a smooth surface and a high basal friction. However, an analogue to this material is not conceivable in nature, as the nearly sediment-bare oceanic crust of tectonically erosive margins is always characterised by high roughness (Lallemand et al., 1994b). Nevertheless, this smooth basal material was used in the experimental setup in contrast with the rough sandpaper. This was to investigate the role of the very high basal friction induced by the roughness, since Adam and Reuther (2000) and Lallemand (1994b) suggested the roughness of the oceanic crust as crucial parameter controlling basal erosion (see Section 4.1.2.4).

experiment			sand wedge			conveyor belt		setup
	material		μ_{PI}	μ_{SI}	μ_{DI}	material	μ_{DB}	
a.	SSC	SIC2	0.73	0.60	0.57	sandpaper	0.56	closed
	PSC	PIC2	0.66	0.66	0.61	sandpaper	0.58	closed
	SSO	SIC2	0.73	0.60	0.57	sandpaper	0.56	open (10 mm)
	ASO	'anisotropic': SIC2 and glass beads	0.73	0.60	0.57 0.43	sandpaper	0.56	open (14 mm)
b.	SSC	SIC2	0.73	0.60	0.57	sandpaper	0.56	closed
	PSC	PIC2	0.66	0.66	0.61	sandpaper	0.58	closed
	SLC	SIC2	0.73	0.60	0.57	latex gum	0.48	closed

Table 4.1: Setup and nomenclature of the experiments simulating steady-state tectonic erosion of a) 1st series (mass transfer) and b) 2nd series (mechanics); (μ_{PI} – peak internal friction; μ_{SI} – stable static friction, μ_{DI} – stable dynamic internal friction; μ_{DB} – stable dynamic basal friction).

4.3 Results of experiments simulating steady-state tectonic erosion

4.3.1 Experimental results of the 1st series (mass transfer)

In the section ‘common features’ I show firstly that all erosive sand wedges of the first series were characterised by a mass-transfer mode, which was governed by the four following processes (Fig. 4.5):

1. Frontal erosion of the frontal part of the wedge by episodic slumping and continuous transport of the erosional debris beneath the wedge in a basal shear zone.
2. Basal erosion along the base of the frontal part of the wedge by continuous mass removal.
3. Underthrusting of formerly-eroded material in the basal shear zone beneath the central part of the wedge.
4. Partial or total basal accretion of the material, which was transported in the basal shear zone, onto the rear wedge base.

Due to the erosive mass-transfer processes (frontal and basal erosion) in the frontal part of the wedge, the wedge-tip continuously migrated towards the rear, i.e. *wedge-tip retreat* (with respect to ‘trench retreat’).

In the section ‘contrasting features’, I outline the differences between the experiments, which were caused by changing the inlet- and global-capacity of the basal shear zone. Moreover, the specific kinematic features of the ASO experiment is presented in detail in this section, as this experiment was excluded from the second series.

Common features

During the experimental runs the sand wedges passed through the three following dynamic phases:

1. In the accretive adjustment phase during the first few centimetres of convergence (< 5 cm conv.), the sand wedge was shortened and thickened by diffuse internal deformation caused by compaction of the sand (see Section 2.3.2). Additionally, the SSC and ASO experiments showed localised thrusting, which thickened their initial thin wedge tip (see Appendix SSC up to 20 cm conv., ASO from 0 to 80 cm conv.).
2. During the erosive adjustment phase (< 100 cm conv.) the mass-transfer processes were still under the influence of the initial conditions of the experiment, as the basal shear-zone formation was not completed. This led to extremely irregular mass-transfer rates (Fig. 4.6).
3. The steady-state phase (> 100 cm conv.) was reached when the whole basal shear zone was filled by frontally-eroded debris. Thus, similar basal material properties were achieved along the whole wedge base and the mass-transfer rates became steady (Fig. 4.6).

I paid most attention to the third phase to investigate the processes of steady-state tectonic erosion with these sandbox simulations.

All erosive sand wedges established a characteristic wedge geometry between 10 and ca. 300 cm conv. (Fig. 4.7 a). In the frontal part, the surface slope reached the angle of repose ($\alpha_{\text{repose}} = 37^\circ$). Therefore, this steep frontal slope was independent of the basal dip, since it was only controlled by the internal frictional strength itself. The central part with

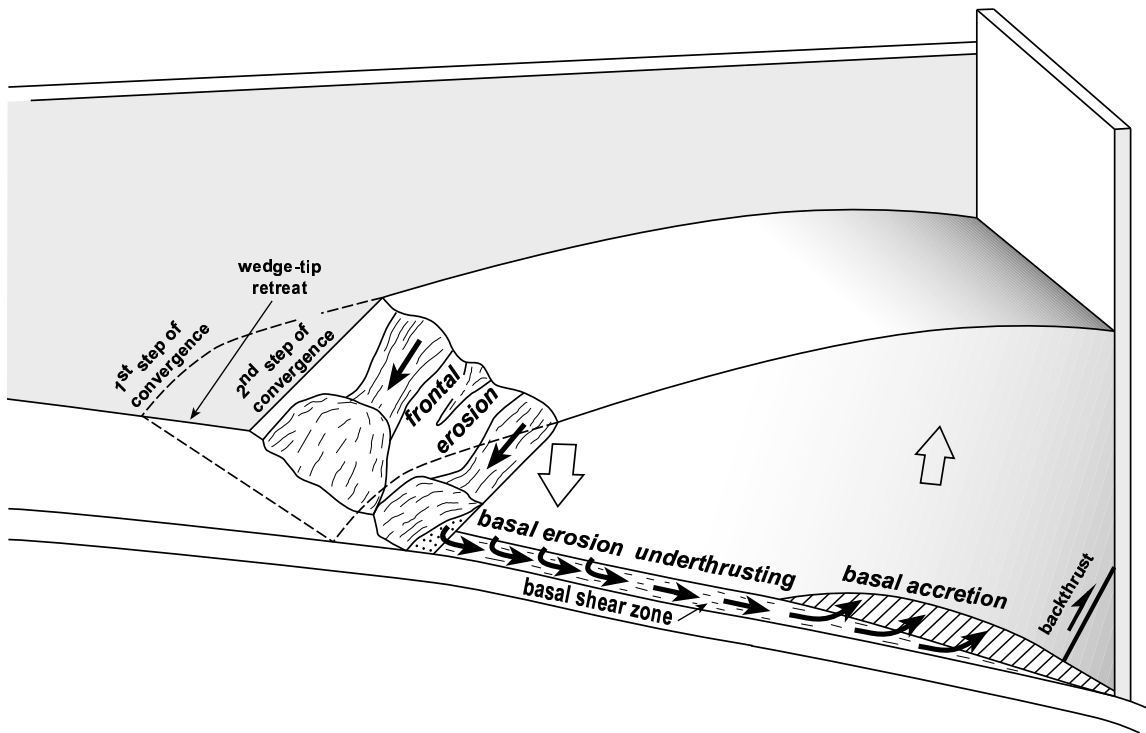


Figure 4.5: Sketch of the mass-transfer processes in a steady-state, tectonically-erosive sand wedge.

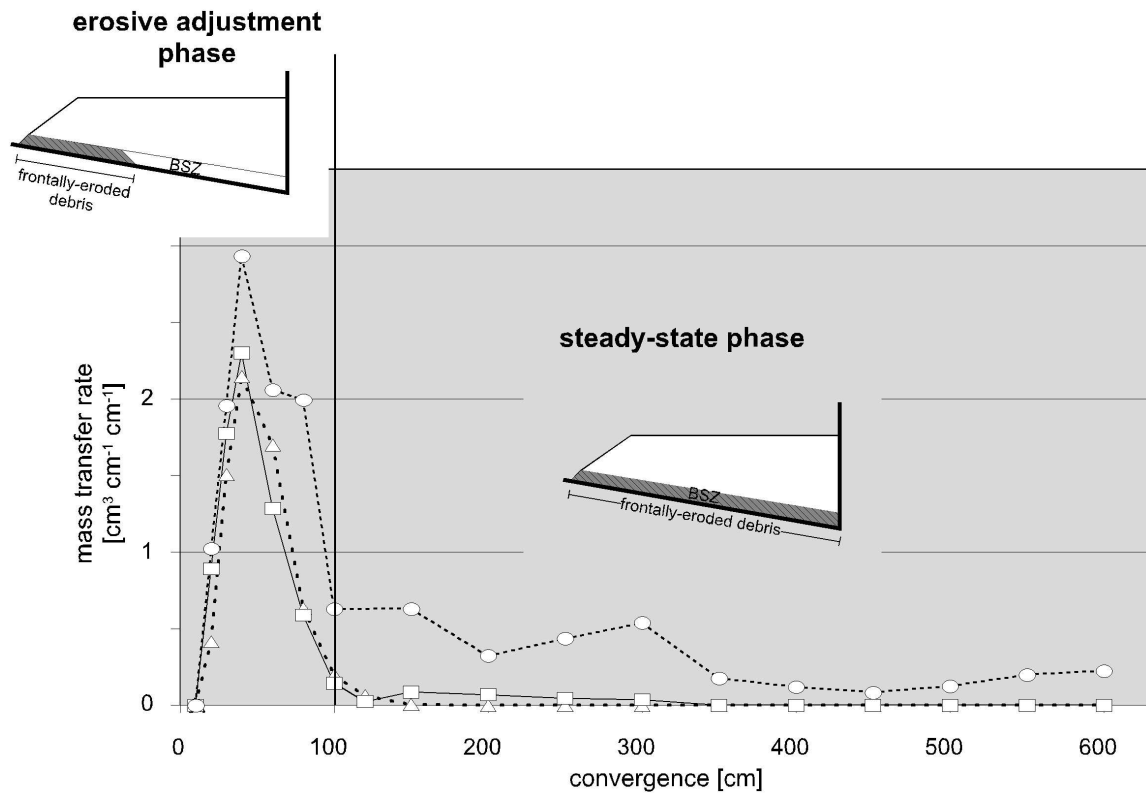


Figure 4.6: Mass-transfer rates of three experiments indicate the erosive adjustment phase before and the steady-state phase after basal shear zone formation.

observed parameter	comment	SSC	PSC	SSO	ASO	
					1 st phase	2 nd phase
1 st suggested χ	μ_{DB}/μ_{SI}	0.93	0.88	0.93
2 nd suggested χ	μ_{DI}/μ_{SI}	0.95	0.93	0.95
frontal erosion	bulk rate [$\text{cm}^3 \text{cm}^{-1} \text{cm}^{-1}$]	0.62	0.64	0.67	1.08	1.2
basal erosion	bulk rate [$\text{cm}^3 \text{cm}^{-1} \text{cm}^{-1}$]	0.05	0.04	0.14	0.48	0.16
wedge-tip retreat	bulk rate [$\text{mm}^2 \text{cm}^{-1}$]	4.50	3.90	5.00		5.3
basal accretion	bulk rate [$\text{cm}^3 \text{cm}^{-1} \text{cm}^{-1}$]	0.49	0.33	0.04		0.04
erosion ratio	basal erosion/frontal erosion [final volumes]	1:13	1:14	1:5	1:2	1:8
measured inlet capacity	thickness of basal flow zone at the wedge tip [mm]	6.8	7.2	6.7	10.0	5.0
calculated inlet capacity	bulk rate of frontal erosion/1 cm conv. [mm]	6.2	6.4	6.7		12
global capacity	[mm]	0.0	0.0	10.0	14.0	14.0

Table 4.2: Quantitative results of the tectonically-erosive experiments of the 1st series.

a length of maximal 15 cm showed a convex topography. In the rear part of the sand wedge, the initial surface slope was nearly preserved ($\sim 0^\circ$).

With ongoing wedge-tip retreat, the steep surface slope migrated rearwards. Contemporaneously, those parts of the wedge, which were initially located in a more rearward position took a more frontal position. Thus, the central part with the convex topography, was possibly missing at this late stage of the experimental run (ca. 300–850 cm conv., Fig. 4.7 b).

The different basal mass-transfer processes were indirectly deduced by the changes in the positions of the marker layers during the experimental run (Fig. 4.8). The surface without vertical motion of the marker layers is named the *neutral surface*. The wedge segment in front of the neutral surface continuously subsided. Up to this point the subsiding segment is named the *toe segment*. It is important to notice that the boundary of the toe segment did not coincide with those of topographical features during the early stages of the experiment (Fig. 4.8 a). In the later stages of some of the experiments, the toe segment was even located within the part with the steep frontal slope (e.g. SSC; Fig. 4.8 b).

The subsidence of the toe segment suggested mass removal along the wedge base. From the video sequences it was observed that active basal erosion occurred dominantly in the first 10 cm from the wedge-tip during the whole experimental run. This area of dominant basal erosion was indicated by a steep gradient of the inclined marker layers (Fig. 4.8). To the rear of this area, the marker layers were only shallowly inclined. Beneath the area of shallowly-inclined marker layers, the frontally- and basally-eroded material was underthrust within the basal shear zone (Fig. 4.8).

The wedge segment to the rear of the neutral surface (i.e. *internal segment*) was uplifted by basal accretion of the underthrust material.

The observation of multiple basal mass-transfer processes suggested that the basal shear zone was of particular importance in further understanding the wedge-internal mass-transfer processes and the mechanics of erosive sand wedges. Therefore the kinematics of the basal shear zone were thoroughly examined: In all experiments, the lower part of the basal shear zone (~ 0.5 cm; i.e. *basal-flow zone*) was characterised by continuous and penetrative shear deformation. The upper part of the basal shear zone (1–2 cm, i.e. *damage zone*) showed episodic and localised shear deformation along an array of base-parallel, spatially discontinuous thrusts. This thrusting caused successive removal of particles from the base of the damage zone (Fig. 4.9).

The kinematics of the erosive sand wedges were inferred from the particle paths of the triangular markers (Fig. 4.10) and not by direct investigation of fault activity, as the major parts of the sand wedges were only diffusely deformed with small displacements. The particle path is the sum of the translation due to wedge-internal deformation and basal mass-transport processes (basal erosion, underthrusting and basal accretion). To estimate wedge-internal deformation, translation due to basal mass transfer has to be removed; this was inferred from the marker-layer interpretation (Fig. 4.8).

In the erosive sand wedges of the first series two kinematic domains occurred, neither of which corresponded to topographical features nor to segments of total subsidence (toe segment) and total uplift (internal segment, Fig. 4.10). In general, the frontal kinematic domain was under extension, as indicated by relative displacement of the particles towards the wedge tip. In contrast, the rear kinematic domain was under compression, as inferred by relative displacement towards the rear (best seen in Fig. 4.15 b and c).

Particles in a more frontal position of the wedge showed more complex paths, since they passed

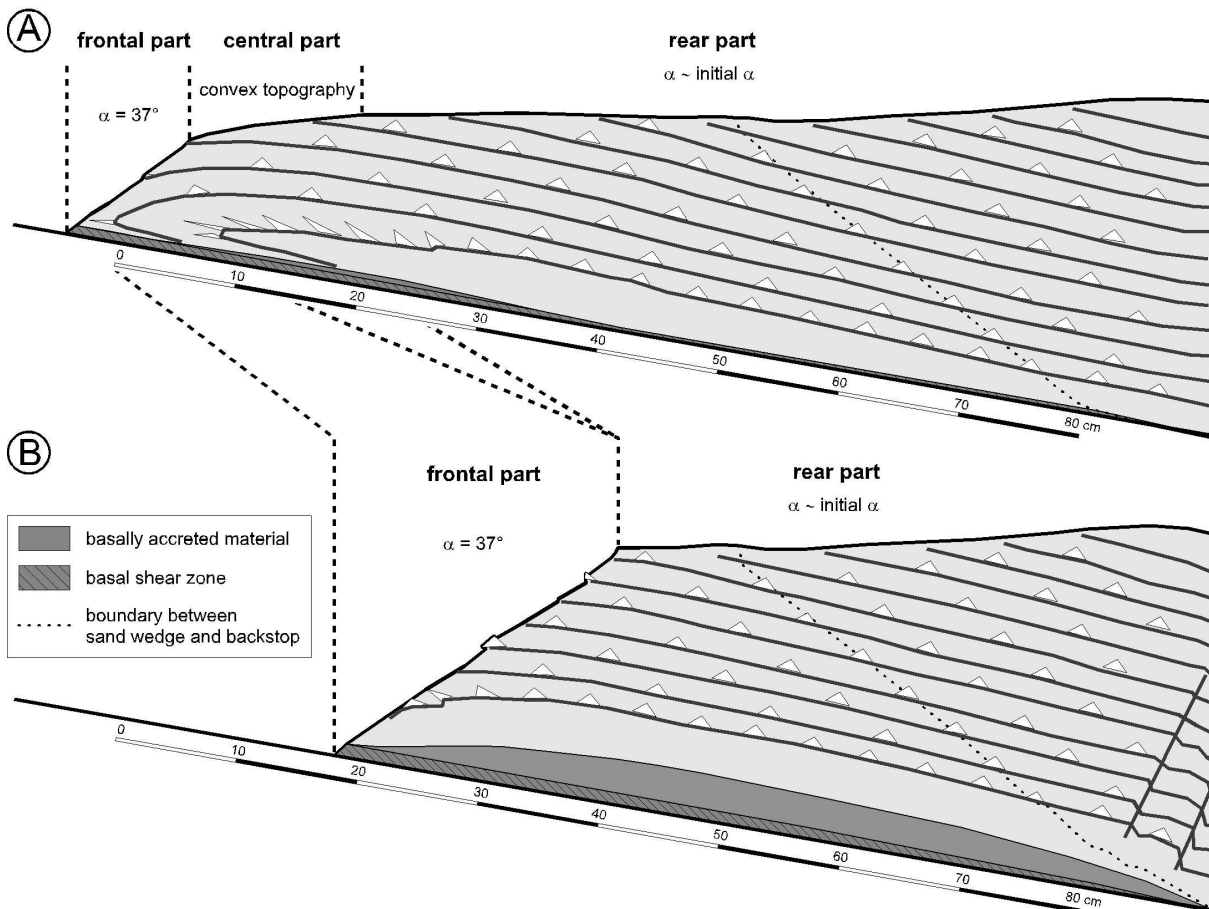


Figure 4.7: General geometrical evolution of a steady-state, tectonically erosive sand wedge. a) beginning of the steady-state phase with a tripartite topography (PSC after 40 cm conv.), b) later steady-state phase with a bipartite topography (PSC after 520 cm conv.).

through different kinematic domains, with respect to particles, which remained in the internal segment during the whole experimental run. Moreover, the particle paths included additional information about the wedge-internal deformation processes, which was fully described by four different particle-paths observed in all experiments of the first series (Fig. 4.10):

1. This particle-path 1 described the particle path of material, which was initially located in the upper part of the internal segment and then frontally-eroded (1 in Fig. 4.10). At first, these particles were strongly uplifted with moderate rearward transport by wedge-internal shortening of the accretive adjustment phase and basal accretion of the erosive adjustment phase. In the steady-state phase, uplift subsequently decreased, with only minor rearward (i.e. compressional uplift) or forward transport (i.e.

extensional uplift). Maximum total uplift was attained when the particles had migrated through the neutral surface into the toe segment, where they suffered extensional subsidence. Finally, the particles were frontally-eroded by slumping.

2. The second particle path attained material initially located near to the base of the internal segment (2 in Fig. 4.10). Maximum base-parallel displacement occurred during the initial formation of the basal shear zone by underthrusting (adjustment phases). In the steady-state phase, moderate compressional uplift occurred until a short stagnation of motion indicated the migration through the neutral surface into the toe segment. Then, material transport was characterised by moderate subsidence with contemporaneous rearward transport in the basal damage zone, indicating basal

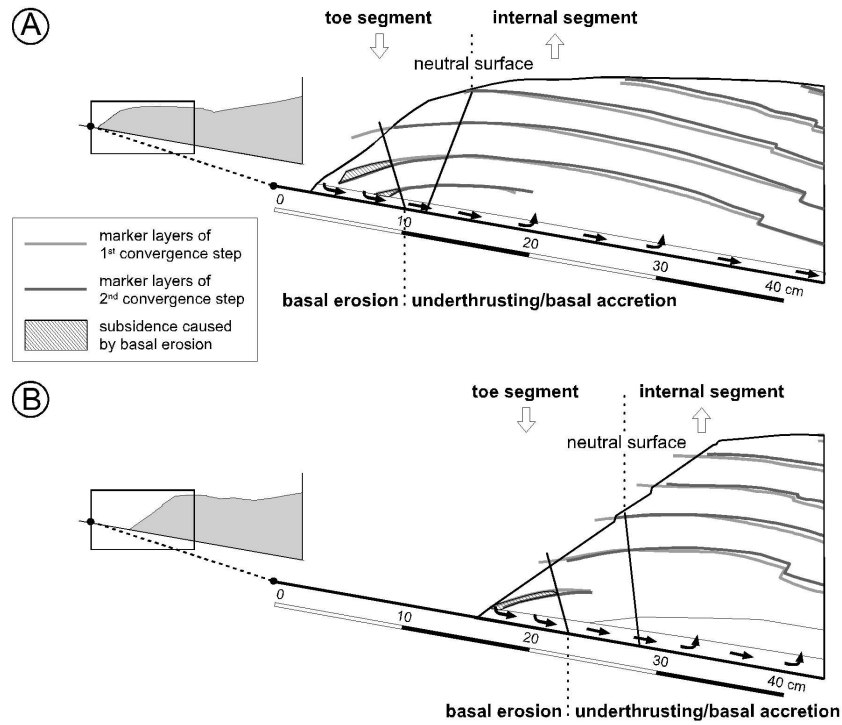


Figure 4.8: Change in the position of marker layers during 40 cm conv. The toe segment and internal segment, as well as the dominant area of basal erosion were identified by this method. a) At the beginning of the steady-state phase, the neutral surface (definition see Section 2.4.3.1) is located at the rear of the steep frontal slope, b) In the later steady-state phase, the neutral surface is located within the steep frontal slope.

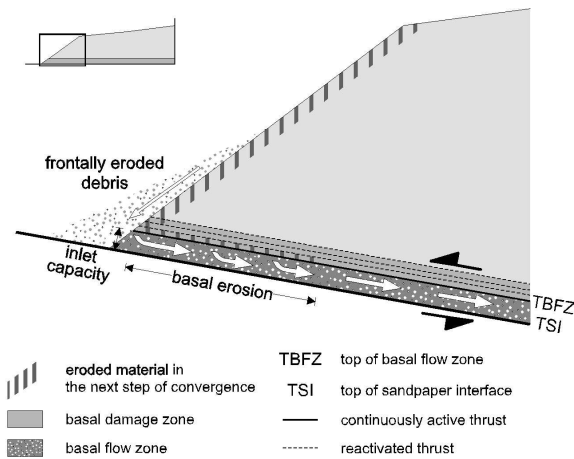


Figure 4.9: Kinematics of the basal shear zone.

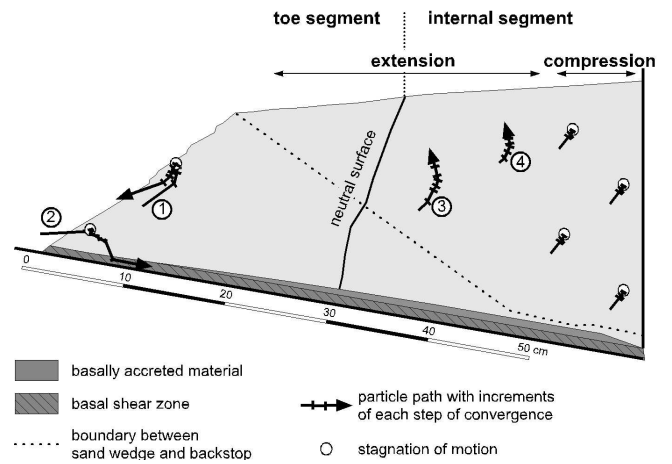


Figure 4.10: Sketch of the four characteristic particle paths. Particle paths 1 and 2 are the results of frontal and basal erosion, respectively. Particle paths 3 and 4 stay in the internal segment and do not migrate through the neutral surface. They are dominantly characterised by uplift (see also Tab. 4.3).

material removal. Finally the particle itself was basally eroded.

3. Particles, which remained in the frontal part of the internal segment during the whole experimental run, were not affected by the erosive processes (3 in Fig. 4.10). This third particle path indicated strong uplift and moderate rearward transport in the adjustment phases and the initial steady-state phase. In the late steady-state phase, all particle paths indicated active extension by minor to moderate relative frontal transport.
4. In the adjustment phases and the initial steady-state phase, particles which were located close to the rigid backwall, migrated along a comparable path to that of particle path of type 3, but with smaller displacements (4 in Fig. 4.10). During the later steady-state phase, the fourth particle paths differed in all experiments (for further description see 'contrasting features').

The increments of wedge-tip retreat, frontal erosion, and basal erosion were determined from the serial photographs to detect potential relationship among the different mass-transfer processes (Fig. 4.11). The rates derived from this investigation were interpreted after 100 cm conv. to focus only on the steady-state phase.

In all experiments of the first series, the final volume of frontally-eroded material exceeded more than fourfold the final volume of basally-eroded material (Tab. 4.2). While the rate of frontal erosion was constantly in the range of $\pm 0.4 \text{ cm}^3 \text{ cm}^{-1} \text{ conv.}^{-1}$ (i.e. cm^3 eroded material $\text{cm}^{-1} \text{ conv.}^{-1}$ width; Fig. 4.12 a), the rate of wedge-tip retreat showed a decreasing trend during the experimental run (Fig. 4.12 c). Moreover, strong increase in the rates of basal-erosion always correlated with increasing frontal erosion rate in the isotropic sand wedges (SSC, PSC, SSO; Fig. 4.12 b).

Contrasting features

The mass-transfer mode of the individual erosive sand wedges differed only in the internal segment (Fig. 4.13). Both experiments with a closed setup (SSC, PSC) showed major basal accretion of the material which was transported within the basal-flow zone. In the experiment with the sifted sand (SSC), the material in the basal-flow zone was basally accreted over a shorter distance onto the wedge base (ca. 35 cm after 330 cm conv.), than in

the sand wedge which consisted of poured sand (ca. 70 cm after 330 cm conv., Fig. 4.13 a and b). In the latter, basal erosion was restricted to the 'frontal part' of the wedge, since basal accretion took place along nearly the whole wedge base, with the exception of the first few centimetres (ca. 10 cm) from the front (this occurred in all the 'isotropic' experiments, but less obvious, see above).

Both experiments in an open setup (SSO, ASO) showed only minor basal accretion during the steady-state phase (Fig. 4.13 c and d). Therefore, the effects of the erosive mass-transfer processes (frontal and basal erosion) on the wedge interior was seen best in these experiments, since the wedge-internal deformation processes were not influenced by basal accretion.

Major differences between the experiments were also observed in the pattern and kinematics of localised shear zones. In the experiments performed in the closed setup (SSC, PSC), localised deformation only occurred in the internal segment and backstop, where uplift by basal accretion was accommodated by backthrusting (Fig. 4.13 a and b). The first backthrusts of the SSC experiment were formed during the accretive adjustment phase (after 40 cm conv., Appendix) in the internal segment. In the later steady-state phase (after 300 cm conv.) when the first backthrusts became inactive, new backthrusts were initiated in their footwall. The contrasting PSC experiment showed only one initiation phase of backthrusts (after 220 cm conv.). These backthrusts were located in the rear of the backstop and met the rigid backwall (Appendix).

In contrast to all other experiments (SSC, PSC, ASO), the SSO experiment did not deform along localised shear zones, neither by backthrusting nor by normal-faulting during the whole experimental run (Fig. 4.13 c).

In the ASO experiment, the pattern of localised shear zones was quite complex during the accretive adjustment phase, since all glass-bead layers were activated as thrusts and backthrusts according to their initial orientation. During the erosive adjustment phase these thrust were successively inactivated from top to bottom. The steady-state phase began when only the lowest glass-bead layer was active (after 100 cm conv., see Appendix). The basal shear zone of this experiment (ASO) strongly differed from that of the isotropic sand wedges (SSC, PSC, SSO) during the initial steady-state phase, since the lens-shaped bodies in the ASO sand wedge were wholly transported as duplexes between the localised roof thrust (lowest glass-bead layer)

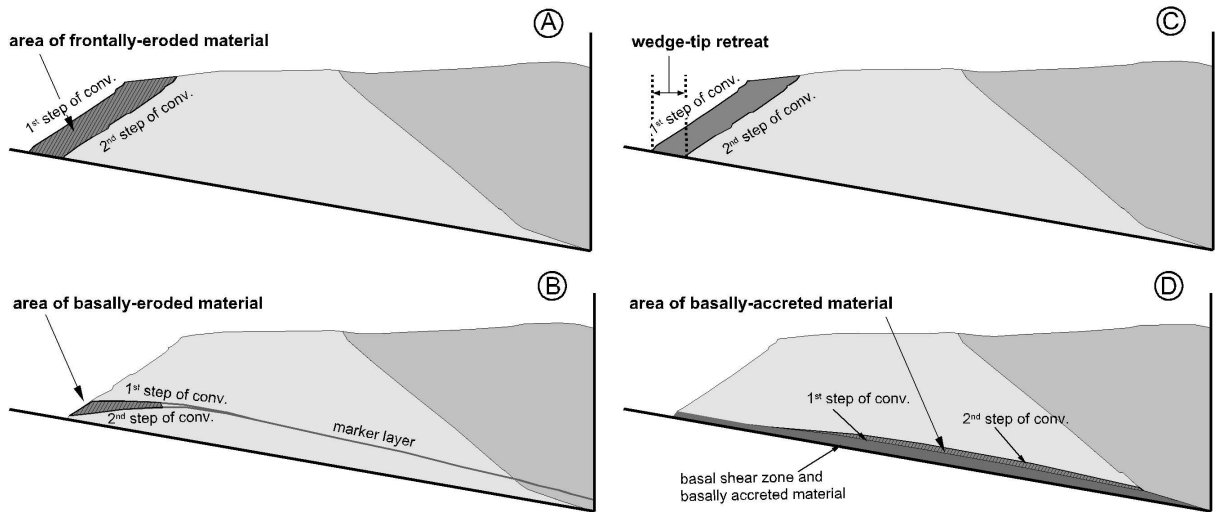


Figure 4.11: Method to detect a) the area of frontal erosion, b) the area of dominant basal erosion, c) the area of basal accretion, d) the distance of wedge-tip retreat. From this the rates and volumes of the mass-transfer processes were determined.

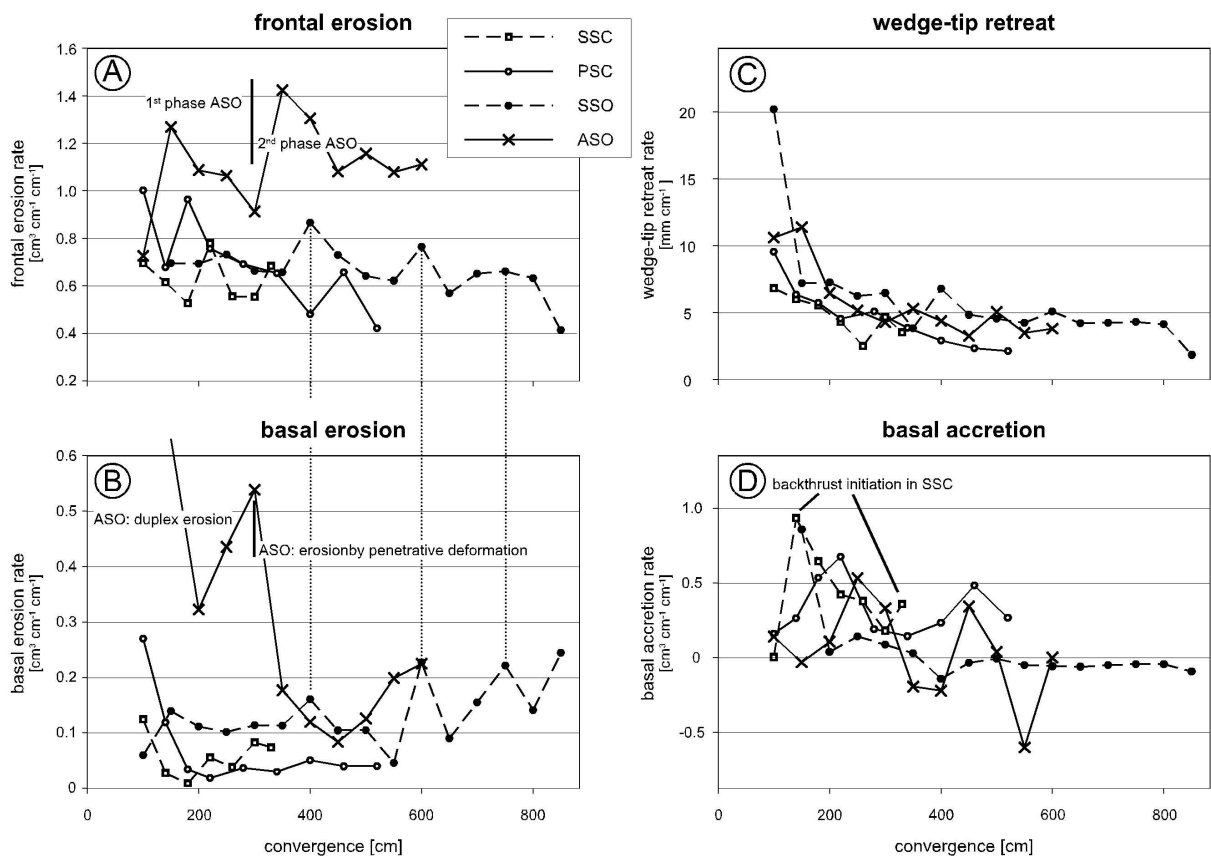


Figure 4.12: Comparison of the mass-transfer rates of the experiments of the 1st series in the steady-state phase a) frontal erosion, b) basal erosion, c) wedge-tip retreat, and d) basal accretion. The coeval increase in basal and frontal erosion rates is best seen in the SSO experiment, as indicated by the dotted lines.

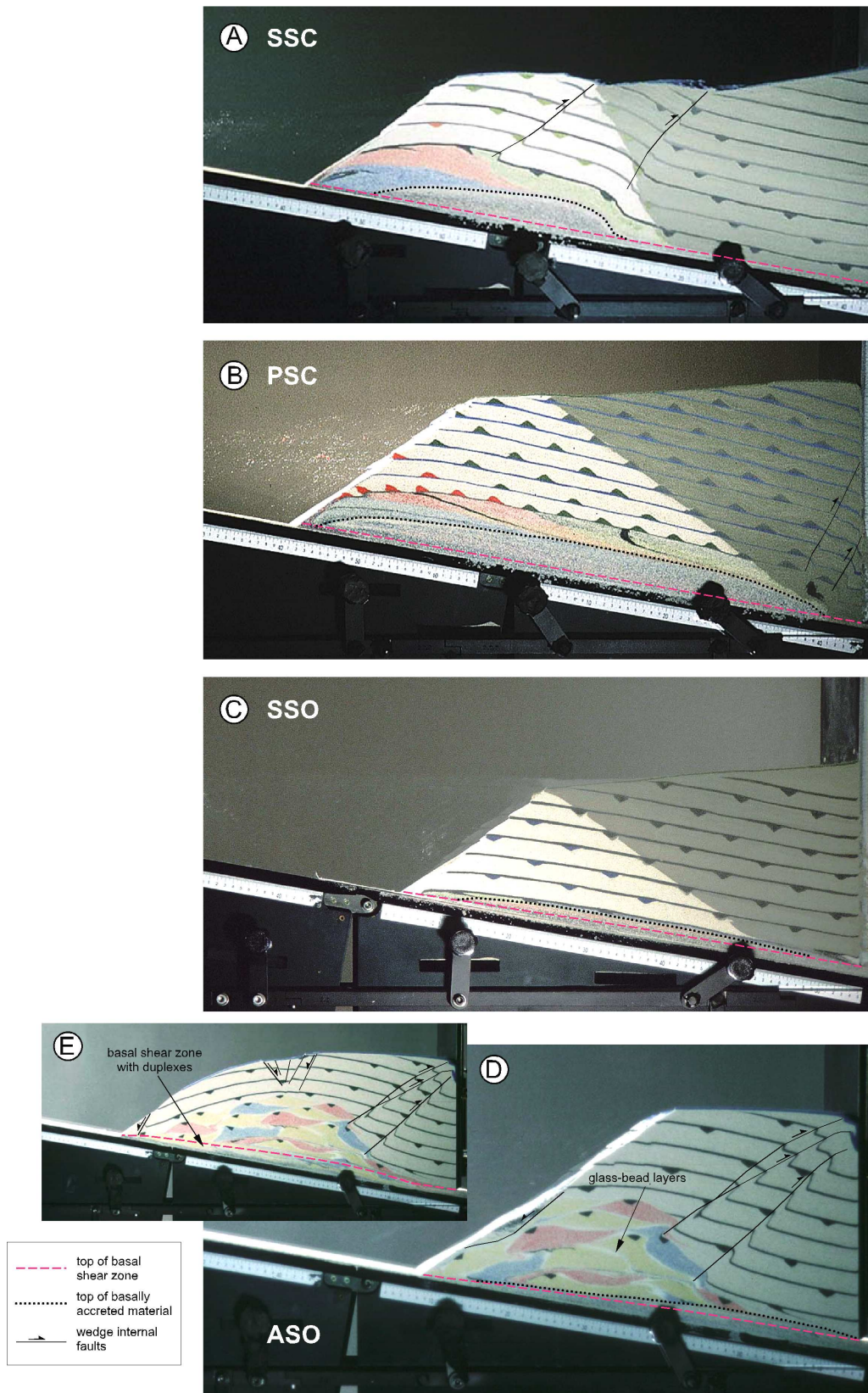


Figure 4.13: Photographs of the final phase of the experiments of the 1st series. a) SSC after 330 cm conv., b) PSC after 520 cm conv., c) SSO after 850 cm conv., d) initial steady-state phase of the ASO experiment with basal duplex erosion after 160 cm conv., and e) later steady-state phase of the ASO experiment, with basal erosion by penetrative shearing after 600 cm conv.

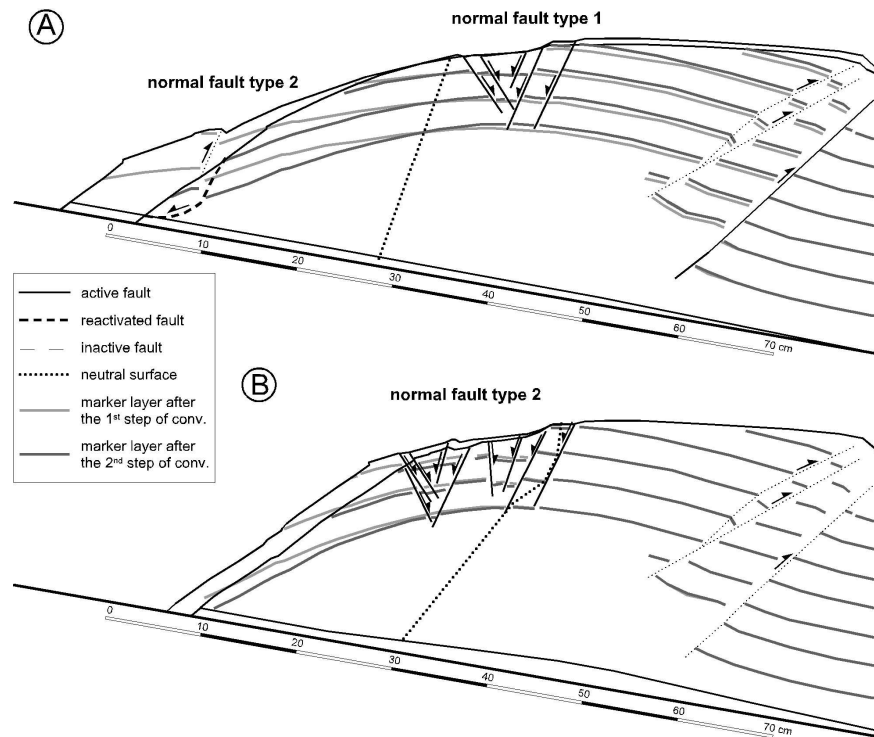


Figure 4.14: Kinematic evolution of the two types of normal faults in the ASO experiment, a) initial steady-state phase (from 80 to 150 cm conv.), b) later steady-state phase (from 200 to 250 cm conv.).

and floor thrust (sandpaper interface, Fig. 4.13 d). However, where the frontally-eroded debris was underthrust beneath the wedge, the division of the basal shear zone into basal-flow zone with diffuse deformation and damage zone was also attained in this experiment. After 300 cm conv. the basal shear zone was formed beneath the whole wedge base (Fig. 4.13 e).

In the ASO experiment, backthrusting occurred much earlier (after 10 cm conv.) than in all other experiments (SSC, PSC, SSO, Appendix). However, during the later steady-state phase (after 200 cm conv.) no further backthrusting was observed, as in the other experiment performed in an open setup (SSO).

The ASO experiment was the only experiment in the first series, which showed extension along localised shear zones. Two types of normal faults were identified:

1. A graben structure was initiated in the uplifted internal segment by normal faulting at the beginning of the steady-state phase (80–150 cm conv., Fig. 4.14 a). Contemporaneously with the inactivation of the backthrusts and the end of basal accretion after 200 cm conv.,

these normal faults also became inactive. This observation indicated that these normal faults were related to the surface extension, which was caused by the bending of the material overlying the basal-accretionary complex (cf. Section 3.3).

2. Another graben structure was formed after 200 cm conv. by normal faults in the subsiding toe segment (Fig. 14 b). The normal faults, which were inclined toward the wedge tip, became the dominant faults later on. After a short phase of inactivity, when the normal faults were positioned on the part of the steep frontal slope, they were finally used as a detachment for extensive slumping at the steep frontal slope.

The inactive normal faults of type 1 were reactivated as type 2, when they reached the toe segment.

The differences in the wedge-internal mass-transfer processes and its related kinematics were more exactly observed in the particle-paths of the individual experiments (Fig. 4.15; Tab. 4.3). In steady state, the particle-paths of type 1 and 2 only varied in the subsiding branch of the paths.

In experiments, in which a closed setup permitted basal accretion (SSC, PSC), particles suffered minor subsidence in the toe segment until they were basally or frontally eroded after only several decimetres of convergence (< 10 dm conv. $<$). In contrast, experiments, in which major basal accretion was avoided by using an open setup (SSO, ASO), substantial subsidence occurred in the toe segment during several metres of convergence (up to 400 cm conv. in ASO).

The particle path of type 3 only varied from the general pattern (see ‘common features’, Fig. 4.10, Tab. 4.3) in the SSC experiment (Fig. 4.15 a). In this sand wedge, the late-stage extensional uplift was not clearly imaged by incremental particle paths, as they were all inclined toward the rear, which was not observed in all of the other experiments (PSC, SSO, ASO). However, I conclude that late-stage extensional uplift in the particle-path of type 3 occurred in the SSC experiment, since the particle paths in a more frontal position showed a decreasing horizontal component compared to the particle paths in the rear. The rearward orientation of particle paths during extensional uplift only occurred in the hanging wall of backthrusts. In this position, transport towards the front was superimposed by strong rearward displacement along the backthrusts, particularly in the experiment, in which the largest displacement along the backthrusts occurred (SSC).

In contrast to the particle paths of type 3, those of type 4 were different in all the experiments of the first series. Persistent compressional uplift was inferred by the particle paths of type 4 in the SSC experiment (Fig. 4.15 a; Tab. 4.3). These particle paths recorded the continuous uplift and rearward transport by backthrusting, which accommodated basal material addition. Although continuous uplift was also observed in the PSC experiment, no horizontal displacement component was present in the rear part of this wedge, as the backthrusts of this experiment met the rigid backwall of the sandbox and therefore, the hanging wall of the backthrusts were not able to escape horizontally (Fig. 4.15 b; Tab. 4.3). The particle paths of type 4 of both experiments performed in an open setup indicated late stage subsidence (SSO, ASO, Fig. 4.15 c and d; Tab. 4.3). In the SSO experiment, the particle paths of type 4 correlated with those of type 3, however, with minor displacements. In contrast, vertical subsidence during the late steady-state phase of the ASO experiment suggested basal material loss at the rear of the wedge (Fig. 4.15 d; Tab. 4.3).

Fig. 4.16 shows the volume balance of erosional mass, its spatial and temporal distribution, and the path of the retreating wedge-tip through the sand wedge (i.e. *wedge-tip line*). Material above and below the wedge-tip line was successively removed by frontal and basal erosion, respectively. In the isotropic sand wedges (SSC, PSC, SSO, Fig. 4.16 a, b, and c), the wedge-tip retreated along a similar path: During the erosive adjustment phase, the initial wedge-tip immediately shifted to a peak level above the wedge base indicating strong initial basal erosion. At the beginning of the steady-state phase, the wedge-tip line gradually stepped down and turned into a nearly base-parallel position. However, this correlation of the shape of the wedge-tip line and the states of the mass-transfer processes was not observed in the anisotropic experiment (ASO, Fig. 4.16 d). The wedge-tip line of the latter did not reach peak level until the basal-flow zone was established over the whole length of the wedge base (300 cm conv., Fig. 4.16 d). After 300 cm conv. the gradual descendance of the wedge-tip line, which was typical for the transition into the steady-state phase of the other experiments (SSC, PSC, SSO), was interrupted at that moment when huge volumes of frontally-eroded material reached the wedge-tip (slumps detached by normal faults of type 2 after 400 cm conv.).

The differences in the wedge-tip lines also infers differences in the mass-transfer process (frontal erosion, basal erosion, basal accretion, wedge-tip retreat) between the experiments. I used the bulk rates of the mass-transfer processes for a detailed analysis of these differences (Fig. 4.17). The bulk rates were derived from the quantities measured in the serial photographs (Fig. 4.11). Again, the experiments were interpreted after 100 cm conv. to only focus on the steady-state phase. For direct comparison of the individual experiments, the quantities were normalised (null values at convergence step 100 cm, Tab. 4.2).

Variation in the ratio of basally- versus frontally-eroded material (derived from the final volume) depended on the setup used, since the closed setup produced lower ratios (SSC, PSC $\geq 1 : 13$) and the open setup higher ratios (SSO, ASO $\leq 1 : 5$; Tab. 4.2).

The bulk rates of basally-eroded and -accreted material, as well as wedge-tip retreat were also controlled by the setup used (Fig. 4.17 b, c, d, and e, Tab. 4.2). The experiments which were performed in a closed setup (SSC, PSC), were characterised by a smaller bulk rate of wedge-tip re-

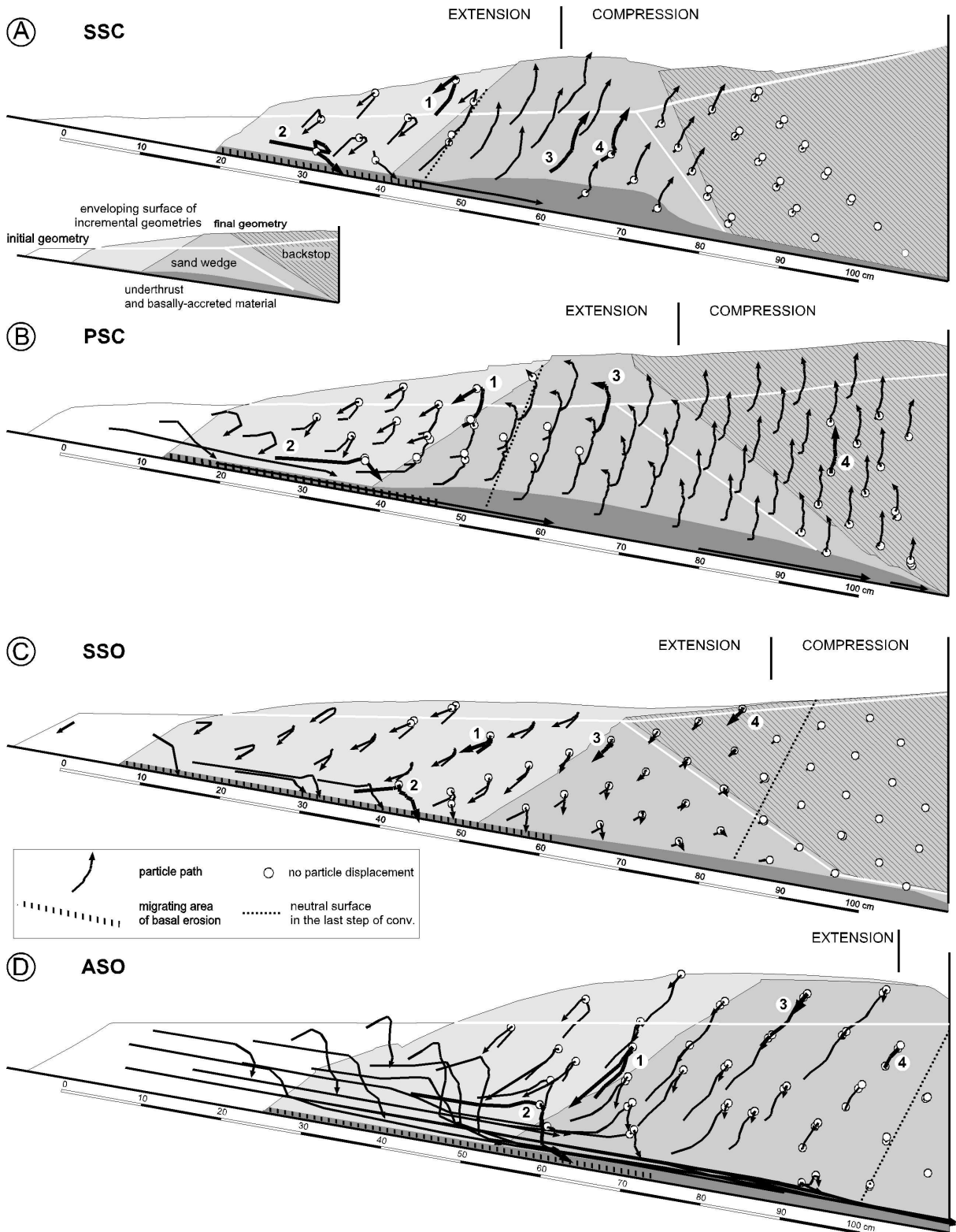


Figure 4.15: Particle-paths of the experiments of the 1st series. Examples of the four typical particle paths are indicated by numbers 1-4 (see Tab. 4.3). a) SSC, b) PSC, c) SSO, d) ASO.

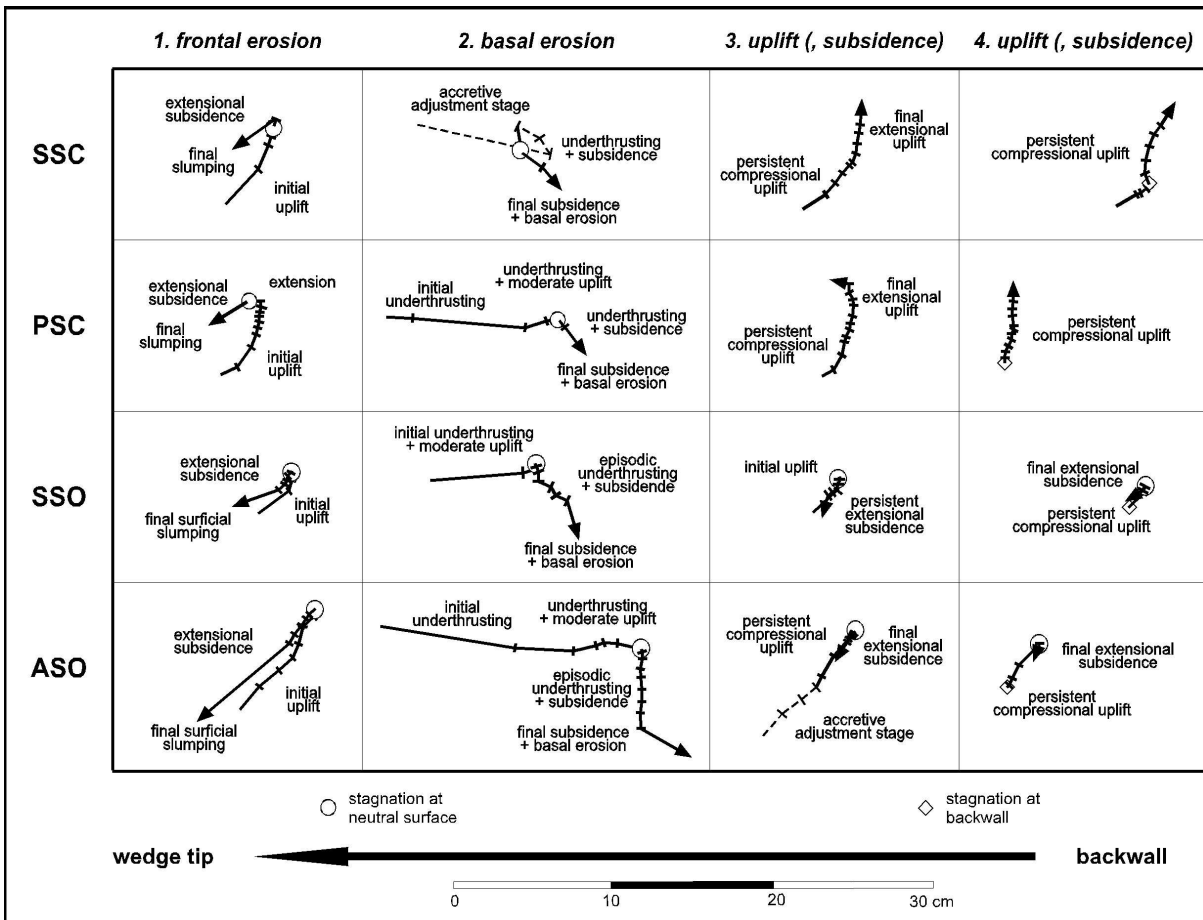


Table 4.3: Characteristic particle paths of the experiments of the 1st series.

treat ($\leq 4.5 \text{ mm cm}^{-1}$; Tab. 4.2), and smaller rate of basally-eroded material ($\leq 0.05 \text{ cm}^3 \text{ cm}^{-1} \text{ cm}^{-1}$, Tab. 4.2), as well as a larger rate of basally-accreted material ($\geq 0.33 \text{ cm}^3 \text{ cm}^{-1} \text{ cm}^{-1}$; Tab. 4.2) than that observed in the experiments, which were performed in an open setup (SSO, ASO, Fig. 4.17, Tab. 4.2). In the latter, the bulk rate of wedge-tip retreat slightly exceeded the bulk rate of the experiments in a closed setup by a factor of 1.1 (Fig. 4.17 d). In contrast, the bulk rate of basally-eroded material was significantly higher by a factor of 2.8 in the SSO experiment compared to the experiments in a closed setup (Fig. 4.17 b). However, the maximum bulk rate of basal erosion of all experiments was observed in the ASO experiment. Here, $0.48 \text{ cm}^3 \text{ cm}^{-1} \text{ cm}^{-1}$ material was basally eroded on average by the underthrusting of the lens-shaped duplexes in the first 200 cm conv. of the steady-state phase. When the basal-flow zone also established in this experiment, the bulk

rate of basal erosion decreased to a rate comparable to that observed in the SSO experiment ($\sim 0.15 \text{ cm}^3 \text{ cm}^{-1} \text{ cm}^{-1}$).

A dependence on the setup used (open or closed) did not occur for frontal erosion. Frontal erosion averaged about $0.65 \text{ cm}^3 \text{ cm}^{-1} \text{ cm}^{-1}$ in all the isotropic sand wedges (SSC, PSC, SSO, Fig. 4.17 a). From this the average thickness of underthrust debris (that was previously frontally eroded) was calculated at 6.5 mm, which was in good agreement with the measured thickness of the basal-flow zone at the wedge tip (6.7–7.2 mm, Tab. 4.2). In contrast, the bulk rate of frontally-eroded material ($12 \text{ cm}^3 \text{ cm}^{-1} \text{ cm}^{-1}$) and the average thickness of underthrust debris (12 mm) of the ASO sand wedge was twice as high as compared to that of the isotropic sand wedges.

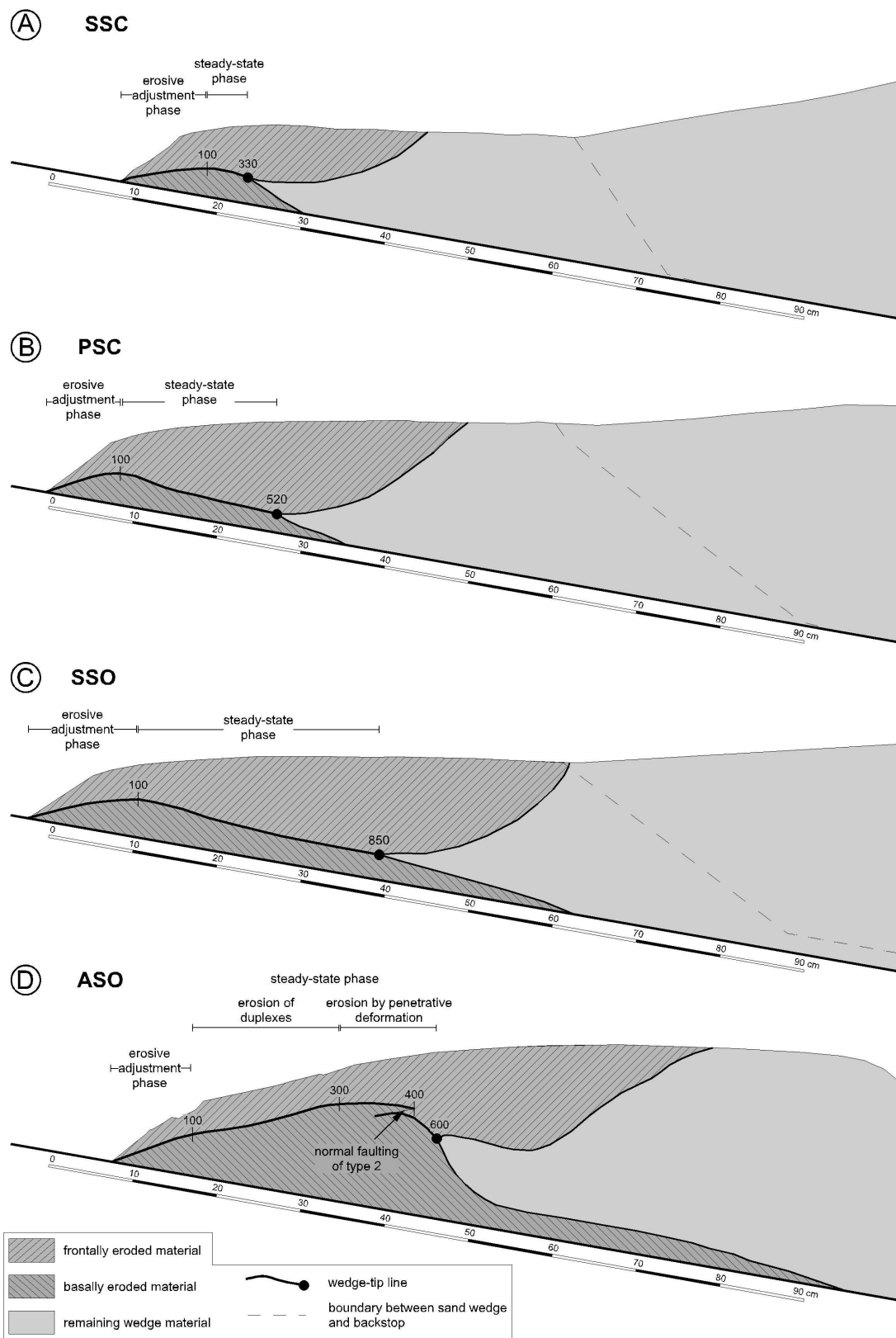


Figure 4.16: Plot of the wedge-tip lines, which were determined by the position of the wedge-tip in the serial photographs, after the accretive adjustment phase. a) SSC, b) PSC, c) SSO, d) ASO. Numbers at the wedge-tip lines indicate cm conv.

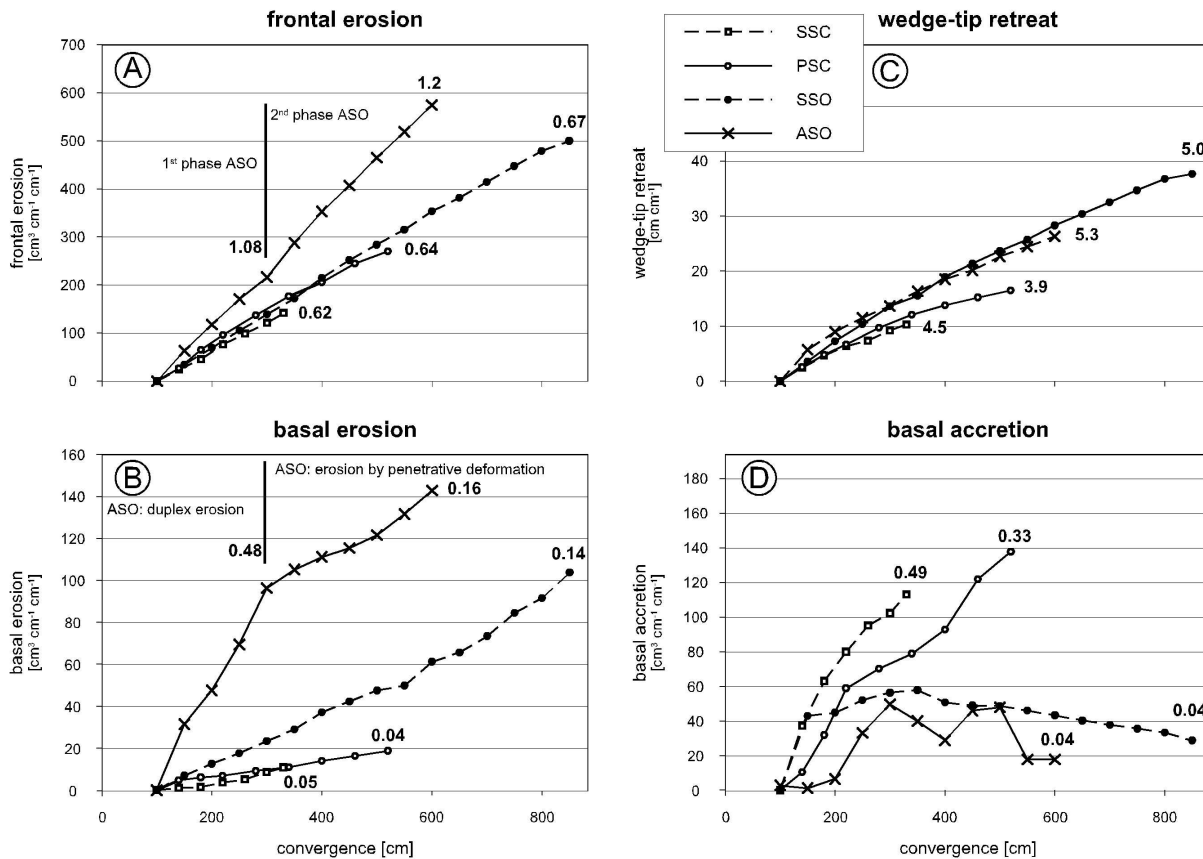


Figure 4.17: Comparison of the mass-transfer volumes of the experiments of the 1st series in the steady-state phase a) frontal erosion, b) basal erosion, c) wedge-tip retreat, and d) basal accretion. The numbers indicate the bulk mass-transfer rates derived from the final values.

4.3.2 Experimental results of the 2st series (mechanics)

The additional experiment (SLC) of this series (Fig. 4.18), which is not included in the first series, contrasted in all features from the other experiments of both series the first and second (SSC, PSC). Therefore, the experimental run of the SLC experiment is separately presented in the first part of this section, followed by the description of the contrasting features of the experiments of the second series, which concerns the mechanics of the tectonically erosive sand wedges.

Experimental run of SLC (SIC2, latex gum, closed setup)

During the accretive adjustment phase of the SLC experiment, diffuse deformation of the whole sand wedge resulted in a total shortening of 2 cm (Fig. 4.18 a). The surface slope of the sand wedge rotated slightly to $\alpha = -0.4^\circ$ due to the initial

compaction increase. Immediately after the accretive adjustment phase, the sand wedge reached the steady-state phase, in which the whole sand wedge stably slid on top of the latex-gum interface without remarkable material transfer. As neither frontal nor basal erosion was initiated after 200 cm conv., the experiment was abandoned, as I did not expect a change during further convergence.

Contrasting features

The SLC experiment, with the conveyor belt made of latex gum, fundamentally differed in the geometrical and kinematical evolution as well as in the mass-transfer mode from all other experiments, which were performed on top of sandpaper (SSC, PSC, and the others of the first series): The SLC experiment did not show an erosive mass-transfer mode, but was stagnant. Therefore, no common features were obtained between the steady-state phase of this sand wedge and the erosive sand wedges.

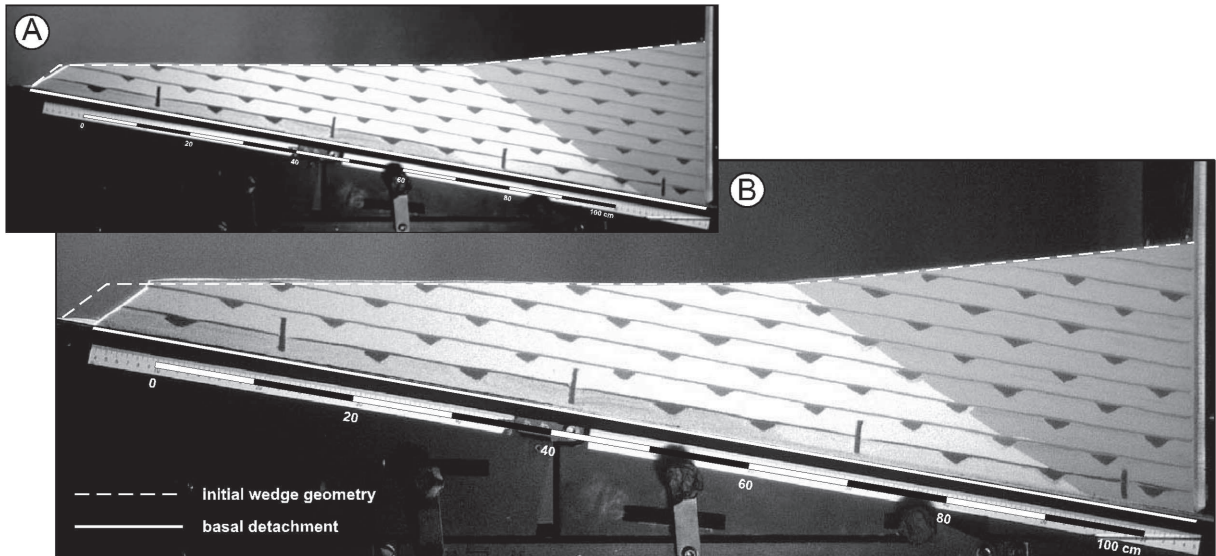


Figure 4.18: Photographs of the SLC experiment after a) 10 cm conv., b) 200 cm conv.

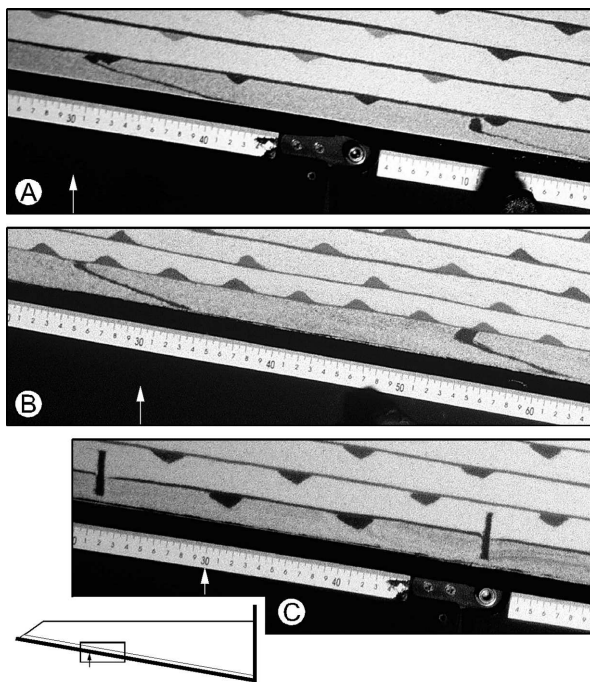


Figure 4.19: Photographs of the initial basal shear zones in the experiments of the 2nd series after 10 cm conv.: a) sandpaper interface/sifted sand (SSO), b) sandpaper interface/poured sand (PSC), c) latex-gum interface/sifted sand (SLC). The initial orientation of the basal markers (black stripes) was vertical, such as seen in (c).

The main difference of the kinematics were observed in the basal shear zone. After 10 cm conv., when the shear zone was not completely formed,

the thickness of the material at the wedge base, which was penetrated by diffuse deformation, were larger in the experiments performed with sandpaper (16 mm beneath 100 mm wedge thickness in SSO, 17 mm beneath 100 mm wedge thickness in PSC; Fig. 4.19 a and b, respectively) than in the SLC experiment (1–2 mm beneath 100 mm wedge thickness, Fig. 4.19 c). This showed that the formation of the basal shear zone was mainly dependent on the roughness of the basal interface and was independent of the preparation technique of the sand. The thickness of the initial shear zone in the sandpaper experiments decreased significantly rearward. This indicated that the shear zone formation partially depended on vertical load.

During the steady-state phase basal shear strain in the SLC experiment was still restricted to the lowest 1–2 mm (Fig. 4.18 b). In contrast, during ongoing basal shear zone formation in the sandpaper experiments, shear strain at the wedge base was progressively localised until the beginning of the steady-state phase, when the basal-flow zone (continuous deformation) and the damage zone (episodic deformation) were established (see also Fig. 4.3.1). A vertical upwards velocity decrease of the continuously transported particles was observed in the basal-flow zone (Fig. 4.20). This vertical velocity decrease is seen best during initial shear zone formation, when the initially-vertical markers indicated minor total displacements of grains at the top of the continuously-deformed material and major displacements of grains located directly on top

of the sandpaper (Fig. 4.19 a and b).

In addition, the bulk rates of the erosional mass-transfer processes in the sifted and poured sand wedge performed with sandpaper in a closed setup (SSC, PSC) were similar with respect to the error range (Fig. 4.17 a and b). (The main error, which occurred by the determination of volumes, was due to the difficulty to distinguish the underthrust material from the undeformed wedge material by colour, Fig. 4.13 a and b). However, the experiments showed differences in the bulk rate of basally accreted material (Fig. 4.17 c). In the poured sand wedge (PSC, $0.3 \text{ cm}^3 \text{ cm}^{-1} \text{ cm}^{-1}$) this bulk rate was lower than that of the sifted sand wedge (SSC, $0.5 \text{ cm}^3 \text{ cm}^{-1} \text{ cm}^{-1}$). This increase of basal accretion in the SSC experiment took place during the backthrusting phases in the overlaying wedge (Fig. 4.12 c, step 100 to 200 cm conv. and 300 to 330 cm conv.).

4.3.3 Summary of experimental results of 1st and 2nd series

Steady-state tectonic erosion only occurred in the experiments with a high frictional and rough basal interface (sandpaper) and not in experiments with a high frictional and smooth basal detachment (latex gum). In additional test runs at the end of accretive experiments a low-friction conveyor belt was drawn against the backwall without an incoming sand-layer. In this case basal erosion did also not occur. Therefore, I conclude that steady-state tectonic erosion requires very high basal friction, which is induced by the high roughness of the sandpaper.

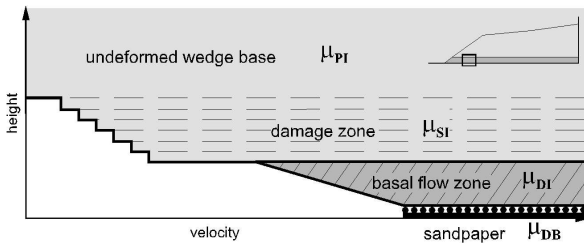


Figure 4.20: Estimated velocity-distribution in the basal shear zone above the sandpaper interface with related frictions (TSI – top of sandpaper interface, TBFZ – top of basal-flow zone, μ_{PI} – peak internal friction; μ_{SI} – stable dynamic internal friction; μ_{DI} – stable dynamic internal friction; μ_{DB} – stable dynamic basal).

The steady-state, tectonically erosive sand wedges are characterised by three kinematic domains (from the front to the rear):

1. extensional subsidence
2. extensional uplift
3. compressional uplift

The formation of these kinematic domains were mainly caused by the three basal mass-transfer processes, respectively: basal erosion, underthrusting, and basal accretion. However, the wedge-internal extension in domain 1 and 2 can not be explained by these basal mass-transfer processes (cf. Section 4.4).

Basal accretion is the mass-transfer process, which is mainly influenced by the choice of the setup, since total basal accretion of formerly-eroded material and the related significant uplift only occurred in the experiments performed in a closed setup.

The isotropic sand wedges deformed diffusely within the kinematic domains, in contrast to the anisotropic sand wedge. The weak layers (glass-bead layers) within the anisotropic sand wedge localised the wedge-internal extension, so that the overlying sand material formed also localised normal faults. The resulting graben and half graben structures were morphologically pronounced and accommodated the extension over a relative short horizontal distance, compared to that of the diffusely deforming sand wedges. Thus, the anisotropic sand wedge was characterised by a more irregular topography with large changes over short horizontal distances.

4.4 Interpretation of experimental results

Firstly, an important difference between the accretive and tectonically erosive sand wedges will be discussed, since this is a key to understand the whole mass-transfer mode in the erosive sand wedges. In such sand wedges the topographical, kinematic, and basal mass-transfer domains did not correspond with each other (cf. Fig. 4.7, 4.8, and 4.10), as it was generally observed in the accretive systems (cf. Fig. 2.11; 2.22 and 3.16 c). Up until now, extension and its related subsidence in the frontal part of the internal segment, and the toe-segment of tectonically erosive sand wedges, could not be explained

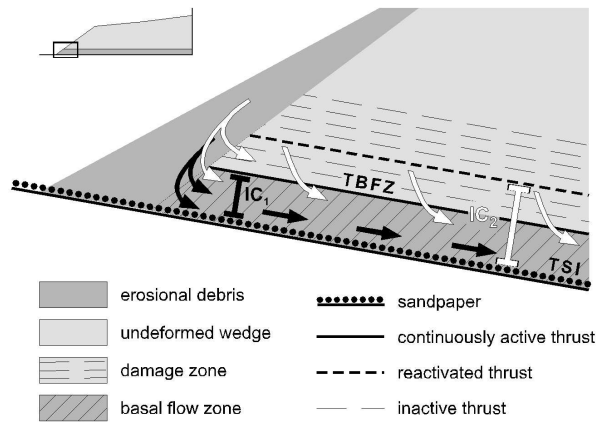


Figure 4.21: Reactivation of thrust in the damage zone causes an increase in the inlet capacity. IC_1 – inlet capacity during inactive damage-zone thrusts; IC_2 – inlet capacity during active damage-zone thrusts.

by the observed mass-transfer processes. The extensional subsidence overprinted the kinematic features of certain basal mass-transfer processes, since it extended over a longer horizontal distance than subsidence due to basal erosion. Therefore, I ascribe the lack of correlation between the wedge domains to extensional subsidence. If basal erosion caused this subsidence, the particle path above the area of basal erosion would be directed towards the base of the wedge. Instead, in the sand wedges in which no material was basally accreted, the particle paths of the upper part of toe segment were directed toward the wedge-tip (Fig. 4.15 c and d). Extension increased from the rigid backwall toward the steep frontal slope (best seen in Fig. 4.15 c). Additional, extension was present over a larger horizontal distance, when the steep frontal slope became successively higher during wedge-tip retreat. Based on these observations, I conclude that extensional subsidence was caused by gravitational collapse induced by the over-steepness of the frontal slope.

4.4.1 Mass transfer

In this section, I focus on the mutual relationship of the erosional mass-transfer processes and on the influence of the capacities of the basal shear zone on the mass-transfer processes. According to the subduction-channel model of Cloos and Shreve (1988b; Section 1.2), the thickness of the basal-flow zone beneath the frontal part of the wedge determines the *inlet capacity* (IC_1 in Fig. 4.21). The *global capacity* (GC) is defined by the thickness of

the material, which was allowed to leave the sand-box at the rear (open and closed setup).

The slumping of the frontal-erosion process induced the steep frontal slope at the angle of repose. Neither the rearward migration of the steep frontal slope influenced the other two topographical domains (convex central part and unmodified rear part) nor did the rates of frontal erosion influence the rates of the other mass-transfer processes in the isotropic sand wedges (Fig. 4.12). Consequently, frontal erosion and the gravitational collapse process did not influence other mass-transfer processes (basal erosion, basal accretion).

However, the rates of frontal erosion itself showed a response on the fluctuations of the basal-erosion rates (Fig. 4.12 a and b). Fluctuation of basal-erosion rates indicates variation of the inlet capacity, as at the moment of basal material removal, the inlet capacity increased from the height of the basal-flow zone up to the height of the active base-parallel shear zones in the damage zone (IC_2 in Fig. 4.21). Therefore, I suggest that frontal erosion was mainly controlled by inlet capacity and was independent of global capacity. This suggestion is made for the isotropic sand wedges (in all of which $IC \geq GC$, since in these experiments the bulk rate of frontal erosion was not influenced by the increase of the global capacity up to the height of inlet capacity (SSO, Fig. 4.17 a). However, the dependence of frontal erosion on the inlet capacity was not confirmed by the ASO experiment. Here, the inlet capacity changed during the experimental run. At the beginning, the inlet capacity was determined by the position of the lowest glass-bead layer above the sandpaper interface (10 mm). While the diffusely-deforming basal-flow zone formed, the inlet capacity decreased down to the top of the basal-flow zone (5 mm). However, the rates of frontally-eroded material did not show a persistent response to this change of inlet capacity (Fig. 4.12 a). Therefore, I suggest that global capacity controls frontal erosion in systems in which $IC < GC$. That frontal erosion is dependent on the IC/GC ratio, can also be inferred from the stronger frontal erosion in the case of $IC \ll GC$ (ASO after 300 cm conv.), in contrast to consistent bulk rates of frontal erosion in all cases of $IC \geq GC$ (SSC, PSC, SSO, Fig. 4.17 a).

The basal erosion process showed a proportional effect on the global capacity in all experiments (Fig. 4.17 b). Therefore, I conclude that global capacity controls the volume of basally-eroded material. The subdivision into systems of different IC/GC ratios was not necessary in the case of basal erosion,

as even in the later stages of the ASO experiment, when $IC \ll GC$, the bulk rate of basal erosion was comparable with the bulk rate observed in the SSO experiment, i.e. $IC = GC$. Nevertheless, basal erosion was additionally controlled by the kinematics of the basal shear zone. In the case of the ASO experiment, in which the setup conditions forced the erosion of basal duplexes, the bulk rate was significantly higher than which would have been induced by the global capacity.

The experimental results inferred that the wedge-tip retreat is controlled by three parameters (Fig. 4.12 d, Fig. 4.17 d):

- the inlet capacity determines how much material will be removed from the wedge tip by frontal erosion (see above),
- the shape of the wedge determines how much material is added to the wedge-tip by slumping of erosional debris (this material addition increased during the experimental run, as the cross-sectional area of the steep frontal slope increased during its rearward migration and truncation of the wedge-shaped body and consequently the rate of wedge-tip retreat decreased during the experimental run, Fig. 4.12 d), and
- the global capacity determines how much material is removed from the wedge base (the dependence of wedge-tip retreat on the global capacity was inferred from the proportional increase of wedge-tip retreat with increased global capacity, Fig. 4.17 d).

Based on these interpretations, I conclude that the inlet- and global-capacity mainly control the mass-transfer mode of steady-state, tectonically erosive wedges. This control was best seen in the ASO experiment, in which an extreme change in the wedge-internal properties (glass-bead layers) induced a pronounced localised deformation as well as higher rates of the erosional mass-transfer processes, but did not change the mass-transfer mode itself. In addition, the change of the mechanical properties secondarily influences the mass-transfer mode and will be discussed in the next section (4.4.2).

I summarise four mutual dependencies of the mass-transfer processes:

1. The height of the steep frontal slope controls the gravitational collapse process at the frontal part of the wedge.
2. Frontal erosion controls the height of the steep frontal slope, since the size of the erosionally truncated surface at the frontal part of the wedge is proportionally related to the frontal erosion rate.
3. Basal erosion near the wedge tip controls frontal erosion.
4. Thus, basal erosion also controls the gravitational collapse process in the frontal part of the wedge.

4.4.2 Mechanics

The experimental results of the second series suggested that the formation of a complex basal shear zone, as it was produced in the experiments with a sandpaper interface, is a pre-condition for the tectonically-erosive mass-transfer mode. Following the method to investigate the mechanics on the basis of the critical-taper theory, as it was successfully applied to the accretive sand wedges (Section 2.4.3, 2.4.4, 3.4.2), the critically-tapered part of the sand wedge must be identified by the comparison of measured and calculated values of basal friction. The experimental results indicate that the convex part with the slight increase in the topographical gradient marks the trailing edge of the area, where dominant basal erosion took place. This wedge geometry reflects the balance of normal stress and shear stress in the transition zone from basal erosion to purely underthrusting. Two aspects of this topographic feature prohibit the comparison of measured and calculated basal friction, as performed in Section 2.4.3: On one hand, this part of wedge topography was consumed by frontal erosion during the experimental run and the convex shape was only maintained in the lower marker layers. On the other hand, it was not possible to measure a taper of a curved shape, and therefore there were not enough data to analyse further.

However, the curved geometry and the absence of basal erosion at the rear of the sand wedge indicates that the frictional strength ratio ($\chi = \mu_B/\mu_I$), which potentially caused basal erosion, changed from the wedge tip to the rear (Fig. 4.22, cf. Section 4.1.2.4). To investigate this, I firstly attempt to identify the certain states of the basal and internal friction (peak, stable static, or stable dynamic) which determine the strength ratio causing basal erosion. Then I discuss which parameter could cause transience of the strength ratio.

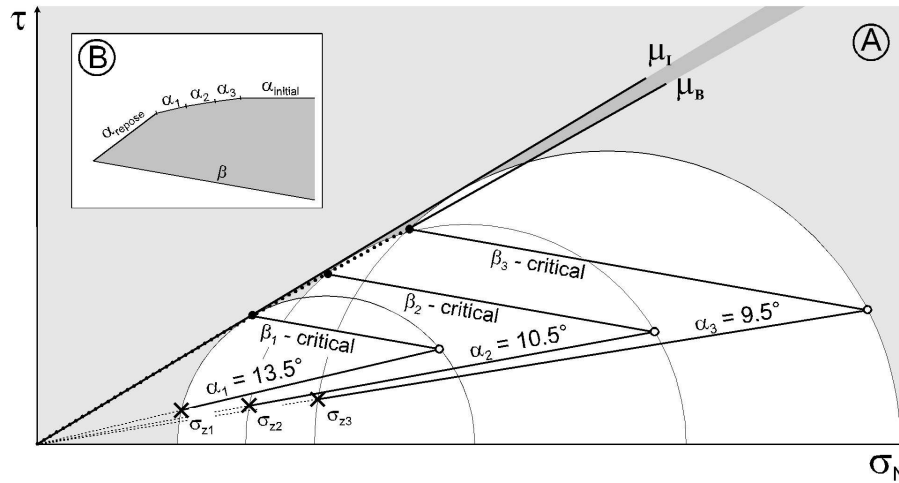


Figure 4.22: a) Schematic Mohr Diagram showing the influence of the transience of basal friction (dotted line) on the inclination of the surface slope (a). The critical state of stress is plotted for three points at the basal interface in different depth ($\sigma_{z1}, \sigma_{z2}, \sigma_{z3}$). (β - basal dip; τ - shear stress; σ_N - normal stress). b) The wedge geometry as constructed in the Mohr space.

Based on the observations of the kinematics of the basal shear zone, only one reasonable state of internal friction exists: The base-parallel, localised shear zones in the basal damage zone, along which the material of the wedge base was basally eroded and transported into the basal-flow zone, were reactivated thrusts (Fig. 4.9). Therefore, I suggest that the internal friction is in the stable static state.

The following are the best basal-friction candidates to cause the frictional strength ratio of basal erosion:

1. In Section 2.4.4, it was shown that the stable dynamic state of the sandpaper best describes the accretive mass-transfer mode. Therefore, the erosive mass-transfer mode might be ascribed to the dynamic-stable friction of the sandpaper.
2. I suggest that the actual basal detachment of the sand wedge is located along the boundary of the basal damage zone and the basal-flow zone (TBFZ in Fig. 4.9 and 4.20), since this boundary acted as continuously-active shear zone and divided the continuously-deforming material in the basal-flow zone from the occasionally-reactivated thrusts in the damage zone. Material of the damage zone, which migrated from the damage zone through this boundary and became part of the underthrust material, and thus it was basally eroded. The top of the sandpaper interface acted as the

basal detachment of the underthrust material (TSI in Fig. 4.9 and 4.20). The underthrust material itself was decoupled from the sandpaper interface by continuous deformation, thus the properties of the sandpaper interface did not directly influence the damage zone, where basal erosion of the sand wedge took place. Therefore, I propose that the stable dynamic friction of the sand material itself is the actual basal friction in tectonically erosive sand wedges.

The second suggestion is validated by the observation of similar bulk rates of the erosive mass-transfer processes in the sifted and poured sand wedge (SSC, PSC Fig. 4.17 b): This observation infers that the frictional strength ratio, which cause basal erosion, has also to be similar in both setups with different materials (sifted and poured), as it was seen in the accretive sand wedges that a different frictional strength ratio was able to cause different rates of mass-transfer processes (e.g. the frictional strength-ratio contrast of 0.05 between the SP and LG experiment led to significantly higher rates of underthrusting, see Section 2.4.4). This restrictive condition is not fulfilled by the combination of stable dynamic basal friction and stable static internal friction (1st suggestion, mentioned above). Here, the frictional strength ratio of sifted sand increases the frictional strength ratio of the poured sand by 0.05 (Tab. 4.2). Thus, this frictional strength ratio is contradictory to the obser-

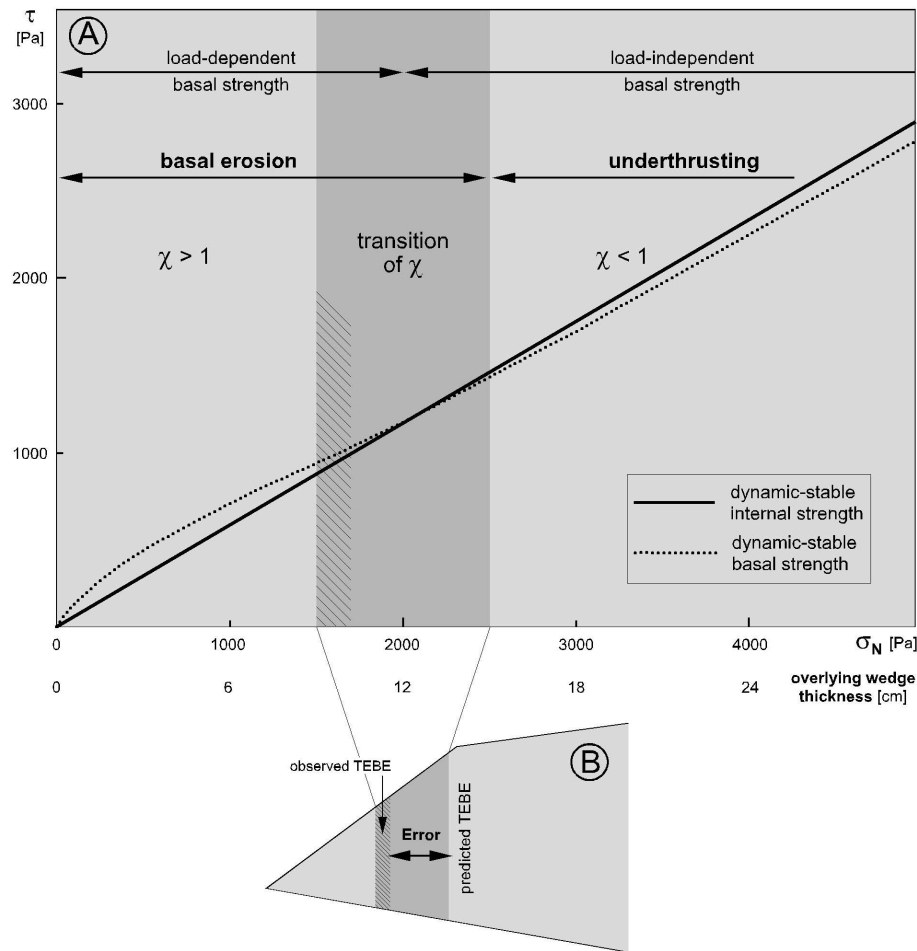


Figure 4.23: a) Strength ratios derived from the comparison of the failure curves of sifted sand during stable sliding and the basal sandpaper interface beneath. b) Estimation of the error caused by the determination method of the TEBE.

vation of similar basal-erosion rates in both experiments (SSC, PSC). However, the frictional strength ratio of dynamic-stable friction of the sand and the stable static friction of the sand fulfils the condition (2nd suggestion, mentioned-above, Tab. 4.2). In this case, the contrast of frictional strength ratios (0.02) of the different sands is negligible, as it was shown in Section 2.3 that the frictional strength within shear zones tend toward a similar value by ongoing shear deformation. Therefore, I favour the hypothesis that the stable dynamic friction of the sand controls the bulk rates of basal erosion.

The difference in the bulk rates of basal accretion in the SSC and PSC experiment is not in conflict with this suggestion. The direct relation between the increased rates of basal accretion and wedge internal deformation (backthrusting, Fig. 4.12 b and c) in the SSC experiment infers that basal accretion

is dependent on the states of wedge-internal frictions. Therefore, it is suggested that the difference in the bulk rates of basal accretion is caused by the 10% difference between the peak internal friction of sifted and poured sand (Tab. 4.2).

However, this interpretation does not explain the restricted occurrence of basal erosion to only the very frontal part of the wedge and is not consistent with the strength ratio predicted by the critical taper theory ($\chi \geq 1$; see Section 4.1.2.4), as the basal and internal friction of this interpretation results in a constant $\chi < 1$ for both experiments ($\chi_{SSC} = 0.95$; $\chi_{PSC} = 0.93$). Moreover, if this interpretation is correct, basal erosion should also occur in the SLC experiment, as a similar frictional strength ratio also existed here at the top of its very thin basal shear zone ($\chi_{SLC} = 0.95$).

To solve these inconsistencies, I examined in

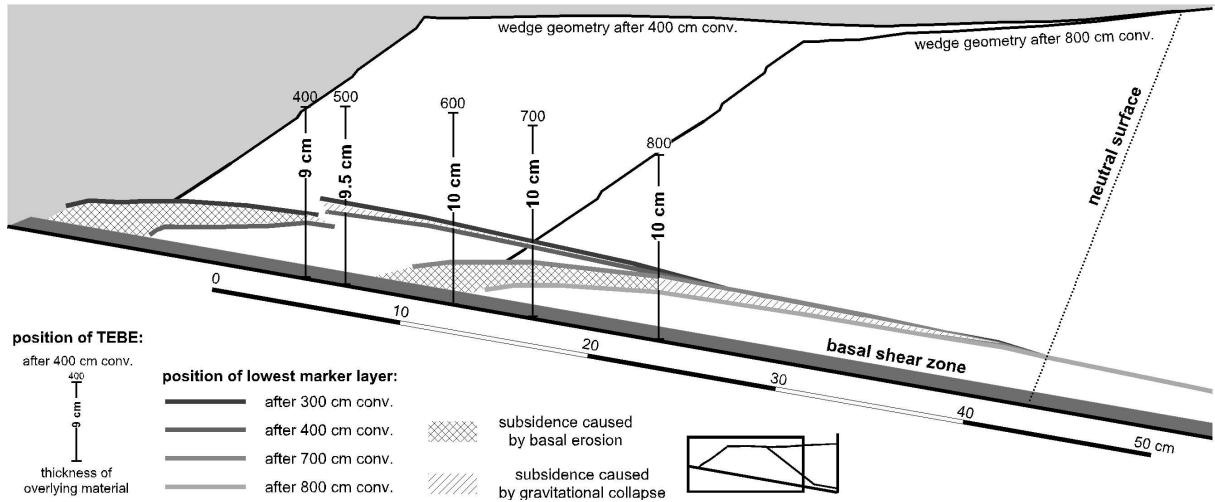


Figure 4.24: Position of the TEBE in several steps of convergence, as determined from the subsidence of the marker layers in the SSO experiment.

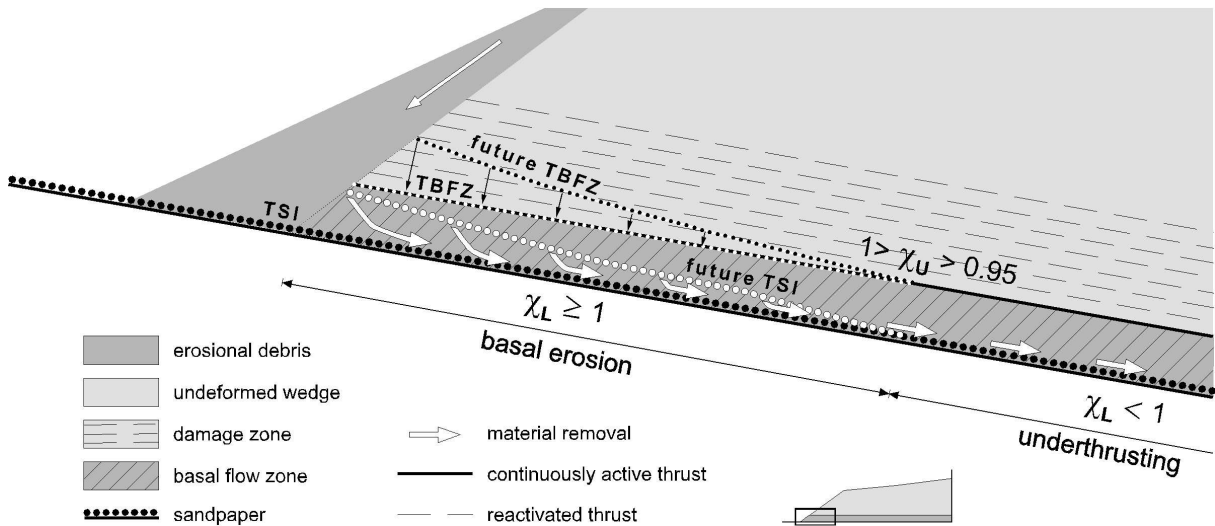


Figure 4.25: Sketch of the process of basal erosion and related mechanical conditions (χ_L – lower strength ratio between the sandpaper interface and basal flow zone; χ_U – upper strength ratio between the basal flow zone and damage zone; TSI – top of sandpaper interface, TBFZ – top of basal-flow zone).

detail the strength ratio between the sandpaper and the continuously-deforming material within the basal-flow zone by the use of stable dynamic states of both the basal and internal strength: The stable dynamic strength of sandpaper is load-dependent for small normal loads (see Section 2.3). For very small normal loads the basal strength exceeds the internal strength (0–2000 Pa, Fig. 4.23 a). With a normal load of 1000 Pa the basal strength begins to decrease until it matches the internal strength at ca. 2000 Pa and the load-independent state of basal friction is reached. This shows that the predicted strength ratio ($\chi \geq 1$) is attained at normal loads of ca. 0–2000 Pa. Accordingly, at the position where this normal load is reached in the sand wedge (i.e. at a wedge thickness of 12 cm sifted sand), the trailing edge of basal erosion (TEBE) is predicted by this scenario. In both experiments (SSC, PSC) the area of dominant basal erosion was overlain by a constant thickness of sand during the whole experimental run (Fig. 4.24). This infers that the TEBE is load-dependent and shows a correlation with the load-dependent maximum strength ratio. Therefore, I conclude that basal erosion only occurs in an area, where the maximum strength ratio at $\chi \geq 1$ is reached.

Nevertheless, the observed thickness of the overlying sand wedge (max. 10 cm, Fig. 4.24) does not match the predicted thickness (12 cm). I suggest, that this inconsistency is due to the amount of error in detecting the TEBE by the change in the inclination of the lowest marker layer (see Section 4.3.1). In this method, I assumed that basal erosion occurs abruptly along the wedge base and is restricted to that part of the wedge, in which subsidence increased. However, Fig. 4.23 shows that the transition from $\chi > 1$ to $\chi < 1$ ranges from 1500–2500 Pa normal load. This infers that basal erosion is not an abrupt, but gradual process. Hence, it is concluded that the method, which was used to detect the TEBE in the experiments is unprecise and results in a slight underestimation of the basal erosion rate and an error in the position of the TEBE (error in horizontal distance ca. 5.5 cm toward the wedge-tip, Fig. 4.23 b). However, a more precise method, which is based on geometrical indicators does not exist, as the geometrical signal caused by basal erosion in the transitional zone is overprinted by that of the subsidence caused by gravitational collapse.

In conclusion, the observation of a stagnant mass-transfer mode in the SLC experiment inferred that the basal properties have a paramount influence on

the basal mass-transfer process, although the rates of basal erosion in the SSC and PSC experiment indicate independence of the material properties of the basal interface. Therefore, I suggest the following process of basal erosion (Fig. 4.25): The load-dependent lower strength ratio of the basal-flow zone (i.e. $\chi_L = \mu_{DB}/\mu_{DI}$) enables basal erosion in the frontal part of the sand wedge. In this part, material of the basal-flow zone is basally eroded, so that the thickness of the basal-flow zone is reduced. However, the load-dependent thickness of the basal-flow zone has to remain constant, as the inclination of the surface slope (angle of repose) and the basal dip remained constant, too. Thus, a reduction of the thickness causes the incorporation of material derived from the damage zone into the basal-flow zone (Fig. 25). Consequently, material transfer from the damage zone into the basal-flow zone is triggered by the strength ratio of stable dynamic friction of the sandpaper and the sand itself (χ_L); but this material transfer is also controlled by the upper strength ratio of the states of internal friction (i.e. $\chi_U = \mu_{DI}/\mu_{SI}$), as these states of friction act at that position, where this material transfer takes place: at the top of the basal-flow zone.

If the range of the upper strength ratio is about 0.93–0.95, basal erosion was observed. The estimated maximum range of the upper strength ratio is about $0.84 < \chi_U < 1$, because:

- during underthrusting of duplexes in the ASO experiment wedge material did not pass through the roof thrust, which was active along the glass-bead layer and hence had an upper strength ratio of 0.84.
- the upper strength ratio would not exceed 1, as the basal detachment and the basal flow zone would then step up to a higher level.

4.4.3 Summary of the basally erosive process

Basal erosion plays a major role in steady-state, tectonically erosive sand wedges. It controls the rate of frontal erosion and gravitational collapse in the upper part of the wedge. The basal erosion rate is controlled by the global capacity and the upper strength ratio ($0.84 < \chi_U > 1$) between the basal flow zone and the damage zone. Thus, this second strength ratio influence the basally erosive process, in addition to the lower strength ratio (χ_L). The lower strength ratio was shown to be $\chi_L \geq 1$ (Section 4.4.2), as predicted by the critical-taper theory

(Dahlen, 1984) and the subduction-channel concept (Cloos and Shreve, 1988b).

The detection of the area of basal erosion from the subsidence in the overlying segment is imprecise, as extensional subsidence caused by gravitational collapse is superimposed upon the signal of subsidence caused by basal erosion. As the subsidence caused by gravitational collapse increase towards the upper parts of the wedge, detection of the area of basal erosion is most precisely carried out from marker layers in the lower wedge part. In addition, an exact determination of the TEBE is not possible, as basal erosion gradually decreases in down-dip and thus lacks a prominent signal.

4.5 Comparison with the North Chilean Forearc

The analogue simulations of steady-state tectonic erosion showed a good first-order agreement with the North Chilean Forearc: The mass-transfer processes interpreted from field evidence (i.e. frontal and basal erosion, see Section 4.1), were simulated in the sandbox experiments using a self-controlled system, which resulted in the retreat of the wedge tip and represents trench retreat in nature. In particular, the experiments in an open setup (SSO, ASO) showed features comparable with the North Chilean Forearc, as the strong wedge-tip retreat of these experiments was accomplished by nearly no basal accretion.

A subduction channel overlain by a damage zone, as inferred from the seismological image of the subduction interface of the Nazca Plate (Shapiro et al., 2001), was also formed as basal-flow zone overlain by the damage zone in the experiments with isotropic sand wedges on top of a sandpaper interface (SSC, PSC, SSO).

The occurrence of extension and strong subsidence in the frontal part of the sand wedge, as well as the migration of extensional deformation up to the rear of the neutral surface are the main consistencies of near-surface kinematics between experiment and nature. Moreover, the pattern of natural subsidence is suggested to be controlled by the interaction of basal erosion and crustal extension (von Huene and Lallemand, 1990). This comparison infers that geometrical, kinematic and subsidence domains independently migrate in nature, as it was also shown for the experiments. Therefore the spatial extension of the basal mass-transfer processes (basal erosion, underthrusting) at the North

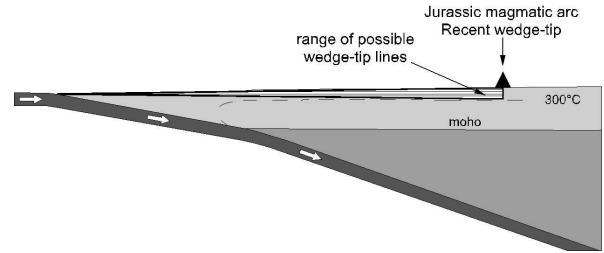


Figure 4.26: Estimated range of wedge-tip lines of the North Chilean Forearc.

Chilean Forearc cannot be concluded from the near-surface kinematics. In contrast to the experiments, the isostatic rebound additionally influences the pattern of vertical motion in natural forearc wedges (Lallemand et al., 1992b; Pelz, 2000). In consequence, the difficulty to determine the TEBE by the subsidence record is even more complicate in nature than it was already in the experiments (cf. Section 4.3.1, 4.4.2, 4.4.3).

The estimated rates of steady-state tectonic erosion for the Japan-, Peru- and Chile-Trench are in the same range of the upscaled total erosion rates (frontal erosion and basal erosion) of the experiments with the isotropic sand wedges (experiment: $68\text{--}81\text{ km}^3\text{ km}^{-1}\text{ km}^{-1}$, nature: $35\text{--}80\text{ km}^3\text{ km}^{-1}\text{ km}^{-1}$; e.g. von Huene and Lallemand, 1990; Lallemand et al., 1992b; Scheuber et al., 1994; Pelz, 2000). This suggests that the isotropic sand wedges simulate best steady-state tectonic erosion. However, the comparison of published erosion ratios for nature [basal erosion (BE)/frontal erosion (FE)] and the observed erosion rates in the experiments did not correlate, so that this suggestion is not validated (experiment: $\text{BE} < \text{FE}$, nature: $\text{BE} > \text{FE}$). The natural erosion rates were all derived by assuming an unknown process for tectonic erosion. Therefore, I decided to compare the wedge-tip lines in nature and experiment. The wedge-tip line approximately depicts the erosion ratio, and can be roughly estimated for nature even if a known process of tectonic erosion cannot be ascertained (Fig. 4.26): When tectonic erosion was initiated during the Jurassic, the wedge tip was located at the very upper part of the continental crust, or at a possibly then existing accretionary wedge. Initially, some fluctuations have to be assumed for the adjustment phase. However, these fluctuations were most probably restricted to the upper crust. Today, the whole near-surface part of the on- and offshore forearc consists of the volcanic and magmatic rocks of the Jurassic arc. This infers that the

wedge-tip line only migrated within the upper crust and never descended to the lower crust (Fig. 4.26). Such a wedge-tip line was only produced during the first steady-state phase of the ASO experiment, during basal erosion of duplexes (Fig. 4.16). In contrast, all isotropic sand wedges showed an descending wedge-tip line. Therefore, I chose the first steady-state phase of the ASO experiment for further comparison with the North Chilean Forearc. Also the presence of the weak layers (glass-bead layers) in the ASO experiment supported this decision, as it has to be expected that the natural forearc also includes heterogeneities (e.g. overpressured layers, material alternations etc.).

Other differences between experiment and nature were seen by correlation of wedge geometry. In part, these are only apparent inconsistencies: The occurrence of more gently-inclined surface slopes in nature are due to the wet and probably overpressured conditions in nature. E.g., the angle of repose in the dry experiments ($\alpha = 37^\circ$) is reduced for fractured continental crust ($\Phi = 37^\circ$) under submarine conditions to the maximum effective surface slope of $\alpha_{\text{eff.max}} \approx 25^\circ$ at nearly hydrostatic pressure ($\lambda = 0.6$) and $\alpha_{\text{eff.max}} \approx 10^\circ$, if the pore pressure is moderately increased ($\lambda = 0.85$).

The North Chilean Forearc is characterised by an explicit trisection in the inclination of the straight surface slope, whereas the tectonically erosive sand wedges formed either a bipartite topography with straight slopes or a tripartite with a convex-shaped middle part. Because of this inconsistency, a direct correlation between experimental and natural wedge geometry and the identification of the steep frontal slope (the typical feature for frontal erosion in the experiments) in the North Chilean Forearc is not possible. Although, the position of the steep frontal slope can not be precisely determined (for further interpretation see Section 4.7), the best candidates are the both slopes with the steepest inclinations, i.e. the lower and middle slope (9° and 6° , respectively). Comparison of this approximated location of the steep frontal slope in nature with that in the experiments shows another difference: In the experiments, the steep frontal slope truncated the sand wedge up to a thickness of 20 cm (20 km in nature; Fig. 4.13) after 700 cm conv. (700 km conv. or ca. 8 Ma in nature). This is the initial thickness of the sand wedge and indicates that at this position material from the wedge base was not removed. The related thickness of the North Chilean Forearc crust does not exceed 13 km at the landward border

of the middle slope. This is well below the original thickness of the Jurassic crust (ca. 30–35 km; Haschke et al., 2002) and suggests that basal erosion takes place at a more landward position than observed in the experiment.

A direct comparison of the kinematic domains between the experiment and the North Chilean Forearc is not possible and will be covered in Section 4.7, as the succession of the kinematic domains show one main difference: In the North Chilean Forearc, the kinematic domains of the lower and middle slope are linked by the topographically-defined areas, whereas this linkage does not exist in the experiment. Nevertheless, I suggest that the experimental observation that near-surface kinematics do not reflect the subsidence caused by basal erosion, might be appropriate for the North Chilean Forearc: The listric normal faults of the upper and middle slope merge into low angle detachments (cf. Fig. 4.2. b; von Huene and Ranero, 2002) and are thus not able to accommodate the subsidence caused by basal erosion.

Possible explanations for the above-mentioned differences between nature and experiment are given in Section 4.7. I previously will discuss the published concepts of steady-state tectonic erosion at the North Chilean Forearc in Section 4.6. There, I will point out the main assumptions of the concepts were incorrect because the mechanics of basal erosion and relations of the mass-transfer processes were not known.

4.6 Discussion of published concepts

The sandbox experiments validate the conclusion that basal erosion occurs only if a strength ratio larger than 1 is present, as predicted by the subduction-channel concept and the critical-taper theory (Dahlen, 1984; Cloos and Shreve, 1988b). Also, the suggestion of a transient strength ratio by Lallemand et al. (1994b) and Adam and Reuther (2000) is confirmed by this study.

Von Huene et al. (1999) and Adam and Reuther (2000) assumed that the topographically- and kinematically-defined parts of forearc wedges are directly caused by basal mass-transfer processes. On this basis, the TEBE of the North Chilean Forearc was determined to be located beneath the landward border of the middle slope (Adam and Reuther, 2000). However, the analogue simulations show that this assumption is not fulfilled by steady-state, tectonically erosive sand wedges: The topographically- and kinematically-defined parts of

the sand wedges do not correlate with areas of the basal mass-transfer processes, since the wedge is additionally overprinted by internal deformation (gravitational collapse). Thus, the strategy to detect the TEBE by a direct correlation of near-surface kinematics and geometry would fail in a steady-state, tectonically erosive sand wedge. The comparison with nature in Section 4.5 suggests that this is also valid for the North Chilean Forearc.

In contrast to the previously-mentioned authors, Pelz (2000) noticed that the vertical motion of the forearc wedge, caused by the basal mass-transfer modes was overprinted by other processes. Therefore he used the record of subsidence to determine the TEBE, while considering the effect caused by isostatic rebound. Nevertheless, he used the boundary between the uplifting and subsiding part of the forearc (i.e. the neutral surface in the experiments) to estimate the position of the TEBE. However, the analogue simulations showed that also the neutral surface does not coincide with the TEBE (cf. Fig. 4.8), as the uplift and subsidence of the sand wedge is not only caused by the basal mass-transfer processes but also by the gravitational collapse process. The fact that the kinematic and subsidence domains of the upper slope and onshore forearc do not coincide (cf. Section 4.5. and 4.7), infers that such an additional process also influences the North Chilean Forearc.

The method used by Pelz (2000) to estimate the mass of tectonically-eroded material (cf. Section 4.1.2.5) would fail in steady-state, tectonically erosive sand wedges, as the slip lines in the upper part of sand wedges were not directly related with the vertical motion caused by the basal mass-transfer processes. As shown in Section 4.5., such independent near-surface kinematics are also suggested for the North Chilean Forearc.

Additionally, the analogue simulations indicate that basal erosion does not abruptly cease and thus does not lead to a prominent topographical signal. Moreover, the ASO experiment suggested that the topographical signal used by Pelz (2000, Coastal Escarpment) could be interpreted as a type 2 normal fault (see Section 4.3.1 and 4.7). In the analogue simulations, these normal faults did not mark the TEBE, as they are a consequence of the wedge-internal extension by gravitational collapse.

Therefore the assumptions used for all previous methods to detect the TEBE could not be validated by the results of steady-state, tectonically erosive sand wedges. To solve this problem, a more probable process of basal erosion in forearc wedges has to

be found, than those assumed in the published concepts. Understanding the inconsistencies between experiment and nature, as mentioned in Section 4.5., might give a better idea of the basally erosive process in nature.

4.7 Discussion of inconsistencies

4.7.1 *Geometric and kinematic inconsistencies?*

To explain the inconsistencies between experiment and nature, the topographically and kinematically defined parts of the steady-state, tectonically erosive sand wedges also have to be identified at the North Chilean Forearc.

Firstly, the most prominent and persistent topographical feature of the sand wedges has to be recognised at the offshore forearc: This is the steep frontal slope at the angle of repose, which is shaped by frontal erosion. As shown in Section 4.5, the angle of repose in the sandbox experiments should correspond to the maximum effective slope of basement rocks, of which the forearc consists. However, the maximum effective slope of rocks mainly depend on the (unknown) pore pressure, so that measuring the inclination of the surface slope does not necessarily identify the steep frontal wedge part. Nevertheless, the steepness of the middle and lower slope and the occurrence of erosional debris suggest that both parts attained the maximum effective slope. The occurrence of two different inclinations (cf. Fig. 4.2) of the maximum effective slope can be explained by the unique material of each of these parts: The middle slope consists of fractured magmatic and volcanic rocks, whereas the erosional debris derived from the continental slope forms the lower slope. Because of possible different pore pressure ratios, the maximum effective slope might vary. Therefore, I suggest that the steep frontal slope of the tectonically erosive sand wedges is an analogue of the lower and middle slope at the North Chilean Forearc.

Based on this, it is possible to compare the near-surface kinematics of the experiments with those of the North Chilean Forearc. The sandbox simulations showed that frontal erosion and the related gravitational collapse mainly cause the near-surface kinematics. If the sandbox simulations actually reflect the process of frontal erosion in nature, the offshore kinematics would be best explained by the kinematics of the type 2 normal-faults observed in the ASO experiment, as these normal faults were

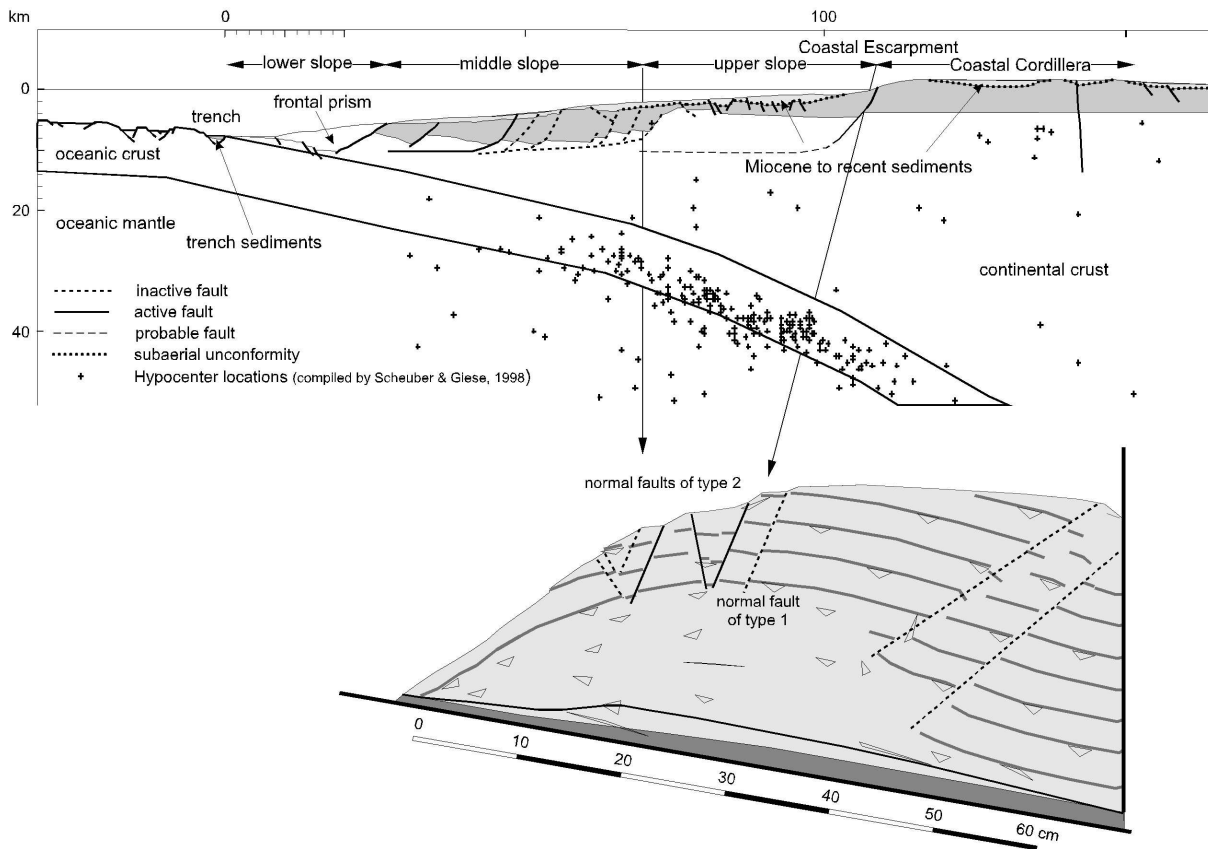


Figure 4.27: Comparison of kinematics and geometry between the a) North Chilean Forearc, modified after Pelz (2000) and von Huene and Ranero (2002) and b) the late steady-state phase of the ASO experiment. The type 2 normal faults in the experiment agree with the kinematics of the offshore forearc. Inactive type 1 normal faults and backthrusts in the experiment were caused by basal accretion in the beginning of the experiment and should not be considered in this comparison.

only caused by the gravitational collapse process (Fig. 4.27; see also Section 4.3.1). During initiation in a relative rearward position, these normal faults showed major displacements forming steep fault scarps. This topographical feature is interpreted as an analogue of the Coastal Escarpment. In the central part of the sand wedge, which is characterised by a shallowly-inclined surface slope, the normal faults are still actively adjusting the surface slope to the angle of repose. The kinematics and the geometry of this part of the sand wedge are in good agreement with the upper slope of the North Chilean Forearc. All the normal faults in the sand wedge, which reached the steep frontal slope, became inactive, as the angle of repose is attained here. This observation matches the middle slope of the North Chilean Forearc, which shows inactive normal faults. A reactivation of the normal faults was observed in the experiment when frontal ero-

sion triggered the final slumping of erosional debris. This slumping process is also well-documented from the North Chilean Forearc (von Huene et al., 1999; von Huene and Ranero, 2002). I conclude that the near-surface kinematics of the offshore forearc are fully explained by the frontal erosion process.

The results of the analogue simulations showed that all features previously used to detect the TEBE do not identify the process of basal erosion (cf. Section 4.6). Nevertheless, the following features still indicate basal erosion and its spatial extension at the North Chilean Forearc:

- From the Coastal Escarpment down to the trenchward limit of the middle slope, the thickness of the continental crust is reduced by about 30%. If this area was not affected by basal erosion, the crustal thinning could have only been caused by crustal extension. To achieve this, horizontal extension of about

230% is required. However, the reflection seismic investigations of CINCA 95 do not substantiate such a large horizontal extension (cf. Fig. 4.2) in the offshore forearc. Therefore, basal erosion is the probable process, which is able to reduce the thickness of the continental crust.

- The crust of the migrated Jurassic Arc (ca. 25 km) is thinner than during the Jurassic (ca. 30–35 km; Haschke et al., 2002). As subaerial volcanites are still preserved in the Coastal Cordillera, the crust must have been thinned by processes acting at base of the onshore forearc.
- The subaerial sedimentation in the Longitudinal Valley since the Miocene is an evidence that this part of the onshore forearc was not affected by major vertical motions (max. 200 m since Miocene). This implies that the onshore forearc beneath the Longitudinal Valley has been neither affected by basal erosion nor accretion.

Therefore I conclude that a deep-seated TEBE is located in the area between the Coastal Cordillera and the Longitudinal Valley. A TEBE located as deep as this would mean that the whole offshore forearc subsides due to basal erosion and vertical adjustment because of basal mass-removal does not have to be accommodated in this area along localised faults. This argument supports the aforementioned kinematic interpretation.

However, the deep-seated TEBE leads to another major inconsistency between experiment and nature: In the sand wedges the maximum area of basal erosion is restricted to the area 20 cm from the front (upscaled natural length: 20 km), whereas the North Chilean Forearc undergoes basal erosion along more than 100 km (see for further discussion Section 4.7.3).

4.7.2 Inconsistencies of the erosion ratios (basal erosion versus frontal erosion)

As mentioned in Section 4.5, the measured erosion ratios of all steady-state, tectonically erosive sand wedges ($BE > FE$) are diametrically opposed to the calculated erosion ratios of nature ($BE < FE$). In Section 4.4.1 it is shown that the mass-transfer processes mainly depend on the relationship between inlet and global capacity. The whole range of possible IC/GC ratios was tested with the first series

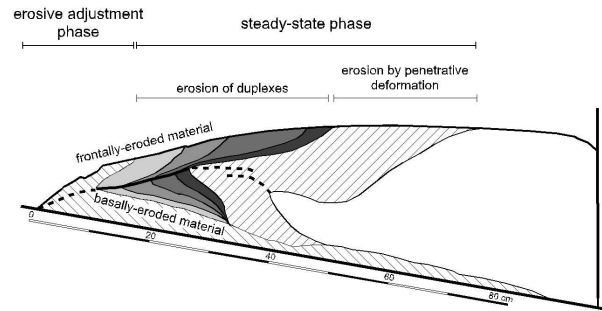


Figure 4.28: Wedge-tip line of the ASO experiment with indicated increments (each increment – 50 cm conv.) of frontal and basal erosion in the phase of duplex erosion. Here the erosion ratio is 1:2 in all increments.

of tectonically-erosive sand wedges. End members and some in-between relationships were realised in the experimental setups (e.g. $SSC - IC \geq GC$; $SSO - IC = GC$; 2nd steady-state phase of $ASO - IC \ll GC$). As all experiments produced an erosion ratio of $BE < FE$, the experimental erosion ratios are in conflict with those calculated for nature.

Several authors (von Huene and Culotta, 1989; von Huene and Lallemand, 1990; Lallemand et al., 1992b; Pelz, 2000) assumed that the volume of eroded material can be calculated from the given thickness of the basally-eroded material (thickness of the subduction channel) and the convergence velocity of the oceanic plate, since the length of the eroded material is given by the convergence velocity over a certain time interval. The application of this method would not work for the experiments, as the basally-eroded material was transported with a significantly slower bulk velocity within the basal-flow zone than that of the conveyor belt (Fig. 4.20; cf. Section 4.3.2). Moreover, the material in the basal-flow zone consisted mainly of frontally-eroded material (cf. Section 4.3.1). Hence, the thickness of the basal-flow zone did not reflect the amount of basally-eroded material. In nature, the geometry of the subduction channel, the transported material within, and its velocity are unknown. Therefore the calculation of basally-eroded mass is an unsolved problem for nature and the quantification of erosion ratios in nature remains uncertain.

Moreover, the wedge-tip lines, which are similar in experiment and nature (Fig. 4.28 and Fig. 4.26), do not reflect the bulk erosion ratio. In the experiment, the wedge-tip line, which remains in the upper part of the wedge, was caused by an increase of basally-eroded mass toward the wedge tip and a decrease of frontally-eroded mass in this direc-

tion (Fig. 4.28). In the experiment, the amount of basally-eroded material never exceeded that of frontally-eroded material. However, based on the arguments of major crustal thinning of the North Chilean Forearc (cf. Section 4.5.) an erosion ratio of $BE > FE$ is expected in nature.

The inconsistency of erosion ratios between experiment and nature might be due to unrealistic IC/GC ratios in the experiments: The experiments show that the variation of the global capacity results in a proportional change of both the frontal and basal-erosion rate (Section 4.4.1). Thus, the inconsistency of the erosion ratio between nature and experiment cannot be explained by different global capacities. However, the experiments did not represent a realistic inlet capacity, as they did not simulate the effects of topographic lows in the oceanic crust. In the moment, when a topographic low is subducted in nature, the inlet capacity is enlarged and the frontal-erosion rate is not only dependent on the thickness of the subduction channel and the basal-erosion rate, as shown for the experiments (Section 4.4.1). However, simulating this effect in analogue experiments would increase the frontal-erosion ratio and also the discrepancy between the erosion ratios of experiment and nature. Consequently, the basal-erosion rate in nature is significantly larger than simulated in the experiments. However, this large basal-erosion rate cannot be due to the basally-erosive process that is restricted to the frontal wedge part as simulated in the experiments, since this would also cause an increase in the inlet capacity and the frontal-erosion rate (cf. Section 4.4.1). Therefore, basal erosion in nature is more efficient in arcward direction, than simulated in the experiments. This conclusion suggests mechanical inconsistencies exist between the basally-erosive process in the experiments and nature, which are covered in the next section.

4.7.3 Mechanical inconsistencies

It was shown that the wedge-internal kinematics of steady-state, tectonically erosive sand wedges basically correlate with those of the North Chilean Forearc from 22 to 24° S (see Section 4.7.1). The last point of discussion is, whether the mechanics of basal erosion, as interpreted in the analogue simulations, are also comparable with those in nature. In Section 4.4.2 it is shown that basal erosion in the experiments was only possible, if the combination of two specific strength ratios ($\chi = \mu_B/\mu_I$; cf. Fig. 4.25) was as follows:

1. The lower strength ratio ($\chi_L \geq 1$) between the basal interface and the basal-flow zone, which changed in the down-dip direction due to the influence of the roughness on the strength of the sandpaper interface, and
2. the upper strength ratio ($\chi_U \approx 0.94$) between the basal-flow zone and damage zone, which was constant in the experiment.

The lower strength ratio ensured down-dip transport of eroded material within the basal flow zone and was required to sustain the capacity of the basal flow zone. The upper strength ratio controlled the mass removal from the wedge base into the basal flow zone. These two processes (mass removal and transport) are also required for basal erosion in nature and therefore I suggest that the combination of these particular strength ratios also controls the basal mass-transfer processes in non-accretive forearc settings.

In contrast previous attempts to understand the mechanics of basal erosion in nature have made use of only one strength ratio. The critical-taper theory, as applied to the North Chilean Forearc (Adam and Reuther, 2000), focused on the strength ratio between the subduction interface and the damage zone, and did not consider the strength of the basal-flow zone, which is located between these two zones (Section 4.1.2.4). The subduction-channel concept (Cloos and Shreve, 1988a) selected the strength ratio between the basal-flow zone and the damage zone as crucial for basal erosion (Section 4.1.2.3). Therefore I question, whether the processes, which were suggested to cause basal erosion in these concepts [influence of the roughness of the oceanic crust (Adam and Reuther, 2000) and weakening of the wedge material by hydro-fracturing (Cloos and Shreve, 1988b)] are actually the processes that control the required combined strength ratio.

The sandbox experiments simulated the influence of the roughness on the strength of the basal interface. This resulted in a more trenchward position of the TEBE (upscaled distance trench-TEBE: 20 km; cf. Section 4.7.1) than that estimated for the North Chilean Forearc (trench-TEBE > 100 km; cf. Section 4.7.1). Therefore, I conclude that the influence of the roughness on the strength of the subduction interface is not the dominant factor controlling basal erosion in nature.

Weakening of the wedge material in the damage zone would lead to a decrease of the upper strength ratio. Under these conditions, wedge material would not be removed from the wedge base

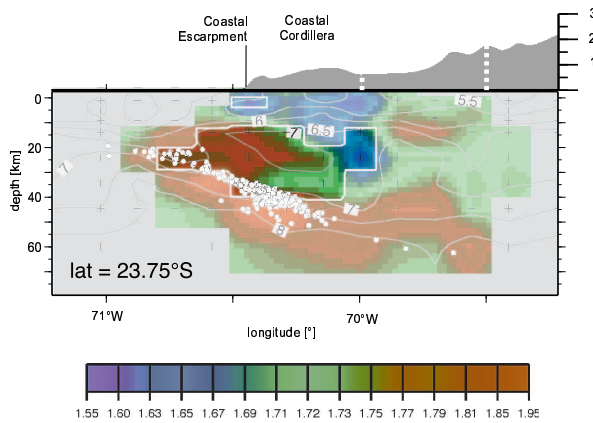


Figure 4.29: Distribution of the V_p/V_s ratio along the dip of the Nazca plate as obtained from the aftershock series of the Antofagasta earthquake (1995; (Husen, 2000)). Areas of good resolution are shown in opaque colours, areas of faint resolution in faded colours (open circles – hypocentre locations of the aftershock series).

into the subduction channel and only frontal erosion would take place.

However, hydro-fracturing and a (partial) weakening of the wedge base by a change in the pore pressure is a process expected at the base of forearc wedges (Cloos and Shreve, 1988b; von Huene and Lallemand, 1990; Lallemand et al., 1994b). Therefore, comparison of the mechanics between dry sandbox simulations and nature has to consider the different mechanical conditions controlling basal erosion in the experiments and at the North Chilean Forearc: The transient strength of the basal interface is only associated with changes of the lower strength ratio in the experiments. In contrast, variations in both the upper and lower strength ratio are able to inhibit basal erosion in nature. In the large area, where basal erosion occurs at the North Chilean Forearc, several parameters are able to change the strength of the subduction channel in down-dip direction [e.g. temperatures up to 300°C (Springer, 1999), dewatering of the frontally-eroded material]. Therefore, I consider that basal erosion is a very sensitive process in nature, since minor changes in the strength of the basal interface, the material in the basal-flow zone, or in the damage zone can be expected to prevent basal erosion. This is in apparent conflict with the geological record of steady-state basal erosion, which suggested that this process is stable over geological time spans and a frequent mass-transfer process along several convergent forearcs (e.g. Peru, Costa Rica, Japan).

To explain this in agreement with the suggested instability of the process, frequent repetition of basal erosion events is required at time intervals, which are shorter than the time resolution of the geological record (i.e. < 1 Ma), is required.

In this regard, fault-valve activity is such a process, which may occur within the seismogenic zone at the plate interface of convergent forearc settings (Sibson, 1990). Here, faults act as impermeable seals during the interseismic period. Fault-valve action is initiated when shear stress or pore pressure within over-pressured zones increases and rupture occurs. The resulting upward discharge of fluids along the fault from the overpressured zone continues until the entire hydraulic gradient reverts to hydrostatic or the fault reseals. This fault-valve behaviour is linked to the earthquake cycle and causes abrupt changes in pore pressure and crustal strength, as pore pressure is one of the main parameters influencing the strength of rocks in the brittle field.

At the North Chilean Forearc, such changes in pore pressure were inferred from earthquake tomography of the North Chilean Forearc, based on the aftershock series of the Antofagasta earthquake (30.07.1995; Husen, 2000). Here, an increased V_p/V_s ratio was found above the seismogenic zone. This V_p/V_s anomaly extends from the Coastal Cordillera to the middle slope (Fig. 4.29). Husen et al. (2000) interpreted the high V_p/V_s ratio to be caused by postseismic discharge of fluids from the oceanic crust, which are able to migrate through the subduction channel into the wedge. This postseismic fluid discharge might cause short-term changes of the strength ratios along the subduction channel, associated with the main shocks of subduction earthquakes. Thus, the combination of the specific strength ratios required for basal erosion is probably present at different locations along the subduction channel for short terms. I consider that the forearc wedge is basally eroded only during these intervals. However, the repeated occurrence of subduction earthquakes enables frequent, short-termed basal-erosion events. In summary, I suggest steady-state basal erosion is probably rather the repetition of a short-term, instable process than a permanent, stable process.

4.8 Conclusions

The comparison of the database obtained from the North Chilean Forearc with the results of the analogue simulation yields new insight in understanding the kinematics, mass-transfer modes, and mechanics of this steady-state, tectonically erosive forearc wedge.

Based on the good agreement of the kinematics between experiment and nature, extension of the offshore forearc is interpreted as caused by gravitational collapse. Thus, the localised extensional shear-zones are only controlled by frontal erosion.

As trench retreat rates in the North Chilean Forearc are in the same order as the upscaled wedge-tip retreat in the experiments performed with an open setup, the analogue simulations are in agreement with the suggestion that nearly no material is basally accreted beneath the forearc.

However, the erosion rates and the mechanics of the experiments are not directly comparable with those of the North Chilean Forearc, as the experimental setup to simulate steady-state tectonic erosion in general was idealised with respect to geometry and mechanics. Therefore, the experiments did not properly represent nature in:

- frontal erosion, as the topographic highs and lows of the oceanic crust were not considered in the experimental setup, and
- basal erosion, as the stable strength of the analogue material used was not transient.

Despite these restrictions, the interpretation of the inconsistencies between experiment and nature shows that idealised experiments are a powerful tool to yield constraints on the mechanics of steady-state, tectonically erosive forearcs.

In the sandbox simulations, basal erosion was controlled by two strength ratios. Consequently, the strength of the subduction interface, the material in the subduction channel and in the damage zone control basal erosion in nature. Changes in pore pressure due to postseismic fluid discharge are a plausible reason, to explain the presence of the specific mechanical conditions required for basal erosion. Therefore, I consider that the North Chilean Forearc is repeatedly affected by basal erosion during postseismic phases of subduction earthquakes.

Chapter 5

Final Discussion

5.1 Hierarchical order of parameters controlling the mass transfer at convergent forearcs

The classification of convergent forearcs into accretive and non-accretive forearc settings (i.e. with and without a frontally-accretionary wedge, respectively; in the terms of von Huene and Scholl, 1991; Section 1.2) is based on geophysical and geological observations. However the parameters, that control these mass-transfer modes and their specific mass-transfer processes (frontal accretion, basal accretion, underthrusting, frontal erosion, basal erosion) have not been identified in nature (cf. Section 1.1). Based on the series of analogue experiments from this study (cf. Chapter 2, 3, 4) and those presented by Gutscher (1996), it is possible to identify parameters, which potentially control the mass-transfer modes of convergent sand wedges. These results are used in this section to identify the ‘real’ controlling parameters and to evaluate their hierarchical order (see below). However, such a mechanical systematics derived from dry sandbox simulations only has the potential to be applied to nature, if the restrictions of the simulation method (Section 1.5; 2.4.1; 4.8) are considered. Consequently, the potentially controlling parameters of convergent forearc settings used in the following discussion, are parameters that are independent of specific material behaviour and specific geometrical conditions, i.e. :

- *Strength ratios*: In this study, great attention was paid to the influence of the internal and basal frictional strength on the mechanics of convergent sand wedges. In particular, the very high basal frictional strength due to the rough interfaces was investigated in accretive and tectonically-erosive experiments. However, the correlation with the North Chilean Forearc revealed that the strength of sand and the rough

sandpaper interface used in the sandbox simulations oversimplify natural conditions (cf. Section 4.7.3). Strength ratios, which are an expression of the relative relationships between the basal and internal strength, are independent of specific material behaviour. Therefore, strength ratios are used to link the results of the sandbox experiments with nature in this chapter.

- *Weak zones*: Several processes are able to produce weak zones in natural rocks (e.g. material changes caused by sedimentation, fracturing, local increase of pore pressure, mineral reactions). In sandbox experiments these processes can not be simulated. However, the influence of such weak zones as potential detachments in the lower crust or in the incoming sediments was simulated by layers of glass beads. Therefore, only the presence of weak layers are considered as a potential controlling parameter and not the processes, which cause material weakening in nature.
- *Sediment supply*: The amount of sediment entering the trench on top of the oceanic crust is seen as crucial parameter by several authors (e.g. Jarrard, 1986; von Huene and Scholl, 1991; Lallemand et al., 1994b; Bangs and Cande, 1997). This parameter was simulated by changing the thickness of the incoming sand-layer. This parameter is linked to nature by the scaling factor (cf. Section 2.4.1).
- *IC/GC ratio*: The inlet capacity (IC) depends on different parameters in accretionary (thickness of the incoming sediments) and tectonically-erosive forearc wedges (load-dependent thickness of the basal flow zone, volume of topographic lows in the oceanic crust).

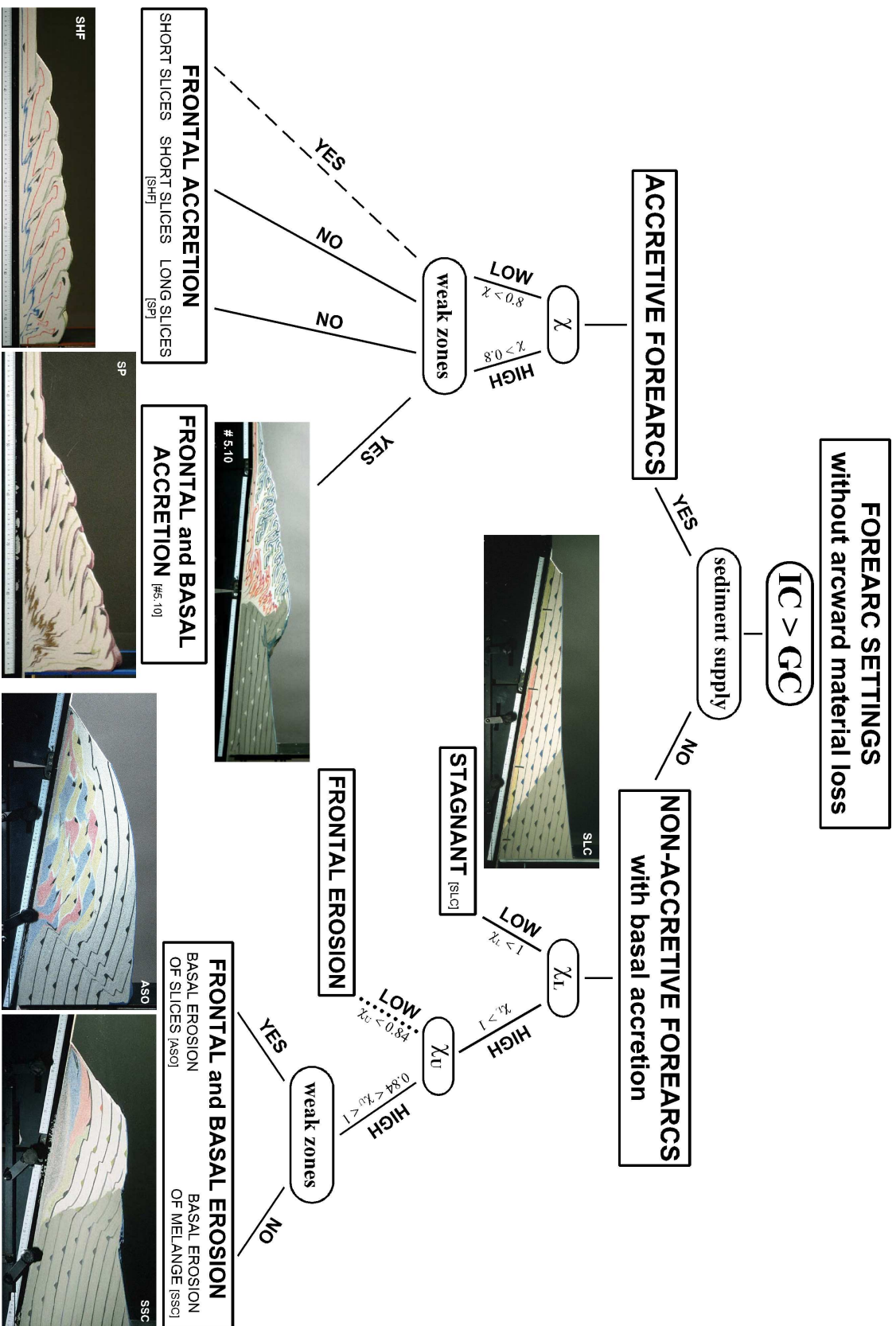


Figure 5.1: Hierarchical order of parameters that control convergent forearc settings without arcward material loss. Dashed lines mark parameter combinations that were not experimentally tested. Dotted lines indicate parameter combinations that were not possible to be experimentally tested.

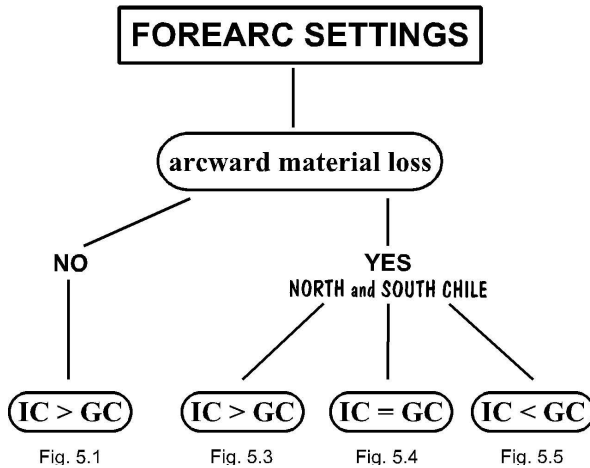


Figure 5.2: Possible IC/GC ratios of convergent forearc settings.

Therefore, a systematics allowing for both scenarios is not able to regard the specific processes regulating the inlet capacity in the individual setting. As shown for tectonically-erosive (Chapter 4) and accretive forearc settings (Gutscher, 1996), the influence of inlet capacity on the mass-transfer mode is strongly dependent on the global capacity (GC). Therefore, the IC/GC ratio best describes these parameters.

- *Distribution of vertical load:* Topographic highs and lows, which are caused by deformation or surficial mass transport (sedimentation, surficial erosion) might change the distribution of vertical load from that of an ideally-shaped wedge. This influences only secondary features of the forearc architecture (e.g. position of the centre of basal accretion), and does not change the general mass-transfer mode (Section 3.3). Therefore, this parameter is not regarded in this section, which focuses on the general mass-transfer modes of convergent forearcs.

The series of experiments presented in this study (cf. Chapter 2, 3, 4) comprise of all combinations of the above-mentioned potentially controlling parameters in closed setups to reveal their hierarchical order (Fig. 5.1). Therefore, these sandbox experiments demonstrated all theoretically-possible forearc settings, where material is not lost in arcward direction. In these forearcs, the inlet capacity is always larger than the global capacity.

As shown in Fig. 5.1, sediment supply is the dominant parameter of these forearc settings: As soon

as sediments enter the trench on top of the oceanic plate, an accretive mass-transfer mode will begin under any mechanical conditions. Non-accretive mass-transfer modes will be produced, if no sediment is supplied.

The subsidiary parameters differ between accretive and non-accretive mass-transfer modes. However, the strength ratio between the subduction interface and its overlying material is a second-order parameter in both types of mass-transfer mode (i.e. χ in accretive modes; χ_L in non-accretive modes), as it determines the ability to underthrust material beneath the wedge. In accretive systems a high strength ratio (> 0.8 ; cf. Section 2.4.4; Gutscher et al., 1996) enables underthrusting of incoming sediments. In contrast, in non-accretive forearc settings underthrusting of frontally- and basally-eroded material requires a significantly higher strength ratio ($\chi_L > 1$) between the subduction interface and the material in the subduction channel. This difference between the second-order parameters of accretive and non-accretive forearc settings is inferred from experiments performed with conveyor belts of latex gum ($\chi_{\text{latexgum/sand}} = 0.84$): Under these conditions the accretive experiments always showed underthrusting of either long frontally-accreted imbricates (LG experiment; cf. Section 2.4.4.1) or the lower portion of the incoming sand-layer beneath a mid-level detachment (experiment 5.10 in Fig. 5.1). In the non-accretive experiments this strength ratio prohibits underthrusting and mass transfer stagnates (SLC experiment; cf. Section 4.3.2).

An additional difference is that the accretive forearc settings are only controlled by one strength ratio (basal strength/internal strength), whereas the non-accretive are influenced by the combination of the lower and upper strength ratios (cf. Section 4.4.2). In the latter, the upper strength ratio (subduction channel/damage zone) is a third-order parameter and controls basal erosion. The scenario of a low strength ratio between the subduction channel and the damage zone, was not possible to test with the setup used in this study (dotted line in Fig. 5.1). However, I propose that in this case, the wedge would be only frontally eroded, since the accretive experiments with such a strength-ratio combination (high χ_L ; low χ_U ; e.g. LF experiment) showed that incoming material is underthrust but material is not basally eroded. Only if both strength ratios are high ($\chi_L > 1$; $\chi_U \approx 0.94$; e.g. SSC experiment) the convergent wedge is frontally and basally eroded.

The presence of weak zones is a third-order parameter in the accretive forearc settings and a

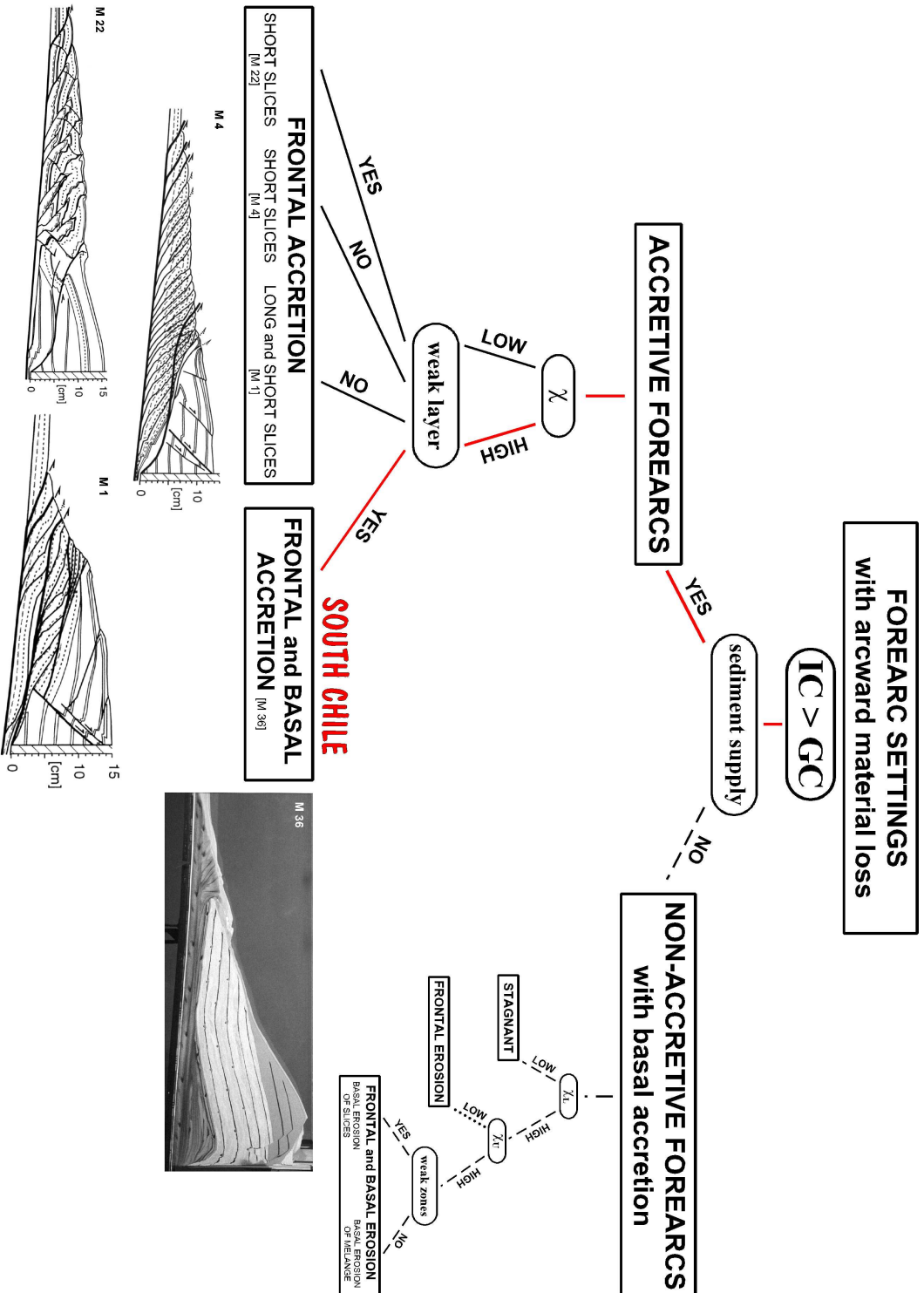


Figure 5.3: Hierarchical order of parameters that control convergent forearc settings with arcward material loss, where $IC > GC$. For the non-accretive forearcs, which have not been experimentally tested, the most probable order is shown. Dashed lines mark parameter combinations that were not experimentally tested. Dotted lines indicate parameter combinations that were not possible to be experimentally tested. Experiments labelled with 'M' were performed by Gutscher (1996).

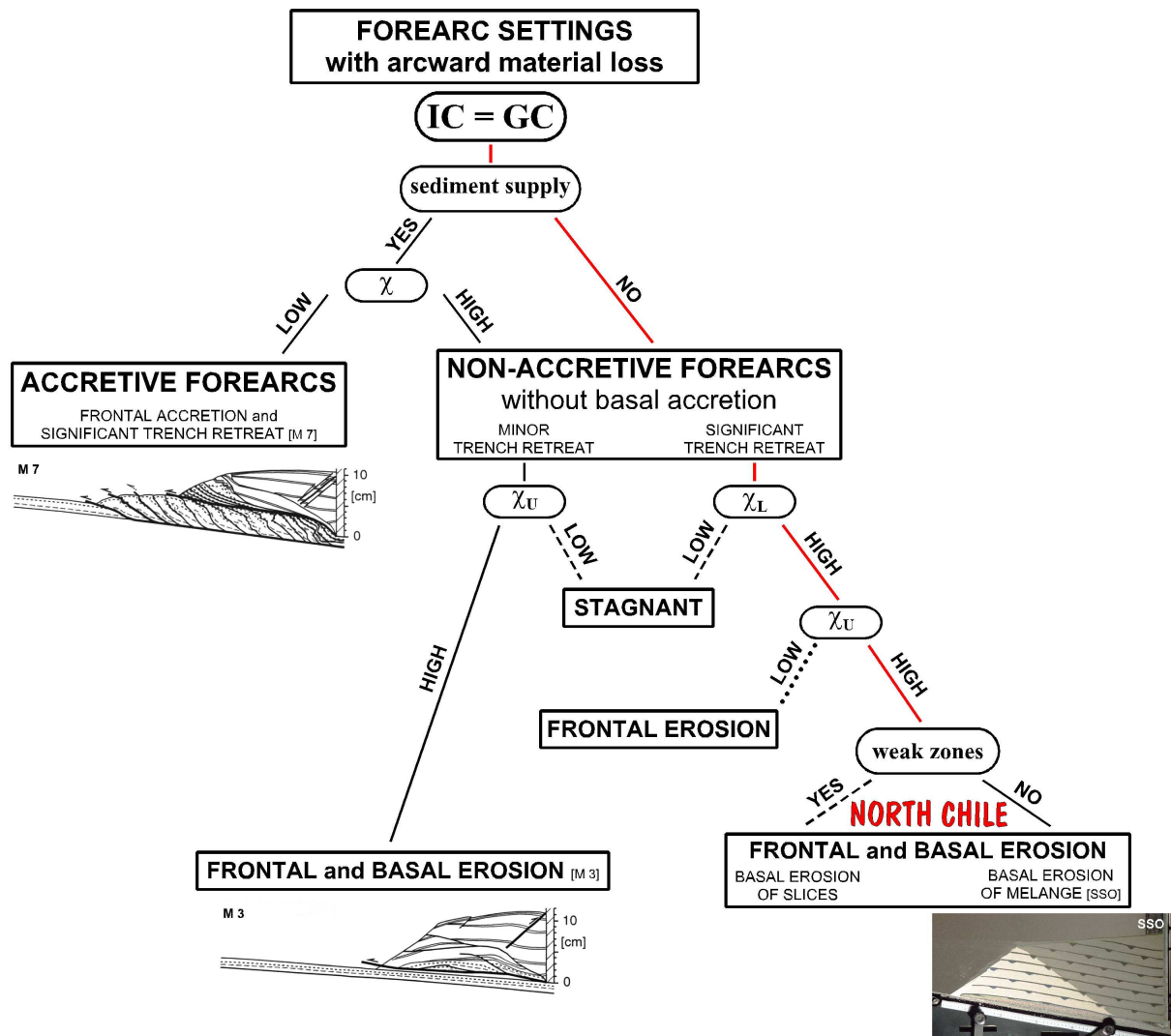


Figure 5.4: Hierarchical order of parameters that control convergent forearc settings with arcward material loss, where $IC = GC$. Dashed lines mark parameter combinations that were not experimentally tested. Dotted lines indicate parameter combinations that were not possible to be experimentally tested. Experiments labelled with 'M' were performed by Gutscher (1996).

fourth-order parameter in the non-accretive forearc settings, as this parameter differently influences the mass-transfer modes of both systems: A weak layer in the incoming sediment pile changes the mass-transfer mode from a purely frontally-accretive to coeval frontal and basal accretion (compare SP experiment and 5.10 in Fig. 5.1). In the case of steady-state tectonic erosion, the presence of lower crustal detachments led to higher rates of arcward material transport and basal erosion, but it did not change the general mass-transfer mode itself (compare 1st phase of experiment 3.14 and SSC; Appendix).

Both the South and North Chilean Forearc, which are investigated in this study, are characterised by arcward material loss (cf. Chapter 3 and 4). As Cloos and Shreve (1988b) have shown that the IC/GC ratio has a dominant control on accretive forearc settings, I questioned whether the hierarchical order (Fig. 5.1) concerning both the accretive and non-accretive forearc settings as discussed above, is also valid for forearc settings with arcward material loss.

Three IC/GC ratios are possible in forearc settings with arcward material loss ($IC > GC$; $IC = GC$; $IC < GC$; Fig. 5.2). Their hierarchical

order of controlling parameters are developed on the base of the experiments performed in this study (cf. Appendix) and by Gutscher (1996) (Fig. 5.3, 5.4 and 5.5). Not each parameter combination for all the IC/GC ratio have been experimentally tested. Therefore, the rank of some of the subsidiary parameters remains presumed (dashed lines in Fig. 5.1 - 5.5). However, comparison of the dominant parameters of the individual IC/GC ratios, proven by experimental results, reveals two systems of forearc settings:

1. IC > GC system: All forearc settings with this IC/GC ratio (with and without arcward material loss) are dominantly controlled by sediment supply, as described above (Fig. 5.1 and 5.3). The accretive and non-accretive mass-transfer modes of this system are able to basally accrete underthrust material.
2. IC ≤ GC system: In these forearc settings, not only the sediment supply determines whether a forearc is in an accretive or non-accretive mode. In the case that sediment is supplied, the strength ratio between the subduction interface and the overlying material additionally controls the subdivision into accretive and non-accretive mass-transfer modes (Fig. 5.4, 5.5). The forearc settings of this system do not allow basal accretion. Thus, the mass-transfer processes of this system are restricted to frontal accretion, stagnation, and frontal and basal erosion.

Within this framework, a forearc such as the North Chilean Forearc, which suffers frontal and basal erosion belongs to the IC ≤ GC system, since it shows nearly no basal accretion (cf. Section 4.5). Although the South Chilean Forearc has also evidence of only minor basal accretion since the Miocene (cf. Section 3.5.3), this forearc is unequivocal assigned to the IC > GC system. This interpretation is based on the following additional features, which differ in both systems:

- A forearc setting with a low strength ratio is not able to activate a mid-level detachment and underthrust material for a long distance, independent of its IC/GC ratio. Consequently, the South Chilean Forearc possesses a high strength ratio, as here material is underthrust beneath a mid-level detachment. However, a high strength ratio in the IC ≤ GC system always lead to a non-accretive mass-transfer

mode (Fig. 5.4 and 5.5). Therefore, the accretive South Chilean Forearc belongs to the IC > GC system.

- All accretive forearc settings of the IC ≤ GC system are characterised by significant trench retreat. No evidence of trench retreat since the Miocene has been found at the South Chilean Forearc.
- All accretive forearc settings of the IC ≤ GC system show a persistent-active, arcward-dipping out-of-sequence thrust, which is the boundary between a small-tapered frontal segment and a large-tapered rear segment. Neither such an out-of-sequence thrust nor such a change in the topography exist at the South Chilean Forearc.

Therefore, the South Chilean Margin represents a forearc setting, which is controlled by the presence of sediments in the trench basin, a high strength ratio, and the presence of a weak layer within the incoming sediment pile (in order of dominant to subsidiary parameters, respectively; red line in Fig. 5.3). Low rates of basal accretion, as observed at the South Chilean Margin, occur in such a forearc settings, when the ratio between the thickness of the underthrust material and the global capacity nearly amounts 1.

Comparison of the North and South Chilean Forearc with this systematics, which was developed on the base of analogue simulations, shows that sediment supply is one of the dominant parameters, which controls the mass-transfer modes of natural forearc settings. This result validates the suggestion of Bangs and Cande (1997), which was based on field investigations (cf. Section 1.1). However, the systematics additionally reveals that sediment supply is not the only parameter that determines, if a forearc setting becomes accretive or non-accretive: the IC/GC ratio is superior among the controlling parameters. This means that the absence of sediments on top of the oceanic crust at the North Chilean Forearc cannot determine alone whether this forearc is in the steady-state, tectonically erosive mode. If sediments would cover the oceanic crust at the North Chilean Forearc, steady-state tectonic erosion is also able to affect the North Chilean Forearc under certain conditions (see red line in Fig. 5.4).

This dominant role of the IC/GC ratio was previously suggested by Cloos and Shreve (1988a). They showed five types of accretive and one non-accretive

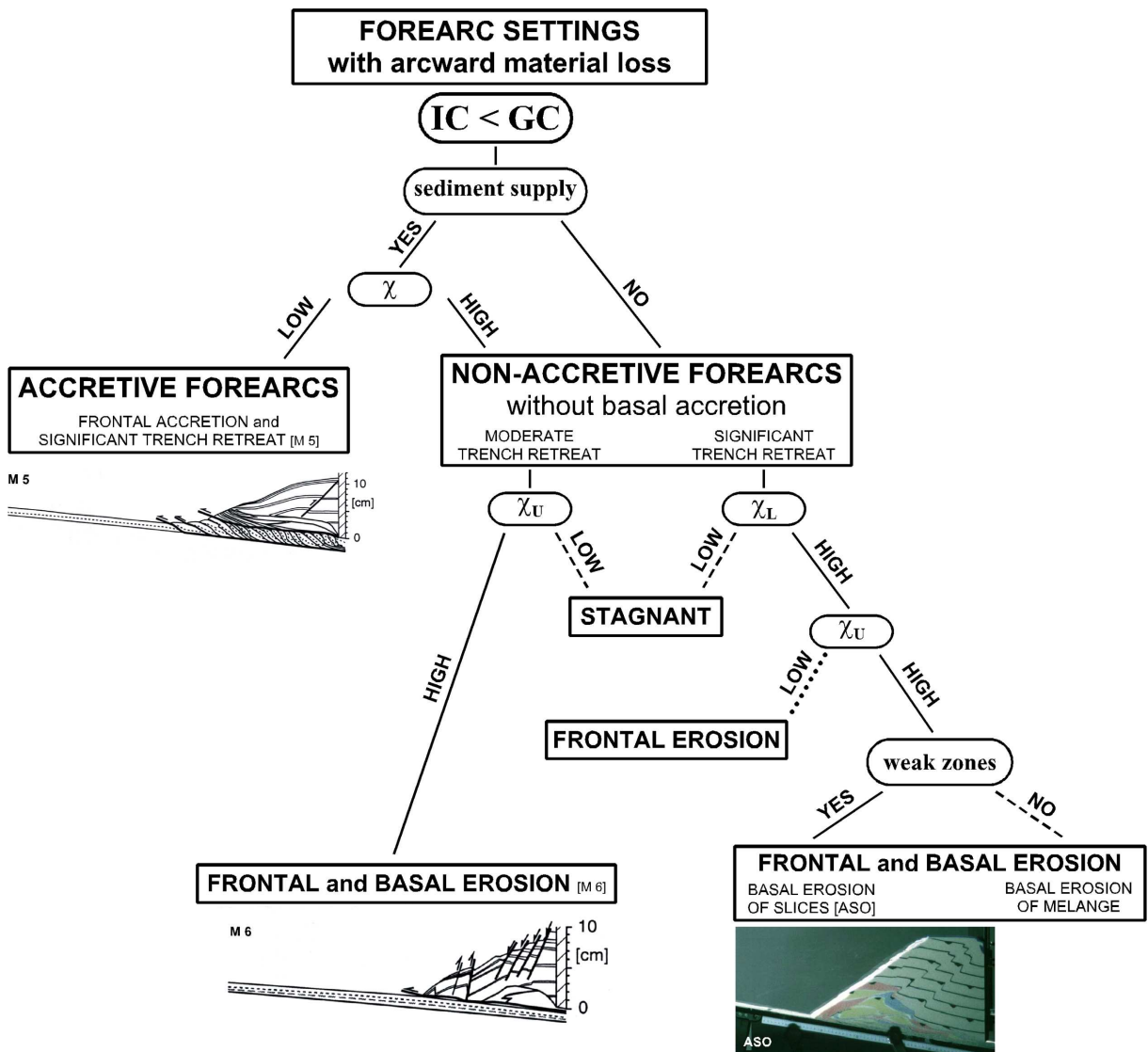


Figure 5.5: Hierarchical order of parameters that control convergent forearc settings with arcward material loss, where $IC < GC$. Dashed lines mark parameter combinations that were not experimentally tested. Dotted lines indicate parameter combinations that were not possible to be experimentally tested. Experiments labelled with 'M' were performed by Gutscher (1996).

forearc setting, which are dominantly controlled by this parameter. The more detailed systematics of non-accretive forearc settings in this study agrees with their suggestion, so that the IC/GC ratio is seen as the dominant parameter that controls the mass-transfer modes of all convergent forearc wedges. Nevertheless, this systematics only begins to explain the mechanics of convergent forearc wedges and the complex interactions of the parameters that control their mass-transfer modes. Some of the questions, which results from this study are listed in the following:

- What are the subsidiary parameters, which control the steady-state, tectonically erosive mass-transfer mode of the North Chilean Forearc? To identify these, one experiment remains to be done: a sand wedge on top of a conveyor belt (10 m) consisting of latex gum should be prepared with an open setup.
- Can the IC/GC ratios of the mass-transfer modes that occur in nature be unequivocally identified by mass-transfer processes, mass-transfer rates, kinematic and geometrical fea-

tures? There are some other experiments must be performed to determine whether each mass-transfer mode of the individual IC/GC ratios has distinctive combinations of these features (dashed lines in Fig 1-5). The results of these experiments will help to understand the position of all subsidiary parameters of all possible IC/GC ratios.

- Is this systematics valid for all natural forearc settings? To answer this question, several other convergent forearc wedges have to be analysed with these systematics, in the same way, as I did with the North and South Chilean Forearc. This would also answer the next question.
- Do all theoretically, experimentally possible forearc settings listed in the systematics, exist in nature? From this study it remains unclear, if forearc settings exist without arcward material loss, as both examples from nature belong to the ‘open forearcs’.
- What is and what controls the global control point? Cloos and Shreve (1988a) defined the global control point as the ‘point’ in the subduction channel, which determines the amount of material subducted to greater depth (global capacity). As shown in this study, the global control point plays a key role in the mass-transfer modes of convergent forearcs. However, this ‘point’ (if it is a ‘point’?) has not been identified or investigated in natural forearc settings yet. It was suggested that this ‘point’ depends on the density of overlying rocks and the geometry of the forearc wedge (Cloos and Shreve, 1988a). Therefore a comparison of mass-transfer rates, gravity field and wedge geometry would enhance the understanding of the global control point.

5.2 Restrictions of quantitative critical-taper analysis of convergent wedges in nature

This study shows that the critical-taper theory can be only applied to convergent sand wedges, when the following restrictions are also considered:

- The theory does not explain the dynamics of steady-state, tectonically erosive sand wedges, as it does not consider all required mechanical parameters (cf. Section 4.7.2). Therefore, the theory is not applicable in this case.

- The theory, which was developed to explain the dynamics of accretionary wedges in nature, includes the simplification that a homogeneous state of stress controls wedge geometry. However, the results of the basic parameter study (cf. Section 2.4.3.2 and 2.4.4.2) suggest that the stress field is only homogeneous within individual kinematic and geometrical segments, which were defined in this study (cf. Section 2.4.3.1).

A new strategy to apply the theory to accretionary sand wedges despite these restrictions was developed and successfully tested in Chapter 2 and 3. Field observations suggest that kinematic segmentation also occurs in natural convergent wedges [e.g. Barbados, (Moore and Byrne, 1987); Sunda, pers. com. H. Kopp] and thus restrictions of the critical-taper theory also exist in nature. This infers that quantitative critical-taper analysis is still appropriate to investigate accretionary wedges in nature, if the new strategy is used. Nevertheless, these restrictions and new insight in the mechanics of accretionary sand wedges resulting from this study, will have consequences for the investigation of accretionary wedges in nature.

Up to now, natural convergent wedges have been treated as wedges in a critical state of stress, when they show active deformation. The theory predicts that each wedge will reach this state, and can only change into a stable or non-stable state by varying of the boundary conditions (cf. Section 1.3). This study shows that this cannot be taken for granted, as:

- only individual segments reach the critical state of stress (FIZ), as the transient bulk wedge strength shifts rear segments into a stable state (IAZ), and
- such critical-tapered segments are built only after an adjustment phase, the duration of which strongly depends on the frictional strength of the accreted material (cf. Section 2.4.3.1).

Consequently, a quantitative critical-taper analysis of accretionary wedges unequivocally requires that the investigated segments are in the critical state. Two features characterise a critical-tapered segment: continuous activity of thrusts and constant wedge taper (cf. Section 2.4.3.1). However, proof that a complete wedge segment in nature is in a critical state of stress, remains an unsolved problem. The main difficulty is that the characteristics of ‘continuously-active’ natural faults are unknown.

In addition, I expect that the area, where a quantitative critical-taper analysis is able to provide results is strongly limited, since the sandbox simulations infer that most segments of accretionary wedges are in a stable state of stress and therefore not suitable for such an analysis. Nevertheless, such investigations would be of major importance, as it would be possible, to estimate the friction of active faults and the bulk strength of individual segments by plotting their kinematic and geometrical features in Mohr Diagrams, as used in this study.

Acknowledgements

This study was part of the Collaborative Research Centre ‘Deformation Processes in the Andes’ (SFB 267), whose support is gratefully acknowledged.

A large number of colleagues and friends gave me their support, advice and encouragement during the course of this work and I can only express my thanks to them properly in our own common language. Some things just don’t translate well, so with apologies to the non-German readers, my personal thanks go to the following people.

Prof. Dr. Onno Oncken hat mir mit viel Geduld und Geschick gezeigt, meine krausen Gedanken mit wissenschaftlicher Logik zu prüfen. Dr. Nina Kukowski hat mir mit Rat und Tat in jeder Phase meiner Doktorandenzeit zur Seite gestanden und mir dabei genug Freiraum gelassen, meinen eigenen Weg zu gehen. Prof. Dr. Hans-Jürgen Götze hat als ‘Fachfremder’ mit konstruktiven Ratschlägen zur allgemeinen Verständlichkeit dieser Arbeit beigetragen. Für diese sinnvolle Betreuung und aufmerksame Begutachtung möchte ich allen dreien meinen herzlichsten Dank aussprechen.

Dr. Dave Tanner hat als Lektor die Arbeit sprachlich mitgestaltet und einen Weg gefunden, mir Freude am Englischen zu vermitteln. Dr. Katrin Huhn hat große Teile der Arbeit in der Erstfassung getestet. An beide ein großes Dankeschön, denn sie haben wesentlich mit zum Gelingen dieser Arbeit beigetragen.

Günter Tauscher, der einfach die schönsten Sandkisten baut, Birgit Michel, Gesine Adam, und die Hiwi-Crew (Anja Pigowske, Olaf Zielke, Kerstin Schemmann und Mariam Sowe) haben mir bei der technischen Umsetzung der Versuche geholfen.

Unter den Wissenschaftlern des SFB 267 habe ich immer einen Ansprechpartner für jede Frage aus anderen Fachgebieten gefunden. Die Mitarbeiter des GFZs, vor allem vom Projektbereich 3.1, haben mich in jeder Hinsicht unterstützt. Ich möchte mich bei allen sehr dafür bedanken, daß ich meine Arbeit in ihrer Umgebung fertigstellen konnte, und sie die kleineren und größeren Schwierigkeiten, die im Laufe der Zeit gemeistert werden mußten, zusammen mit mir bewältigt haben. In diesem Zusammenhang möchte ich mich besonders bei Helmut Echtler, Lotte Krawczyk, Michael Köhler, Dieter Berger, Gabi Arnold, Tim Vietor, Kirsten Elger, Gisela Wolff, Manuela Dziggel, Brigitte Stöcker, Janina Baier, Kirsten Gräfe und Daniel Acksel bedanken. Bei Jürgen Adam bedanke ich mich für die achtjährige Zusammenarbeit.

Meine Freunde haben dazu beigetragen, daß ich die Doktorandenzeit dazu nutzen konnte eigene Standpunkte zu finden. Besonders möchte ich mich für die Tips von Frau zu Frau bei L. Reimers, für kultige Kiez-Erlebnisse bei den Kreuzbergern, für die schöne Sizilien-Unterbrechung bei Klaus Pelz, Maria Panateri und Marinella Sineri bedanken. Und mein neuer großer Bruder war einfach für mich da.

Den umfassendsten Dank richte ich an Jonas für die große Liebe.

Alle diese Menschen haben für mich eine wichtige Rolle bei der Umsetzung dieser Arbeit gespielt und mir dieses Erlebnis ermöglicht. Mir hat es Spaß gemacht.

References

- Adam, J. 1996. Kinematik und Dynamik des neogenen Falten- und Deckengürtels in Sizilien (Quantifizierung neotektonischer Deformationsprozesse in der zentralmediterranen Afro-Europäischen Konvergenzzone), *Berliner Geowiss. Abh. (A)* **185** 171.
- Adam, J., Kukowski, N. and Lohrmann, J. 2000. Mechanics and mass transfer patterns of tectonic erosive convergent margins: quantitative results from analogue sandbox models and their implications for natural forearc systems. In: *AGU, Fall Meeting. EOS, San Francisco*, 81/F.
- Adam, J. and Reuther, C.-D. 2000. Crustal dynamics and active fault mechanics during subduction erosion. Application of frictional wedge analysis on to the North Chilean Forearc. *Tectonophysics* **321**, 297-325.
- Aguirre, L., Hervé, F. and Godoy, P. B. 1972. Distribution of metamorphic facies in Chile. *Krystalinikum* **9**, 7-19.
- Anand, L. and Gu, C. 2000. Granular materials: constitutive equations and strain localization. *Jour. Mech. Phys. Solids* **48**, 1701-1733.
- ANCORP and group, w. 1999. Seismic reflection image revealing offset of Andean subduction-zone earthquake locations into oceanic mantle. *Nature* **397**, 341-344.
- Angermann, D., Klotz, J. and Reigber, C. 1999. Space-geodetic estimation of the Nazca-South American Euler Vector. *Earth Planet. Sci. Lett.* **171**(3), 329-334.
- Armijo, R. and Thiele, R. 1990. Active faulting in northern Chile: ramp stacking and lateral decoupling along a subduction plate boundary? *Earth and Planetary Science Letters* **98**, 40-61.
- Asch, G., Schurr, B., Lüth, S., Belmonte, A., Bohm, M., Bruhn, C., Giese, P., Rietbrock, A. and Wigger, P. 2001. Structure and rheology of the upper plate from seismological investigations. In: *Deformation Processes in the Andes, Interaction between endogenic and exogenic processes during subduction orogenesis* (edited by SFB-267). *Report for the Research Period 1999-2001*, 177-209.
- Bangs, N. L. and Cande, S. C. 1997. Episodic development of a convergent margin inferred from structures and processes along the southern Chile margin. *Tectonics* **16**(3), 489-503.
- Beaumont, C., Fullsack, P. and Hamilton, J. 1992. Erosional control of active compressional orogens. In: *Thrust tectonics*. (edited by McClay, K. R.). Chapman & Hall, London, United Kingdom, 1-18.
- Behrmann, J. H. and Kopf, A. 2001. Balance of tectonically accreted and subducted sediment at the Chile Triple Junction. *Geologische Rundschau* **90**(4), 753-768.
- Behrmann, J. H., Lewis, S. D., Cande, S. C., Musgrave, R., Bangs, N., Boden, P., Brown, K., Collombat, H., Didenko, A. N., Didyk, B. M., Froelich, P. N., Golovchenko, X., Forsythe, R., Kurnosov, V., Lindsley, G. N., Marsaglia, K., Osozawa, S., Prior, D., Sawyer, D., Scholl, D., Spiegler, D., Strand, K., Takahashi, K., Torres, M., Vega, F. M., Vergara, H. and Waseda, A. 1994. Tectonics and geology of spreading ridge subduction at the Chile triple junction; a synthesis of results from Leg 141 of the Ocean Drilling Program. *Geologische Rundschau* **83**(4), 832-852.
- Boettcher, M. 1999. Tektonik der Halbinsel Arauco und angrenzender Forearc-Bereiche (südliches Zentral-Chile). *Mitt. Geol.-Paläont. Inst. Univ. Hamburg* **83**, 1-53.
- Brace, W. F. and Byerlee, J. D. 1966. Stick-slip as a mechanism for earthquakes. *Science* **153**, 990-992.
- Brudy, M., Zoback, M. D., Fuchs, K., Rummel, F. and Baumgaertner, J. 1997. Estimation of the complete stress tensor to 8 km depth in the KTB scientific drill holes; implications for crustal strength. In: *The KTB deep drill hole*. (edited by Haak, V. & Jones, A. G.). *Journal of Geophysical Research, B, Solid Earth and Planets* **102**. *American Geophysical Union, Washington, DC, United States*, 18,453-18,475.
- Buske, S., Lüth, S., Meyer, H., Patzig, R., Reichert, C., Shapiro, S., Wigger, P. and Yoon, M. 2002 in press. Broad depth range seismic imaging of the subducted Nazca Slab, North Chile. *Tectonophysics*.
- Byerlee, J. 1978. Friction of rocks. *Pure. Appl. Geophys.* **116**, 615-626.
- Byrne, D. E., Wang, W. H. and Davis, D. M. 1993. Mechanical role of backstops in the growth of forearcs. *Tectonics* **12**, 123-144.
- Cadell, H. M. 1888. Experimental researches in mountain building. *Royal Soc. of Edinburgh Transactions* **35**, 337-360.
- Chapple, W. M. 1978. Mechanics of thin-skinned fold-and-thrust belts. *Geol. Soc. of Americ. Bull.* **89**, 1189-1198.
- Chu, J. 1995. An experimental examination of the critical state and other similar concepts for granular soils. *Can. Geotech. J.* **32**, 1065-1075.
- Cisternas, M. E. and Frutos, J. 1994. Evolución tectónico-paleogeográfica de la cuenca terciaria de los Andes del sur de Chile (34°30'-40°30'). *VII Congreso Geológico Chileno* **1**, 6-12.
- Clift, P. D., Pecher, I., Kukowski, N., Hampel, A. and Ruppel, C. Tectonic erosion of the Peruvian Forearc, Lima Basin, by steady-state subduction and Nazca Ridge Collision. *subm. to Tectonics*.
- Cloos, M. and Shreve, R. L. 1988a. Subduction-channel model of prism accretion, melange formation, sediment subduction, and subduction erosion at convergent plate margins; Part I, Background and description. *Pure and Applied Geophysics* **128**(3-4), 455-500.
- Cloos, M. and Shreve, R. L. 1988b. Subduction-channel model of prism accretion, melange formation, sediment subduction, and subduction erosion at convergent plate margins; Part II, Implications and discussion. *Pure and Applied Geophysics* **128**(3-4), 501-545.
- Cobbold, P. R. 1999. Sand as an analogue material in tectonics; advantages, limitations and future developments. In: *European Union of Geosciences conference abstracts; EUG 10*. (edited by Anonymous). *Journal of Conference Abstracts* **4**, Cambridge Publications, 602.
- Cobbold, P. R. and Castro, L. 1999. Fluid pressure and effective stress in sandbox models. *Tectonophysics* **301**(1-2), 1-19.
- Cobbold, P. R., Cosgrove, J. W. and Summers, J. M. 1971. Development of internal structures in deformed anisotropic rocks. *Tectonophysics* **12**, 223-253.
- Cobbold, P. R., Durand, S. and Mourgues, R. 2001. Sandbox modelling of thrust wedges with fluid-assisted detachments. *Tectonophysics* **334**(3-4), 245-258.
- Cobbold, P. R., Rosello, E. and Vendeville, B. C. 1989. Some experiments on interacting sedimentation and deformation above salt horizons. *Bull. Soc. Géol. France*, 453-360.

- Colletta, B., Letouzey, J., Pinedo, R., Ballard, J. F. and Bale, P. 1991. Computerized X-ray tomography analysis of sandbox models; examples of thin-skinned thrust systems. *Geology* **19**(11), 1063-1067.
- Corrado, S., Di, B. D., Naso, G. and Faccenna, C. 1998. Influence of palaeogeography on thrust system geometries; an analogue modelling approach for the Abruzzi-Molise (Italy) case history. *Tectonophysics* **296**(3-4), 437-453.
- Dahlen, F. A. 1984. Noncohesive Critical Coulomb Wedges: An Exact Solution. *J. Geophys. Res.* **89**(B12), 10125-10133.
- Dahlen, F. A., Suppe, J. and Davis, D. 1984. Mechanics of Fold-and-Thrust Belts and Accretionary Wedges: Cohesive Coulomb Theory. *J. Geophys. Res.* **89**(B12), 10087-10101.
- Davis, D., Suppe, J. and Dahlen, F. A. 1983. Mechanics of fold-and-thrust belts and accretionary wedges. *J. Geophys. Res.* **88**(B2), 1153-1172.
- Davis, D. M. and von Huene, R. 1987. Inferences on sediment strength and fault friction from structures at the Aleutian Trench. *Geology* **15**, 517-522.
- Davy, P. and Cobbold, P. R. 1991. Experiments on shortening of a 4-layer model of the continental lithosphere. In: *Experimental and numerical modelling of continental deformation.* (edited by Cobbold, P. R.). *Tectonophysics* **188**, 1-25.
- Delouis, B., Philip, H., Dorbath, L. and Cisternas, A. 1998. Recent crustal deformation in the Antofagasta region (northern Chile) and the subduction process. *Geophysical Journal International* **132**(2), 302-338.
- DeMets, C., Gordon, R. G., Argus, D. F. and Stein, S. 1994. Effect of recent revisions to the geomagnetic reversal time scale on estimates of current plate motions. *Geophys. Res. Lett.* **21**(20), 2191-2194.
- Díaz-Naveas, J. L. 1999. Sediment subduction and accretion at the Chilean convergent margin. *PhD-Thesis, Ch. Albrechts Universität Kiel.* pp. 130.
- Dominguez, S., Lallemand, S. E., Malavieille, J. and von Huene, R. 1998. Upper plate deformation associated with seamount subduction. *Tectonophysics* **293**(3-4), 207-224.
- Elgueta, S., McDonough, M., Le Roux, J., Urqueta, E. and Duhart, P. 2001. Estratigrafía y sedimentología de las Cuencas cenozoicas de la región de Los Lagos (39°-42°S). *Bol. Serv. Nac. Geol. Miner.* **57**, in press.
- Elliot, D. 1976. The motion of thrust sheets. *Journal of Geophysical Research* **81**(5), 949-963.
- Gosh, S. K. and Ramberg, H. 1968. Buckling experiments on intersecting fold patterns. *Tectonophysics* **5**, 89.
- Gräfe, K., Echtler, H., Glodny, J., Seifert, W., Kemnitz, H. and Rosenau, M. 2000. Structure and evolution of the active continental margin in South-Central Chile (36°-42°S); Universität Stuttgart, 2000. In: 17. Geowissenschaftliches Lateinamerika-Kolloquium. *Profil* **18**, Stuttgart, 47.
- Gutscher, M. A. 1996. Growth, erosion and material transfer in accretionary wedges: A quantitative analysis based on analog modeling and the implications for the evolution of convergent margins. *PhD-Thesis, Christian-Albrechts-Universität zu Kiel.* pp. 114.
- Gutscher, M. A., Kukowski, N., Malavieille, J. and Lallemand, S. 1996. Cyclical behaviour of thrust wedges; insights from high basal friction sandbox experiments. *Geology* **24**(2), 135-138.
- Gutscher, M. A., Kukowski, N., Malavieille, J. and Lallemand, S. 1998a. Episodic imbricate thrusting and underthrusting; analog experiments and mechanical analysis applied to the Alaskan accretionary wedge. *Journal of Geophysical Research* **103**(B5), 10,161-10,176.
- Gutscher, M. A., Kukowski, N., Malavieille, J. and Lallemand, S. 1998b. Material transfer in accretionary wedges from analysis of a systematic series of analog experiments. *Journal of Structural Geology* **20**(4), 407-416.
- Hall, J. S. 1815. On the vertical position and convolution of certain strata and their relation with granite. *Royal Soc. of Edinburgh Transaction* **7**, 79-108.
- Han, C. and Drescher, A. 1993. Shear bands in biaxial tests on dry coarse sand. *Soils and Foundations* **33**(1), 118-132.
- Haq, B. U., Hardenbol, J. and Vail, P. R. 1988. Mesozoic and Cenozoic chronostratigraphy and cycles of sea-level change. In: *Sea-level changes; an integrated approach.* (edited by Wilgus, C. K., Hastings, B. S., Ross, C. A., Posamentier, H. W., Van, W. J. & Kendall, C. G. S. C.). Special Publication - Society of Economic Paleontologists and Mineralogists 42. SEPM (Society for Sedimentary Geology), Tulsa, OK, United States, 72-108.
- Harris, L. B. and Cobbold, P. R. 1984. Development of conjugate shear bands during bulk simple shearing. *Journ. Struct. Geol.* **7**, 37-44.
- Haschke, M., Siebel, W., Günther, A. and Scheuber, E. 2002, in press. Repeated crustal thickening and recycling during the Andean orogeny in north Chile (21°-26°S). *JGR* **107**(B1).
- Hervé, F. 1977. Petrology of the crystalline basement of the Nahuelbuta Mountains, Southcentral Chile. In: *Comparative studies on the geology of the Circum-Pacific Orogenic Belt in Japan and Chile* (edited by Ishikawa, T., Aguirre, L.). Japan Soc. f. Promotion of Science, 1-51.
- Hilde, T. W. C. 1983. Sediment subduction versus accretion around the Pacific. *Tectonophysics* **99**, 381-397.
- Hinz, K., Reichert, C. J., Flueh, E. R. and Kudrass, H. R. 1998. *Final report: Crustal Investigations off- and on-shore Nazca Central Andes (CINCA).* Bundesanstalt für Geowissenschaften und Rohstoffe, Hannover, pp 217.
- Hoshino, K., Koide, H., Inami, K., Iwamura, S. and Mitsui, S. 1972. *Mechanical properties of Tertiary sedimentary rocks under high confining pressure.* pp. 200.
- Hubbert, M. K. 1937. Theory of scale models as applied to the study of geological structures. *Geol. Soc. Am. Bull.* **48**, 1459-1520.
- Hubbert, M. K. 1951. Mechanical basis for certain familiar geologic structures. *Geological Society of America Bulletin* **62**(4), 355-372.
- Huhn, K. 2002. Analyse der Mechanik des Makran Akkretionskeils mit Hilfe der Finiten und der Diskreten Elemente Methode sowie analoger Sandexperimente. *Scientific Technical Report STR02*(02), 159.
- Huhn, K., Morgan, J. K. and Kukowski, N. 2000. Investigating the mechanics of the Makran accretionary wedge with analog and distinct element model. *AGU 2000 Fall Meeting. EOS, San Francisco*, 81/F.
- Huiqi, L., McClay, K. R. and Powell, D. 1992. Physical models of thrust wedges. In: *Thrust tectonics.* (edited by McClay, K. R.). Chapman & Hall, London, United Kingdom, 71-81.

- Husen, S., Kissling, E., Flueh, E.R. 2000. Local earthquake tomography of shallow subduction in North Chile: A combined onshore and offshore study. *JGR* **105**(B12), 18,183-28,198.
- Husen, S., Kissling, E., Flueh, E. and Asch, G. 1999. Accurate hypocentre determination in the seismogenic zone of the subducting Nazca Plate in northern Chile using a combined on-/ offshore network. *Geophysical Journal International* **138**(3), 687-701.
- Hussong, D. M. and Uyeda, S. 1982. Tectonic processes and the history of the Mariana Arc; a synthesis of the results of Deep Sea Drilling Project Leg 60. In: Leg 60 of the cruises of the drilling vessel Glomar Challenger; Apra, Guam to Apra, Guam; March-May 1978. (edited by Lee, M., Powell, R., Hussong, D. M., Uyeda, S., Blanchet, R., Bleil, U., Ellis, C. H., Francis, T. J. G., Fryer, P., Horai, K. I., Kling, S., Meijer, A., Nakamura, K., Natland, J. H., Packham, G. H. & Sharaskin, A. Y.). *Initial Reports of the Deep Sea Drilling Project* **60**, 909-929.
- Hyndman, R. D., Wang, K., Yuan, T. and Spence, G. D. 1993. Tectonic sediment thickening, fluid expulsion, and the thermal regime of subduction zone accretionary prisms: the Cascadia margin off Vancouver Island. *J. Geophys. Res.* **98**, 21865-21876.
- Jaeger, J. C. and Cook, N. G. W. 1969. *Fundamentals of Rock Mechanics*. Methuen, London. pp. 593.
- Jarrard, R. D. 1986. Relations among subduction parameters. *Reviews of Geophysics* **24**(2), 217-284.
- Jordan, T. E., Burns, W. M., Veiga, R., Pángaro, F., Copeland, P., Kelley, S. and Mpodozis, C. 2001. Extension and basin formation in the southern Andes caused by increased convergence rate: A mid-Cenozoic trigger for the Andes. *Tectonics* **20**(3), 308-3024.
- Kaizuka, S., Matsuda, T., Nogami, M. and Yonekura, N. 1973. Quaternary Tectonic and recent seismic crustal movements in the Arauco Peninsula and its environs, Central Chile. *Geographical Report* **8**, 39-42.
- Karig, D. E. and Kagami, H. 1983. Varied responses to subduction in Nankai Trough and Japan Trench forearcs. *Nature* **304**(5922), 148-151.
- Karig, D. E. and Sharman, G. F., III. 1975. Subduction and accretion in trenches. *Geological Society of America Bulletin* **86**(3), 377-389.
- Kato, T. and Godoy, E. 1995. Petrogenesis and tectonic significance of Late Paleozoic coarse-crystalline blueschist and amphibolite boulders in the Coastal Range of Chile. *Int. Geol. Rev.* **37**, 992-1006.
- Kelm, U., Cisternas, M., Helle, S. and Méndez, D. 1994. Diagenetic character of the tertiary basin between Los Angeles and Osorno, southern Chile. *Rev. Geol. Chile* **21**, 241-252.
- Kopf, A. 1995. Festoffbilanzierung akkretierten und subduzierten Sedimentes und computergestützte Rückwärtsmodellierung deformierter Krustenquerschnitte am Kontinentalrand von S-Chile. *Gießener Geol. Abhandlungen* **55**, 225.
- Kopp, H., Klaeschen, D., Flueh, E. R. and Bialas, J. 2002. Crustal structure of the Java margin from seismic wide-angle and multichannel reflection data. *JGR* **107**(B2), ETG 1-1 - ETG 1-24.
- Koyi, H. 1988. Experimental modelling the role of gravity and lateral shortening in Zagros mountain belt. *AAPG Bull.* **72**, 82-94.
- Krantz, R. W. 1991. Measurement of friction coefficients and cohesion for faulting and fault reactivation in laboratory models using sand and sand mixtures. *Tectonophysics* **188**, 203-207.
- Kudrass, H. R., von Rad, U., Seyfried, H., Andruleit, H., Heinz, K. and Reichert, C. 1998. Geological sampling. In: *Final report: Crustal Investigations off- and onshore Nazca Central Andes (CINCA)* (edited by Hinz, K., Reichert, C.J., Flueh, E.R., Kudrass, H.R.). Bundesanstalt für Geowissenschaften und Rohstoffe, Hannover, 44-52.
- Kukowski, N., Adam, J., Huhn, K., Lohrmann, J., Hampel, A. and Oncken, O. in press. Geodynamische Prozesse an konvergenten Plattenrändern: Simulation mit analogen und numerischen Methoden. *Scientific Technical Report*.
- Kukowski, N., Adam, J. and Lohrmann, J. 1999. Erosive mass transfer at convergent margins: constraints from analog models and application of Coulomb wedge analysis. In: *ISAG. Andean Geodynamics*. Institut de Recherche pour le Développement, Göttingen, 400-403.
- Kukowski, N., Hampel, A., Lohrmann, J., Hübscher, C. and Bialas, J. 2001a. Tectonic erosion at the Peruvian margin resulting from extraordinary roughness of the plate interface: evidence from new swath bathymetry data, seismic wide angle data, and sandbox analogue modelling. *Geophysical Research Abstracts* **3**, CD-Rom.
- Kukowski, N., Lallemand, S. E. and Malavieille, J. 1997. Complex deformation styles in sandbox accretionary wedges caused by two active décollements and changing basal conditions. *EOS* **78**(46), F707.
- Kukowski, N., Malaville, J., Gutscher, M.-A. and Lallemand, S. E. Mechanical decoupling and basal duplex formation observed in sandbox experiments with application to the Western Mediterranean Ridge. *Marine Geology* **187**(3-4), in press.
- Kukowski, N., Schillhorn, T., Huhn, K., v. Rad, U., Husen, S. and Flueh, E. R. 2001b. Morphotectonics and mechanics of the central Makran accretionary wedge off Pakistan. *Marine Geology* **173**, 1-19.
- Kukowski, N., von Huene, R., Malavieille, J. and Lallemand, S. E. 1994. Sediment accretion against a buttress beneath the Peruvian continental margin at 12°S as simulated with sandbox modeling. *Geologische Rundschau* **83**, 822-831.
- Kulm, L. D., Schweller, W. J. and Masias, A. 1977. A preliminary analysis of the subduction process along the Andean continental margin near 6° to 45°. In: *Island Arcs, Deep-sea Trenches, and Back-arc Basins* (edited by Talwani, M., Pitman III, W.C.). *Maurice Ewing Series* **1**. AGU, 285-301.
- Ladage, S., Reichert, C., Schreckenberger, B., Block, M., Bönnemann, C., Canuta, J., Damaske, D., Diáz, J., Gaedicke, C., Krawczyk, C., Kus, J., Sepulveda, J. and Urbina, O. 2002. SPOC-Experiment: Seismic Imaging and Bathymetry of the Central Chile Margin - First Results. *Geophysical Research Abstracts* **4** EGS, Nice, France, April 2002.
- Lallemand, S. E., Lewis, K. B. and Collot, J. Y. 1994a. Sandbox modelling of seamount subduction and possible applications in New Zealand. In: *Geological Society of New Zealand 1994 annual conference; programme and abstracts*. (edited by Neil, H., Gillespie, J. L., Moon, V. & Briggs, R.). *Geological Society of New Zealand Miscellaneous Publication* **80a**, 109.

- Lallemant, S. E., Malavieille, J. and Calassou, S. 1992a. Effects of oceanic ridge subduction on accretionary wedges: Experimental modelling and marine observations. *Tectonics* **11**(6), 1301-1313.
- Lallemant, S. E., Schnuerle, P. and Malavieille, J. 1994b. Coulomb theory applied to accretionary and nonaccretionary wedges; possible causes for tectonic erosion and/or frontal accretion. *JGR* **99**(6), 12,033-12,055.
- Lallemant, S. E., Schnurle, P. and Manoussis, S. 1992b. Reconstruction of subduction zone paleogeometries and quantification of upper plate material losses caused by tectonic erosion. *JGR* **97**(1), 217-239.
- Lavenu, A. and Cembrano, J. 1999. Compressional- and transpressional-stress pattern for Pliocene and Quaternary brittle deformation in fore arc and intra-arc zones (Andes of central and southern Chile). *Journal of Structural Geology* **21**(12), 1669-1691.
- Leeman, W. P., Carr, M. J. and Morris, J. D. 1994. Boron geochemistry of the Central American volcanic arc; constraints on the genesis of subduction-related magmas. *Geochimica et Cosmochimica Acta* **58**(1), 149-168.
- Lehner, F. K. 1986. Comments on Noncohesive Critical Coulomb Wedges: An Exact Solution by F. A. Dahlen. *JGR* **91**(B1), 793-796.
- Leturmy, P., Mugnier, J. L., Vinour, P., Baby, P., Colletta, B. and Chabron, E. 2000. Piggyback basin development above a thin-skinned thrust belt with two detachment levels as a function of interactions between tectonic and superficial mass transfer; the case of the Subandean Zone (Bolivia). *Tectonophysics* **320**(1), 45-67.
- Lüth, S. 2000. Auswertung und Interpretation der weitwinkelseismischen Messungen des AN-CORP-Projektes. *Berliner Geowiss. Abh.*, pp. 153
- Malavieille, J. 1984. Modélisation expérimentale des chevauchements imbriqués: application aux chaînes de montagnes. *Société Géologique de France Bulletin* **7**, 129-138.
- Marone, C. 1998. Laboratory-derived friction laws and their application to seismic faulting. *Annu. Rev. Earth. Planet. Sci.* **26**, 643-96.
- Martin, M. W., Kato, T. T., Rodriguez, C., Godoy, E., Duhart, P., McDonough, M. and Campos, A. 1999. Evolution of the late paleozoic accretionary complex and overlying forearc-magmatic arc, south central Chile (38°-41°): Constraints for the tectonic setting along the southwest margin of Gondwana. *Tectonics* **18**(4), 582-605.
- McClay, K. R. 1976. The rheology of plasticine. *Tectonophysics* **33**, 7-15.
- McClay, K. R. and Ellis, P. G. 1987. Analogue models of extensional fault geometries. In: *Continental Extensional Tectonics* (edited by Coward, M. P., Dewey, J. F. & Hancock, P. L.). *Spec. Publ. Geol. Soc. London* **28**, 109-125.
- McDonough, M. R., Duhart, P., Herrero, C., van der Velden, A., Cook, F. A., Martin, A. W., Ugalde, H., Villeneuve, M. and Mpodozis, C. in prep. Accretionary tectonics and forearc basin evolution on the Southwestern margin of Gondwana, Southern Chile: Implications of new seismic and geochronological results.
- Miller, H. 1970. Das Problem des hypothetischen 'pazifischen Kontinentes' gesehen von der chilenischen Pazifikküste. *Geol. Rundschau* **59**(3), 927-938.
- Moore, J. C. and Byrne, T. 1987. Thickening of fault zones: A mechanism of melange formation in accreting sediments. *Geology* **15**, 1040-1043.
- Moore, J. C., Watkins, J. S. and Shipley, T. H. 1982. Summary of accretionary processes, Deep Sea Drilling Project Leg 66; offscraping, underplating, and deformation of the slope apron. In: *Leg 66 of the cruises of the drilling vessel Glomar Challenger; Mazatlan, Mexico to Manzanillo, Mexico; March-May, 1979.* (edited by Lee, M., Watkins, J. S., Moore, J. C., Bachman, S. B., Beghtel, F., Butt, A., Didyk, B. M., Dmitriev, Y. I., Leggett, J. K., Lundberg, N. F., McMillen, K. J., Niitsuma, N., Rodriguez, T. R., Shephard, L. E., Shipley, T. H., Stephan, J. F. & Stradner, H.). *Initial Reports of the Deep Sea Drilling Project* **66**, 825-836.
- Mordojovich, C. 1981. Sedimentary Basins of Chilean Pacific Offshore. *AAPG* **12**, 63-82.
- Morris, J. D., Leeman, W. P. and Tera, F. 1990. The subducted component in island arc lavas; constraints from B-Be isotopes and Be systematics. *Nature* **344**(6261), 31-36.
- Mortimer, C., Farrar, E. and Saric, N. 1974. K-Ar ages from Tertiary lavas of the northern-most Chilean Andes. *Geologische Rundschau* **63**(2), 484-490.
- Mulugeta, G. 1988. Modelling the geometry of Coulomb thrust wedges. *J. Struct. Geol.* **10**, 847-859.
- Mulugeta, G. and Koyi, H. 1987. Three-dimensional geometry and kinematics of experimental piggyback thrusting. *Geology* **15**, 1052-1056.
- Mulugeta, G. and Koyi, H. 1992. Episodic accretion and strain partitioning in a model sand wedge. *Tectonophysics* **202**(2-4), 319-333.
- Murauchi, S. and Ludwig, W. J. 1980. Crustal structure of the Japan Trench; the effect of subduction of oceanic crust. In: *Legs 56 and 57 of the cruises of the drilling vessel Glomar Challenger; Yokohama, Japan to Yokohama, Japan; Leg 56, September-October 1977; Leg 57, October-December 1977.* (edited by Lee, M., Stout, L.N., Langseth, M., Okada, H., Adelseck, C.G., Jr., Bruns, T.R., Harper, H.E., Jr., Kurnosov, V.B., Mueller, G., Murdmaa, I.O., Pisciotto, K.A., Robinson, P., Sakai, T., Thompson, P.R., Whelan, J.K., Worries, H., von Huene, R., Nasu, N., Arthur, M.A., Barron, J.A., Bell, G.D., Cadet, J.P., Carson, B., Fujioka, K., Honza, E., Keller, G., Moore, G.W., Reynolds, R., Sato, S. & Shaffer, B.L.). *Initial Reports of the Deep Sea Drilling Project* **56-57**, 463-470.
- Nelson, A. R. and Manley, W. F. 1992. Holocene coseismic and aseismic uplift of Isla Mocha, south-central Chile. *Quaternary International* **15/16**, 61-76.
- Nieuwland, D. A., Leutscher, J. H. and Gast, J. 2000. Wedge equilibrium in fold-and-thrust belts; prediction of out-of-sequence thrusting based on sandbox experiments and natural examples. *Geologie en Mijnbouw* **79**(1), 81-91.
- Pardo-Casas, F. and Molnar, P. 1987. Relative motion of the Nazca (Farallon) and South American Plates since Late Cretaceous time. *Tectonics* **6**(3), 233-248.
- Paterson, M. S. 1978. *Experimental rock deformation.* Springer, New York. pp. 254.
- Paterson, M. S. 2001. Relating experimental and geological rheology. *Int. Jour. Earth Science* **90**(1), 157-167.
- Patzig, R., Shapiro, S. A., Asch, G., Giese, P. and Wigger, P. subm. Seismogenic plane of the Andean subduction zone

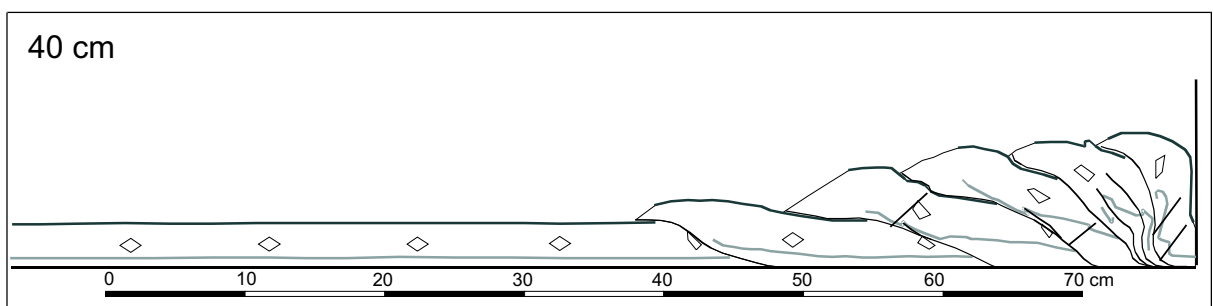
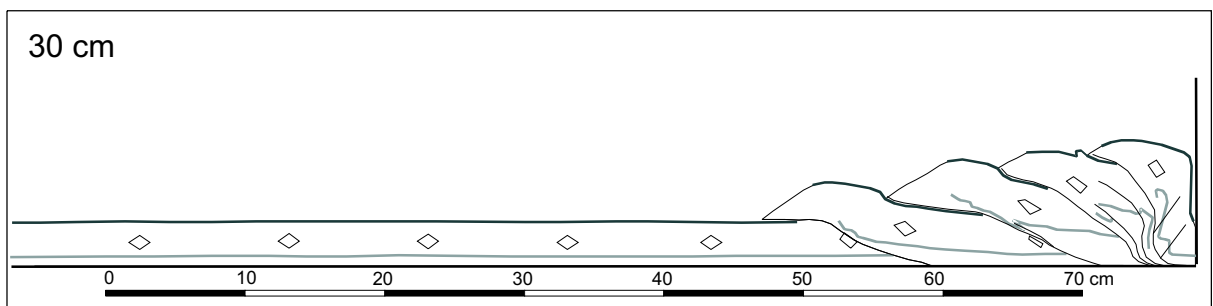
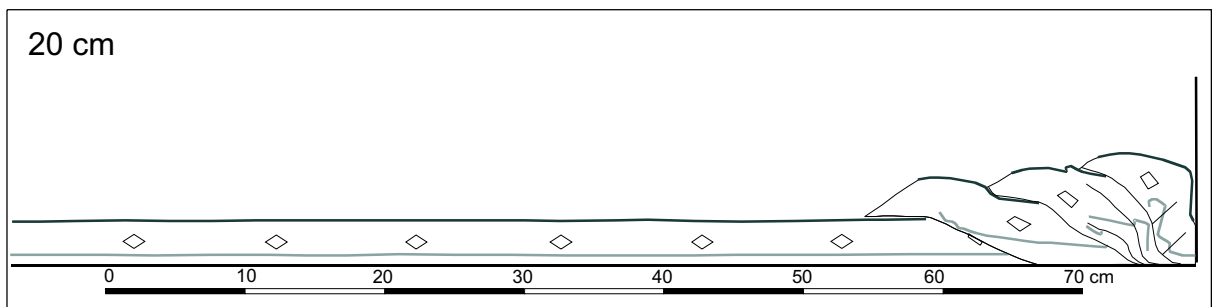
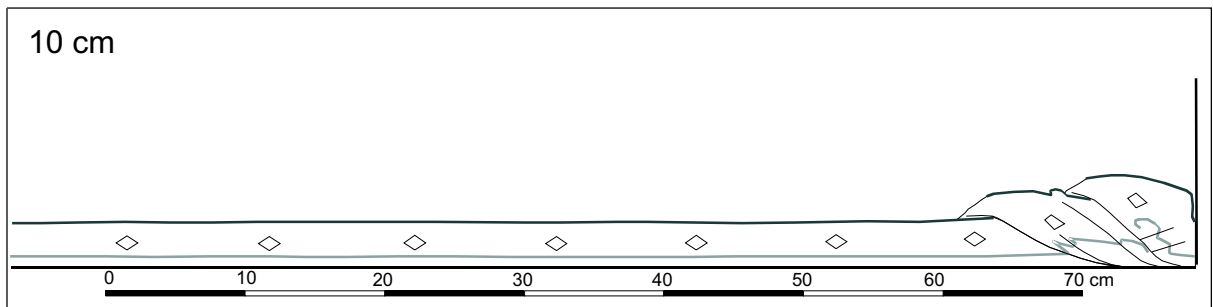
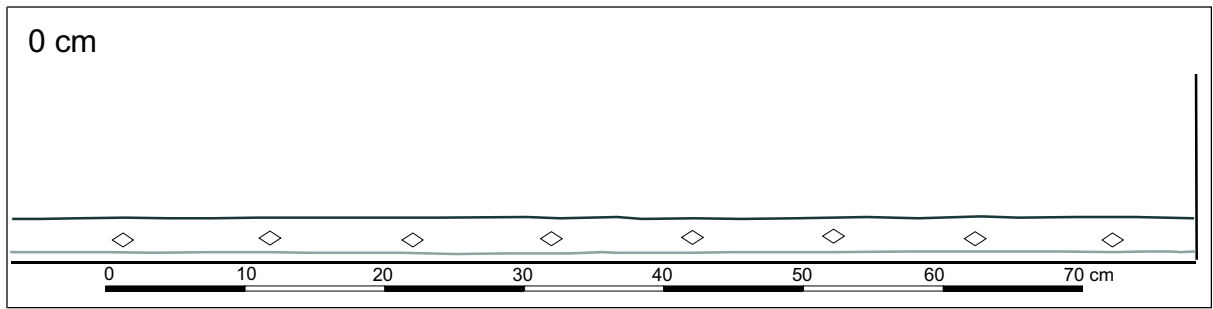
- from aftershocks of the 1995 Antofagasta (Chile) earthquake.
- Patzwahl, R., Mechie, J., Schulze, A. and Giese, P. 1999. Two-dimensional velocity models of the Nazca Plate subduction zone between 19.5 degrees S and 25 degrees S from wide-angle seismic measurements during the CINCA95 project. *JGR* **104**(4), 7293-7317.
- Pelz, K. 2000. Tektonische Erosion am zentralandinen Forearc (20°-24°S). *Scientific Technical Report STR00/20*, 118.
- Pineda, V. 1986. Evolución paleogeográfica de la cuenca sedimentaria Cretácico-Terciaria de Arauco. In: *Geología y Recursos Minerales de Chile* (edited by Frutos, J., Oyarzun, R., Pinchaera, M.). Universidad de Concepcion, 375-390.
- Platt, J. P. 1986. Dynamic of orogenic wedges and the uplift of high-pressure metamorphic rocks. *Geol. Soc. of Americ. Bull.* **97**, 1037-1053.
- Platt, J. P. 1988. The mechanics of frontal imbrication; a first-order analysis. *Geologische Rundschau* **77**(2), 577-589.
- Platt, J. P. 1990. Thrust mechanics in highly overpressured accretionary wedges. *JGR* **95**(B6), 9025-9034.
- Platt, J. P., Leggett, J. K., Young, J., Raza, H. and Alam, S. 1985. Large-scale sediment underplating in the Makran accretionary prism, southwest Pakistan. *Geology* **13**, 507-511.
- Radke, U. 1989. Marine Terrassen und Korallenriffe - Das Problem der quartären Meeresspiegelschwankungen erläutert an Fallstudien aus Chile, Argentinien und Barbados. *Düsseldorfer Geologische Schriften* **27**, 195-203.
- Ramberg, H. 1981. Gravity, deformation and the earth's crust. Academic Press, New York. pp. 452.
- Ranalli, R. 1987. Rheology of the earth. Allen & Unwin, Wellington. pp. 366.
- Ranero, C. R. and von Huene, R. 2000. Subduction erosion along the Middle America convergent margin. *Nature* **404**(6779), 748-752.
- Reuther, C.-D. and Potent, S. 2001. Neotectonics and active movements at the Southern Chilean Plate Margin - dynamics of the Arauco-Bio-Bio trench-arc system. *Schriftenreihe DGG* **14**, 162-613.
- Rutland, R. W. R. 1971. Andean orogeny and ocean floor spreading. *Nature* **233**(5317), 252-255.
- Schanz, T. and Vermeer, P. A. 1996. Angles of friction and dilatancy of sand. *Géotechnique* **46**(1), 145-151.
- Schellart, W. P. 2000. Shear test results for cohesion and friction coefficients for different granular materials; scaling implications for their usage in analogue modelling. *Tectonophysics* **324**(1-2), 1-16.
- Scheuber, E. 1994. Tektonische Entwicklung des nordchilenischen aktiven Kontinentalrandes: Der Einfluß von Plattenkonvergenz und Rheologie. pp. 131.
- Scheuber, E., Bogdanic, C. T., Jensen, A. I. and Reutter, K. J. 1994. Tectonic development of the North Chilean Andes in relation to plate convergence and magmatism since the Jurassic. In: *Tectonics of the southern Central Andes; structure and evolution of an active continental margin*. (edited by Reutter, K. J., Scheuber, E. & Wigger, P. J.). Springer-Verlag, Berlin, Federal Republic of Germany, 121-139.
- Scheuber, E. and Reutter, K.-J. 1992. Magmatic arc tectonics in the Central Andes between 21° and 25°S. *Tectonophysics* **205**, 127-140.
- Scholl, D. W. and von Huene, R. 2001. Evolution of convergent margins - impact of new and reassessed observations on rates of crustal recycling and arc magmatic additions. *Schriftenreihe der DGG* **14**, 190-191.
- Scholl, D. W., von Huene, R., Vallier, T. L. and Howell, D. G. 1980. Sedimentary masses and concepts about tectonic processes at underthrust ocean margins. *Geology* **8**(12), 564-568.
- Schulze, D. 1994. Entwicklung und Anwendung eines neuartigen Ringschergerätes. *Aufbereitungs-Technik* **35**(10), 524-535.
- Schweller, W. J., Kulm, L. D. and Prince, R. A. 1981. Tectonics, structure, and sedimentary framework of the Peru-Chile Trench. *Mem. Geol. Soc. Am.* **154**, 232-349.
- Seely, D. R., Vail, P. R. and Walton, G. G. 1974. Trench slope model. In: *The geology of continental margins*. (edited by Burk, C. A. & Drake, C. L.). Springer-Verlag, New York, United States, 249-260.
- SERNAGEOMIN. 1980. Mapa Geológico de Chile. 1:1000000. Instituto de Investigaciones Geológicas.
- Shapiro, S. A., Buske, S., Lüth, S., Orlowski, B., Patzig, R., Rothert, E., Sperlich, S., Wigger, P. and Yoon, M. 2001. Fluid-related structures and processes in the seismic image of the North Chilean subduction zone (between 20°S and 25°S). In: *Deformation Processes in the Andes, Interaction between edogenic and exogenic processes during subduction orogenesis* (edited by SFB-267). Report for the Research Period 1999-2001, 213-233.
- Shemenda, A. I. and Grocholsky, A. L. 1992. Physical modelling of lithosphere subduction in collision zones. *Tectonophysics* **216**, 273-290.
- Sibson, R. H. 1974. Frictional constraints on thrust, wrench and normal faults. *Nature* **249**, 542-544.
- Sibson, R. H. 1990. Conditions for fault-valve behaviour. In: *Deformation Mechanisms, Rheology and tectonics* (edited by Kneipe, R. J., Rutter, E.H.). *Geological Society Special Publications* **54**, 15-28.
- Smith, W. H. F., Sandwell, D. T. 1997. Global Seafloor Topography from Satellite Altimetry and Ship Depth Soundings. *Science* **277**, 1956-1962.
- Springer, M. 1999. Interpretation of heat-flow density in the Central Andes. *Tectonophysics* **306**, 377-395.
- Stern, C. 1991. Role of subduction erosion in the generation of Andean magmas. *Geology* **19**, 78-81.
- Stern, C. R. 1989. Pliocene to present migration of the volcanic front, Andean Southern Volcanic Zone. *Revista Geologica de Chile* **16**, 145-162.
- Storti, F. and McClay, K. 1995. Influence of syntectonic sedimentation on thrust wedges in analogue models. *Geology* **23**(11), 999-1002.
- Straffelini, G. 2001. A simplified approach to the adhesive theory of friction. *Wear* **249**, 79-85.
- Terzaghi, K. 1943. Theoretical Soil Mechanics. John Wiley, New York.
- Turrini, C. and Ravaglia, A. 1999. Compressional structures in a multi-layer mechanical stratigraphy: Insights from the sand-box modelling. *Jour. of Conf. Abstracts, EUG* **4**, 607.

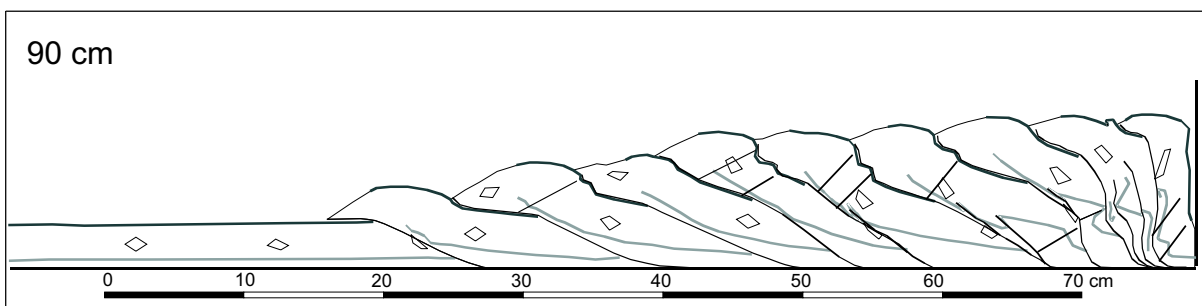
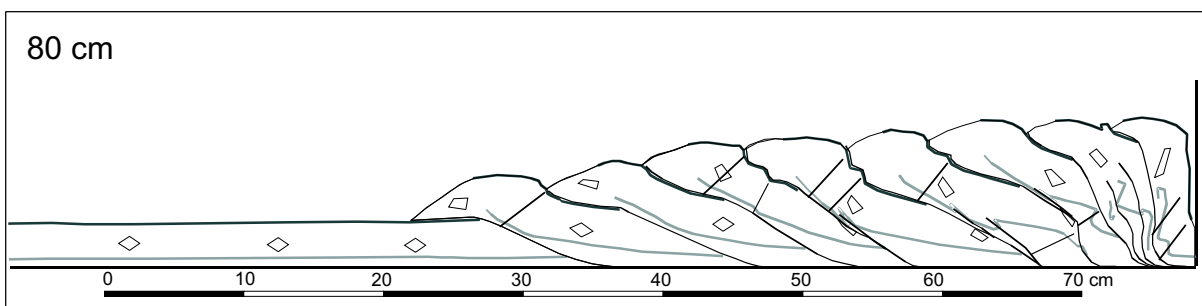
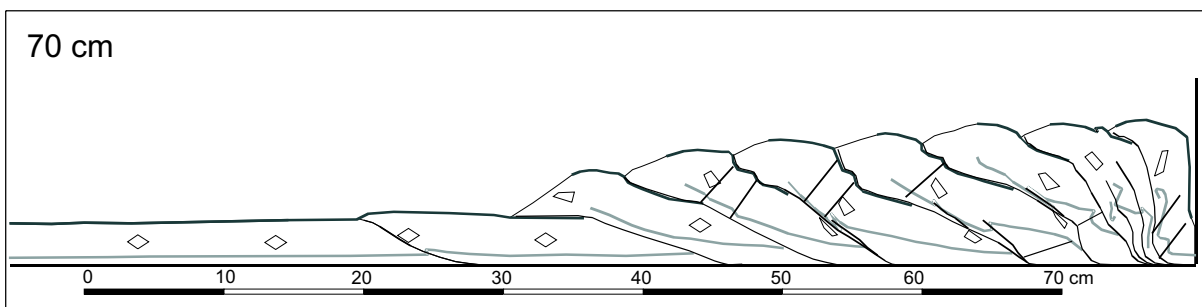
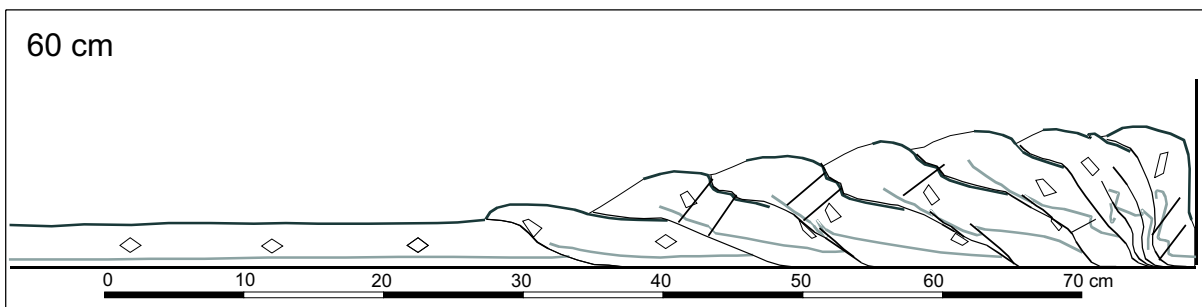
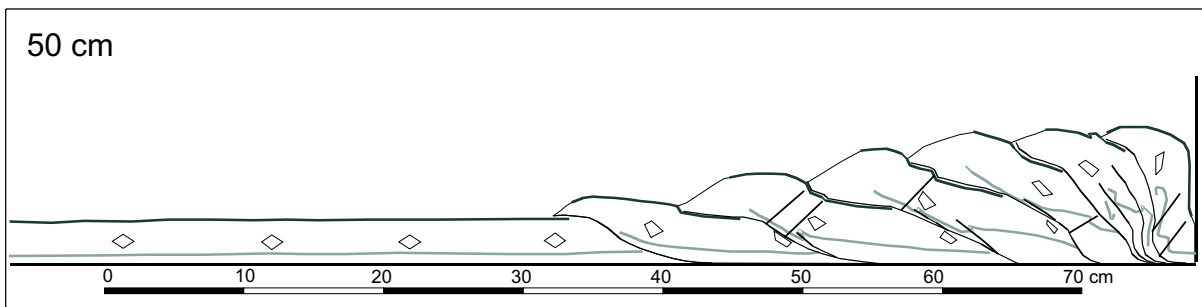
- Vaid, Y. P. and Sasitharan, S. 1992. The strength and dilatancy of sand. *Can. Geotech. J.* **29**, 522-526.
- Victor, P. 2000. Die Entwicklung der Altiplano Westflanke und ihre Bedeutung für die Plateaubildung und Krustenverdickung in N-Chile (20-21°S). *Scientific Technical Reports STR00/13*, 100.
- von Huene, R. and Culotta, R. C. 1989. Tectonic erosion at the front of the Japan Trench convergent margin. In: *Subduction zones; the Kaiko Project.* (edited by Cadet, J. P. & Uyeda, S.). Tectonophysics 160. Elsevier, Amsterdam, Netherlands, 75-90.
- von Huene, R. and Lallemand, S. E. 1990. Tectonic erosion along the Japan and Peru convergent margins. *Geological Society of America Bulletin* **102**(6), 704-720.
- von Huene, R. and Ranero, C. R. in press. Subduction erosion and basal friction along the sediment starved convergent margin off Antofagasta, Chile. *JGR*.
- von Huene, R. and Scholl, D. 2001. The true seaward edge of the continent at modern convergent margins. In: Margins Meeting, Int. Conf. and Annual Meeting of DGG and GV (edited by Roth S., R., A.). *Schriftenreihe DGG* **14**, Kiel, 99.
- von Huene, R. and Scholl, D. W. 1991. Observations at convergent margins concerning sediment subduction, subduction erosion, and the growth of continental crust. *Reviews of Geophysics* **29**(3), 279-316.
- von Huene, R., Weinrebe, W. and Heeren, F. 1999. Subduction erosion along the North Chile margin. In: Lithospheric structure and seismicity at convergent margins. (edited by Flueh, E. R. & Carbonell, R.). *Journal of Geodynamics* **27**, 345-358.
- Wang, W. H. and Davis, D. M. 1996. Sandbox model simulation of forearc evolution and noncritical wedges. *JGR* **101**(B5), 11,329-11,339.
- Weijmar, R. and Schmeling, H. 1986. Scaling of Newtonian and non-Newtonian fluid dynamics without inertia for quantitative modelling of rock flow due to gravity (including the concept of rheological similarity). *Phys. Earth Planet. Inter.* **43**, 316-330.
- Westbrook, G. K., Smith, M. J., Peacock, J. H. and Poulter, M. J. 1982. Extensive underthrusting of undeformed sediment beneath the accretionary complex of the Lesser Antilles subduction zone. *Nature* **300**(5893), 625-628.
- Wigger, P. J., Schmitz, M., Arandeda, M., Asch, G., Baldzuhn, S., Giese, P., Heinsohn, W. D., Martinez, E., Ricaldi, E., Roewer, P. and Viramonte, J. 1994. Variation in the crustal structure of the southern Central Andes deduced from seismic refraction investigations. In: *Tectonics of the southern Central Andes; structure and evolution of an active continental margin.* (edited by Reutter, K. J., Scheuber, E. & Wigger, P. J.). Springer-Verlag, Berlin, Federal Republic of Germany, 23-48.
- Willett, S., Beaumont, C. and Fullsack, P. 1993. Mechanical model for the tectonics of doubly vergent compressional orogens. *Geology* **21**(4), 371-374.
- Willett, S. D. 1992. Dynamic and kinematic growth and change of a Coulomb wedge. In: *Thrust tectonics.* (edited by McClay, K. R.). Chapman & Hall, London, United Kingdom, 19-31.
- Woodcock, N. H. 1986. The role of strike-slip fault systems at plate boundaries. *Philos. Trans. R. Soc. London* **A317**, 13-29.
- Wosnitza, E. M. 2002. Mountains of Wax - Continental Collision in Scaled Thermomechanical Analogue Experiments and Data Analyses. *Unpublished PhD Thesis, Freiburg University.* pp. 202.
- Zhao, W.-L., Davis, D., Dahlen, F. A. and Suppe, J. 1986. The origin of convex accretionary wedges; Evidence from Barbados. *JGR* **91**, 10246-10258.
- Ziegler, A. M., Barrett, S. F. and Scotese, C. R. 1981. Palaeoclimate, sedimentation and continental accretion. *Philosophical Transactions of the Royal Society of London, Series A: Mathematical and Physical Sciences* **301**, Royal Society of London, 253-264.

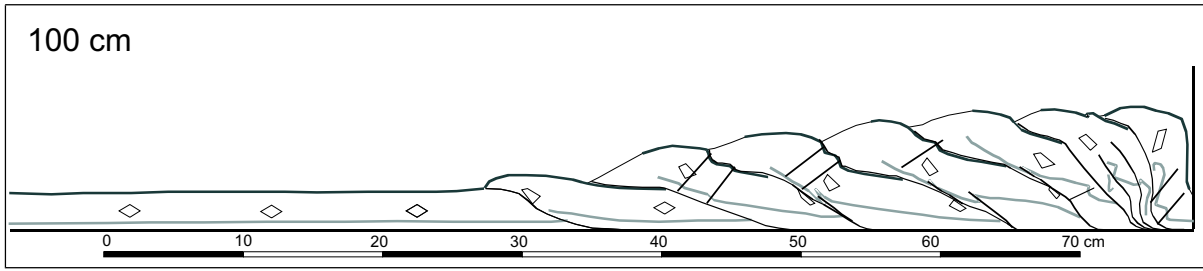
Appendix A

experiment	nr.	setup	incoming sand-layer thickness [mm] and material	initial wedge	initial surface slope [°]	conveyor belt	basal dip [°]	page
purely frontal accretion: variation of internal friction (Chapter 2):								
SIF	# 2.6	closed	35 (SIF)	no	0	paper	0	144
PIF	# 2.5	closed	35 (PIF)	no	0	paper	0	146
SIC1	# 2.7	closed	35 (SIC1)	no	0	paper	0	149
SHF	# 2.8	closed	35 (SHF)	no	0	paper	0	151
purely frontal accretion: variation of basal friction (Chapter 2):								
SP	# 2.11	closed	35 (SIC2)	no	0	sandpaper (< 400 μm)	0	153
LG	# 2.10	closed	35 (SIC2)	no	0	latex gum	0	157
coeval frontal and basal accretion (Chapter 3):								
HC	# 5.2	closed	32 (SIC2 with glass-bead horizon)	mortar	6	sandpaper (> 630 μm)	5	159
LC	# 5.3	closed	39 (SIC2 with glass-bead horizon)	mortar	6	sandpaper (> 630 μm)	5	169
LF	# 5.6	closed	39 (SIC2 with glass-bead horizon)	mortar	6	sandpaper (< 400 μm)	5	165
steady-state tectonic erosion (Chapter 4):								
SSC	# 3.3	closed	no	SIC2/mortar	37/0	sandpaper (< 400 μm)	10	173
PSC	# 3.5	closed	no	PIC2/mortar	37/0	sandpaper (< 400 μm)	10	176
SSO	# 3.6	open (10 mm)	no	SIC2/mortar	37/0	sandpaper (< 400 μm)	10	180
ASO	# 3.16	open (14 mm)	no	SIC2/lenses of SIC2 and glass-bead horizons (large)	37/0	sandpaper (< 400 μm)	10	185
SLC	# 3.7	closed	no	SIC2/mortar	37/0	sandpaper (< 400 μm)	10	184

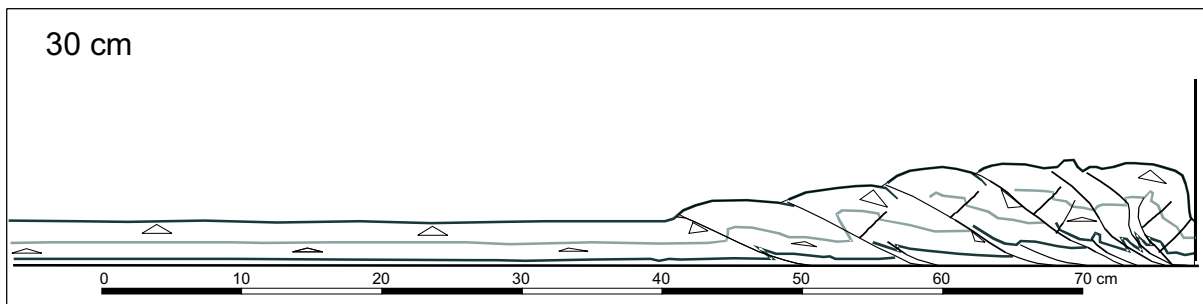
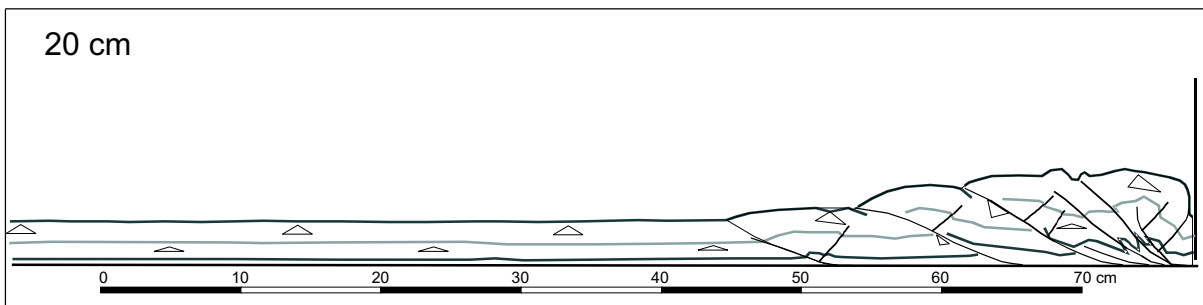
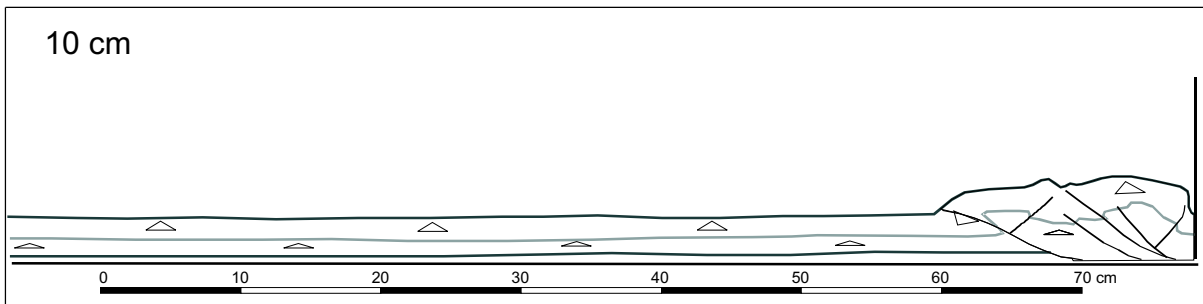
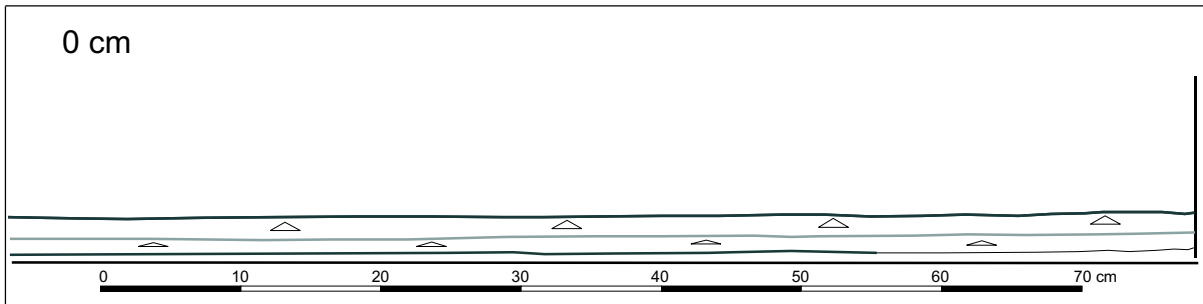
SIF experiment

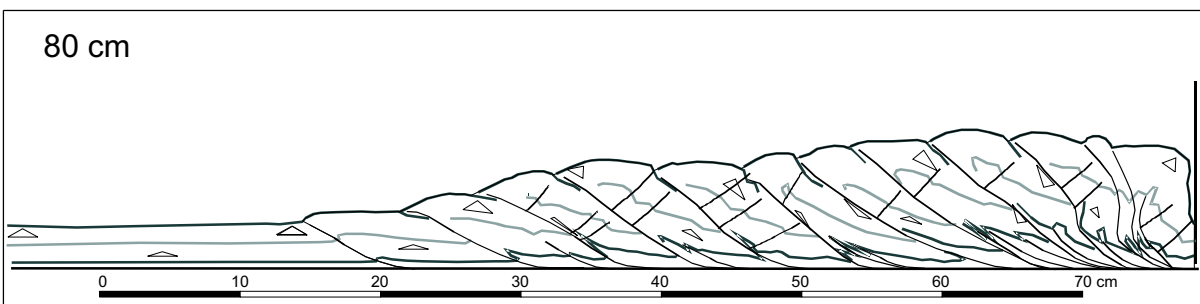
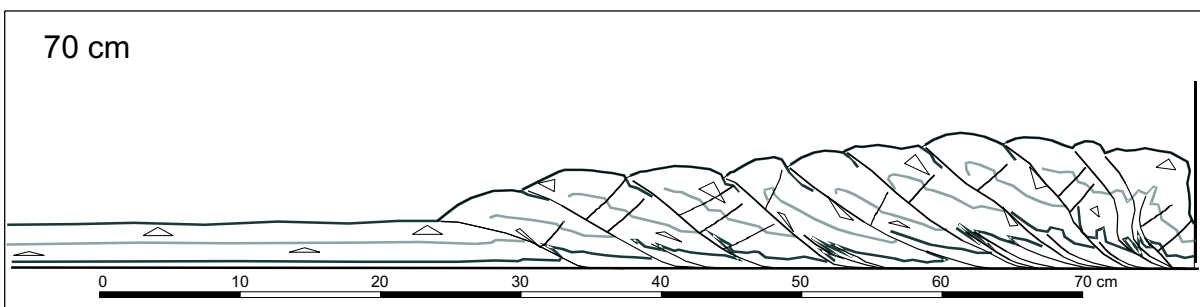
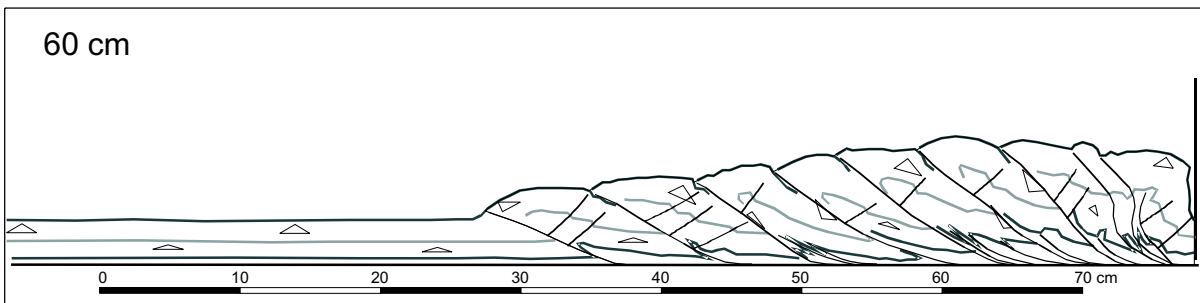
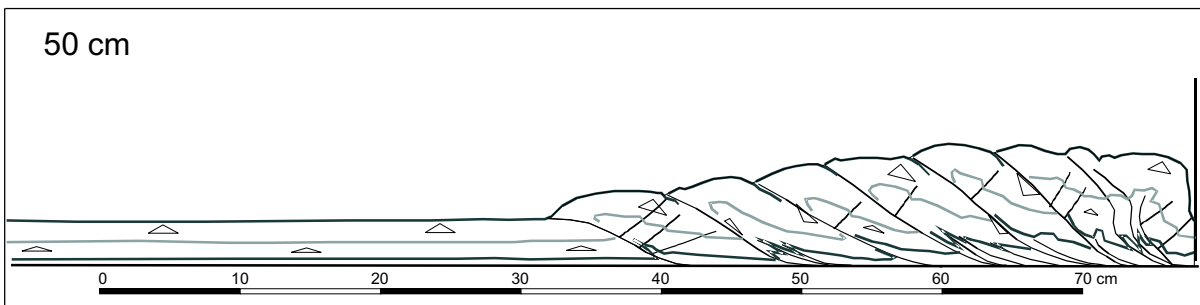
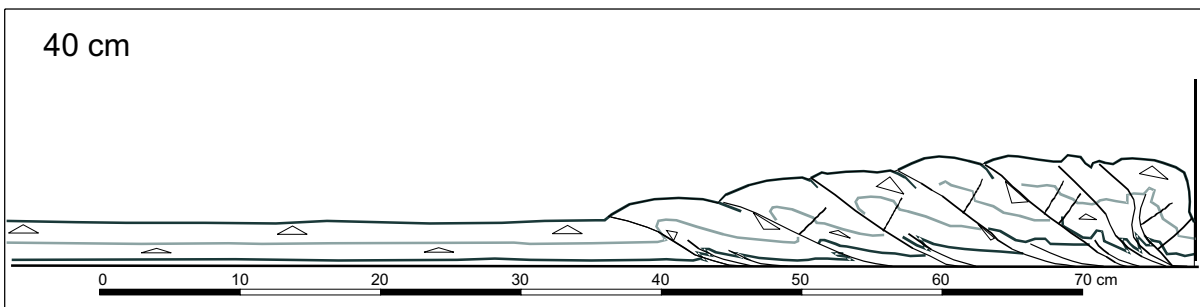




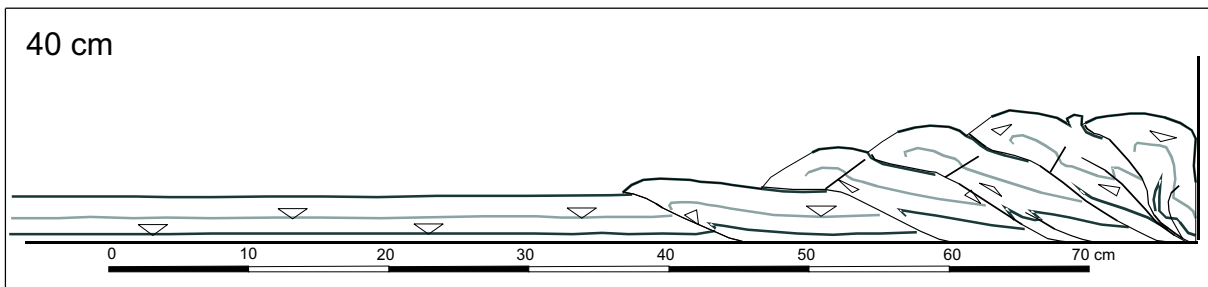
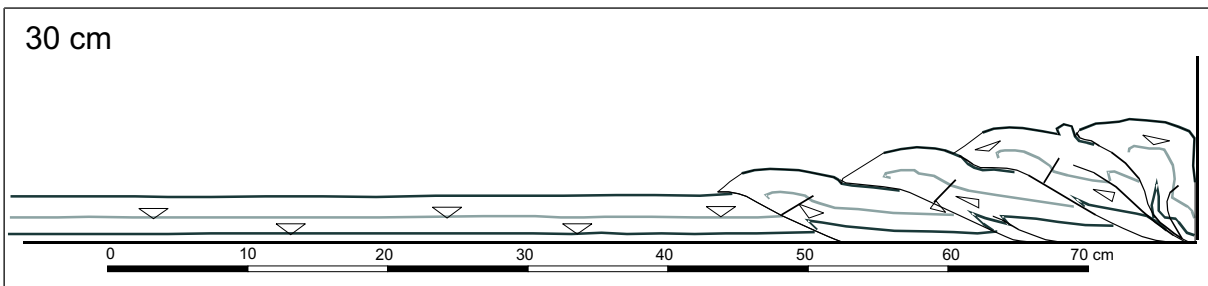
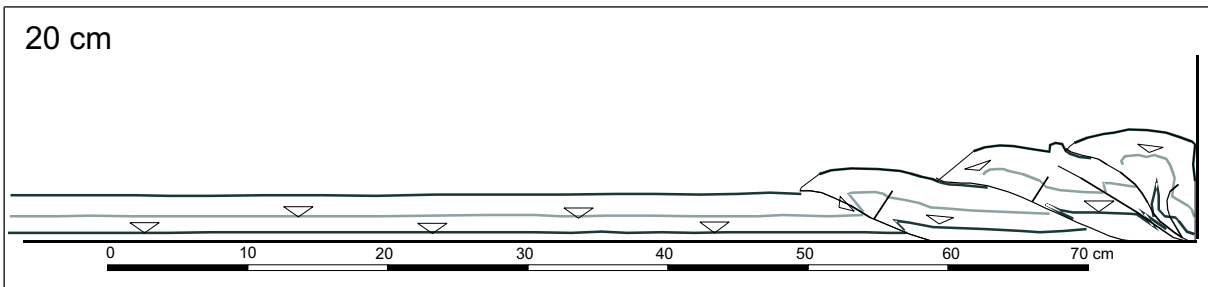
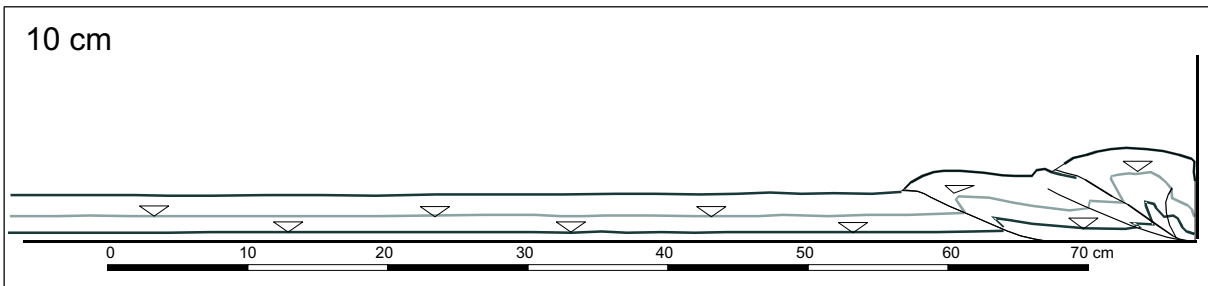
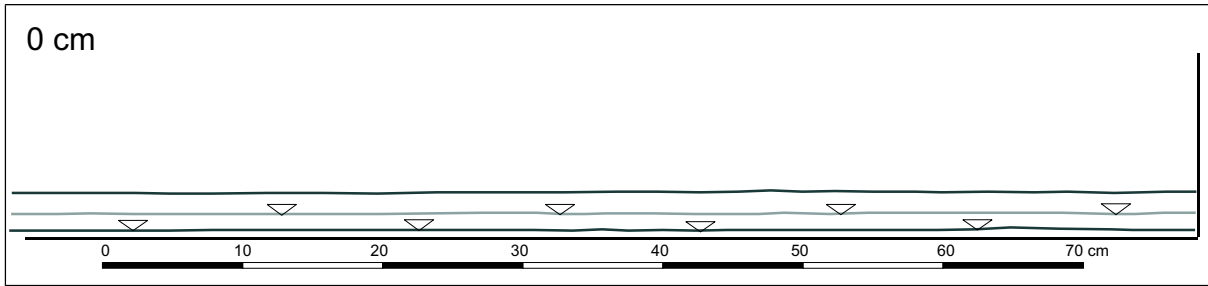


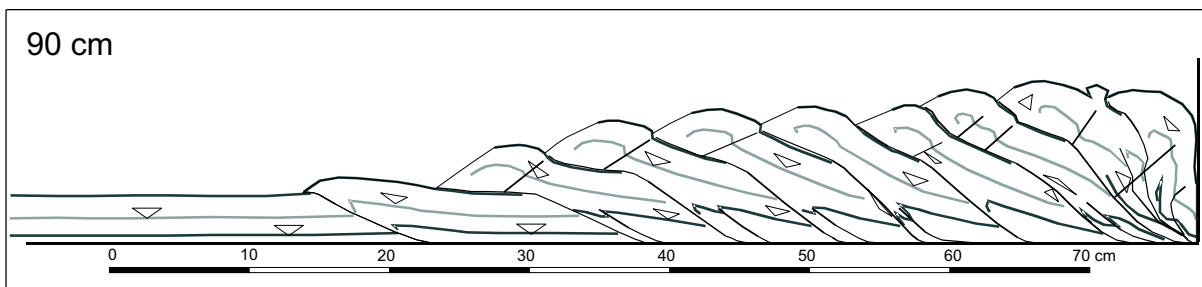
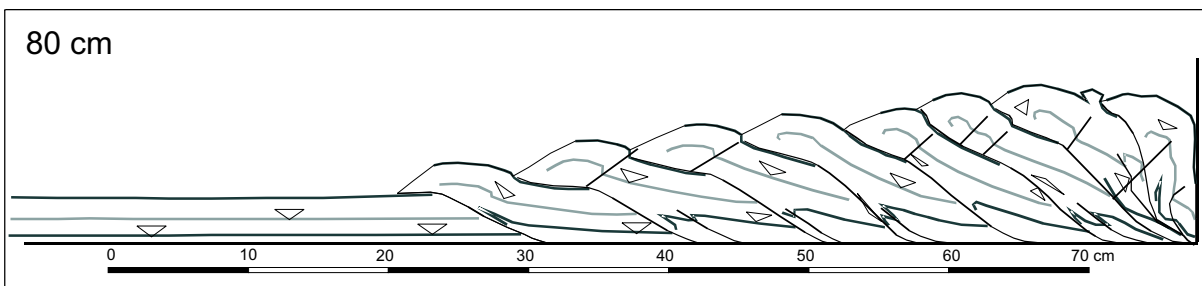
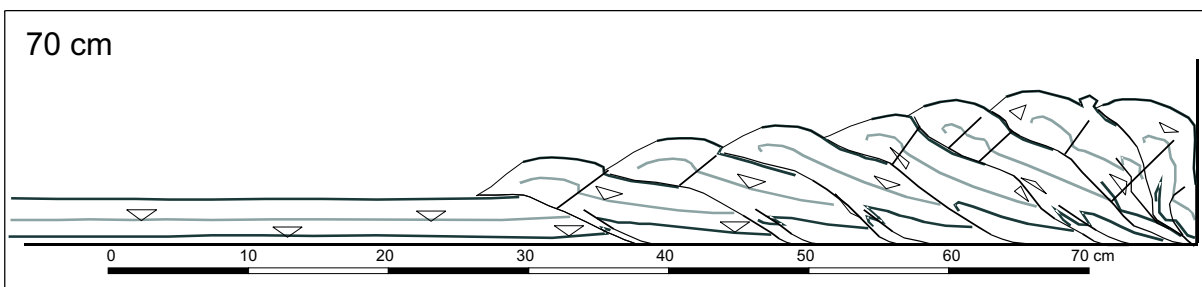
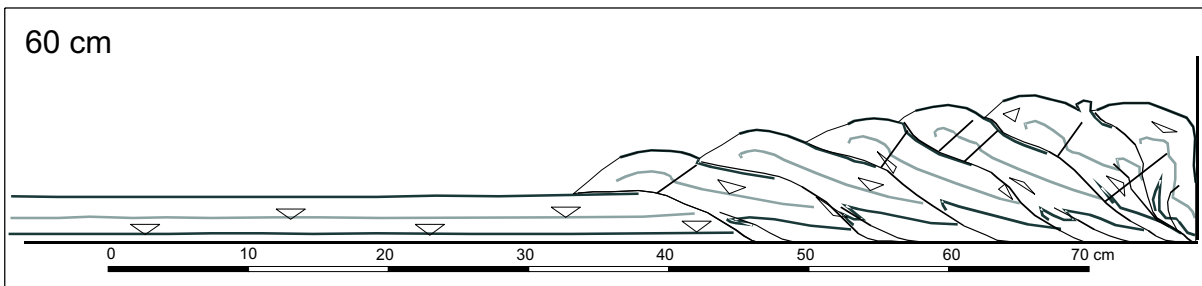
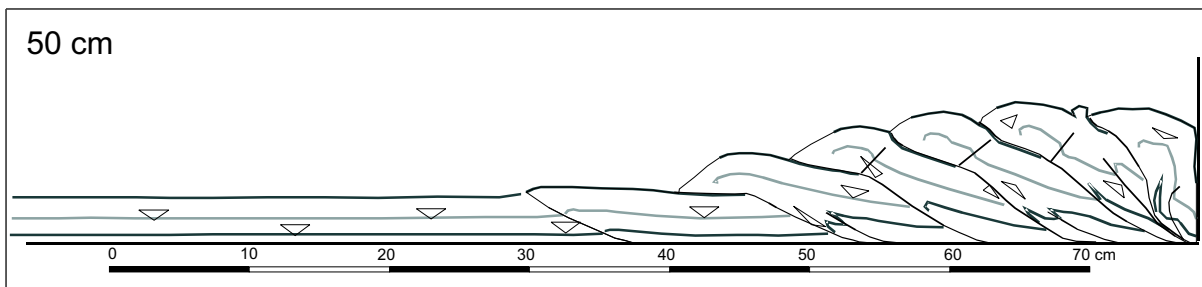
PIF experiment

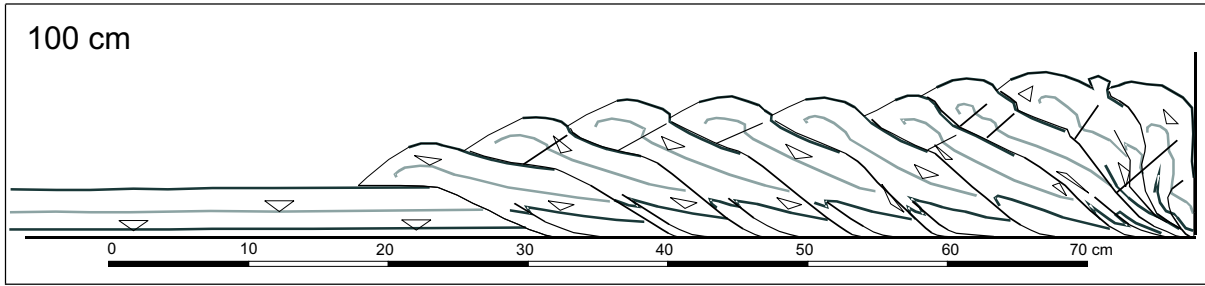




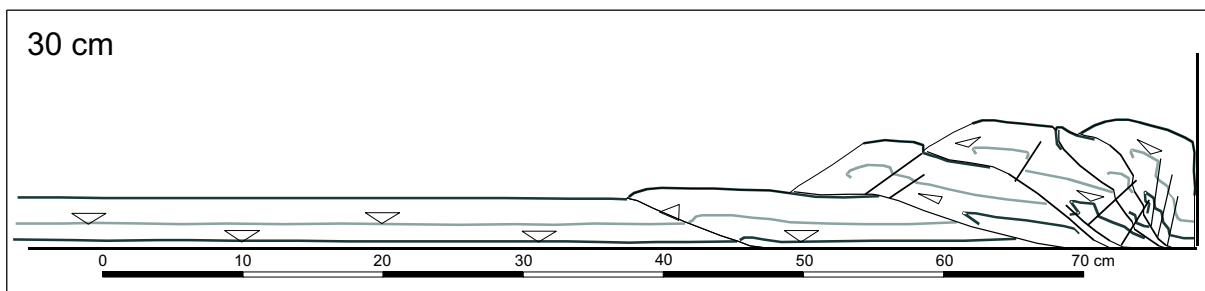
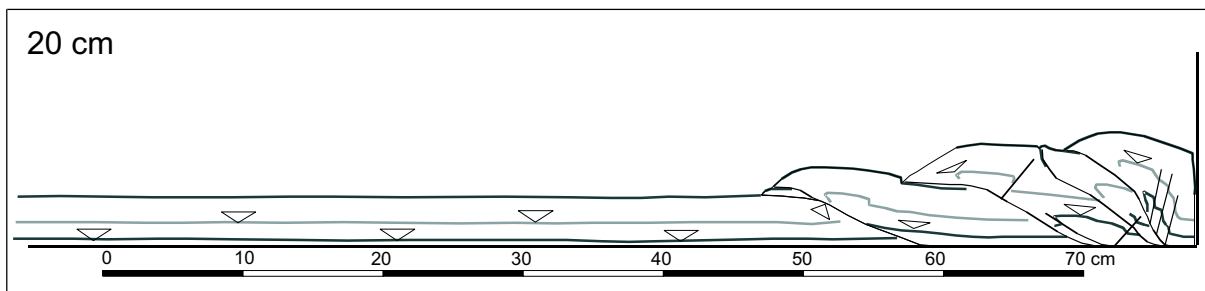
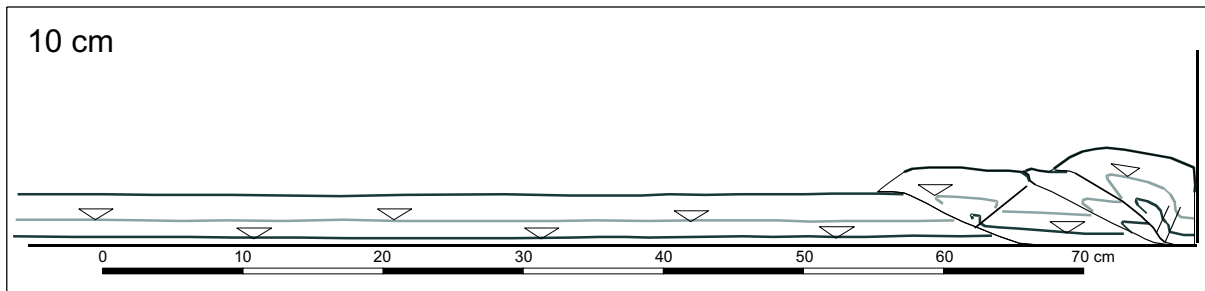
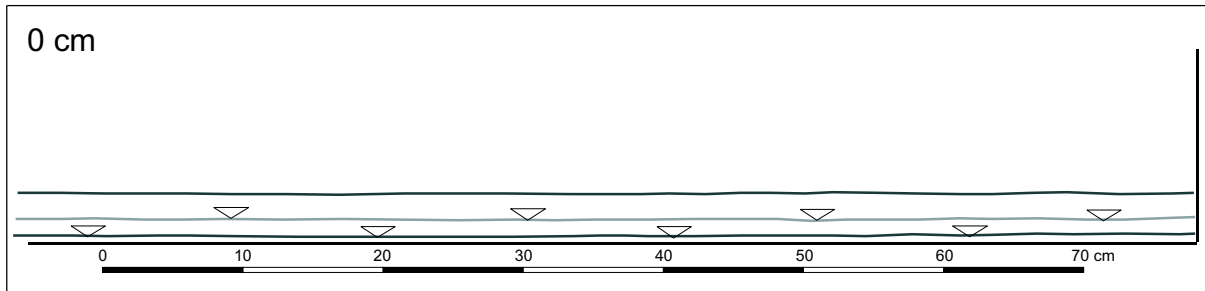
SIC1 experiment

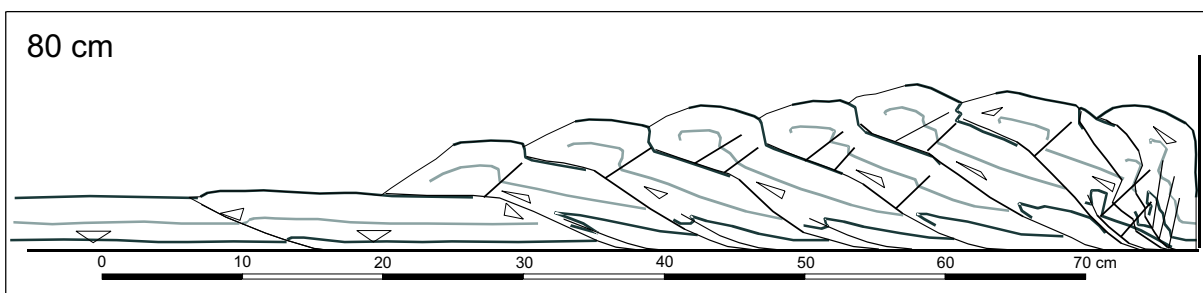
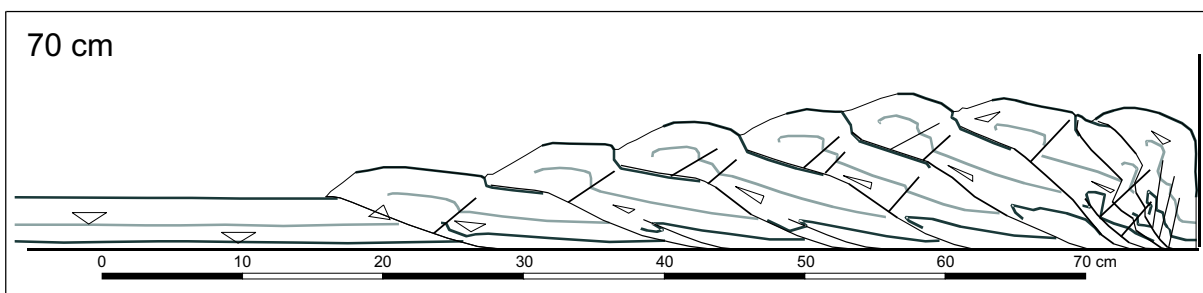
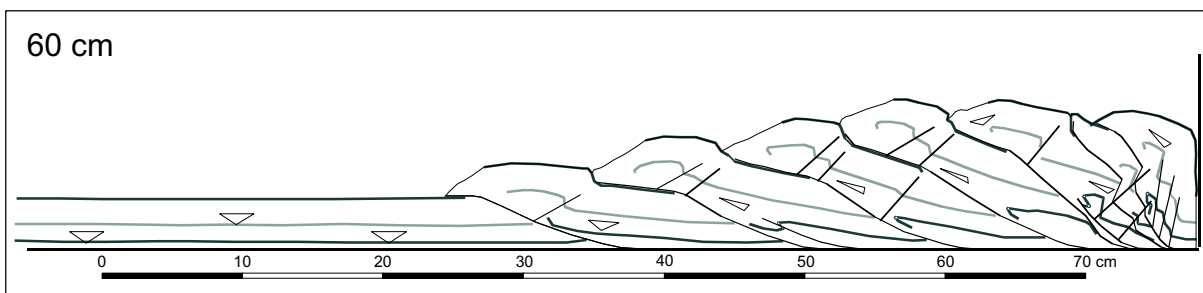
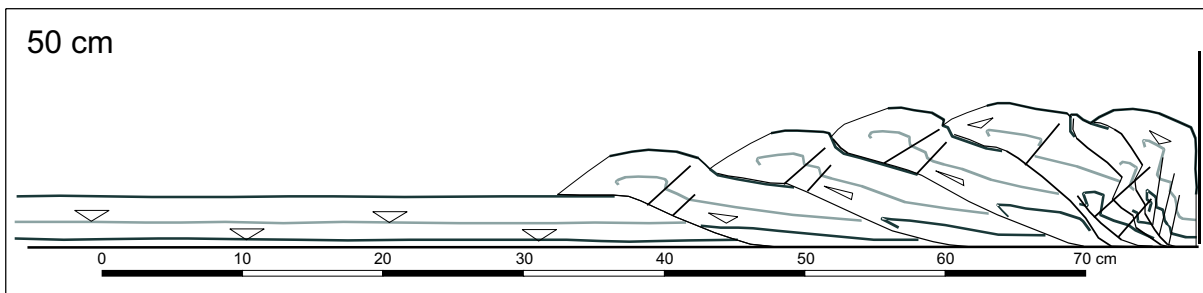
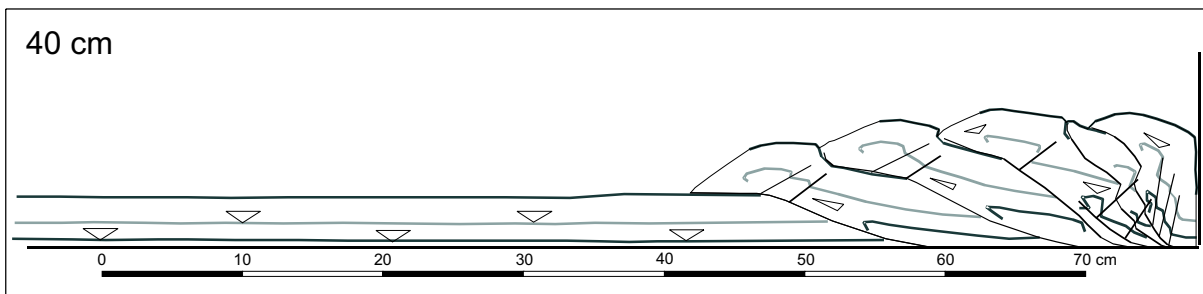


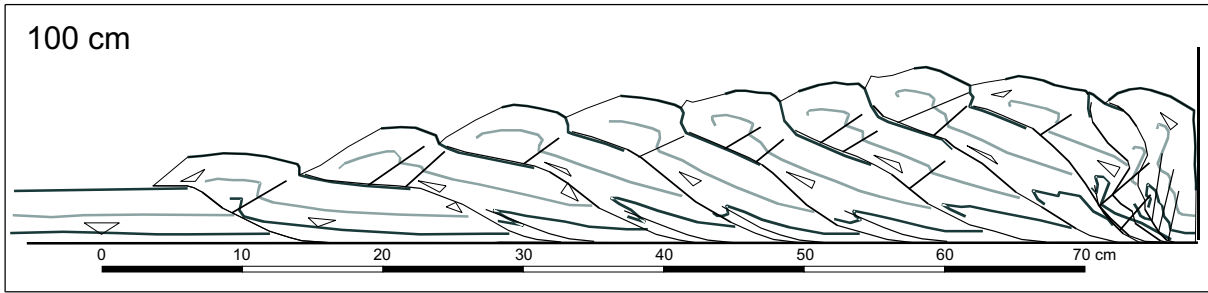
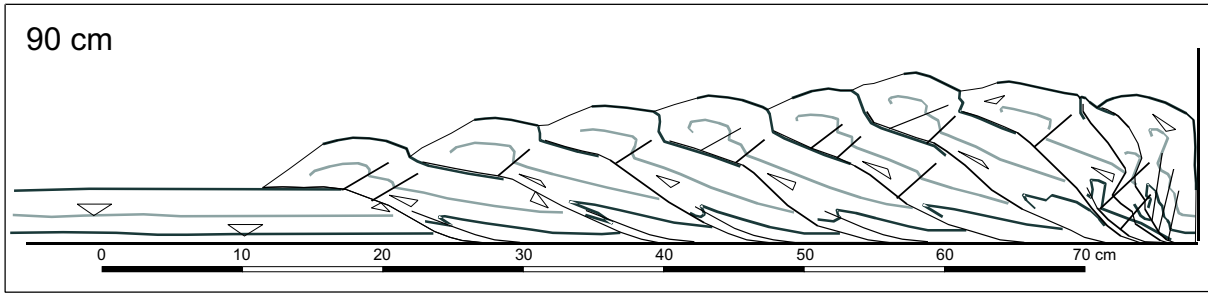




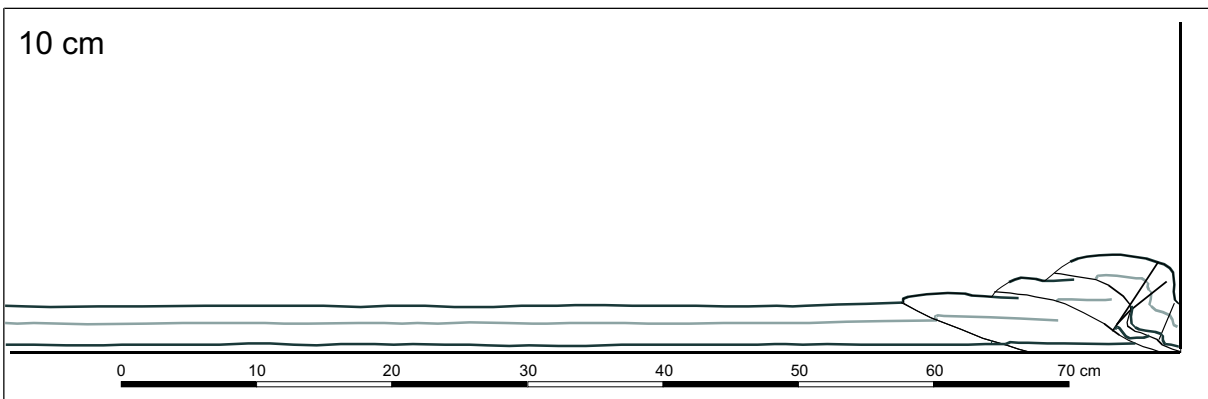
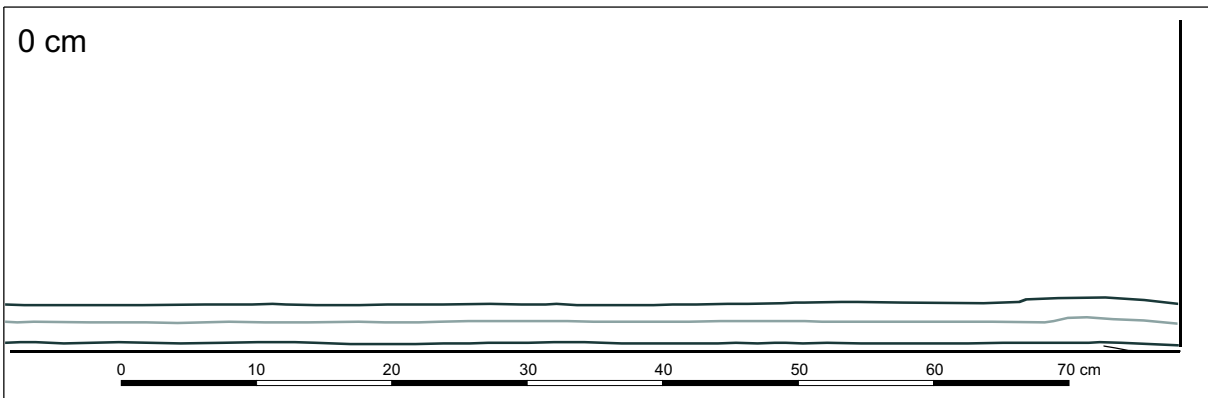
SHF experiment

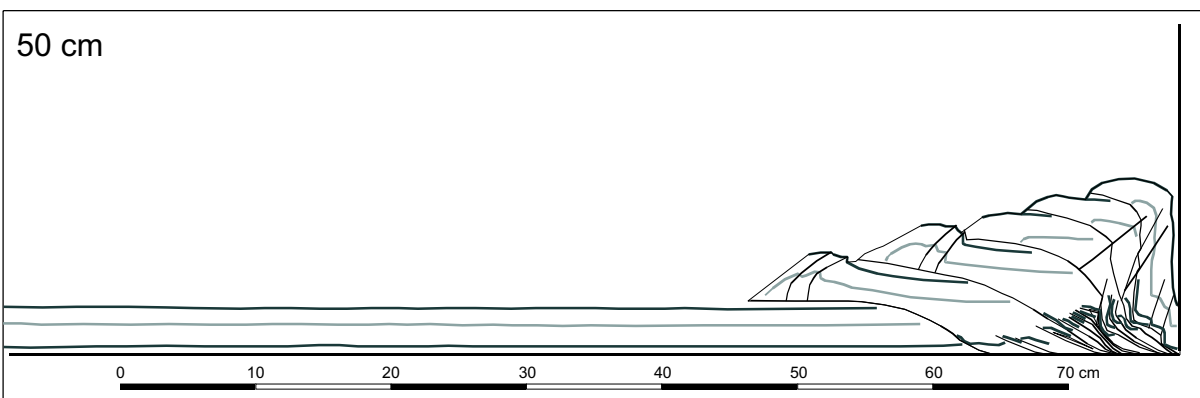
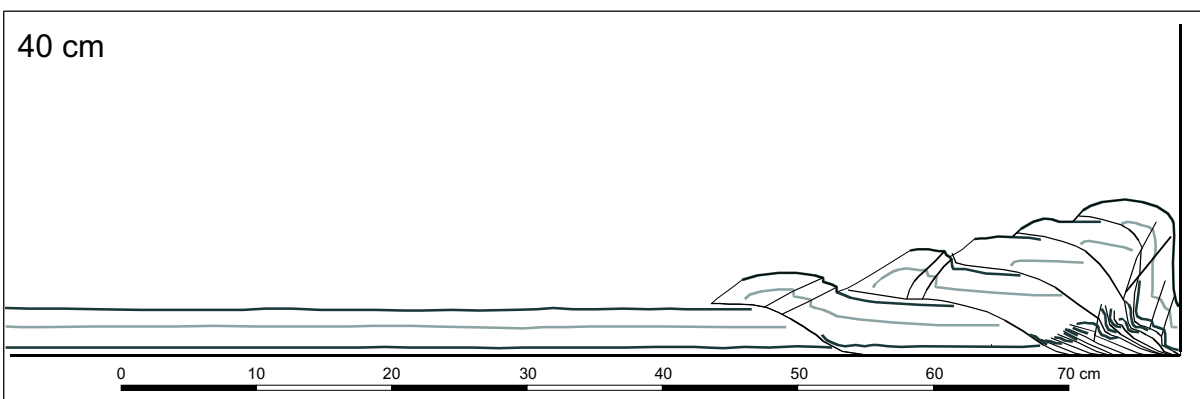
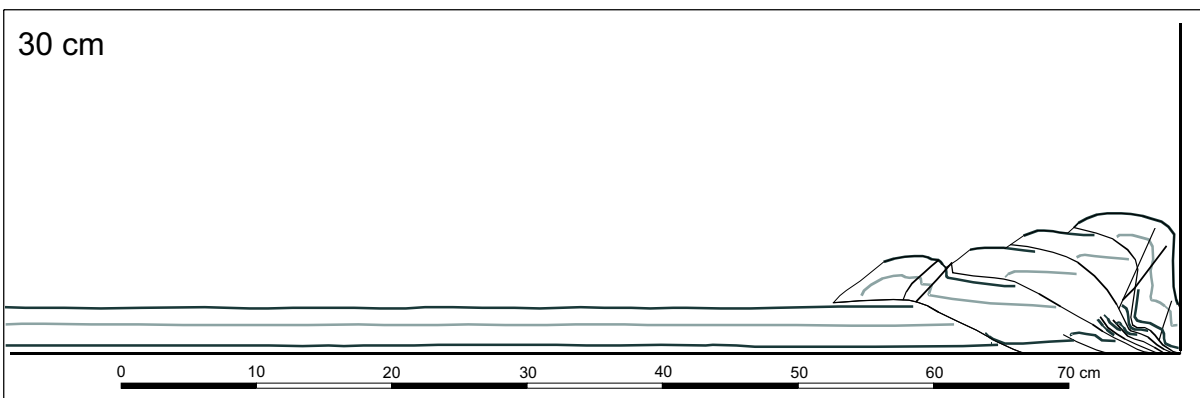
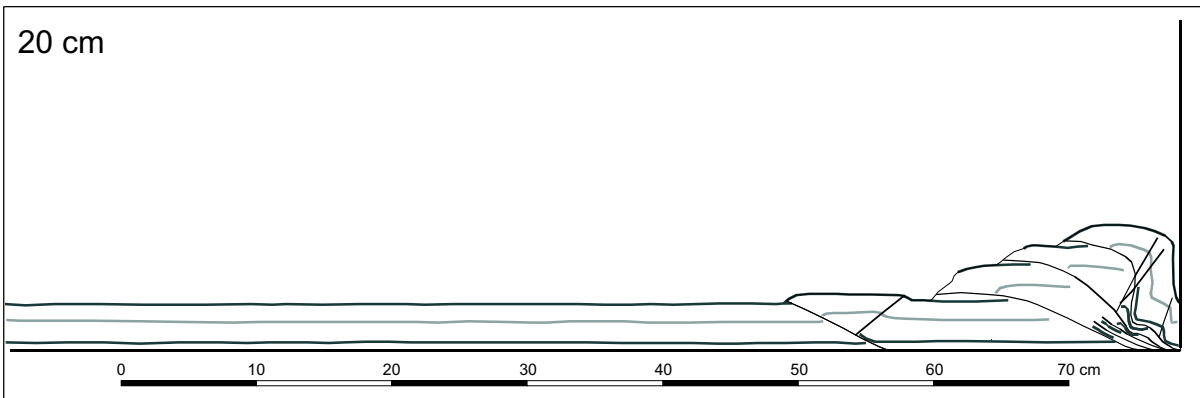


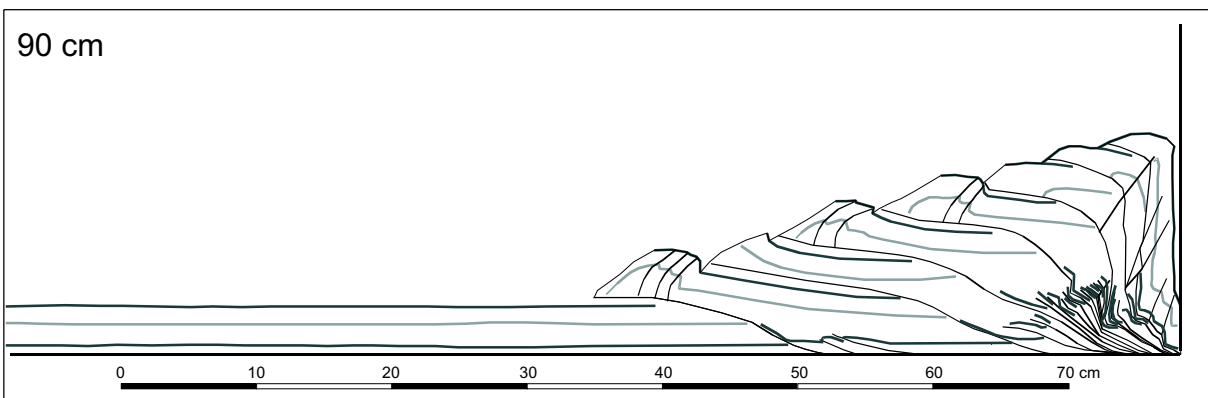
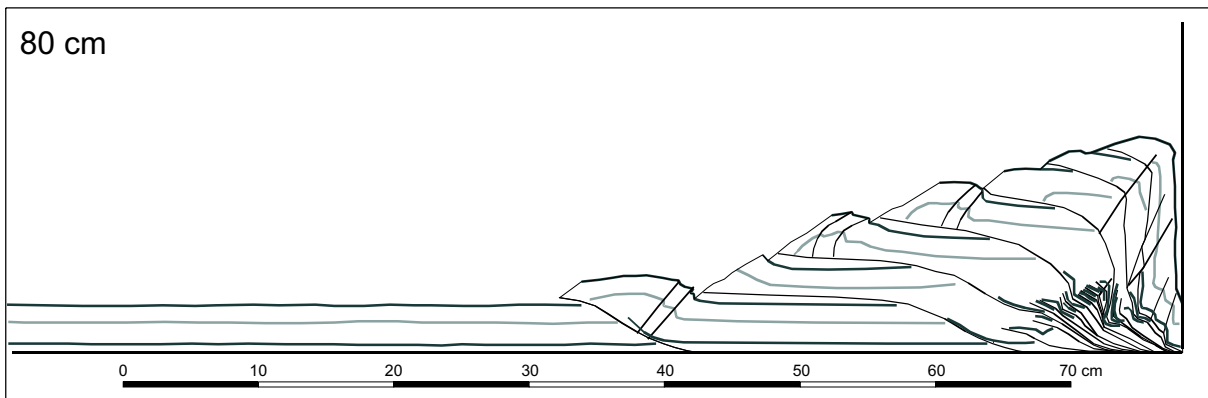
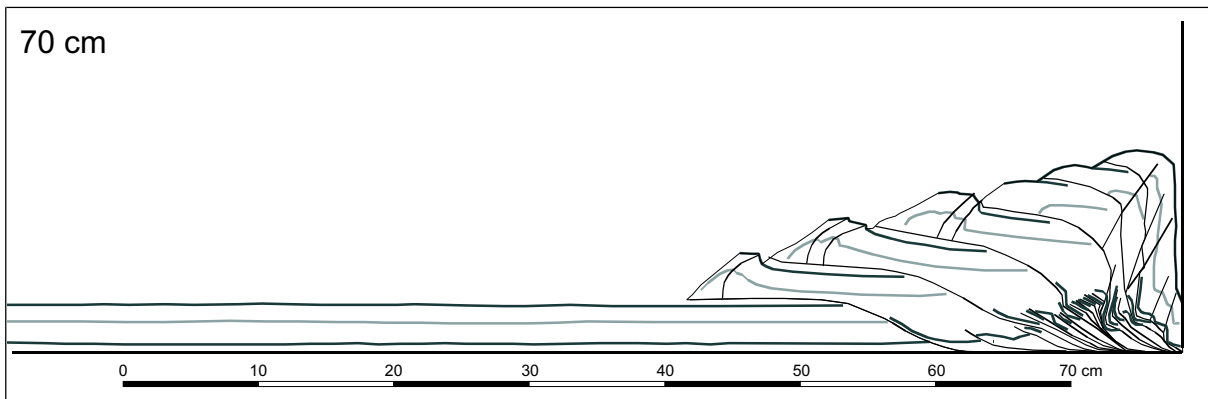
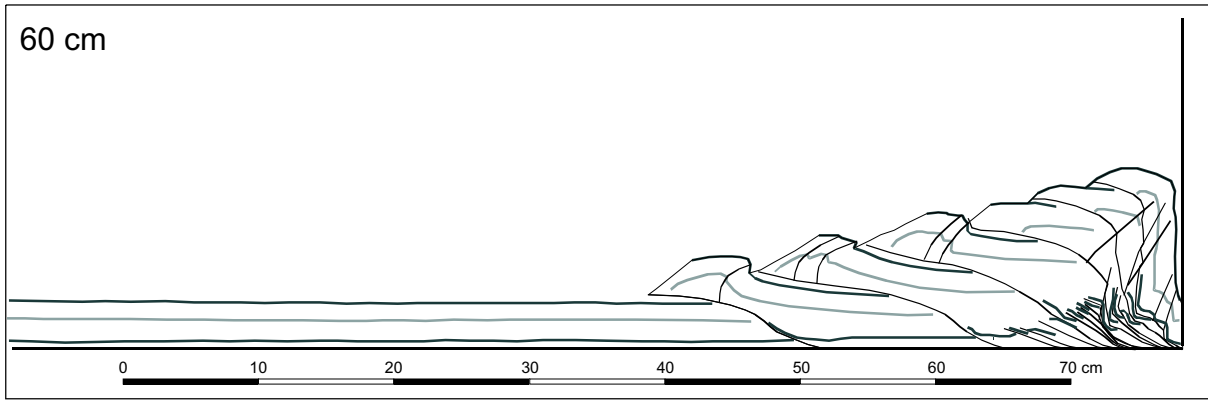


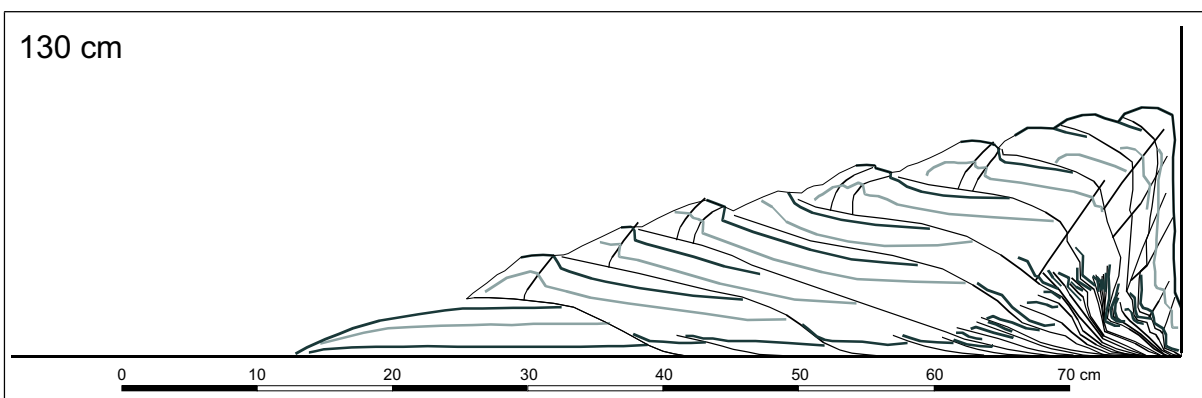
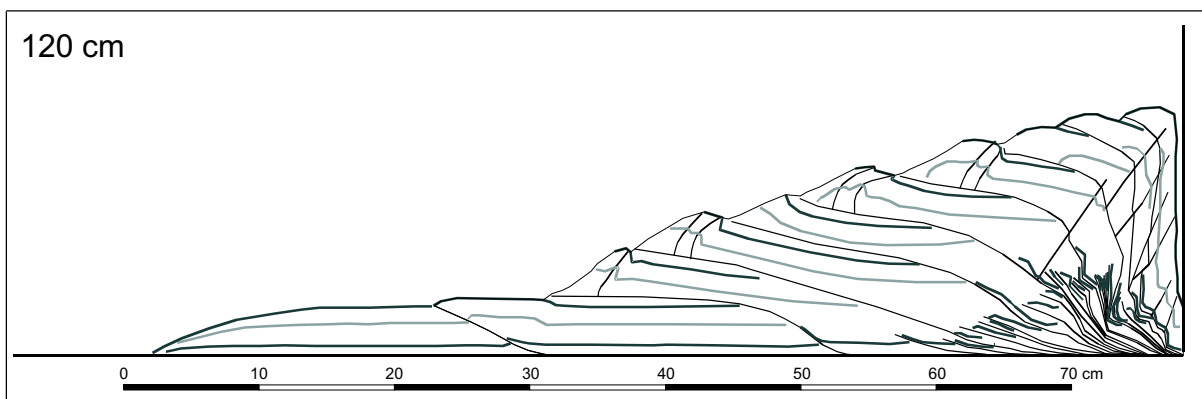
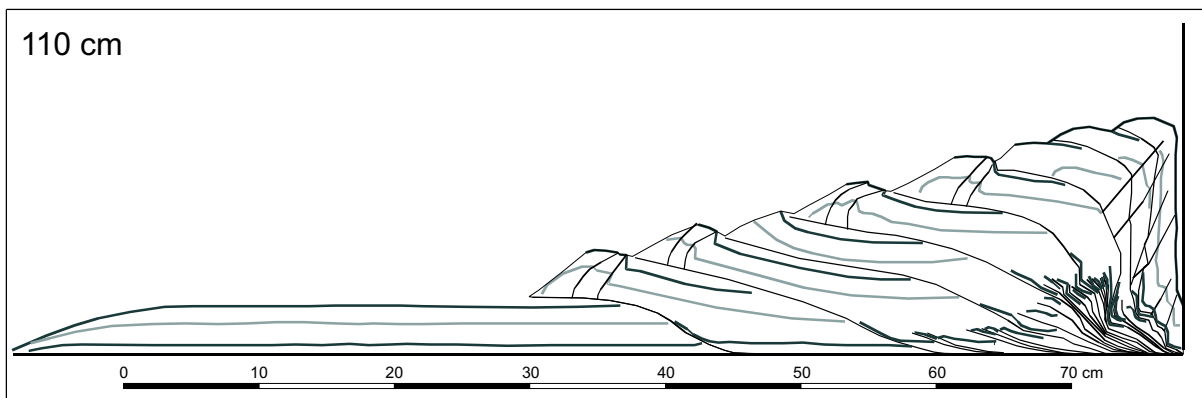
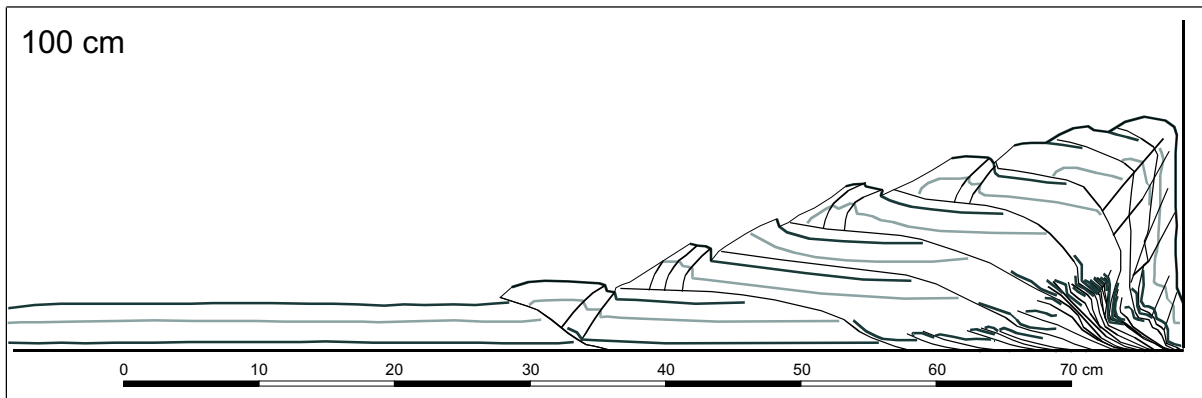


SP experiment

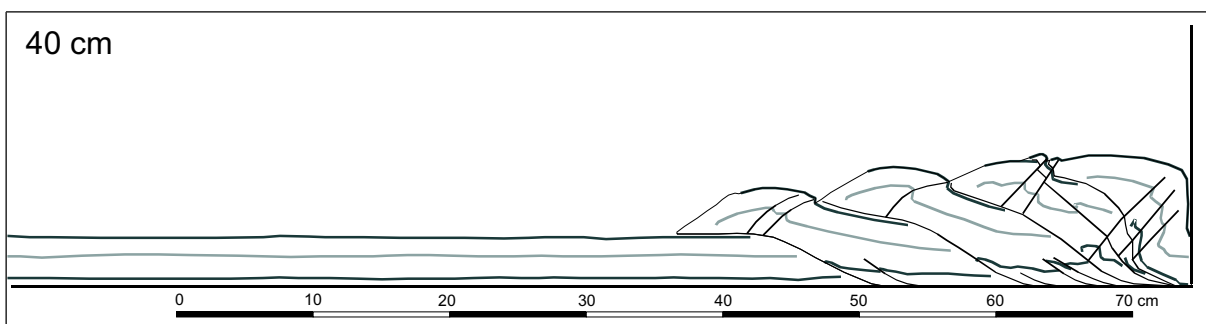
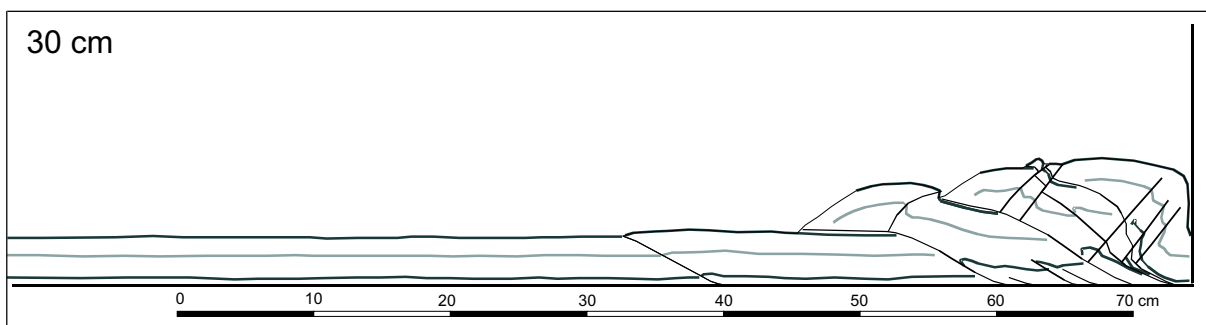
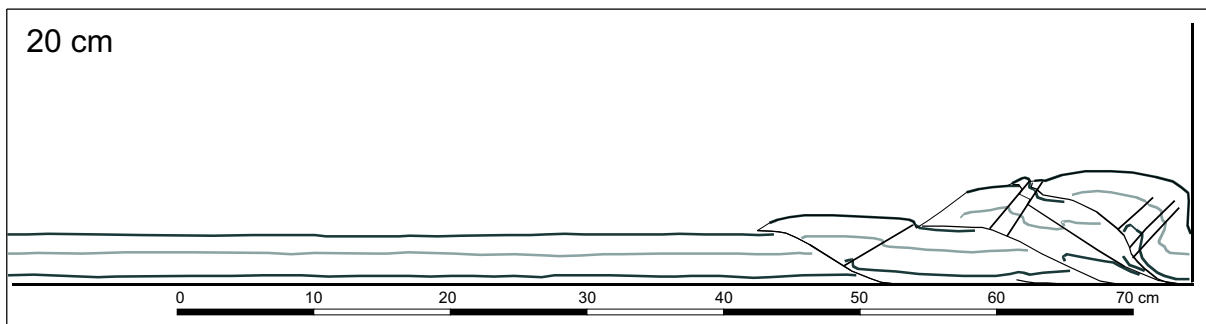
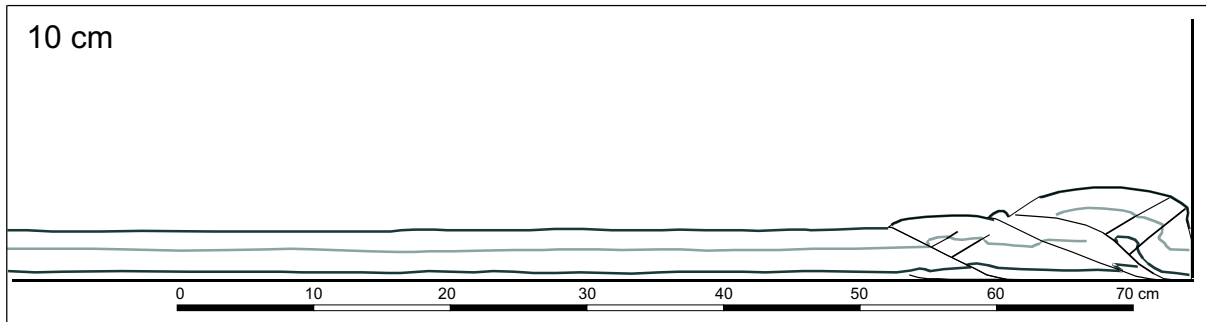
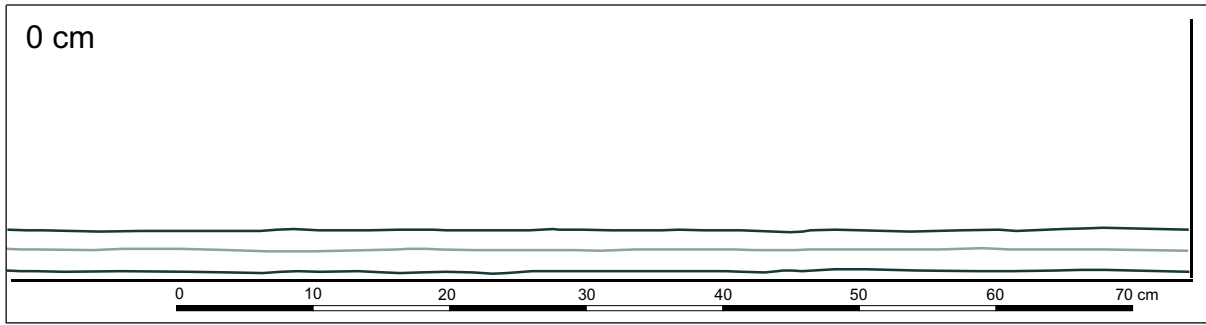


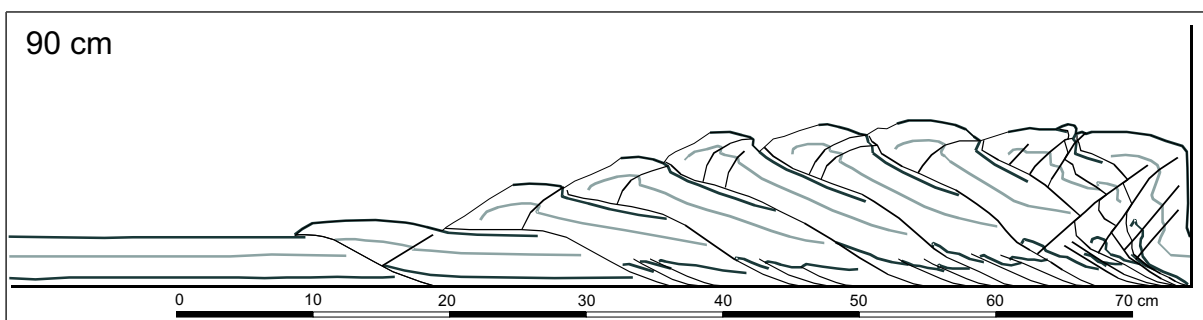
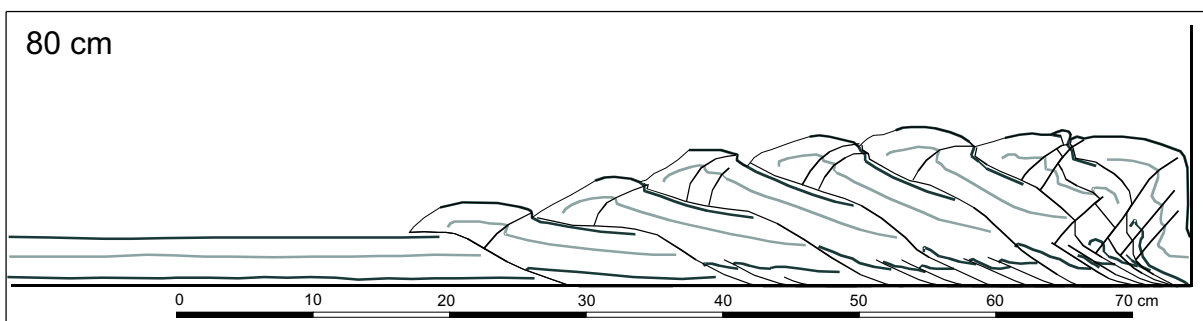
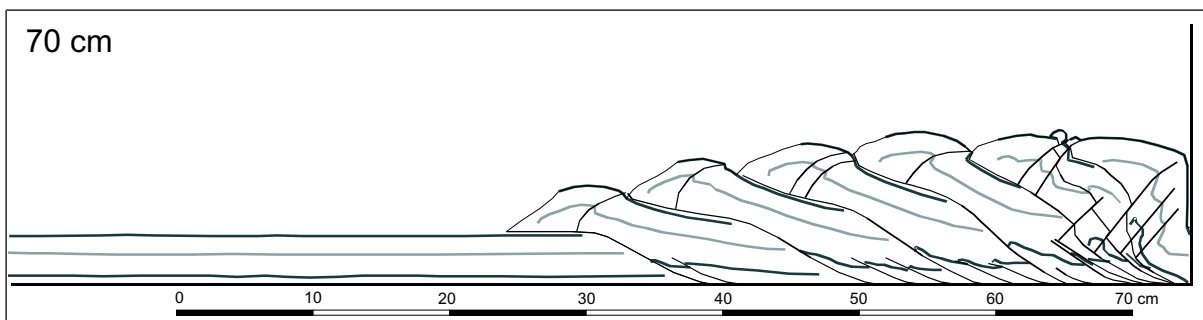
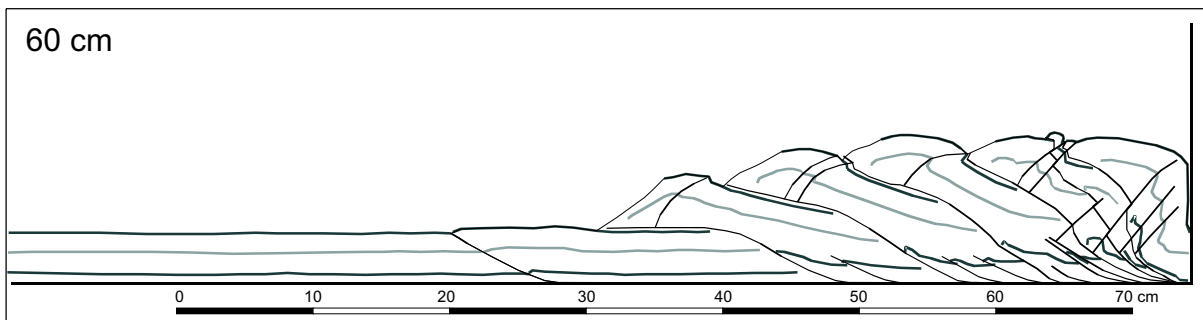
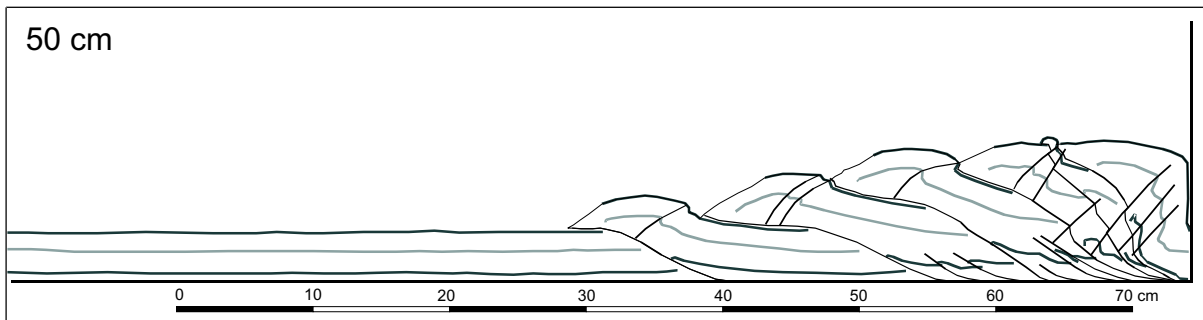


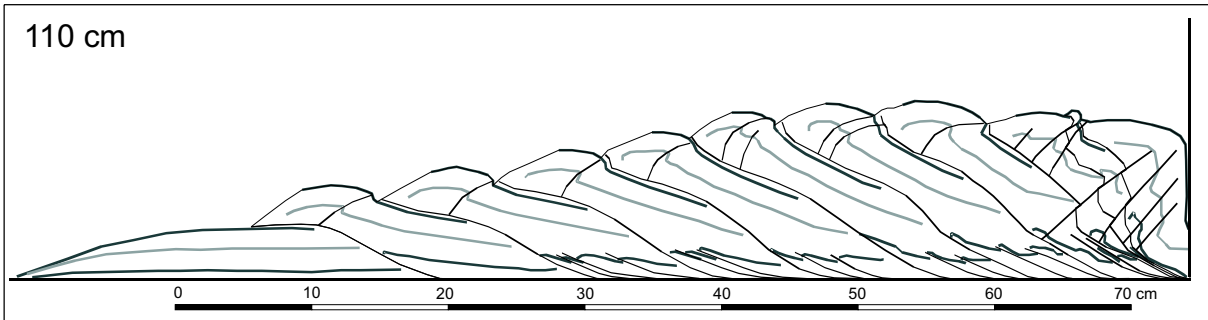
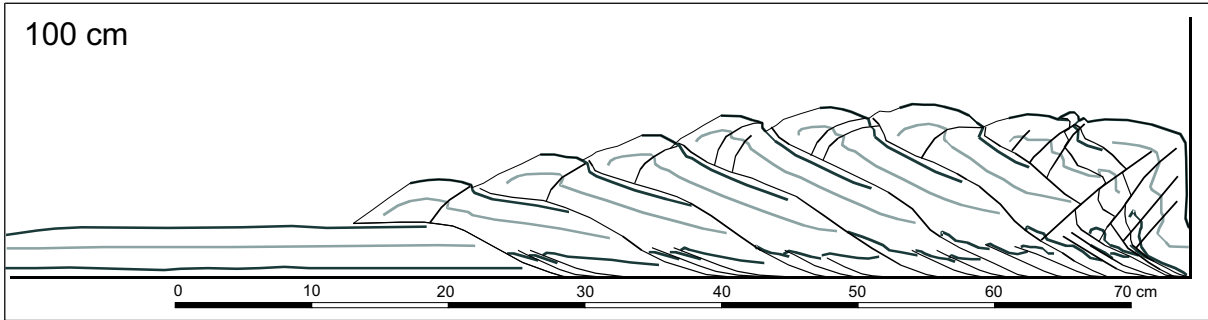




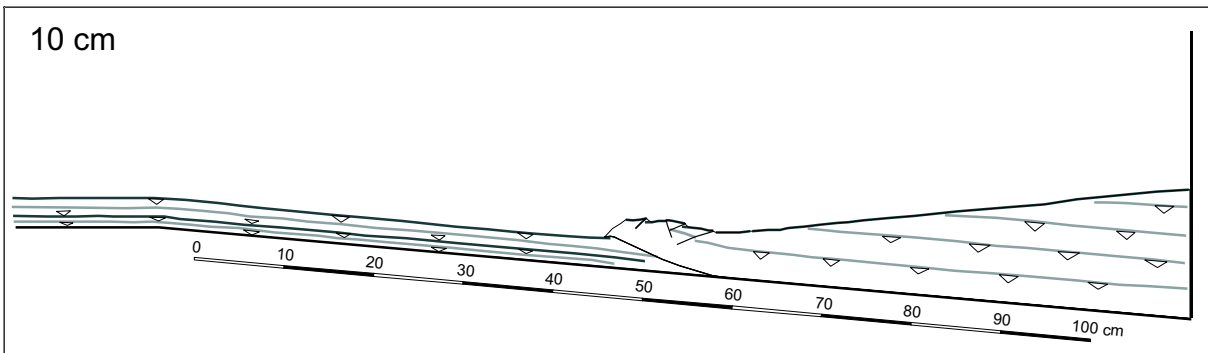
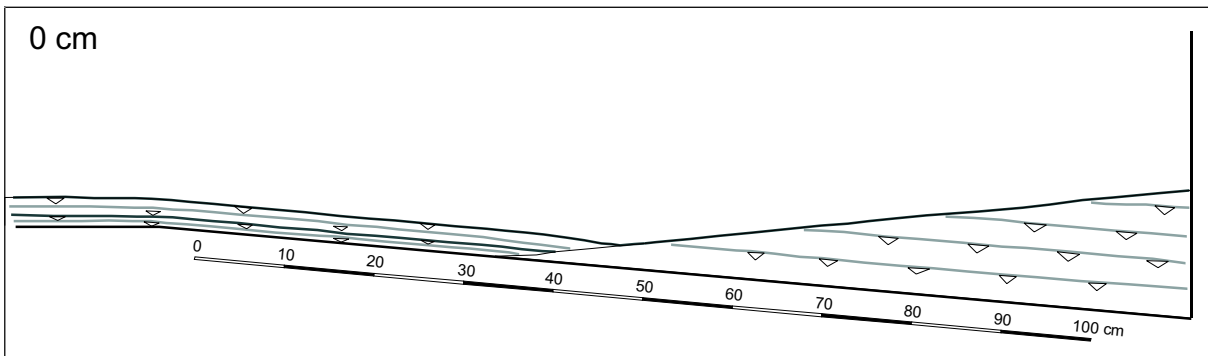
LG experiment

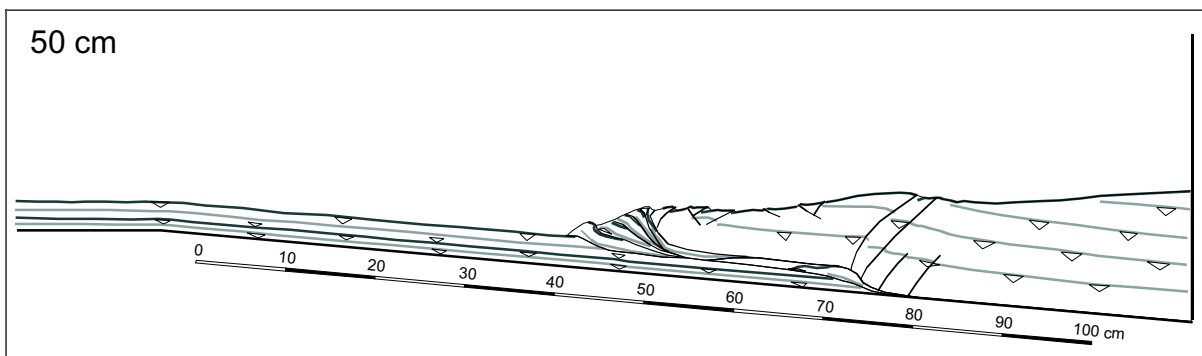
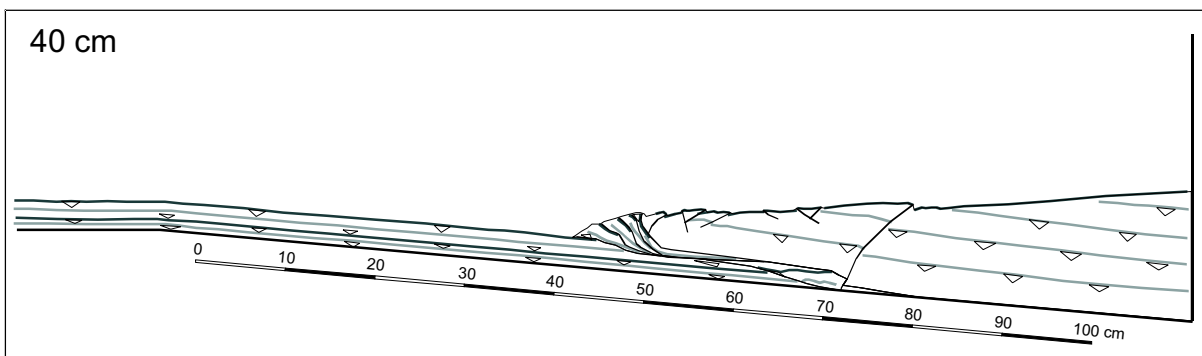
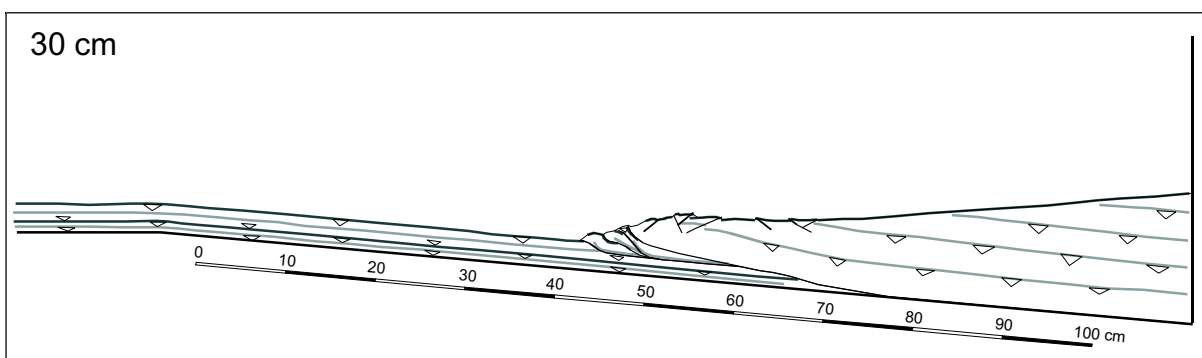
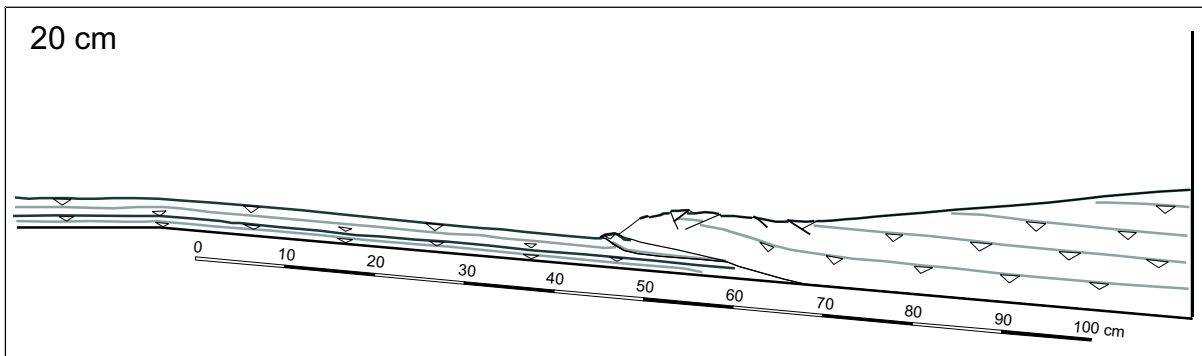


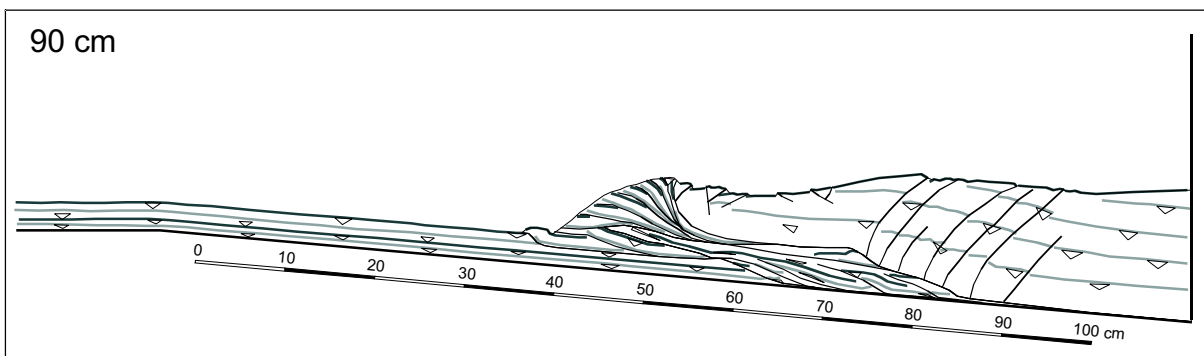
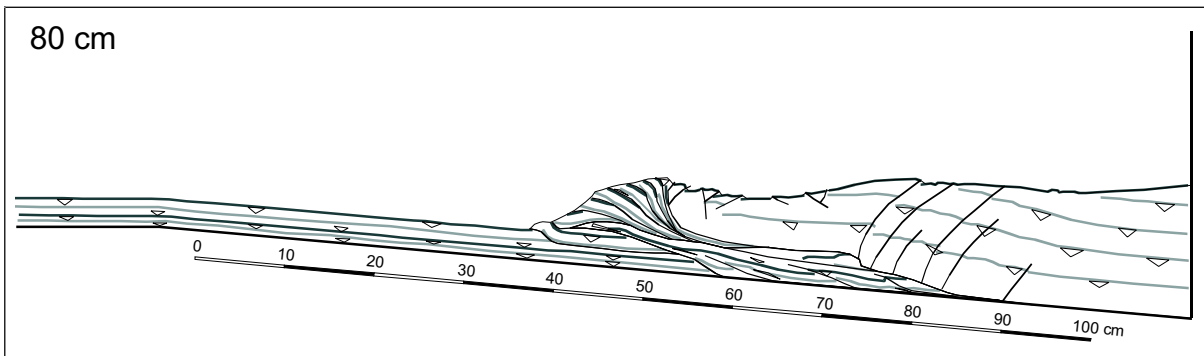
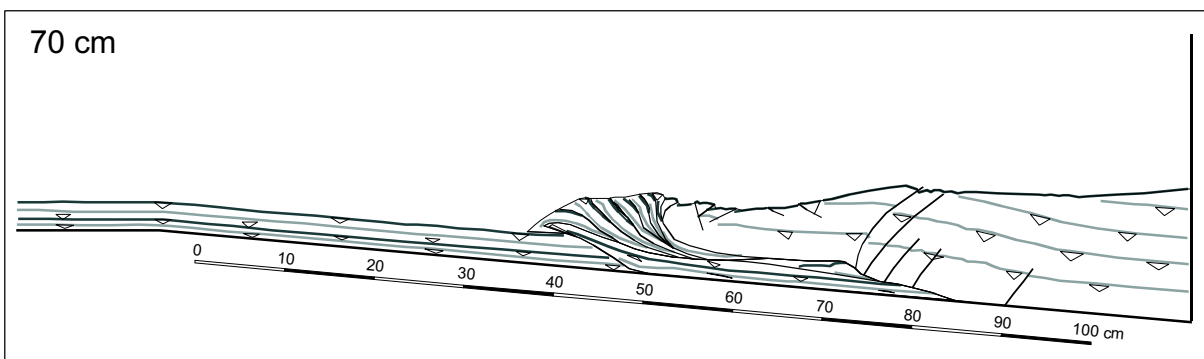
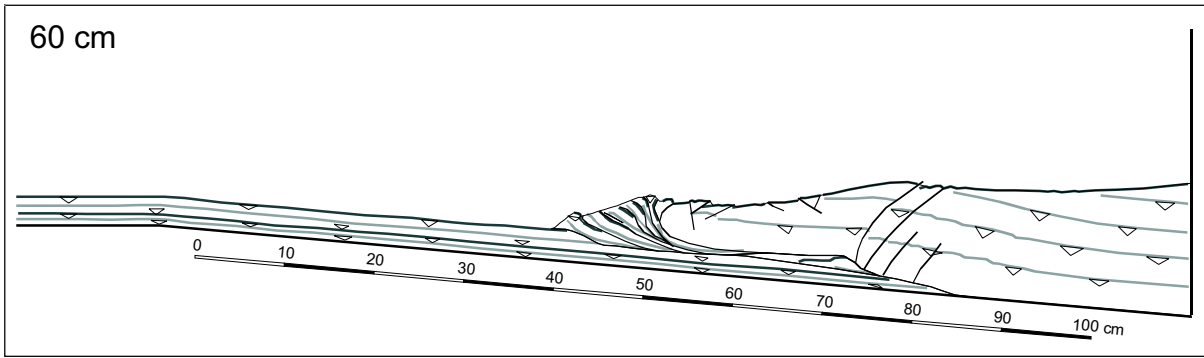


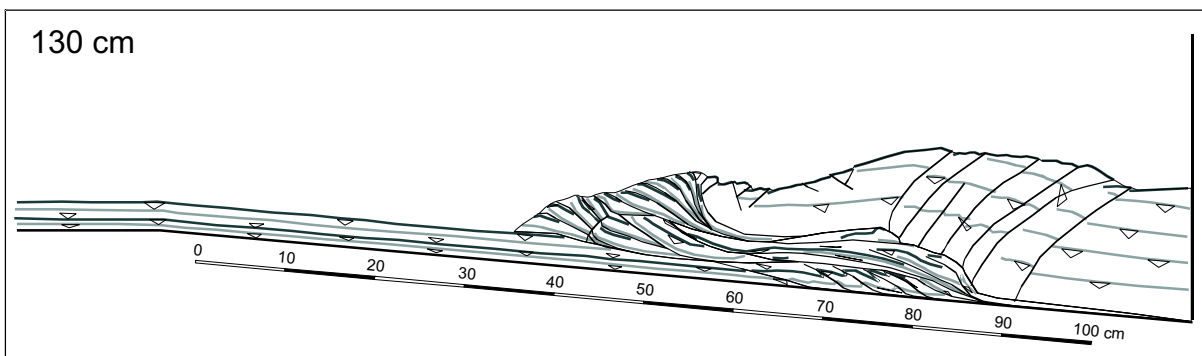
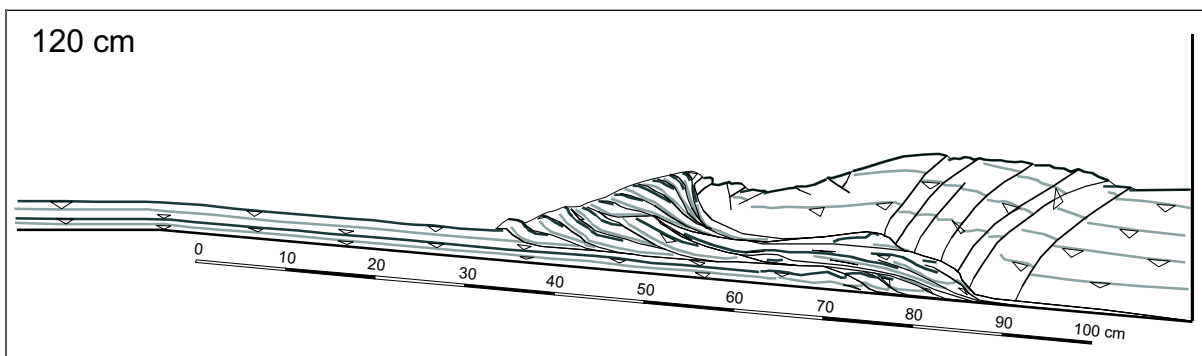
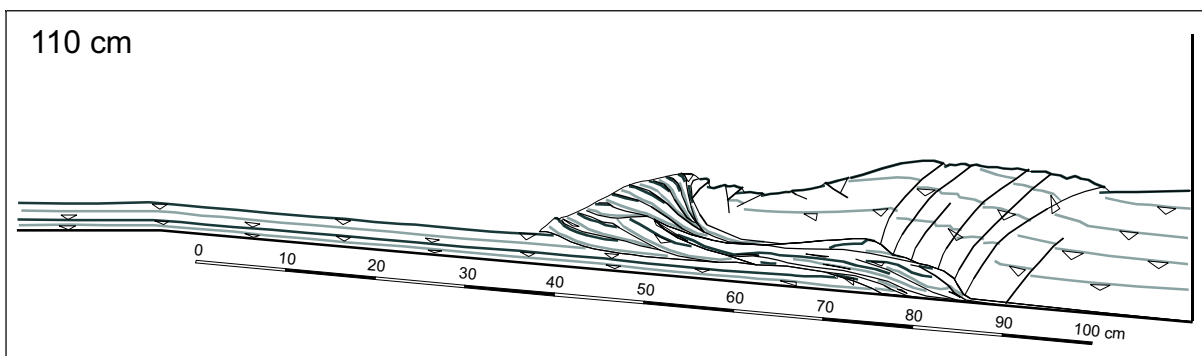
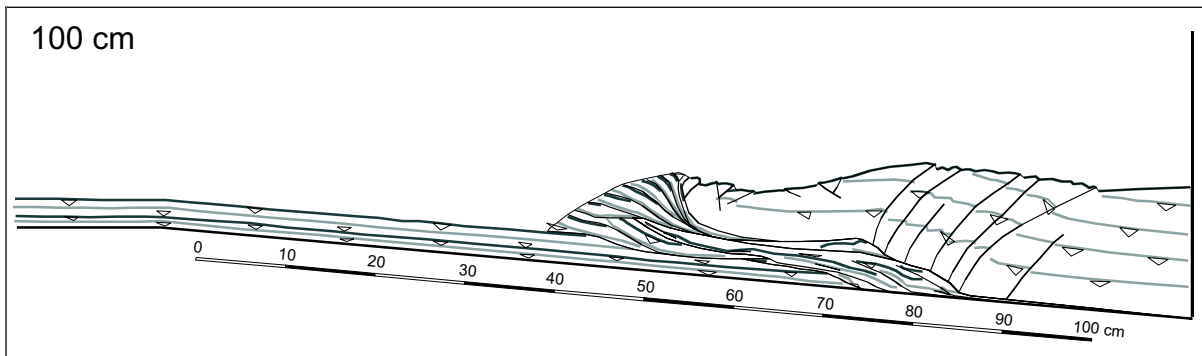


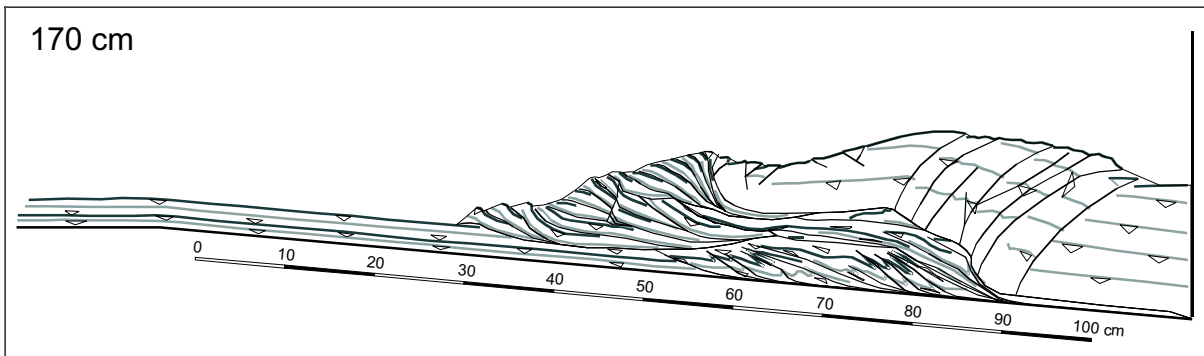
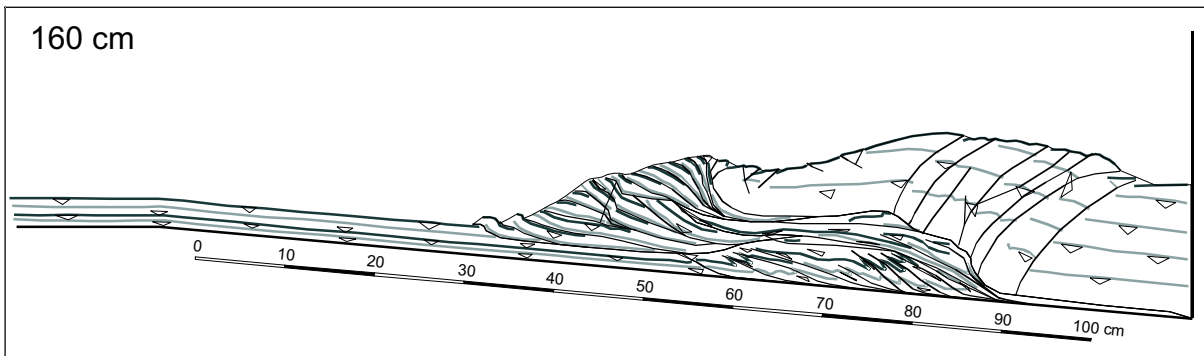
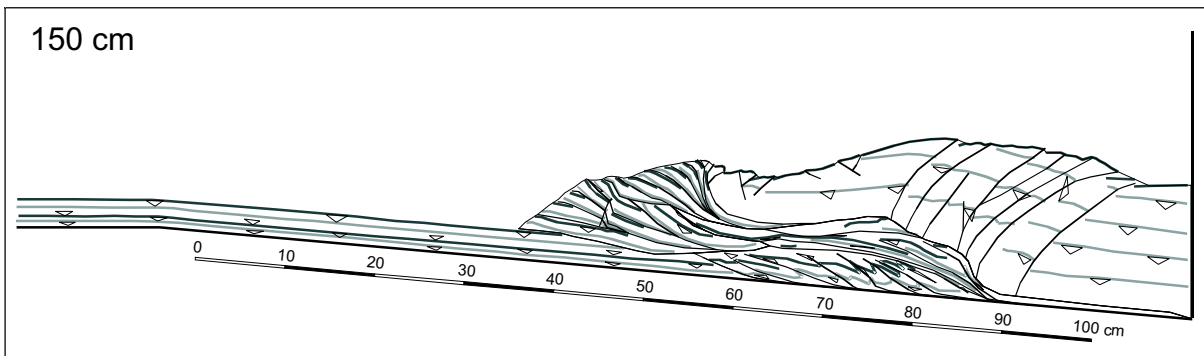
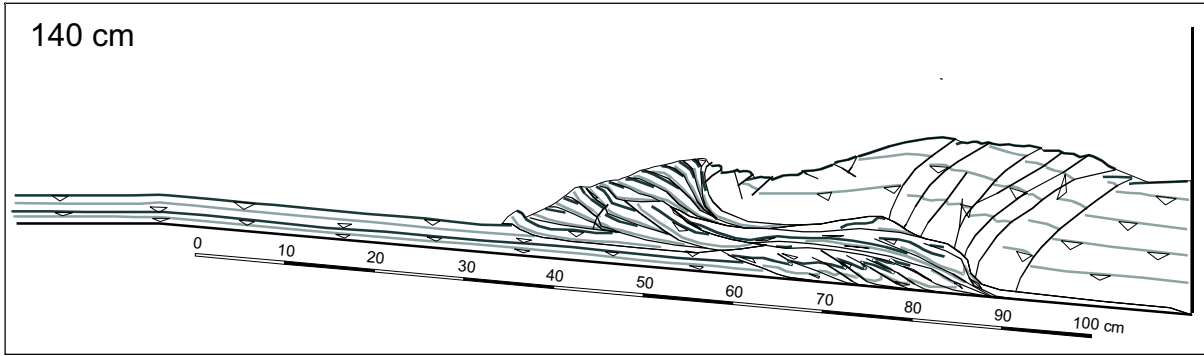
HC experiment

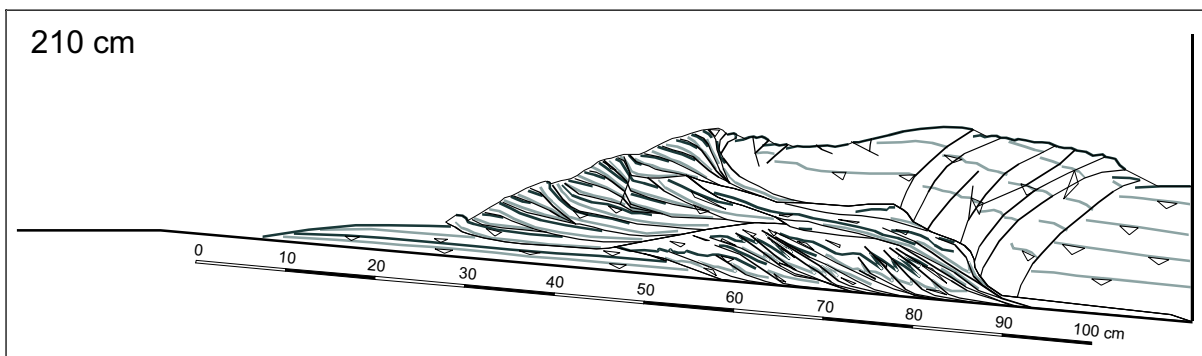
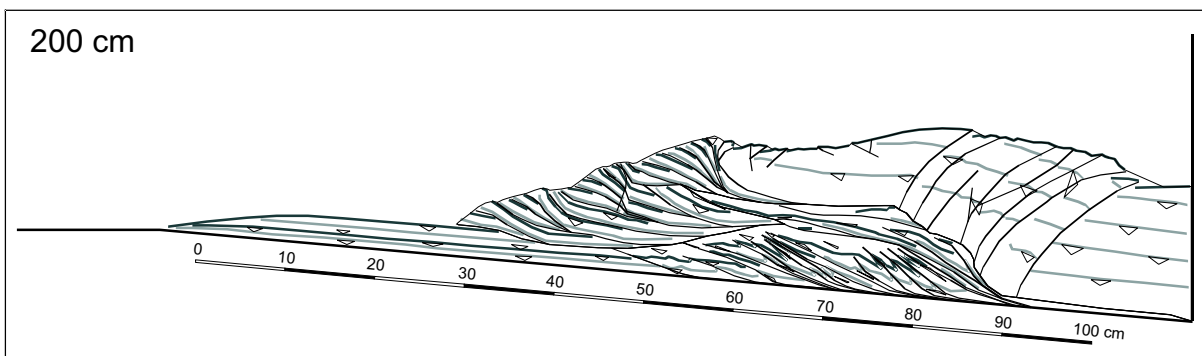
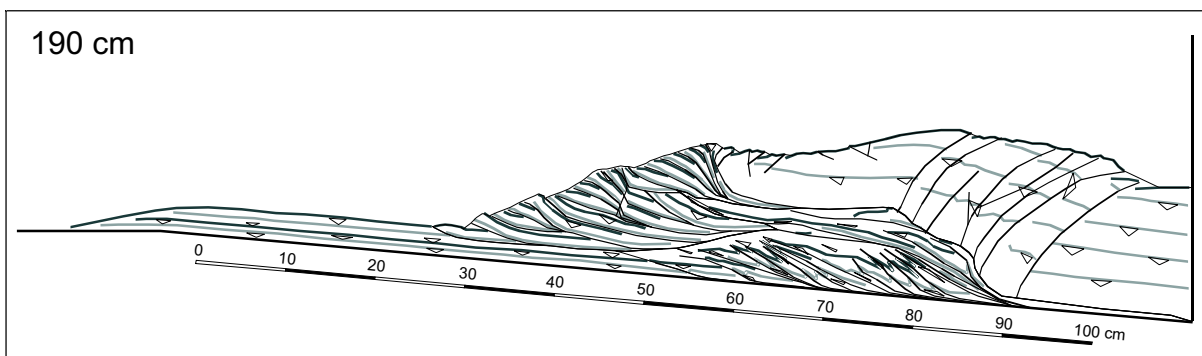
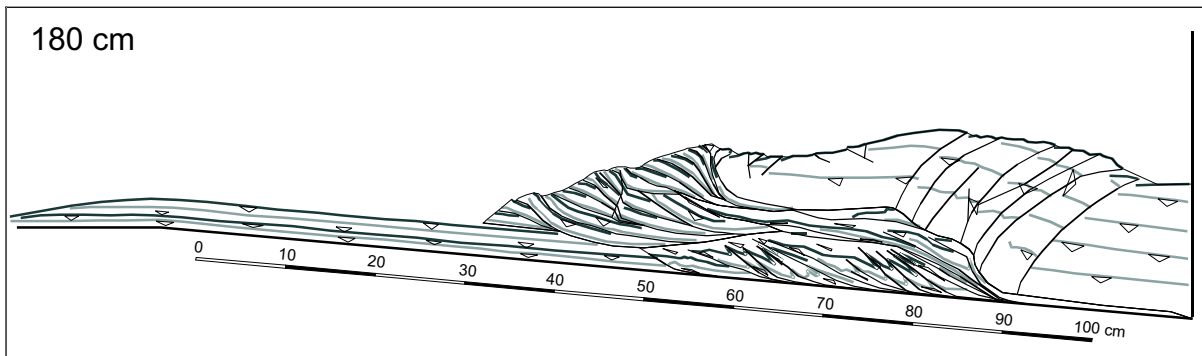


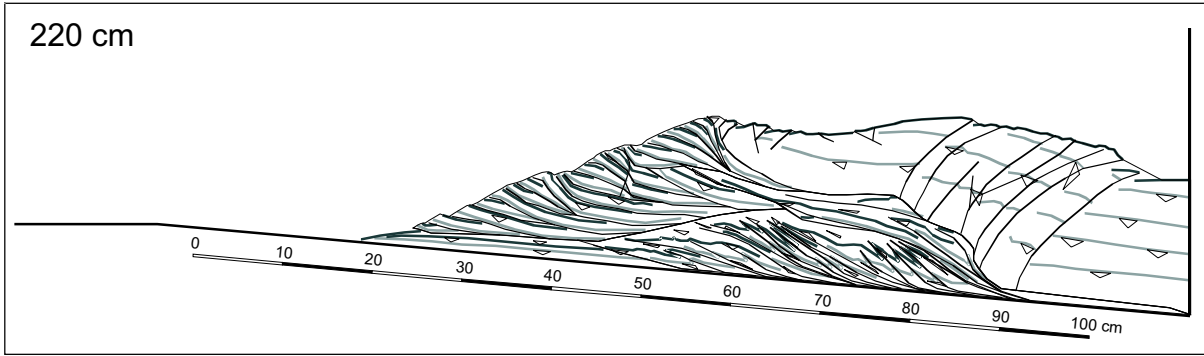




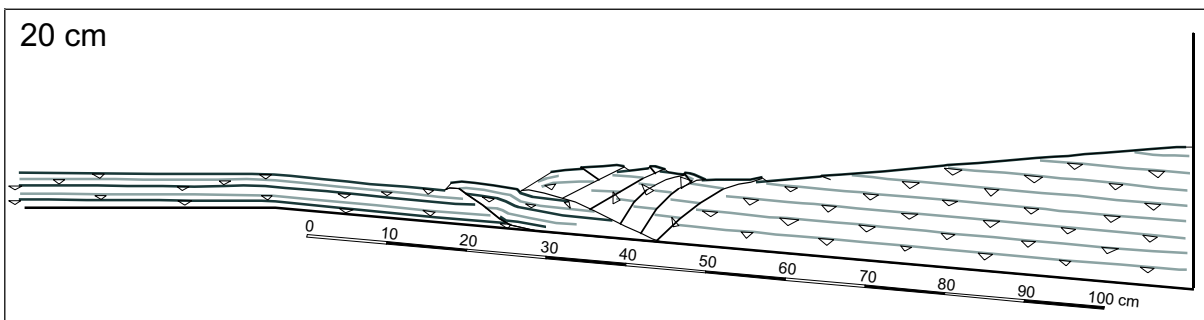
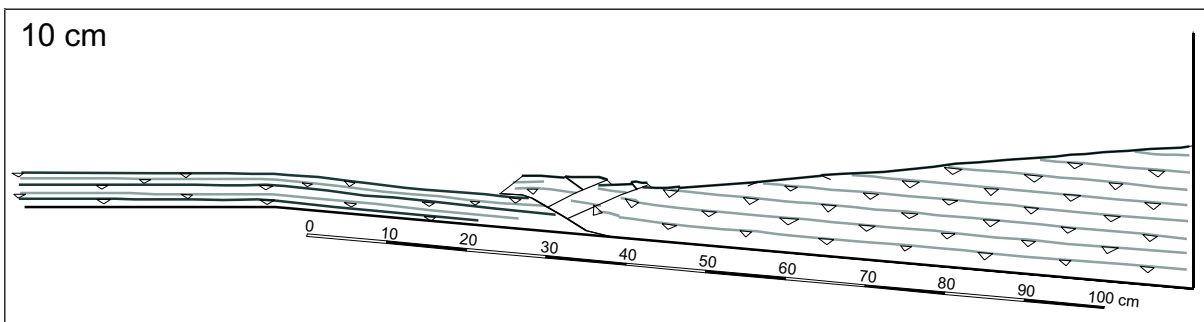
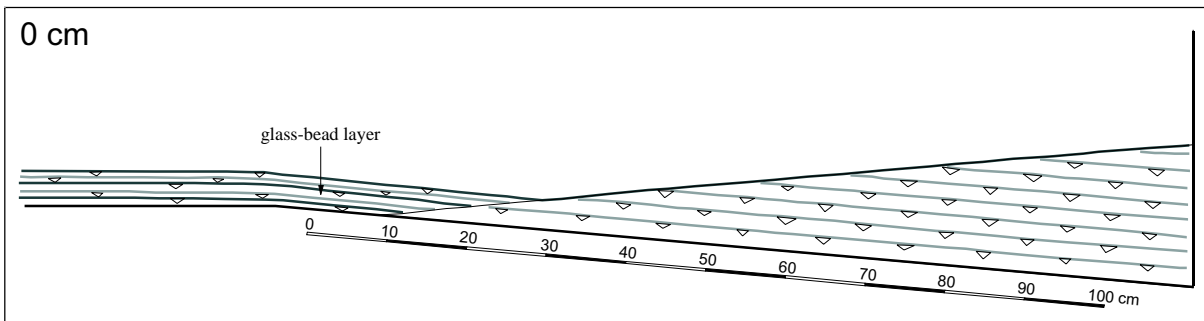


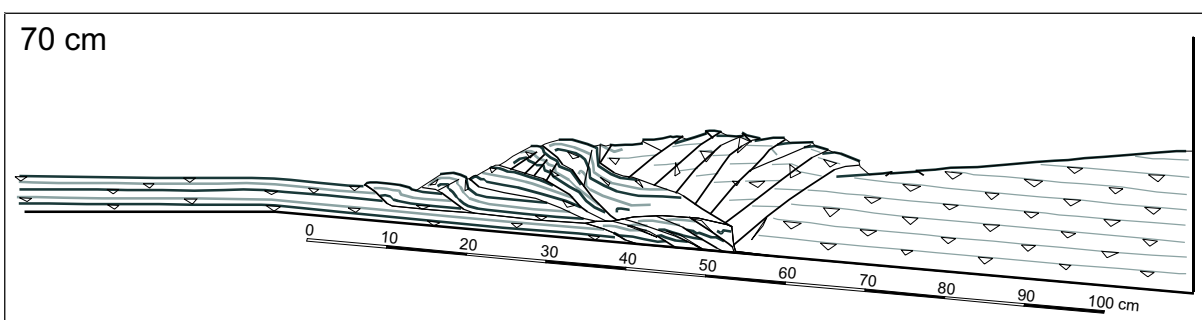
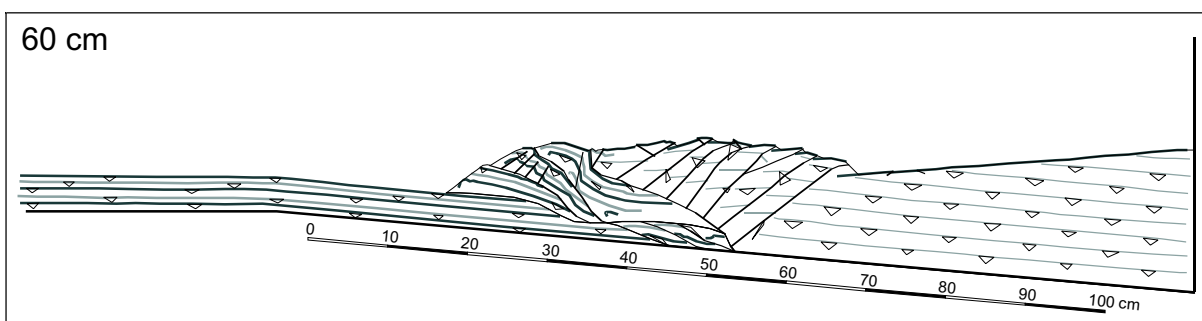
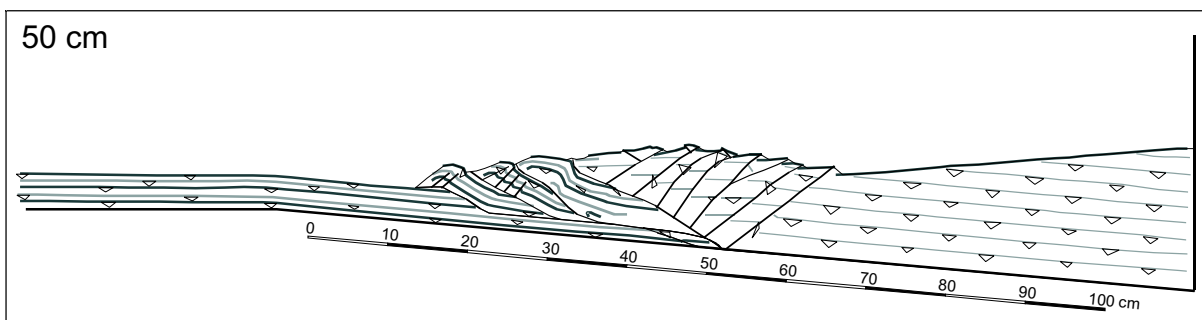
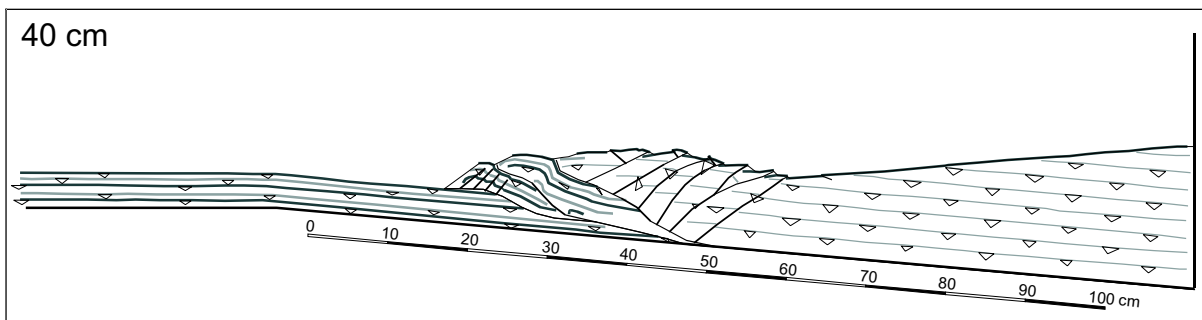
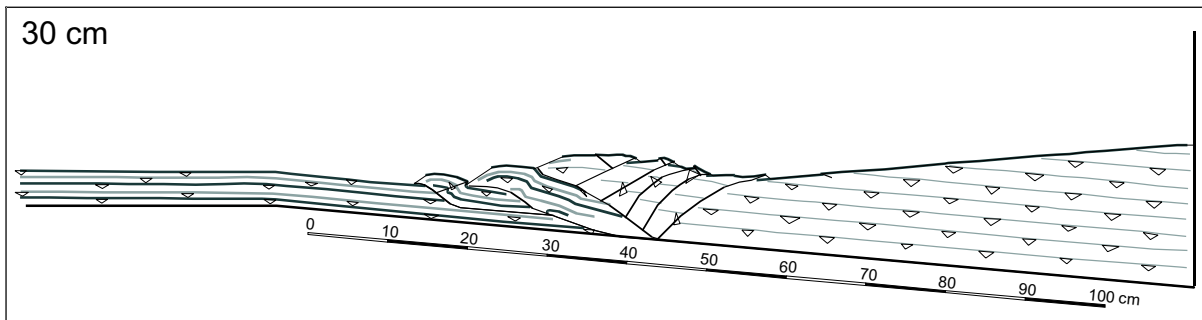


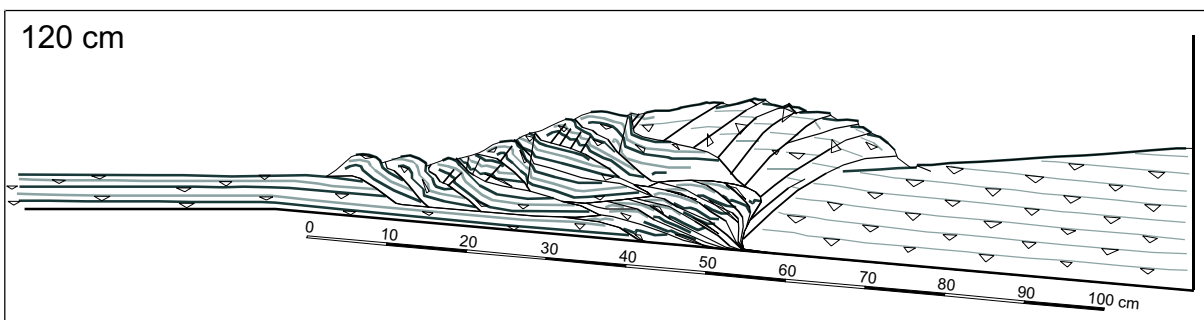
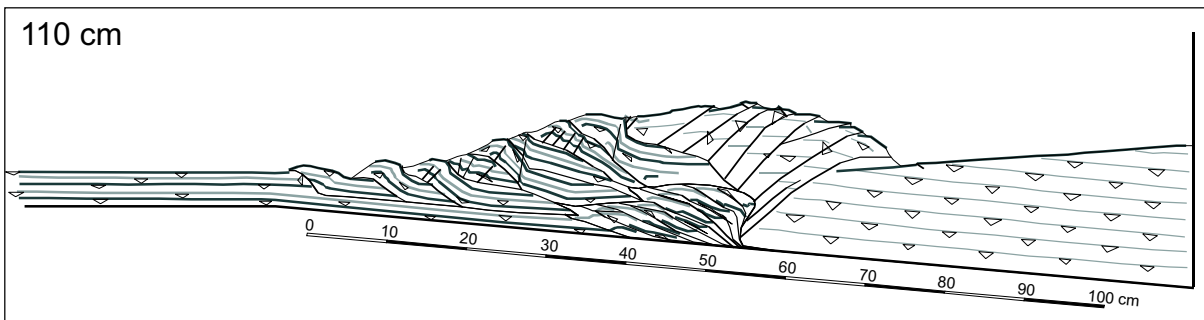
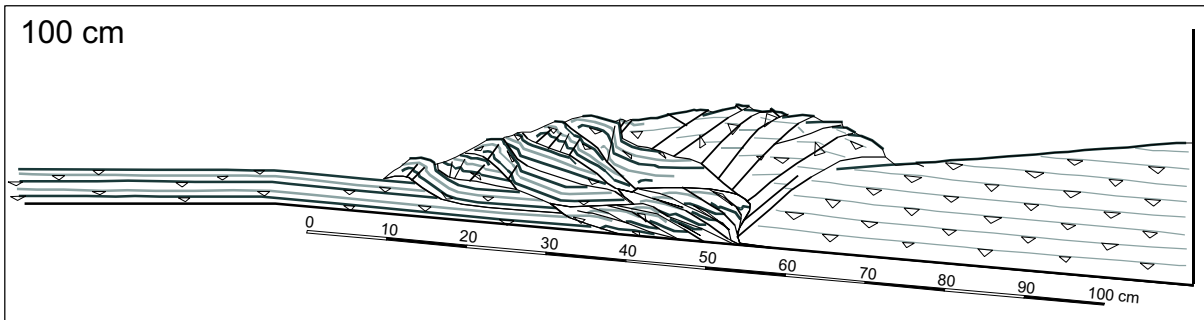
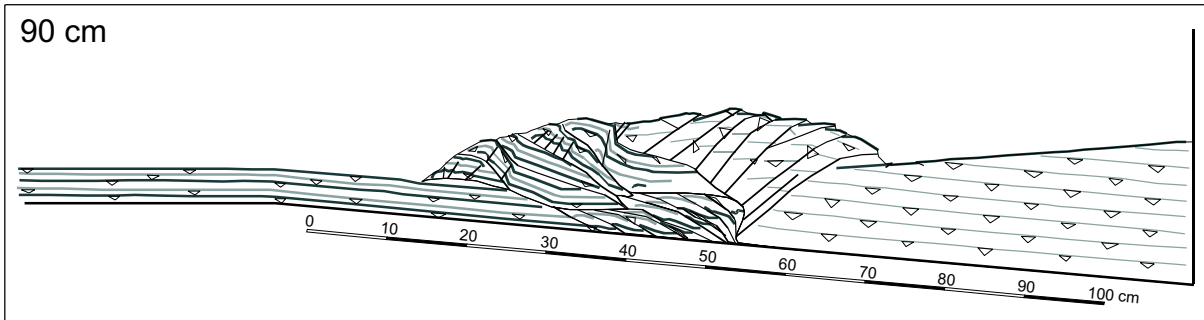
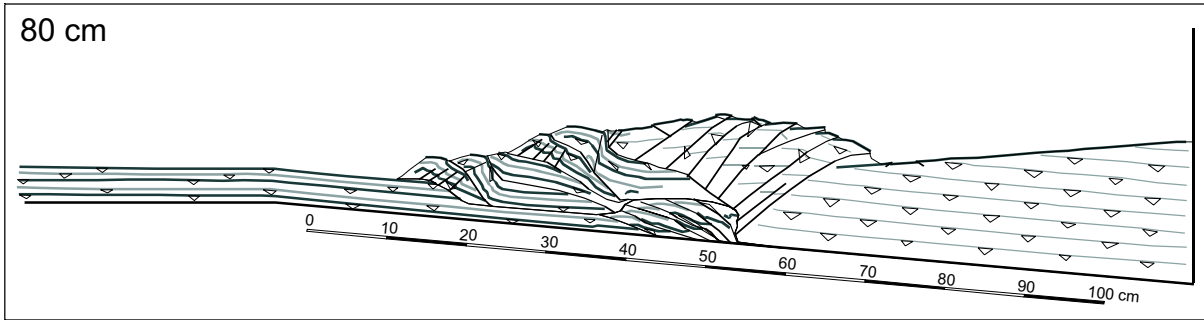


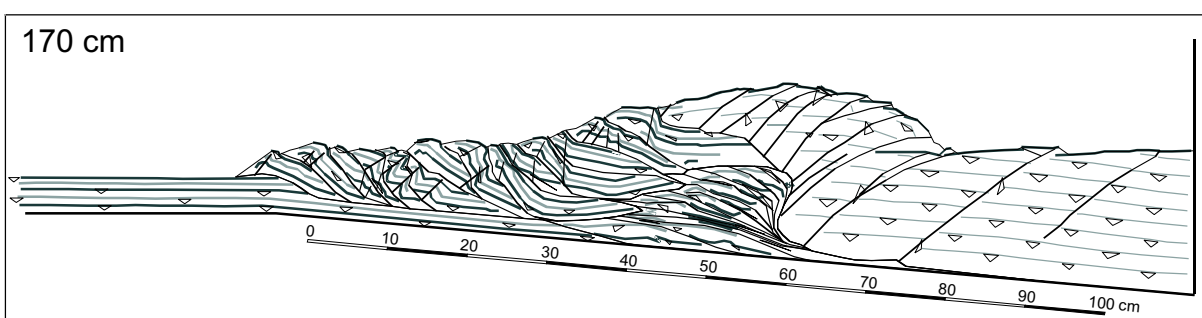
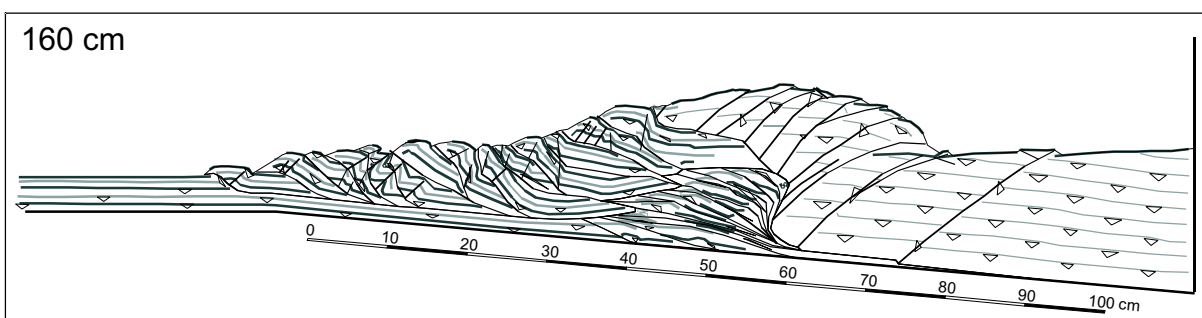
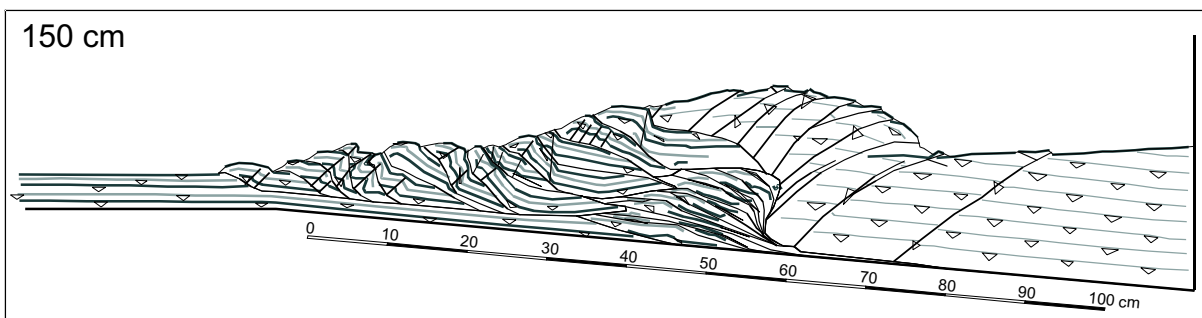
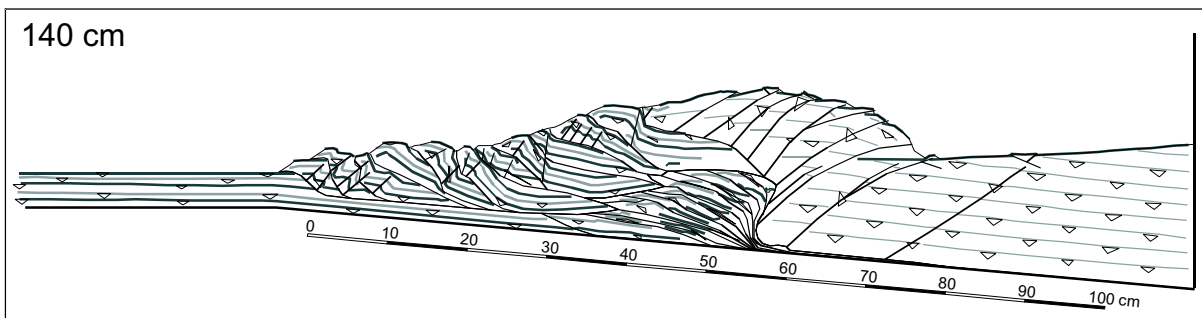
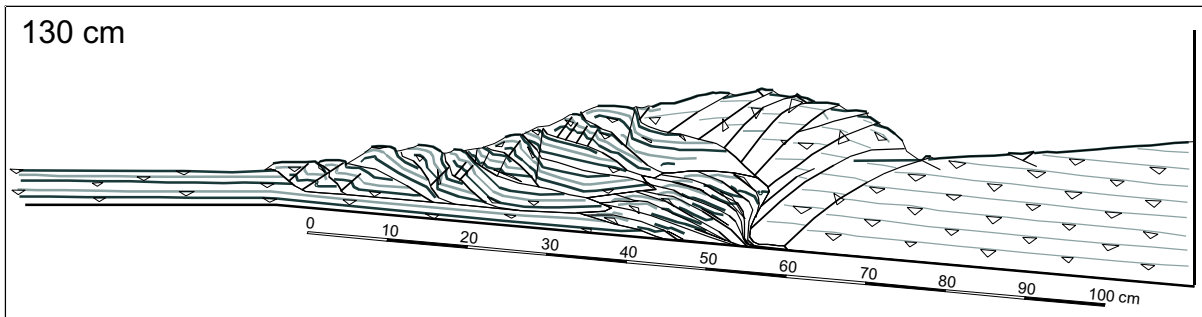


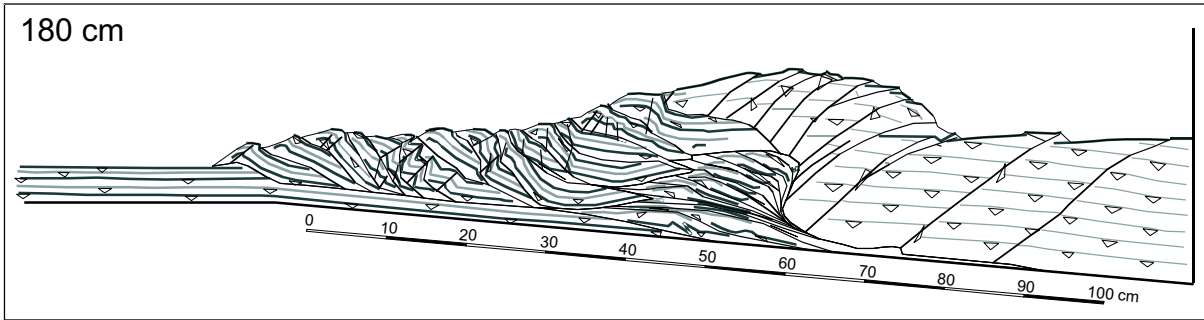
LF experiment



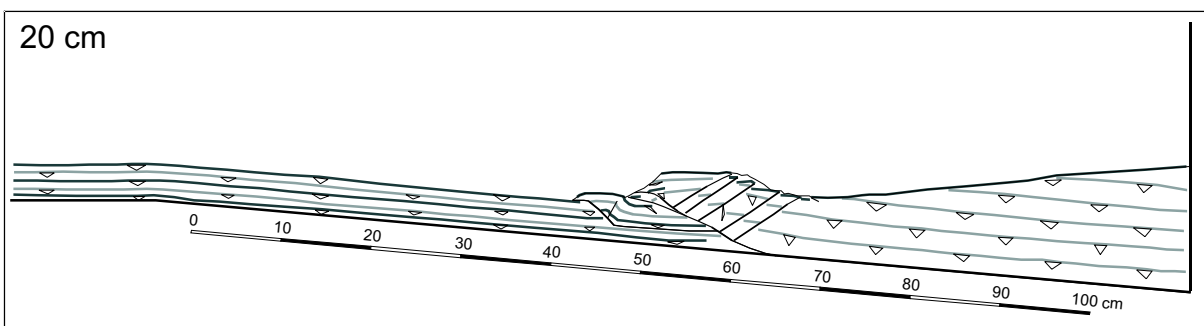
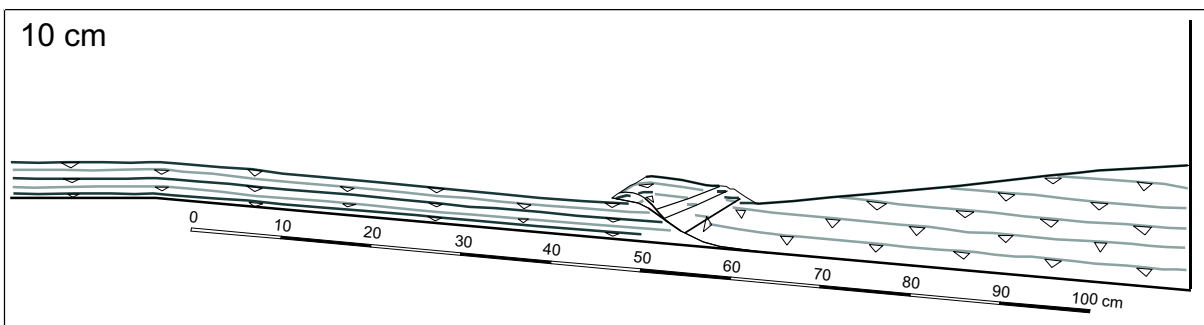
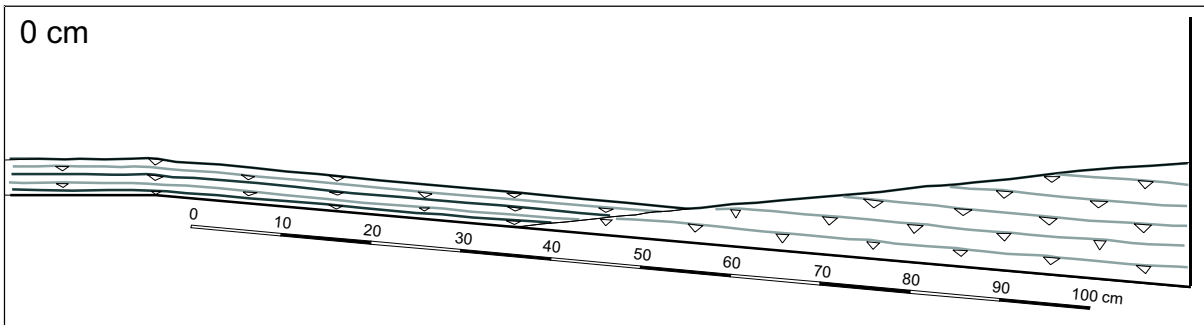


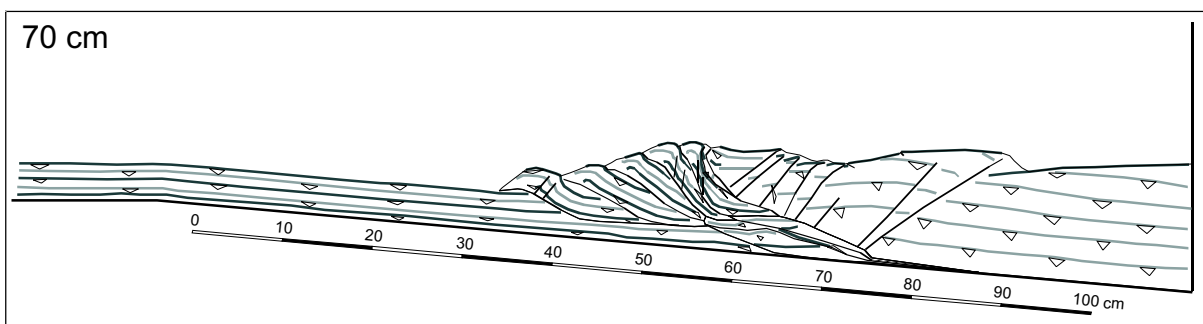
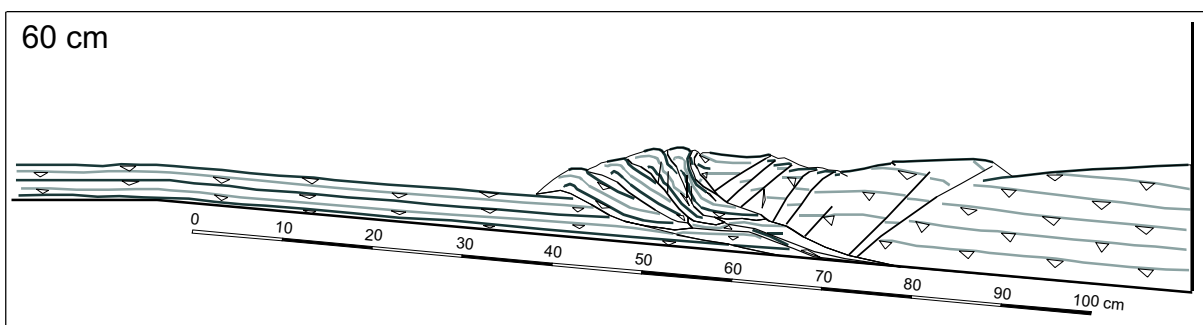
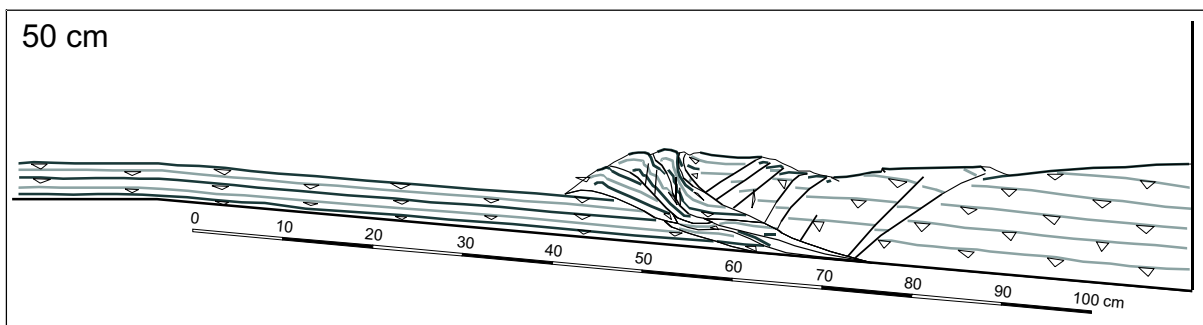
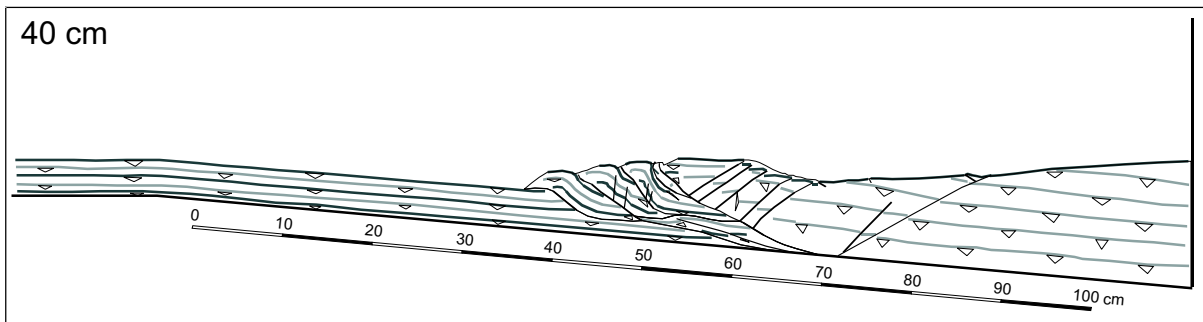
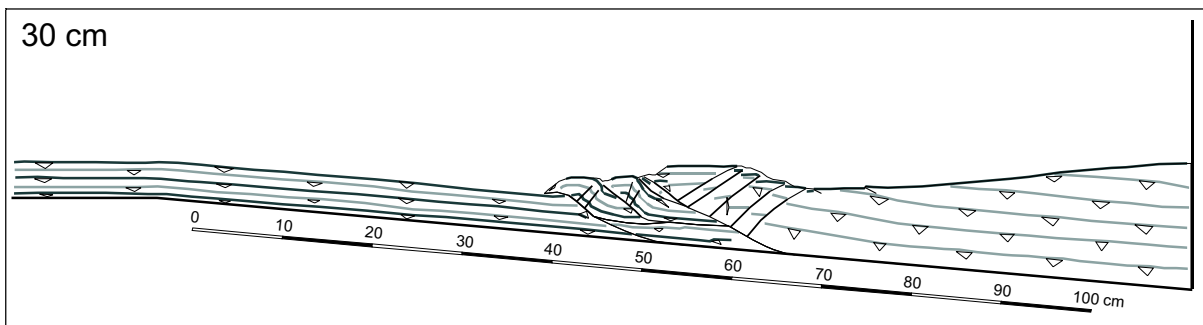


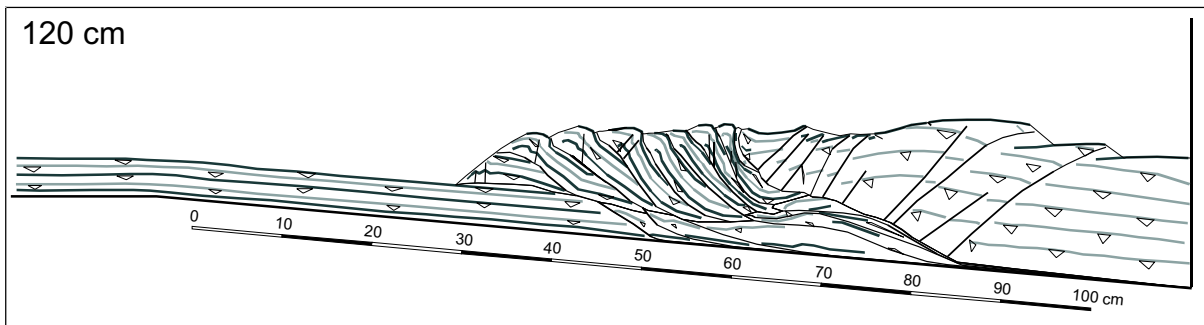
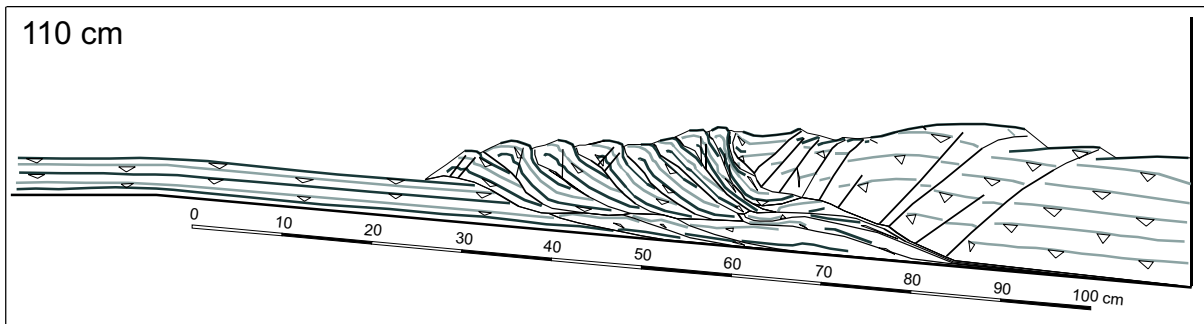
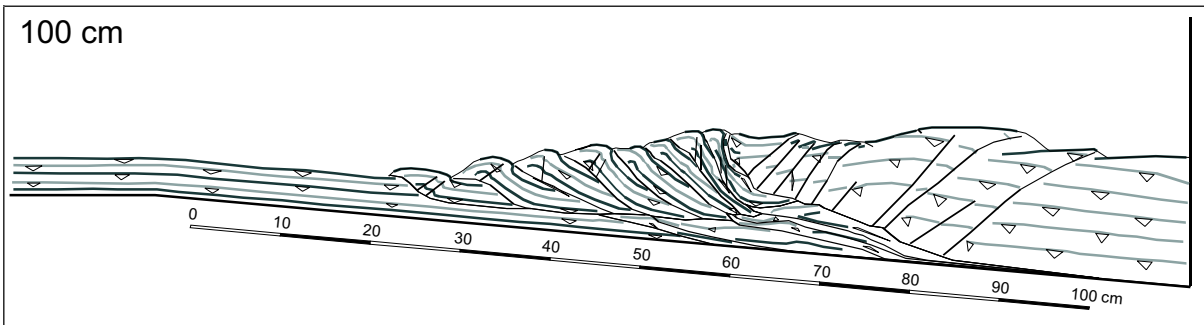
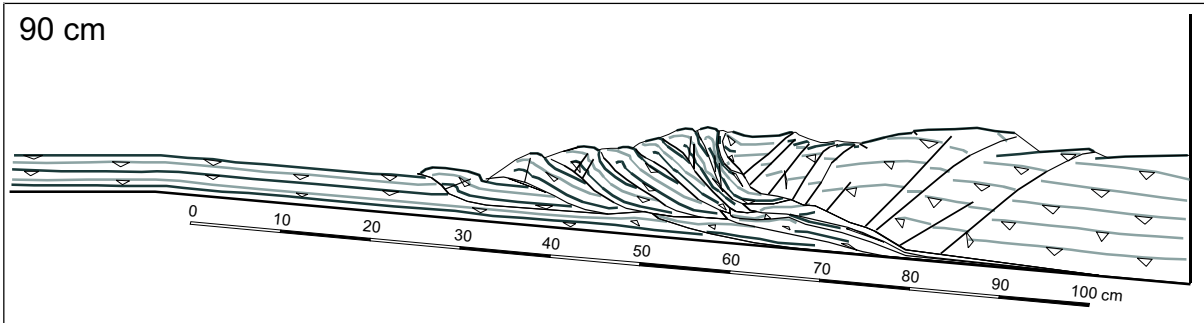
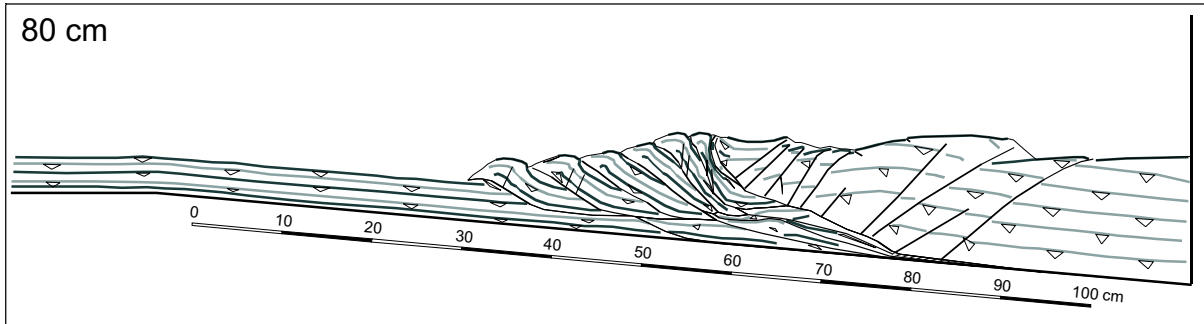


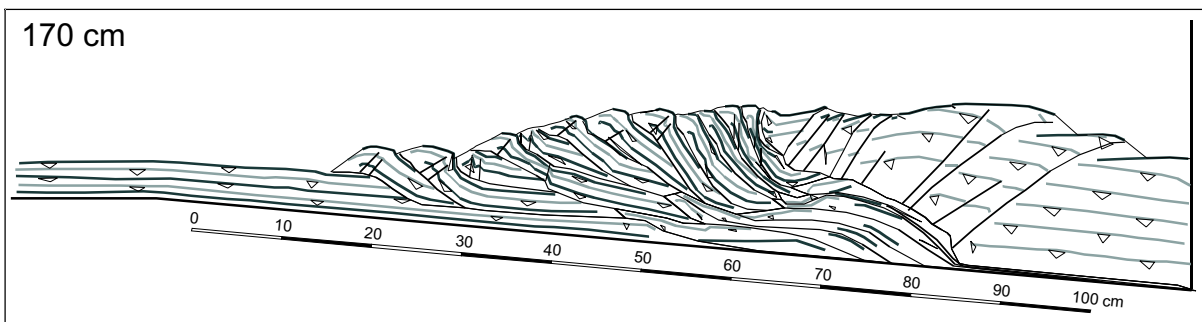
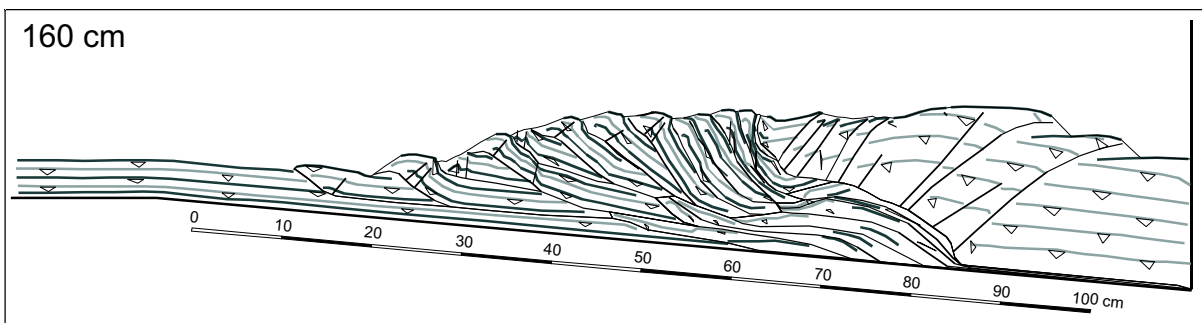
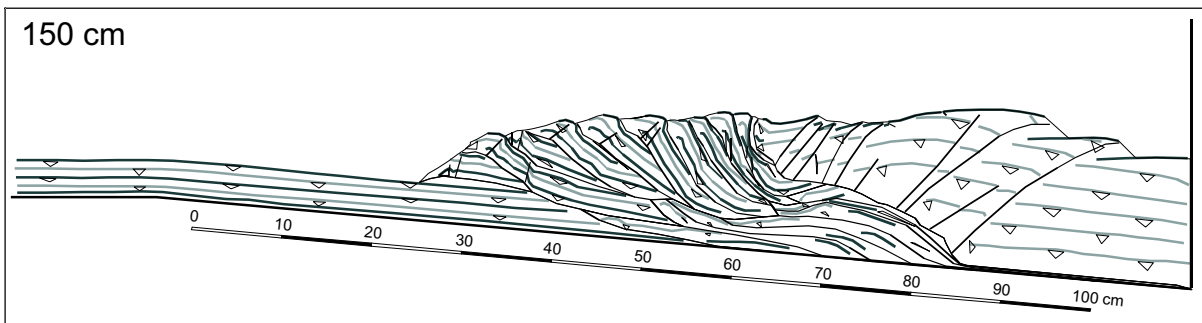
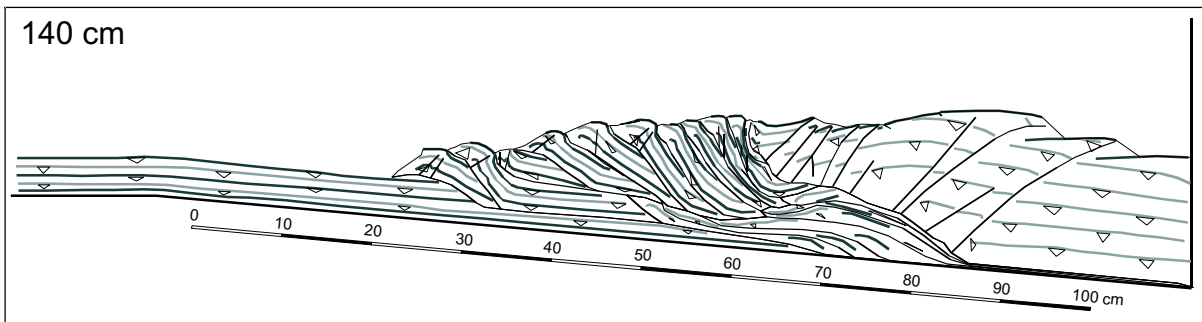
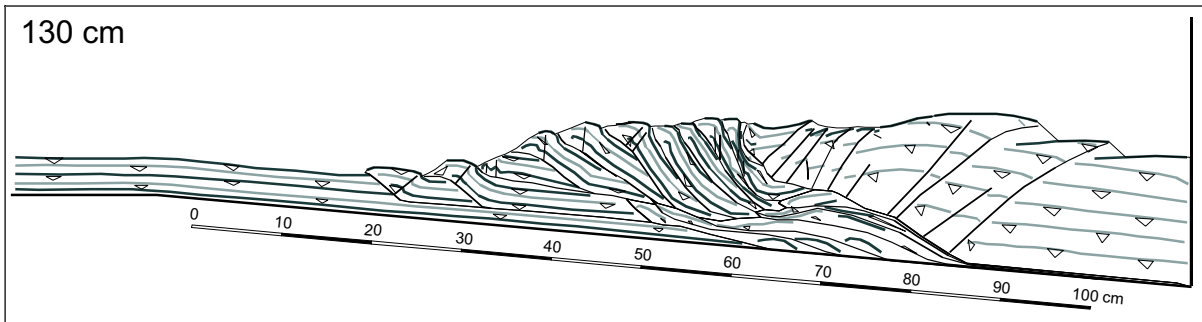


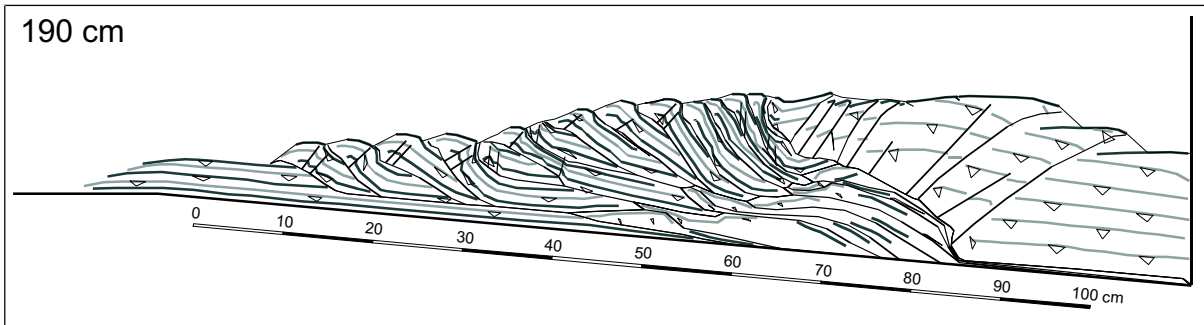
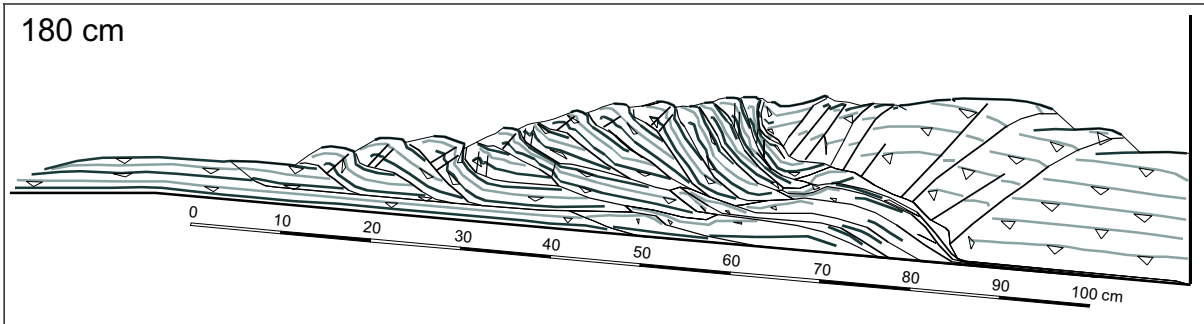
LC experiment



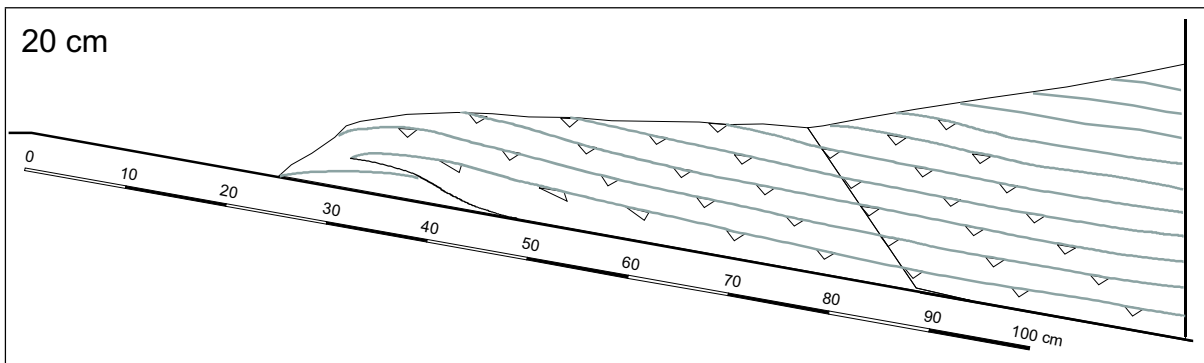
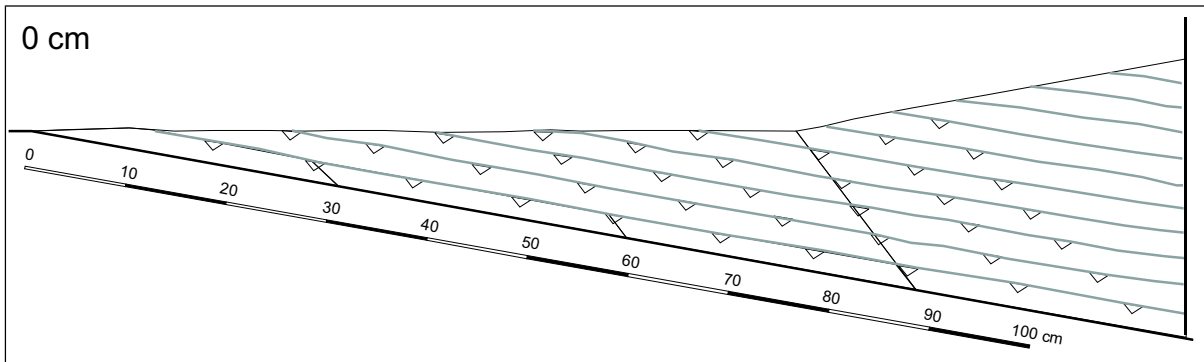


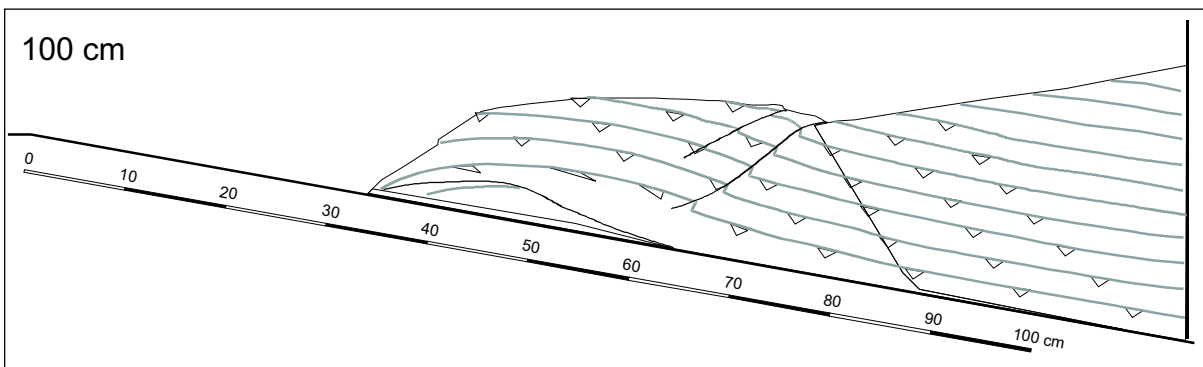
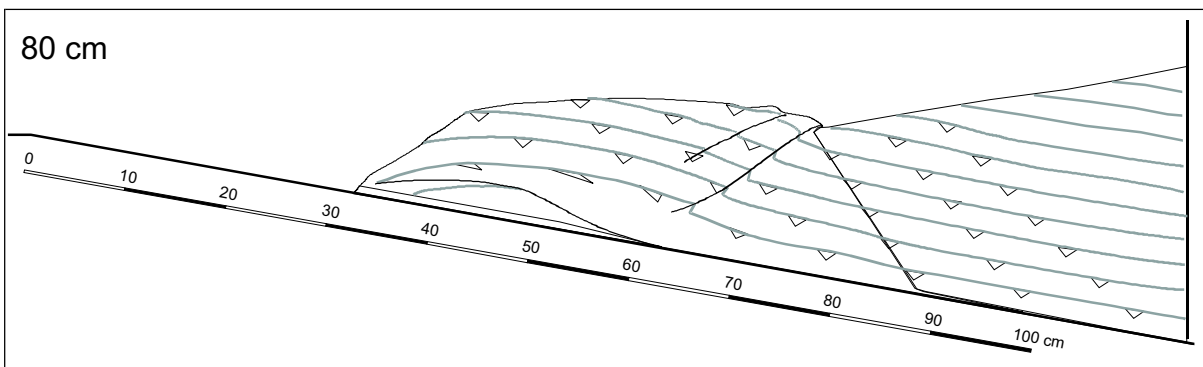
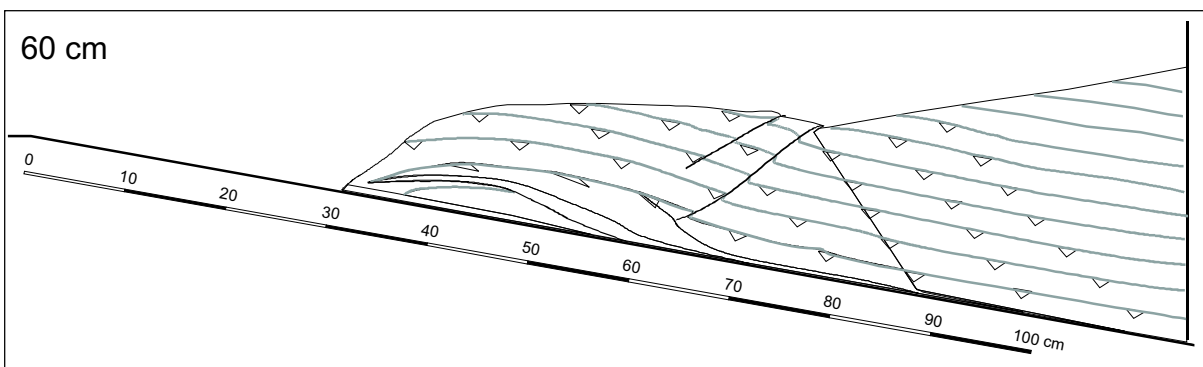
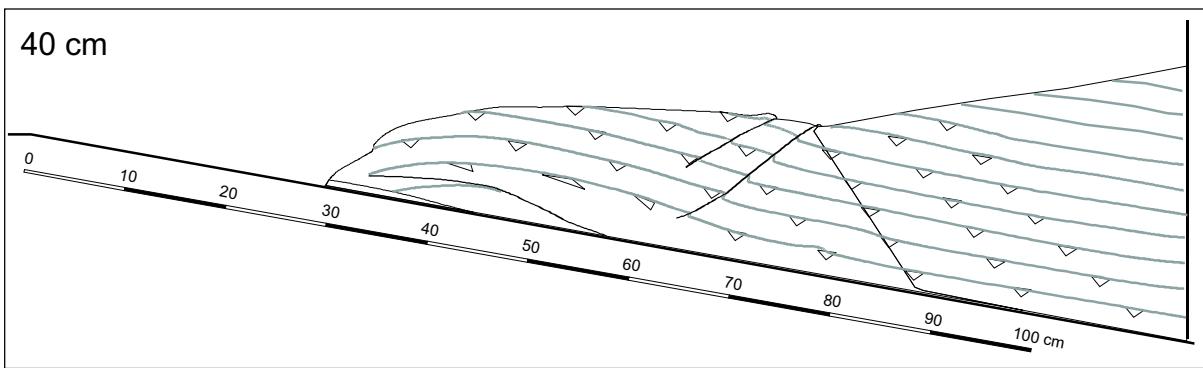


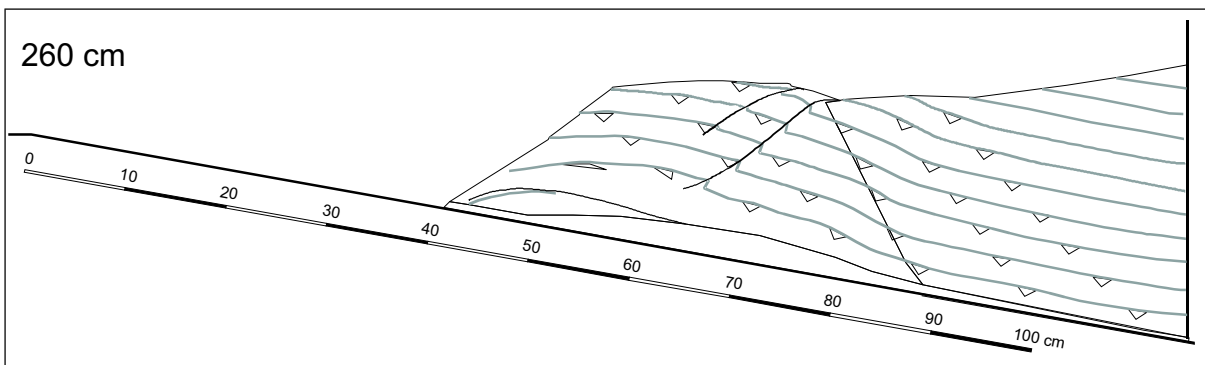
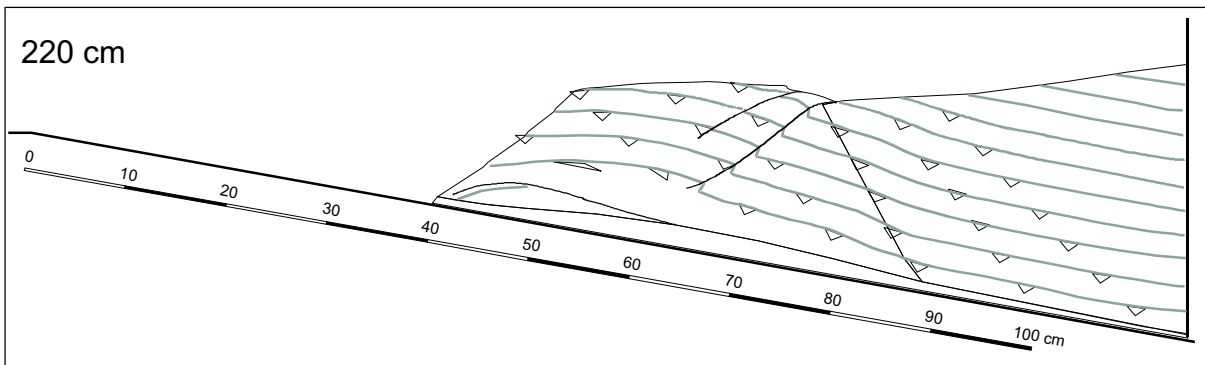
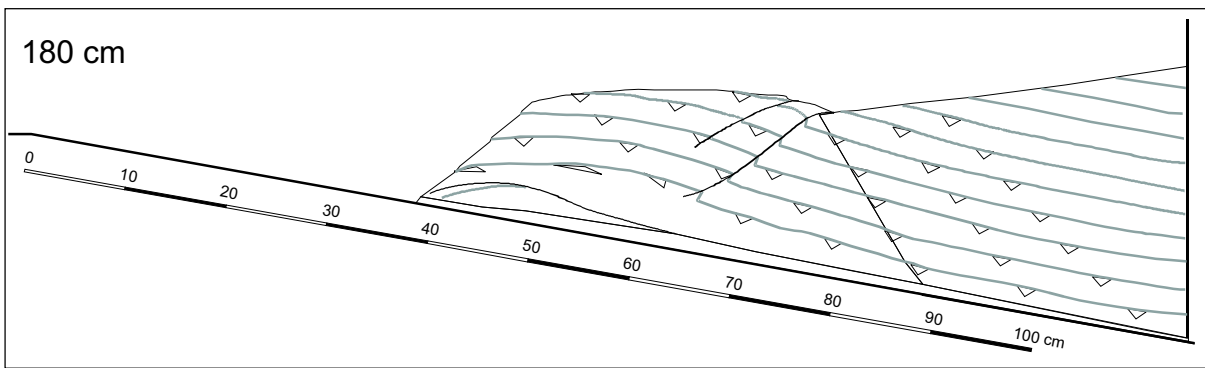
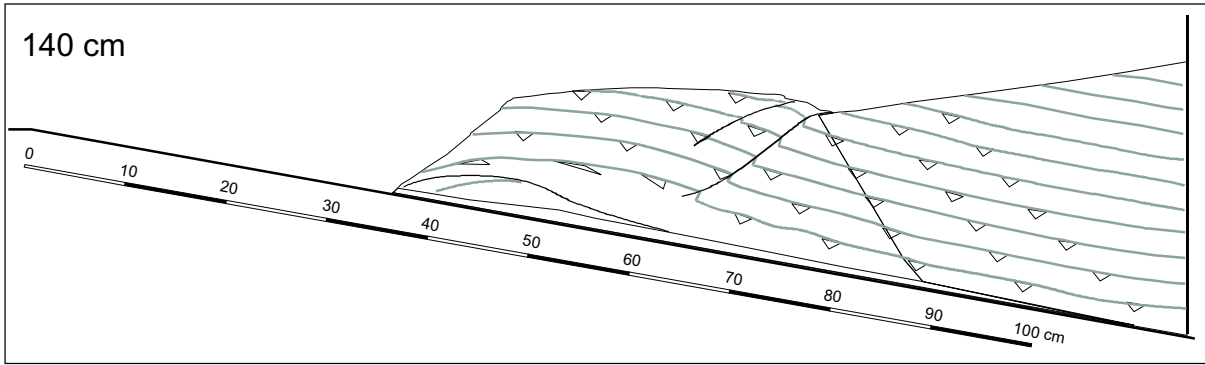


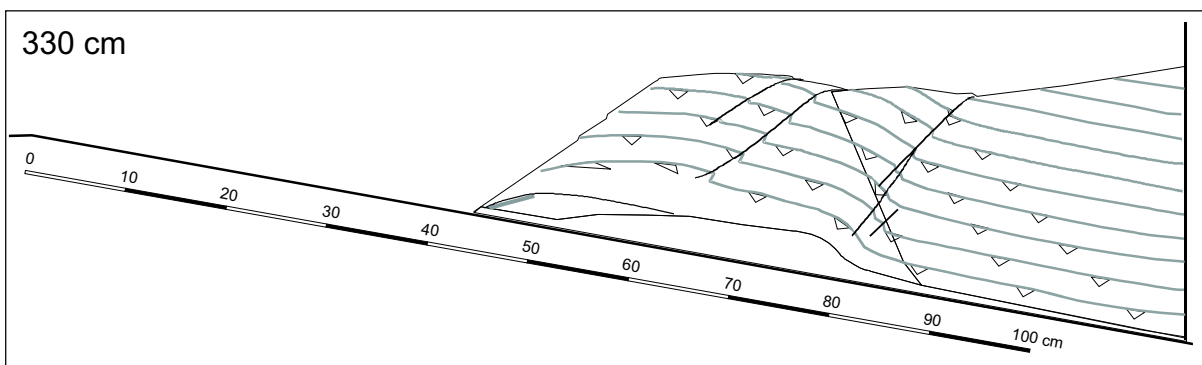
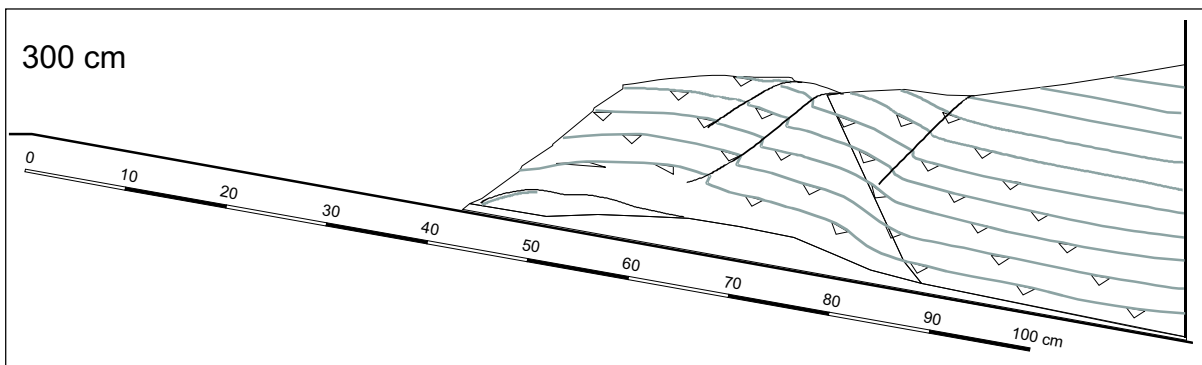


SSC experiment

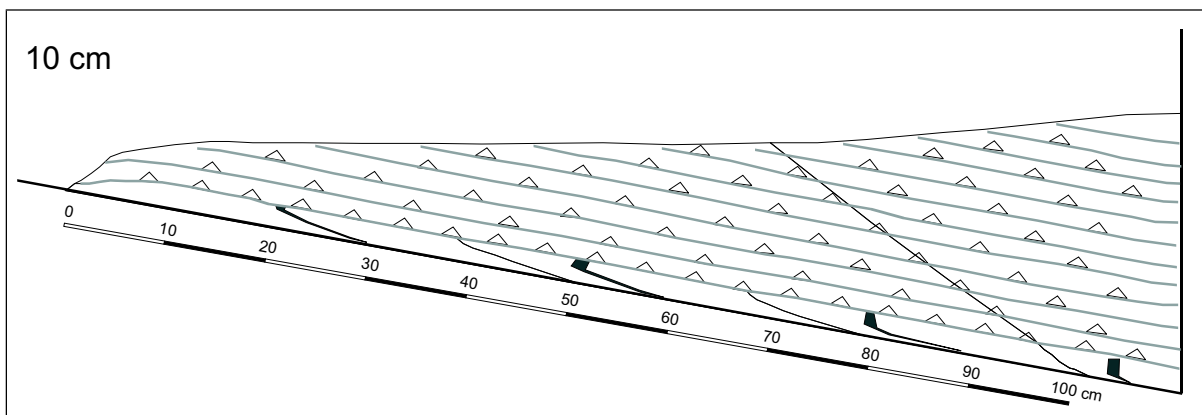
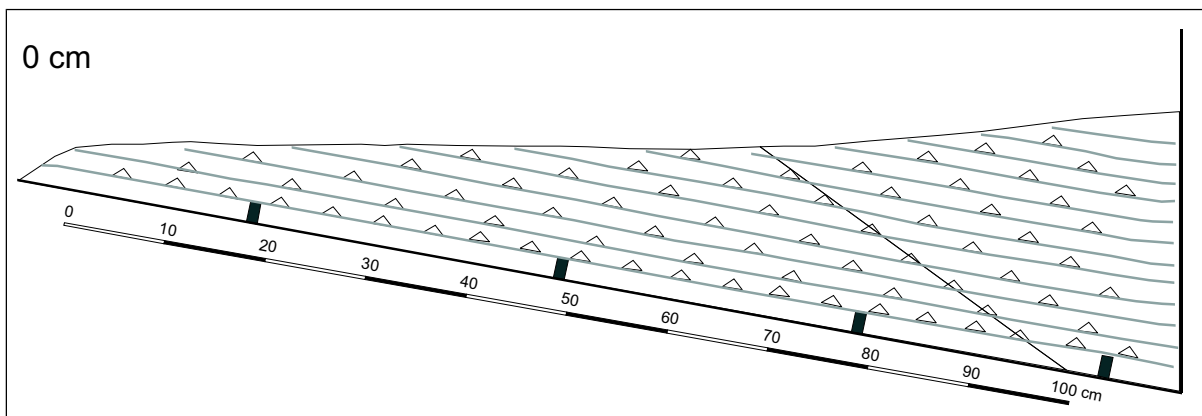


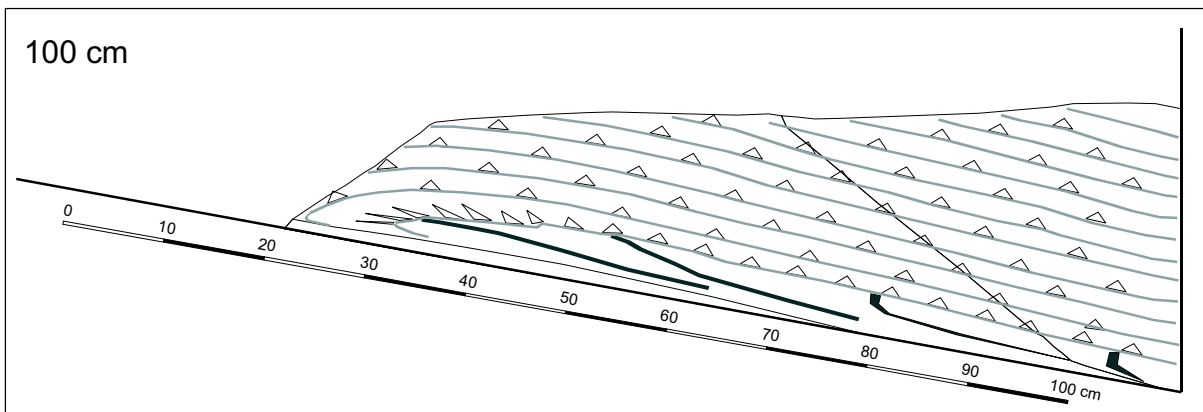
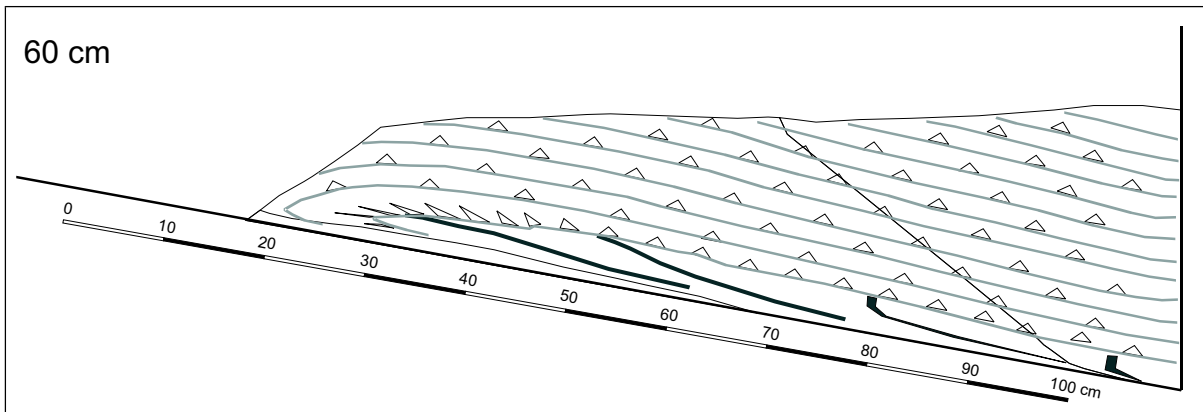
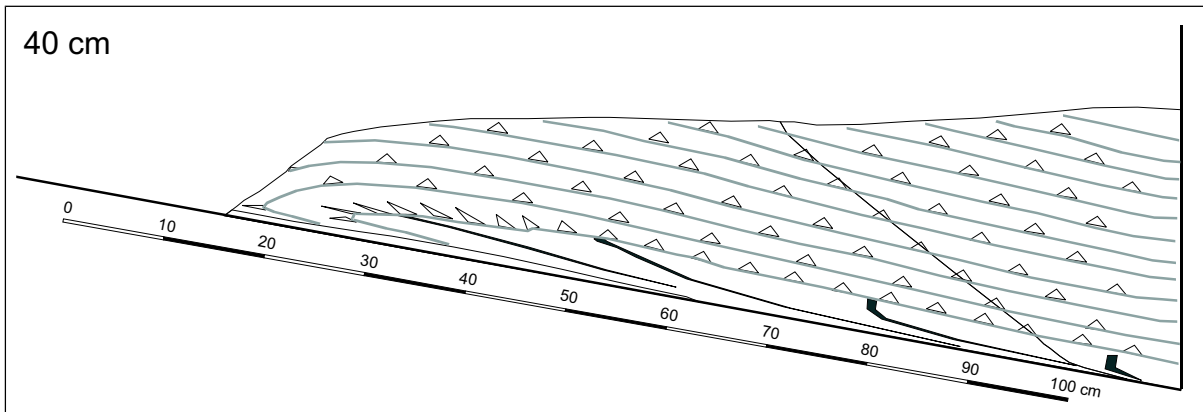
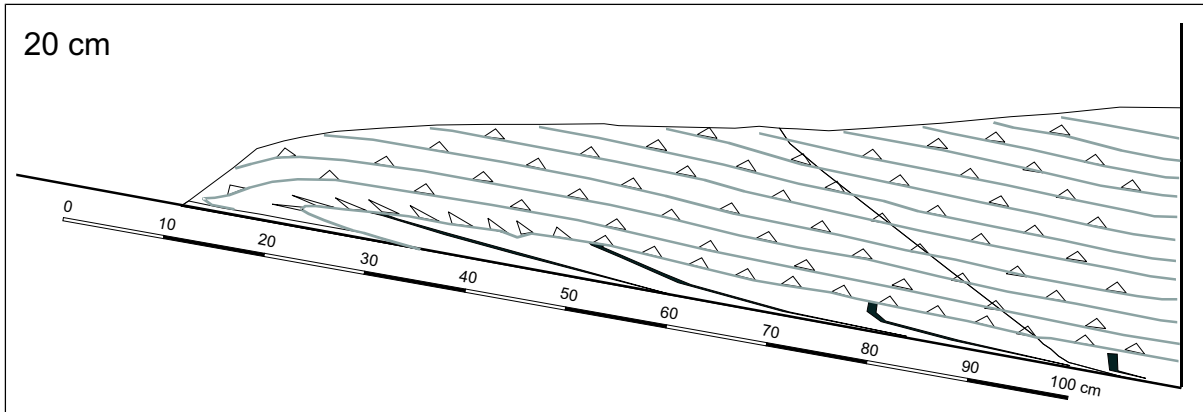


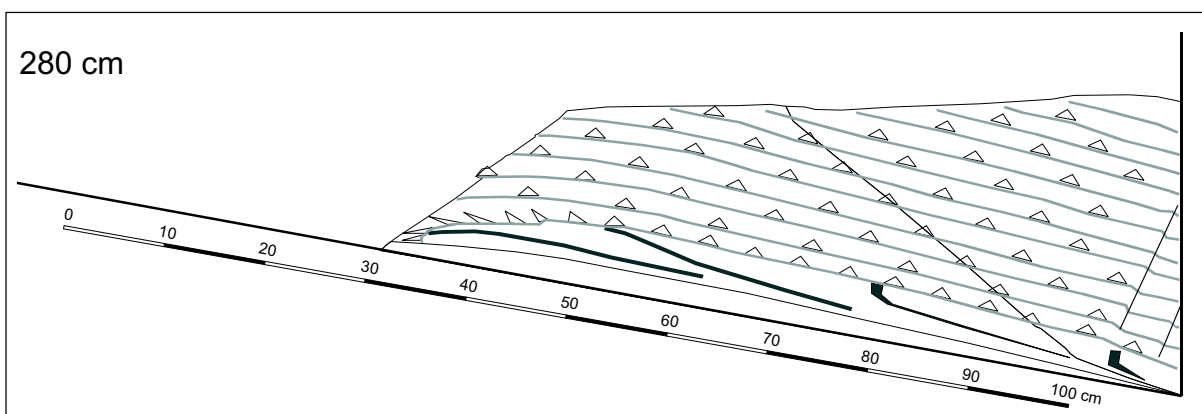
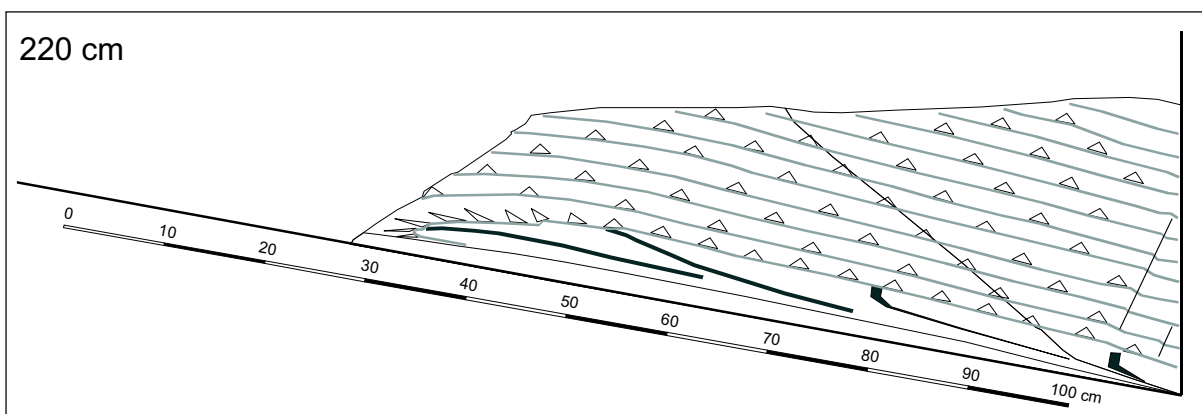
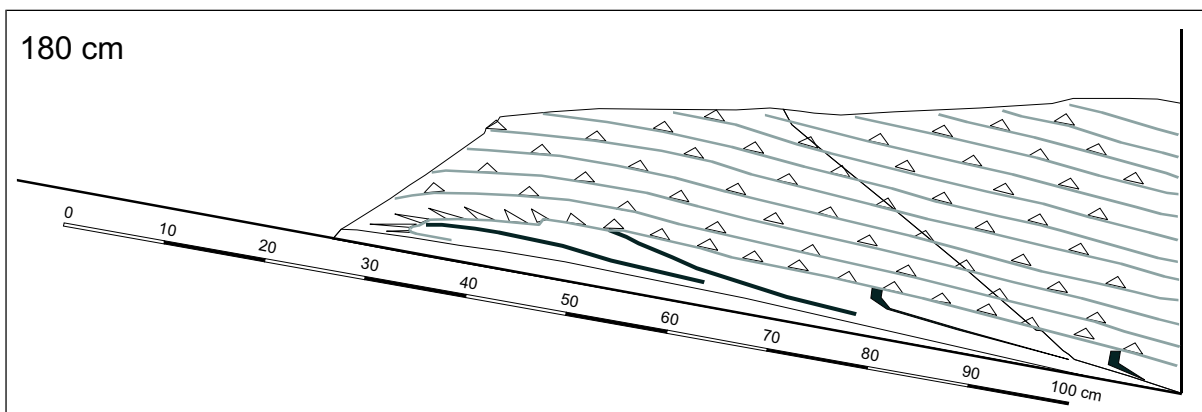
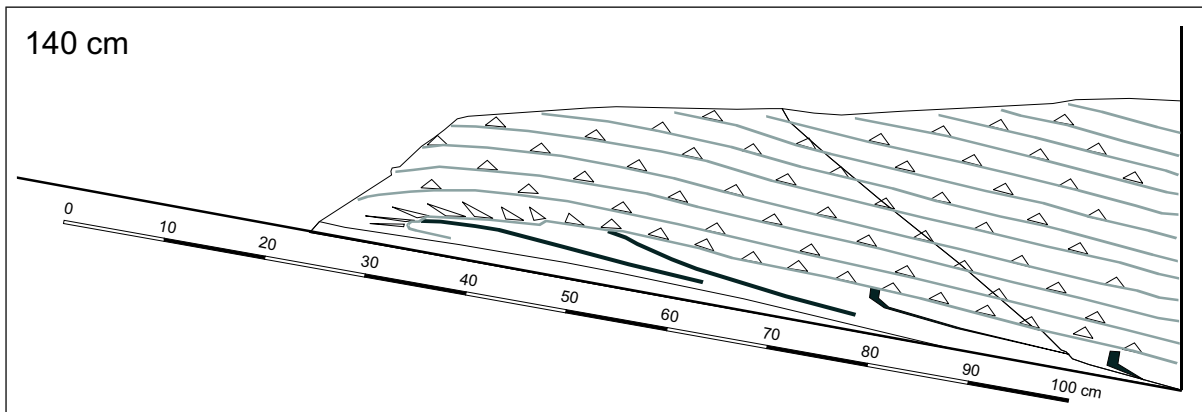


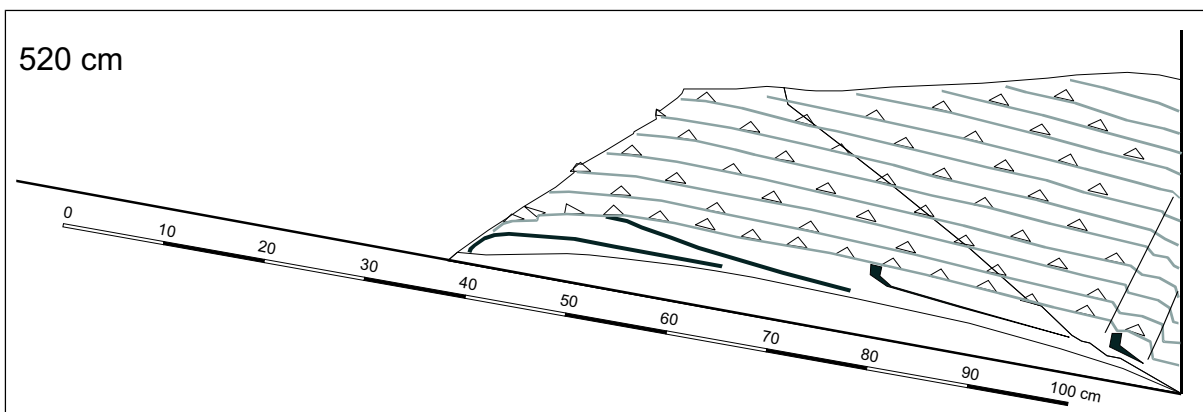
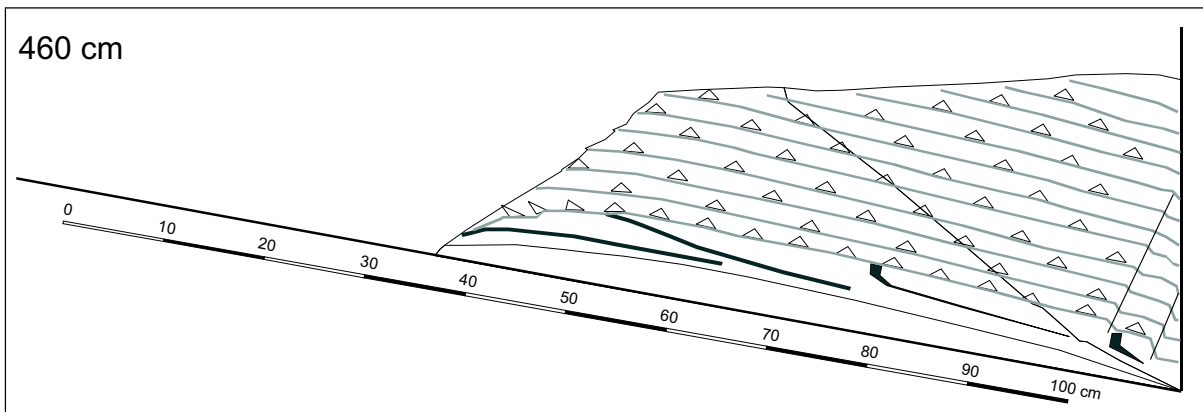
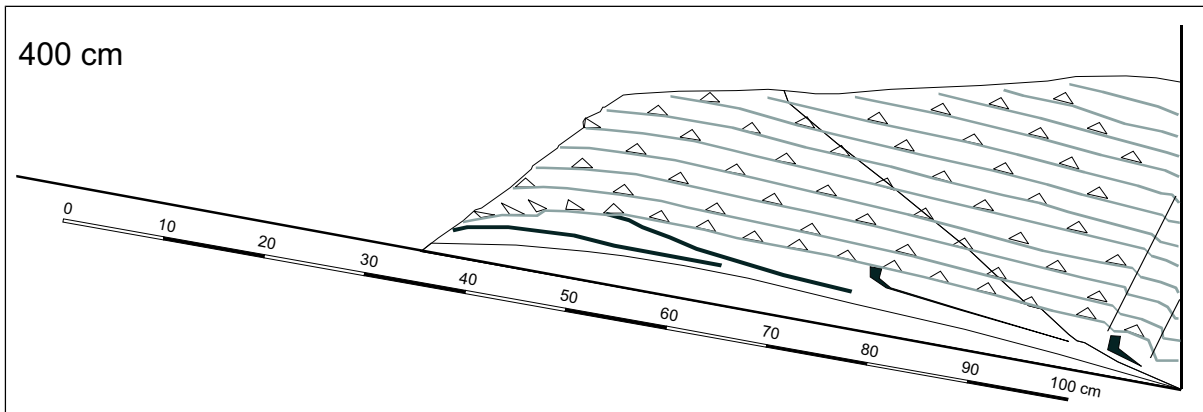
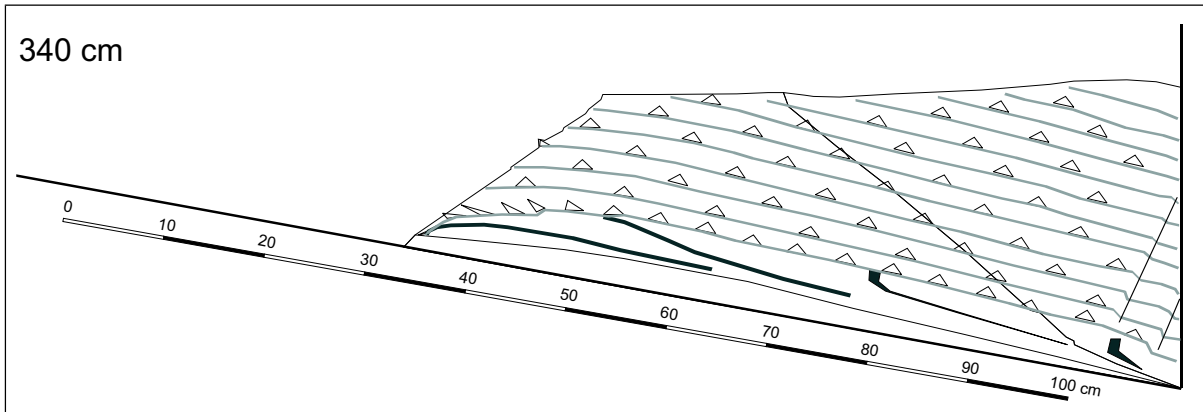


PSC experiment

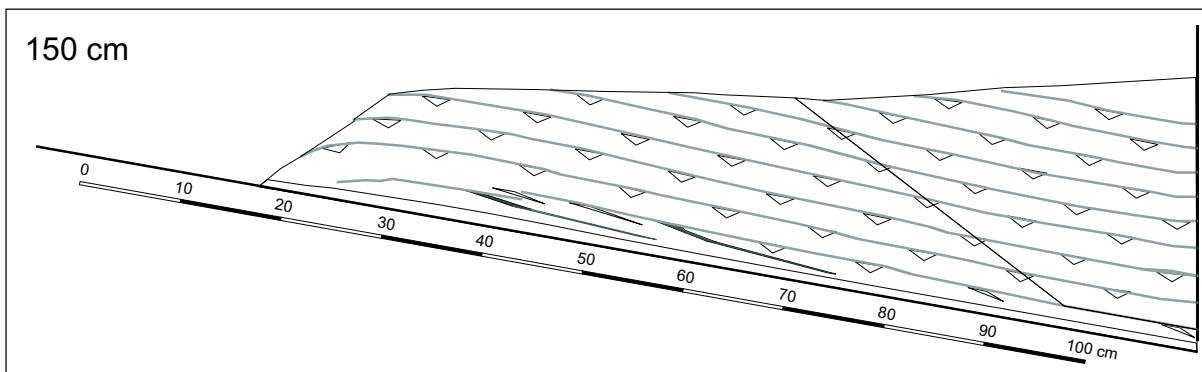
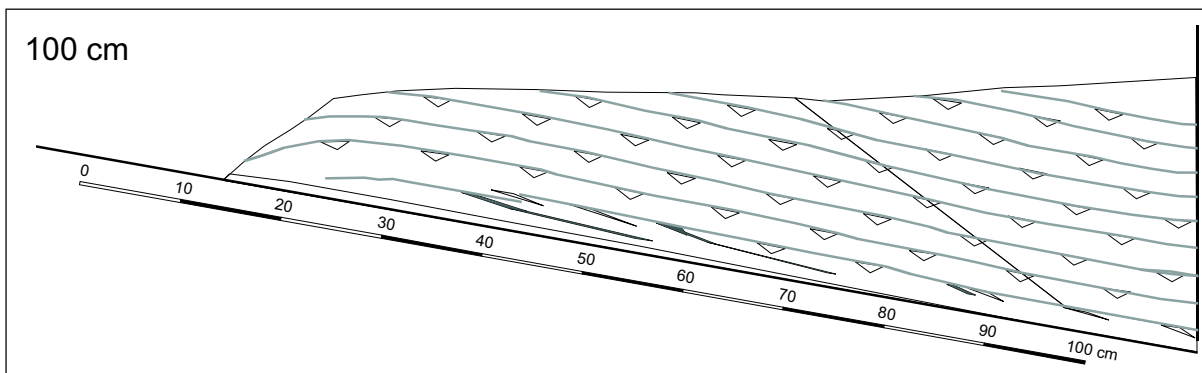
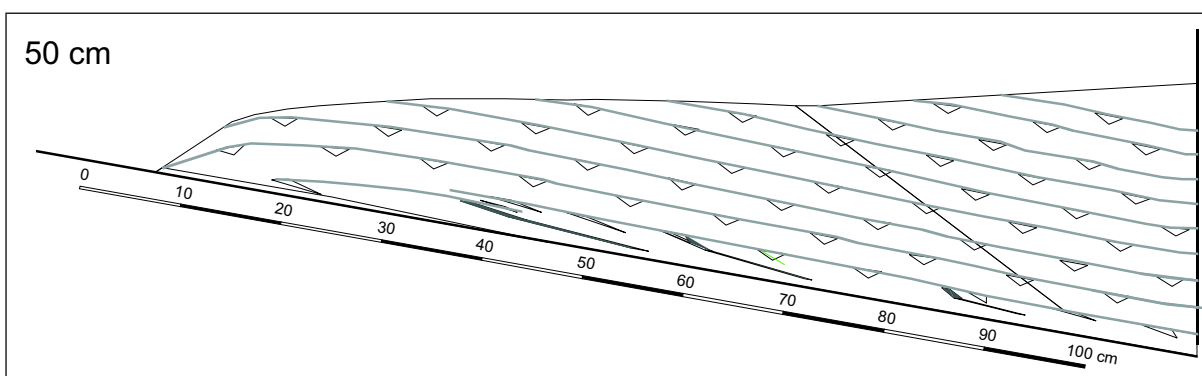
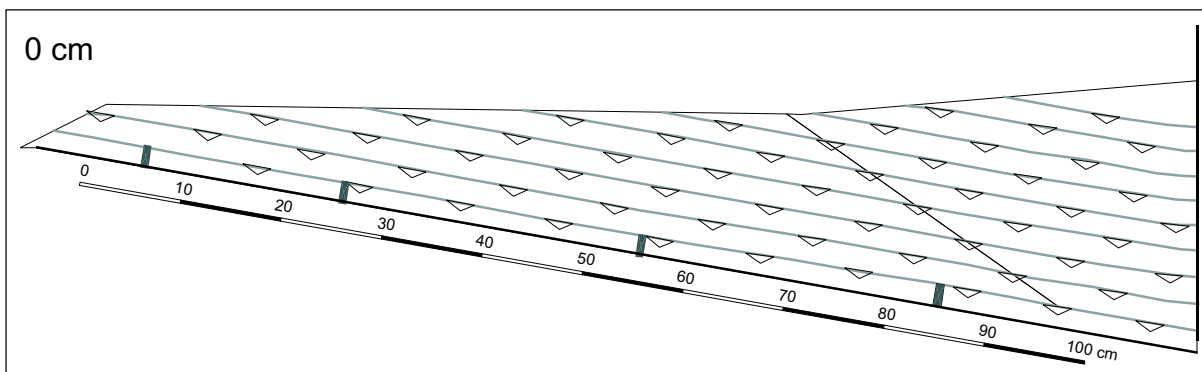


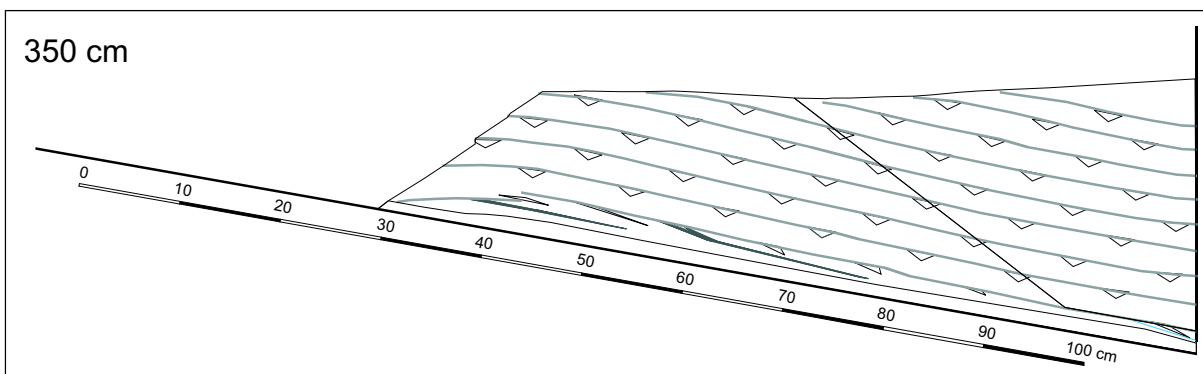
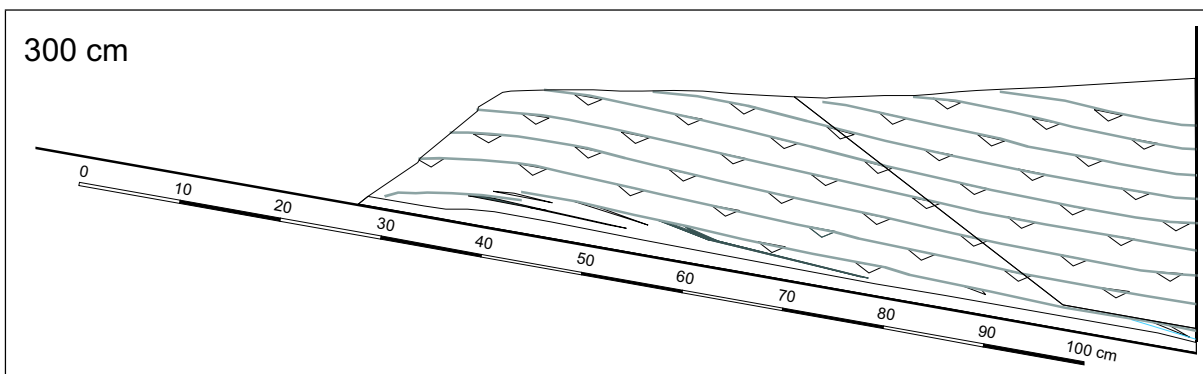
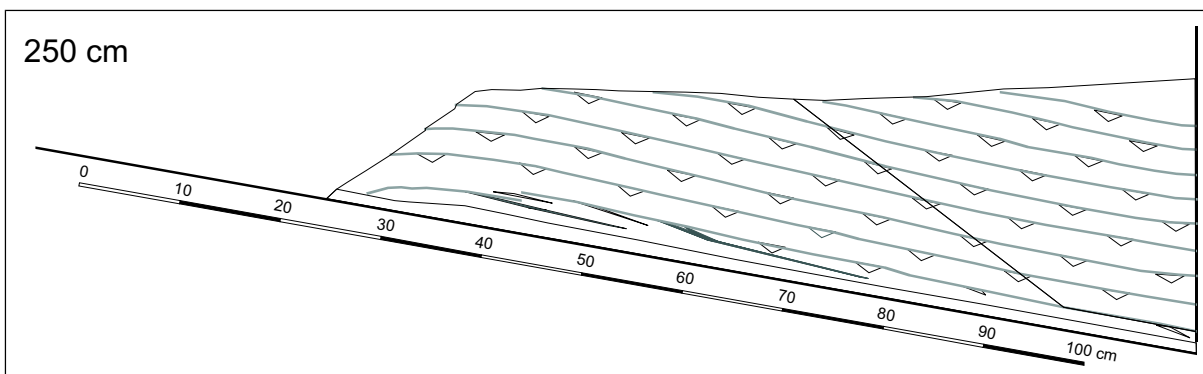
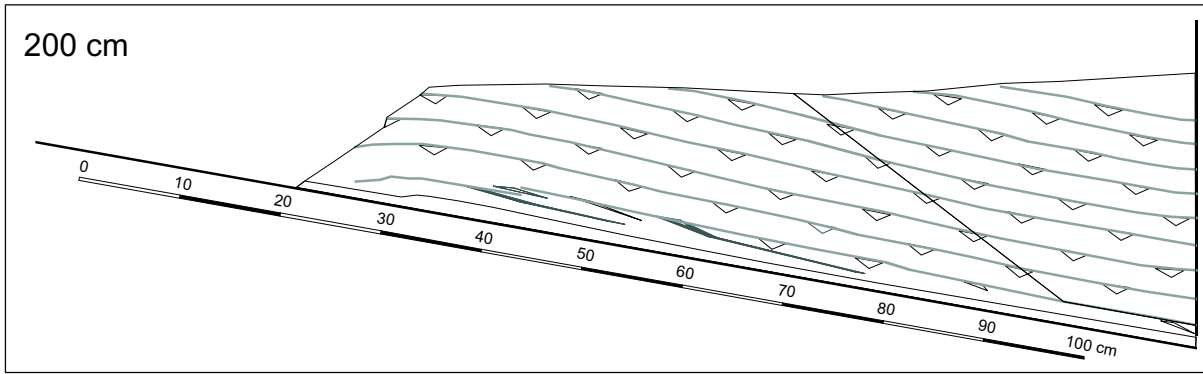


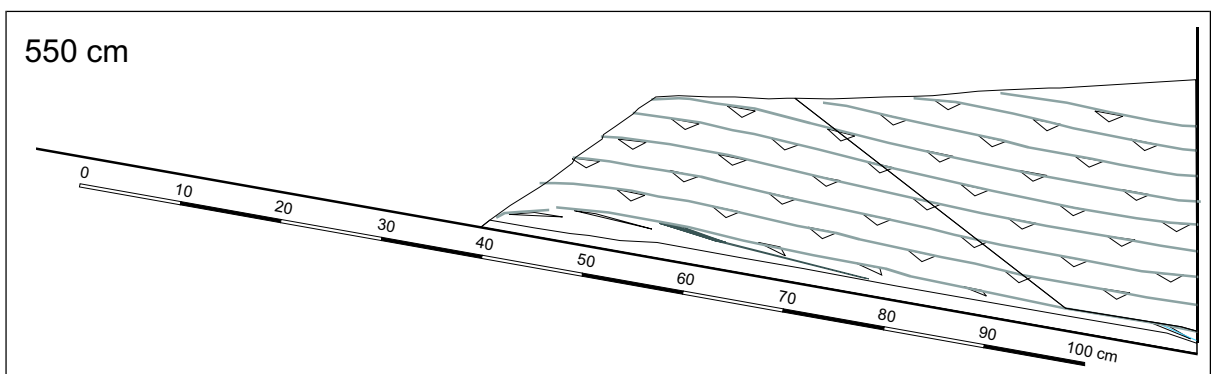
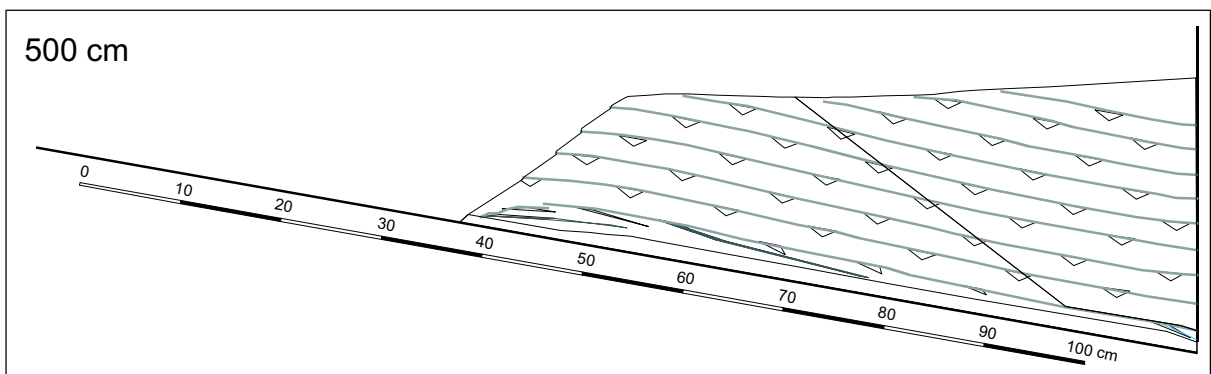
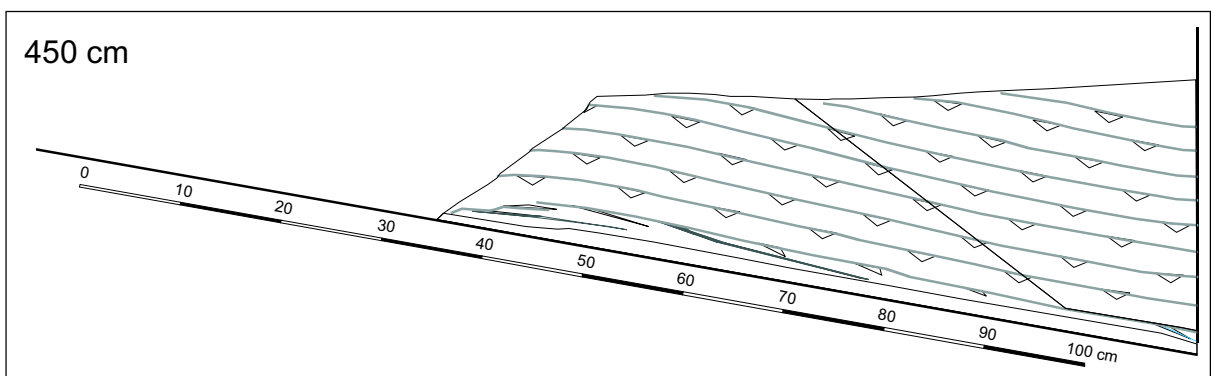
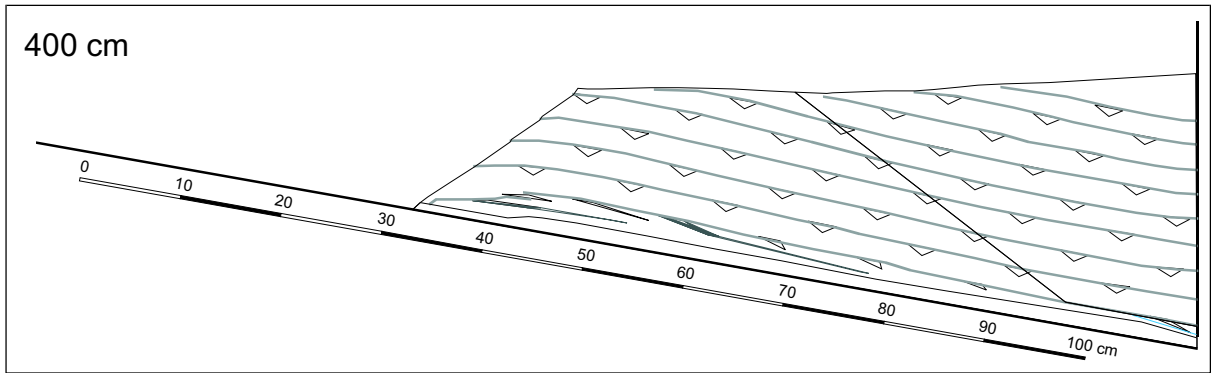


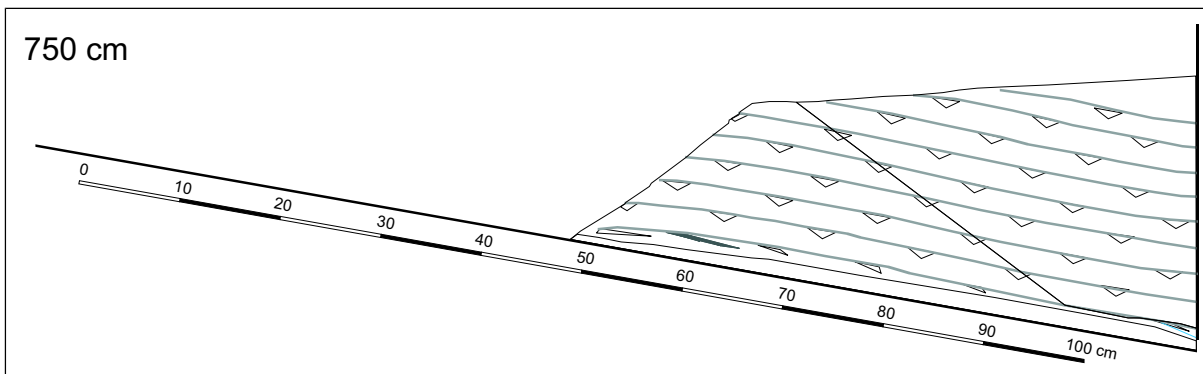
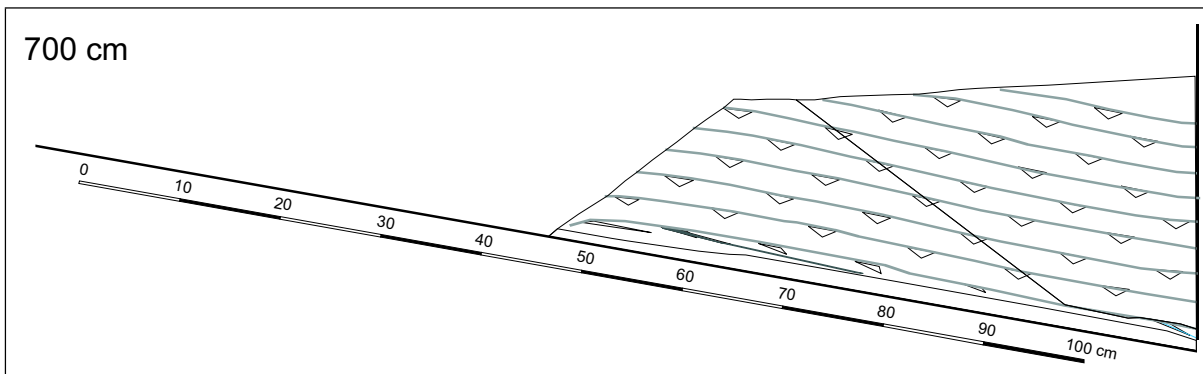
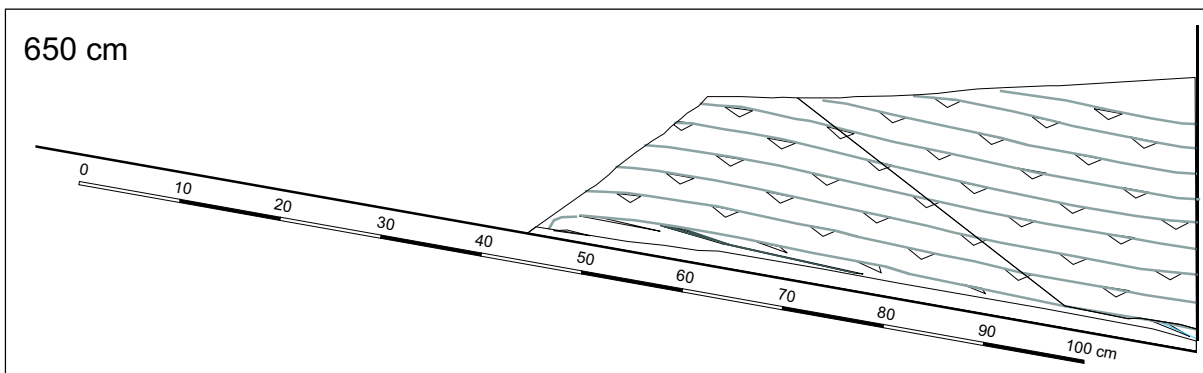
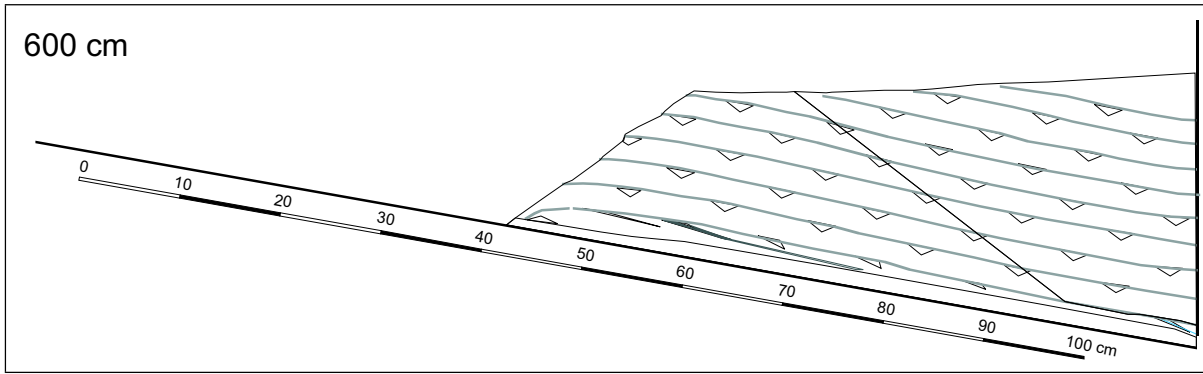


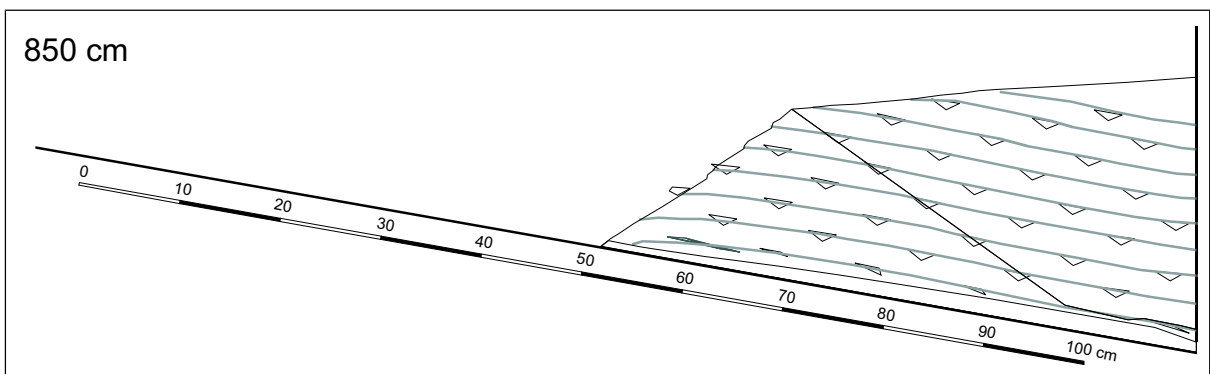
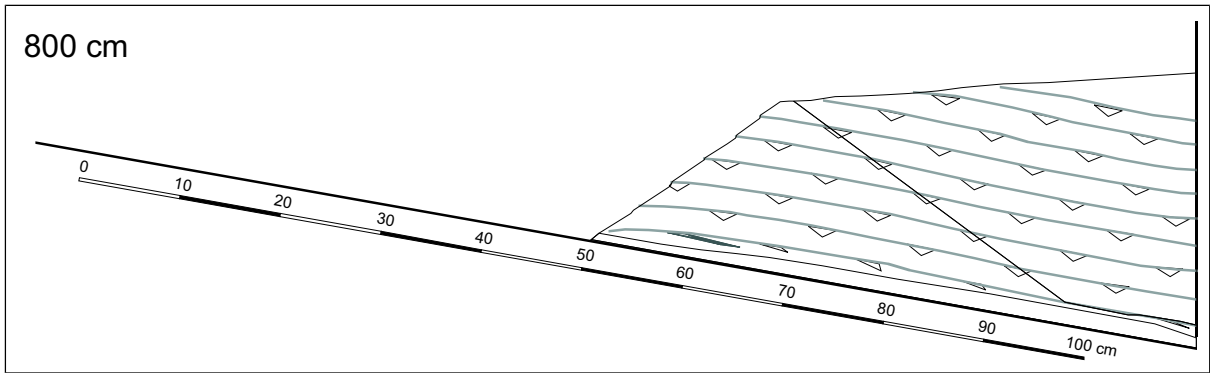
SSO experiment



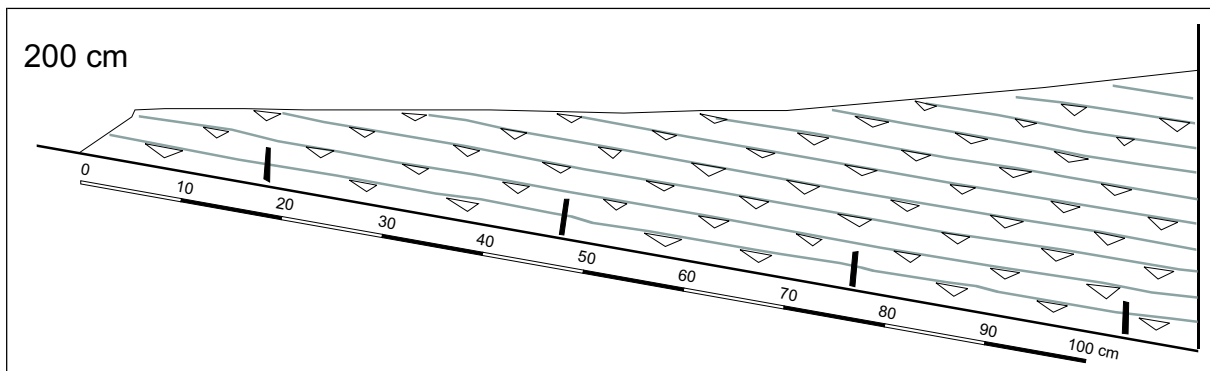
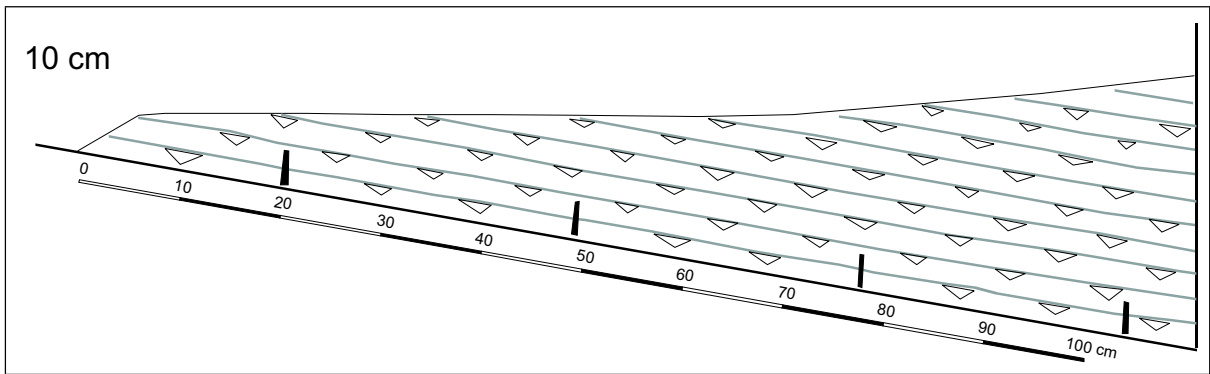




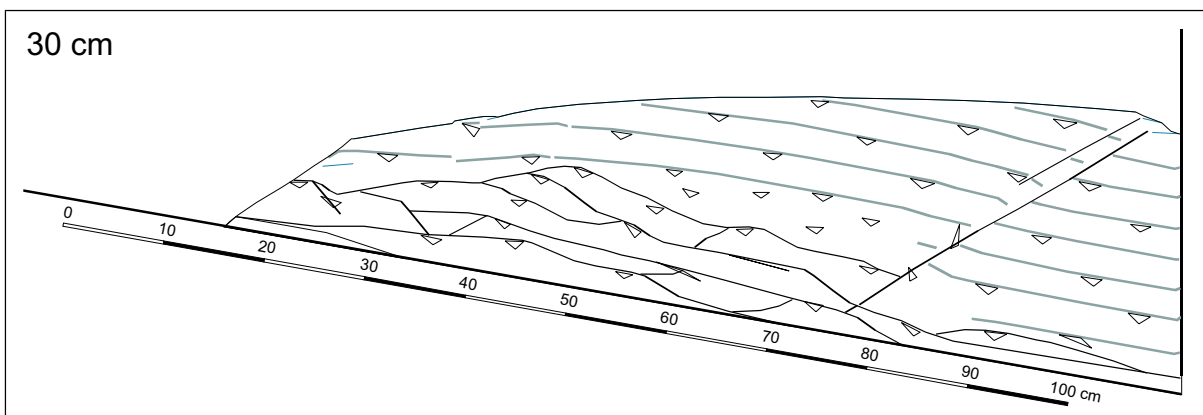
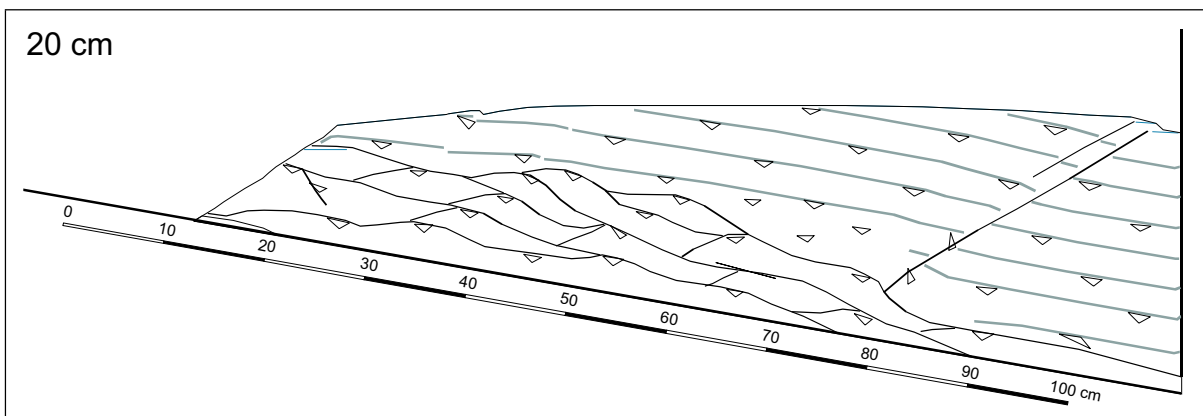
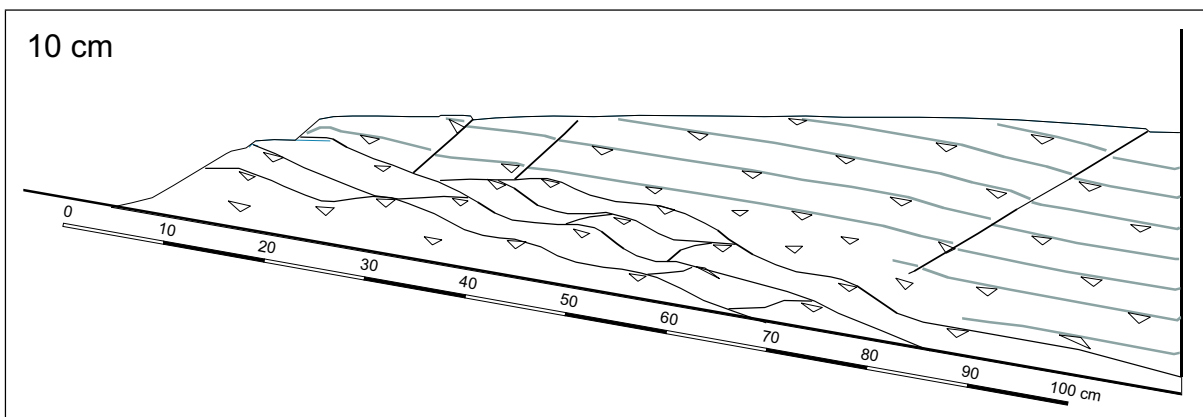
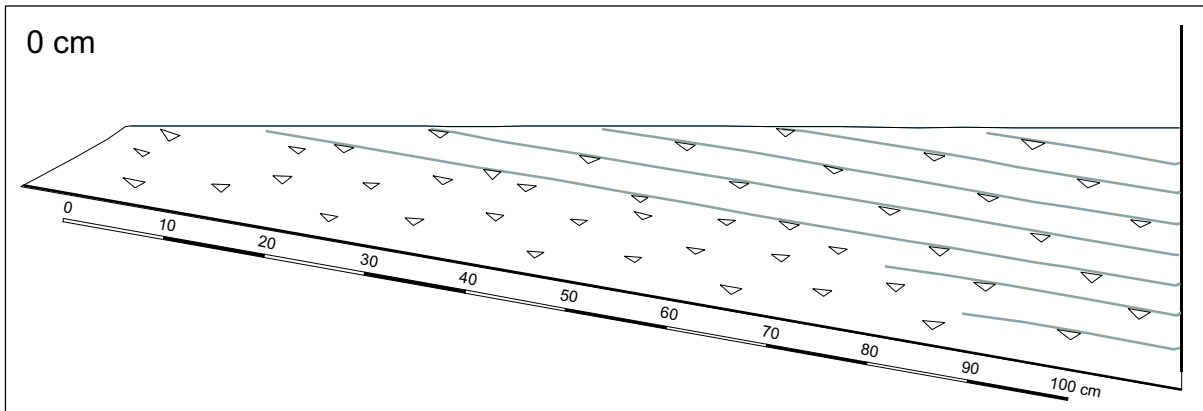


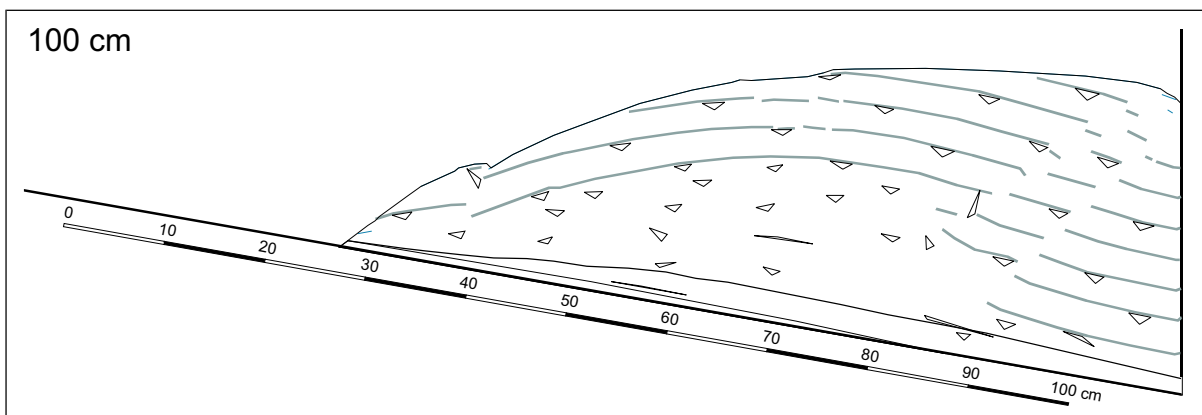
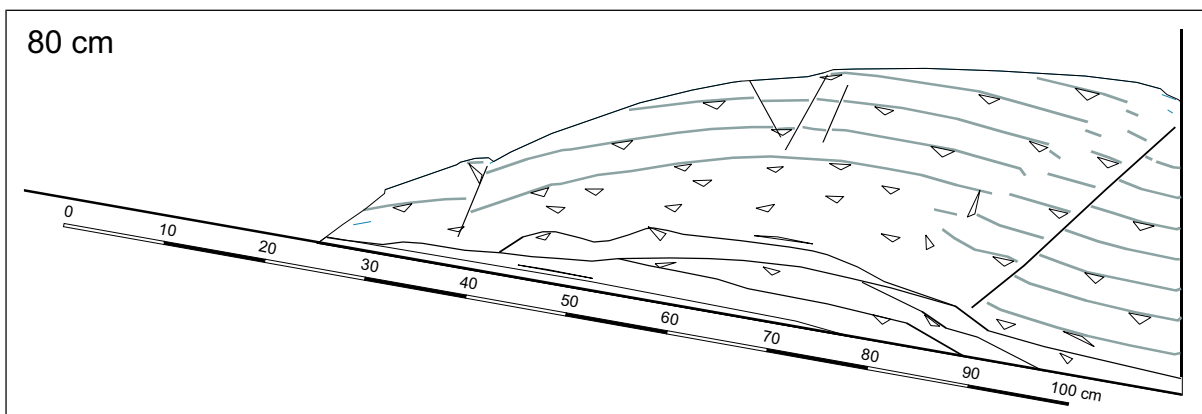
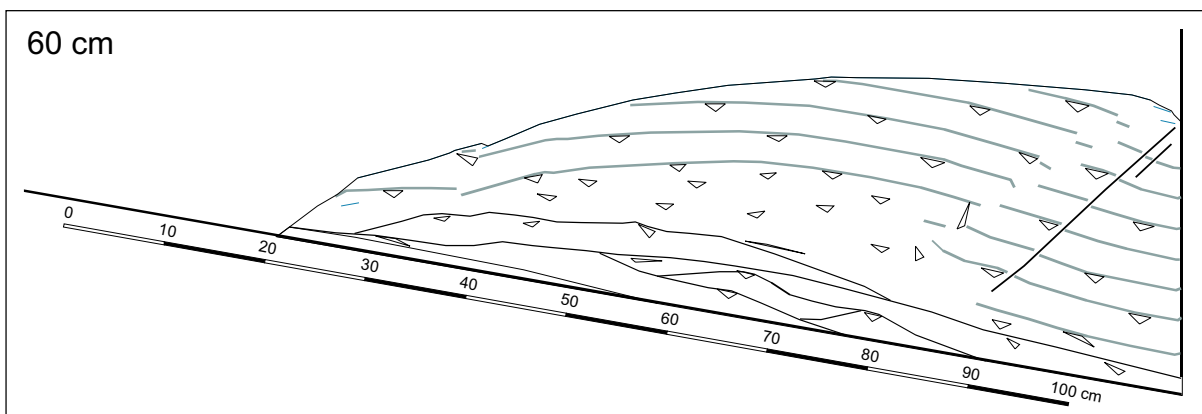
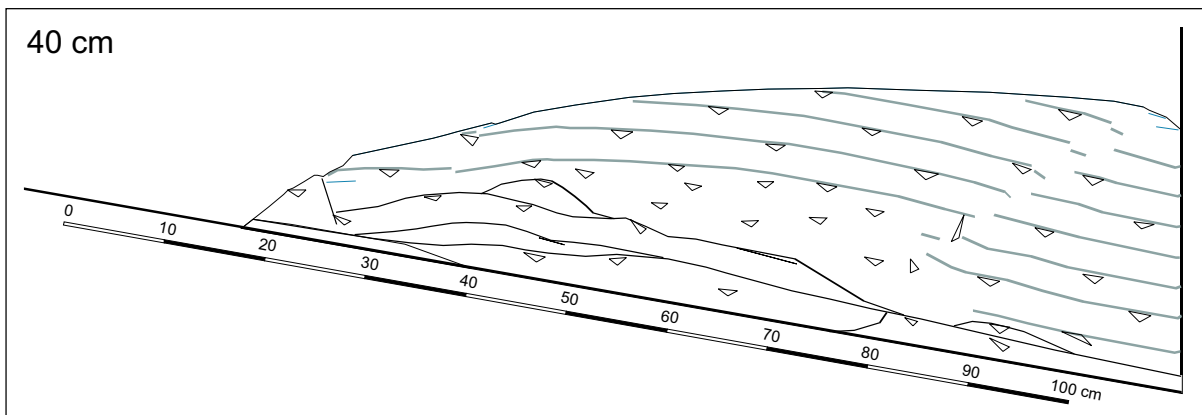


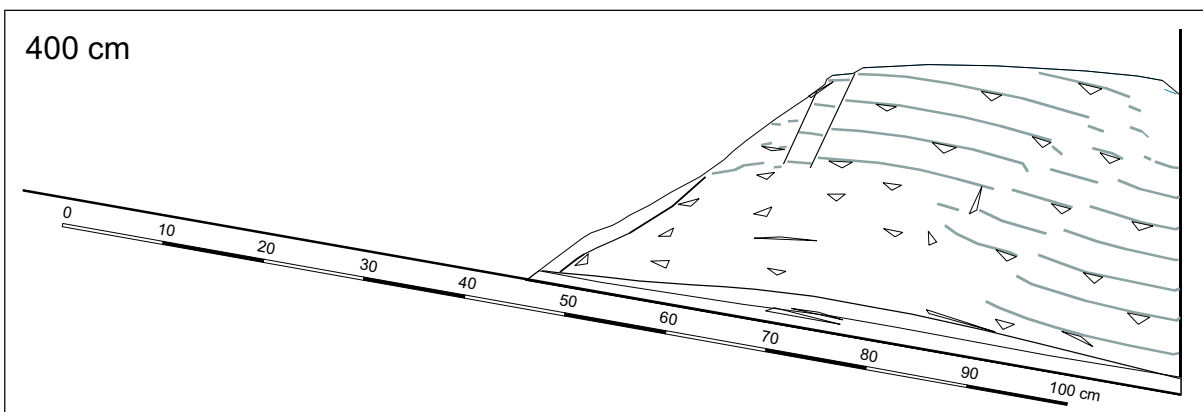
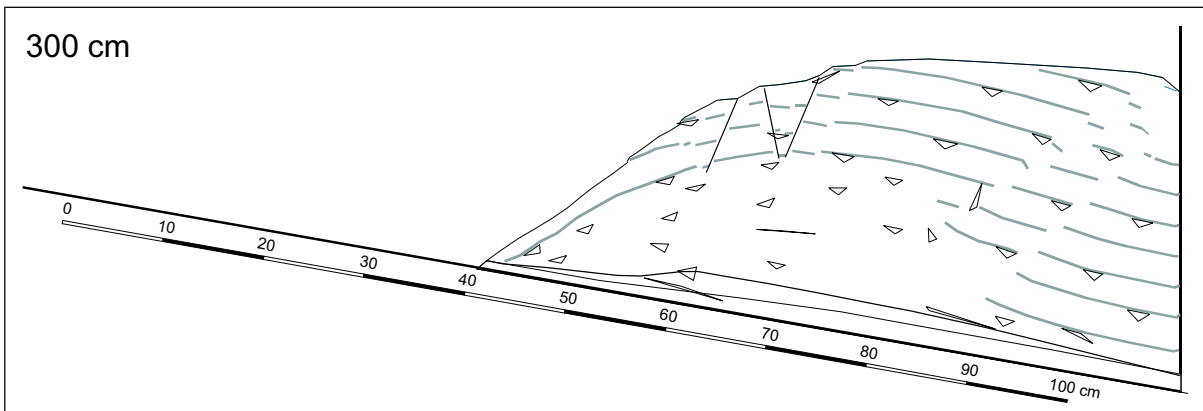
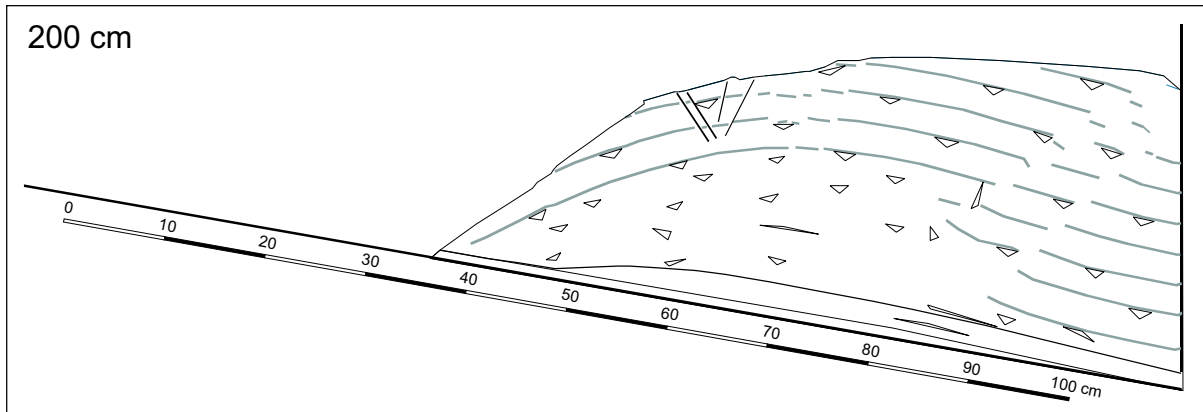
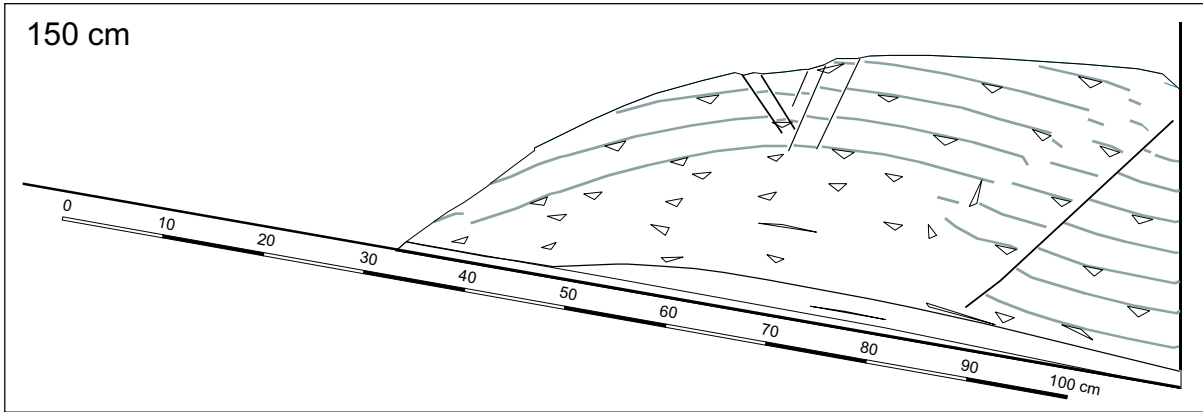
SLC experiment

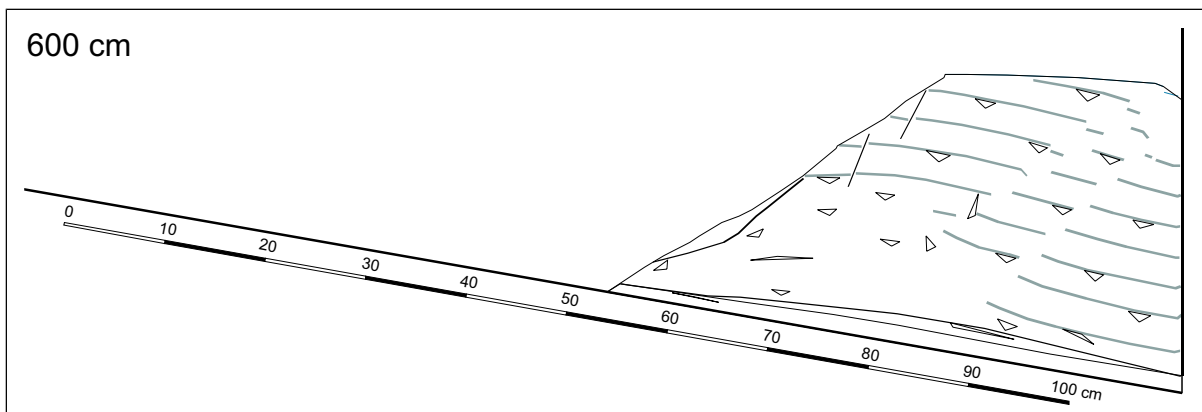
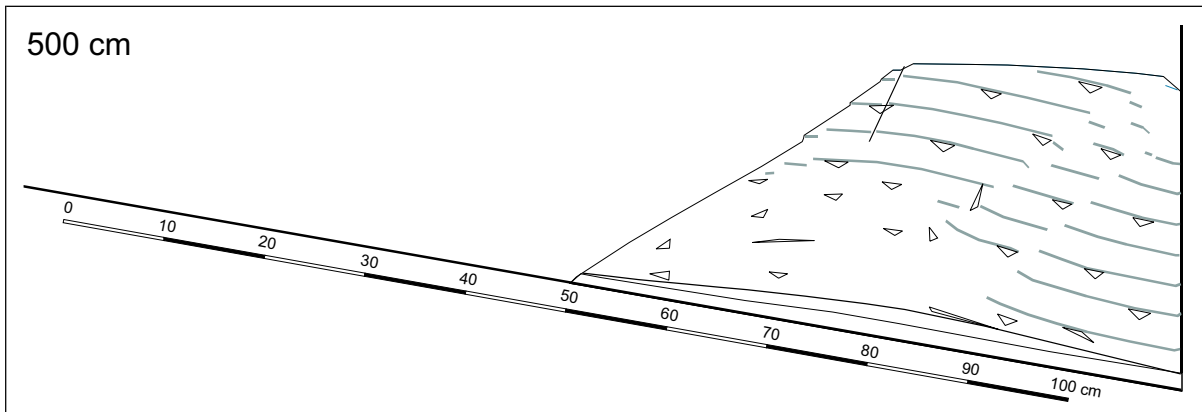


ASO experiment







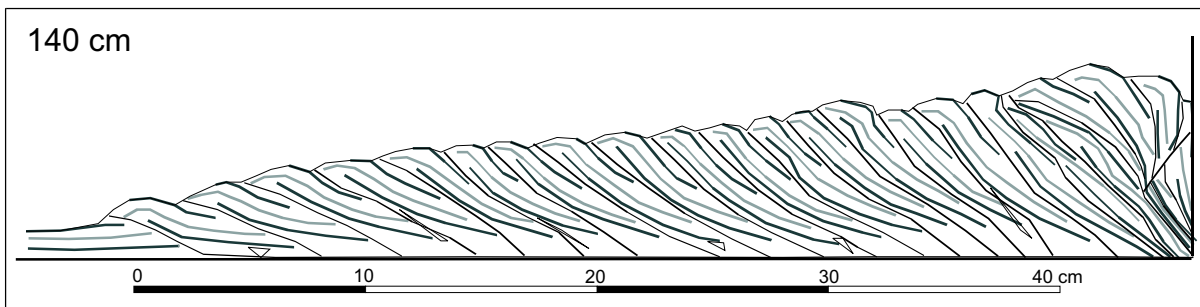
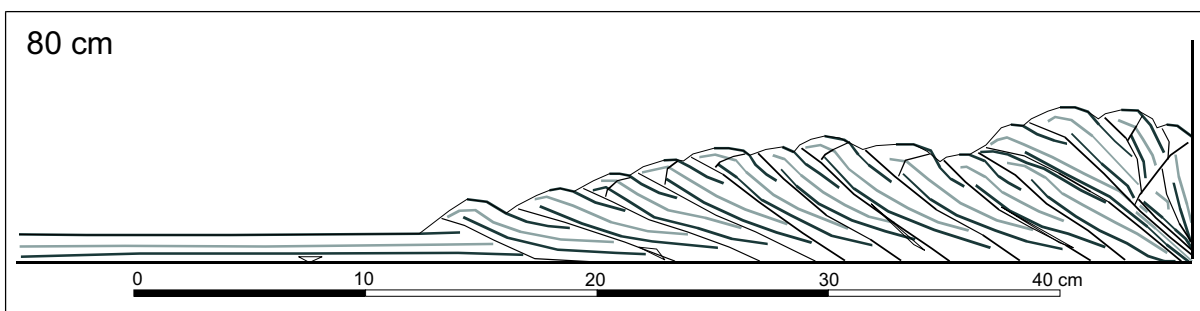
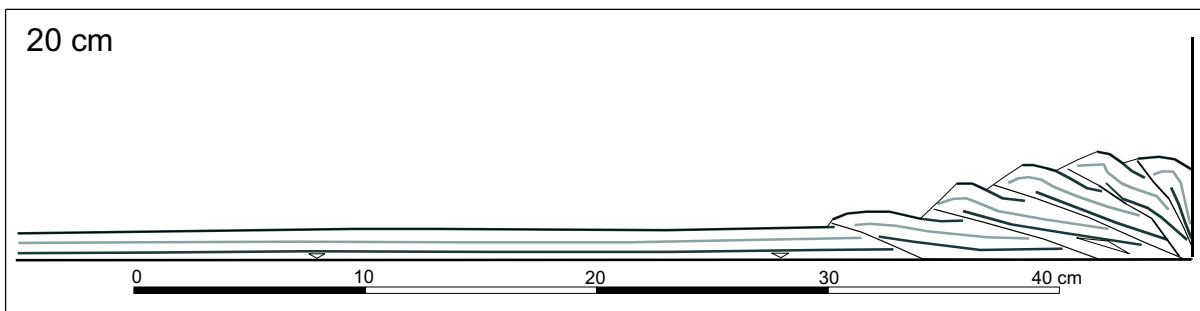


Appendix B

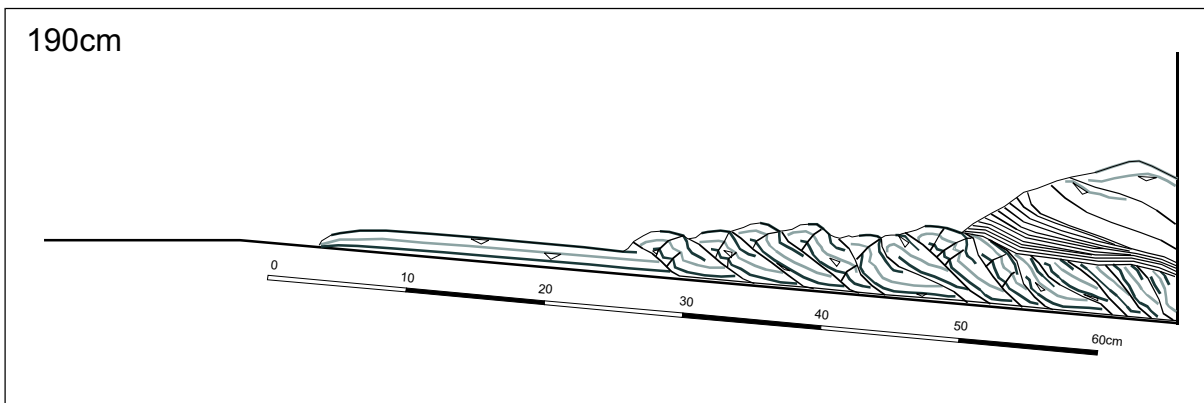
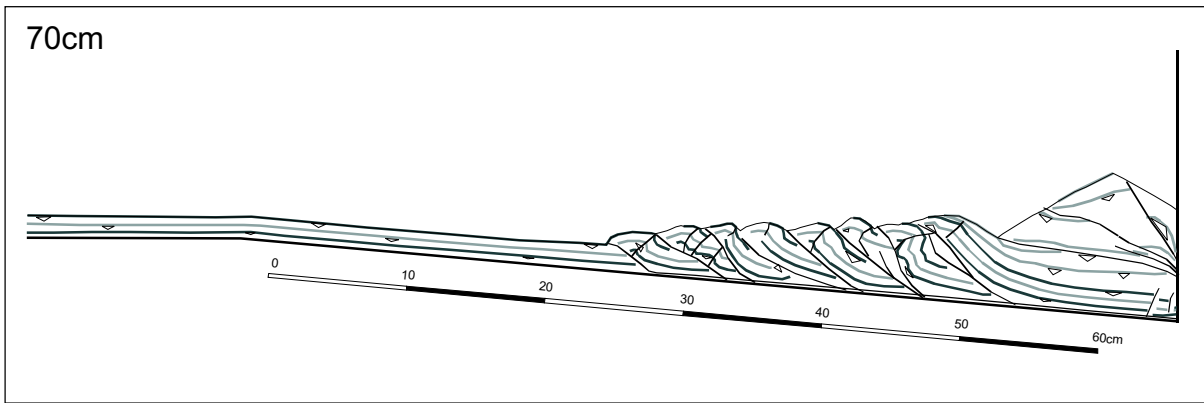
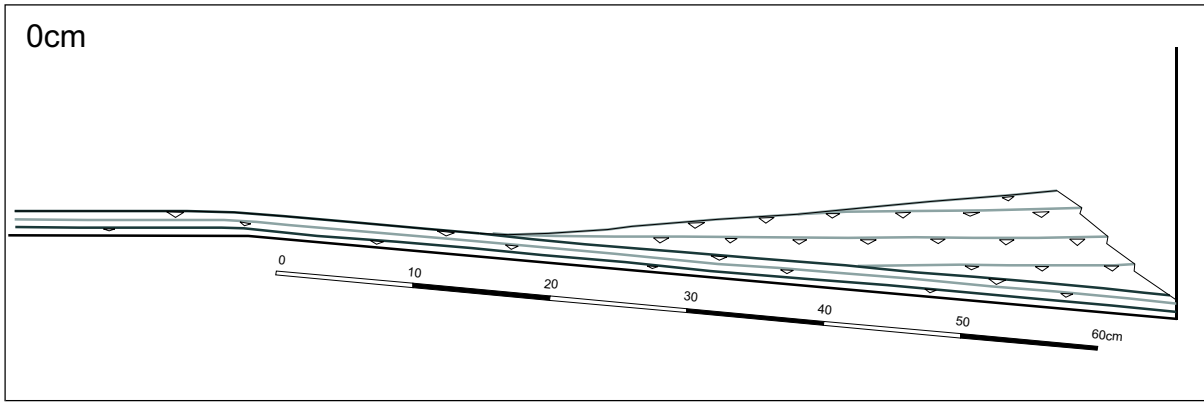
nr.	setup	incoming sand-layer thickness [mm] and material	initial wedge	initial surface slope [°]	conveyor belt	basal dip [°]	comment	page
purely frontal accretion: variation of internal friction								
# 1.5	open (5 mm)	14 (S30T)	no	0	Mylar	0	test experiment for documentation	191
# 2.1	open (16 mm)	16 (S30T, sifted)	S30T, sifted	5	PVC	5	test experiment for device, default (initial material loss)	192
# 2.2	open (16 mm)	16 (S30T, sifted)	S30T, sifted	5	PVC	5	test experiment for device	193
# 2.3	open (16 mm)	16 (S30T, sifted)	S30T, sifted	5	sandpaper (< 400 µm)	5	test experiment for device	194
# 2.4	closed (16 mm)	16 (> 630 µm, sifted)	> 630 µm, sifted	5	Mylar	5	test experiment for material	195
purely frontal accretion: variation of basal friction:								
# 2.12	closed	15 (SIC2)	no	0	latex gum	0	test experiment for setup	196
# 2.13a	closed	15 (SIC2)	no	0	sandpaper (< 400 µm)	0	test experiment for setup	199
# 2.13b	open (13 mm)	15 (SIC2)	sand wedge produced in # 2.13a	0	sandpaper (< 400 µm)	0	test experiment for setup	202
coeval frontal and basal accretion:								
# 5.1	closed	no / 5 (SIC2)	SIC2/mortar	37/6	sandpaper (< 400 µm)	6.5	test experiment: transition from tectonic erosion to accretion	206
# 5.4	closed	39 (SIC2 with glass-bead horizon)	mortar	6	sandpaper (< 400 µm)	5	default (backstop was too short)	208
# 5.5	closed	20 (SIC2) 5 (basal glass-bead layer)	no	-6	sandpaper (< 400 µm)	5	test experiment: frontal accretion above glass beads	209
# 5.7	closed ^a	40 (SIC2 with glass-bead horizon)	mortar and basal glass-bead layer	6	sandpaper (< 400 µm)	5	default (failure of the conveyor belt)	210
# 5.8	closed ^a	40 (SIC2 with glass-bead horizon)	mortar and basal glass-bead layer	6	sandpaper (< 400 µm)	5	no conveyor belt beneath the backstop	211
# 5.9	closed	40 (SIC2 with glass-bead horizon)	mortar	6	sandpaper (< 315 µm)	5	experiment for TV presentation; default (backstop was too short)	212
# 5.10	closed	39 (SIC2 with glass-bead horizon)	mortar	6	latex gum	5	experiment for final discussion	213
steady-state tectonic erosion:								
# 3.8	closed	no	SIC2/mortar	37/0	sandpaper (> 630 µm)	10	default (failure of the backwall)	214
# 3.9	closed	no	SIC2/mortar	37/0	sandpaper (> 630 µm)	10	default (failure of the conveyor belt)	217
# 3.10	closed	no	SIC2/mortar	37/0	sandpaper (> 630 µm)	10	default (failure of the conveyor belt)	218
# 3.11	closed	no	SIC2/lenses of SIC2 and glass-bead horizons (small)	37/0	sandpaper (< 315 µm)	10	test experiment for tectonic erosion of lens-shaped bodies; default (lateral material loss)	219
# 3.12	closed	no	SIC2/lenses of SIC2 and glass-bead horizons (very large)	37/0	sandpaper (< 315 µm)	10	test experiment for tectonic erosion of lens-shaped bodies	220
# 3.14	closed	no	SIC2/lenses of SIC2 and glass-bead horizons (large)	37/0	sandpaper (< 315 µm)	10	tectonic erosion of lens-shaped bodies	221
# 3.15	closed	no	SIC2/lenses of SIC2 and glass-bead horizons (small)	37/0	sandpaper (< 315 µm)	10	tectonic erosion of lens-shaped bodies	225

^ano conveyor belt beneath the backstop

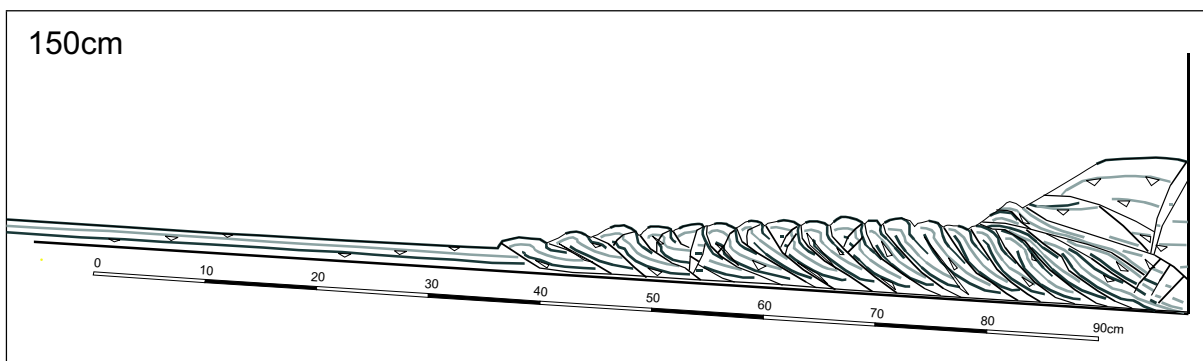
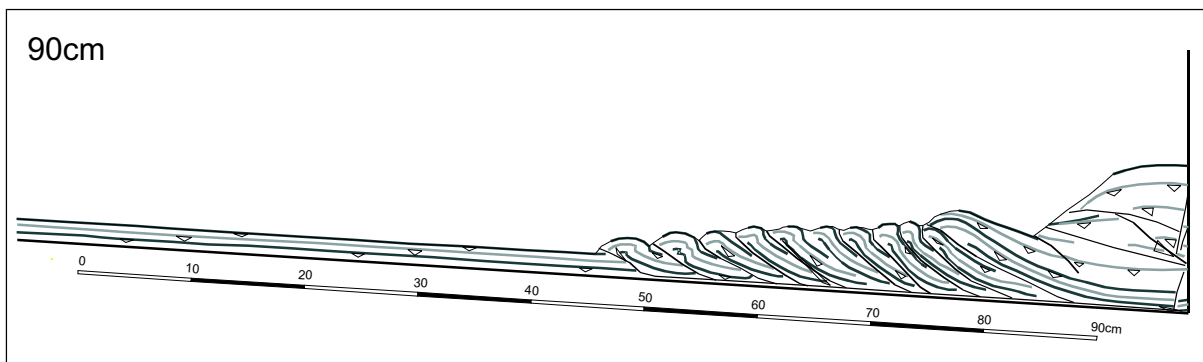
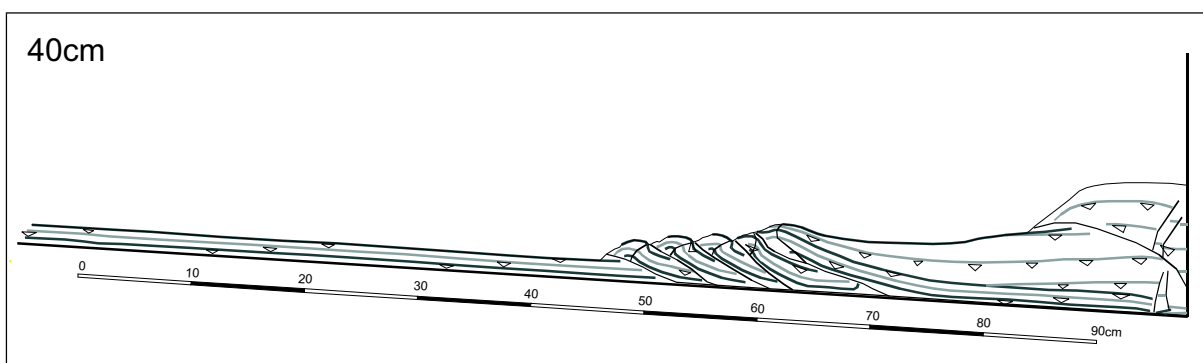
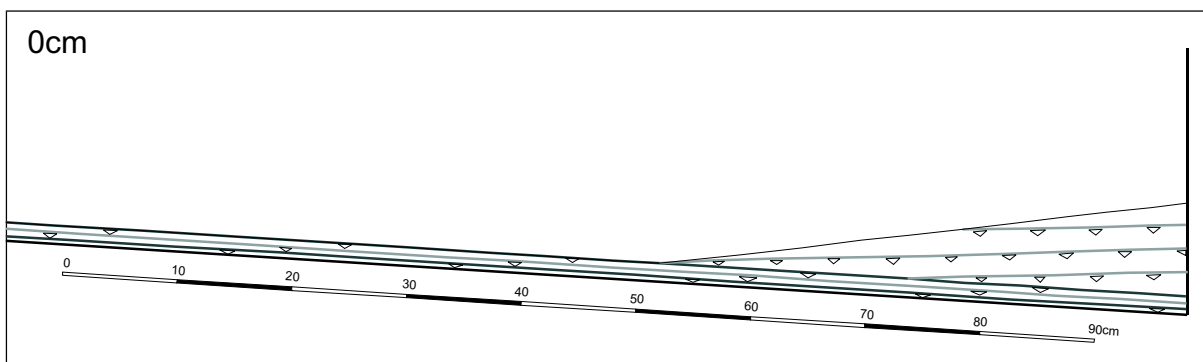
1.5 experiment



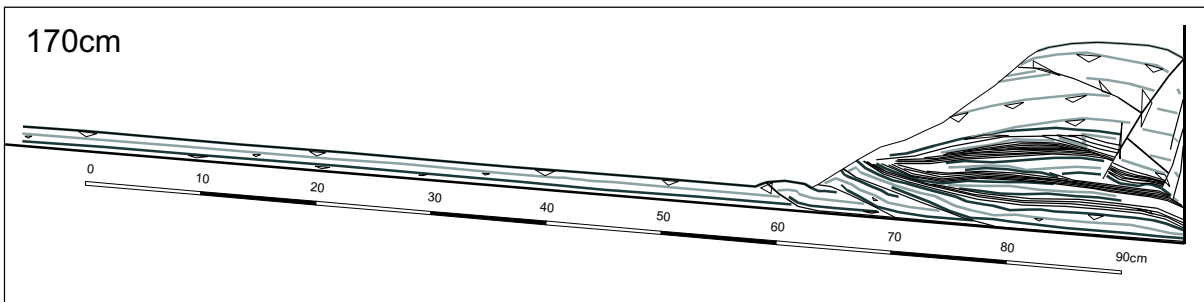
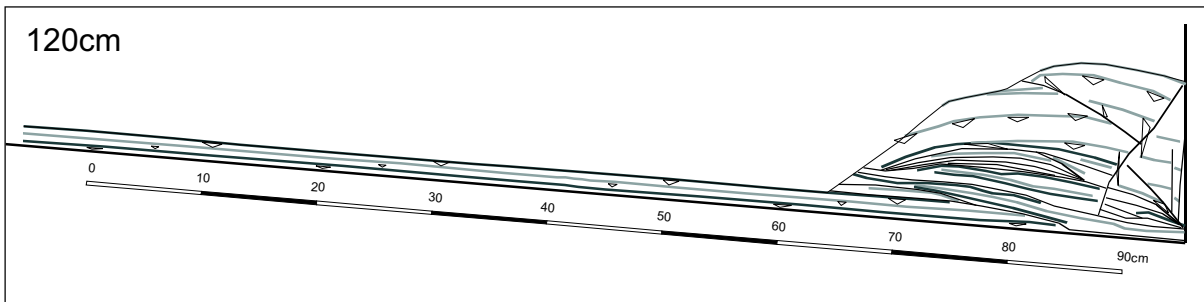
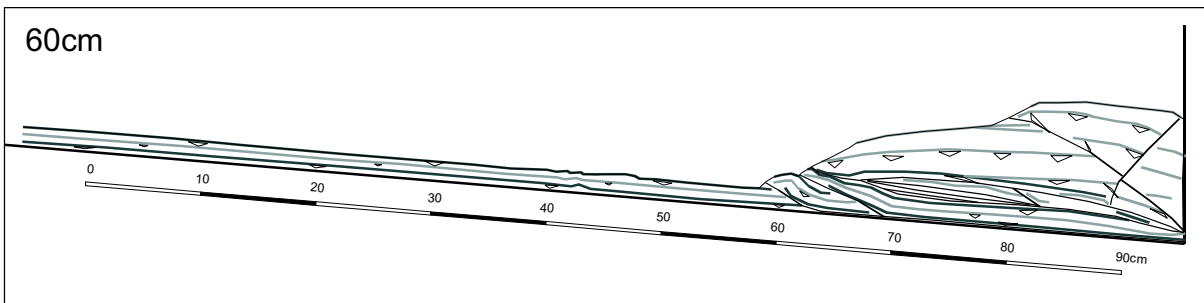
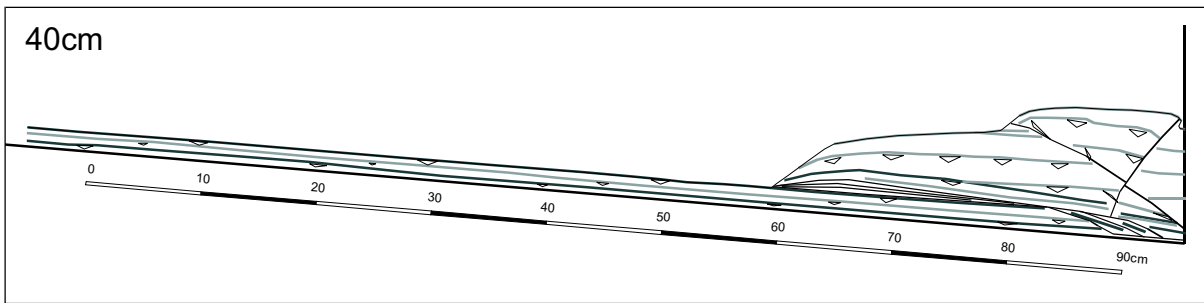
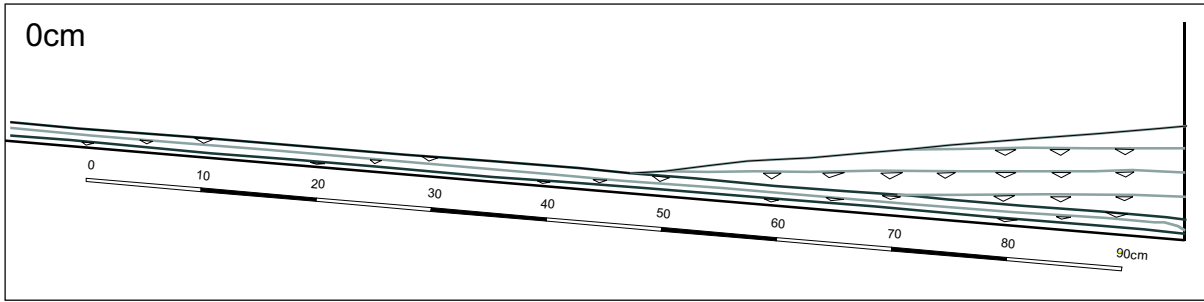
2.1 experiment



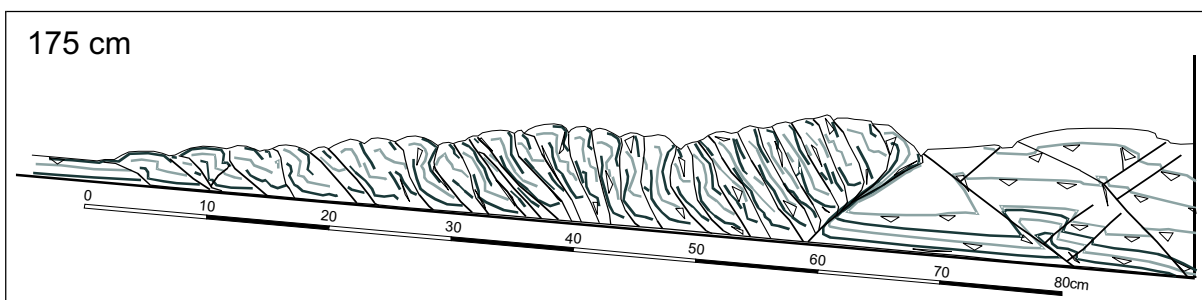
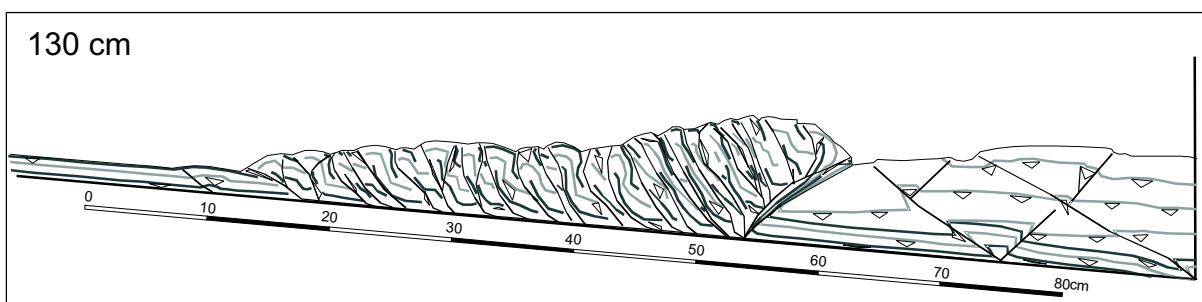
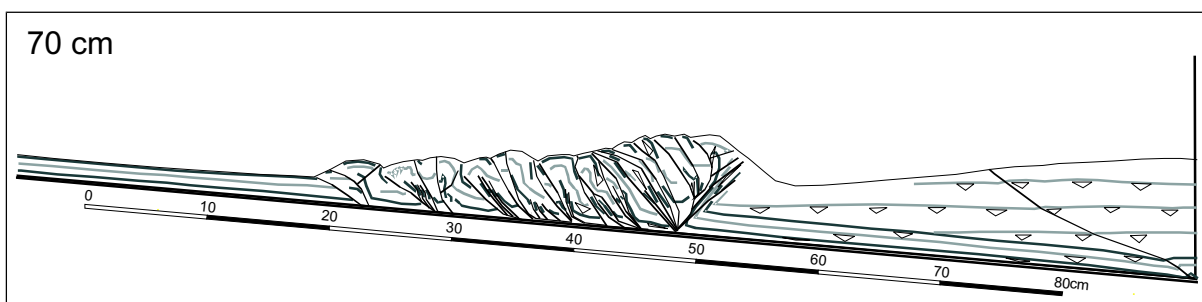
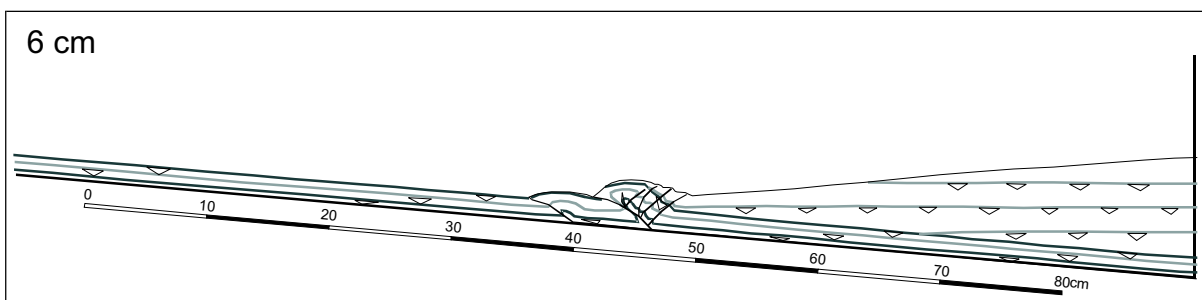
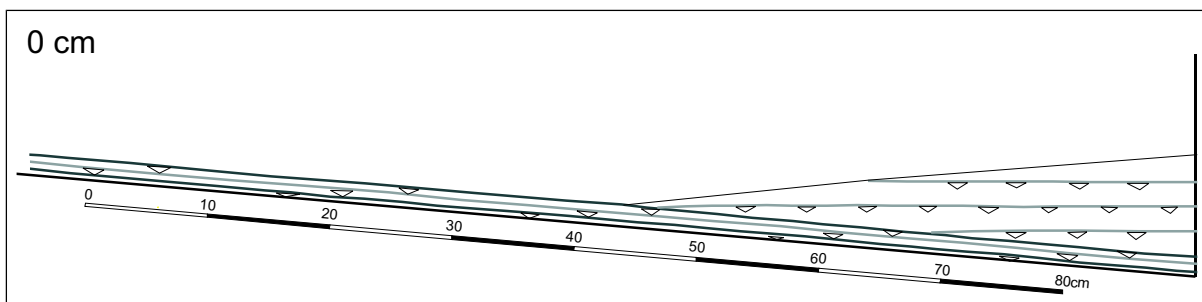
2.2 experiment



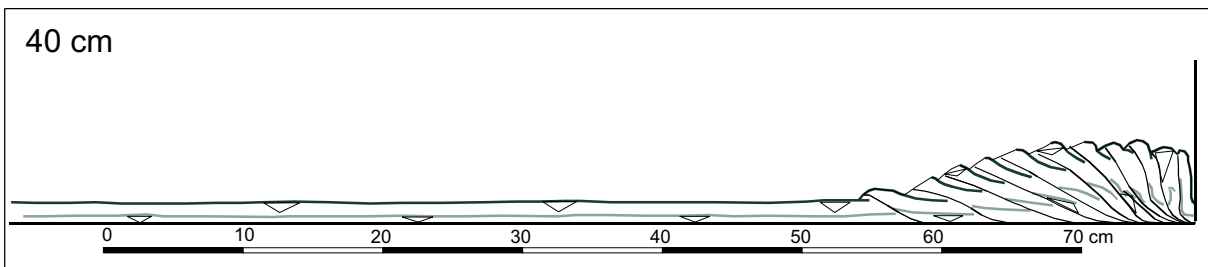
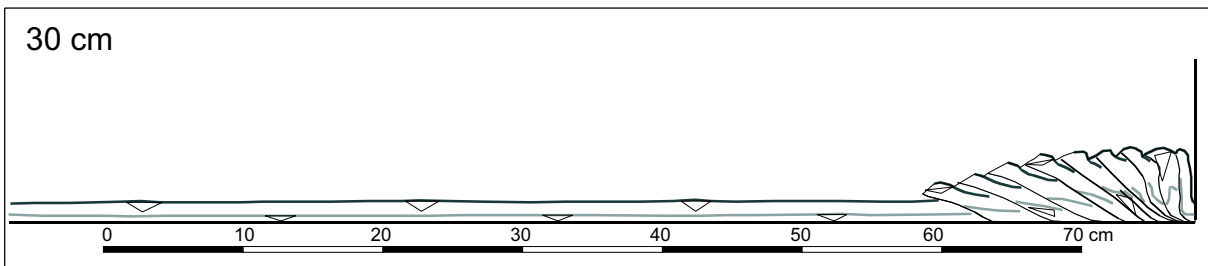
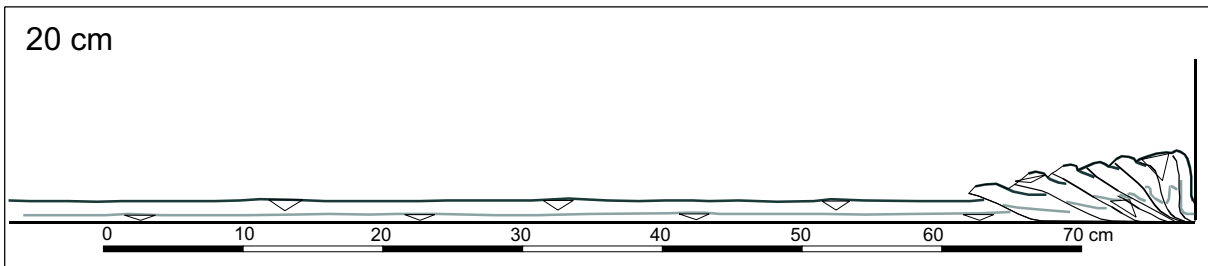
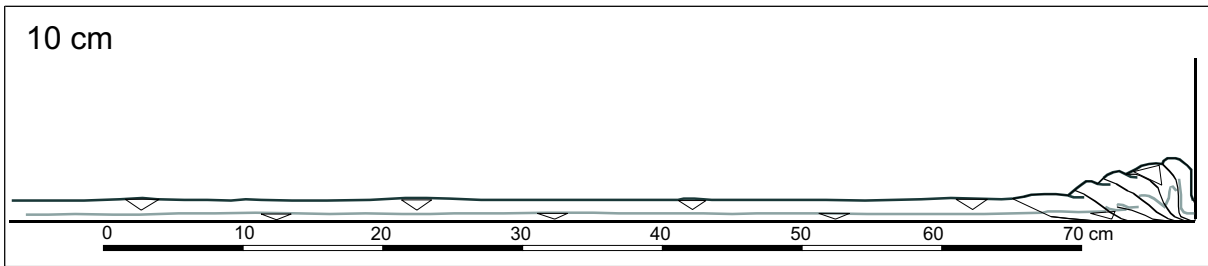
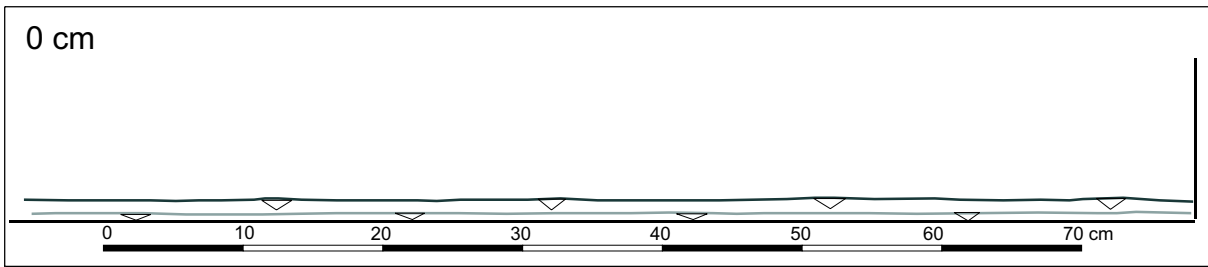
2.3 experiment

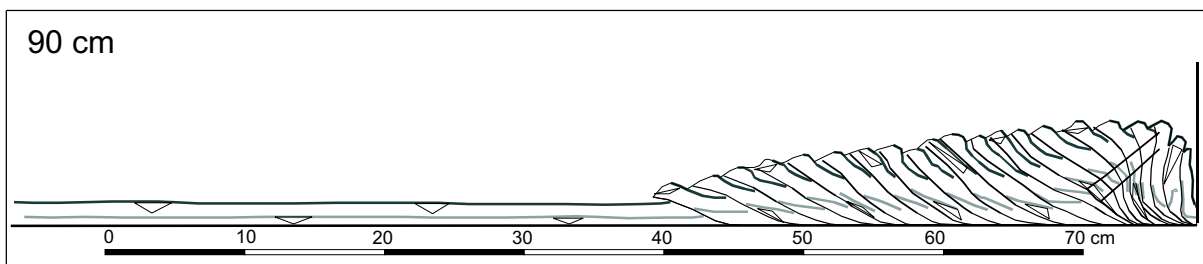
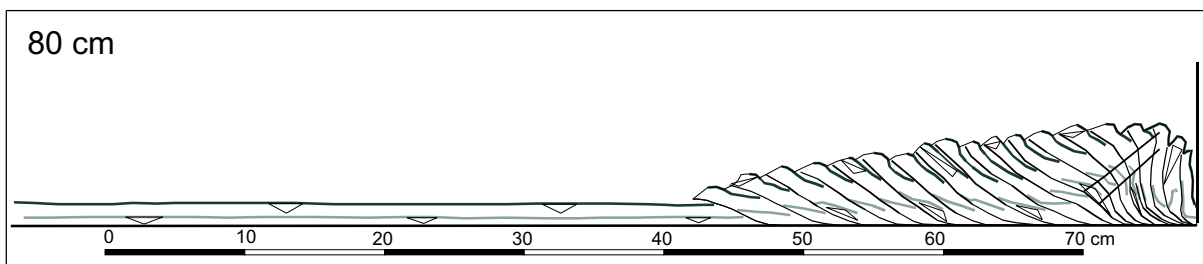
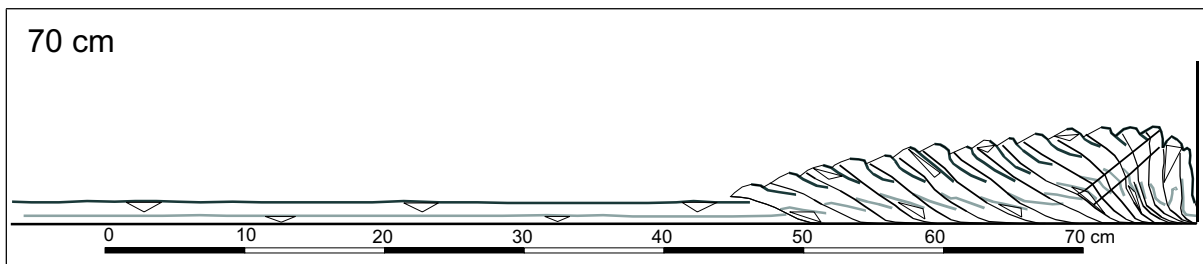
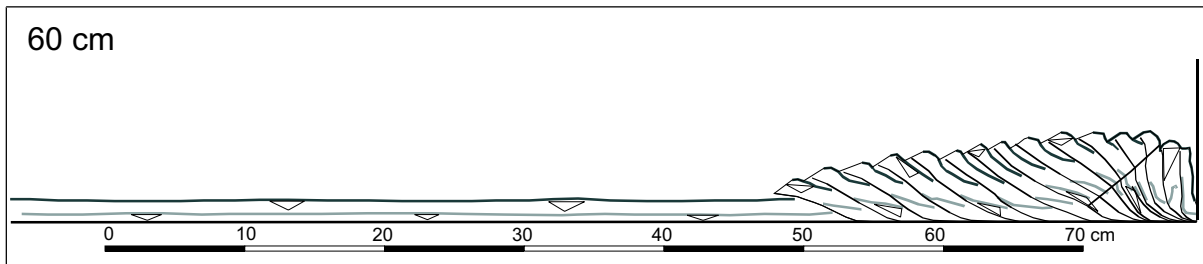
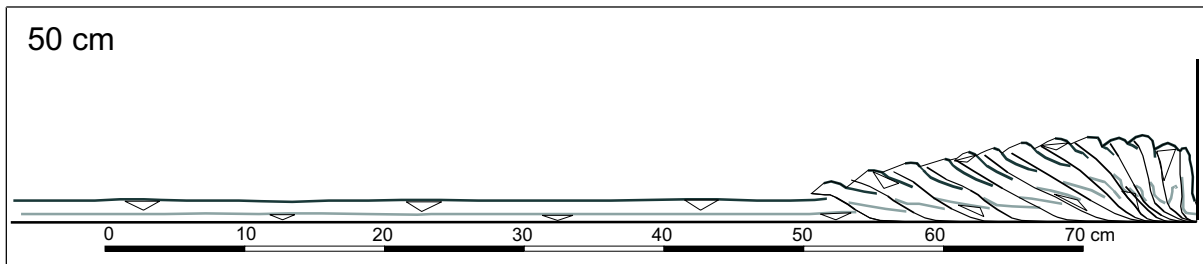


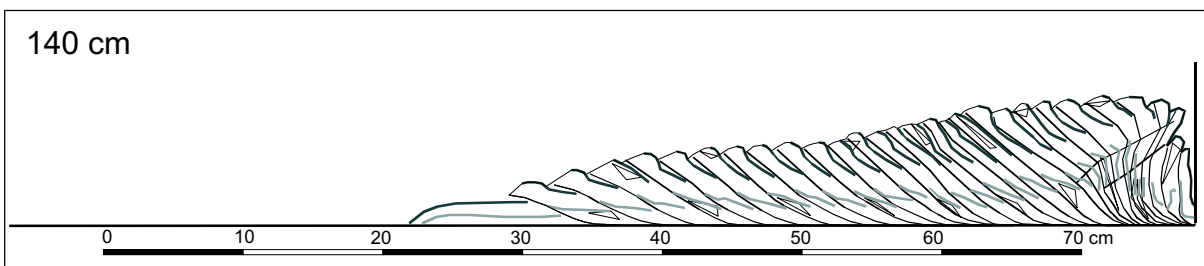
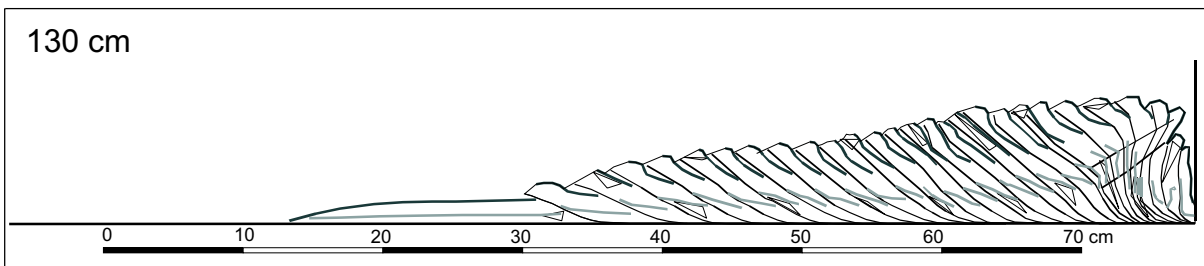
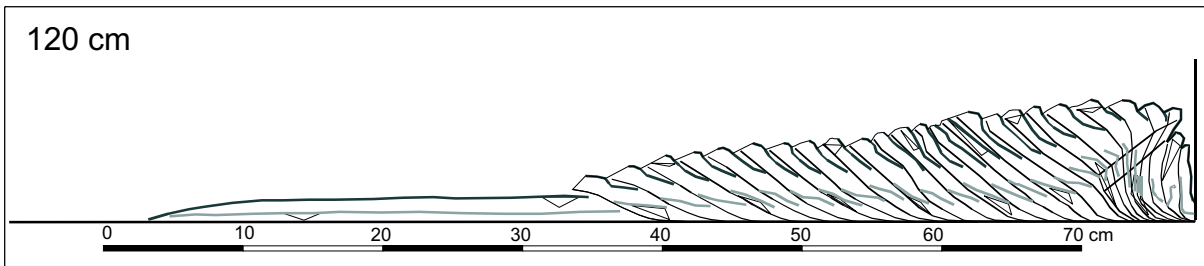
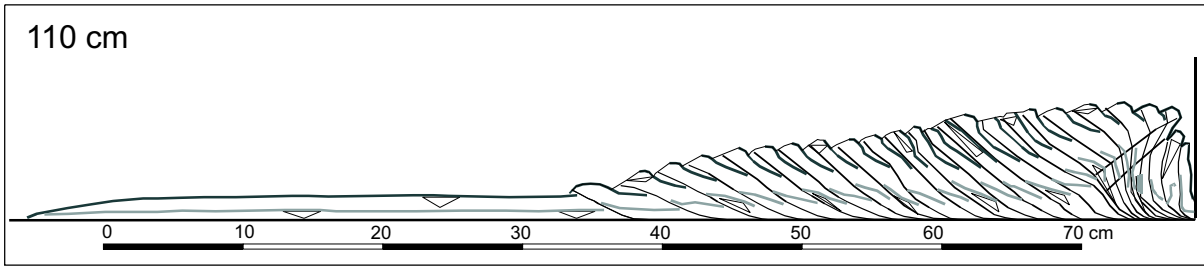
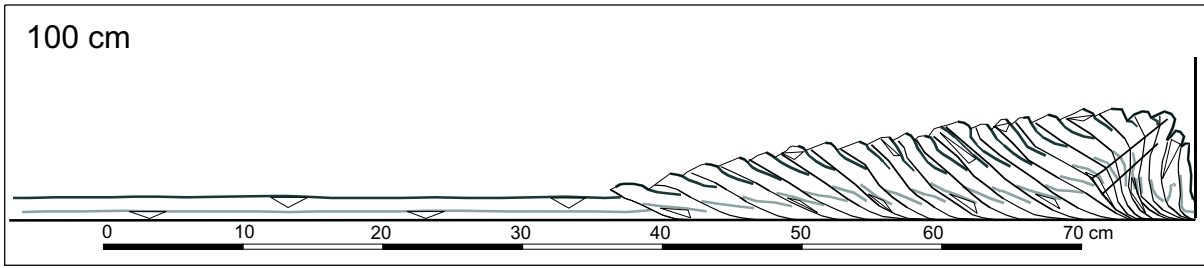
2.4 experiment



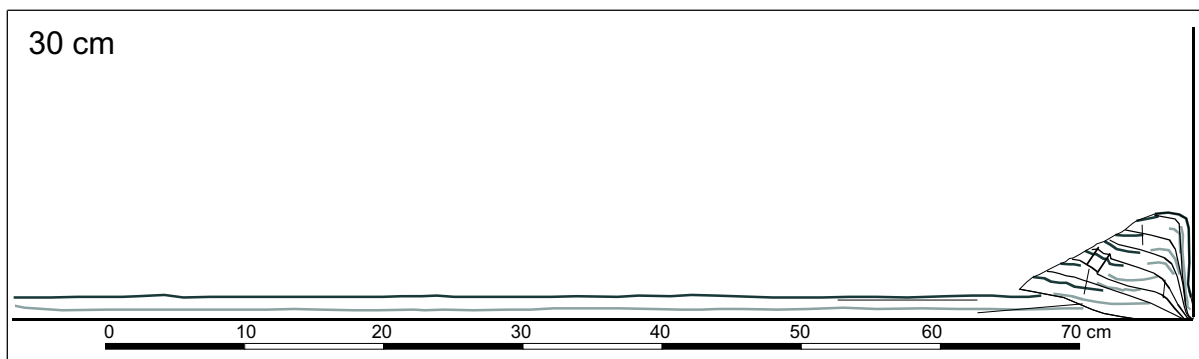
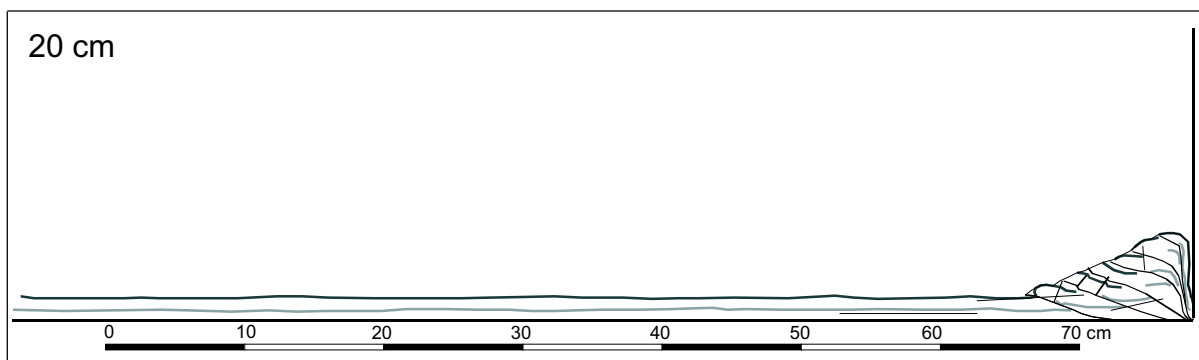
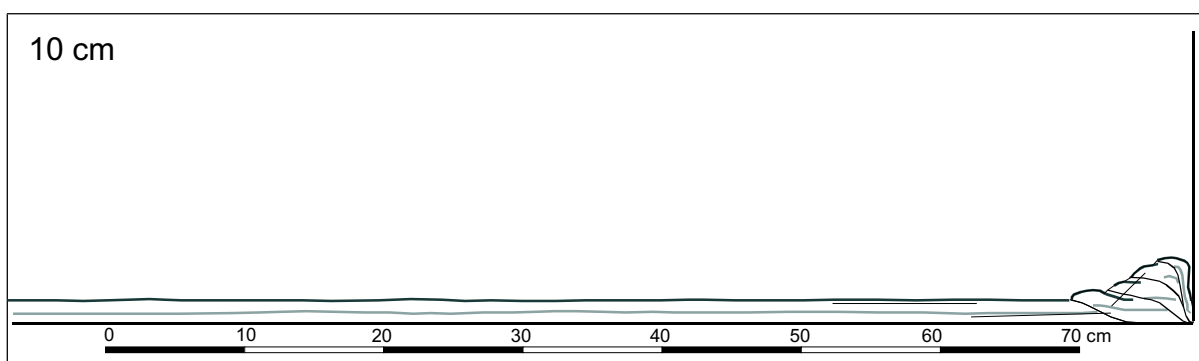
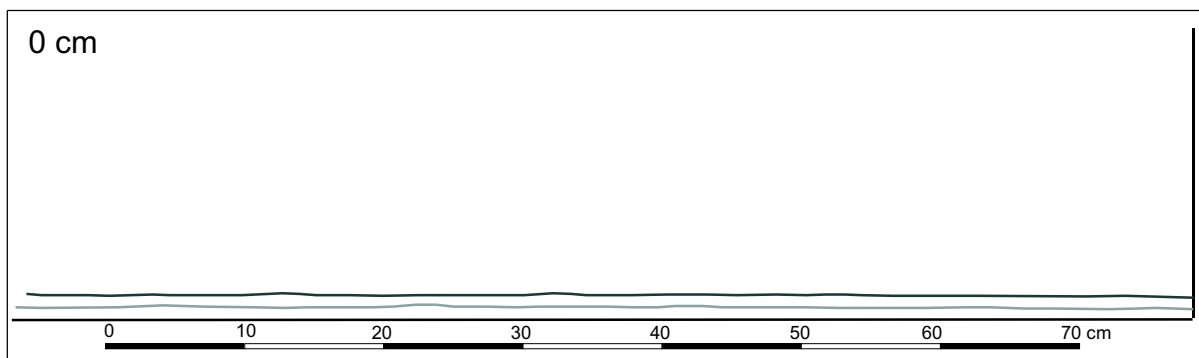
2.12 experiment

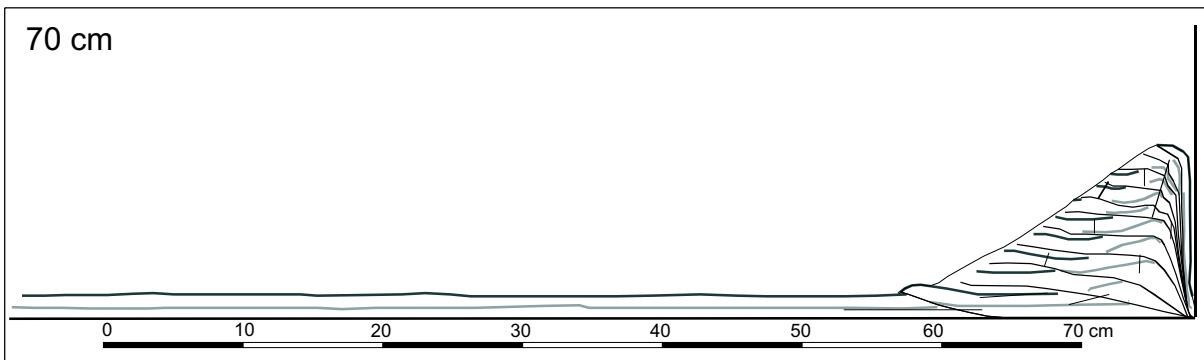
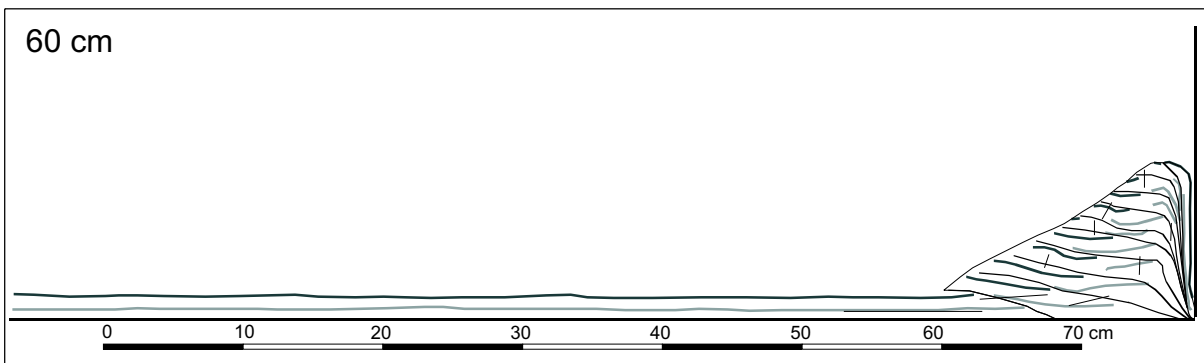
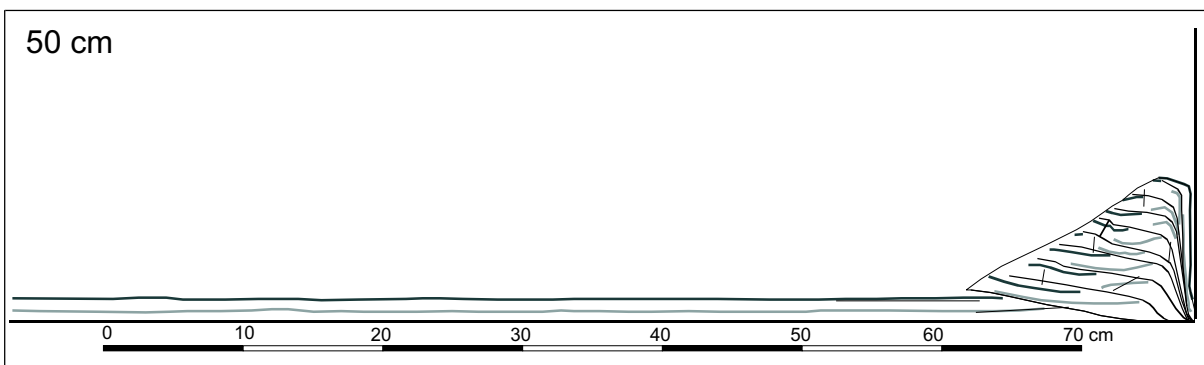
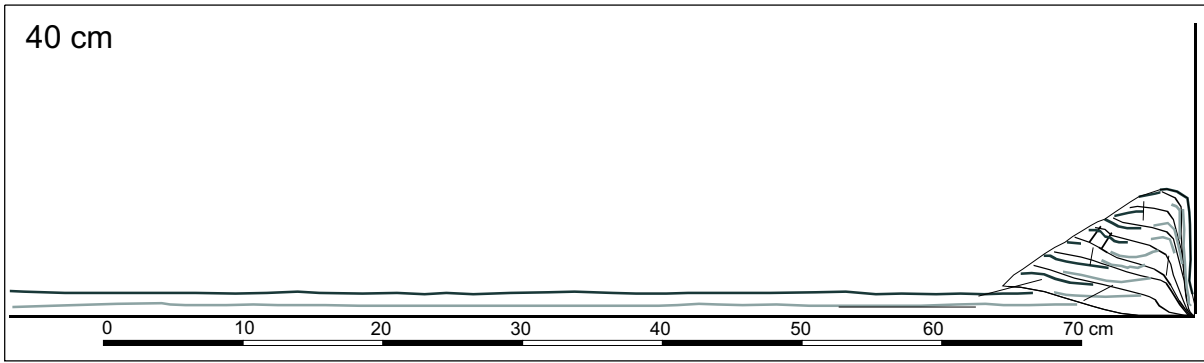


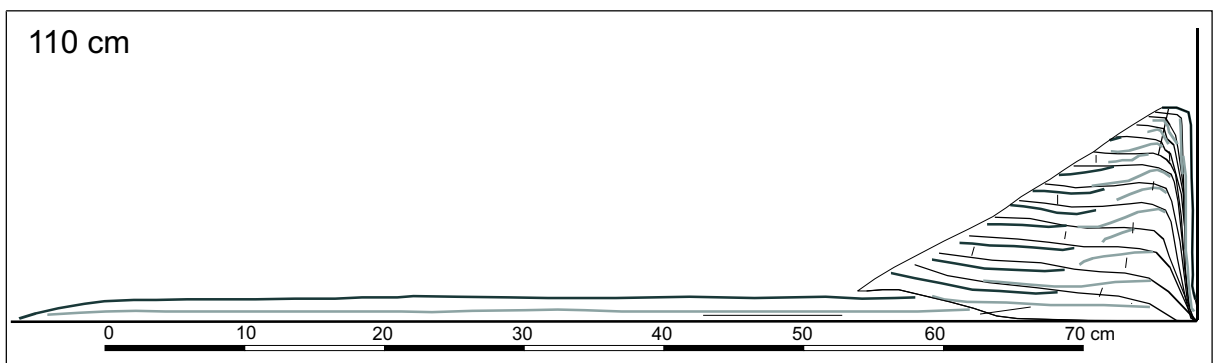
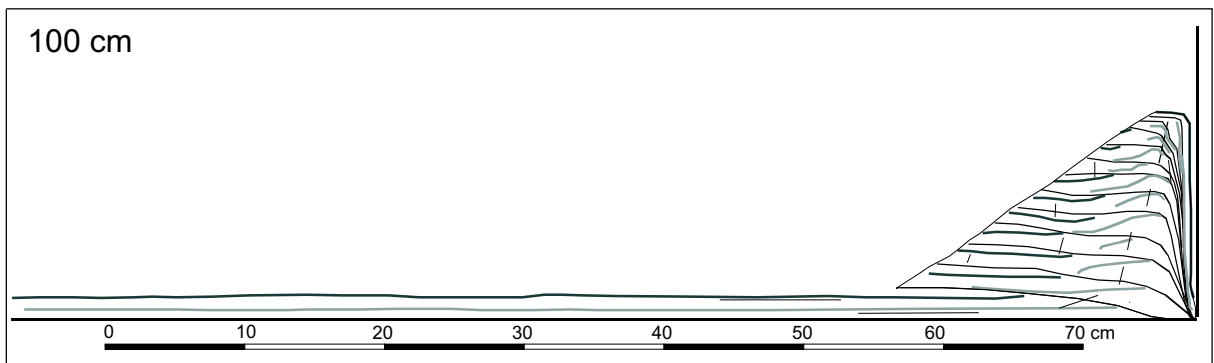
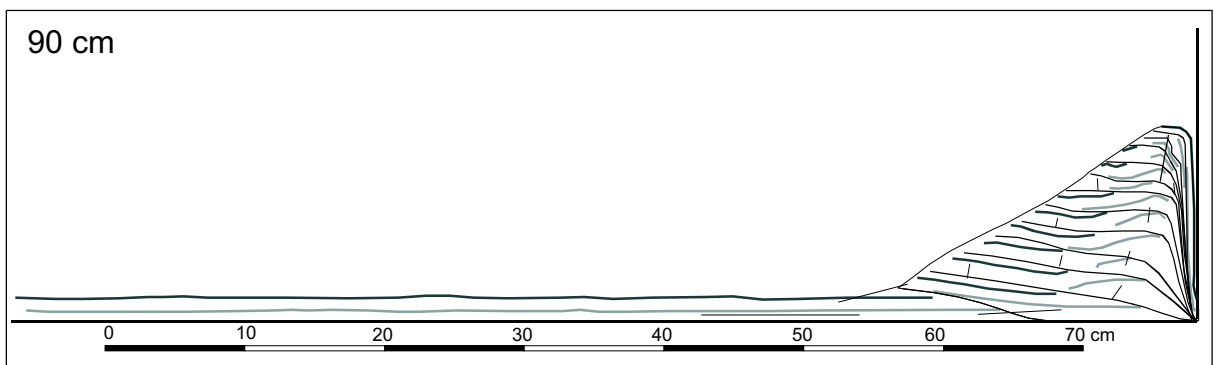
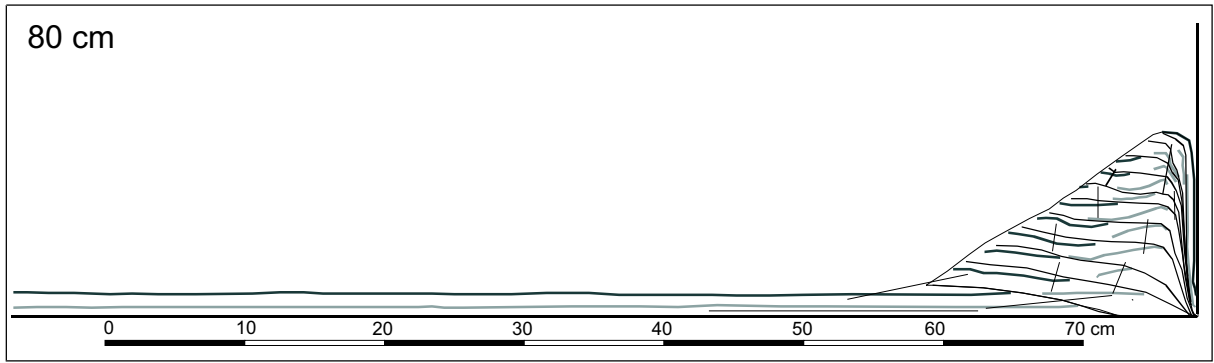


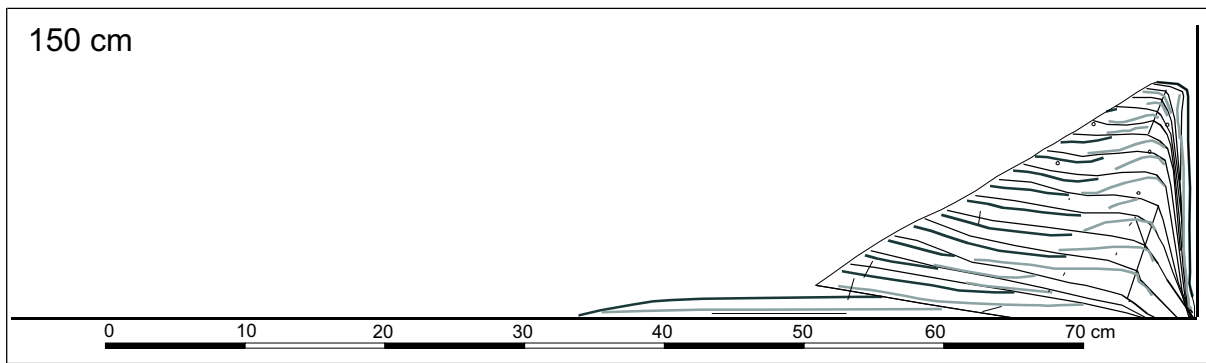
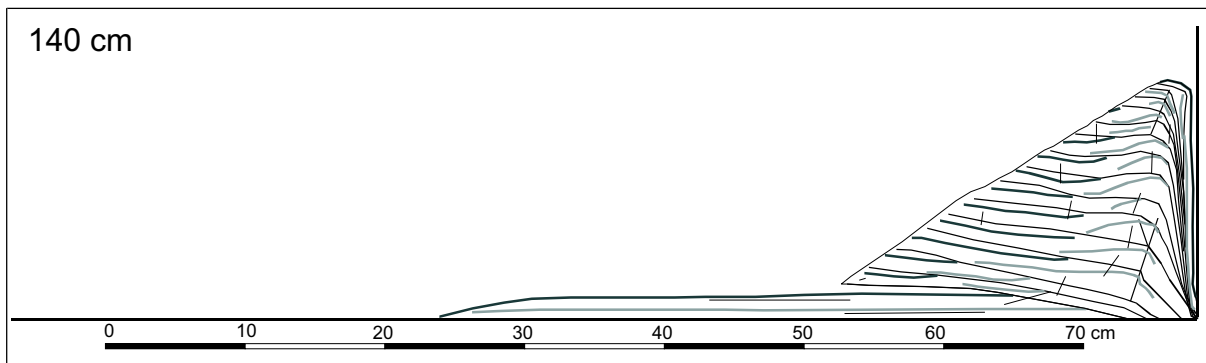
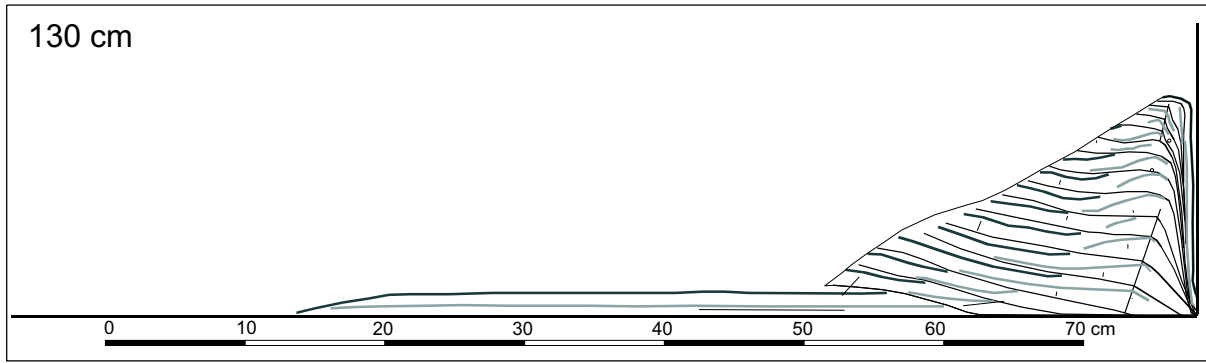


2.13A experiment

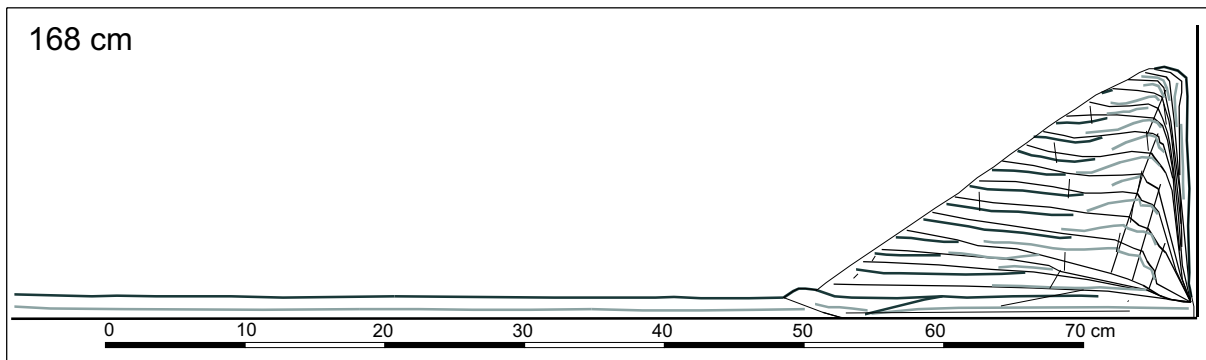


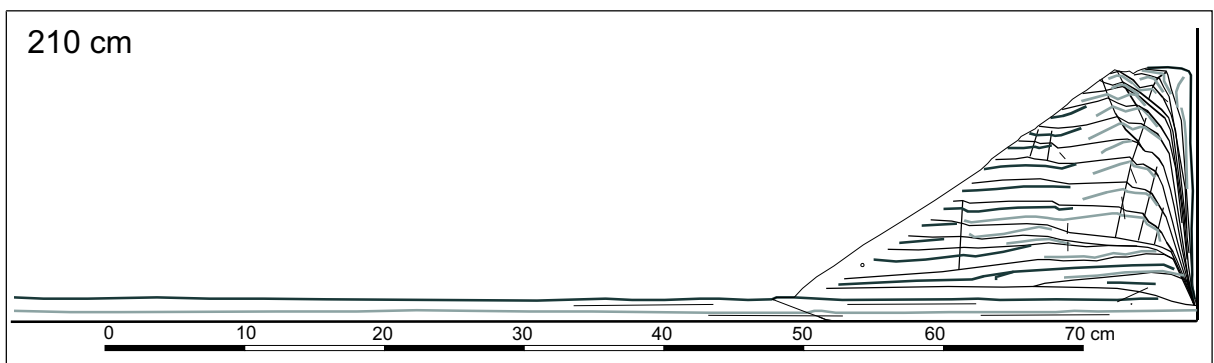
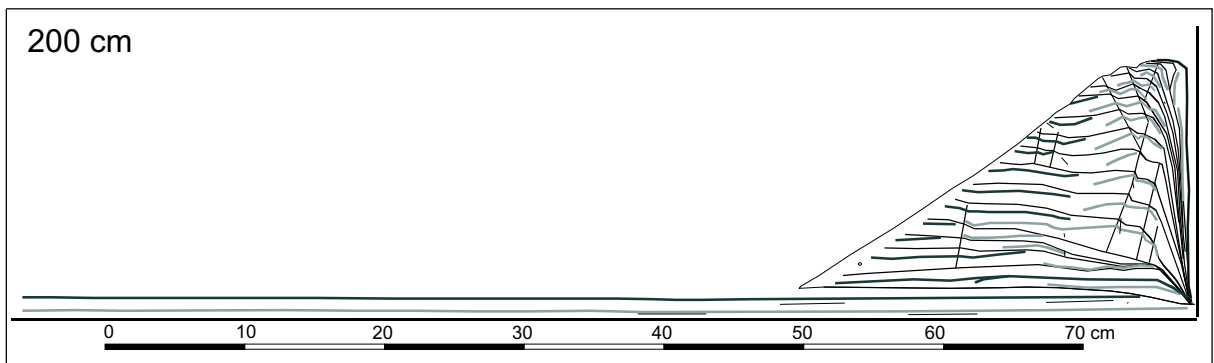
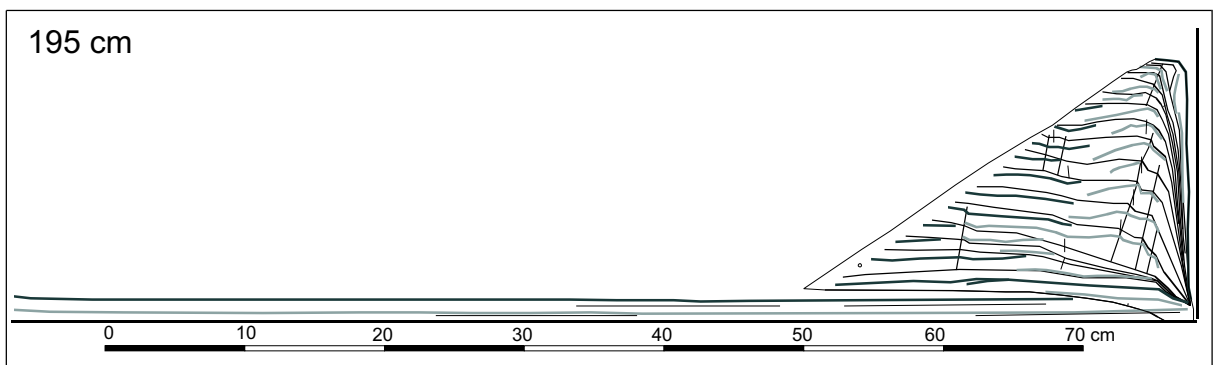
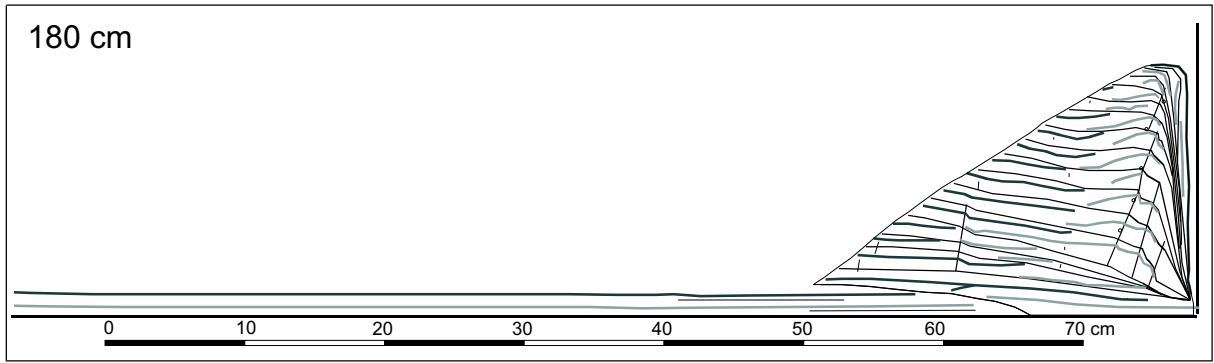


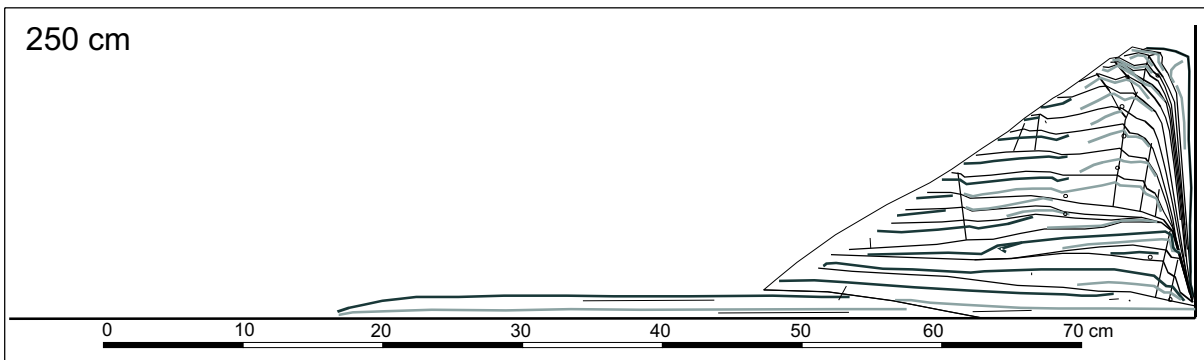
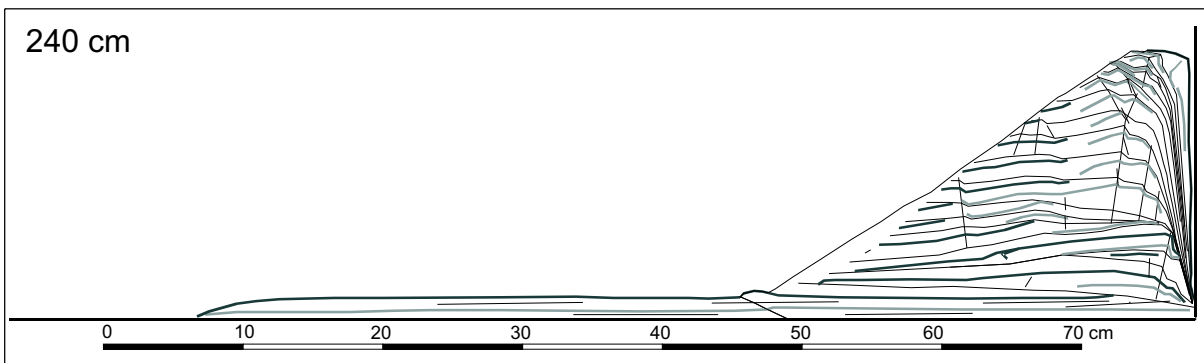
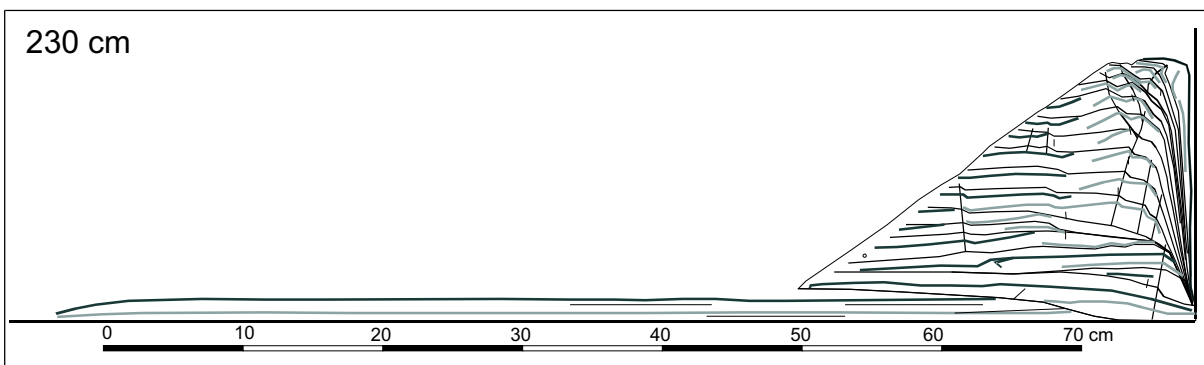
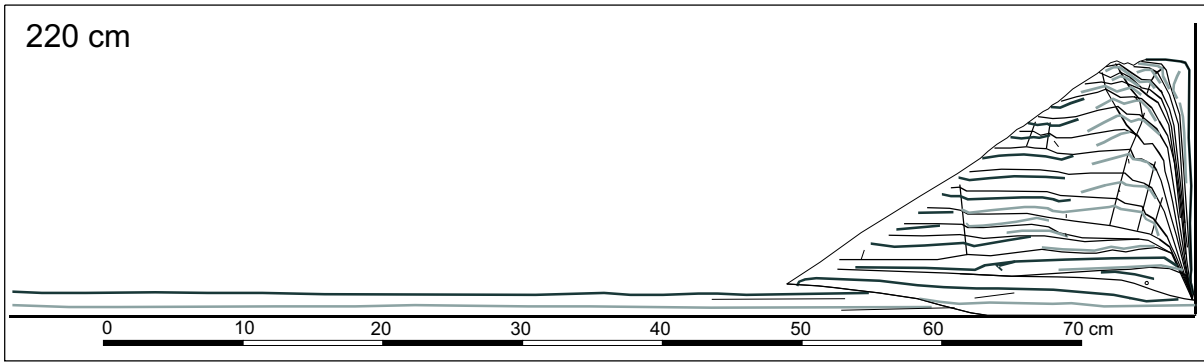


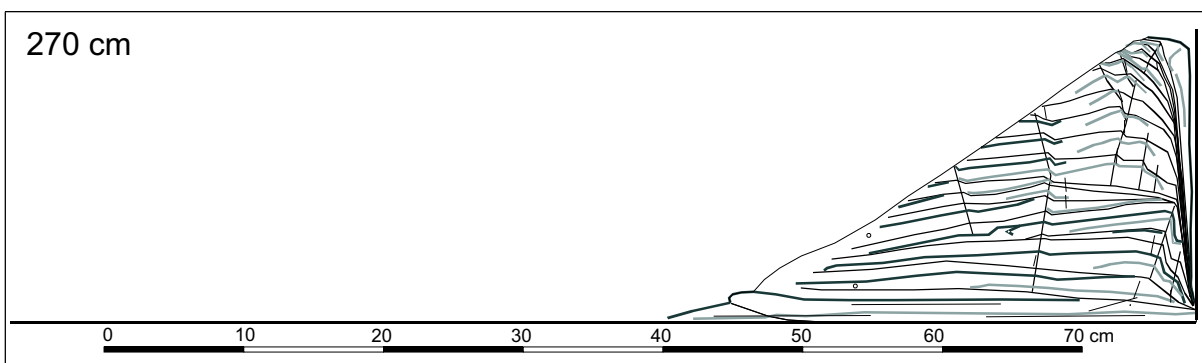
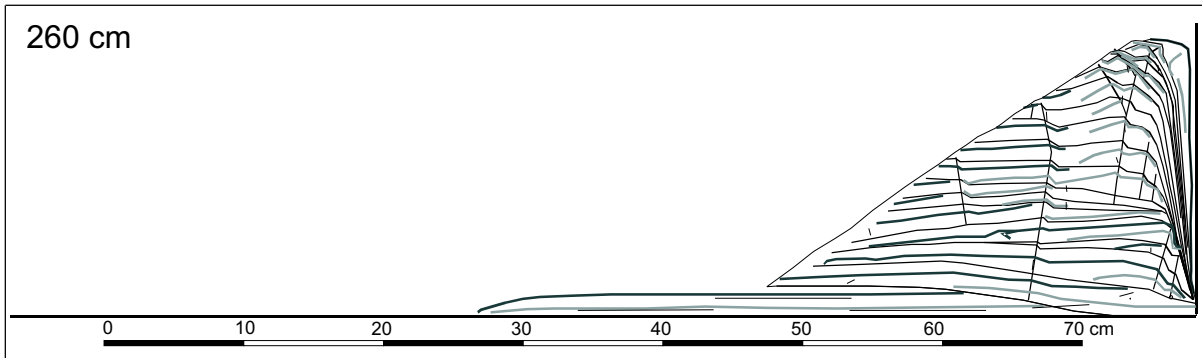


2.13B experiment

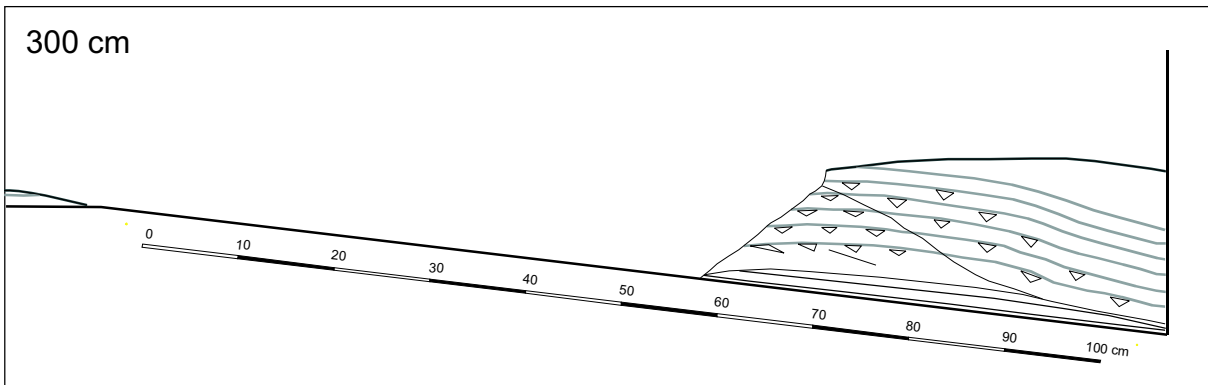
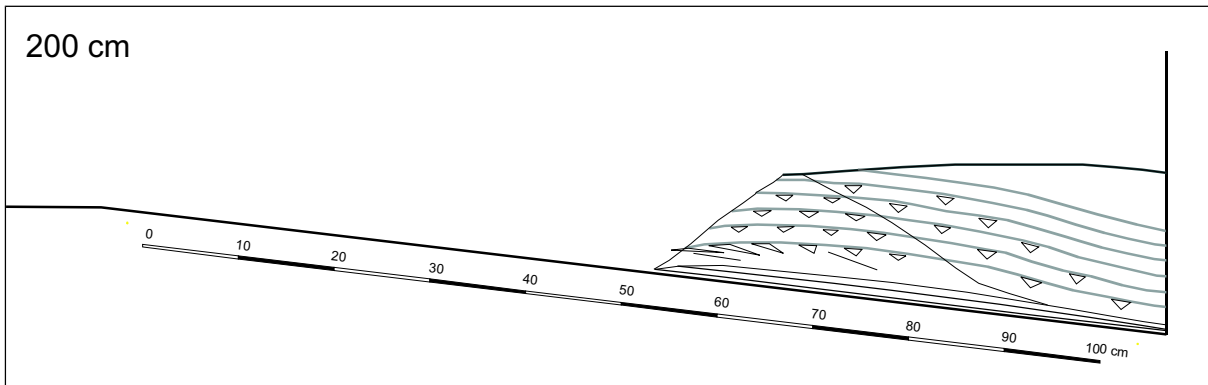
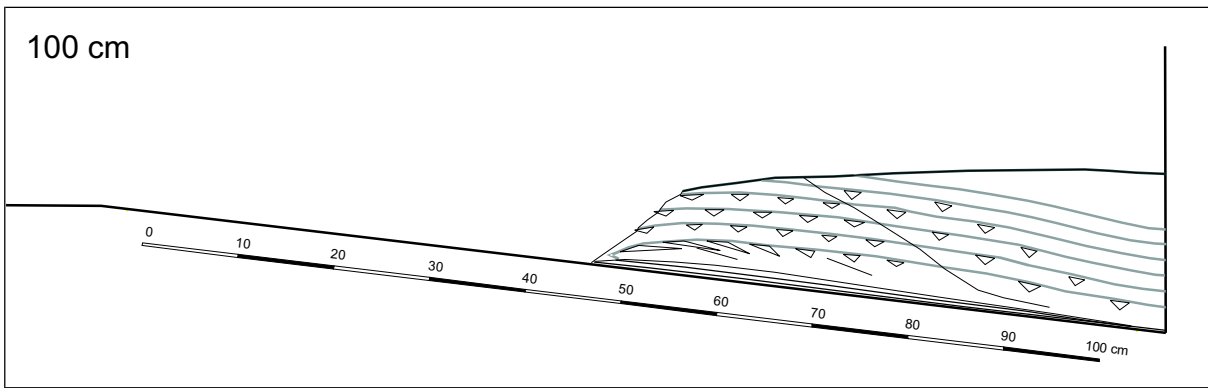
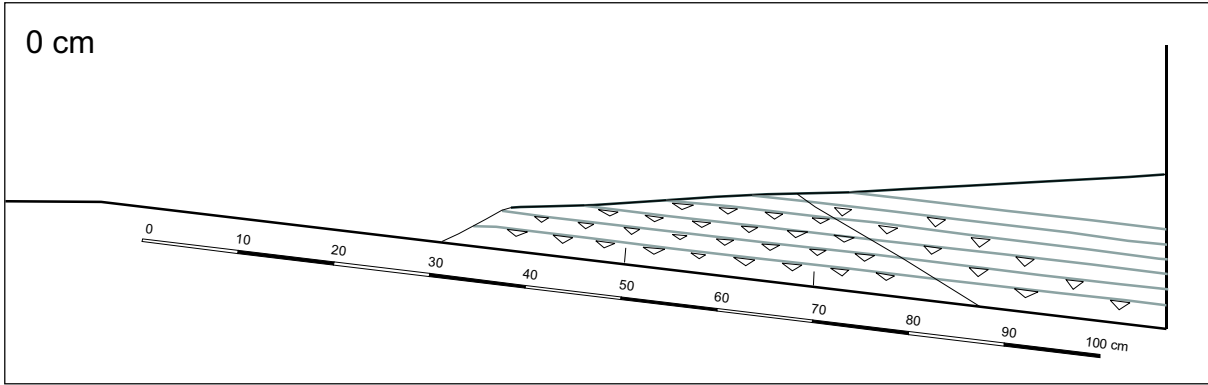


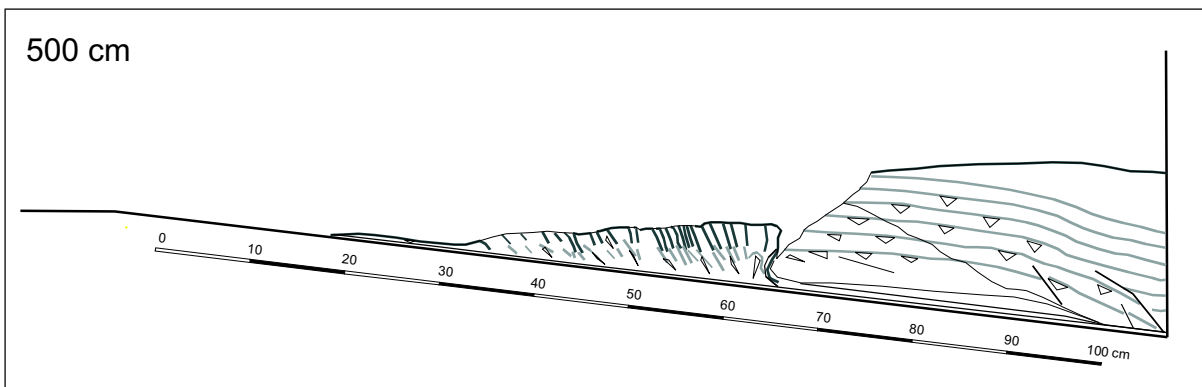
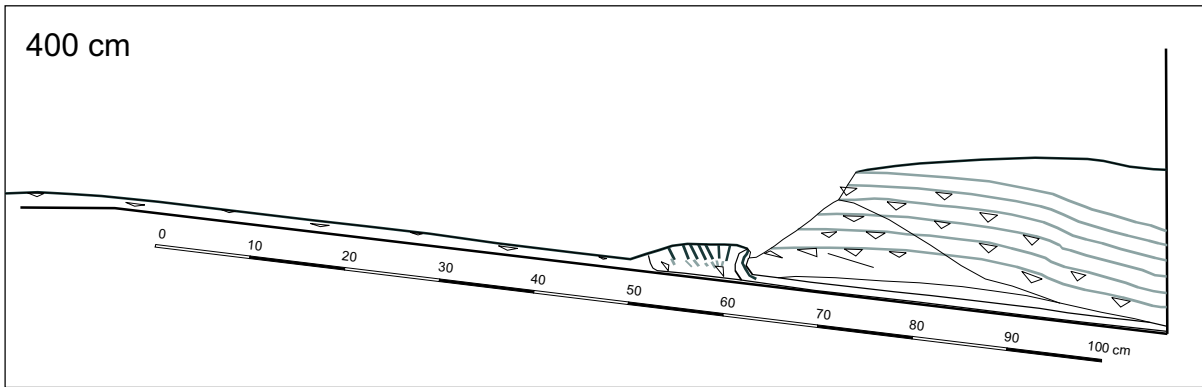




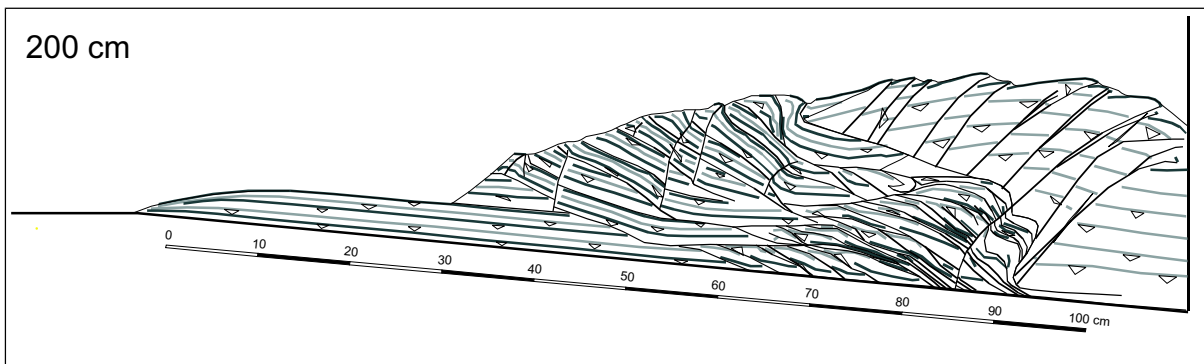
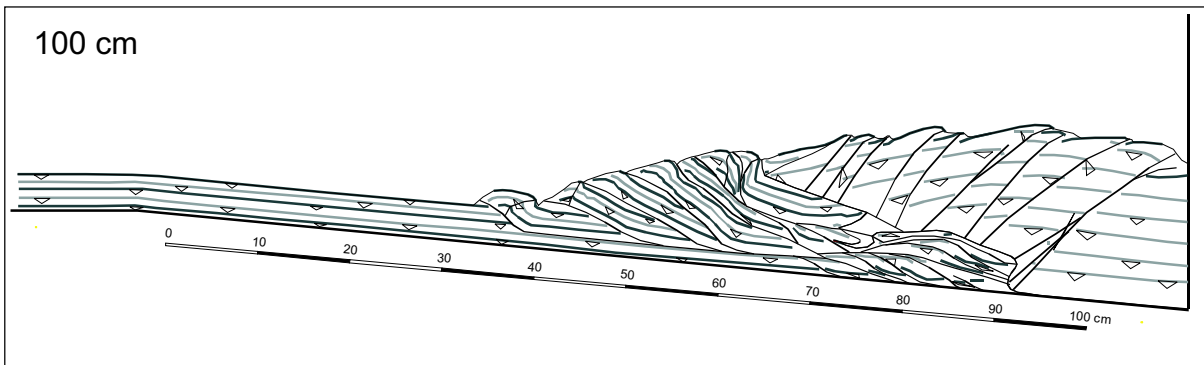
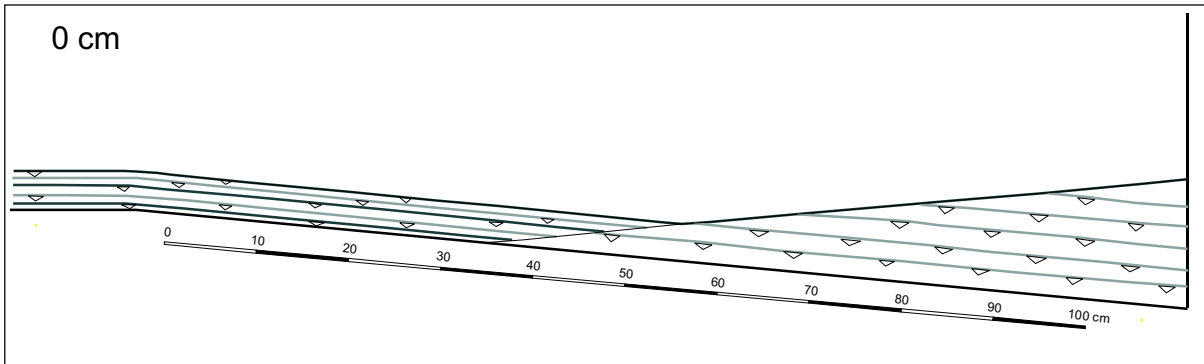


5.1 experiment

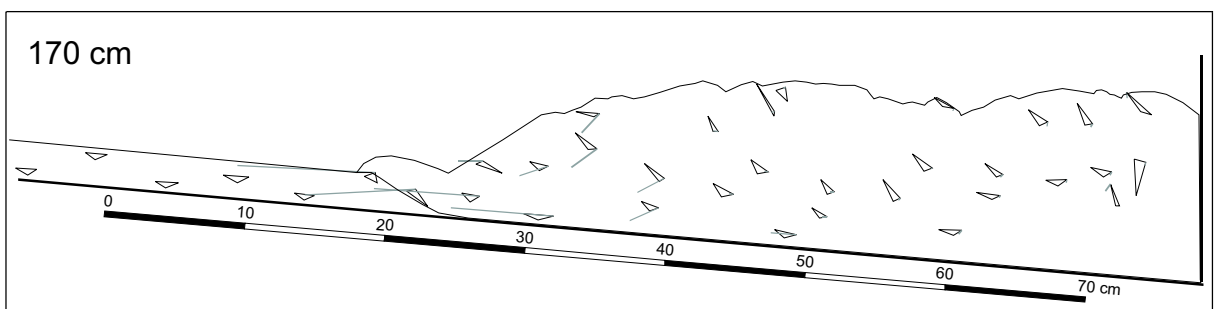
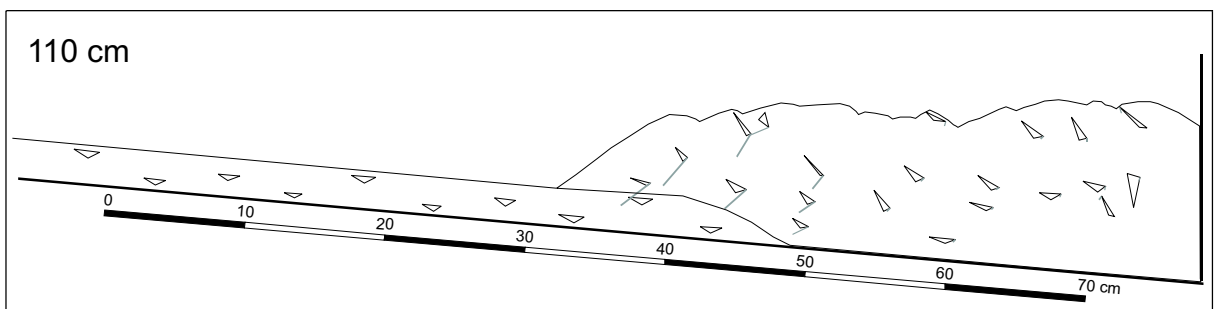
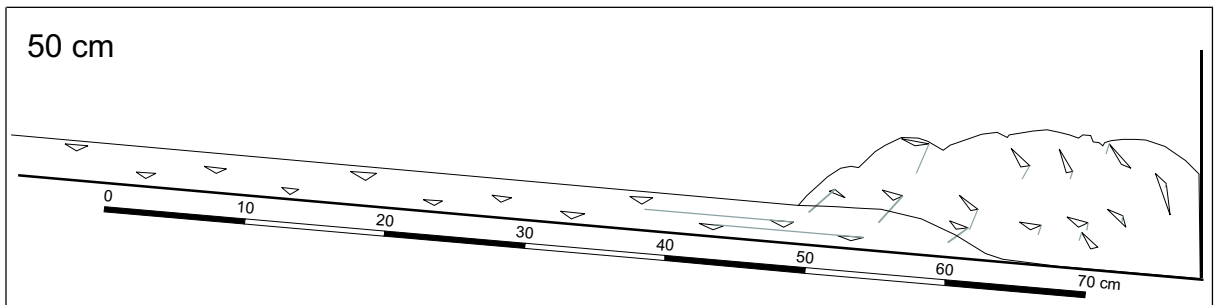
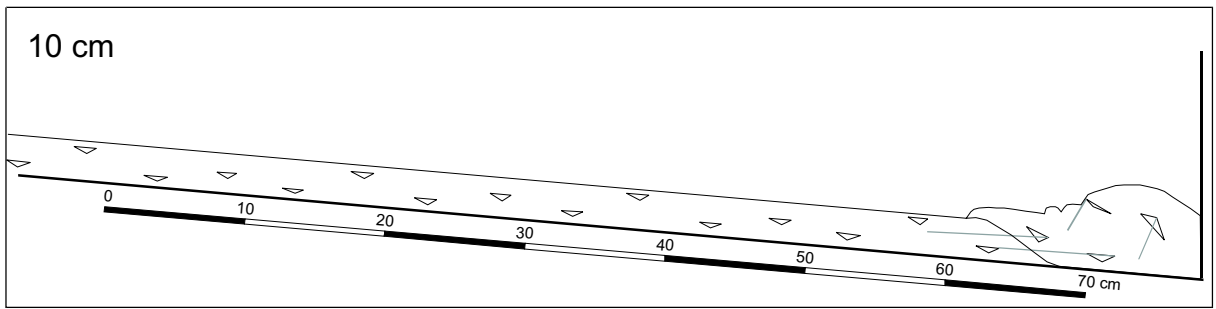




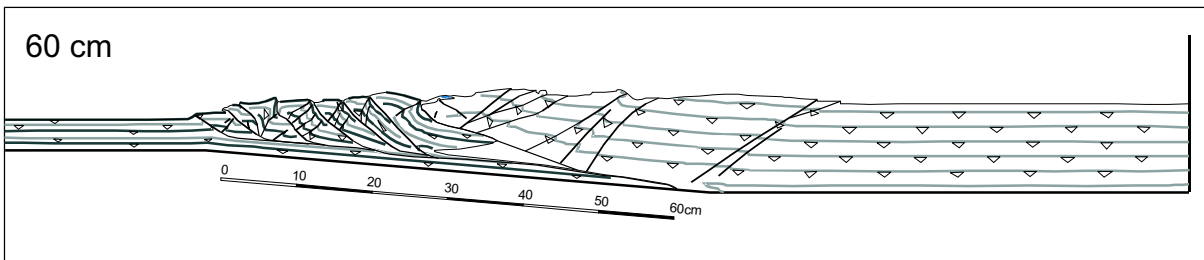
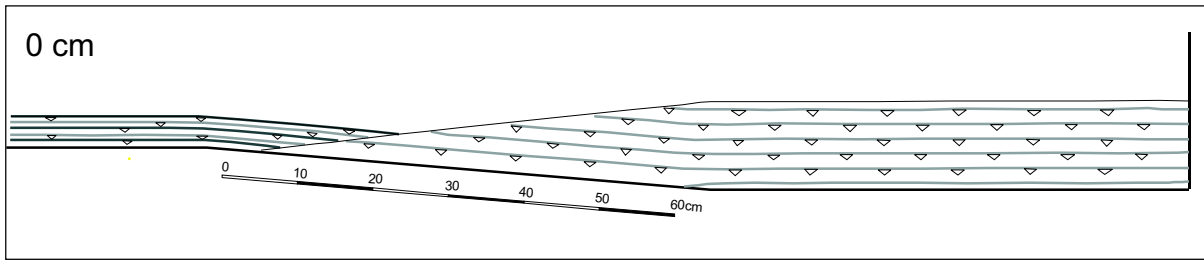
5.4 experiment



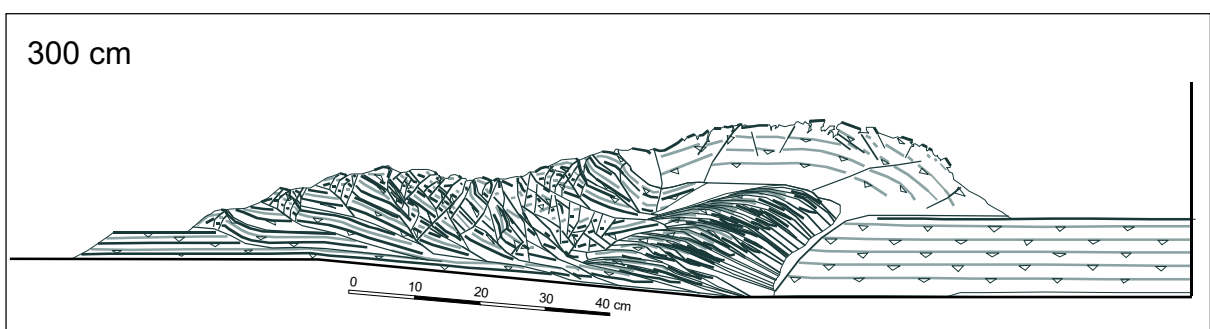
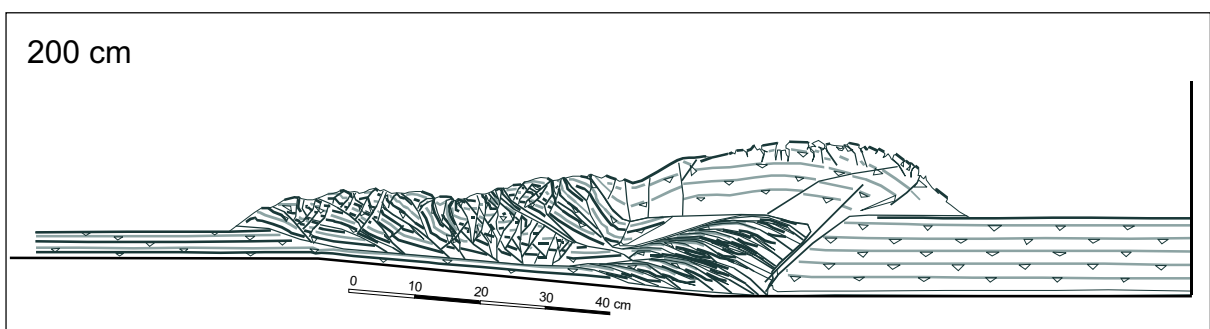
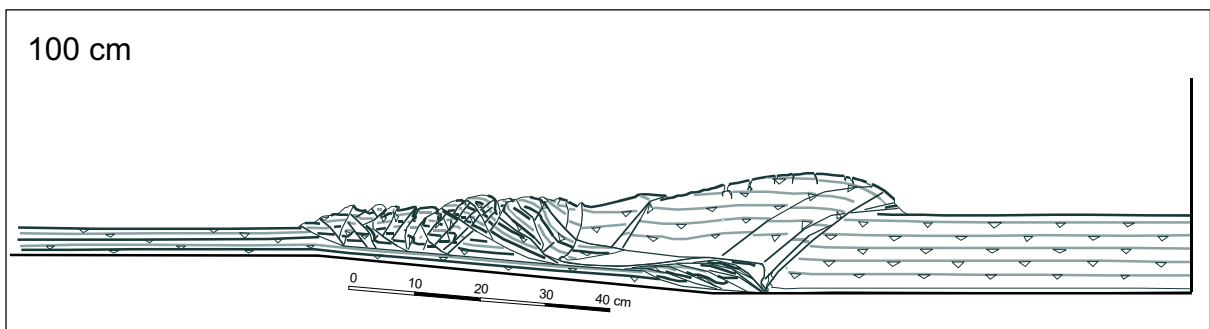
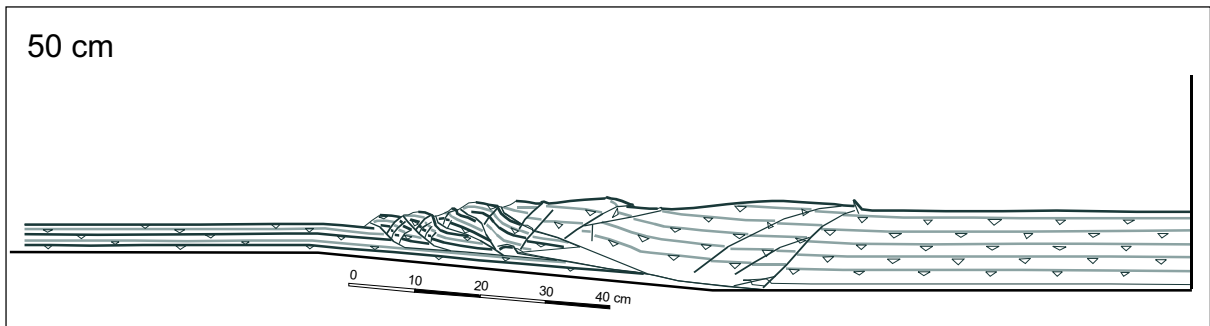
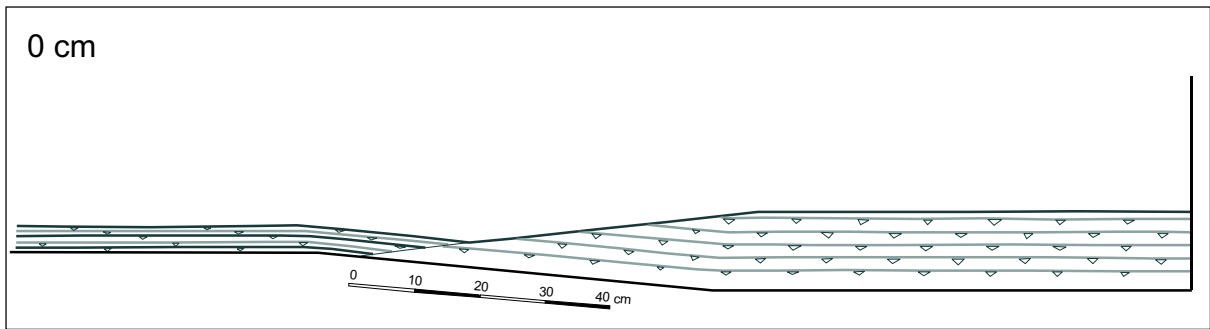
5.5 experiment



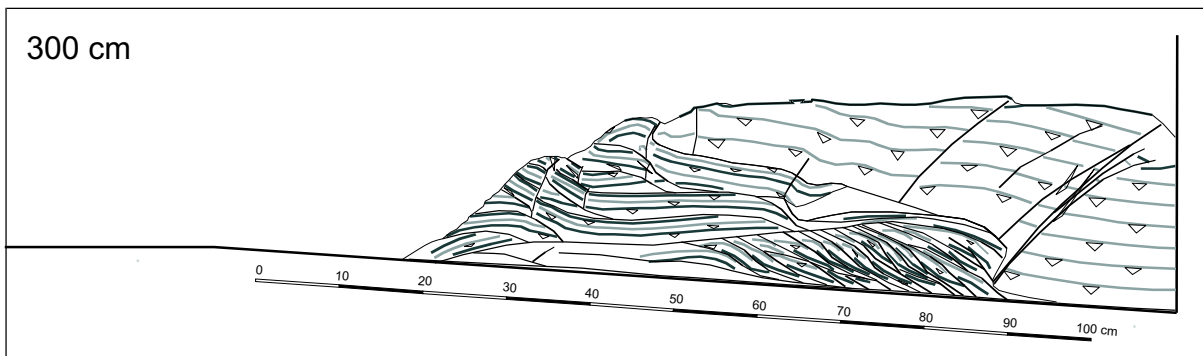
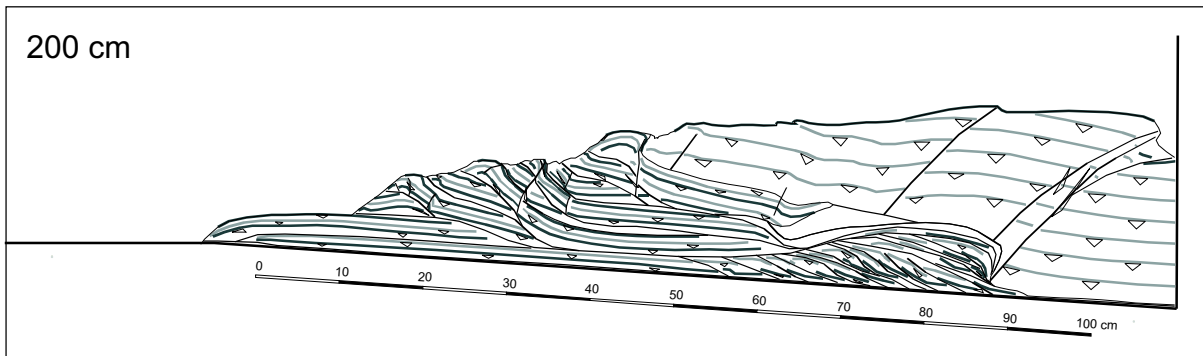
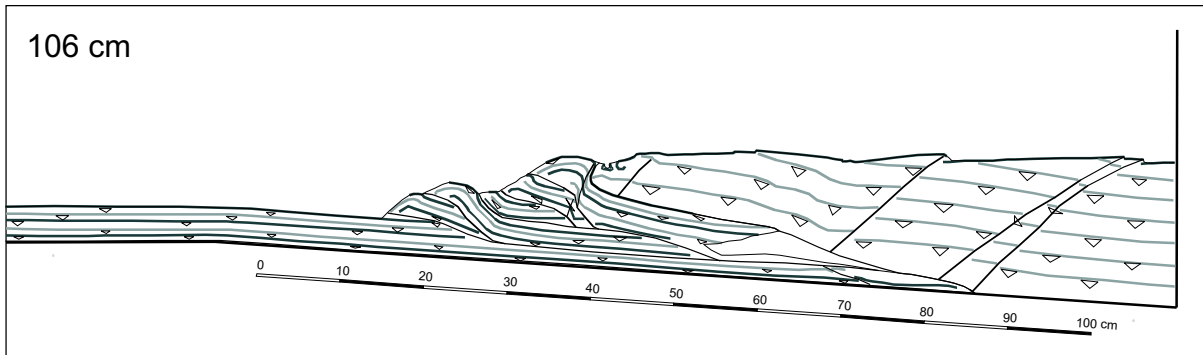
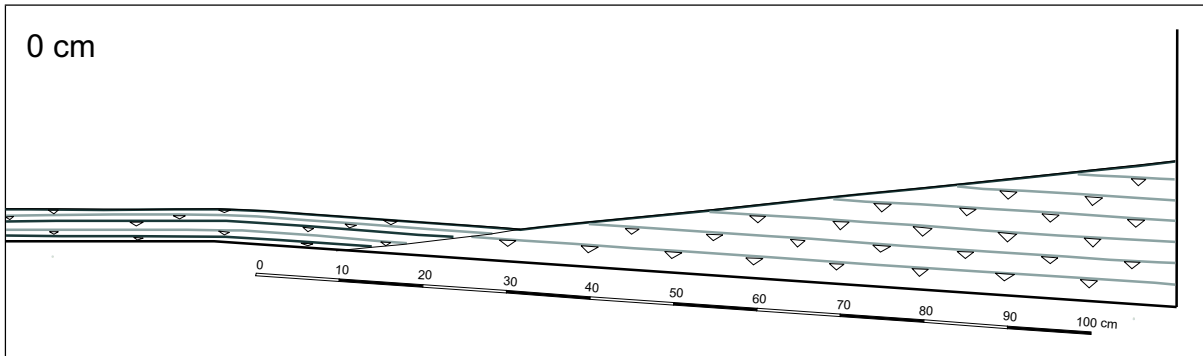
5.7 experiment



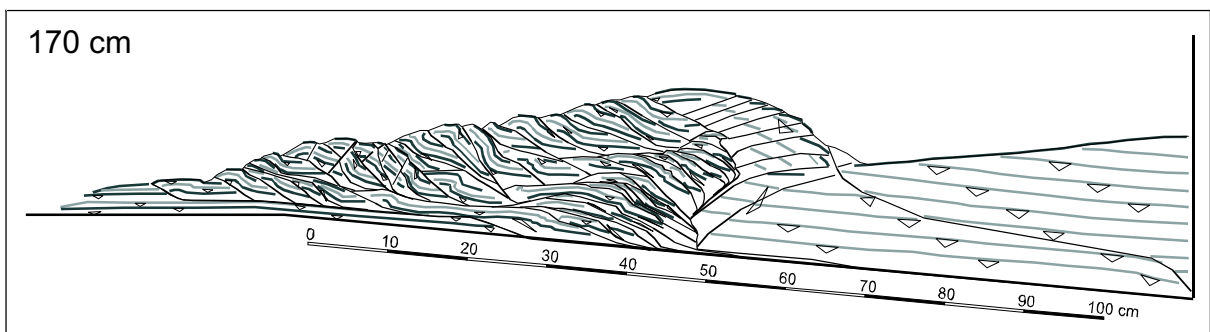
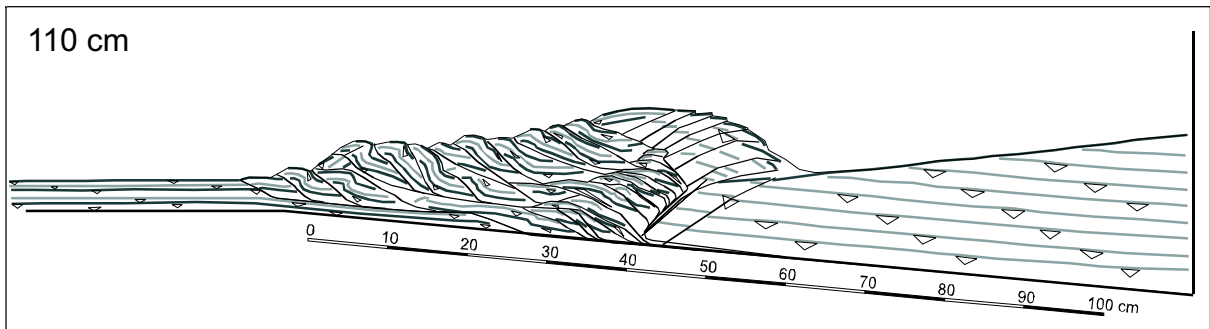
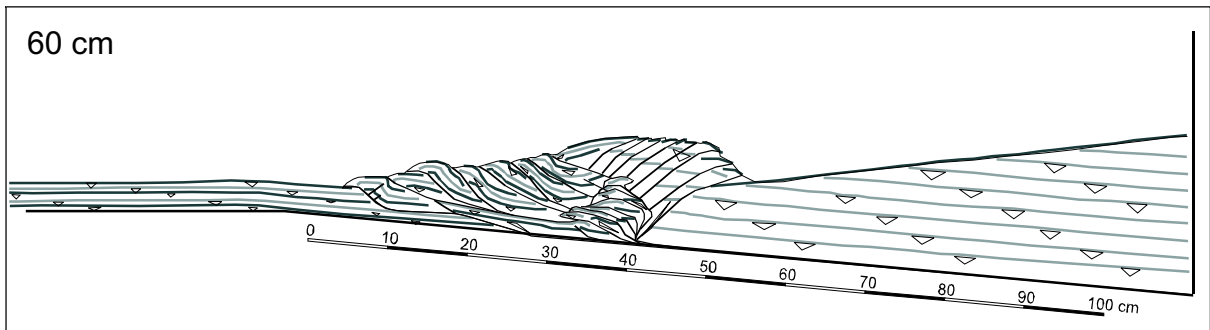
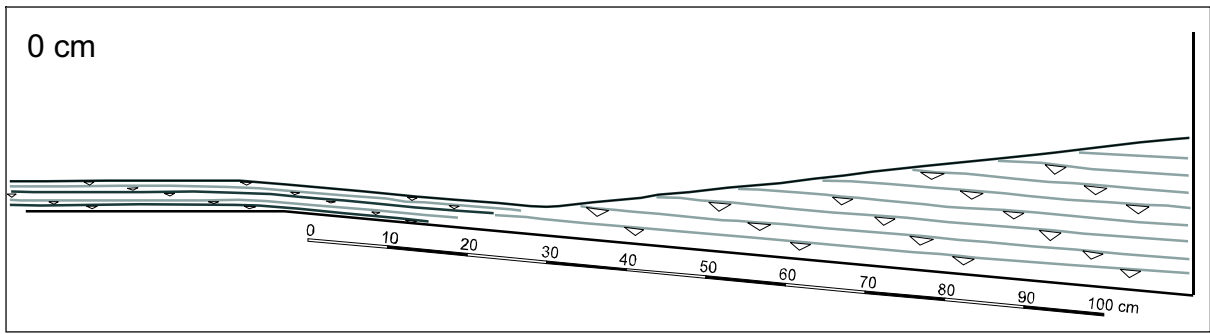
5.8 experiment



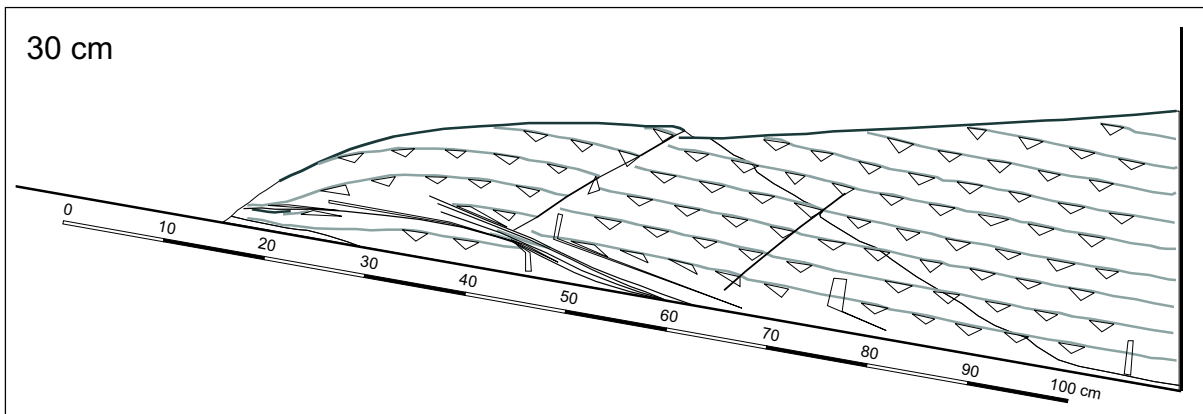
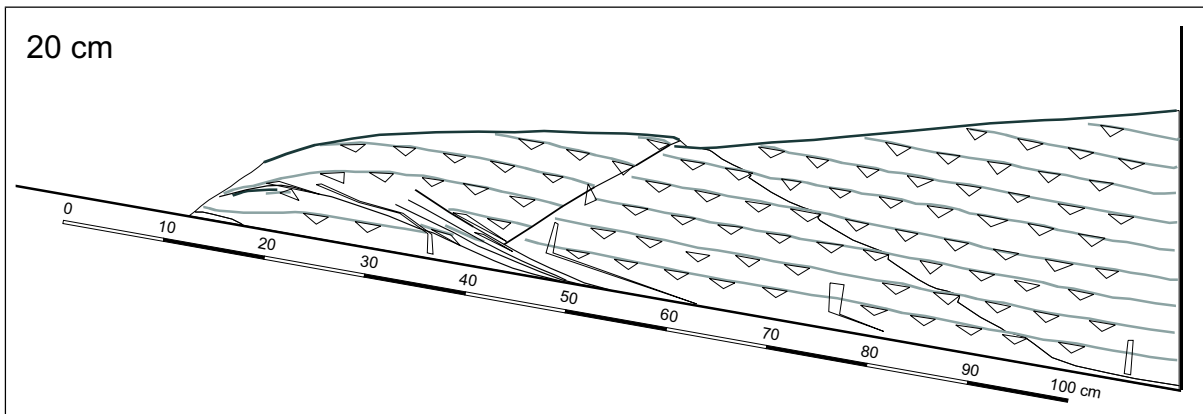
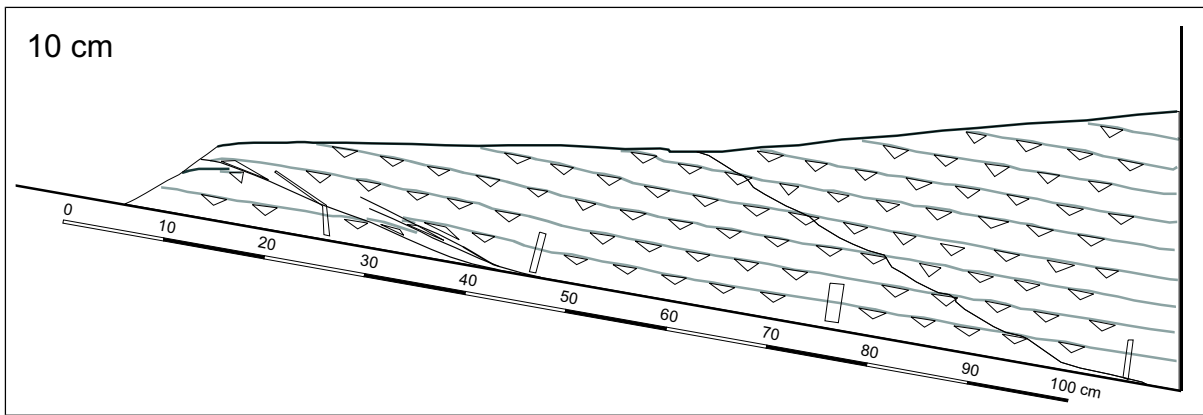
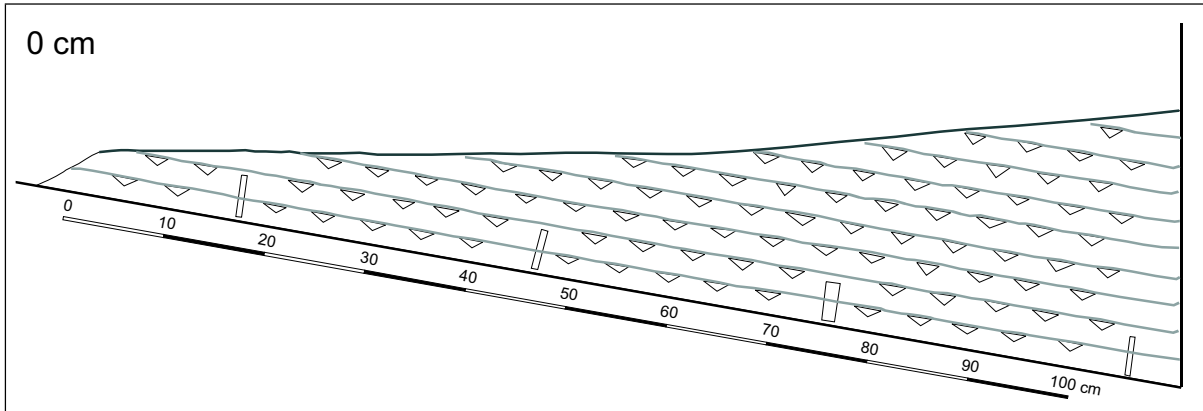
5.9 experiment

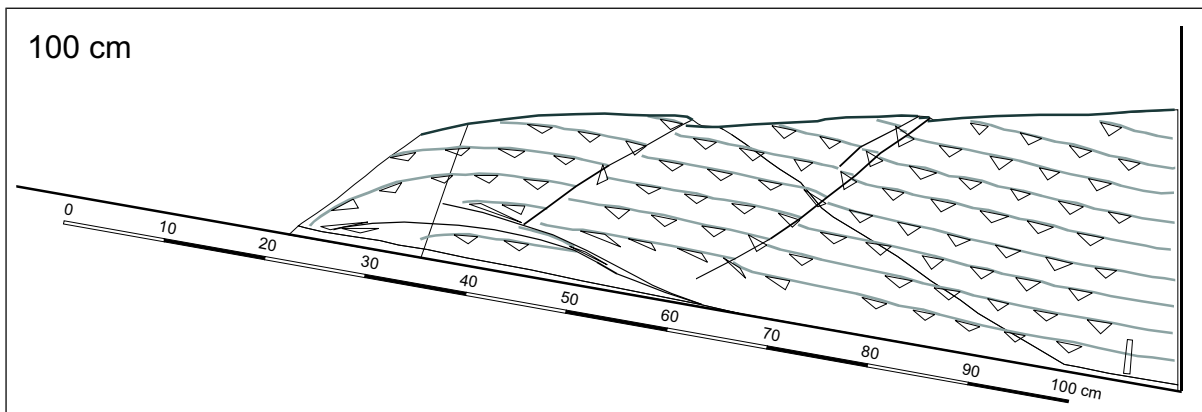
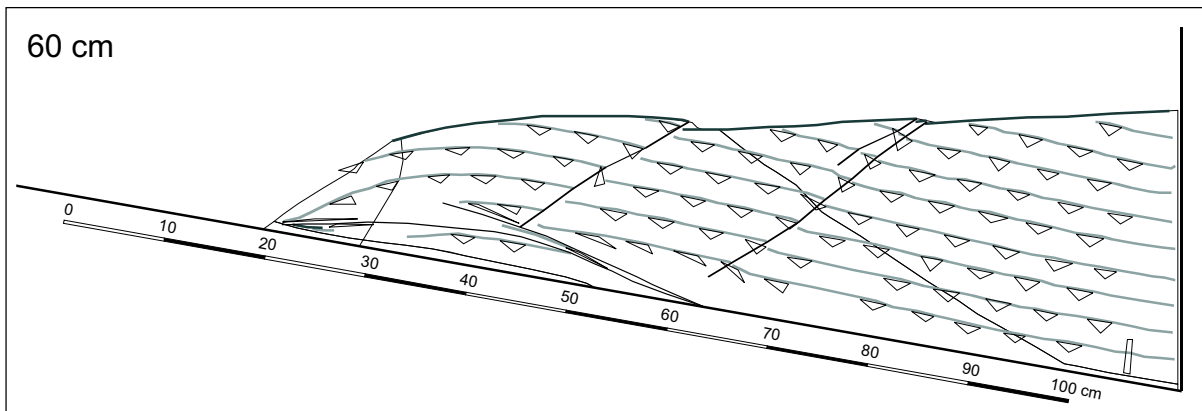
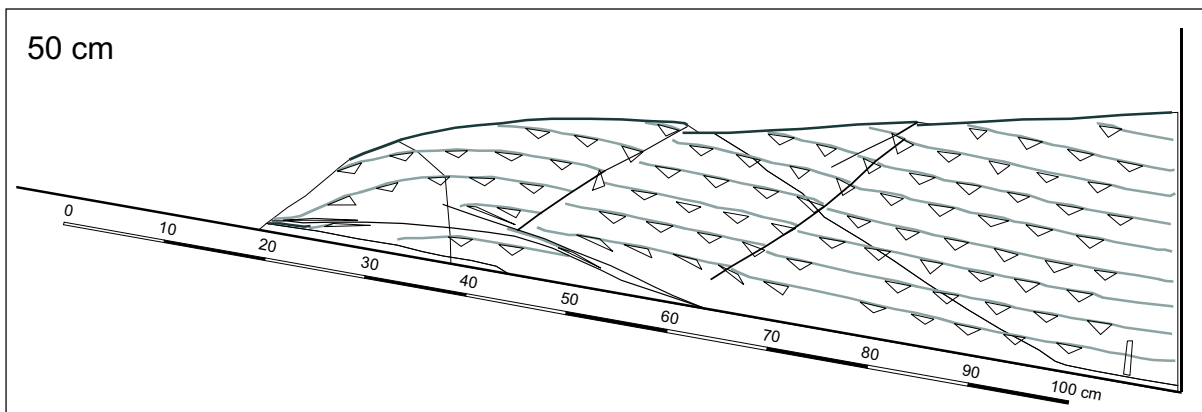
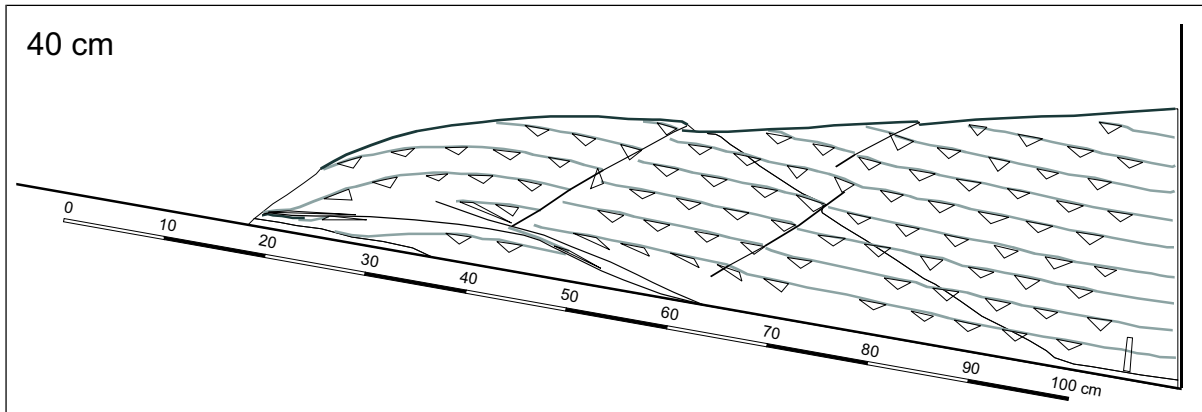


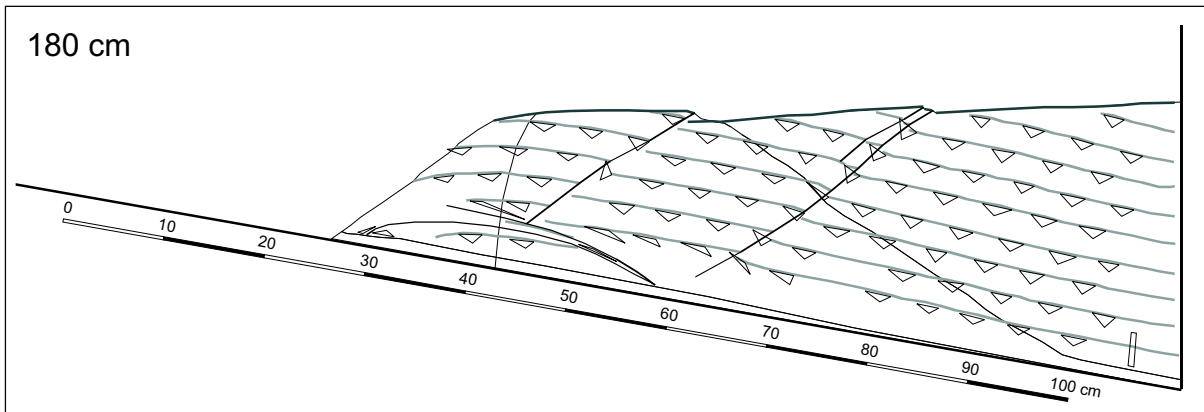
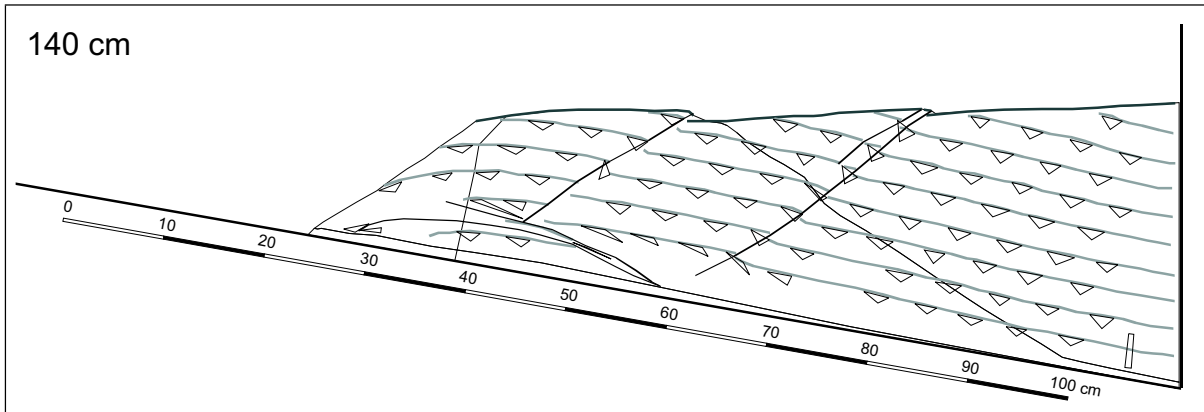
5.10 experiment



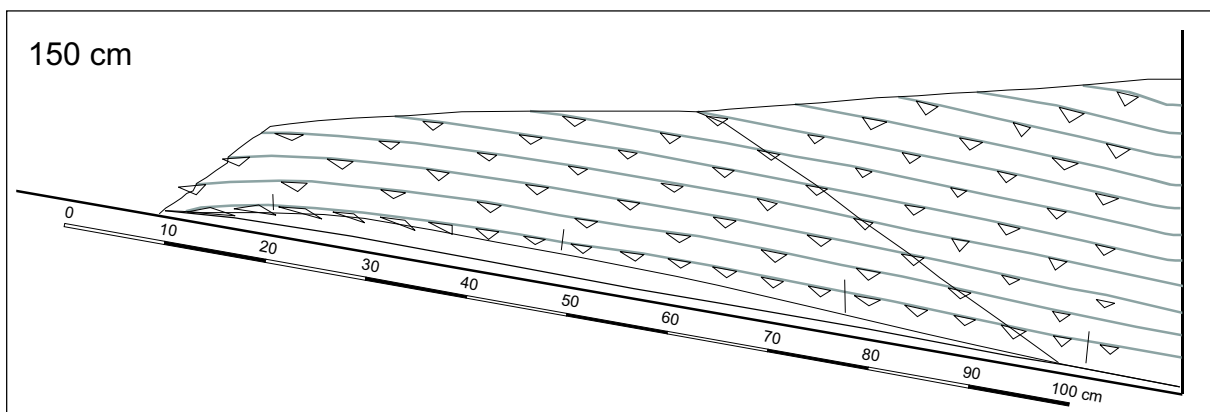
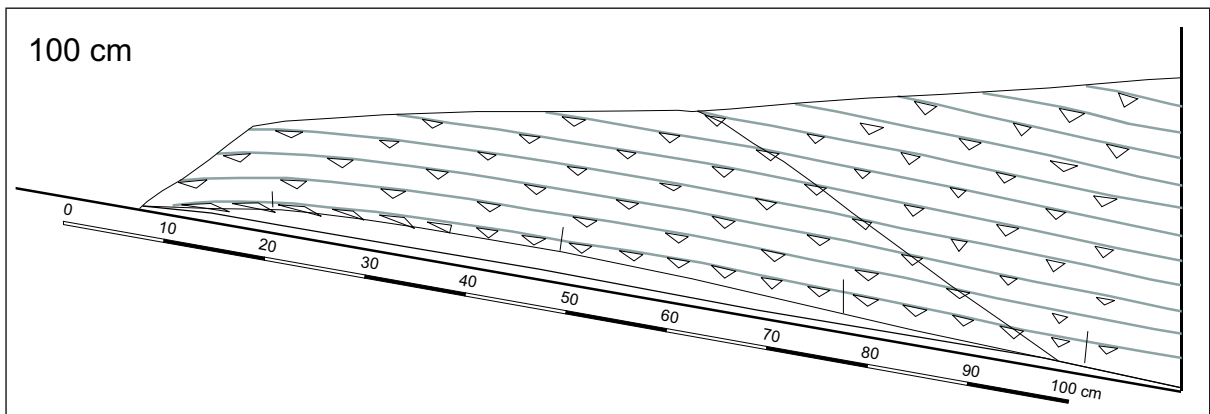
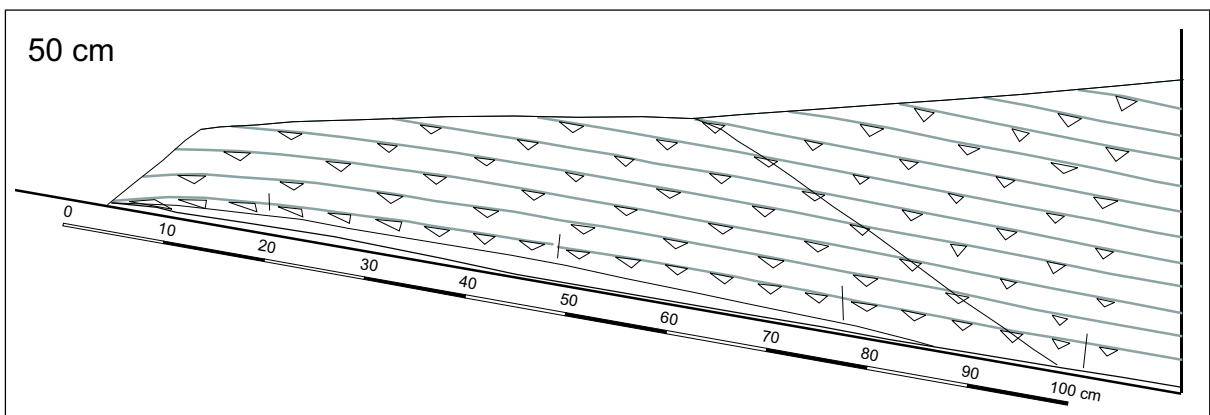
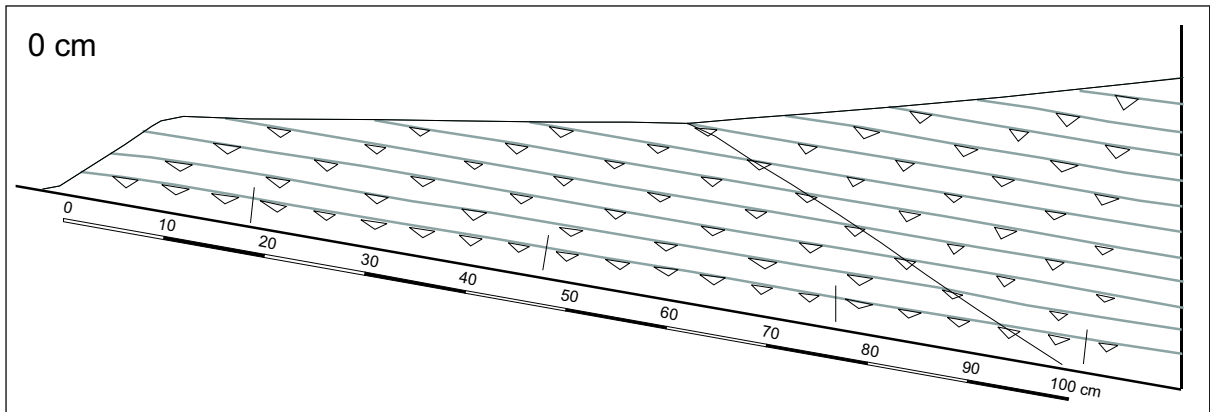
3.8 experiment



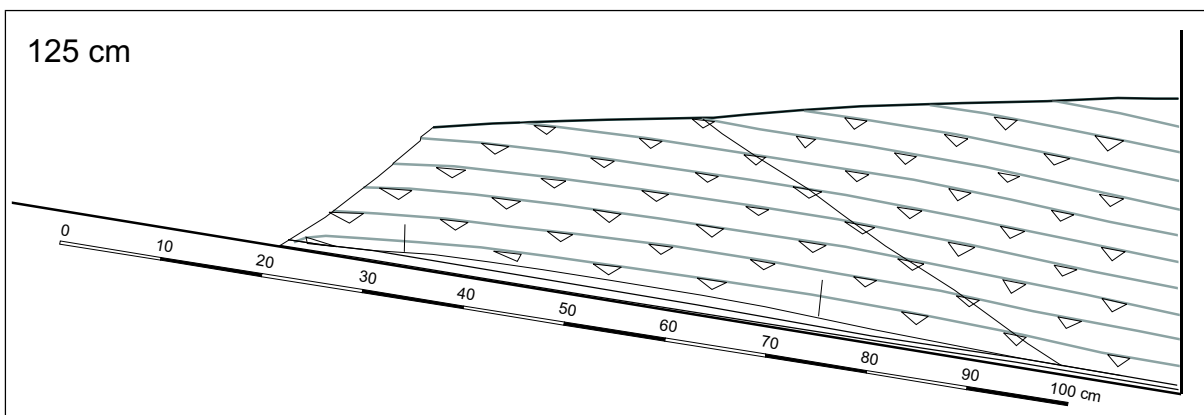
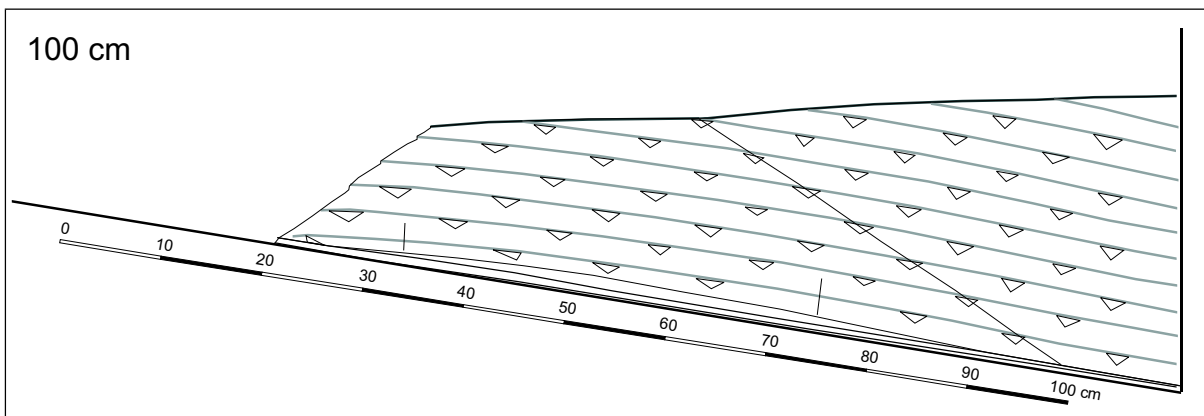
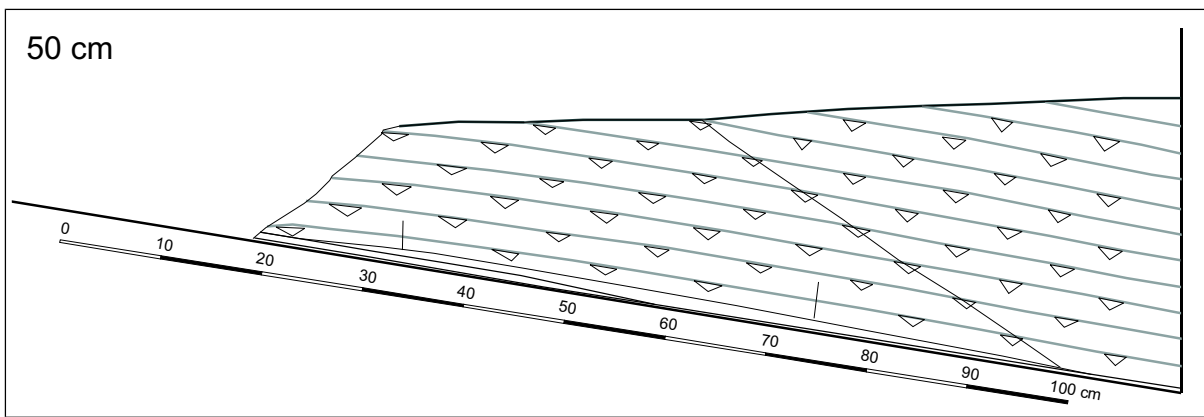
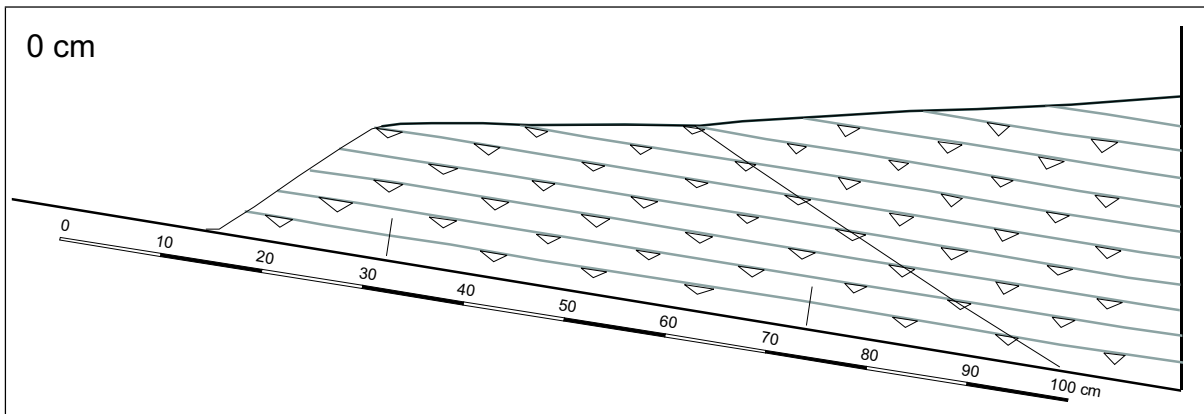




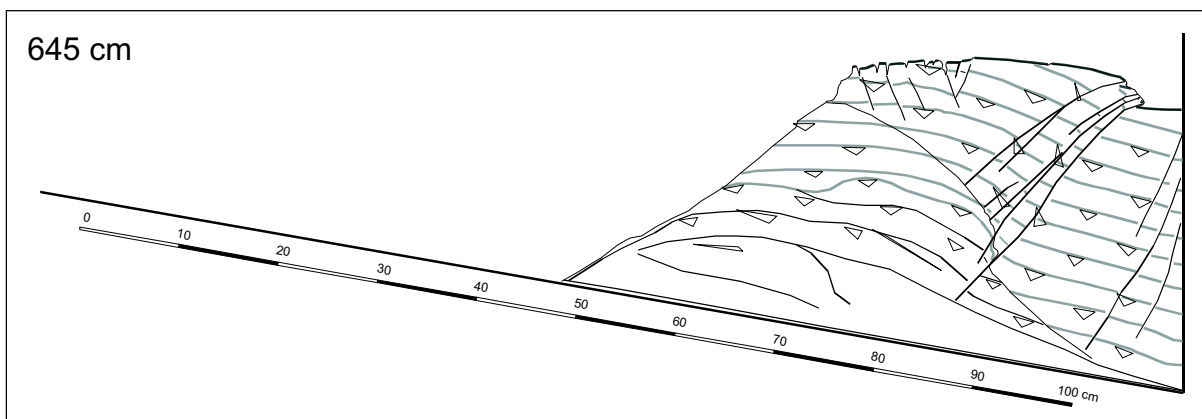
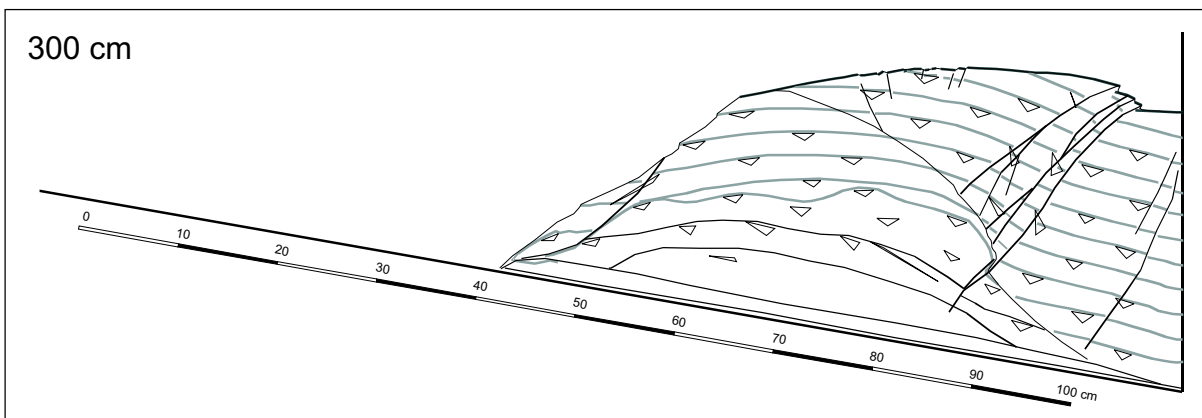
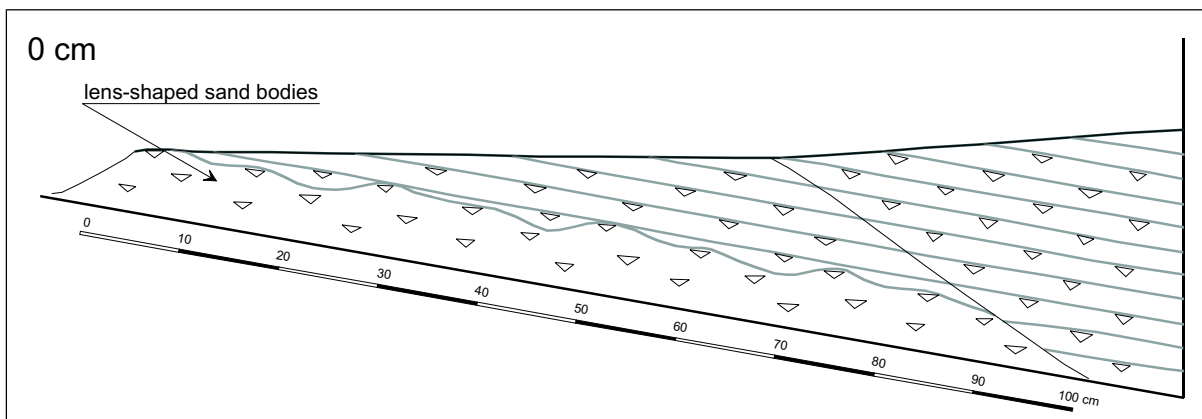
3.9 experiment



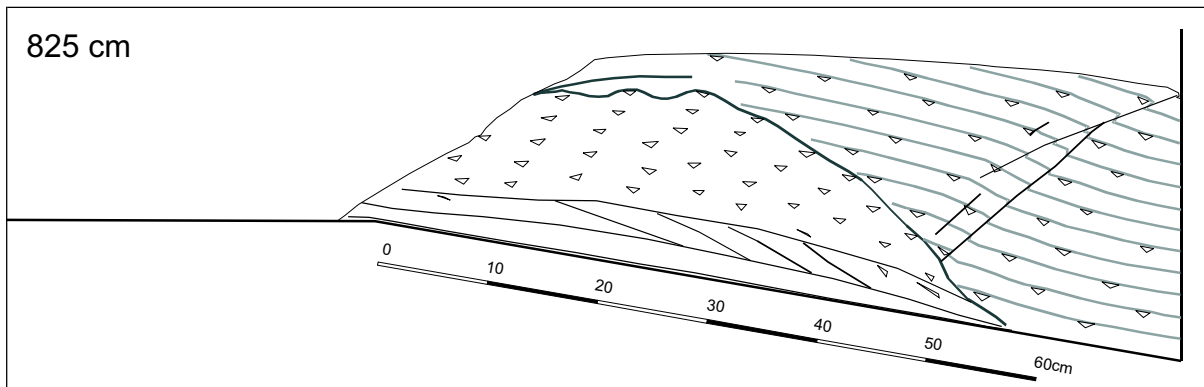
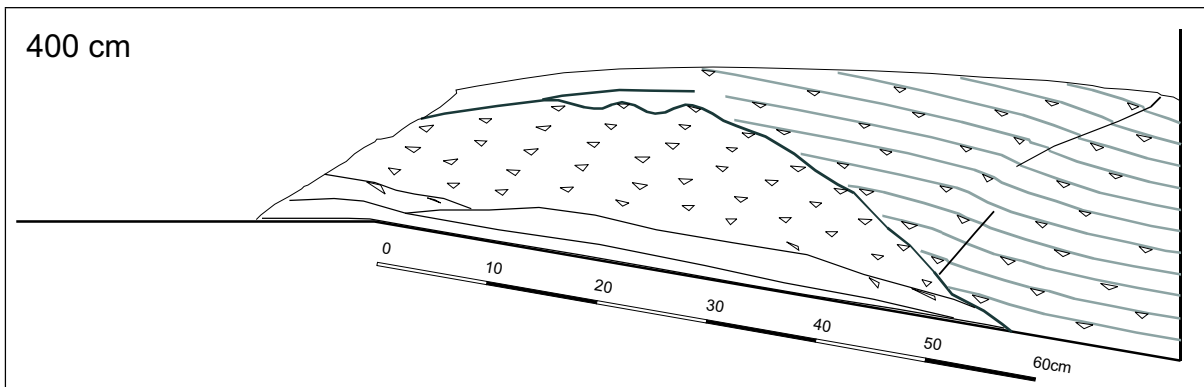
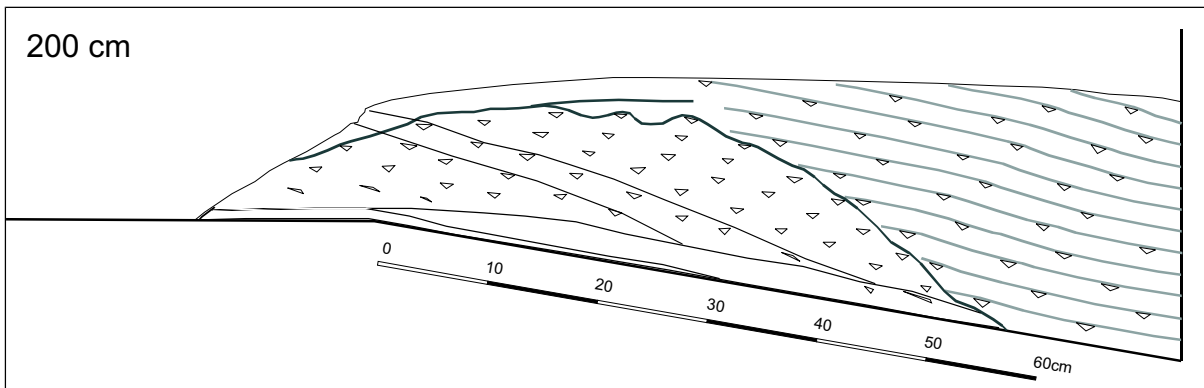
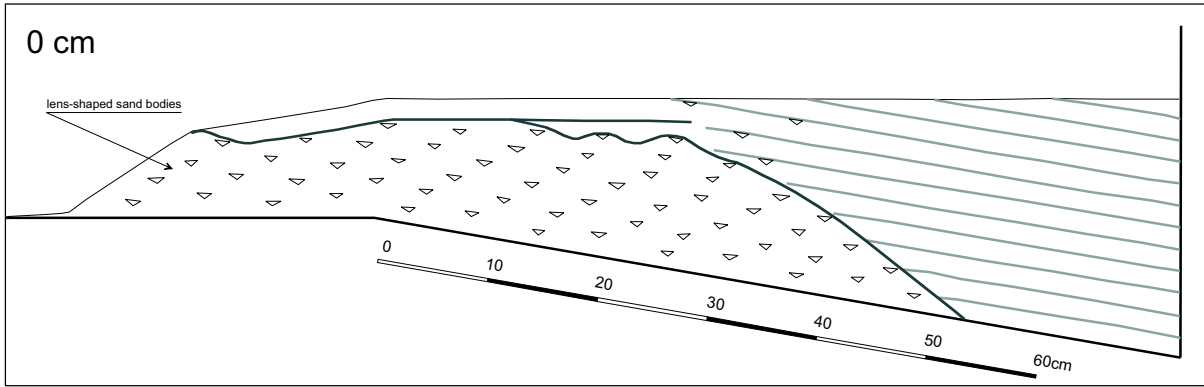
3.10 experiment



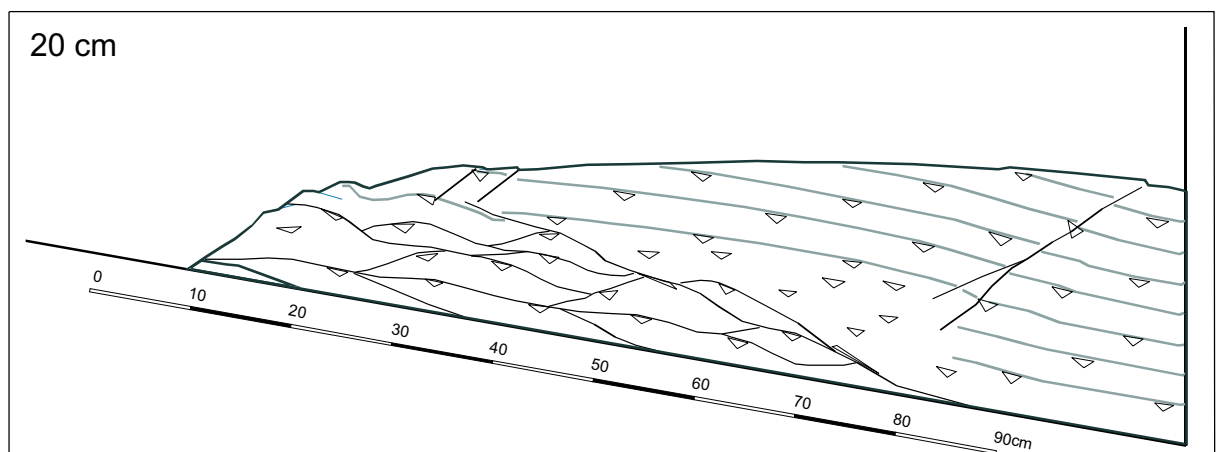
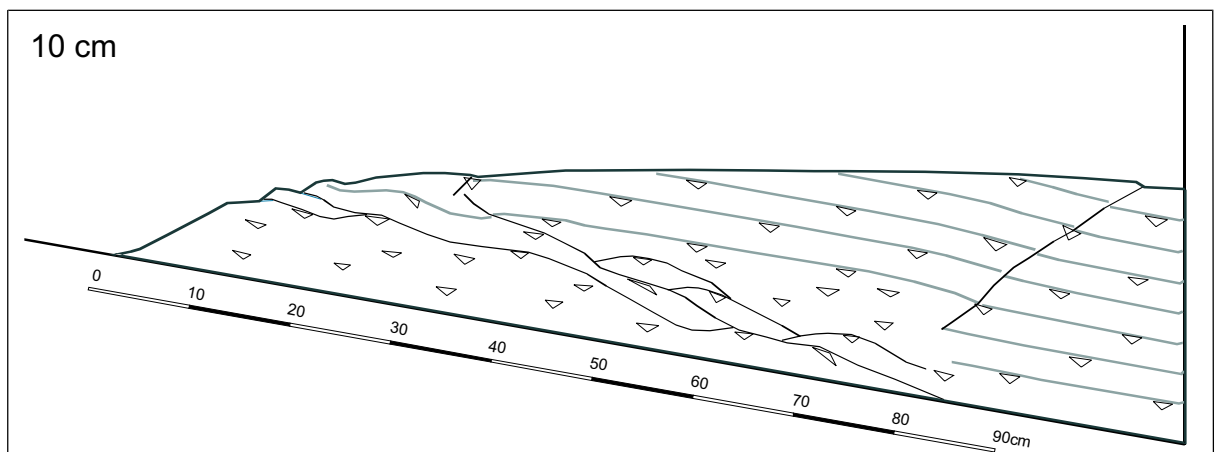
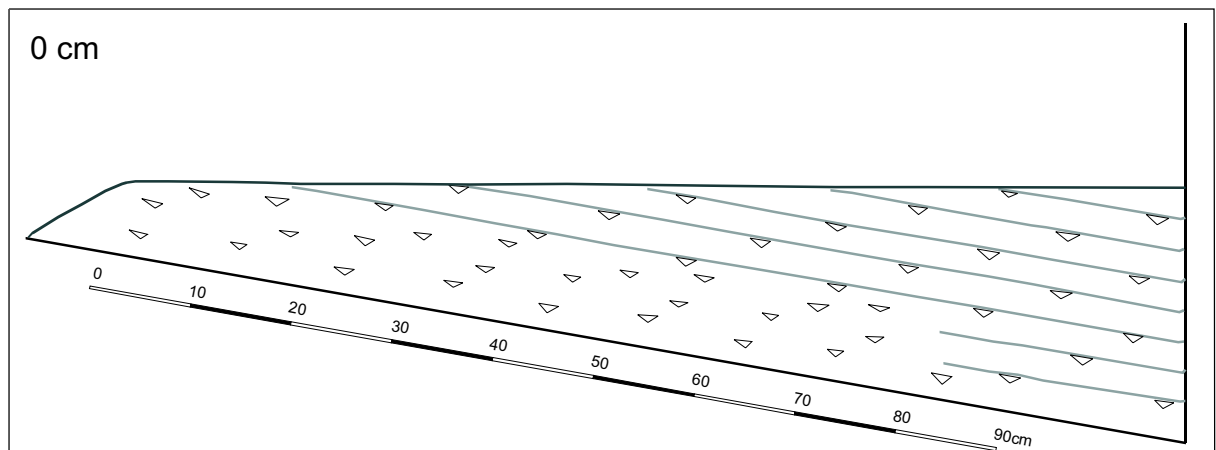
3.11 experiment

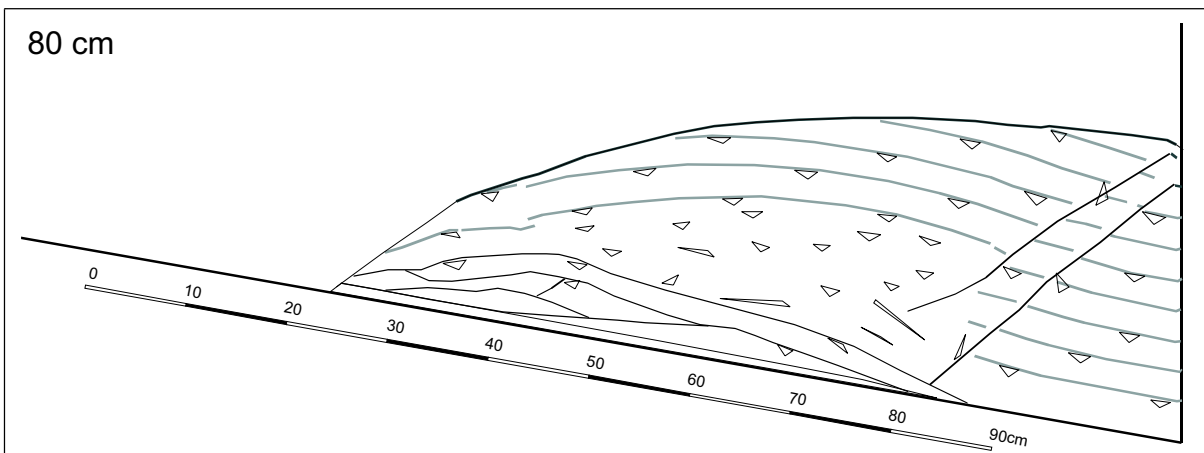
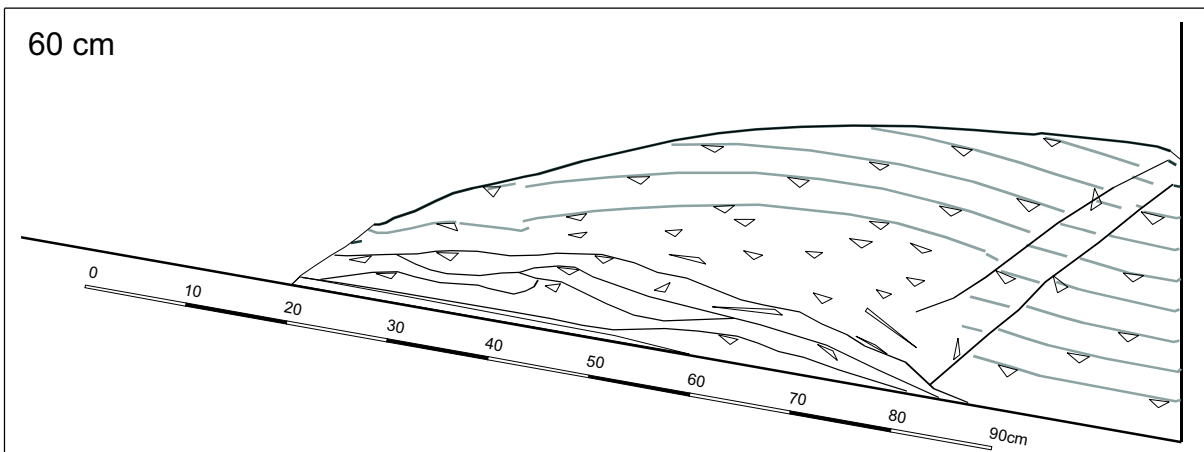
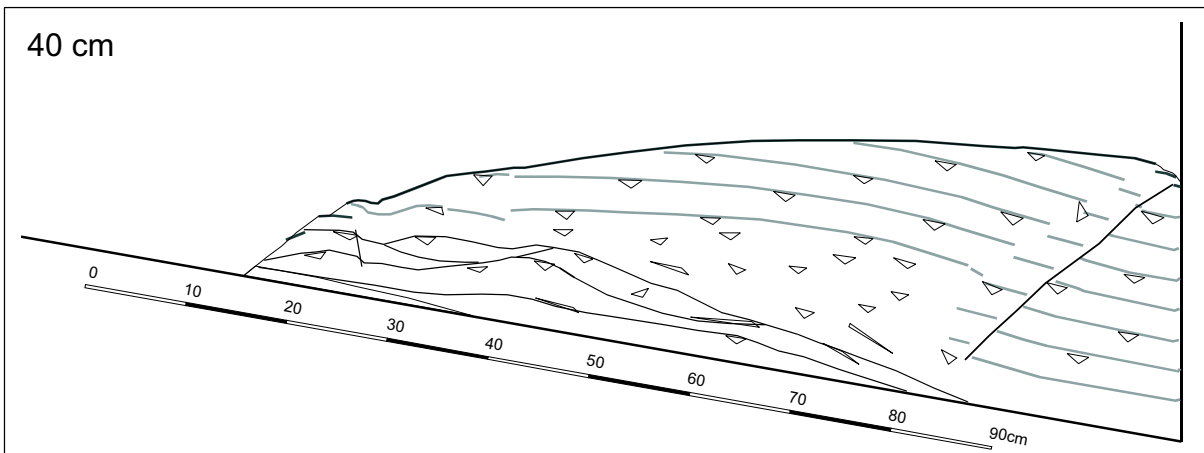
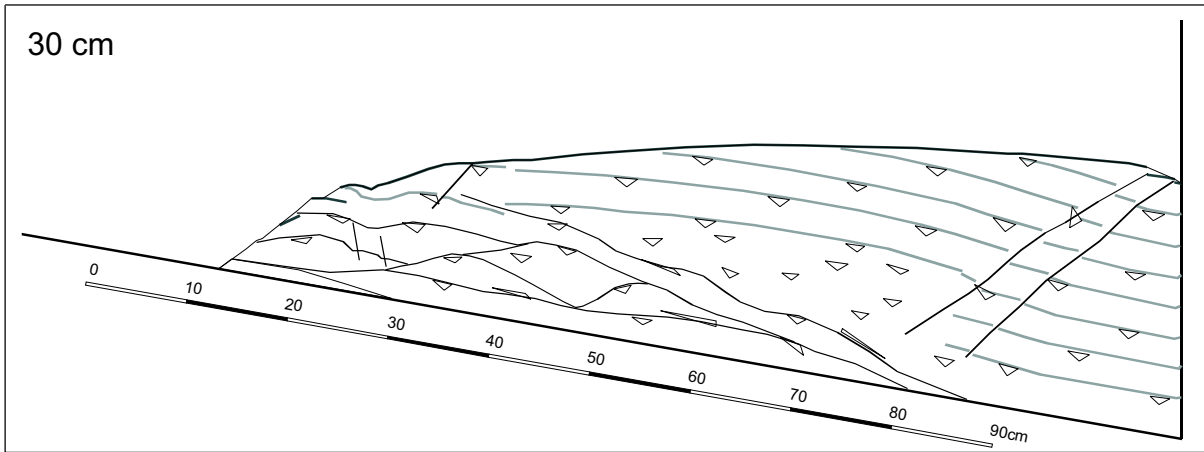


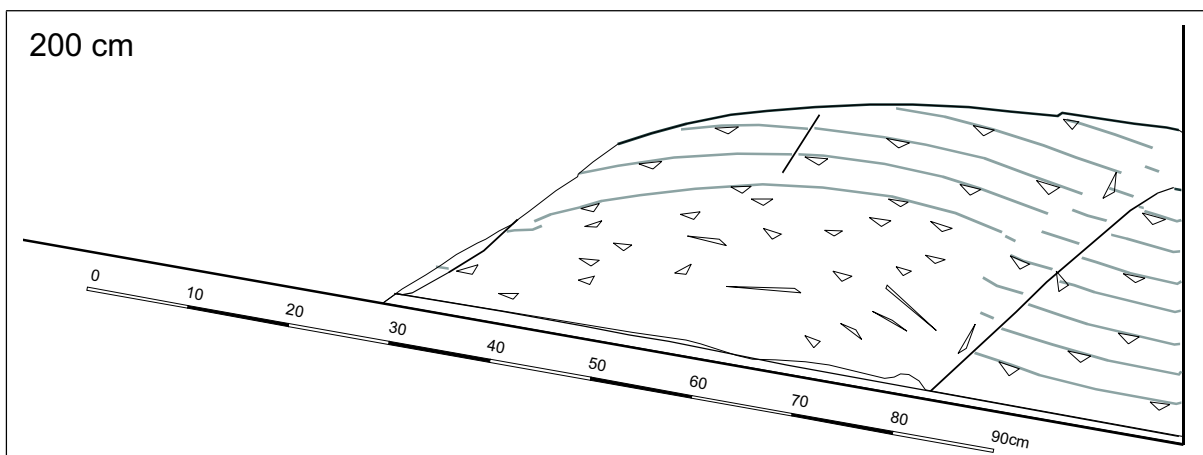
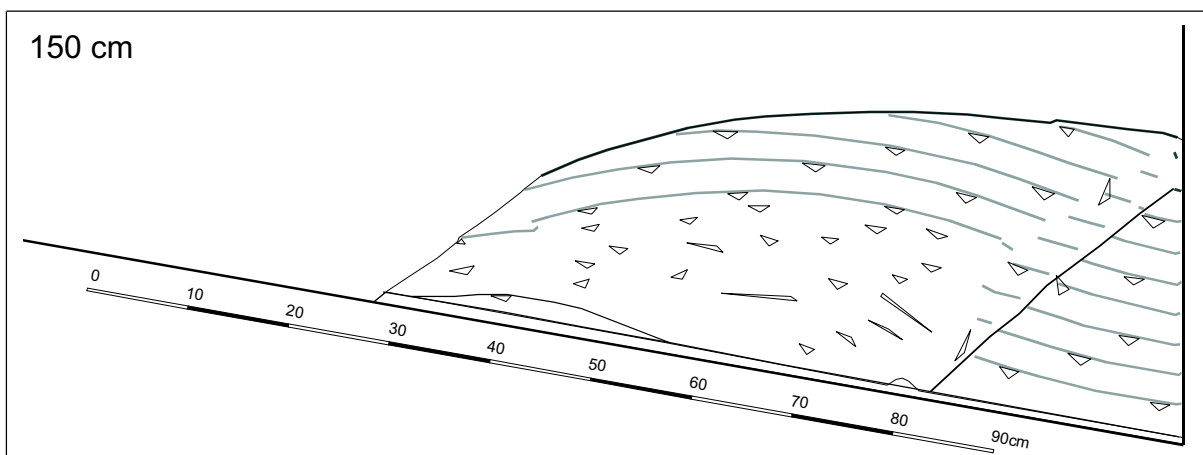
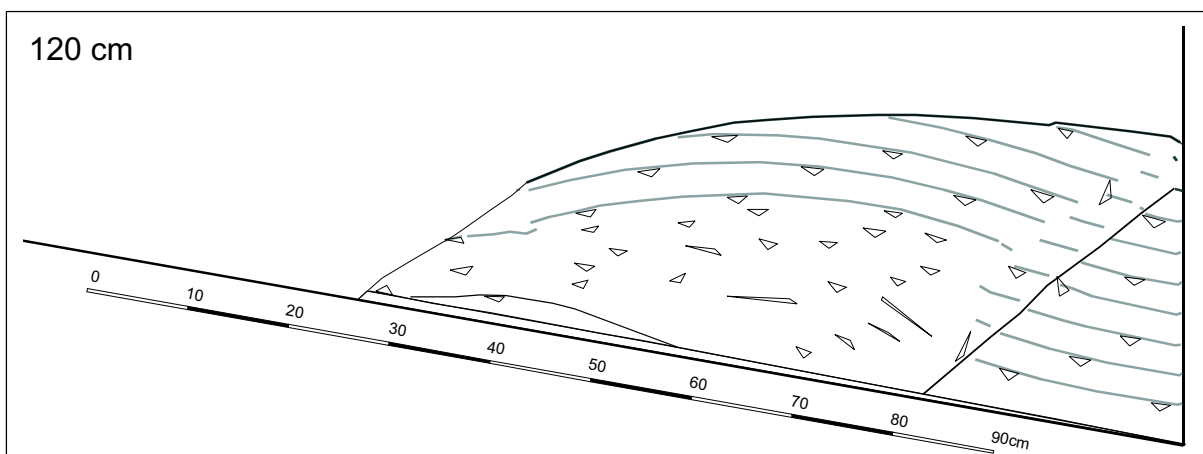
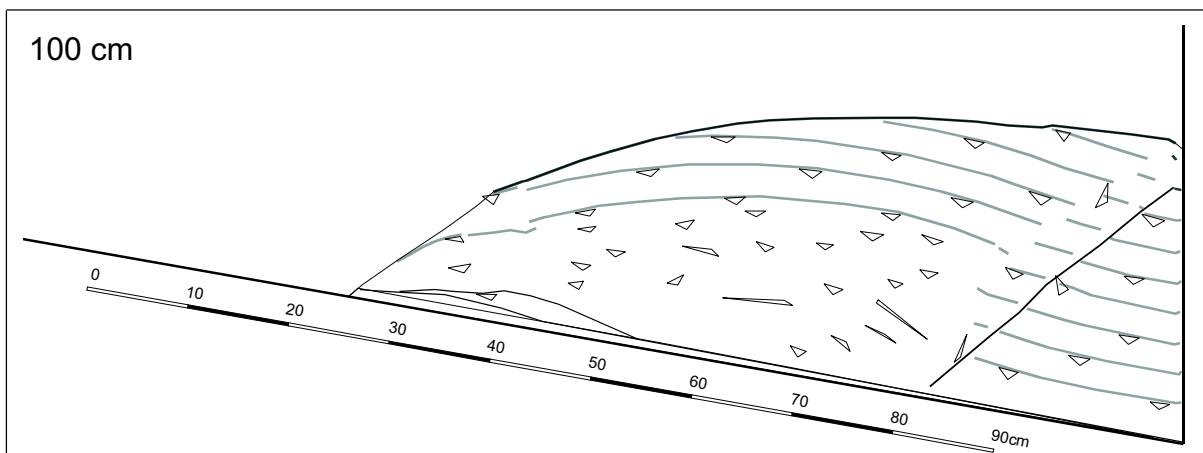
3.12 experiment

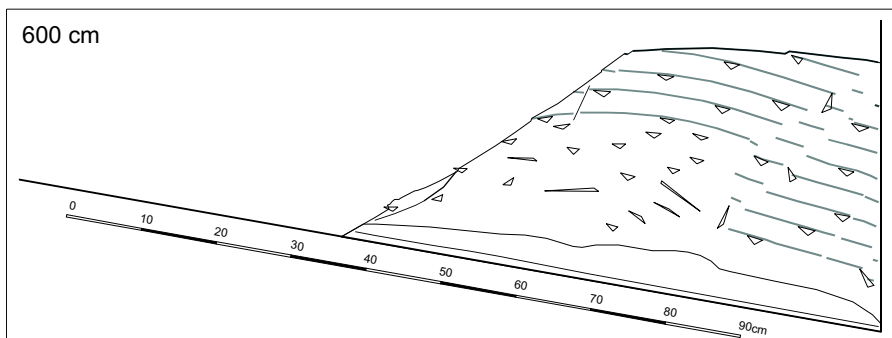
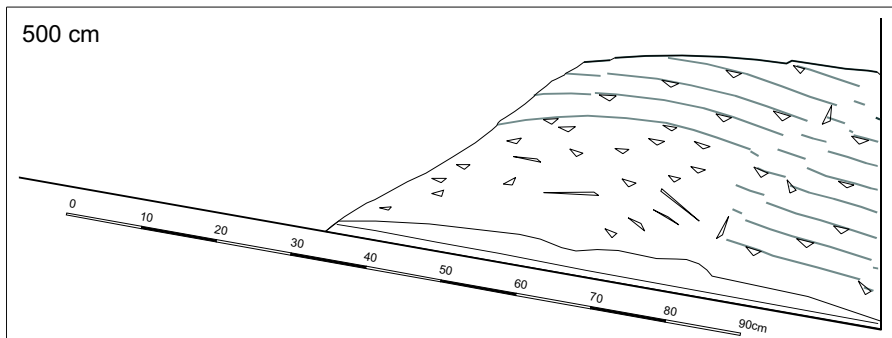
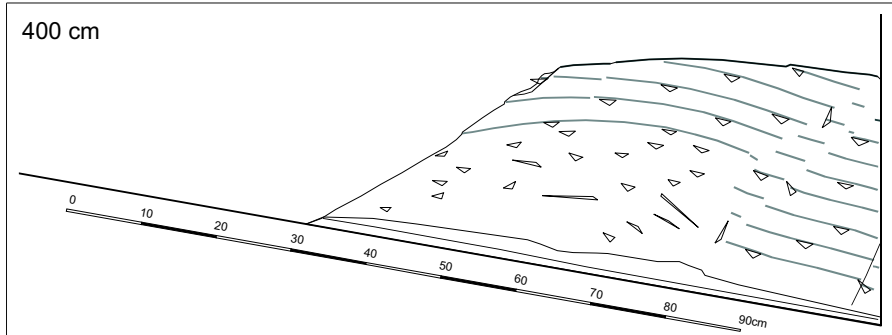
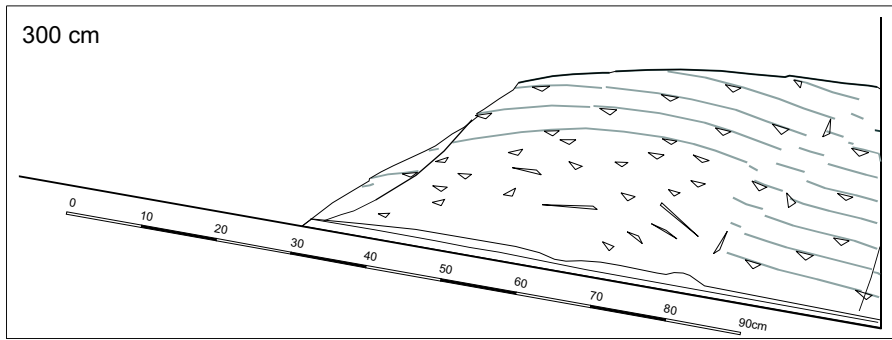


3.14 experiment

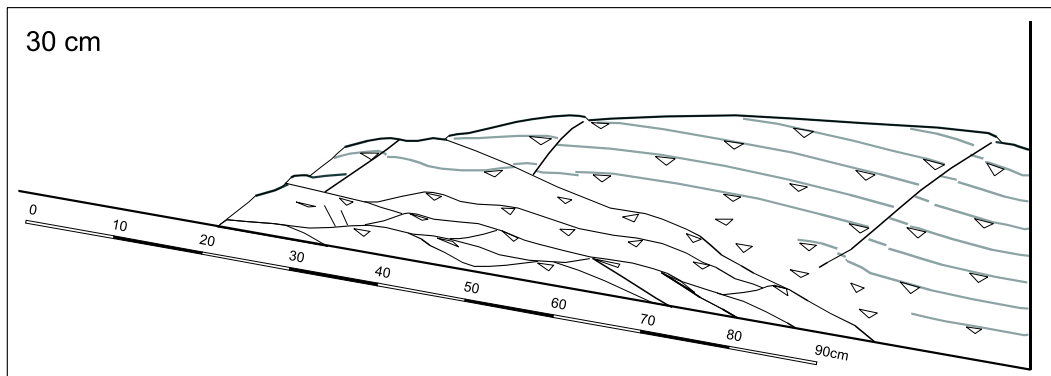
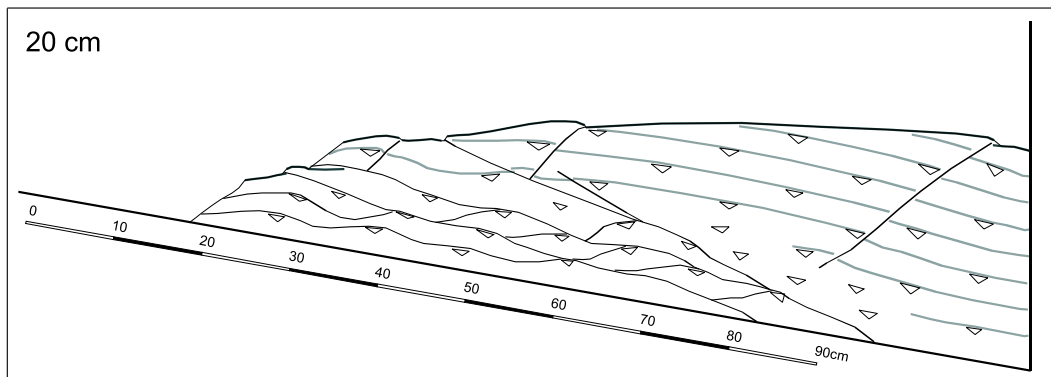
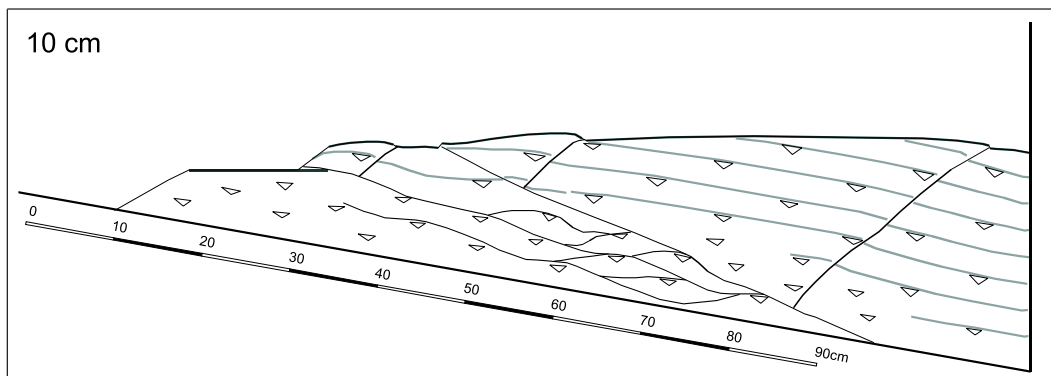
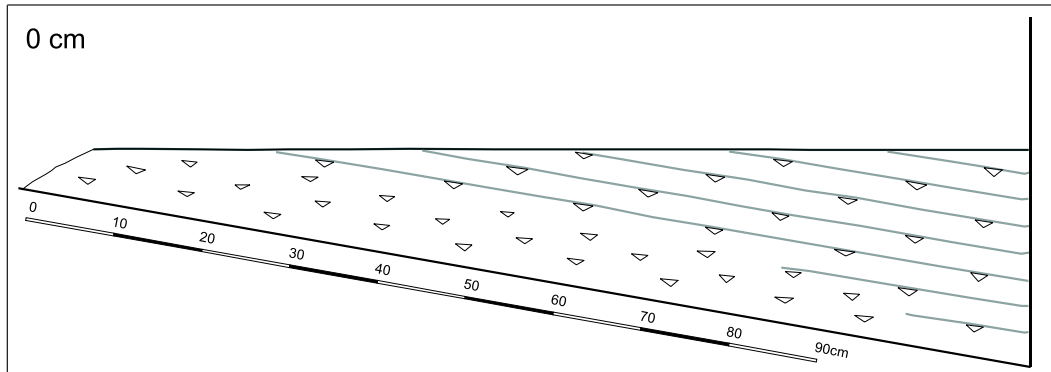


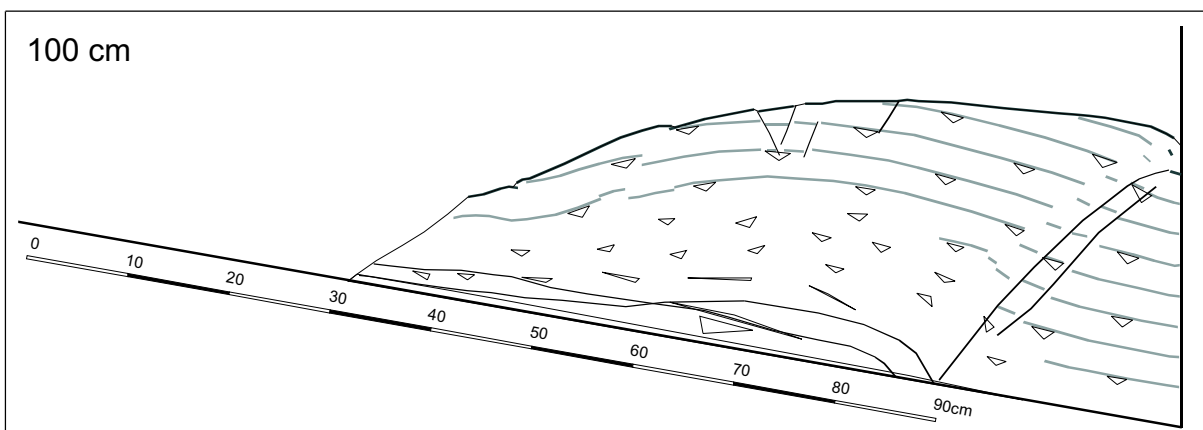
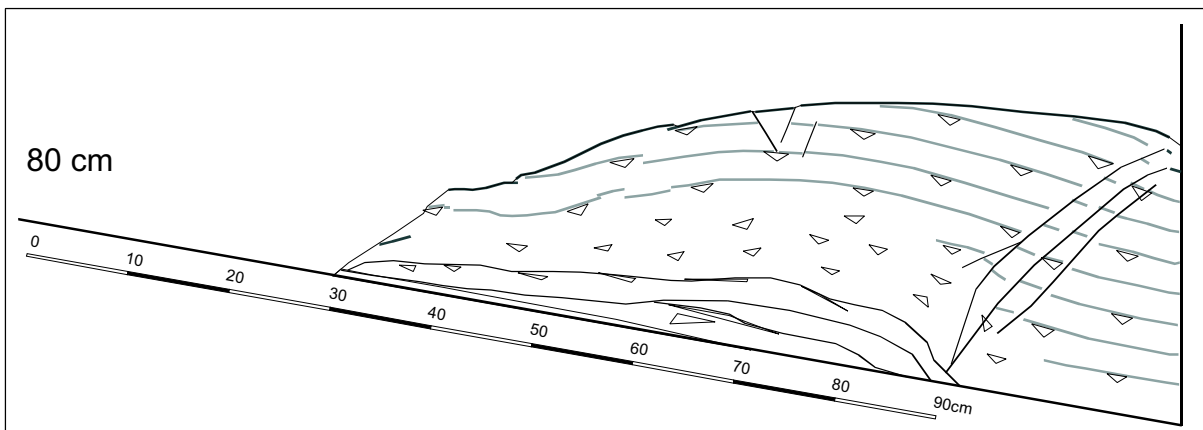
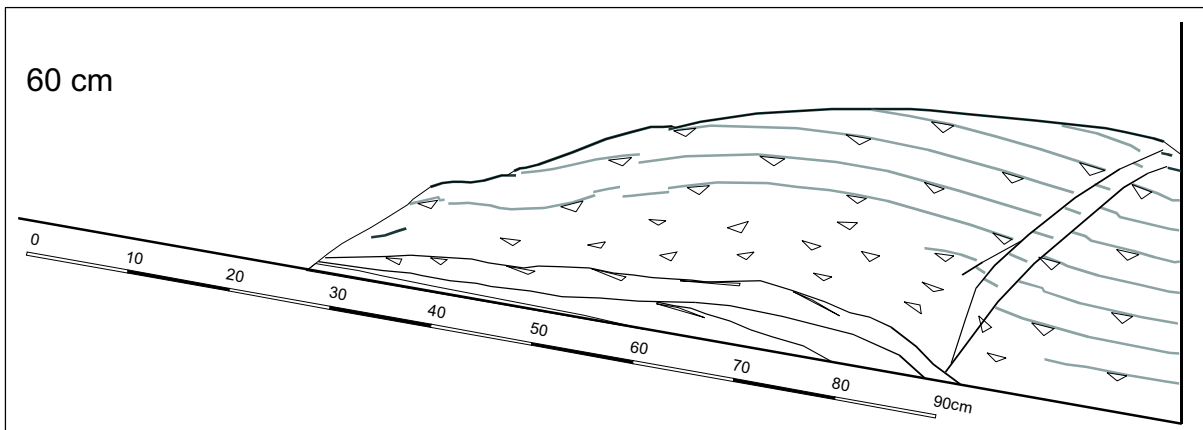
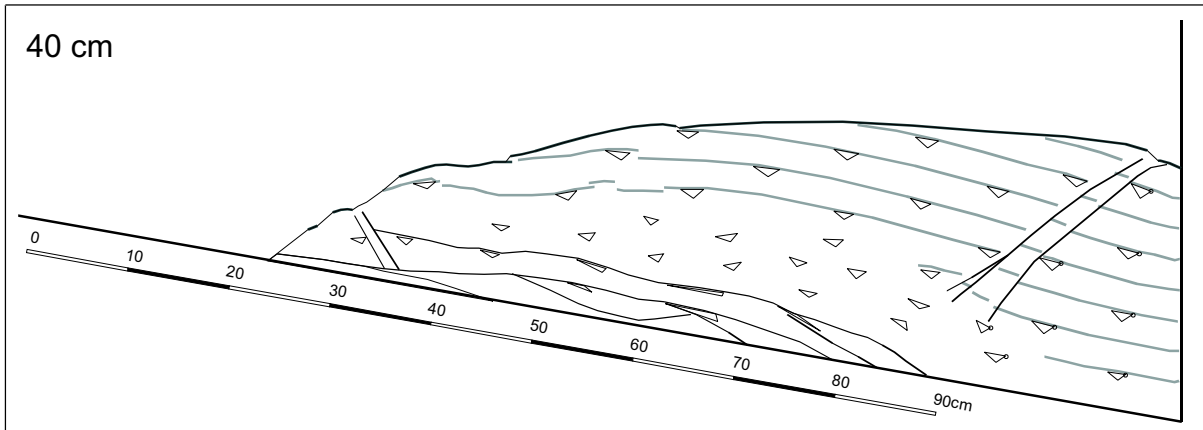


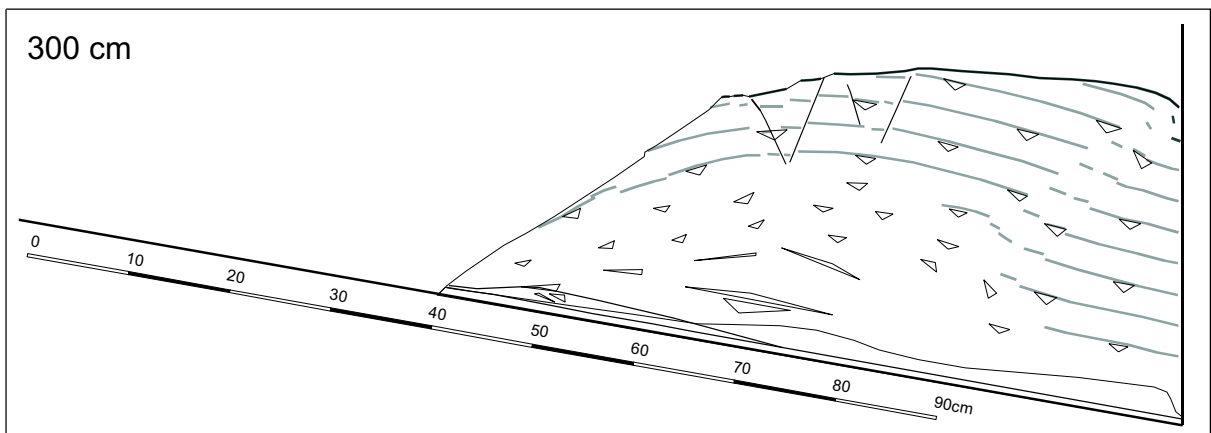
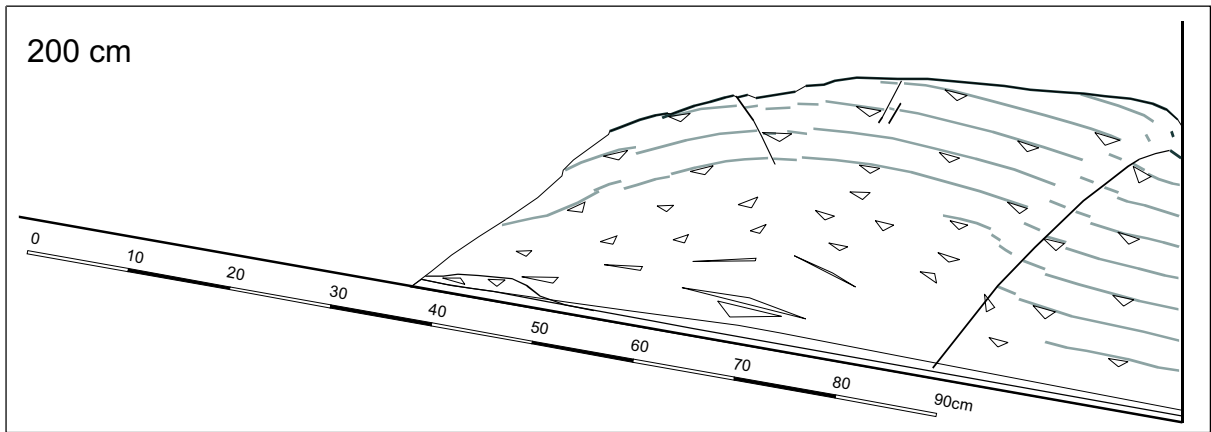
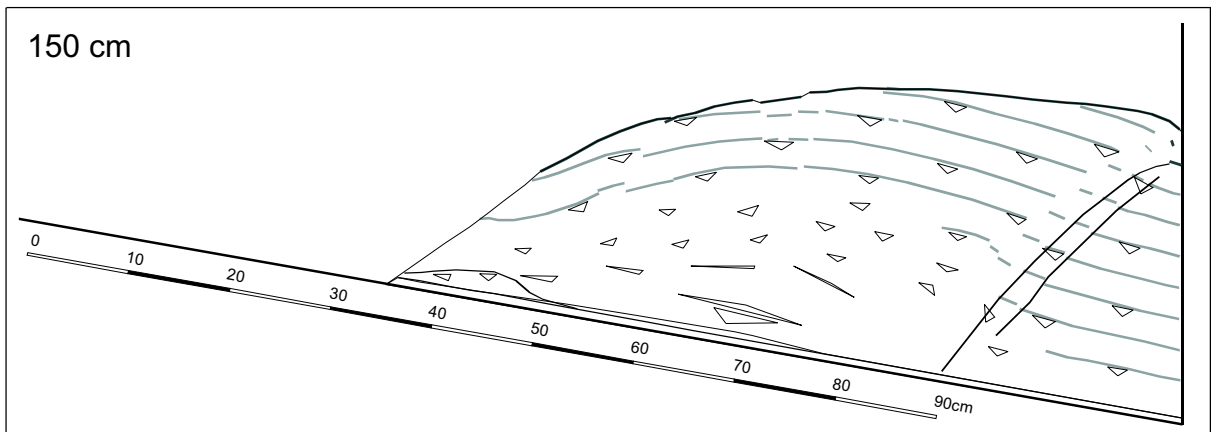
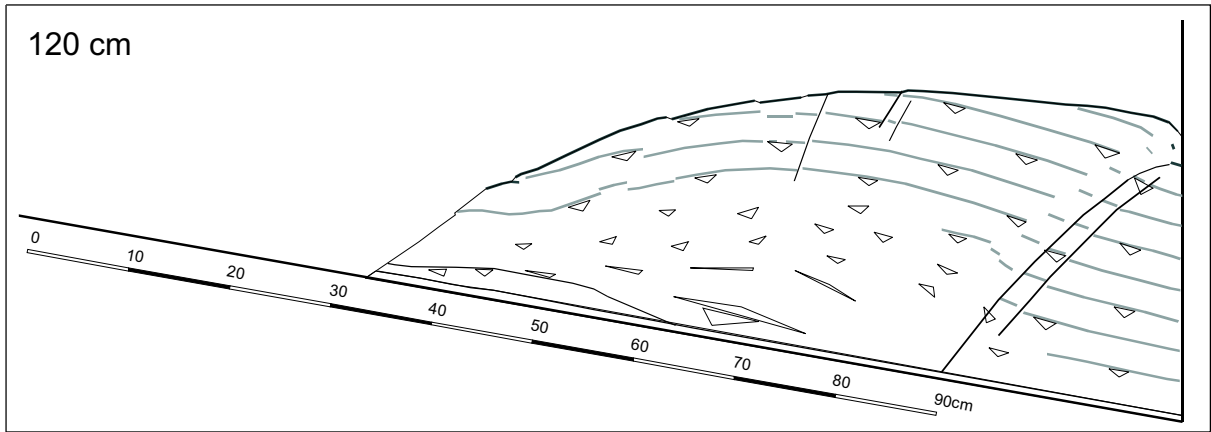


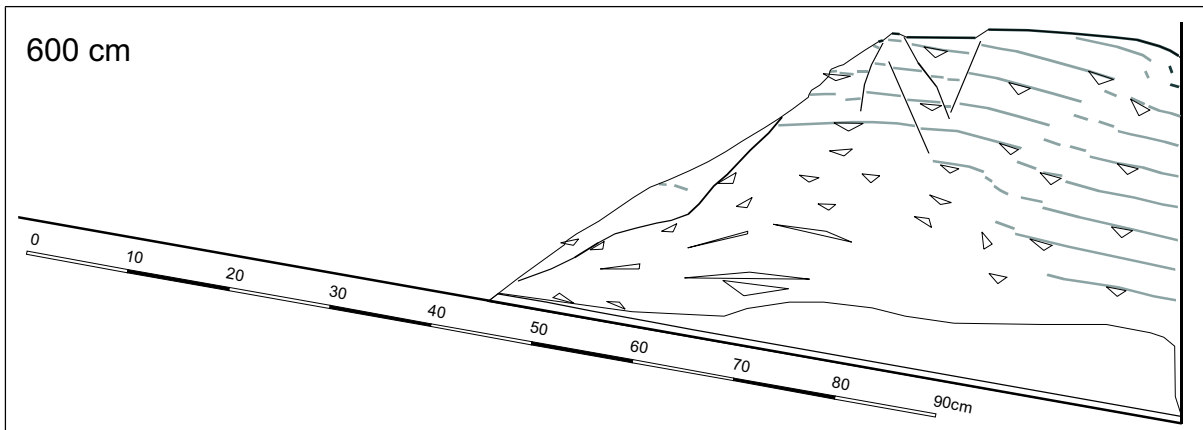
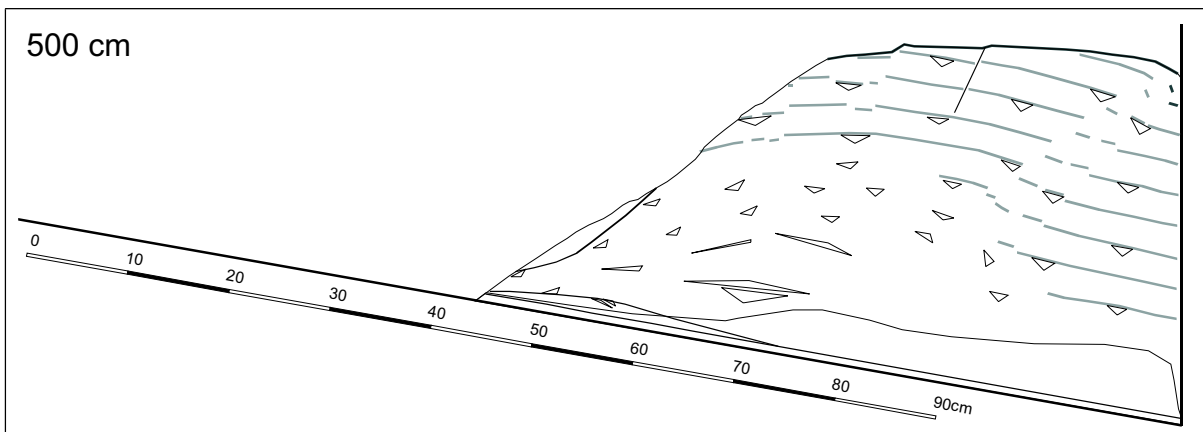
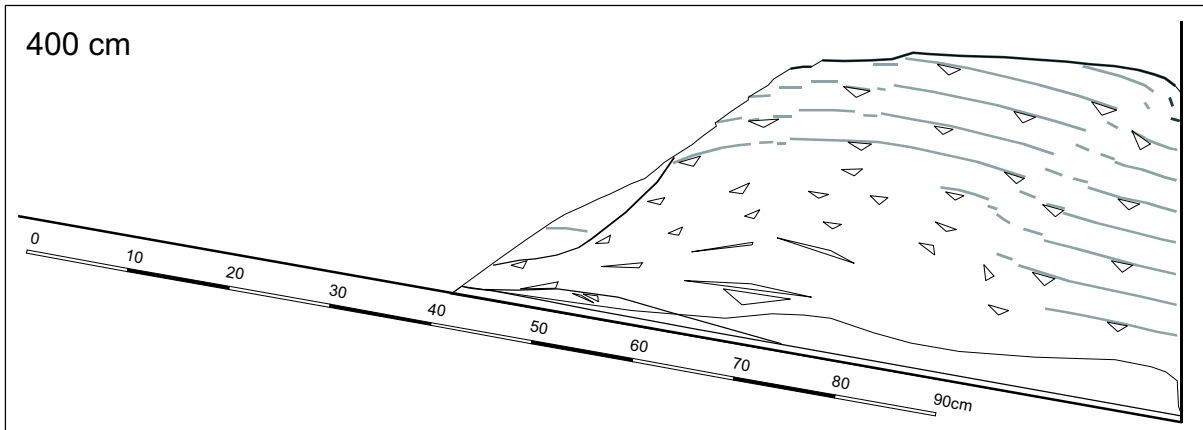


3.15 experiment









Appendix C

Zusammenfassung

Das Ziel dieser Arbeit war es, die Steuerparameter, die den Massentransfer im spröden Bereich von tektonisch erosiven und akkretiven *Forearc*-Keilen kontrollieren, zu identifizieren und zu quantifizieren. Skalierte Analogsimulationen, die speziell für diese Fragestellung ausgelegt waren, wurden mit dem konvergenten chilenischen Plattenrand verglichen, da hier beide dieser Massentransfermodi auftreten. Für Analogsimulationen geodynamischer Prozesse müssen granulare Materialien (z.B. Sand) verwendet werden, deren Deformationsverhalten dem von typischen krustalen Gesteinen entspricht. Daher wurde eine Parameterstudie durchgeführt, die Erkenntnisse zur generellen Mechanik von idealisierten konvergenten Sandkeilen lieferte.

Mit statischen und dynamischen Schertests wurde die Festigkeit verschiedener Sande gemessen. Die analysierten Sande zeigten ein reibungsabhängiges elastisch-plastisches Deformationsverhalten, welches durch eine transiente *strain-hardening* und *strain-softening* Phase vor dem Erreichen des stabilen Gleitens gekennzeichnet ist. Dieses komplexe Materialverhalten ist vergleichbar mit dem natürlicher Gesteine, auch wenn es im Widerspruch zu der Annahme eines ideal kohäsionslosen Coulombmaterials mit konstanten Reibungseigenschaften steht. Das Verhalten von Coulombmaterialien wird in üblichen Interpretationen der Mechanik von konvergenten *Forearc*-Keilen, Falten-Überschiebungsgürteln und Orogenen verwendet. Der Einfluß der transienten Materialeigenschaften auf die Kinematik, den Wachstumsmechanismus und die interne Deformation von konvergenten Sandkeilen erzeugte in den Experimenten dieser Arbeit charakteristische Keilsegmente: die frontale Deformationszone an der Keilspitze, die frontale Imbrikationszone im Zentrum des Keils und die interne Akkumulationszone im hinteren Keil. Abhängig vom Kompaktionsgrad des Materials variierte die Segmentierung von gut definierten Keilsegmenten zu einer konvexen Keiltopografie. Es wurde eine neue Strategie der *critical-taper* Analyse, die auf die einzelnen Keilsegmente beschränkt ist und das komplexe Materialverhalten berücksichtigt, entwickelt. Diese Analyse der konvergenten Sandkeile zeigte, daß die meisten Sande nur ein Segment (frontale Imbrikationszone) mit kritischem Keilwinkel ausbilden konnten. Der Keilwinkel und die Durchschnittsfestigkeit der Keilsegmente wurden bei der Materialaddition durch die Festigkeit der aktiven Störungen kontrolliert. Die keilinternen Überschiebungen rotierten während der Materialaddition in mechanisch unvorteilhafte Orientierungen und riefen damit einen Anstieg der Durchschnittsfestigkeit im hinteren Bereich der Keile hervor, so daß die Segmentierung der Keile entstehen konnte.

Auf der Basis dieser Parameterstudie wurden der Massentransfer der tektonischen Erosion am nordchilenischen und der der Sedimentakkretion am südchilenischen Kontinentalrand untersucht. Dazu wurden unterschiedliche Szenarien dieser Massentransfermodi durch systematische Parametervariation simuliert, deren Schwerpunkt auf der Veränderung folgender Parameter lag: Menge des zugeführten Materials, Anwesenheit von mechanisch weichen Lagen als potenzielle Abscherhorizonte, Festigkeit und Oberflächenrauigkeit der Plattengrenzfläche sowie die Transportkapazität des 'Subduktionskanals'. Letztere ist durch die Inletkapazität (d.h. die Menge Material, die unter dem Keil unterschoben werden kann) und die Globalkapazität (d.h. die Menge Material, die in größere Tiefen subduziert werden kann) bestimmt. Die Experimente wurden in Hinsicht auf die Störungs kinematik, die Keilgeometrie, das Partikelverschiebungsfeld, das Subsidenzmuster und die Massentransferraten analysiert. Diese Merkmale der

konvergenten Sandkeile wurden dann mit den entsprechenden Merkmalen des nord- und südchilenischen *Forearcs* verglichen und mögliche Szenarien für die Massentransfermodi dieser Naturbeispiele entworfen. Dieser Vergleich verband die Beobachtungen aus der Natur mit den experimentellen Untersuchungen und erlaubte somit die Identifizierung der Steuerparameter der in der Natur beobachteten Massentransfermodi.

Interpretationen reflektionsseismischer Profile und Oberflächengeologie zeigen, daß die Sedimente, die auf der ozeanischen Platte dem südchilenischen *Forearc* zugeführt werden, zum einen Teil frontal akkretiert und zum anderen Teil unter den *Forearc*-Keil unterschoben und vielleicht unterhalb der Küstenkordilliere basal akkretiert werden. Dieser Massentransfermodus wurde experimentell in einem Versuchsaufbau simuliert, in welchem eine Sandschicht auf einem hochreibenden basalen Förderband einem Sandkeil zugeführt wurde und Entkopplung an einem weichen Horizont innerhalb der zugeführten Schicht stattfand. Dieser komplexe Modus der Sedimentakkretion erzeugte, ähnlich wie die frontal akkretierenden Sandkeile der Parameterstudie, kinematisch segmentierte konvergente Keile. Die basale Akkretion erzeugte Hebung, Verbiegen und horizontale Extension in dem überlagernden Keilsegment. Gleichzeitige Hebung, Verkippung und oberflächennahe Extension sind daher die Indikatoren für diesen basalen Massentransferprozeß. Diese kinematischen Merkmale kennzeichnen auch den südchilenischen *Forearc*, so daß die anfängliche, auf Geländedaten basierende Vermutung, daß basale Akkretion unterhalb der Küstenkordilliere stattfindet, durch die experimentellen Untersuchungen bestätigt wurde. Allerdings zeigt der Vergleich von der Massenbilanz in der Natur und den Experimenten, daß nur ein kleiner Anteil der unterschobenen Sedimente am südchilenischen *Forearc* auch basal akkretiert und der Hauptanteil in größere Tiefen subduziert wird.

Die *critical-taper* Analyse der komplex akkretionierenden Sandkeile zeigte, daß sich kein Keilsegment im kritischen Spannungszustand befand. Die Keilsegmente, die durch frontale Akkretion gebildet wurden, wurden aufgrund der Veränderung von Keileigenschaften durch Störungsrotation, der Ausbildung des basalen Abscherhorizontes in unterschiedlichen Materialien auf verschiedenen Niveaus und dem Verkippfen gesamter Segmente im stabilen Spannungszustand gehalten. Das Keilsegment, welches durch basale Akkretion gebildet wurde, war während des gesamten Experimentablaufs im subkritischen Spannungszustand, da seine Anpassung an den kritischen Spannungszustand durch den kontinuierlichen Anstieg der Normallast durch Materialzufuhr zum überlagernden, frontal akkretierenden Keilsegment verhindert wurde.

Steady-state tektonische Erosion, wie sie am nordchilenischen *Forearc* beobachtet wird, entstand in Analogexperimenten nur, wenn der Sandkeil auf einem hochreibenden basalen Förderband plazierte war und ihm kein Material zugeführt wurde. In diesen Experimenten wurden vier Massentransferprozesse identifiziert: i) frontale Erosion, ii) basale Erosion, iii) Unterschiebung und iv) basale Akkretion des vorher erodierten Materials. Diese Massentransferprozesse erfordern die Ausbildung einer mächtigen basalen Scherzone mit einer besonderen Kinematik. Im unteren Bereich dieser Scherzone wird frontal und basal erodiertes Material kontinuierlich unter penetrativer Zerschering unterschoben, wohingegen im oberen Bereich der Scherzone das Keilmaterial entlang von reaktivierten, lokalisierten Scherzonen von der Keilbasis entfernt wird (basale Erosion). Die frontale Erosion erzeugte Subsidenz durch keilinterne Extension eines Gravitationskollapses, welcher auch am nordchilenischen Kontinentalrand identifiziert wurde. Diese Subsidenz überprägte solche Subsidenz- und Hebungssignale, welche durch die basale Erosion und Akkretion hervorgerufen wurden. Daher ist eine kinematische Segmentierung, wie sie in den akkretiven Sandkeilen festgestellt wurde, in den tektonisch erosiven nicht vorhanden, so daß hier die einzelnen basalen Massentransferprozesse nicht anhand von Oberflächeninformationen identifiziert werden konnten. Die exakte Position der basalen Erosion am nordchilenischen *Forearc* kann somit nicht rekonstruiert werden, obwohl eindeutige Hinweise auf basale Erosion in den geophysikalischen und geologischen Daten dieses *Forearcs* vorliegen.

Die Analyse der Analogexperimente zeigte, daß die Raten der basalen Erosion stark von den physikalischen Eigenschaften des Keilmaterials abhängen. Die basale Materialabfuhr wird nur ermöglicht, wenn bestimmte Festigkeitsverhältnisse innerhalb der basalen Scherzone ($\chi_L > 1$) und dem darüberliegenden Keilmaterial ($\chi_U \approx 0.94$) erreicht werden. Da schon geringfügige Veränderungen in der Festigkeit dieser Materialien die basale Erosion verhindern würden, wird vermutet, daß basale Erosion in der Natur ein sehr anfälliger Prozeß ist. Daher treten in der Natur die erforderlichen Bedingungen wahrscheinlich eher

kurzfristig und in häufigen Wiederholungen auf, als daß sie kontinuierlich vorhanden sind. Ein plausibler Prozeß welcher diese speziellen Bedingungen hervorrufen kann, ist die Variation des Porendrucks während der postseismischen Phasen von Subduktionsbeben.

Innerhalb der großen Bandbreite von Massentransfermodi, die an konvergenten Plattenrändern auftreten, sind die untersuchten Massentransfermodi am nord- und südchilenischen *Forearc* nur zwei Beispiele und werden als repräsentativ für andere *Forearc*-Systeme, die einen vergleichbaren Modus zeigen, gesehen. Daher konnten die experimentellen Ergebnisse dieser Arbeit dazu genutzt werden, die Steuerparameter, die den Massentransfer an konvergenten Plattenrändern kontrollieren, und ihren Einfluß auf die *Forearc*-Entwicklung, im allgemeinen Zusammenhang zu untersuchen. Das Verhältnis zwischen der Inlet- und der Globalkapazität (IC/GC-Verhältnis) spielt in der Hierarchie dieser Steuerparameter die entscheidende Rolle. Die Zuordnung des nord- und südchilenischen *Forearcs* zu der in dieser Arbeit entwickelten Systematik zeigt, daß der Unterschied in ihren Massentransfermodi durch Unterschiede im IC/GC-Verhältnis und in den Mengen an zugeführten Sedimenten hervorgerufen wird. Diese Zuordnung zeigt, daß die Systematik der Steuerparameter dazu genutzt werden kann, die IC/GC-Verhältnisse von *Forearc*-Systemen durch die Identifikation und den Vergleich von mehreren Merkmalen der Massentransferprozesse, Massentransferraten, Kinematik und Keilgeometrie in der Natur und den Experimenten eindeutig zu bestimmen.

Appendix D

Lebenslauf

persönliche Daten

Geburtstag: 11.05.1969
Geburtsort: Schöttmar jetzt Bad Salzuflen
Staatsangehörigkeit: deutsch

Ausbildung

1988 allgemeine Hochschulreife
1988–1993 Studium der Freien Kunst an der Hochschule für Bildende Künste Hamburg bei Sigmar Polke und Stanley Brown
1993 Diplom der Freien Kunst, *Auswendiges Zeichnen der Verzeichnisse zum Budapester Staub*
1993–1999 Studium der Geologie und Paläontologie an der Universität Hamburg
1995–1999 Stipendiatin der Heinrich-Böll-Stiftung
1999 Diplom der Geologie-Paläontologie, Thema: *Kinematische Entwicklung des Leonforte-Agira thrust-top Beckens (E-Sizilien)*
1999–2002 Promotionsstelle am GeoForschungsZentrum Potsdam im Projektbereich *Struktur, räumlich-zeitliche Evolution und Geodynamik*
2002 Promotion an der Freien Universität Berlin